esa

SP-381

GEN87

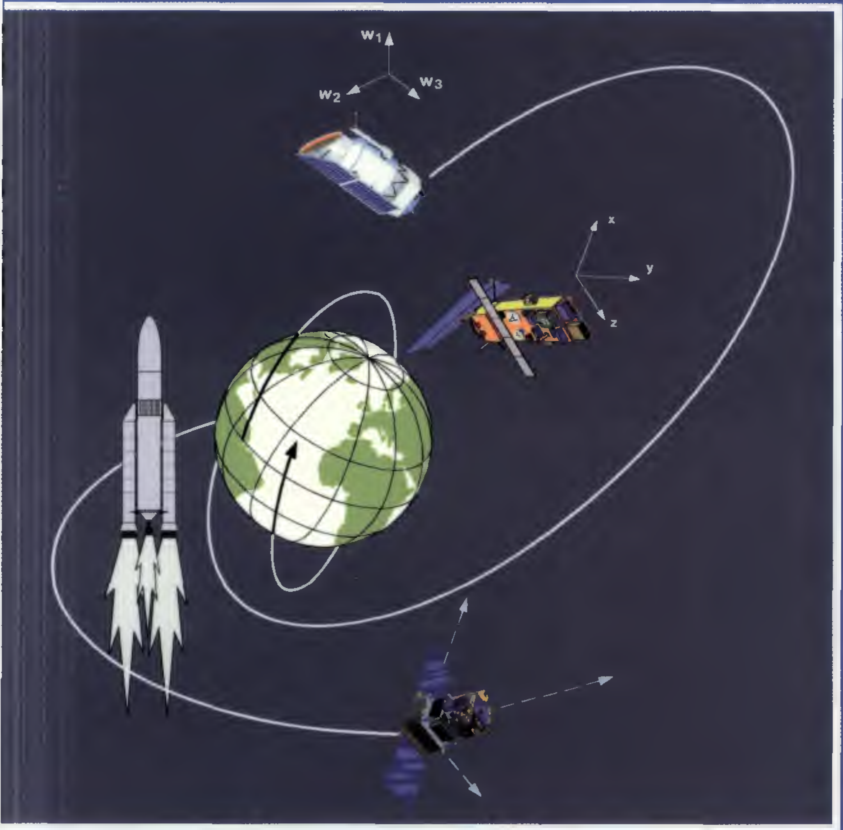

Third ESA International
Conference on

Spacecraft Guidance, Navigation and Control Systems

26-29 November 1996
ESTEC, Noordwijk, The Netherlands

European Space Agency
Agence spatiale européenne

SP-381
February 1997

3rd ESA INTERNATIONAL CONFERENCE ON SPACECRAFT GUIDANCE, NAVIGATION AND CONTROL SYSTEMS

and

Tutorial on Microsats: Design, Development and Execution of Minimum Missions

26-29 November 1996
ESTEC, Noordwijk, The Netherlands

European Space Agency
Agence spatiale européenne

PROGRAMME COMMITTEE

D.N. Soo	ESA/ESTEC (Chairman)
M. Weinberger	ESA/ESTEC
D. Wilson	ESA/ESTEC
W. Fehse	ESA/ESTEC
Ph. Marchal	CNES, France
Th. Lange	DLR, Germany
K. Ninomiya	ISAS, Japan
B. Suresh	ISRO, India
F. Tolivar	NASA/JPL, USA
C. Arduini	CRA, Italy
Z.H. Zhou	BICE, China
L. Virdee	Intelsat, USA
M. Huddleston	DRA, UK
W. McMath	CSA, Canada

LOCAL ORGANISING COMMITTEE

R. Creasey
P. Brazzale
R. Guerrand
G. Elfering
B. Kaldeich-Schürmann, ESA Editor

Published by: *ESA Publications Division*
ESTEC, Noordwijk, The Netherlands

Compiled by: *Brigitte Kaldeich-Schürmann*

Price: *Dfl 100.00*

ISBN: *92-9092-207-9*

© *1997 European Space Agency*

Autonomous Attitude Determination from Stars 295
I. Barraco & F. Donati

The Advanced Stellar Compass onboard the Oersted Satellite 303
J.L. Joergensen, C.C. Liebe, A. Eisenmann & G.B. Jensen

SESSION 11: GPS ANALYSIS

Chairman: F. Sarti, ESA/ESTEC

The GPS Tensor^{TM} Receiver Development 311
L. Marradi & D. Fossati

Multipath Rejection and Attitude Determination Using GPS Experiment 321
M. Sghedoni & D. Guichon

A Visibility-Based Algorithm for the GPS Initial Integer Ambiguity Problem 327
A. Pasetti, P. Colmenarejo & F. Gottifredi

SESSION 12: LAUNCHERS

Chairman: D. Paris, ESA/ESTEC

Guidance and Control System for J-I Launch Vehicle 337
H. Suzuki, W. Kobayashi, Y. Suzuki & K. Ayabe

Reliability of Launcher Control System 343
V.V. Malyshev, V.T. Bobronnikov, K.A. Karp et al.

H_∞ Method Applied to Launcher Control During Atmospheric Flight 349
S. Mauffrey, F. Chabert & M. Schoeller

Hardware-in-Loop Simulation of Brazilian Launcher VLS 355
W. De Castro Leite Filho & D. Salvio Carrijo

SESSION 13: MISSIONS II

Chairman: L. Virdee, Intelsat, USA

Galaxy III-R Transfer Orbit Attitude Control 361
J. Salvatore, M. Barsky & R. Quartararo

ODIN Attitude Control System — Design, Development and Test 367
O. Jirlow, A. Ptak & R. Augustsson

Attitude and Orbit Control System for an Infrared Imaging Surveyor 373
K. Ninomiya, T. Hashimoto & H. Iida

Tethered Satellite System Reflight Mission Attitude Dynamics and Control: On-Flight Results 379
B. Musetti, B. Cibrario & P. Martella

SESSION 4: RVD

Chairman: W. Fehse, ESA/ESTEC

ATV GNC During Rendezvous 85
J. Fabrega, M. Frezet & J.-L. Gonnaud

ARPK Design and GNC Performance Evaluation for ATV-Rendezvous 95
J.L. Gonnaud, J. Sommer & M. Tsang

Rendezvous Strategy of the Japanese Logistics Support Vehicle to the International Space Station 103
K. Yamanaka

Remote Intervention in Automatic Onboard GNC Systems 109
A. Vankov, A. Alyoshin, P. Chliaev et al.

SESSION 5: MISSIONS 1

Chairman: F. Tolivar, JPL,USA

The Design and Development of the Attitude and Orbit Control Systems for the XMM and INTEGRAL Scientific Spacecraft 121
D. Jukes & D.H. Parker

The GNC&C Design of the New Earth-Observing System Common Spacecraft 127
T.P. Nosek

Attitude and Orbit Control System for Multimission Spacecraft Platform 133
M. Sghedoni, J.L. Beaupellet, J. Busseuil & F. Douillet

Attitude and Orbit-Control System Design for X-Ray Astrophysics Space Observatory ASTRO-E 141
K. Ninomiya, T. Hashimoto, K. Maeda et al.

SESSION 6: RE-ENTRY

Chairman: S. Strandmoe ESA/ESTEC

Navigation, Guidance and Control of the Atmospheric Re-entry Demonstrator 149
G. Pigné, Ph. Clar, E. Ferreira et al.

Re-entry and Aeroassisted Transfer Trajectory Optimal Control: the Gradient Restoration Algorithm 163
M. Belló Mora & G. Dutruel-Lecohier

Analysis of a CTV Re-entry Navigation Concept 175
H. Malthan, J.M. Fraile Ordónez & M. Krischke

Parafoil Technology Demonstrator OBC Development: A Successful Exercise in Timely and Low-Cost Development 183
P.H. van Rossem, P.G. Beerthuizen, J.B. Geerdes et al.

CONTENTS

SESSION 1: IN-ORBIT RESULTS

Chairman: D. Wilson, ESA/ESTEC

ISO AOCS In-Flight Experience — The Exceptional Story of how Everything Turned out Better than Expected 3
M.J.A. van Oort, P. Van Hulzen, P. Lammertse, W. Van Leeuwen, M.E. Houck, J. Busseuil, P. Scott & M. Buemi

Life Test, In-Orbit Operations and Further Development of the Type 125 Gyroscope 9
D. Reid & P. Scott

SAX AOCS Design and In-Flight Experiences 17
F.H. van der Laan, L. Karsten, S. Kampen, E.A. Silkens et al.

Attitude Control System Experiment on Engineering Test Satellite-VI 31
T. Sekiguchi, S. Ishikawa, M. Kudo, et al.

The Use of Magnetic Field Data to Estimate Attitude and Trajectory for the Rossi X-Ray Timing Explorer (RXTE) 37
J. Deutschmann & I. Bar-Itzhack

SESSION 2: STAR SENSOR DESIGN

Chairman: P. Underwood, ESA/ESTEC

Further Evaluation of an Autonomous CCD Star Tracker by the Monte Carlo Method 45
J.B. Crowden & D.M. Priestley (presented by P. Cope)

Intelligent Modular Star and Target Tracker: A New Generation of Attitude Sensors 53
U. Schmidt, D. Wunder & E. Graf

SESSION 3: GPS Systems Aspects

Chairman: P. Silvestrin, ESA/ESTEC

MOMSNAV: First Analysis of GPS Flight Data from Space Station MIR 61
S. Föckersperger, J.M. Fraile-Ordónez, O. Montenbruck & E. Gill

A GPS-Based Orbit Positioning System for the European Archimedes Mission 67
J. Potti, M. Bello & A. Pasetti

Relative GPS Navigation Design and Validation for ATV Rendez-Vous 77
H. Marcille, G. Moreau & V. Pascal

SESSION 14: LANDING AND PLANETARY MISSIONS

Chairman: M. Lang, ESA/ESTEC

Hazard Avoidance Based on Optical Sensing for Lander Missions 389
E. Zekri & F. Guettache

A Preliminary Assessment of Various Autonomous Navigation Techniques for Interplanetary Missions 395
J.B. Serrano, J. Prieto & S.E. Strandmoe

Navigation for Autonomous Landing on Unknown Planetary Surface Using Conical Laser Scanner 405
T. Kubota, I. Nakatani, T. Yamaizumi & H. Hayashida

Vision-Based GNC Design for the LEDA Mission 411
B. Frapard, C. Champetier, S. Kemble et al.

SESSION 15: HIGH ACCURACY POINTING SYSTEMS I

Chairman: Ph. Marchal, CNES, France

Towards GAIA: A Ground Demonstration of Nanoradian Sensing and Control 423
P. Cope

A Two-Stage OPD Control System for Free-Flyer Interferometry Missions 433
I. Laine, L. Vaillon, H. Lambert et al.

Digital Controllers for Attitude Manoeuvring: Experimental Results 439
S. Di Gennaro, S. Monaco, D. Normand Cyrot & A. Pignatelli

Dynoptix: A Software Tool for Dynamics and Control Analysis of Optical Systems 447
I. Laine, D. Dubet, A. Defendini & C. Champetier

SESSION 16: SMALL SATELLITES

Chairman: M. Huddleston, DRA, UK

Onboard Attitude Determination for a Small Satellite 457
T. Bak

A New Approach for CHAMP Safe Mode Attitude Control 463
H. Bauer & C. Schmitt

Passive Aerodynamic Stabilisation of Low Earth Orbit Satellite 469
T. Bak & R. Wisniewski

SESSION 17: HIGH ACCURACY POINTING SYSTEMS II

Chairman: C. Philippe, ESA/ESTEC

Test Results on the High Accuracy Optical Pointing Payload OASIS 477
J.L. Carel, J.M. Michelin, B. Groult & M. Le Du

GOMOS Dynamics and Pointing, an Innovative Concept for High-Accuracy Pointing Instruments 483
C. Lemercier, J. Dekneudt, M. Bréart de Boisanger et al.

SOHO Microvibrations: Analyses, Tests and Flight Results 489
Ph. Laurens, E. Decoux & M. Janvier

Passive and Active Microvibration Control for Very High Pointing Accuracy Space Systems 497
L. Vaillon, C. Champetier, V. Guillaud et al.

SESSION 18: CONTROL HARDWARE

Chairman: G. Coupe, ESA/ESTEC

In-Flight Experience of the Space Inertial Reference Unit Utilizing the Solid State HRG 507
G. Londerville, R. Ciolino & D. Haley

Control Moment Gyroscopes (CMG's) and their Application in Future Scientific Missions 523
X. Roser & M. Sghedoni

Intelsat VII DIRA Calibration Using an Extended Kalman Filter 529
K.V. Raman

SESSION 19: ANALYSIS II

Chairman: F. Ankersen, ESA/ESTEC

Spillover Reduction Technique for Flexible Spacecraft Control Problem 537
F. Curti & C. Arduini

Non-Linear Control for Large Angle Attitude Slew Manoeuvres 543
C.R. McInnes

Tether Deployment by Fuzzy Logic Controller 549
R. Licata

SESSION 20: CONTROL SYSTEMS

Chairman: M. Weinberger, ESA/ESTEC

Optimization of Magnetic Attitude and Angular Momentum Control for Low Earth Orbit Satellites 559
J. Bals, W. Fichter & M. Surauer

Attitude Control of Geostationary Satellites with Minimal Use of Gyros 569
M. Surauer, P. Zentgraf & W. Fichter

Spacecraft Attitude Rate Measurement Systems without Gyros 577
J.B. Serrano, E.J. Mora, F. Sarti et al.

Software to Support the ESA Pointing Error Handbook 587
D.G. Dungate

POSTERS AND STORYBOARDS

The PRONAOS Pointing and Stabilisation System 597
S. Berrivin, M. Le Du & A. Robert

An Autonomous and Integrated Attitude and Orbit Measurement System for Future Communication Satellites in Non-Conventional Orbits 603
E.J. Mora & J.B. Serrano

Improved Star Tracker for ODIN Satellite 611
P. Pissavin, J.P. Krebs, P. Lelong et al.

An Interactive Software for Orbit and Attitude Parameters Specification 617
W. de Castro Leite Filho

Star Trackers for Accurate Pointing and Attitude Determination 621
— In-Flight Results of High-Accuracy Star Trackers of ISO and SAX
— New Development Towards Navigation Autonomy
A. Landi, M. Buemi & D. Procopio

AOCS Design Software 631
Y. Roche & M. Sghedoni

Attitude Control Simulation for Equator-S Using Object Oriented Modelling 633
W. Enderle, U. Feucht & D. Moormann

A Prototypal Platform for Attitude and Configuration Control 639
P. Di Giamberardino, F. La Gala & S. Monaco

CFIE: In-Orbit Active Damping Experiment Using Strain Actuators 645
A. Conde Reis, N. Loix, J. Dettmann & P. Brazzale

An Overview on Aerospatiale Magnetic Bearing Products for Spacecraft Attitude Control and for Industry 649
A. Samuel & B. Lechable

Strategies for Orbit Injection that Includes Yaw Manoeuvre 657
W. de Castro Leite Filho

LIST OF PARTICIPANTS 663

LATE PAPERS

FEEP Thrusters Applications to Constellations and Small Satellites 689
S. Marcuccio, A. Genovese, M. Andrenucci et al.

Drag-Free, Attitude and Orbit Control for LISA 695
H. Klotz, H. Strauch, W. Wolfsberger et al.

SESSION 1:

IN-ORBIT RESULTS

Chairman: D. Wilson (ESA/ESTEC)

ISO AOCS In-Flight Experience

*The exceptional story of how everything turned out **better** than expected*

M.J.A. Oort, P. Van Hulzen, P. Lammertse, W. Van Leeuwen, M.E. Houck
Fokker Space B.V., the Netherlands
J. Busseuil
Aerospatiale Espace & Defence, France
P. Scott
G.E.C. Marconi, Scotland
M. Buemi
Officine Galileo, Italy

ABSTRACT

The Infra-Red Space Observatory [ISO] was launched on November 17. From the start, it was evident that the satellite as a whole, and the AOCS in particular was in a very good shape. Now, after one year of operation, the AOCS is still functioning well within spec, with only a single glitch during a negative safe-corridor period. This paper to focuses on the functional performance of the AOCS as a whole, and the performance of the two most critical sensors within the AOCS, the Gyro package [GYR] and the Star Tracker [STR].

1. INTRODUCTION

ISO is a 1½ year astronomical pointing mission dedicated to studying in detail infra-red objects detected in previous missions (notably IRAS). The satellite was developed as part of the ESA scientific program, with Aerospatiale as Prime Contractor. Fokker Space was responsible for the Attitude and Orbit Control System [AOCS]. The units comprising the AOCS and their developers are listed (in arbitrary order) in Table 1. For more information, see [ref1, ref2]

Unit	Developer
Computer + Operating System	Saab Ericsson Space
Application S/W [ASW]	CAPTEC
Gyroscopes [GYR]	GEC Marconi
Star Tracker [STR]	Officine Galileo
Quadrant Star Sensor [QSS]	Officine Galileo
Earth Limb Sensor [ELS]	Officine Galileo
Fine Sun Sensor [FSS]	Adcole
Sun Acquisition Sensor [SAS]	TNO-TPD
Reaction Wheel System [RWS]	Teldix
Distrib. & Mon. Unit [DMU]	ETCA

Table 1: AOCS units

Two sensors used for nominal control of ISO were considered critical. The STR is the main sensor for accurate pointings, and is essentially a new design. The use of gyros in AOCS design has been the centerpoint of many discussions in the past due to a number of in-orbit failures. Because these sensors are the main sources of the high performance of ISO, they deserve special attention (sections 3.2 and 3.3).

The critical sensor for contingency operations is the ELS, the only sensor which can detect the Earth. The finer subtleties of the ELS performance and its interaction with the on-board FDIR functions are addressed in section 4.2

2. THE EARLY ORBIT PHASE

ISO was launched at $2^h\,20^m\,04^s$ (MET) on November 17 '95 with the Ariane 4. The first twenty minutes after separation took place outside ground contact, during which time the AOCS would have to de-spin the satellite and acquire a stable sun-pointing. When ground contact was restored, ISO was indeed in a stable pointing under RCS control. Ariane 4 had ejected ISO perfectly, and all the autonomous provisions to cope with high-rotation, off target separation proved unnecessary.

The major sensors and AOCS modes were checked during the first six revolutions. It already became apparent then that the units were performing within specification.

During Revolution 2 and 6 two main delta-V maneuvers were carried out to bring ISO into its final 24-hour orbit. In accordance with the trend of success, the delta-Vs produced an orbit accurate to within 0.1%. The performance of the thruster-control could be predicted very well on the basis of a short rehearsal done in revolution 2. During this rehearsal, a relatively large misalignment of the thrusters was found, which was taken into account during the main delta-Vs.

The most crucial event in the commissioning phase was the ejection of the cryo cover. A time-critical sequence of operations was needed to determine that the cover had indeed successfully been ejected out of reach of ISO, and then to move away quickly to avoid reflections of sunlight by the cover into the telescope. Fortunately, cover ejection could be confirmed by its jolting effect on the main body of ISO (see fig 2.2). Minutes later, first star-light was seen by the QSS through the telescope. By the end of the day, the first instrument image (M51 by CAM) had been collected.

Proceedings Third International Conference on Spacecraft Guidance, Navigation and Control Systems, ESTEC, Noordwijk, The Netherlands, 26-29 November 1996, ESA SP-381 (February 1997)

Errors	Spec Value
SF change	< 0.04% in one month
Short term SF change	< 0.02 % in one hour
SF linearity	within 0.02%
SF change in orbit	< 0.1 % in 18 months
Noise	< 0.2 arcsec for 2Hz sampling

Table 3.2.1 GYR specifications

3.2.2.1 Bias drift

The following table 3.2.2 gives various bias drift values obtained at different stages in the program dating back to the initial tests of the gyro instruments in 1989/90. Bias drift is measured routinely as part of Gyro Instrument tests. During the Acceptance, this test is repeated with the Gyros inverted to determine the "float drop effect". Due to freedom of movement of the gyro float and the presence of gravity a "float drop effect" can give two distinct values of bias drift dependent on the up/down direction of the gyro output axis during tests (provided all other factors are constant). This float drop effect is allowed for in the ground to orbit drift change figure.

Test	Date	Gyr 1	Gyr 2	Gyr 3	Gyr 4
Gyro	'89 / '90	0.939	-0.079	0.253	-0.187
Accept.	Jul '94	0.931	-0.082	0.196	-0.212
Accept.	Jul '94	0.993	-0.152	0.233	-0.282
In-orbit	Nov '95	0.9908	-0.1257	0.208	-0.269
In-orbit	Nov '96	1.0105	-0.1333	0.1731	-0.2654
In-orbit	Avg.	0.9931	-0.132	0.1902	-0.272
In-orbit	StdDev	0.0104	0.0037	0.0106	0.0052

Table 3.2.2. Units are deg/hr

The initial in-orbit bias drift values obtained agree very well not only with the final ground test figures but also with the measurements made during the initial testing of the gyroscopes.

The evolution of the drift calibration results for each gyro channel up to the end of October are shown in the plots., as well as a composite plot of all four gyro drift results with the means removed.

The average drift values are comfortably within the initial in-orbit specification value of +/- 2 deg hr. Any ground to orbit change in drift can be attributed to the transition from 1g to zero g and the consequential "float drop effect" and this is well within the limit of 0.3 deg/hour. The long term change in drift is comfortably within the value allowed for in the specification.

There are some points of interest in the day to day behavior of the drift results.

These are:

- during the first ten days or so of the mission (initial check out period prior to cover ejection) there is less apparent noise in the drift values.
- following the initial "quiet period" there is an increase in the day to day variations which appear in all four gyros. This suggests that some common environmental / operational factor such as slewing activity is influencing the drift calibrations activity.
- at approximately day 50 into the mission there is evidence of a small step change in the drift values of gyros 2 and 3. It is understood that at around this time the Star Tracker was commanded off for about 40 minutes.
- over the last month or so the day to day variation appears to have reduced slightly.

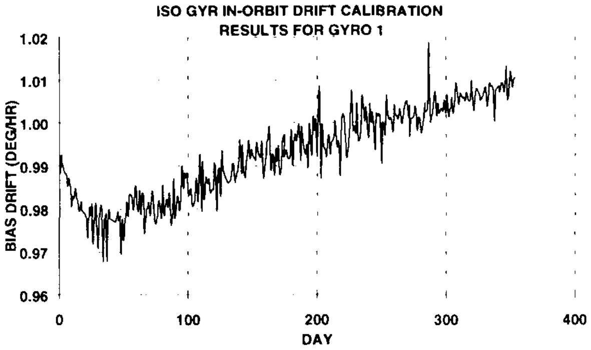

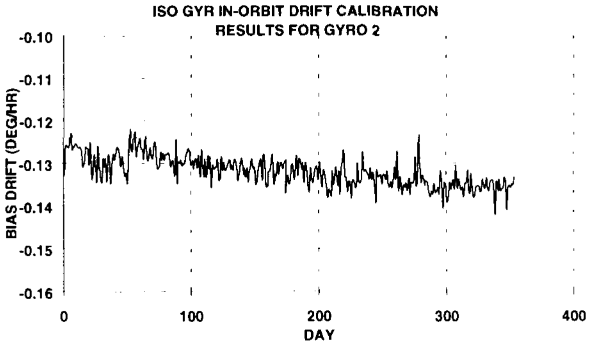

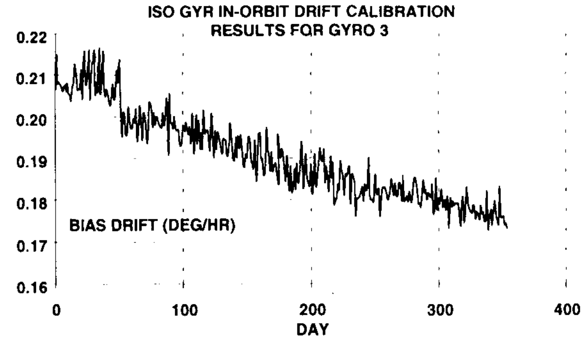

the measured NEA was lower than the requirement (**1.5 arcsec**).
Fig. 3.3.1-1 shows an example of STR output (CCD Unit, 1 CCD Unit=0.245 arcsec) as function of time during 30 minutes pointing.

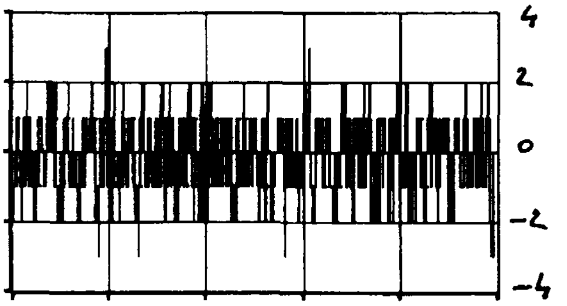

Figure 3.3.1-1: STR output example

3.3.2 STR Pointing Stability

The good stability of the pointing has been indirectly confirmed by the data relevant to the QSS/STR misalignment. In figure 3.3.2-1 the complete history of the Z component of the misalignment between STR optical axis and telescope is shown. The peak of 10 arcsec is a consequence of a change of the STR base-plate temperature of 15°C in one night.

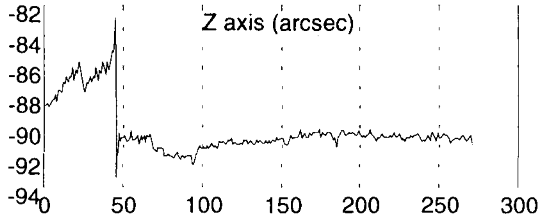

Figure 3.3.2-1 QSS/STR Misalignment history

After the stabilisation of the STR thermal control the optical head base-plate temperature in now around -11°C and its variation is less than 0.1°C/orbit. The current Z misalignment variation is less than **1 arcsec** after each orbit (see Fig 3.3.2-2).

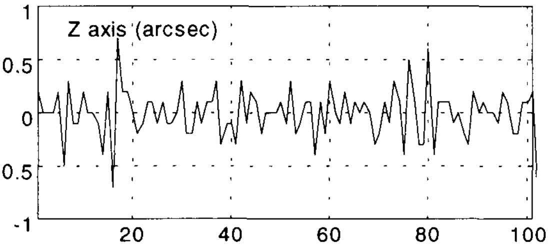

Figure 3.3.2-2 QSS/STR Misalignment variation

3.3.3 STR functionality in radiation environment

The STR tracking capability in presence of false event due to the effect of SEU on CCD produced by cosmic radiation has been verified.

The frequency of the false events measured outside the radiation belts (due to cosmic rays) show a mean value of **5 SEUs** per day on a tracking window with a maximum peak of **17 SEUs** in one orbit. This results is in agreement with the radiation analysis.

3.3.4 STR End of Life Performance

Degradation of the dark current over the life in the ISO radiation environment is of a great interest because it affects the STR accuracy performance. In table 3.3.4-1 the dark current values estimated on the basis of CCD radiation test results and the currently measured values are reported. The dark current End of Life (*) has been estimated on the basis of the current increasing trend. From these results it is clear that if the dark current increase follows the current trend, the final value will be well below the expected one and the detection and STR performance will remain below the EoL specification..

Time (months)	CCD Dark Curr (el) estimated	CCD Dark Curr (el) measured
0	15	10
4	130	35
10	325	89
18	585	149 (*)
24	780	196 (*)

Table 3.3.4-1 Dark current in ISO environment

4. ON-BOARD AUTONOMY

The ISO AOCS has an unprecedented level of autonomy for a European spacecraft of this type [see ref3]. Two experiences are highlighted here; one a successful one, the other not so successful.

4.1 STR Single Event Upsets

As a result of the requirement to retain the highest possible mode of operation, the AOCS contains an autonomous function to recover from STR Single Event Upsets [SEU], e.g. caused by cosmic rays. A single upset is ignored, and data from the previous cycle are used. An double SEU results in an autonomous re-search of the guide star, and pointing is resumed. As can be seen in section 3.3, these SEUs occur frequently, and the autonomy has prevented significant loss of observation time and effort on the part of the ground segment.

4.2 Anomaly #12

Perigee passages outside ground contact with very narrow safe attitude corridors necessitated highly complex autonomous functionality in the AOCS. The ground is primarily responsible for charting a safe course through the passage, and loading this as a set of time-tagged pointings prior to the passage. On the other hand, the AOCS is designed to react to possible errors in

Life Test Results, In-Orbit Operation and Further Development of the Type 125 Gyroscope

David Reid, Peter Scott

GEC Marconi Radar and Defence Systems
Navigation and Electro-Optics Systems Division
Silverknowes, Ferry Road
Edinburgh EH4 4AD
Telephone 0131-332-2411, Fax 0131-343-5050
e-mail: David.Reid@gecm.com
Peter.Scott@gecm.com

ABSTRACT

In 1975, twelve Type 125 mechanical gyros were installed on a life test. The gyros were subjected to a simulated launch environment and then run in vacuum conditions with periodic performance testing. The twelve gyros are all still running and have now accumulated in excess of 170,000 hours each. In addition, a four gyro test was started in January 1987 to investigate long term drift changes under contract to ESA. The four gyro test has also been kept in operation and the gyros have each accumulated in excess of 81,000 hours running. In total, 2.4 million hours of operation have been accumulated by the sixteen gyros without a single failure.

This paper presents a review of the Type 125 gyro design and performance and discusses its continuing suitability for satellite attitude control applications.

This paper also describes a new two-axis gyro unit which is designed for use with a new Enhanced Gyro Electronics module, suitable for operating the Type 125 gyro. The aim of these developments is to provide a cost effective and flexible modular package design to meet future AOCS requirements.

1. INTRODUCTION

The Type 125 Gyroscope was originally licenced in 1962 to GEC Marconi (Ferranti at the time) from Singer-Kearfott in the United States. The gyroscope originated from the King II series and was of a well considered conceptual and detailed design. Painstaking development followed and the instrument gained application in the GEC FIN series of gimballed navigation systems.

There has been continuous development of the gyroscope and its high performance has found suitability for a wide range of application. Originally fitted to Harrier GR3 and Phantom F4 aircraft, it has also been installed on land and mine survey equipment, PADS (Position Azimuth Determining System) and satellite AOCS systems. The gyroscope was selected for the second generation digital navigation systems produced by GEC which remain in production for application in front-line fighter aircraft such as the Tornado. To date there have been fifty-seven Ariane launches involving the Type 125 gyroscope. The gyro was installed as the prime system in thirty-nine of these launches and in all cases there has not been a single gyro related failure.

2. REVIEW OF TYPE 125 GYROSCOPE DESIGN

The Type 125 is a conventional single axis floated rate integrating gyroscope. The flywheel is constructed using a beryllium hub and a heavy metal rim manufactured from NIMONIC 75. The hub houses the hysteresis ring and is also used to locate two radio metal magnetic shields. The assembly is driven by a three phase hysteresis motor. The beryllium shaft is held stationary and the flywheel is supported on R3 size outer rotating bearings. Beryllium is chosen as the main material used in the flywheel, motor shaft and float as a result of its high specific stiffness. The thermal expansion coefficient of beryllium matches that of the bearing steel exactly. The flywheel has an angular momentum of 4.375×10^5 gm cm^2/sec at 350 Hz excitation.

The bearing system must have low noise characteristics and also be robust enough to withstand the rigours of high performance aircraft application. The inner of the bearing is shrunk onto the shaft and ground in position. Each bearing, inner and outer, is lapped and polished to a finish of better than 0.025 micron and roundness to better than 0.5 micron. Track dimensions are measured in-house and bearings are matched with ball sets which are sized to within 0.076 micron. Bearing retainers are impregnated with Teresso V150 mineral lubricating oil, the quantity of oil being chosen to minimise mass shifts and maximise bearing life.

Proceedings Third International Conference on Spacecraft Guidance, Navigation and Control Systems, ESTEC, Noordwijk, The Netherlands, 26-29 November 1996, ESA SP-381 (February 1997)

4. REVIEW OF LIFE TEST RESULTS

Twelve Gyro Test

The first life-test set of twelve gyros remain on test in simulated space conditions and all are operating within specification. These gyros are maintained under vacuum, are temperature controlled and run at one third normal speed (117Hz) in an open loop mode. They are positioned with their output-axis vertical, to eliminate g-dependent bias effects and input-axis south to subject the gyro to approximately -8.4 deg/hour input rate. The gyros have each been tested for mean indicated drift rate and random drift over a three hour period using an integration period of five minutes. Each instrument has now achieved in excess of nineteen years of continuous operation without failure and the total population running hours, for all twelve instruments, is of the order of 2.0 million. A plot of mean drift against running hours, for gyro serial number 4469, is shown in Figure 4.1.

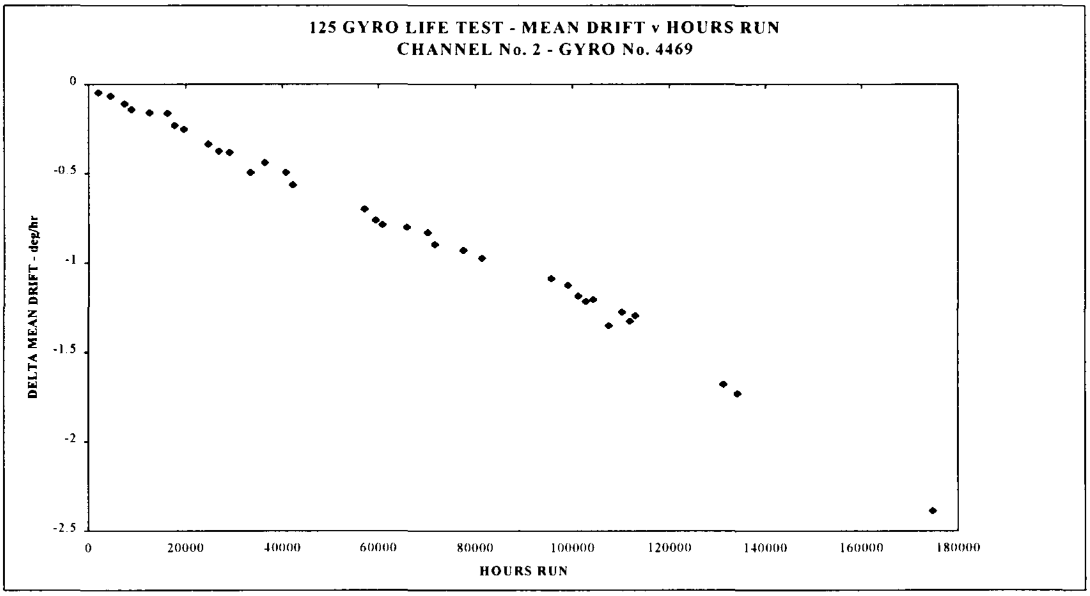

Figure 4.1

The long term trend of gyro bias, as indicated by the shift in measured rate over the nineteen year period, shows a systematic effect averaging (-)0.12deg/hour/year. All twelve gyros show a similar trend-all have a negative coefficient and the overall average is (-)0.068 deg/hour/year.

A result of running the gyros uncaptured between tests is that the float will precess to an end stop at approximately 0.75° from its null position. This places a slight strain on the gold alloy ligaments, used to conduct electrical signals into the float assembly, which are displaced from their null position. It is postulated that this ligament strain gives rise to the systematic behaviour of gyro bias observed. It must be emphasised that the gyros would not be held against an end stop in any normal application and would thus not be subjected to this effect.

The average random drift at the start of life test for all twelve instruments was 0.002 deg/hour. After 19.4 years of life test, the random drift was found to be 0.003 deg/hour indicating that there has not been any significant deterioration in performance over the entire period.

Four Gyro Test

A second life test, comprising four gyros, was initiated by ESA to confirm the ligament displacement postulate above. These instruments are kept running at 117Hz at their normal operating temperature, at atmospheric pressure, with their output axis vertical and their input axis North. The capture loop is applied at all times to keep the float nulled. Mean indicated drift rate and random drift are regularly measured. All four instruments continue to operate satisfactorily, without failure, and have each accumulated in excess of 81,000 continuous running hours.

The following observed mean drift changes with time do not show the systematic trend experienced with the twelve gyro test.

Gyro Serial No.	Mean Drift Change (deg/hour/year)
8858	0.038
8866	0.033
8872	0.0012
8880	-0.018

A simple analysis of the modulus of each drift slope yields a figure of 0.022 deg/hour/year which is significantly better than the (-)0.068 deg/hour/year figure observed in the twelve gyro test.

DIRA Life Test

A Digital Integrating Rate Assembly (DIRA) life test model comprising two type 125 gyroscopes has undergone 2000 hours of test in thermal vacuum conditions. Requirements of the test were a total running time of 2000 hours, a minimum of 630 gyro turn-on/offs and at least 75 thermal cycles. A total of 77 thermal cycles were actually performed over the temperature range -20°C to +55°C.

Three hours of stabilisation were allowed at each temperature extreme followed by one hour of testing. Testing was directed at gyro run-down times which were felt to be a measure of gyro performance. The results of the test demonstrated stability of performance with thermal cycling. It was also demonstrated that repeated switch-ons and switch offs did not result in performance degradation.

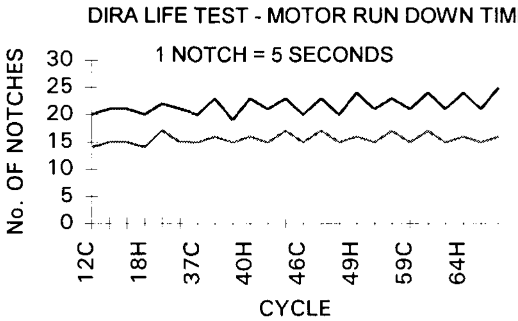

Figure 4.2

Figure 4.2 above demonstrates repeatability of motor run time during the DIRA life test.

CONCLUSION

A total of 274 years running have been accumulated by the sixteen Type 125 life test gyros. The instrument has been shown to be extremely reliable and to be capable of satisfying demands for future long life space applications.

5. IN-ORBIT APPLICATIONS OF THE TYPE 125 GYRO.

The Type 125 Gyro has seen operational service in Launcher and Spacecraft applications for as long as the 12 gyro life test has been running and even longer in the case of the earlier launcher applications of ELDO and BLACK ARROW. The first Type125 gyro based rate sensing package for space use (comprising separate sensor and electronics units) was designed for the UK MIRANDA satellite (launched in 1974) which was an experimental engineering spacecraft. Since then, there has been a continuing supply of Type 125 Gyro Packages for a variety of Scientific and Communications Satellite missions, demonstrating the versatility of the gyro. (FIG 5.1) Altogether 84 Type 125 gyroscopes have been "put-into-orbit" in a total of twenty spacecraft (in many cases on Ariane launchers stabilised by Type 125 Gyros).

Fig 5.1

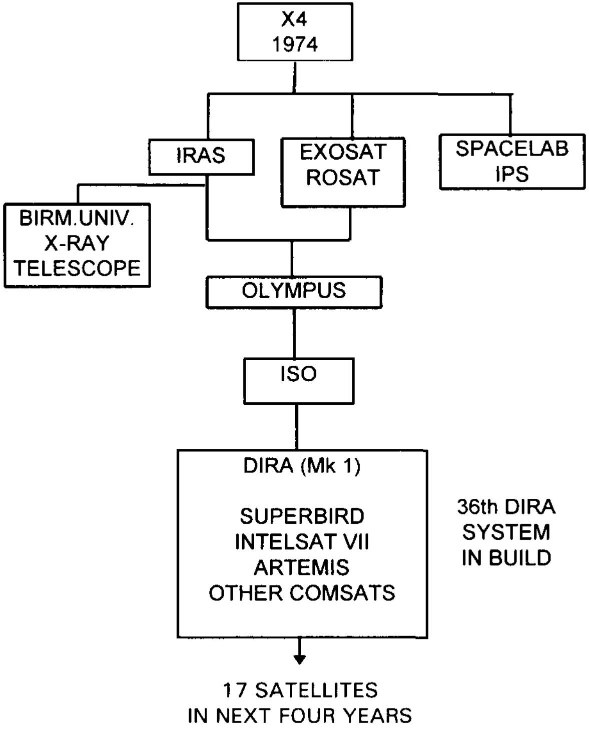

The passage of the years has seen the steady rise in vibration test levels and mission lifetime requirements. Radiation requirements have become more rigourously defined and interfacing requirements more sophisticated. As a result, the Gyro Electronics Units have been repeatedly redesigned for each successive new application up to the current DIRA (Mk1) system.

The Type 125 gyro has demonstrated its excellent mechanical robustness throughout, not least by virtue of it's successful qualification at random vibration levels of up to 19 g r.m.s. on more than one occasion. The total accumulated in-orbit running hours of all the gyros that have been launched (not including those on the launchers) is approximately 480,000 with an estimated total number of start / stops of 960. Of these 84 gyros, 52 are in currently operational spacecraft: either running continouously as in the case of scientific satellites or periodically for station keeping manoeuvres,.as in the communications satellites.

Over the next four years a further 17 communications satellites are to be fitted with the DIRA gyro package including ESA's ARTEMIS satellite.
Although the gyro instrument has demonstrated it's excellent reliability and performance capabilities, there have been a few in orbit problems with our Gyro Packages in the past (as there have been with other gyro packages) though none have been reported in recent years.
Two gyro channels (out of the 84) became permanently unuseable due to problems with the electronics Spin-Motor Supply. There have also been two instances (one in OLYMPUS and another in ROSAT) where suspected transient disturbances resulted in wheel run down (this is normally a recoverable situation).
In the current Gyro Packages, margins have been increased in the design and operation of the Spin-Motor Supply and more rigorous testing is performed at equipment level to verify these margins. There have never been any problems that could be attributed to the gyro instrument itself and, in our view, the long history of life testing, qualification and acceptance testing backed up by the evidence of in-orbit success serves only to emphasise the suitability of the mechanical Type 125 design for both high and normal performance Satellite Attitude Control applications.

6 DEVELOPMENT OF THE DIRA MK2 GYRO PACKAGE.

6.1 Introduction

Under a collaborative study and development contract with ESTEC which commenced in late 1994, GMRDS Navigation Systems Department (NESD) have designed, built and tested a prototype of a new Gyro Electronics module which is refered to as the Enhanced Gyro Electronics (EGE) module.

In addition, NESD have been separately conducting preliminary studies of suitable designs for a Two-Gyro unit, known as the Enhanced Gyro Unit (EGU), which could be used in conjunction with a number of EGE Modules to make up complete (DIRA Mk2) Gyro Packages comprising 2, 4, 6 or 8 independent gyro Channels.

A major aim in designing the EGE was to arrive at a design which could yield lower cost Gyro Packages while retaining the ability to exploit the high performance, reliability and longevity features of the Type 125 Gyroscope to meet a variety of possible future applications ranging from the purely scientific to communications satellite missions.

While the Gyro sensor units have changed little since the first design was implemented for the UK Miranda (X4) satellite in 1974, subsequent programmes have required a number of different designs for the Electronics Unit which have been largely dictated by particular mission specifications. Traditionally, our approach has been to optimise the electronics configuration for any particular Mission and Contractual requirement.

As a result, each different programme has incurred significant development and qualification costs which, in the present highly cost conscious climate, are difficult to justify.

The primary development task has been to repackage the pre-existing gyro electronics to reduce their mass and simplify the assembly while, at the same time, incorporating any design changes that would enhance the current gyro electronics design, provide flexibility and apply the lessons learnt from our experience in the Satellite Gyro field to date.

6.2 Description of the EGE

A schematic of the EGE is shown in Fig 6.1. At a functional block level the architecture is very similar to existing designs (particularly the ISO GYR design). At a detailed circuit level however there are significant changes and new features added.
The more radical design changes that have been implemented are:-

- the use of a Field Programmable Gate Array (FPGA) for the majority of the timing, control, encoding and interfacing logic functions
- additional features in the spin motor supply
- "new" encoder design
- "off-the-shelf" DC-DC converter module
- cage frequency notch filter in the capture loop
- surface mount parts for small passive components and diodes
- the overall mechanical construction

In addition the manner in which the circuitry is partitioned makes it feasible to accomodate alternative interface types such as MIL Std. 1553, MACS or other data interface standard.
Some of the"enhancements" and major features of the EGE are summarised in the following sections.

6.2.1 Notable features of the EGE

a) Gate Array
The design is based on an Actel RH1280 FPGA. The introduction of the gate array provides a degree of flexibility in the design that has not been possible with our Gyro Packages so far while at the same time enabling a considerable reduction in circuit volume.

logical system architecture partitioning while achieving thermal, vibration and radiation shielding requirements at the lowest possible mass.

Internal cable-forms are eliminated by the use of 90 deg solder spill 'D-Type' external connectors fitted directly onto the PCBs and a Hypertac inter-PCB connector within each module. EMI protection is provided by multi-point contact gaskets between each module and around each 'D-Type' connector while a metal shield between each module attenuates inter-module cross-talk and protects against catastrophic failure propagation.

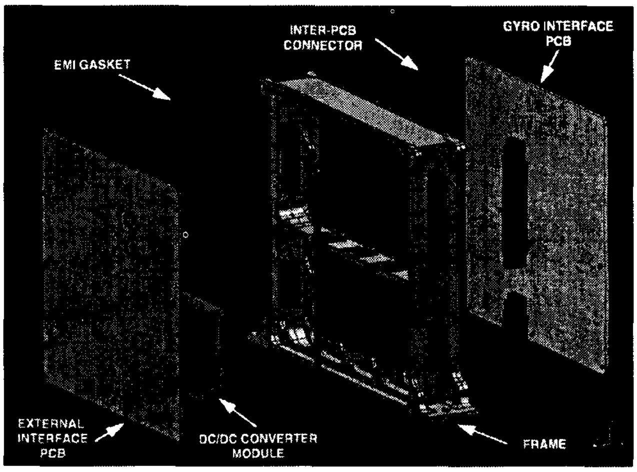

Fig 6.2

Prototype Evaluation

The development EGE Module is currently undergoing tests. So far, the majority of the circuit and gate array functions have been verified including the operation of the Spin-Motor Supply at the different selectable wheel speeds and for supply voltages over the range +20 to +50 Volts. Preliminary performance measurements with a representative gyro unit, indicate as good or better performance as is obtained with the current electronics.

6.3 Enhanced Two-Gyro Unit (EGU)

Preliminary study work on the design of a two gyro unit (fig 6.3) based on the Type 125 Gyro has been conducted.

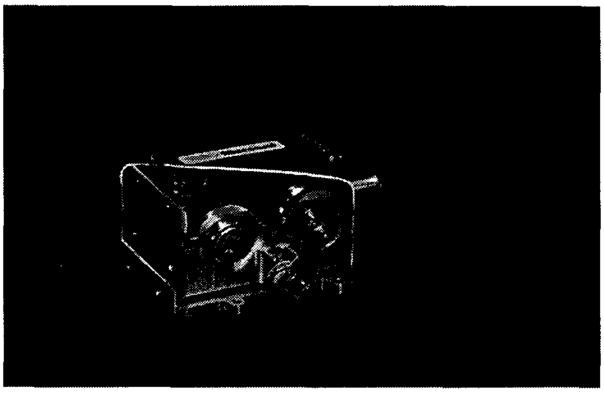

Fig 6.3 Model of the EGU

The reasons for considering a new Gyro Sensor Unit design were:

- to capitalise on the flexibility and mass savings offered by the EGE modular electronics unit design.
- to provide a simple two gyro package which for some applications such as Yaw axis control of COMSATS.is considered an adequate rate sensing provision
- to increase the environmental temperature range in which gyro temperature control can be maintained.

Fig 6.4 shows the basic construction of the two-gyro unit.

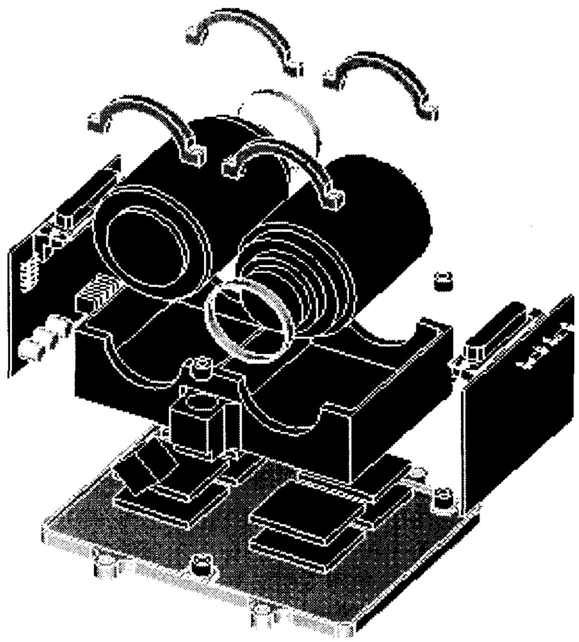

Fig 6.4 EGU Exploded View

The EGU contains two Type 125 gyros with their output axes parallel to each other and to the base of the unit. The gyroscopes can be clamped in any orientation (within 180 deg) about the output axis (longitudinal) direction. By mounting units on the appropriate surfaces of the spacecraft virtually any axis configuration can be achieved. For example a fully redundant or skewed six axis configuration would be achieved with three EGU's

The design mass of the two-gyro unit (~1.6kg) is less than 50% of the current four gyro DIRA type unit and, in multiple combinations, allows a wide choice of measurement axes configurations. The gyroscopes are arranged in opposite orientation to make the thermal loads symmetric and their input axes can be rotated to any position about their output axes.

Twin redundant arrays of four thermoelectric cooler/heaters assist in maintaining the gyros at their operating temperature of 55 degC over an external floor temperature range of -35 to +70 degC. Fine temperature control is provided by the instrument 'wrap-around' foil heaters to eliminate any requirement for temperature modelling. Temperature control circuits are mounted on individual instrument PCBs, each fitted with a 90 deg solder spill 'D-Type' external connector, to minimise cableforms.

Gyro axis alignment reference is provided by an optical cube attached to the instrument support frame while an eccentric spacer ring allows each instrument to be accurately harmonised to the optical reference. The overall package is magnetically shielded to reinforce the gyro shielding and attenuate the effects of external fields impinging on the sensitive output axes of the instruments

6.4 Conclusions

The basic design of the Type 125 gyroscope has been demonstrated to be eminently suitable for a wide variety of space attitude and guidance control applications. Furthermore, it is readily available in significant quantities "off the shelf".

It has a degree of flexibility in the manner in which it can be operated, using relatively simple, conventional electronics, to optimise its performance for any specific space application.

As a rate measuring instrument, it is extremely sensitive yet it is also robust and exhibits stable performance over long periods of time.

The new Enhanced Electronics and Sensor Units described in this paper have been designed to reliably exploit the full capabilities of the Type 125 gyro while aiming to minimise development costs that would inevitably be incurred in producing a Type 125 Gyro Package tailored for a particular application.

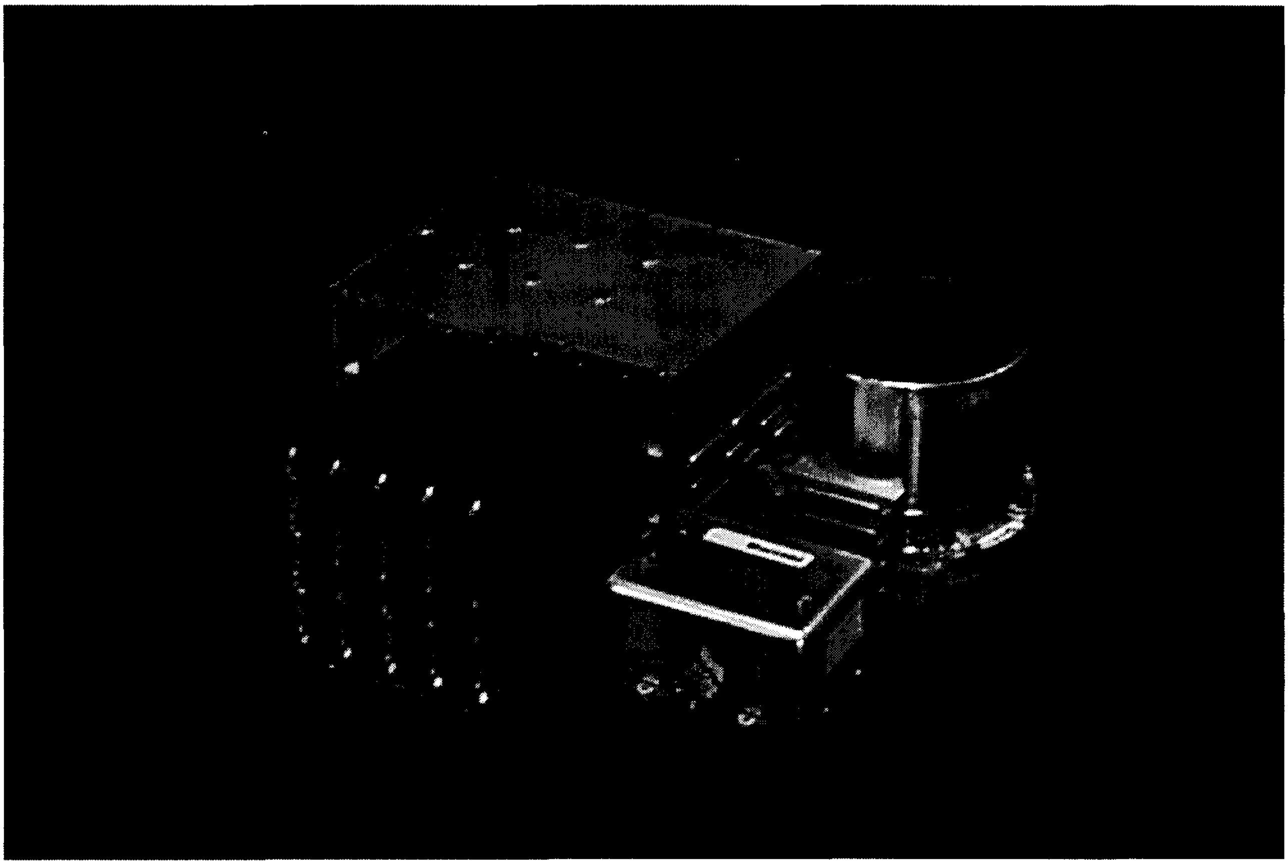

Fig 6.5 Comparison of DIRA Mk1 (at rear) with DIRA Mk2.
NB: only one EGU shown.

SAX AOCS DESIGN AND IN-FLIGHT EXPERIENCES

F.H.van der Laan, L.Karsten, S.Kampen, E.A.Silkens
Fokker Space B.V.
Leiden, The Netherlands

A.Tramutola, G.Chlewicki, A.Bacchetta, M.Montagna
Alenia Spazio
Turin, Italy

ABSTRACT

The paper is composed of two parts. The first part describes the functions and hardware configuration of the SAX Attitude and Orbit Control subsystem (AOCS). The mode logic is described in detail and for each mode attention is given to the use of relevant sensors and actuators. Because of the short ground contact each orbit, relatively long eclipse duration and because SAX is not a spinner, the autonomy requirement has been a serious driver for the SAX AOCS design. For that reason, special attention is paid to the fault-tolerance strategy, which includes full redundant hardware, extensive health check logic, redundancy management, and numerous autonomous fallbacks to safe conditions.

The second part of the paper focuses on the in orbit commissioning of the AOCS covering the initial mission phases, subsystem calibration and performance as well as a summary of problems encountered in flight. The measurements of the AOCS performance reported in this section demonstrate that, after in orbit calibration, all performance requirements have been satisfied and in some cases significantly exceeded. In the section devoted to problems encountered during commissioning emphasis is placed on practical solutions that have been implemented including modifications and tuning of AOCS software.

1 INTRODUCTION

The "Satellite per Astronomia a Raggi X" (SAX) is an orbiting X-ray observatory developed as a joint Italian-Dutch programme under ASI-NIVR contract. Alenia Spazio was the prime contractor for the SAX spacecraft. The AOCS has been designed by Fokker Space, with Alenia's participation in unit procurement and subsystem testing. Commissioning of the AOCS, the primary responsibility for which rested with Alenia, was carried out with Fokker and NLR support, and in close co-operation with Nuova Telespazio, which was responsible for all tasks related to operational control of the spacecraft, including the development of ground station facilities at Malindi and the SAX Operations Control Centre in Rome.

PART ONE

2 SAX MISSION DEFINITION

The SAX satellite has the objective to carry out systematic and comprehensive observations of celestial X-ray sources over the 0.1 to 300 keV energy range using both Narrow Field Instruments and Wide Field Cameras. The scientific objectives of the SAX mission include the following:

- imaging with moderate resolution and broad-band spectroscopy over the energy range from 1 to 10 keV,
- continuum and cyclotron line spectroscopy over the energy range from 3 to 200 keV,
- time variability studies of bright sources, both on short-term (msec) and long-term (days/months) time scales,
- systematic studies of long-term variability of X-ray sources

The satellite is operated from a near circular low Earth Orbit (600 -450 km) with an inclination of less than 5°. The operational lifetime is at least 2 years. Ground contact will be 8 to 10 minutes, depending on the altitude, in a 97 minute orbit.

The SAX AOCS guarantees pointings to last up to 28 hrs with an Absolute Pointing Error (APE) better than 90" for the main instrument axis, when 2 star trackers are used. An Absolute Measurement Accuracy for this axis better than 22" can be achieved. Because of the restriction that the Sun vector remains within 30° from the +X axis for safety reasons, only a part of the sky can be covered at a given time. Within a period of 4 months, the complete sky can be covered.

Figure 1 shows the satellite and the satellite coordinate frame. The X-axis is normal to the solar arrays; the Z axis is aligned with the boresight of the narrow-field

---

Proceedings Third International Conference on Spacecraft Guidance, Navigation and Control Systems, ESTEC, Noordwijk, The Netherlands, 26-29 November 1996, ESA SP-381 (February 1997)

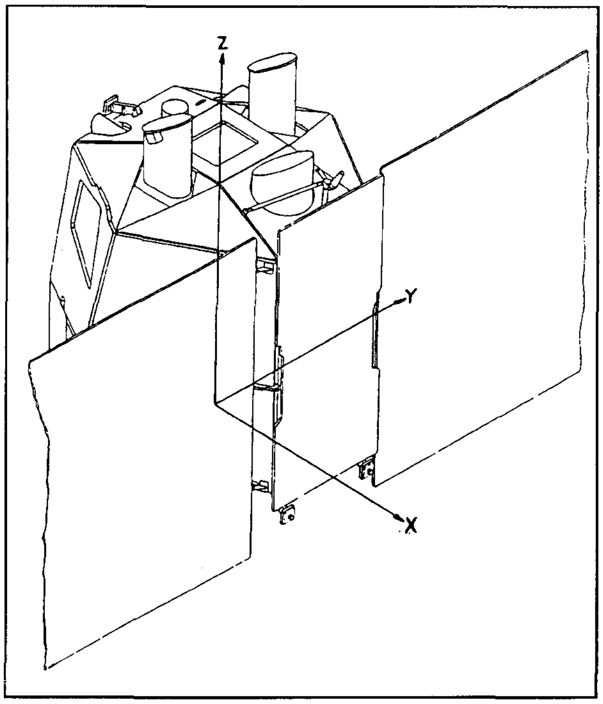

Figure 1: SAX and its coordinate frame definition.

instruments and the Y axis completes the right-hand coordinate system.

In order to point the Narrow-Field Instruments accurately at an X-ray source, the field-of-view of one star tracker is in +Z direction. As can be seen in Figure 1, the two Wide-Field Cameras look to the -Y and +Y direction. They are used to scan for variable X-ray sources during pointings. For this reason, accurate attitude knowledge about the Z axis is provided by two more star trackers, one in +Y direction and one in -X direction. They provide redundancy and shorten the duration of star obscurations by the Earth. Gyroscopes are used to maintain the attitude knowledge during star obscuration and to extrapolate the Sun vector position during eclipses.

Because the NFI's are very sensitive to sunlight, the Sun vector is not allowed more than 30° out of the XY plane. When the Sun vector is in the XY plane, rotations about the Z axis are possible up to 45° to achieve a large coverage with the WFC, called the 'Extended Pointing Domain'. If the Sun vector is not in the XY plane, the Sun vector is restricted with 30° of the +X axis, called the 'Normal Pointing Domain'. Upon ground command, transitions between the two pointing domains can be made.

3 AOCS FUNCTIONS

The SAX AOCS performs the following functions:

- attitude safe keeping
- attitude changes (slews) upon ground command
- accurate pointings
- unloading of excess angular momentum
- delta-V manoeuvres to increase orbit altitude
- special attitude and instrument calibrations
- software reprogrammability
- extensive unit health checking
- autonomous reconfiguration to redundant units
- autonomous transitions to safe modes

Attitude safe keeping

Attitude safe keeping is achieved by the Acquisition Mode (AM) which uses the Sun Sensors (QSS and SPI's) and magnetometer (MGM) as sensors to determine the attitude. The Reaction Wheels (RWS) are used as actuators to align the +X axis with the sun vector. AM is implemented in ROM and is entered automatically after separation and upon a fallback by the safeguard function. This safeguard is implemented as a separate function which resets the ACC when the Sun vector moves outside the pointing domain, or if some other unsafe condition is detected. The safe attitude guarantees that the sun cannot enter the field of view of the sun-sensitive scientific instruments, and provides an attitude that is favourable for power and thermal reasons. If during separation, or due to some external effect, the satellite body angular momentum would increase to a level above 14 Nms, there will be an autonomous transition to 'Detumble Mode' (DTM), which is a submode of AM, in which the thrusters are activated to remove the momentum and to bring the satellite in a safe and stable attitude relative to the Sun vector.

Attitude changes upon ground command

Because the SAX mission is intended to perform measurements over prolonged periods while pointing to X-ray sources, attitude changes have to be performed accurately to guarantee that the star trackers can find their target stars when going from one pointing to the next. During attitude changes, the new target is obtained by ground command via the Attitude Operations Plan (AOP). The on-board attitude is maintained using the star trackers while attitude changes are registered by gyroscopes and integrated by the On-board Software.

To reduce the effects of sensor noise and discretisation steps, sensor data is filtered by combining an augmented state reconstructor with a PD control law. Attitude bias due to permanent disturbances is integrated by augmenting the state reconstructor with models for disturbance torques and gyro drift. Feed-forward compensation of the estimated disturbance is applied and the estimated gyro drift removes the gyro bias from the filter velocity estimate. An extra low-

pass filter has been added in the loop between the sensor output and estimator to deal with solar array flexibility effects.
The RWS is used as actuators during slews, providing a maximum slew speed of 15 deg/min. The maximum slew (180°) takes less than 20 minutes to complete. The Reaction Control System (RCS) is only used for attitude changes during non-nominal situations and when performing a delta-V manoeuvre.

Accurate pointings
When in Science Pointing Mode (SPM), SAX is capable of maintaining a pointing accuracy (Absolute Pointing Error) of 1.5 arcmin in target direction and an accuracy better than 16.5 arcmin normal to that direction. The target direction corresponds with the direction of the satellite +Z axis which is the main instrument axis. To achieve this pointing accuracy, three star trackers are used according to a timing schedule that is given in the AOP. In this way, obscurations of stars by the Earth are predicted and loss of star references during a pointing is avoided by changing the use of the STRs during the orbit.

Unloading excess angular momentum
Due to external disturbance torques, angular momentum gets stored in the RWS. As saturation of the wheels would inhibit attitude control, the MTRs are used to exert an external torque as soon as the total momentum exceeds 3.5 Nms. Unloading stops when the momentum is reduced to 2 Nms.

Delta-V manoeuvres
To extend the nominal 2-year lifetime, SAX is equipped with a Reaction Control System that can be operated on ground command to perform a 'delta-V' manoeuvre which raises the orbit altitude. During this manoeuvre, the satellite Z axis will be kept aligned with the velocity vector while the RCS is used both for orbit change and attitude control. Because a failure of the RCS during this operation can result in an excess of angular momentum that can not be absorbed in the RWS and cannot be quickly unloaded by the magnetic torquers (MTR), a large number of safety measures are taken to prevent autonomous activation of the RCS.

Special attitude and instrument calibrations
A number of special modes of operation has been implemented to support attitude calibration and calibration of instruments. The transition from AM to the Science Pointing Mode (SPM), for instance, requires an accurate attitude in order to guarantee that the star trackers successfully find their guide stars. This attitude calibration is achieved by means of the 'Default Pointing Mode' (DPM). In SPM, the gyroscopes have to be calibrated for drift and misalignment errors. To be able to correct for these errors in the software, they must first be measured, which requires a set of accurate slews. This is achieved by pointing a STR at a guide star and rotate about the inertially fixed axis. Finally, a Slow-Scan Mode has been implemented which allows the spacecraft to be rotated about any axis with a well-defined rotational speed. This mode is used to calibrate some of the instruments during the mission.

Software reprogrammability
All AOCS functions that are important for the safety of the satellite, are loaded in ROM. These functions include the 'operating system' called BSW (Basic SoftWare) and the BAC (Basic Attitude Control) functions. At initialisation, this software is copied to RAM, which is divided into a 'code' segment and a 'data' segment. Functions that are not essential for the safety are loaded in RAM before launch and can be uplinked to the satellite during the mission. These functions (such as the SPM logic) are called the Extended Attitude Control (EAC) functions.

Part of the data segment can be used for code. This option was investigated during the project when the code margin was becoming too small. It is possible to replace all code and data in RAM during flight by means of 'patch' procedures. For some parameters in the data segment, regular replacement by patching is nominal for calibration purposes. For code, patching is non-nominal and will only be done if a serious software failure is detected during the mission. It provides a flexibility to adjust the design during operation, increasing its robustness against failures.

4 AOCS MODES

Figure 2 gives an overview of the SAX AOCS modes.

Initialisation Mode (IM)
When the PDU is powered, the ACC and MRU become automatically powered and the ACC gets a hardware reset, initialises and enters IM. Next, a process of switching on the sensors and actuators is executed, followed by a transition to Acquisition Mode (AM).

Acquisition Mode (AM)
In this mode, the satellite searches for a safe attitude, independent of its initial conditions: it aligns the +X axis with the Sun vector and rotates about this axis with the objective to get the Earth-Magnetic Field (EMF) vector in the satellite XZ plane. Care is taken that during the slew no sunlight can enter the instruments which are oriented parallel to the Z axis.

If this mode is entered during eclipse (e.g. as a result of separation in eclipse), the Z axis will be aligned with the EMF vector until eclipse exit.

AM is the safe mode and is implemented in ROM. When the ROM software (which is running from RAM) executes AM, it is called 'BAC-AM'. As soon as also the EAC functions can operate, AM is called from the EAC environment and called 'EAC-AM'. The mode remains AM until the ground commands a transition to Default Pointing Mode.

Default Pointing Mode (DPM)

This mode has two objectives: (a) to serve as intermediate step between AM and the Science-Pointing Mode (SPM) for accurate attitude calibration, and (2) to keep the satellite in a safe position with full attitude accuracy when no scientific pointings are commanded. To achieve the attitude calibration, the satellite starts a slew upon entering DPM, to align the +Z axis with Polaris. To this end, the STR on the +Z axis is commanded in 'mapping' mode. When Polaris is not directly found, a search process is started in which the satellite rotates a few degrees about the Sun vector, and the Z-STR starts mapping the sky again. This process is repeated until Polaris is found, or until it becomes clear that the attitude error is too large, resulting in a fallback to EAC AM.

Science Pointing Mode (SPM)

SPM consists of a number of submodes that result in a slew towards the new target, followed by a pointing at that target until the ground decides to command a new pointing or to change the mode. Initialisation of SPM includes copying the new target quaternion from the SPM AOP and calculating the Sun vector setpoint from the new target quaternion. Next, the star obscuration prediction process is started to determine which STR is to be used at 'AOP enable' (ground confirmation to use the new target) and to set timers for the defined STR obscuration start and stop events. Then, a slew is started, using the GYR as sensors and the RWS as actuators. The GYR data is used to continually update the on-board attitude quaternion. The controller determines the slew errors from the changing attitude quaternion and the target quaternion. Close to the end of the slew, the STRs are commanded and the final part of the slew is performed using a combination of GYR and STRs.

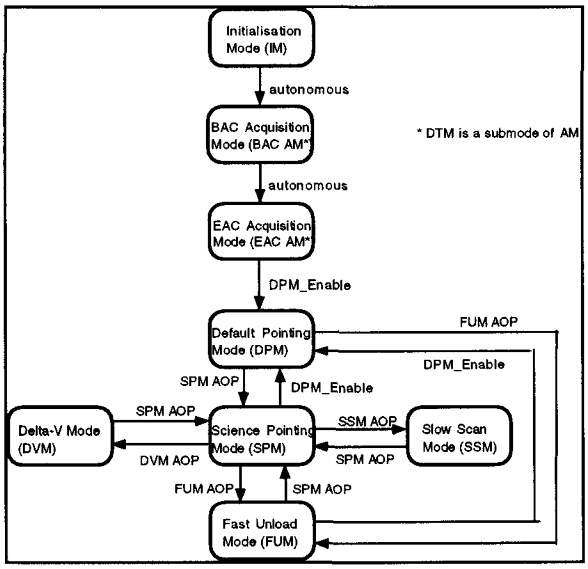

Figure 2: SAX AOCS Mode overview.

During the pointing, the STR data is used to calibrate the on-board quaternion to prevent that GYR drift can introduce errors in the absolute attitude knowledge on board.

Delta-V Mode (DVM)

Delta-V mode is especially designed to raise the orbit altitude. During this manoeuvre, the Sun must be kept within the Normal Pointing Domain, while the +Z is kept perpendicular to the velocity vector. In addition to an acceleration of the satellite (ΔV), it requires a constant rotation about the -Y axis of about 4 deg/minute. The AOCS manages this attitude change by updating the target attitude each AOCS cycle of 0.5 s with a 'delta quaternion'. Both the initial attitude quaternion and the delta quaternion have to be provided by a ground-commanded DVM-AOP. DVM is a critical mode because it requires a number of ground preparations, such as commanding the thruster heaters 'on' and commanding the GYR to 'coarse mode'. When DVM is executed, the GYR-related health checks will autonomously use thresholds related to these coarse mode setting to prevent that the induced angular accelerations (including solar array flexibility) would trigger these checks and risking that one of the GYR is (incorrectly) declared to be unhealthy.

De-Tumble Mode (DTM)

De-Tumble Mode has been introduced as a special safe mode (submode of AM), against launcher failures. If, during separation from the third stage of the Atlas-Centaur, too much angular momentum is put in the satellite body (a small chance), this could theoretically lead to GYR saturation, which could mean loss of control during AM. It is essential to bring the satellite in a favourable attitude relative to the sun for solar array deployment, during the initial attitude acquisition phase.

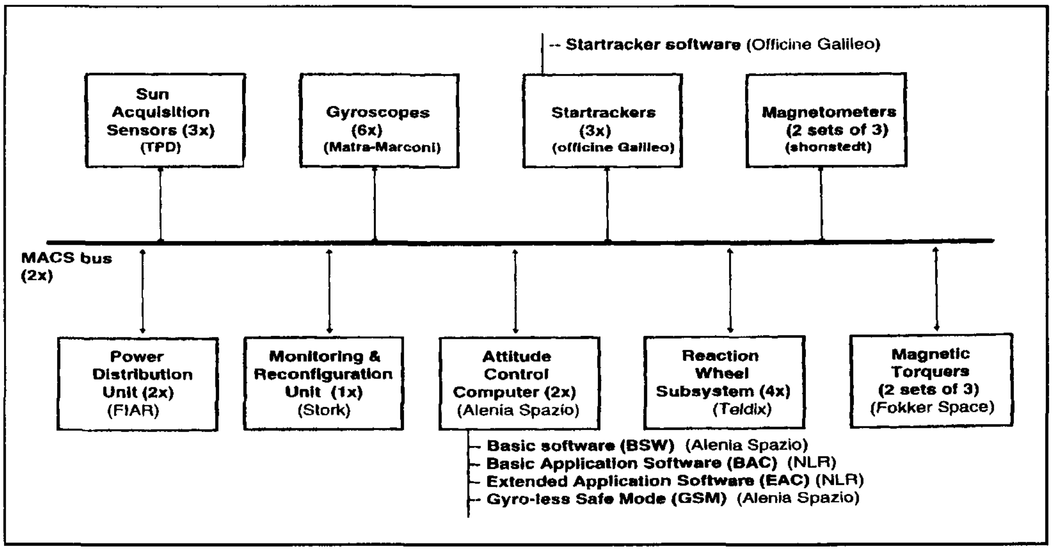
-- Startracker software (Officine Galileo)
Sun Acquisition Sensors (3x) (TPD)
Gyroscopes (6x) (Matra-Marconi)
Startrackers (3x) (officine Galileo)
Magnetometers (2 sets of 3) (shonstedt)
MACS bus (2x)
Power Distribution Unit (2x) (FIAR)
Monitoring & Reconfiguration Unit (1x) (Stork)
Attitude Control Computer (2x) (Alenia Spazio)
Reaction Wheel Subsystem (4x) (Teldix)
Magnetic Torquers (2 sets of 3) (Fokker Space)
- Basic software (BSW) (Alenia Spazio)
- Basic Application Software (BAC) (NLR)
- Extended Application Software (EAC) (NLR)
- Gyro-less Safe Mode (GSM) (Alenia Spazio)

Figure 3. AOCS hardware configuration.

If the launcher would have brought SAX into an incorrect orbit which would lead to rapid accumulation of angular momentum due to high external drag torques, DTM would also interfere and autonomously remove the momentum and restore the satellite's attitude.

Finally, DTM acts as 'safety net' in case a thruster failure occurs during DVM. DTM uses the GYR in coarse mode as sensors and has its own, dedicated health checks.

Fast-Unload Mode (FUM)

If the launcher would have left SAX in an incorrect orbit, the ground would have to raise this orbit by means of a DVM manoeuvre. Properly executing DVM, however, requires first a number of attitude calibrations to guarantee that STRs will be able to lock on guide stars before the DVM is executed. To unload the satellite body angular momentum during the process of preparing for DVM, the ground can also control the RCS-momentum unloading directly by commanding the AOCS in "Fast Unload Mode' (FUM). The FUM is very similar to DVM (same control laws and health checks) but results only in RCS-controlled momentum relieve, not in a Delta-V manoeuvre.

Slow Scan-Mode (SSM)

Finally, an attitude-control mode has been designed specifically to calibrate a number of scientific instruments. This mode guarantees a well-controlled angular rate about a well-defined axis. Both the scan rate and scan axis have to be provided in the SSM AOP. Similar to the DVM control, the mode logic updates the target quaternion each AOCS cycle.

5 AOCS HARDWARE CONFIGURATION

Figure 3 shows the AOCS subsystem block diagram. It shows that the AOCS is a modular system, consisting of a number of units which communicate with the 'Attitude Control Computer' (ACC) via a redundant digital, serial 'Modular Attitude Control Subsystem' (MACS) bus.

Attitude Control Computer

The ACC communicates with the satellite's On-Board Data Handling system (OBDH) through a 'Digital Bus Unit' (DBU). It executes the 'Remote Bus Interface' (RBI) protocol to receive commands, send telemetry and to synchronise the AOCS to on-board time. The ACC is the master of the MACS bus. It initiates communications to command AOCS units, to acquire data, and to distribute the AOCS control cycle time reference. The ACC consists of two identical computers, one is constantly powered while the other is cold standby. Each computer is based on the 80C86 microprocessor, supplemented with a 8087 co-processor. Each computer contains 48 Kbytes of PROM for the Basic Software and part of the Application Software, and 128 Kbytes of RAM for operational application software. After switch-on, the PROM software is copied to RAM from which it runs, and the PROM is switched off to safe power.

Power Distribution Unit

Power switching of all AOCS units is controlled by the 'Power Distribution Unit' (PDU). The PDU receives 8 'live' 28V system power lines from the satellite Power Protection and Distribution Unit. All AOCS units except the Magnetometer (MGM) have their own power converter. For the MGM, the power converter is housed inside the PDU. The PDU contains 16 bits RAM Subsystem Status Memory and 5 relays to store vital AOCS information for initialising the ACC after a computer reset or switchover to the redundant computer. The PDU's monitor and command electronics is redundant. It can switch on and off all AOCS units, and powers the 'Magnetic Torquer Rods' (MTR), thruster Flow Control Valves and thruster heaters upon command. The PDU provides status monitoring to the ACC about the VRAM and NVRAM registers, the power switch status of all units, and the current status of the thrusters and MTR, and thruster temperatures.

Monitoring & Reconfiguration Unit

The 'Monitoring and Reconfiguration Unit' (MRU) contains the subsystem watchdog (MRU-WD) and the A/D converter for the 'Sun Acquisition Sensor' signals. The MRU-WD receives a checkword from the ACC each cycle, indicating the health status of the computer. If the checkword indicates a failure, the MRU-WD informs the PDU, which switches to the redundant computer in the ACC. The MRU-WD can only command an autonomous switchover from ACC/A to ACC/B.

Magnetometer

The 'Magnetometer' (MGM) measures the Earth Magnetic Field vector, decomposed in its own coordinate frame. There are two MGM sensors, each with their own electronics, in cold redundancy. Each MGM electronics has its own interface with the MACS bus and is powered by a secondary power line from its DC/DC converter in the PDU. The magnetic field vector is used as attitude reference in AM and as reference for angular momentum unloading by the MTR.

Sun Acquisition Sensors

There are three 'Sun Acquisition Sensors' (SAS), each with a hemispherical field of view, which provide information on the position of the sun relative to the spacecraft. Two SAS's are mounted on the +X side, one is mounted on the -X side. The two +X SAS's use a 'Quadrant Sun Sensor' (QSS) to measure the angle between the QSS boresight and the Sun vector. The QSSs have a field-of-view of more than 90° x 90°. The bias error of each sensor is less than 0.3°. The sensor-head consists of a truncated pyramid surrounded by a square baffle. Each side of the pyramid carries two 'Sun-Presence Indicators' (SPI's) that provide a coarse position of the Sun vector in all directions. The -X SAS only provide SPI's; the +X SAS's provide two QSS's and two sets of SPI's in hot redundancy. The SAS electronics is housed inside the MRU.

The Sun vector as measured by the QSS is used as attitude reference in AM and both QSS and SPI's are used by the safeguard function to check if the Sun vector crosses the Pointing Domain boundaries.

Gyroscopes

Changes in attitude are measured by means of gyroscopes. There are six gyroscopes, of which four are active in hot redundancy. The input axes of the four gyro's in the 'default' (launch) configuration, are oriented in an 'all skewed' configuration. With four gyro's in a hot redundant configuration, a correct velocity vector can be measured, even if one of these four has failed. Two gyro's are permanently switched off and not addressed via the MACS bus. In case a gyro fails, the ground can decide to switch on one of these two gyro's and switch off the failed one, and patch the new MACS addresses and software parameters that correspond with the new gyro configuration. In orbit, the gyro output will be corrected for scale-factor errors and drift errors which are determined by calibration procedures. After calibration, typical drift residue can be as high as 13.3" during a 40 minutes period of star tracker obscuration.

The GYR are used for attitude reference during slews, and to maintain the attitude during pointings when stars become obscured by the Earth. The GYR are also used to extrapolate the EMF vector in between MGM measurements (once per minute) and to extrapolate the Sun vector during eclipses.

Star Trackers

During pointings, 'Star Trackers' (STR) provide inertial attitude reference data. Three Star trackers are used, with optical axes that point in the +Z, +Y and -X direction respectively. This configuration provides redundant attitude measurement about all control axes. Because of obscuration of the guide stars by the Earth during pointings, the combination of star trackers that is used is changed a few times during the orbit. Each STR has a field-of-view of 3 x 4 degrees. The detector of an STR is a CCD with 384 x 288 light-sensitive pixels that each has a size of 23 μm x 23 μm. To maintain a low noise level, the CCD is thermally controlled at a temperature of -20° by a Peltier cooler. The STR electronics are microprocessor-based, and contain software for processing sensor data and executing STR tasks upon command. During pointings, the STR is commanded by the on-board software in 'search tracking' mode, in which it starts tracking a guide star that is found at the indicated part of the field-of-view. Stars with a visual brightness between 2 and 8 can be tracked. In 'Default Pointing Mode' (DPM), the on-board software commands one of the Star Trackers in 'Mapping Mode'. This means that all 36 'Elementary Search Windows' that cover the field of view, are automatically scanned while searching for the unique guide star (default is Polaris). The resolution of an STR is 0.25 arcseconds, while an STR is capable of tracking stars while slewing up to 40 arcseconds per second.

Reaction Wheels

The 'Reaction Wheel System' (RWS) is the actuator for all the normal modes. Four wheels in an 'all skewed' configuration are powered by two electronics boxes which each contain two channels. The RWS provides wheel speed information (tacho output) to the health checks that are implemented in the on-board software; this speed information is not used for control purposes. For the RWS, there is a three-out-of four redundancy: the wheel which is not used, is not powered. Each wheel can store up to 20 Nms of angular momentum, and can provide a torque up to 0.245 Nm in 63 torque steps.

Magnetic Torquers

The 'Magnetic Torquers' (MTR) provide the capability to unload angular momentum via interaction with the Earth's Magnetic Field. Three MTR's are mounted along the major satellite axes. Each torquer contains two coils, a prime and a redundant one. The torquers are powered directly and independently via the PDU to provide zero, maximum positive or maximum negative magnetic dipoles. Upon powering, an MTR will generate an average magnetic moment of 95 Am².

Reaction Control System

The 'Reaction Control System' (RCS) consists of two (redundant) branches of six thrusters each. The RCS is used as actuator during the special modes only, like the 'Delta-V Mode', 'Detumble Mode' and the 'Fast Unload Mode'. The RCS thrusters can deliver a thrust of 11 N at BOL and 3 N at EOL conditions. The thrusters are operated via the PDU and can be commanded either in 'open', 'closed' or 'pulse' mode. When used in 'pulse' mode, the thruster valves are opened during 100 ms only of the 500 ms AOCS cycle.

6 AOCS FAULT TOLERANCE

The Fault Tolerance strategy for the SAX AOCS is based on the implementation of (a) full redundancy of all hardware, (b) extensive health check logic, (c) redundancy management logic to recover the effect of the failure by switching to the redundant unit and (d) autonomous fallbacks to a safer mode.

Extensive unit health checking

The SAX AOCS is designed to be Single Point Failure free. It is fully redundant and supported by extensive health checks implemented in the software. An overview of the health checks and cross checks is given in the following table.

unit health checks	
RWS	continuity check, accumulation check
MACS	self test, deadlock check
GYR	continuity check, sum check
SAS	frozen output check, accuracy check, eclipse time-out check
MTR	current check, polarity check
PDU	commanding response checks
MGM	frozen-output check
unit cross checks	
GYR/ RWS	based on conservation of total angular momentum
GYR/ QSS	based on predicted and measured sun movement

Autonomous reconfiguration to redundant units

Because there is limited ground contact (10 minutes each orbit), and because the instruments are very sensitive to damage by sunlight, extensive measures have been taken to guarantee an automatic transition to a safe attitude upon the occurrence of non-nominal events. These are either transitions to another (safer) BAC or EAC mode, a 'hardware' reset of the ACC, or ACC switchover. These transitions are listed in the following table.

Check	**initial mode**	**result**
BSW ROM test	initialisation	ACC switch
BSW ROM copy test	initialisation	ACC switch
BSW RAM test	initialisation	ACC switch
BSW processor test	initialisation	ACC switch
BSW process. i/f test	initialisation	ACC switch
BAC ROM-copy (sg)	initialisation	ACC h/w reset
BAC RAM test (sg)	initialisation	ACC h/w reset
BAC 8087 check	all modes	ACC switch
BAC RT clock test	all modes	ACC switch
BAC Macs self test	all modes	ACC switch
ACC/MRU var. bit	all modes	ACC switch
ACC/MRU time-out	all modes	ACC switch
ACC h/w watchdog	all modes	ACC h/w reset
EAC pos/vel check (sg)	all modes	ACC h/w reset
EAC SOL check (sg)	all modes	ACC h/w reset
Sat. body rate test (sg)	all modes	ACC h/w reset
Hrws limit check (sg)	all modes	ACC h/w reset
BSW division by zero	all modes	BAC-AM
BSW unused memory	all modes	BAC-AM
BSW mult. event upset	all modes	BAC-AM
BSW BCP missing	all modes	BAC-AM
BAC QSS consist chck	all modes	BAC-AM
BAC gyr sum check	all modes	EAC-AM

BAC Htot unloading	all modes	EAC-AM
BAC Htot RCS check	all modes	DTM
RWS health checks	all modes	BAC-AM
MGM health checks	all modes	BAC-AM
star not found	SPM	DPM
star not found	DPM	EAC AM
STR unhealthy	SPM	DPM
STR unhealthy	DPM	EAC AM
AOP time-out	DVM or FUM	EAC-AM
AOP time-out	SSM	DPM
attitude error too large	DVM or FUM	EAC-AM
Htot too high	DVM or FUM	EAC-AM

sg = safeguard check

Autonomous transitions to safe modes

The Redundancy Management function handles the health status reported by the health checks and takes action to reconfigure unhealthy units if necessary. The unit health status is stored in a 16-bit RAM Subsystem Status Memory (VRAM) of the PDU. This memory preserves the unit status upon an ACC switchover and indicates for each set of units, which is the active configuration, and if reconfiguration is allowed. For the RWS, MGM, ACC and PDU, automatic reconfiguration after a transition has taken place to the redundant unit, is not possible (cold redundant), unless the ground enables this upon command. For all other units, an autonomous transition back from redundant to primary unit after a second health check trigger is possible (hot redundant).

PART TWO

7 INITIAL MISSION PHASES

The SAX satellite was launched by a Lockheed Martin Atlas I/Centaur from the Cape Canaveral Air Station. Lift-off was on 30 April 1996 at GMT time 4:31 as scheduled. After injection into the elliptical parking orbit and a coasting period of about 14 minutes the Centaur main engine brought the spacecraft in the planned equatorial orbit. Separation occurred at 4:59:23. The first ground contact was as expected at about 5:05 and the first telemetry which reached the Operational Control Centre in Rome showed SAX in Sun pointing with target attitude acquired. Solar array deployment occurred during first visibility. Orbital parameters computed by Nuova Telespazio on 4 May 1996 gave further confirmation of the correct operating orbit: apogee = 616443 m; perigee = 579814 m; period = 96.675 minutes; eccentricity = 0.2625×10^{-2}; inclination = 3.95°. The average visibility duration from the Malindi station is 10’30” and the eclipse duration is about 34’40”. All orbital parameters are therefore nominal.

Telemetry covering separation is not available but a rough estimate of the S/C total angular momentum at separation yields a value of about 6 Nms. (The maximum expected angular momentum remaining after the rate pre-compensation manoeuvre carried out by the Centaur autopilot was 6.72 Nms). The effects of ongoing solar array deployment on spacecraft dynamics became visible at about 7’51” after the SEL acquisition and the locking of the panel hinges occurred at about 8’10”. The disturbance in the satellite body velocity induced by the solar panel flexible modes lasted about 60 cycles causing spacecraft velocities mainly about the Z axis in the range 0.012 ÷ -0.01 rad/sec. As was expected on the basis of sub-system simulations and tests, these effects caused a reconfiguration of the gyro assembly. Spikes of total angular momentum reached about 16 Nms but did not activate the RCS based Detumble Mode because they were filtered by the DTM initialisation logic. This critical phase of the mission, autonomously executed by the spacecraft, lasted about 16’7” and was successfully completed at about 05:15:30 by the “Solar array deployed” command sent from the OBDH SW to the AOCS.

SAX remained in Acquisition Mode up to orbit 36 and the ground activity carried out during this period was devoted to the activation of the nominal S/S configuration, S/S check-out, EAC code verification and preparation for the activation of scientific modes. During this period all AOCS functions were nominal. OBDH interface was checked by the AOCS telemetry acquisition and by proper execution of AOCS telecommands. No triggering of any of the unit health checks occurred. Angular momentum unloading functioned correctly. Unloading was activated 9 times and the angular momentum was normally reduced from 3.5 Nms to 2 Nms within a time interval in the range 8’15” ÷ 18’39”. In two extreme cases, unloading remained active for as long as 1^{h}41’34” and 1^{h}10’25” apparently as a result of an unfavourable configuration of the total angular momentum vector which was nearly parallel to the average direction of the EMF.

The transition to a stable DPM was carried out during passage 36. A previous attempt was not successful because STRZ detected Polaris as a bright object and the AOCS fell back to EAC AM. The problem was successfully avoided by replacing the default guide star in the ACC database with a less luminous high declination star, Yildun (δ = + 86°35’10.8”, Mv = 4.4, Sp = A1V).

Polaris was restored as the default guide star before the end of commissioning, when the problem of bright object detection was solved by patching the brightness threshold in the STR database (Polaris is variable with the maximum visual luminosity of 1.9, which is just outside the nominal magnitude range of the STR).

The first slew performed to reach Yildun was about 14° long. The star was acquired in the first DPM mapping window at a distance of less than 1°20′ from the centre of the STR FOV. This points out to an excellent accuracy of attitude calibration in Acquisition Mode, especially the attitude with respect to the magnetic field which is affected both by errors in modelling the EMF and the effects of residual magnetic field generated by the spacecraft.

8 AOCS CALIBRATION IN ORBIT

The objective of the calibration procedures carried out in flight is to determine systematic errors due to factors, such as sensor alignment, that have direct impact on pointing and slew performance in the science operating modes of the AOCS. The sensors to be calibrated are the STR's and the gyroscopes, which together determine the performance characteristics of the subsystem. The onboard software database was primed before launch with values of calibration parameters corresponding to either ideal design settings (alignment) or measurements obtained during qualification tests by AOCS equipment suppliers. The objective of commissioning was to carry out the initial calibration of the AOCS, which is relatively more difficult than subsequent routine maintenance because of large ground-to-orbit variations in the values of parameters that must be calibrated. Subsequent calibrations make part of routine operational housekeeping and are outside the scope of this discussion (the discussion below indicates only what type of regular maintenance is required for individual parameters).

The following list summarises the parameters subject to calibration, and indicates for each of them the procedure used for calibration as well the impact of calibration errors on the performance of the AOCS. The parameters are listed in the order in which the calibrations were carried out during commissioning.

1. GYR drift.

Procedure. Calculate the average output of each gyroscope during a stable science pointing in which the attitude about all three axes is STR-controlled - with the average body rate maintained at zero by the controller, the result represents directly the drift.

Impact of errors. Uncertainties in attitude maintenance during STR occultation. Maximum errors allowed during operations are limited by the need to remain within APE requirements stated in Part I during the longest STR occultation of approximately 43′.

Maintenance. Continuous monitoring needed with updating as soon as variations become large enough to violate pointing requirements (APE).

2. Relative STR alignment.

Procedure. With the inertial attitude of the spacecraft maintained using gyroscopes, all STR's are commanded to find and track two stars each with a large angular separation in the FOV. The star vectors determined from the measurements are used to obtain the orientation of the internal reference frame of each sensor with respect to the equatorial coordinate system. Since the optical axes of the Z and Y STR's define the AOCS control frame, the transformations between the STR instrument frames automatically determine the relative alignment of the sensors.

Impact of errors. Change of attitude when control about a single axis switches between two STR's: transitory effect on RPE, persistent systematic error in APE.

Maintenance. No regular updating appears necessary. Occasional monitoring may be carried out to check for effects of secular and seasonal variations.

3. GYR scale factor and alignment

Procedure. A set of three slews about the principal axes of the spacecraft control frame is carried out. Each slew uses the special control strategy discussed in part I in which the inertial pointing of the slew axis is maintained using STR data (allowing the angular rate vector to have a nearly constant direction during the slew). The integrated GYR output of each channel is used to determine the direction cosines of the input axis, and its normalisation yields the scale factor.

Impact of errors. Inaccuracies lead to attitude errors during slews with amplitude proportional to the traversed angle. Maximum allowed error is limited by the requirement to place the target star within the STR search window at the end of the longest allowed slew (180° about X).

Maintenance. Nominally, scale factor calibration should be repeated approximately once a month. Post-commissioning data indicate better than required stability over the long term and indicate that less frequent calibrations are sufficient.

The following tables summarise the values of calibration parameters measured in flight with respect to pre-flight values entered in the onboard software database (gyroscope data include the currently used GYR6 rather than the nominal GYR2 replaced in flight). Table 1 quotes only the initial value of GYR drift. The orbit-to-orbit variations, which are one of the essential factors influencing the APE during pointings, are generally below 40″/h (except for GYR3). In general, during stable pointings lasting more than one orbit the drift stability is several times better. Variations at the indicated level have been observed after a change of attitude with respect to the

Table 1. GYR drift calibration (all values in °/h)

	GYR1	GYR6	GYR3	GYR4
Qualification test	-0.02	-0.25	0.48	0.46
First in-flight calibration	-0.28	-0.13	0.29	0.47

Table 2. GYR scale factor and alignment calibration

	GYR1	GYR6	GYR3	GYR4
Scale factor qualification(rad/count)	4.583×10^{-7}	4.545×10^{-7}	4.789×10^{-7}	4.745×10^{-7}
Scale factor in-orbit (rad/count)	4.578×10^{-7}	4.54×10^{-7}	4.786×10^{-7}	4.739×10^{-7}
In-orbit misalignment (deg)	0.25	0.18	0.25	0.21

Sun vector, which suggests that they are due to small changes in the external temperature of the GYR sensors and electronics. Only limited data are available on the stability of the GYR scale factors, since a long monitoring period is required. There are clear indications, however, that the stability is significantly better than the required value of 0.0004/months (in terms of relative scale factor error).

Actual in-flight performance

The two principal measures of pointing performance are the Relative Pointing Error (RPE) and the Absolute Pointing Error (APE) covered by requirements discussed in Part I. In flight, the RPE can be estimated directly from the output of sensors used in the control loop during normal pointings. The APE requires dedicated experiments in order to obtain an estimate of the absolute errors in attitude references used by the control (*e.g.*, the position of the optical axis of the STR). The results obtained for the two parameters are discussed separately below.

RPE

The worst case values observed in orbit for the principal factors that influence the RPE are listed below. RPE requirements for SAX are defined over intervals of **100 seconds**. The RPE is defined as an axis pointing error with respect to the average attitude over the reference interval. All the measurements quoted below refer to rotations about a single control axis; therefore, conservative worst case estimates of the RPE can be obtained by multiplying the values given below by $\sqrt{2}$.

- ***Control dead-band*** is defined by the discrete resolution of RWL torque commands and corresponds to no more than **3.25″** per control axis.
- ***Sensor noise.*** Typical 2σ values in flight are **0.5″ - 2″** (lower values are obtained for GYR-controlled axes) indicating sensor performance significantly better than required. Since the values are well below the control deadband, the effect on actual spacecraft attitude should be negligible.
- ***STR pixel boundary crossings.*** The largest discontinuity in star coordinates observed in TM is about **7″**. The effect on control is much smaller because of successful filtering by the state estimator.
- ***Disturbance due to MTR switching*** has a maximum amplitude of about **3″**.
- ***Effect of RWL zero crossing*** (causing a large disturbance in state estimation and control because of change of sign of RWL friction) has the largest values observed in TM of about **8″**.

The RPE is required by the specification of the SAX AOCS to remain below the 30″ threshold for 95% of the pointing time. Since the largest effects listed above can occur only sporadically (RWL zero crossings typically occur no more than twice in a single orbit), the RPE is normally limited by the actuator-determined deadband. At the required 95% level, the value obtained in flight is therefore about an order of magnitude better than the 30″ requirement.

APE

The technique used during the commissioning of SAX to obtain an approximate measure of the APE was based on a pointing during which STRZ was maintained in tracking mode locked on a guide star never obscured by the Earth, while its data were not

Table 3. STR misalignment

	STR Z	STR Y	STR -X
Misalignment (arcmin)	Reference (both coordinates)	Reference × 1.6	3.1 × 8.9

used for attitude control (the control loop used the orthogonal STR's and the GYR data).

The estimates of the main factors affecting the APE are listed below. As in the discussion of the RPE above, all error estimates below are for single axis control errors (except when indicated otherwise) and can be multiplied by √2 to obtain the worst case pointing error.

- **Thermal drift of STR optical axis** amounts to about **10″** and is consistent with pre-launch estimates.
- **Residual STR misalignment after calibration** is difficult to measure directly, but its values are likely to be similar to those obtained for optical axis drift.
- **Orbital aberration** displaces the stellar positions by up to **5″** at the SAX orbital velocity of ~7.5 km/s.
- **GYR drift variations.** The impact of the error depends on the AOCS sensor configuration during the pointing. Two separate cases must be considered. (1) Gyroscopes used for control about only one control axis (one STR remains available). The maximum occultation time of the second STR, during which attitude propagation has to rely on GYR data is 43′. With the worst case combination of errors on the individual GYR channels, the drift uncertainty of 40″/h leads to an attitude error of **58″** (since only the attitude about one control axis is derived from GYR data, this value represents the full attitude error). (2) Gyroscopes used for control about all three axes (all STR's obscured). The maximum duration of a three-STR occultation is below 20′ and the worst case effect of drift on the pointing error (including the multiplication by √2) amounts to **38″**.

Careful programming of scientific operations can reduce the impact of GYR drift errors on the APE by making sure that guide stars are defined for all three STR's during each pointing in order to minimise the duration of GYR-based control. The compound effect of all listed errors remains in any case below the requirement threshold of 1.5′. Although the measurements in flight have been carried out only for the Z axis (covered by the more stringent 1.5′ requirement), available data suggest similar errors also for the orthogonal axes.

Slew performance

A performance test consisted of a slew about the X (Sun vector) axis of 90°. Errors at the moment of guide star acquisition were below 2 pixels (80″) on both target STR's and were within the minimum approach error box of 90″ (STR search commands are sent when the norm of the three-axis error vector is within this error limit). This result was achieved after the first scale factor calibration which consisted of slews of only 21° (nominally calibration slews should exceed 50°; the reduction was due to relatively large misalignment errors which prevented successful execution of larger rotations). Several successful slews of approximately 180° have subsequently been carried out.

9 PROBLEMS AND RELEVANT SOLUTIONS

STRs problems & solutions

Background

The tracking of Yildun by STRZ has shown significant variations of the background level during the sunlight/eclipse and eclipse/sunlight transitions. The data collected by STRY in mapping mode with low limiting magnitude that were used to perform the on-ground attitude reconstruction were affected by a large number of background pixels with illumination levels above the detection threshold. Both phenomena pointed to the presence of stray light on the CCD in the sunlit portion of the orbit (maximum background levels reached about 260% of the nominal dark current, and the dispersion was 50% higher than nominal). A set of measurements have been performed to evaluate the worst case conditions for both affected sensors (STRY and STRZ) in terms of background level. For STRZ the background level is related to the angle between the Sun vector and the Z axis (SIA). For STRY no systematic trend as a function of Sun vector angle has been observed, probably because of shadowing by solar panels.

The increased STR background gave rise to the following problems:

- Uncertainty in the detection of the dimmest stars;
- Poor tracking of low luminosity stars;
- Detection of background pixels as stars.

The solution of the problem consisted of a modification of the STR SW which introduced adaptive background calculation during the star detection cycle (the nominal STR SW assumed fixed background during star searches based on the ground calibration of dark current). A feature of the existing STR SW, which reads out a 16×16 block of CCD pixels when the instrument is in stand-by mode, made it possible to obtain an estimate of the dark current in the star detection cycle without extensive modifications of STR SW. Dedicated measurements carried out in orbit showed that stray light illumination was not uniform on the CCD so that the position of the background evaluation window had to be variable.

The implementation of the workaround required modifications of both STR and ACC SW consisting of the following items:

- Use of adaptive background (derived in the previous cycle) during star detection (STR).
- Recalculation of star detection thresholds to account for the change in background calculation. Additionally, detection margins had to be widened to take into account the increased dispersion of the background (STR).
- Automatic commanding of STR in stand-by mode prior to a star search and patching of background window co-ordinates (ACC).

The increased margin in star detection thresholds had as an inevitable consequence a reduction of STR sensitivity from Mv=8 to Mv=7.3.

Dedicated procedure for efficient uplinking of modified software (including automatic down-loading by the OBDH) have been developed and tested on Alenia's facilities in Turin. The complete package (including other modifications of ACC SW discussed below) have been successfully tested in flight in the final phase of commissioning.

False events

A *false event* condition is reported by the STR SW during the tracking of a star in case of a sudden change of either the magnitude or the position of the guide star. The most likely cause of such events is the impact of high energy cosmic ray particles on the CCD. The filtering of single false events was implemented in the ACC SW, but in spite of the filter, during the commissioning phase several cases of lost tracking occurred. Two phenomena were observed:

- Long lasting false event (maintained for at least 2 cycles);
- Permanent false event.

The physical effect of particle impact that gives rise to both types of false events lasts for only one cycle and is removed when the star tracking window on the CCD is read out. The extension of the event to following cycles is due to the response of the STR software and depends on the position of the pixel affected by the particle impact with respect to the image of the guide star. Both types of false event problems have been solved by modifications of the ACC SW. Events of increased - but not permanent - duration are handled by increasing the filter threshold. The effect of permanent false events (which normally cause the termination of science pointings with a fallback to DPM) is avoided by automatically re-commanding the STR search after the event has been registered.

SEU

During the commissioning phase an unexplainable behaviour of STRX was observed when the value of star coordinates reported by the STR were outside the maximum physically possible range. After an STR code dump and a comparison with the reference file, a SEU (bit flip) in the STR RAM was detected. No error message was given by the unit because the autonomous run-time checks (data checksum, code flow, wrong op-code) were not triggered by the SEU. To restore the correct memory contents, the unit was switched off and on, and the software was reloaded (the code loaded from ROM does not contain the background workaround). Three more SEU events in the STR RAM have been reported after the end of commissioning (all on STRY), only one of which was automatically detected by the STR SW. An optimised recovery procedure was used in all these cases, in which only the locations directly affected by the SEU are reloaded from ground.

Visual and instrumental magnitude

Comparison between expected guide star magnitudes and the values reported by the STR software indicated significant differences (as large as 1^{m}), with the stars in general appearing brighter than expected. The effect has been alleviated by applying a correction function which predicts the instrumental magnitude on the basis of the visual magnitude of the star and its colour index, B-V. The correction accounts fully for the wavelength dependence of the transfer function of the STR optics. However, apart from the systematic effect due to STR optics, the observed magnitude discrepancies appear to be affected as well by uneven quality - and consequently large dispersion - of photometric data used in the guide star catalogue.

QSS problems & solutions

The Sun sensor has caused a number of health check triggers during the commissioning of the science modes of the AOCS. Some of the triggers indicated minor performance problems within the sensor itself, whereas others were related to the subtle tuning of health check thresholds. The list below summarises the most significant events.

Degradation of output current. The irradiation of the QSS window by the solar UV caused a gradual reduction of transparency in the early phase of the mission, which led to a corresponding reduction of the output current of all four QSS cells (there is no effect on the calculated Sun vector, since this relies on current ratios). On SAX, this degradation reached about 26.5% after 41 days in orbit and led to a safeguard trigger in passage 565. No further significant degradation has been observed. The problem was solved by a minor modification of safeguard code and an adjustment of sensor illumination thresholds.

Baffle displacement. A slew towards the edge of the extended domain (taking the Sun 44° away from the X-Z plane of the satellite) caused a trigger of the consistency check between the prime and redundant QSS. TM data indicated a growing error in the Sun vector angle measured by QSSB which set in at about 43.8° during the slew. Immediate analysis led to the conclusion that the error was due to the shadowing of the QSS sensor cells by the external baffle, which should normally set in only at the 45° limit of the nominal field of view of the QSS. Subsequent analysis by the supplier of the sensor (TPD) confirmed this conclusion and suggested that the external structure of the sensor was probably altered during launch. The redundant QSS remains in any case fully operational and slews to any target in the extended pointing domain (with Sun vector angles up to 45°) are possible with appropriately modified health check thresholds.

Earth albedo effects. Because of its wide field of view, the QSS is susceptible to relatively large errors when the Earth enters its field of view. These errors, which are difficult to calibrate by simulation and modelling, led to a number of spurious triggers of the GYR-QSS consistency check. The problem was solved by recalculating one of the thresholds of the check using data collected in flight.

Gyro 2 drift variation and Gyro 2 replacement.

A series of events, starting with a fallback from SPM to DPM in orbit 274, indicated that large variations were occurring in the drift of the one of the gyroscopes in the active control configuration used by the ACC SW. The science pointing which was autonomously aborted in orbit 290 for similar reasons provided extensive data for analysis, since the Z STR continued to track its guide star for several orbits also in periods when the attitude was controlled using only gyroscopes. The analysis of body rates derived from STR data supplemented by the output of the redundant gyroscope (GYR4) clearly identified GYR2 as the source of the problem. This analysis showed that during orbit 274 GYR2 underwent two short periods of about 3.5′ each when its drift changed by -1.0° ÷ -1.3°/h, followed by a third longer period lasting 25′ with a similar variation of drift. The analysis of the period leading up to the fallback in passage 290 revealed similar changes of the drift of GYR2, with duration as long as 100′. The amplitude of the variation was also increased up to -1.8 °/h which brought the total drift of GYR2 to about 2.5°/h. Since continuation of scientific pointings appeared impossible, the AOCS was commanded to fall back to AM. GYR2 was identified as unhealthy by the onboard GYR-QSS consistency check, which however triggered only during transitions between eclipse and sunlight when the sensitivity of the check to GYR errors is strongly increased by the inaccuracies in Sun vector determination. This pattern of health check triggers together with the results of consistency checks between the four gyroscopes indicated that the amplitude of the drift variations suffered by GYR2 remained contained within several °/h and therefore posed no immediate threat to the safety of the spacecraft. Since further use of GYR2 in science pointings was ruled out, the decision was nevertheless taken to replace it by one of the cold redundant gyroscopes in order to allow the mission to continue with a full complement of four hot redundant GYR channels. The GYR chosen for the replacement was GYR6, because its input axis lies in the +Z,-X plane (-cos 27.33°, 0, sin 27.33°) and is closer to the input axis of GYR2 than that of GYR5 (cos 27.33°, 0, sin 27.33°).

The replacement of GYR2 with GYR6 was carried out during visibility 313. The additional gyro is powered by the Primary Power Distribution Unit and it is switched on and off by a relay driver command which is directly sent from the central decoder. The replacement procedure uses the nominal OBDH protocol which dispatches commands to the AOCS SW. Each replacement sequence is composed of 69 (one gyro replacement) or 73 (two gyros replacement) macrocommands. The sequence modifies the MACS address table, corrects the gyro transformation matrices for the new direction of the input axis, and activates the gyro health checks with thresholds updated for the new gyro configuration. The macrocommand sequence is first loaded in the CTU memory and then downloaded by a special OBDH process into the ACC. The macrocommand transfer lasts about 18 seconds and is executed when the satellite is in safe configuration and the AOCS mode is BAC.

All modifications performed in the ACC RAM in order to install the new GYR configuration are lost in case of an ACC reset which restores the contents of the PROM into the RAM (HW reset, ACC switchover, BSW commanded SW reset). If two cold redundant gyros were included in the current assembly, the HW reset can result in a loss of control for the satellite. The solution to this problem was found by implementing a process inside the OBDH ASW which monitors the current AOCS status and recognises destructive ACC resets. If such a reset is detected, the OBDH ASW sends again to the ACC the MCMD sequence which performs the gyro replacement. This procedure limits the period in which incorrect GYR parameters may be used by the ACC to about 20 seconds and guarantees that no significant loss of attitude control can occur as a result.

The replacement procedure carried out in flight was ended when GYR2 was switched off. It is foreseen that its health status will be checked again during one of the future maintenance intervals.

10 AOCS STATUS AT THE END OF COMMISSIONING

At the end of commissioning, (13 July 1996), the AOCS configuration was different from the launch default only in a few aspects as summarised below.

(1) The gyroscope assembly includes GYR6 instead of GYR2, which has become a cold redundant unit still available for use in safety modes.

(2) GYR3 has been excluded from the current control configuration, but remains in hot redundancy. This decision was taken because changes of drift detected during commissioning make this unit insufficiently reliable for scientific pointings. The other gyro units (GYR 1,6,4) can be considered healthy with all characteristics remaining at least at nominal levels.

(3) The QSS's (both prime and redundant) have suffered a 27% degradation of output levels which, however, has no impact on Sun vector determination. The problem of QSSB baffle has been solved by specifying database patches to be used in extreme extended domain pointings. Both sensors remain fully available for use in attitude control.

(4) RWL, MTR and MGM are nominal. The PDU works properly and ACC health checks did not signal any anomalous behaviour.

(5) No SEU has been detected by the EDAC circuitry of ACCA. Cold redundant units, such as MGM2, ACCB, GYR5, RWL1, have not been checked during commissioning.

(6) The sensitivity of STRY and STRZ has been reduced from Mv = 8.0 to Mv = 7.3 for normal search/tracking commands in science pointings.

(7) AOCS SW has been modified during commissioning by uplinking a new release of EAC code, which has been generated and tested on Alenia's facilities in Turin. The software was loaded on board on July 8th and successfully commissioned during the subsequent week. The modifications introduced have been outlined in the relevant sections above. The BAC SW stored in ROM has been demonstrated to be reliable and no patches have been necessary. The updated values of database parameters modified during commissioning have been stored as a macrocommand sequence to be uplinked from ground if the ACC RAM contents are lost after a HW reset.

(8) The STR SW release 6.0 has been loaded in all three units. If the STR's are switched off (as happens after every ACC SW reset), the streamlined OBDH procedure discussed above is used to reload the STR SW.

11 LESSONS LEARNED

The work carried out during about 74 days of commissioning can be considered to represent nominal in-flight tuning of a very complex subsystem. The star tracker sensitivity reduction does not imply severe limitations of scientific observation because several work-around solution can be adopted in order to reach the planned target. The new application software release together with the new STR SW release can manage the problem of the high dark current on the CCD and permanent false events providing the necessary stability for scientific observations. GYR2, even though it has been switched off, is still considered to be a valid cold redundant unit available for future emergency use in safety modes. The robustness and the high degree of autonomy of the SAX AOCS design have been demonstrated by the autonomous and commanded mode transitions carried out during the commissioning. Measurements of pointing performance indicate that APE values can be improved further by optimising ground procedures for the updating of GYR drift.

The experience gained during the commissioning of SAX leads to several conclusions that may be useful in the development of future scientific missions.

- The AOCS SW requires the greatest possible flexibility so that in-orbit tuning can be carried out without modifying code. In particular, sensitive algorithms, such as spike filters, should be parametric rather than hard-coded.
- TM should guarantee full observability of critical events. In accordance with the usual practice, the SAX ACC provides two types of TM streams: intensive attitude reconstruction data (0.5 sec. sampling rate) and subcommutated housekeeping data (4-second sampling). A circular buffer can also be defined in the ACC RAM for user-selectable data. A user-selectable block in intensive TM (not implemented on SAX) would be of great value in analysing problems such as STR false events and guide star search failures.
- The ACC SW performed remarkably well during the early mission phase of SAX. Among the few problems that were encountered (especially threshold tuning), most are related to the effects of Earth albedo and sunlight/eclipse transitions on the Sun sensors. These happen to be the only aspects of the spacecraft environment that were not simulated during closed loop tests. Our experience therefore indicates once again that any features in the OBS not explicitly tested on ground are likely to require adjustments in orbit, whereas appropriate testing can increase the reliability of SW to nearly 100%.

ATTITUDE CONTROL SYSTEM EXPERIMENT ON ENGINEERING TEST SATELLITE - VI

Takeshi Sekiguchi,* Shinichi Ishikawa,* Masato Kudo*
Takashi Kida, Isao Yamaguchi****
Yuji Awa*, Yoshitake Yamaguchi******
**National Space Development Agency of Japan, Sengen2-1-1, Tsukuba, Ibaraki, 305, JAPAN*
***National Aerospace Laboratory, 7-44-1 Jindaiji-higashi, Chofu, Tokyo 182, JAPAN*
****Mitsubishi Electric Corporation,325 kamimachiya, kamakura, kanagawa, 247, JAPAN*
*****Toshiba Corporation, 1 komukaitoshibachou, saiwaiku, kawasaki, kanagawa, 210, JAPAN*

ABSTRACT

In order to establish basic attitude control technology for large flexible structures and satellites susceptible to dynamic disturbances, we conducted the Attitude Control System Experiment (ACSE) using Engineering Test Satellite-VI (ETS-VI) which was launched in 1994. The ACSE consists of several experiments such as Flexible Structure Control Experiment (FLEX). This paper outlines the results of ACSE, as well as the analysis of the data obtained by the experiments.

1. INTRODUCTION

In recent years, satellites have grown larger and larger and require higher and higher accuracy due to increased mission requests, increased amount of information, and progress in rocket launching technology. However, as space structures grow larger, various engineering problems arise. These include structural vibration, disturbances, and errors in structural parameters estimated on the ground.

As the satellites become large, and the stiffness decreases, the structures become flexible and easily cause vibration. In addition, frequency of the vibration approaches the attitude controller frequency. The satellites then become unstable because of the interference between the structural vibration and the attitude control. There are many natural disturbances, such as the gravity gradient, the solar pressure, and so on. In addition, there are disturbances caused by the large components in the satellite such as the large gimbals antennas. Moreover, the space environment is hard to simulate on Earth. Estimation errors are thus inevitable when the parameters are estimated by the ground test. Controllers using such parameters could become unstable because of the parameter errors. These problems must be solved to attain the proper attitude control of Large Space Structures (LSS).

In the near future, high-precision attitude control will be required for large flexible structures, satellites with large gimbal antennas, and satellites susceptible to dynamic disturbances.

With this concern in mind and in order to establish the basic attitude control technologies, we conducted Attitude Control System Experiment (ACSE) using Engineering Test Satellite-VI. ACSE consists of three experiments; Flexible Structure Control Experiment (FLEX), Torque Control Experiment (TRQCNT), and Attitude Control System using Antenna Pointing System Experiment (APSACS).

Proceedings Third International Conference on Spacecraft Guidance, Navigation and Control Systems, ESTEC, Noordwijk, The Netherlands, 26-29 November 1996, ESA SP-381 (February 1997)

2. EXPERIMENT SYSTEM

ETS-VI is a 2-ton, three-axis stabilized satellite. It is large enough to be regarded as a flexible structure. (Frequency of the solar paddle vibration is very low (~ 0.1 Hz)).

ETS-VI was launched by the National Space Development Agency of Japan (NASDA) using an H-II rocket in August 1994. Figure 1 shows the general view of the ETS-VI.

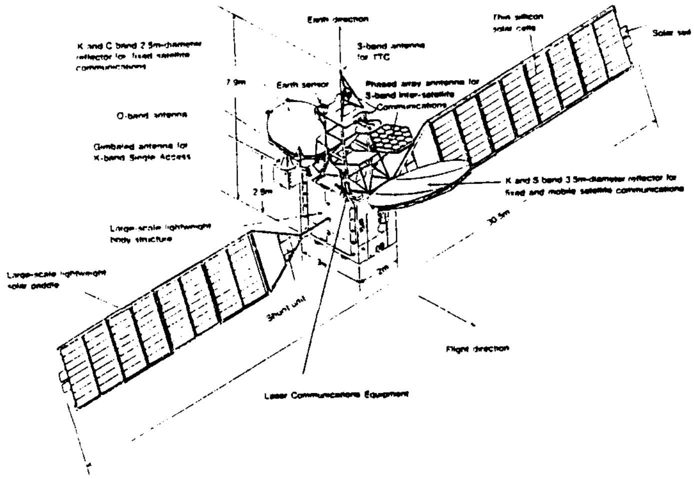
Earth direction
Thin silicon solar cells
K and C band 2.5m-diameter reflector for fixed satellite communications
S-band antenna for TTC
7.9m
Earth sensor
Phased array antenna for S-band inter-satellite Communications
O-band antenna
Gimbaled antenna for K-band Single Access
2.9m
K and S band 3.5m-diameter reflector for fixed and mobile satellite communications
30.5m
Large-scale lightweight body structure
Large-scale lightweight solar paddle
3m
2m
Shunt unit
Flight direction
Laser Communications Equipment

Fig.1 General view of the ETS-VI

ETS-VI was put into an elliptical orbit which differed from the originally planned geosynchronous orbit. The elements of the orbit are as follows.

Ascending node	80.9812	[deg]
Inclination	13.2869	[deg]
Semimajor axis	29999.2395	[km]
Eccentricity	0.5007	
Argument of Perigee	227.6421	[deg]
Mean anomaly	179.9977	[deg]
Perigee height	8601.9431	[km]
Apogee height	38640.2600	[km]

(March 1995)

In order to carry out the experiment, feasibility studies of the visibility from Japan, the relation of the location between the satellite and the sun, and many disturbances were conducted. The solar array paddle has to be fixed, and in order to maintain the electronic power, the angle between sun direction and the normal direction of the paddle must be within 30 degree, especially with FLEX. As a result, the experiment was replanned to be carried out in the orbit above the Indian Ocean.

Figure 2 shows the ACSE experiment system. The Attitude Control System (ACS), Reaction Control System (RCS), Launch Environment Monitor Unit (LEMU), and Telemetry Tracking and Command Subsystem (TTC) are utilized. The experiment is conducted by sending commands and the software for experiment from the ground. Data are also sent to the ground by TTC and LEM. The software for the experiment is loaded into RAM by re-programming from the ground. On the ground, the experiment is conducted from Tracking and Control Center (TACC) in Tsukuba Space Center (TKSC) using the Tracking and Control Station (TACS) from which the satellite is visible.

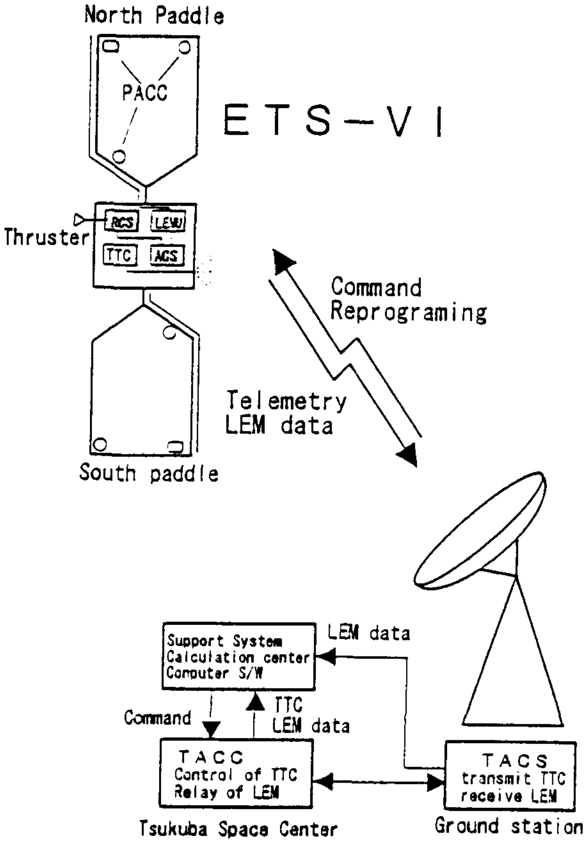
North Paddle
PACC
ETS−VI
Thruster
RCS
LEMU
TTC
ACS
Command
Reprograming
Telemetry
LEM data
South paddle
Support System
Calculation center
Computer S/W
LEM data
Command
TTC
LEM data
TACC
Control of TTC
Relay of LEM
TACS
transmit TTC
receive LEM
Tsukuba Space Center
Ground station

Fig.2 ACSE experiment system

3. FLEXIBLE STRUCTURE EXPERIMENT

FLEX consists of following three experiments.

(1)Observation of the solar array paddle extension
(2)Parameter identification experiment
(3)flexible structure control experiment

The information of the attitude and vibration is obtained from various attitude sensors (the Earth sensor, the fine sun sensor, the inertial reference unit, and the rate integrated gyro) and the Paddle Accelerometer (PACC) which is prepared for FLEX. Three PACCs are mounted on the edge of the solar array paddle, and detect the vibration of the out-of-plane mode, the in-plane mode, and the twist mode.

(1) Observation of the solar array paddle extension

The vibration of the paddle initiated by the extension of the solar array paddle and the several antennae for communication is observed using the PACC. The following are monitored by PACC:

- Solar array paddle full extension
- Main reflecting mirror and the sub-reflecting mirror of the 20 GHz antenna
- Main reflecting mirror and the sub-reflecting mirror of the 30 GHz antenna
- K band antenna

Figure 3 shows PACC response. From FFT analysis, the vibration frequency of the first order out-of-plane mode was founded to be 0.1 to 0.12 Hz. These data approximately agree with the data estimated on the ground.

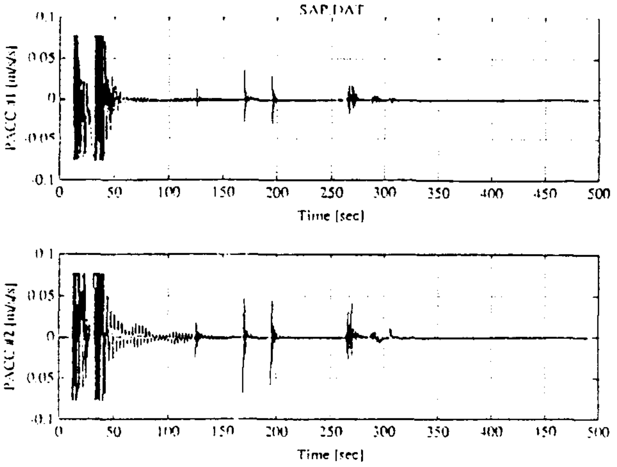

Fig.3 The response of the paddle extending monitor

(2) Parameter identification experiment

The parameter identification experiment aims to establish standards for designing satellite controllers, to evaluate the identification methods, and to compare the identified parameters with the parameters estimated in the ground test.

Acceleration data and Attitude Control System (ACS) data of the thruster-accelerated solar array paddle is used in this experiment. There are two kinds of the acceleration.

i) Impulse acceleration

In this case, thrusters are fired in bursts, which simulates impulse disturbance. The transfer function from the input to the output was then identified. From these data, analysis methods in time domain such as Eigensystem Realization Algorithm (ERA) method and Ibraham's Time Domain (ITD) methods are used to identify the flexibility parameter.

ii) Random acceleration

In this case thrusters are fired according to the M series signals, which is regarded as random disturbance. The transfer function from the input to the output was then identified. From these data, analysis methods in frequency domain such as FFT or maximum entropy methods are used to identify the flexibility parameter.

From these accelerations, we gathered attitude angle, angular rate, and the vibration data and identified the resonance frequency and the damping ratio. Figure 4 shows the response of the impulse acceleration, Fig.5 shows the random acceleration. Table 1 shows the result of the identification.

Parameters estimated on the ground were found to be close to the parameters identified in orbit, so the test technology for flexible structures on the ground was verified to be useful.

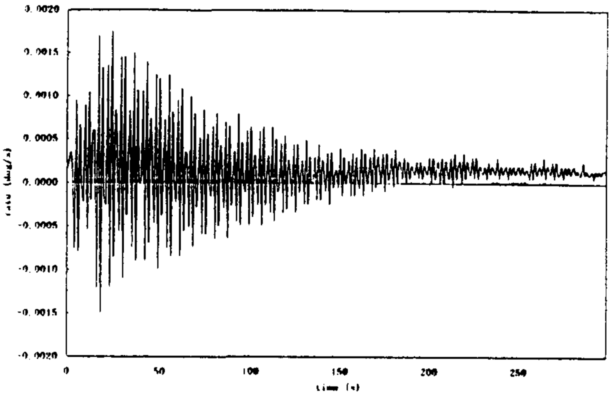

Fig.4 Response of the impulse acceleration

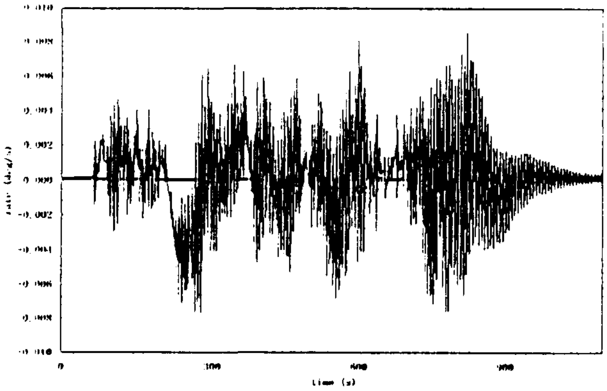

Fig.5 Response of the random acceleration

Table 1 Result of the identification

Mode	Ground test	On-Orbit -Identified		
	Frequency (Hz)	Frequency (Hz)	Frequency (Hz)	Damping Ratio
Out-of-Plane Syn 1st	0.106	0.0893	0.0938	0.45
Out-of-Plane Asyn 1st	0.197	0.163	0.164	0.57
In-Plane Syn 1st	0.263	0.2299	0.2286	0.33
Torsion Syn 1st	0.395	0.400	0.397	
Torsion Asyn 1st	0.398	0.393	0.398	0.47
I-Plane Asyn 1st	0.471	0.457	0.457	0.51
Out-of-Plane Syn 2nd	0.748		0.656	
Out-of-Plane Asyn 2nd	0.772	0.676	0.680	0.44
Torsion Syn 2nd	1.259	1.284	1.277	0.12
Torsion Asyn 2nd	1.260	0.390	1.371	0.42

(3) flexible structure control experiment

Control experiments aim to verify the efficiency and the effectiveness of the modern attitude control theory and to verify the fundamental controller design.

The problem in designing the controllers of the LSS is that the mathematical models usually include the uncertainty due to the truncation of high-frequency modes and parameter estimation errors. If the controller is designed with such uncertainty it might cause spillover and be unstable. Modern control theories are adopted to design robust stable controllers. In this experiment, several control theories are verified such as the H_∞ control, Frequency Shaping Linear Quadratic Gaussian control (FSLQG), Low Authority Control / High Authority Control (LAC/HAC), the non-collocation control using Paddle Accelerometer (PACC).Table 2 shows the operation.

The result of the LAC/HAC theory is presented below. In this paper, the result of the FS H_∞ control experiment is presented as an example of the control experiment.

Table 2 Experiment operation.

Date(UT)	Paddle angle (deg)	Experiment
1-16-1995	270	I-PD control, H_∞control
1-22-1995	270	FSLQG^{*1}, LAC/HAC control
1-25-1995	270	I-PD control, H_∞control
1-28-1995	270	FS H_∞control
3-17-1995	180	FSLQG, DVFB control^{*2}
3-20-1995	180	Non collocation control
3-23-1995	180	I-PD control, H_∞control 1DOF^{*3}, H_∞control 2DOF
3-26-1995	180	FSLQG, DVFB, LAC/HAC, H_∞control 2DOF
5-10-1995	180	Non collocation control, FS H_∞control
7-24-1995	90	FS H_∞control

*1 Frequency Shaping Linear Quadratic Gaussian

*2 Direct Velocity Feedback

*3 Degree of Freedom

The LAC/HAC controller has two feedback loops. The LAC loop guarantees the stability of the system, and the HAC loop achieves the high performance. In this case, the LAC loop adopts the Direct velocity Feedback (DVFB) control theory, and the HAC loop adopts the H_∞control theory. The H_∞ control adopts the mixed-sensitivity method and mainly controls the satellite attitude.

Figure 6 shows the response of the FS H_∞ control, and Fig.7 shows the Bode plot of the loop transfer function. The results of this experiment show that the controller achieves stability and high performance. The efficiency of this control theory has been verified. Similarly, other theories have also been verified.

The result of this experiment shows that the controller could realize the stable system and the high performance. In results, the efficiency of this control theory has been verified. Similar to this case, other theories have been well verified.

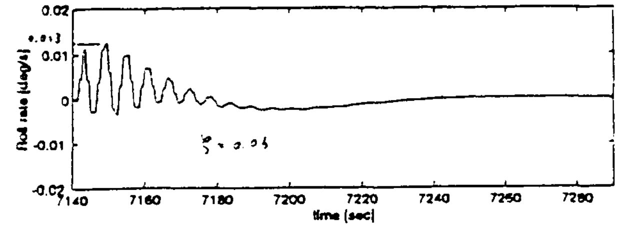

Fig. 6 Response of the FS H_∞ control

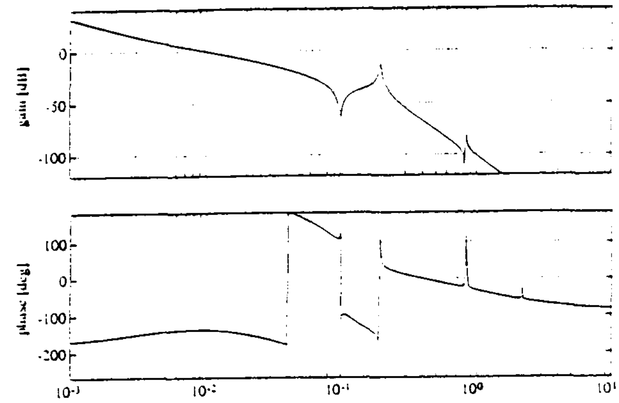

Fig. 7 Bode plot of the loop transfer function

4. Torque Control Experiment (TRQCNT)

TRQCNT estimated dynamic disturbances in an attitude control experiment using the solar radiation pressure imposed on the simulated solar sail. Opening and closing four sails using the shape keeping alloy generated the torque around the pitch and yaw axis by the solar radiation pressure. The concept of the solar sail control is shown in Fig. 8.

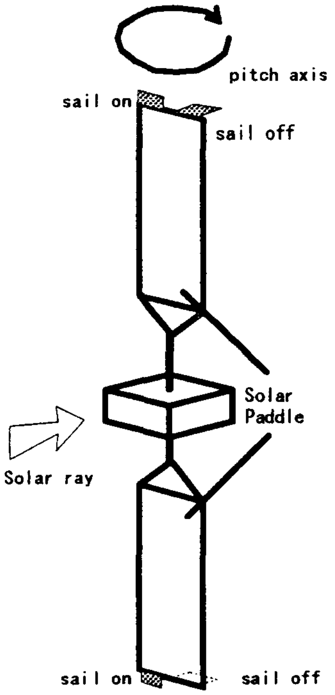

Fig. 8 The concept of the solar sail control

TRQCNT was used to conduct two experiments.

(1) Disturbance estimation experiment

The disturbance of the satellite is estimated by off-line analysis of the attitude data including attitude, rate, and the number of rotations of the wheel.

The opening and closing pattern of the sail is established according to the pattern of the estimated disturbance.

(2)Control of the disturbance experiment

Sails are opened and closed based on the opening and closing pattern. The ability of the decreasing accumulated angular momentum is verified.

Figure9 shows the angular momentum generated by sails. Although there isn't enough time in comparing the case on geosynchronous orbit, angular momentum generated 0.1 to 0.3 Nms and the angular momentum of the satellite changed. So the efficiency of disturbance control by sail was verified.

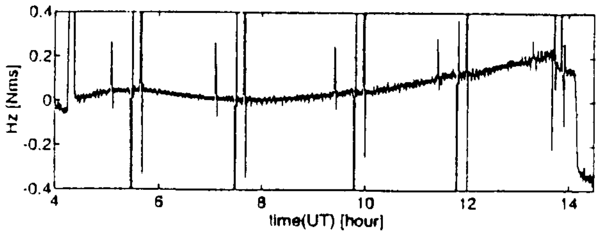

Fig.9 Result of the TRQCNT

5. Attitude control system using antenna pointing system (APSACS)

In order to establish the technology to control internal disturbances such as from large ginbal antennas, APSACS was used to conduct a feedforward attitude control experiment using the momentum signal from the Antenna Pointing System (APS) and the K-Band antenna. Figure 10 Shows the block diagram of the feedforward control.

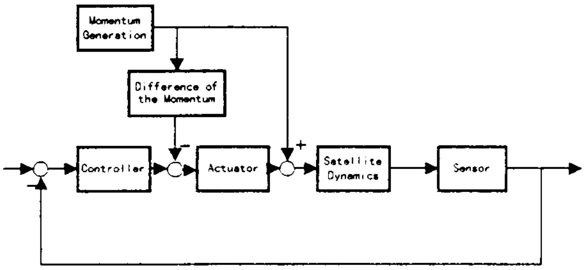

Fig.10 Block Diagram

Figure 11 and 12 shows the estimated control reference of the normal control and the feedforward control. As the figure shows, the change of the attitude by feedforward control is less than the normal control, so the efficiency of the feedforward compensation was verified.

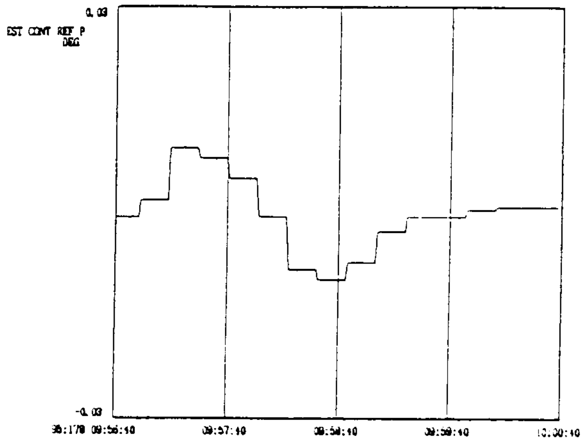

Fig.11 Ordinary control

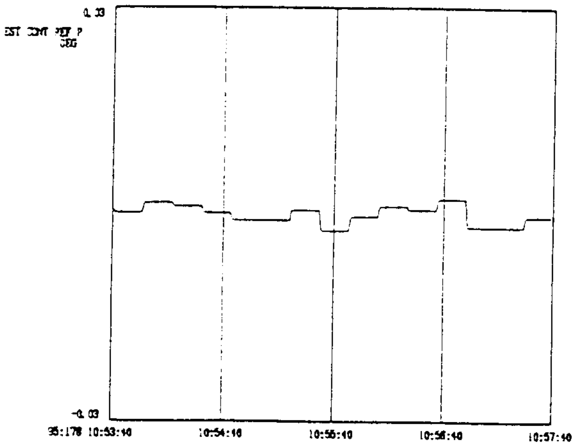

Fig.12 Feedforward control

6. CONCLUSION

Problems associated with LSS have been studied in great detail recently. However, there is very little data from the real structures or satellites in orbit. Although ETS-VI was put into an elliptical orbit instead of the originally planned geosynchronous orbit, all ACSE experiments were successfully conducted and we could obtain useful data. Through these experiments, actual data from ACSE will contribute to advancing LSS control technology. Finally we would therefore like to thank all those who supported these experiments.

Reference

[1] The final report of the joint research between NAL and NASDA, National Aerospace Laboratory and National Space Development Agency of Japan

[2] Flexible Structure Control Experiment on Engineering Test Satellite-VI, T.Suzuki, S.Ishikawa, T.Sekiguchi, S.Tanaka, S.Ichikawa, T.Kida, I.Yamaguchi, K.Komatsu, M.Sano, T.Kasai, Proceedings of the 39th Space Science and Technology Conference, 1995

[3] Survey on Control of Large Space Structure '86, Research Group on Control of Flexible Space Structures, 1987

THE USE OF MAGNETIC FIELD DATA TO ESTIMATE ATTITUDE AND TRAJECTORY FOR THE ROSSI X-RAY TIMING EXPLORER (RXTE)

Julie Deutschmann
National Aeronautics and Space Administration
Flight Dynamics Division/Code 552
Goddard Space Flight Center
Greenbelt, Maryland 20771
email: julie.deutschmann@gsfc.nasa.gov
fax: 301-344-8909

Itzhack Bar-Itzhack
Sophie and William Shamban Professor of Aerospace Engineering
Faculty of Aerospace Engineering
Technion-Israel Institute of Technology
Haifa 32000 Israel
email: ibaritz@techunix.technion.ac.il
fax: 972-4-823-1848

Abstract

Traditionally satellite attitude and trajectory have been estimated with completely separate systems, using different measurement data. Recently, trajectory estimation for low earth orbit satellites was successfully demonstrated in ground software using only magnetometer data. Since the earth's magnetic field is a function of time and position, and since time is known quite precisely, the differences between the computed and measured magnetic field components, as measured by the magnetometers throughout the entire spacecraft orbit, are a function of both the spacecraft trajectory and attitude errors. Therefore, these errors can be used to estimate both trajectory and attitude. This work proposes a single augmented Extended Kalman Filter (EKF) to simultaneously and autonomously estimate both spacecraft trajectory and attitude with data from the Rossi X-Ray Timing Explorer (RXTE) magnetometer and gyro-measured body rates.

In this work, we outline the derivation of the EKF, including both the measurement update and the propagation. Results from a 12 hour span of RXTE magnetometer and gyro data are processed by the EKF. Comparisons are made with very accurate operational estimates computed at the NASA Goddard Space Flight Center's Flight Dynamics Division. These comparisons are presented in the paper.

Many future low-budget missions, such as the NASA Small and Mid-Size Explorer Series are looking for low cost and autonomous approaches to orbit and attitude estimation. This work could prove valuable to these missions as a prime trajectory and attitude estimation system, with coarse accuracy requirements, or a backup to a prime system where more stringent accuracy is required.

Introduction

The magnetometer, due to its reliability and low cost, has been the focus of many studies in the recent past. Emphasis has been placed on using the magnetometer alone, without any additional input, to estimate the spacecraft trajectory (References 1, 2, and 3) and attitude (References 4 and 5). Studies have also been performed to determine the ultimate accuracy of the magnetometer in estimating attitude when accurate rate information is available (Reference 6).

Both attitude and trajectory have been successfully estimated using simulated magnetometer data and gyro data (Reference 7). Large initial errors were applied with resulting accuracies of 4 km (RSS) in position and less than 1 degree (RSS) in attitude. In this work, we

Proceedings Third International Conference on Spacecraft Guidance, Navigation and Control Systems, ESTEC, Noordwijk, The Netherlands, 26-29 November 1996, ESA SP-381 (February 1997)

continue the testing of Reference 7, applying the EKF to real RXTE data. The ability of the filter to overcome large initial errors is presented, along with the final accuracies achieved once the filter has reached steady state.

Extended Kalman Filter Algorithm

The EKF algorithm is based on the following assumed models:

System Model:

$$\dot{\underline{X}} = \underline{f}(\underline{X}(t),t) + \underline{w}(t) \qquad (1)$$

Measurement Model:

$$\underline{Z}_k = \underline{h}_k(\underline{X}(t_k)) + \underline{v}_k \qquad (2)$$

where $\underline{w}(t)$ is a zero mean white process noise, $\underline{v}_k$ is a zero mean white sequence measurement error, and $\underline{X}(t)$ is the state vector defined as

$$\underline{X}^T = [a, e, i, \Omega, \omega, \theta, C_d, \underline{q}]$$

The first six elements of $\underline{X}(t)$ are the classical Keplarian elements which determine the spacecraft position and velocity, namely, the semi-major axis (a), eccentricity (e), inclination (i), right ascension of the ascending node (Ω), argument of perigee (ω), and true anomaly (θ). C_d is the drag coefficient and $\underline{q}$ represents the attitude quaternion.

Measurement Update Stage:

The linearization of equation (2) results in

$$\underline{z}_k = H_k \underline{X}'_k + v_k \qquad (3)$$

where $H_k = [H_o \mid H_a]$

$X'_k = [a, e, i, \Omega, \omega, \theta, C_d, \alpha]$

H_o is the measurement matrix for the orbital states and is derived in Reference 1. H_a is the measurement matrix for the attitude states, $\underline{\alpha}$, a vector of three small angles, representing the error in the attitude estimate. The derivation of H_a is given in Reference 7. The effective measurement used by the filter is given as

$$\underline{z}_k = \underline{B}_{m,k} - \underline{B}(\hat{\underline{X}}_k, t_k) \qquad (4)$$

where

$B_{m,k}$ = the magnetic field vector measured by the magnetometer

$\underline{B}(\hat{\underline{X}}_k, t_k)$ = the estimated magnetic field vector as a function of the estimated state at time t_k

The estimated magnetic field vector is dependent on both the position and attitude, which is seen in the expansion of equation (3) in Reference 7.

The state update equation is

$$\hat{\underline{X}}_k(+) = \hat{\underline{X}}_k(-) + K_k \underline{z}_k \qquad (5)$$

where K_k is the Kalman gain computed according to

$$K_k = P_k(-)H_k^T[H_k P_k(-) H_k^T + R_k]^{-1} \qquad (6)$$

R_k is the covariance matrix of the measurement error, $\underline{v}_k$, and the covariance matrix of the estimation error is updated as usual with

$$P_k(+) = [I - K_k H_k]P_k(-)[I - K_k H_k]^T + K_k R_k K_k^T \qquad (7)$$

Equation (5) is used to update the orbital states, but not the attitude states. The update of the attitude states is done as follows. As shown above, the state vector contains the attitude represented by a quaternion. The EKF estimates an error in the attitude, expressed as $\underline{\alpha}$. The estimated error is converted to a quaternion and is appropriately combined with the current estimate of the quaternion to give an updated estimate of the quaternion, which is then propagated to the next time point.

Propagation Stage:

The filter dynamics model is given as

$$\underline{X}'_{k+1} = A_k(\underline{X}'_k)\,\underline{X}'_k + [\underline{w}^T_o \ \underline{w}^T_a]^T \qquad (8)$$

$A_k(\underline{X}'_k)$ is the transition matrix of the linearized dynamics equation. It is composed of A_o, the transition matrix for the linearized orbital dynamics and is a function of the estimated orbital states; and A_a, the transition matrix for the attitude error, $\underline{\alpha}$. A_a is based on the development from Reference 7. A_o is defined in Reference 8. The transition matrices A_o and A_a are first order approximations computed from the Jacobian $F_k(\underline{X}_k)$ derived from the linearization of equation (1).

The covariance matrix is propagated from time t_k to time t_{k+1} using:

$$P_{k+1}(-) = A_k(\hat{\underline{X}}'(+)_k)P_k(+)A_k(\hat{\underline{X}}'(+)_k)^T + Q_k \quad (9)$$

Q_k is the process noise covariance matrix for both the orbit and attitude states. The orbit and attitude states are propagated by solving equation (1) numerically, without the noise component

Results

The EKF was tested with 12 hours of real magnetometer and gyro data from the RXTE satellite. The data selected was from January 19, 1996, within a month of the launch. The spacecraft underwent a series of attitude maneuvers throughout the data span. Figure 1 shows the spacecraft attitude angles yaw, roll, and pitch, respectively. The attitude angles represent a 3-1-2 Euler rotation from inertial to spacecraft body coordinates.

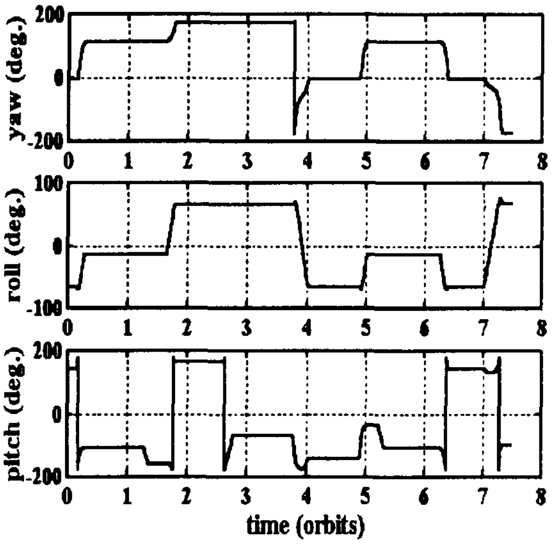

Figure 1: RXTE True Attitude

The filter was initially started with large errors in position, velocity and attitude. The initial RSS position error was 1425.4 km, the initial velocity error was 1.6 km/sec and the RSS attitude error was 17.2 degrees. The errors are determined by comparing the filter position, velocity, and attitude estimates to accurate position, velocity, and attitude estimates computed on the ground at the NASA Goddard Space Flight Center.

In an effort to improve the filter accuracy, the filter state was expanded to include a first order Markov process and bias component as was done in Reference 8, with the exception that the Markov and bias are uncoupled. The filter results, with the addition of the Markov and bias, are shown in Figures 2, 3, 4 (RSS position and velocity errors), and 5 (RSS attitude error). The final RSS position and velocity errors are reduced to averages of 25-30 km and less than 0.05 km/sec, respectively, and 1-3 degrees RSS for the attitude errors.

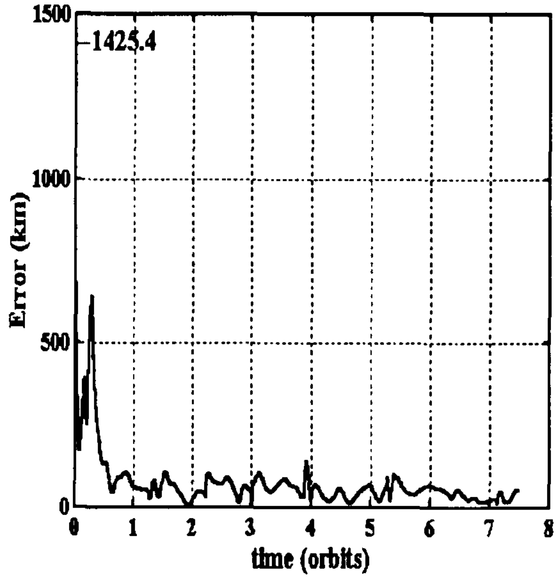

Figure 2: RSS Position Error

The steady state results of Figures 2, 3, 4 and 5 still contain significant error. One possible cause of these errors may be the strong correlation of the position estimate to errors in the attitude estimate. When there is an increase in the attitude covariance, as shown in Figure 6, the position error increases. The attitude covariance increases when the spacecraft undergoes an attitude maneuver, as would be expected. After a maneuver, the attitude estimate also must have time to converge to the new attitude, this too affects the position estimate. The final filter estimates are also dependent on the choice of the a priori state and a priori covariance and also the values selected for the measurement noise matrix and the process noise covariance matrix. Finally, the additional Markov parameters improve the final estimates but perhaps do not adequately model the disturbance in the measurement data.

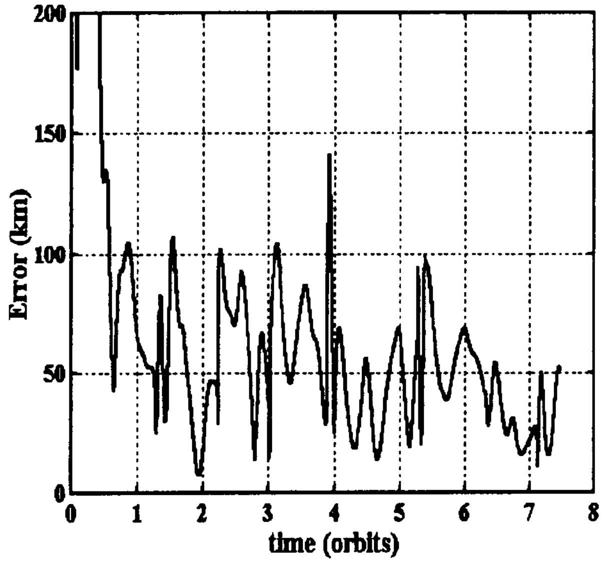

Figure 3: RSS Position Error with an Expanded Vertical Axis

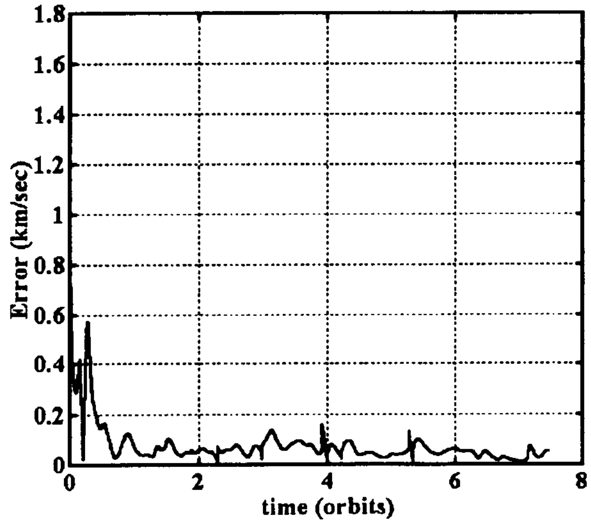

Figure 4: RSS Velocity Error

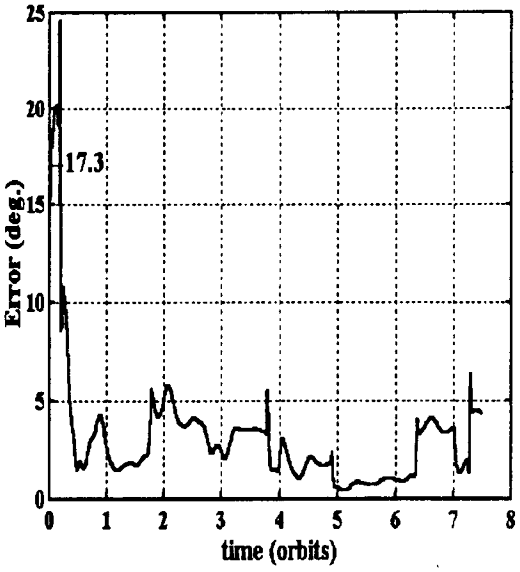

Figure 5: RSS Attitude Error

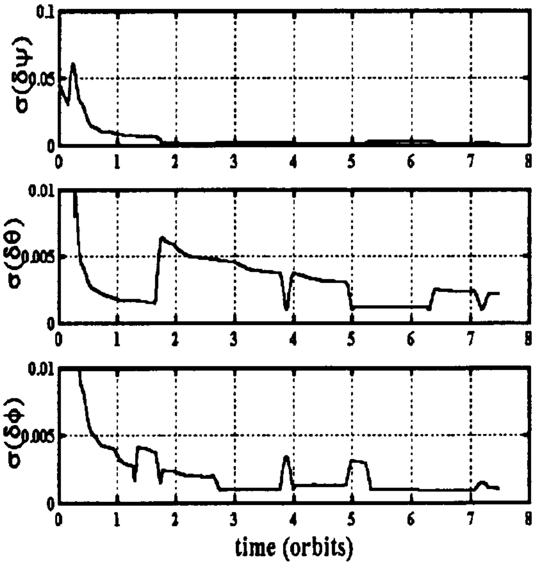

Figure 6: Uncertainty in Attitude Error

Conclusions

The EKF presented was tested with real magnetometer and gyro data from the RXTE spacecraft. The filter was able to overcome very large initial errors, 1425.4 km in position, 1.6

km/sec in velocity, and 17.2 degrees in attitude (all RSS), and converge to steady state averages less than 30 km in position, 0.05 km/sec in velocity, and 3 degrees in attitude (RSS). Due to several attitude maneuvers and unknown disturbances in the measurement data, the final errors could not be reduced further. Future testing on a longer span of RXTE data that is inertially pointing would help to determine the extent of the correlation between the position estimates and attitude error estimates, and additional analysis of the measurement data may identify additional disturbances that could be removed and thus improve the final estimates.

References

1. Shorshi, G. , and Bar-Itzhack, I., “Satellite Autonomous Navigation Based on Magnetic Field Measurements”, Journal of Guidance, Control, and Dynamics, Vol. 18, No. 4, July-August, 1995, pp. 843-850.

2. Ketchum, E., “Autonomous Spacecraft Orbit Determination Using the Magnetic Field and Attitude Information”, Paper No. AAS 96-005, presented at the 19th Annual AAS Guidance and Control Conference, Breckenridge, Colorado, February 1996.

3. Psiaki, M., “Autonomous Orbit and Magnetic Field Determination Using Magnetometer and Star Sensor Data”, Journal of Guidance, Control, and Dynamics, Vol. 18, No. 3, May-June 1995, pp. 584-592.

4. Challa, M., Natanson, G., Deutschmann, J., and Galal, K., “A PC-Based Magnetometer-Only Attitude and Rate Determination System for Gyroless Spacecraft”, Paper No. 07, presented at the GSFC FDD Flight Mechanics/Estimation Theory Symposium 1995, NASA Goddard Space Flight Center, Greenbelt, Maryland, May 16-18, 1995.

5. Martel, F., Pal, P., and Psiaki, M., “Three-Axis Attitude Determination via Kalman Filtering of Magnetometer Data”, presented at the GSFC FDD Flight Mechanics/Estimation Theory Symposium 1988, NASA Goddard Space Flight Center, Greenbelt, Maryland, May 10-11, 1988.

6. Hashmall, J., Liu, K., and Rokni, M., “Accurate Spacecraft Attitudes from Magnetometer Data”, Paper No. MS95/007, presented at the CNES International Symposium on Space Dynamics, Toulouse, France, June 19-23, 1995.

7. Deutschmann, J. and Bar-Itzhack, I., “Attitude and Trajectory Estimation Using Earth Magnetic Field Data”, Paper No. AIAA-96-3631, presented at the AIAA/AAS Astrodynamics Conference, San Diego, CA, July 29-31, 1996.

8. Shorshi, G. and Bar-Itzhack, I., “Satellite Autonomous Navigation Based on Magnetic Field Measurements”, TAE No. 714, Technion-Israel Institute of Technology, Haifa, Israel, April 1994

SESSION 2:
STAR SENSOR DESIGN

Chairman: P. Underwood (ESA/ESTEC)

3rd ESA Conference on Spacecraft GNC

TITLE: FURTHER INVESTIGATIONS INTO WIDE ANGLE AUTONOMOUS STAR SENSING USING THE MONTE CARLO METHOD.

by Dr.J.B.Crowden & D.M.Priestley,M.Sc.

MATRA MARCONI SPACE

Directorate of Science & Remote sensing

Engineering Division

Guidance Navigation & Control Department

Anchorage Road Portsmouth Hants

PO35PU England

Telephone 44-1705-704681, Telefax 44-1705-708290

Abstract

Following work on the Wide-Angle Autonomous Star Sensor (WASS) reported at the 2nd GNC Conference the software has been extended to take into account specific types of radiation-induced CCD defect, i.e. single pixel proton blemishes, pixel (dark current & sensitivity) non-uniformity, and the degradation in charge transfer efficiency to be expected during the mission. The autonomous star identification method used is based on a 44° diameter sensor field of view and a reduced star catalogue of only 200 stars in which star triads are recognised by matching the star separations observed with a short separations catalogue (2000 entries.). Work carried out on component asessment is capable of quantifying the defects induced by various levels of space radiation exposure but the type of modelling described in this paper is necessary to translate these findings into terms like successful star identification probability and rms angular pointing measurement noise and/or noise spectral density which are more meaningful to the spacecraft systems engineer. A tool is also provided for "software hardening" i.e. developing algorithms to recover, at least partially, sensor performance lost due to radiation-induced defects. Results presented include dependence of whole sky identification probability and of rms angular noise versus degree of radiation damage.

Key words: Spacecraft, Autonomy, Star sensing, CCD, radiation damage

1. Introduction

At the last ESA conference on GNC in April 1994, a paper was presented describing pattern recognition algorithms for use with a wide angle autonomous star sensor (ref 2). The results given at that time concerned reliability of acquisition (~98%), data rate (~5Hz) and overall error (50μrad rms, 15μrad rms noise). The duration of future satellite missions, especially geosynchronous communications satellites will tend to increase to levels of the order of 15 years. In assessing the suitability of such a star sensor for future applications it is now necessary to address the effect of CCD radiation damage, since this may be the limiting factor in its lifetime.

2. Radiation damage

2.1 Types of defect

Published results from previous research into the effects of radiation on CCD arrays has suggested that 3 main effects arise due to natural irradiation:

- A new fixed pattern dark current contribution over the whole CCD

Proceedings Third International Conference on Spacecraft Guidance, Navigation and Control Systems, ESTEC, Noordwijk, The Netherlands, 26-29 November 1996, ESA SP-381 (February 1997)

- Isolated "proton spikes" of high dark current with different statistics
- A general increase in charge transfer inefficiency, (CTI)

This paper sets out to address the effects of these types of CCD defect in terms of star sensor performance degradation meaningful to the attitude control engineer who may wish to assess the suitability of WASS for long life missions.

The estimates of the most likely effects resulting from radiation-induced CCD defects have been made in consultation with Dr. S.Watts and Professor A.Holmes-Siedle of Brunel University, who have made available the results of their extensive researches into this subject. After studying this work in detail, the main effects may be summarised as follows:-

The total dose received, measured in terms of deposited ionisation, is composed mostly of Bremsstrahlung from which the effects are limited to chemical changes in the surface dielectrics which causes an increase in dark current. The effects of surface leakage can be highly reduced in MPP CCDs operating in slow scan in the inverted mode but not where integration times are short and readout is continuous. Dark current is not a major problem at these speeds and thus does not indicate troublesome damage to the CCD.

The greatest influence on performance is caused by bulk damage, which can affect many important electrical parameters. Bulk damage is caused mainly by the the Proton flux arising from either primary Cosmic Ray or Solar particles which can become trapped in the Radiation Belts. These protons can also eject secondary neutrons in the CCD shielding and either particle can cause damage to the CCD crystal lattice structure. The main effects on CCD performance are:

1. An increase in the level of dark current. This normally follows a Gaussian distribution but, after irradiation, an additional gaussian distribution with different parameters and a tail of much higher than normal dark current are added. This is mainly composed of Proton Spikes, which are isolated pixels with increased dark current. This contribution to the dark current is the one most likely to reach the threshold of detection in a Star Sensor. The shape of this modified distribution has been assessed by reference to the results of irradiation tests carried out by Brunel on CCD samples and approximates to the additional dark current gaussian plus a much broader gaussian spread of the logarithm of the damage level. The intensity of all these effects is related in different ways to total dose. MMS have assumed that the highest damage level (log gaussian) component simply accumulates in more pixels pro rata as the dose increases.

2. An increase in the Charge Transfer Inefficiency (CTI). This represents the charge left behind in the previous pixel during the transportation process. This causes an asymmetric smearing effect on the shape of the Star Spot Image which, in turn, has an adverse effect on the accuracy of determination of the Star Centroid coordinates. The effect is present in both axes, but is generally worse in the frame transfer direction than in the line readout register.

2.2 Radiation-induced dark current

Normal CCD dark current varies from pixel to pixel and can be considered to follow a Gaussian distribution. It has a mean and standard deviation broadly in line with the basis used in the 1993 paper. The advent of MPP inverted mode CCDs with reduced dark current has not materially changed the picture as far as attitude sensors are concerned because the need for rapid data necessitates a readout process, during which inverted mode cannot be used. This produces a source of noise which dominates that produced during the integration time.

The effect of radiation is to build up a new noise distribution, normally distributed again but with different mean and standard deviation parameters from the normal dark current noise. This process can be modelled by adding code identical to the normal dark current model but drawing its parameters from new elements in the data array.

2.3 Radiation-induced spikes

The so-called proton spikes constitute a third dark current effect with a higher mean and a much larger standard deviation but affecting only a limited number of pixels, depending on the radiation dose. This process has been modelled using a log Gaussian MonteCarlo draw method but with the total number of damaged pixels restricted to correspond to the experts' predictions with one or two arbitrary safety factors.

2.4 Degradation in charge transfer efficiency

An increase in CTI will result in a slight tendency to smear images arising in the parts of the CCD remote from the readout corner(s). Since the impairment of the charge transfer is a general and gradual process affecting the whole CCD its effect on the star centroid coordinates will be to cause a bias error proportional to the remoteness of the source pixels. This will produce an effect on the data similar to a slight change in scale of the CCD dimensions. If a simple diagnostic test was available indicating the extent of the change in each axis, such a change could be corrected by just two telecommands. It would be possible, for example, to run the star separation search with two or more close but different scale factors and to telecommand a shift towards the change giving the better match statistics.

In order to assess the effects of impaired charge transfer efficiency on the Sensor performance, a simulated degree of smearing of the star spot image has been modelled, based upon the predicted increase in CTI during a typical mission of interest. In addition, an investigation of the damage threshold of uncorrected scale factor changes has been carried out to provide a rationale for the choice of tolerance and frequency in making telecommanded scale factor corrections during the satellite life.

3. Description of WASS simulation

The present work is a further development of an existing Monte-Carlo simulation model, which was originally produced to demonstrate the feasibility of using Autonomous Star Sensors for spacecraft acquisition and control. The results were reported at the previous ESA GNC conference in 1994 (ref 2). The model contains a simulated CCD sensor head with parameters arranged to be as realistic as possible. It is based upon a frame transfer CCD of active area 1000x1000 pixels, which should be available and qualified in time for a future space mission. An objective lens of 28mm. focal length will give a field of view of 43x43 degrees. This is optimised to give the best compromise between sensor accuracy and size of star catalogue.The field of view of each pixel will be 162 arcseconds, which should yield an rms. accuracy of 8 arcseconds after centroiding. The modelled CCD has been attributed with dark current and noise values based upon manufacturers data and results from tests on similar real sensors.

The next stage is to project simulated star images on to the CCD array from a star catalogue which defines the positions and intensity of the stars within the field of view. During the Monte-Carlo process the sample area of sky selected is different each time. The shape of the projected simulated star spot profile has been modelled by reference to experimental observations during previous projects in which the size was optimised to give the best centroiding accuracy. The light inputs to each pixel from the idealised star spot are then processed to give the CCD sensor response taking into account all the modelled defects and noise sources. It is normally sufficient to retain only the 256 brightest pixels from the array output for further processing.

The star identification and attitude determination process is based upon measuring the separations between the centroid coordinates of each pair of simulated star spot images.These are then compared with an ordered star separations catalogue to identify the source objects The correct identification is confirmed by forming the separations into triangles ,known as "triads". If the same triad can not be reproduced from the separations catalogue entries, the "connectivity test" is considered to have failed, and the search is extended to the neighbouring entries in the catalogue. Normally the search process finds a three star match (triad) before the tolerance limits of the separations search have been reached.

The Monte-Carlo analysis involves repeating the above process many times with a random selection of the sky field and all the other sensor and noise source parameters.This enables the success rate, reliability and accuracy of the modelled sensor to be estimated. The object of the present study is to extend the model to include realistic radiation damage defects and to measure their effect on sensor accuracy and detection performance.This has been done by comparing the results from simulations carried out with and without the modelled radiation degradation effects.

4. Radiation damage models

4.1 Radiation induced dark current

A further addition to the simulation model has now been made to take account of the increased dark current produced by the exposure to radiation This has been based upon the results of radiation damage evaluation tests carried out by Brunel University (ref 1). These show that the dark current normally follows a Gaussian distribution. After irradiation the main component of the dark current is still a Gaussian distribution but the mean level is now higher depending on the level of radiation exposure. Consequently, the Monte-Carlo runs to simulate performance after irradiation were done with a mean level of dark current increased to the value expected at end of life for the model mission. However, even with this increased mean level it is expected that the dark current will still be well below the threshold of detection except for the extreme limits of the tail of the distribution.With the relatively bright stars in the proposed catalogue this can be set at a high enough level.

4.2 Radiation induced Proton spikes

A more significant effect on the sensor performance is likely to arise from the effect of protons which can cause bulk damage to the silicon lattice structure. This results in isolated pixels with much larger dark current.The effect is to produce a tail to the dark current distribution extending towards the higher levels. The shape of this extended tail has been estimated from the results of the Brunel Univ. tests. It was found that the most convenient mathematical simulation was achieved by assuming that the log of the proton spike amplitude followed a Gaussian distribution. By selecting appropriate parameters it was possible to produce a shape to the frequency distribution which fitted the experimental data.

The total number of proton spikes to be expected was calculated, taking into account the CCD area, the radiation level, and the proposed mission duration.This contribution was then added directly to the general Gaussian distribution produced in the previous section

4.3 Radiation-induced CTI

The other important degradation in CCD performance resulting from radiation, is an increase in the Charge Transfer Inefficiency (CTI). This represents the charge left behind in the previous pixel during the readout transportation process. It causes a smearing effect on the shape of the Star Spot Image, which has an adverse effect on the accuracy of determination of the Star Centroid coordinates.

The effect of this smearing on the attitude determination accuracy has been estimated by calculating the change in shape of the star spot image profile which would result from the estimated increased CTI value at end of life . By applying the expected charge shift, as measured in the Brunel tests, to the ideal image spot profile, the End of Life shape can be calculated. This is now slightly skewed owing to the smearing, and a shift in the Centroid coordinates will be caused. The magnitude of the expected shift has been calculated by applying the centroid algorithm to the simulated skewed star spot image. The attitude measurement error resulting from this will be proportional to the number of pixels which the charge has been shifted through, in each axis. This has been built into the Monte Carlo simulation model as an additional modification to the data, enabling the occurrence of misidentifications and attitude errors to be assessed. Since the CTI changes will produce systematic bias errors with a linear spatial relationship, it should be possible, in a real spacecraft application, to introduce a correction by periodic calibration during the mission.

5. Results

5.1 Effects of increased dark current and proton spikes

The first series of simulations was carried out to assess the effect of radiation induced background noise on the sensor performance. Each run consisted of 2000 Monte-Carlo drawn events with a realistic statistical spread in noise and performance parameters.

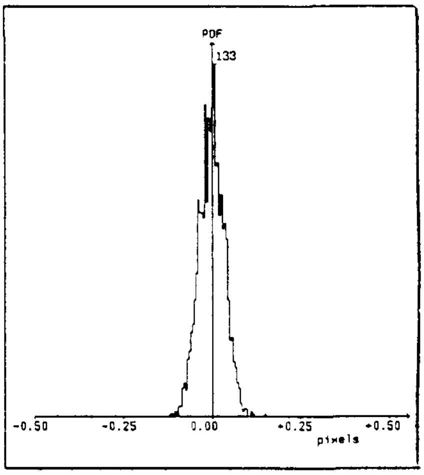

Figure 1 Sensor performance before degradation

Figure 1 shows the results from the first run which represents the normal CCD noise levels to be expected at the beginning of life, before the exposure to radiation. This can be taken as a baseline level of performance to enable the degradation to be measured. The histogram on the left shows the attitude error as the difference between the true sensor boresight based upon star positions from the star map

and the sensor boresight calculated from the star positions as measured by the sensor. In this case the rms. error was 0.035 pixels representing 5.7 arcseconds for the real sensor. This would be a very satisfactory performance for a geosynchronous communications spacecraft. The number of correct triad identifications out of 2000 frames was 1985. In a real case most of these errors would be corrected at the next data frame.

Figure 2 shows a similar run with a realistic level of damage for a typical geosynchronous mission. This includes the expected increased general level of dark current and randomly distributed proton spikes. The estimated number of proton spikes at end of life was 1500. The number of successful identifications at the first frame has now fallen to 1959, and the.rms. attitude error is almost identical at 0.036 pixels. This suggests that a realistic level of radiation would produce very little effect on sensor performance, probably because the induced noise is still well below the minimum star intensity of interest, and will be rejected by the detection threshold.

	Clear	Dark current and proton spikes						CTI Smear		Total
Parameter	0	1500	5000	10000	20000	35000	50000	0.05	0.5	1500 0.05
No. of events	2000	2000	2000	2000	2000	2000	2000	2000	2000	2000
Number of successes	1985	1959	1851	1687	1499	1338	1259	1984	1982	1959
Proton spike errors	0	23	125	299	485	651	726	0	0	26
Attitude error	0.035	0.036	0.038	0.037	0.042	0.045	0.045	0.043	0.257	0.045

Table 1 Summary of Damage Effects

The result suggests that only proton spikes are ever likely to exceed the threshold during a real mission.

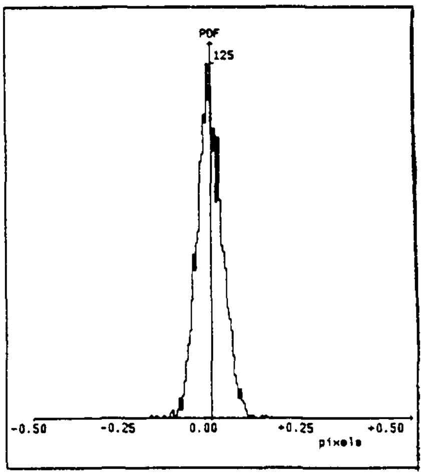

Figure 2 Performance with 1500 proton spikes

In order to assess the margin, further simulation runs were carried out with the numbers of proton spikes increased to 5000, 10000, 20000, 35000, and 50000. The results are summarised in table 1 and show that the reliability of successful attitude determination gradually decreases owing to the presence of large numbers of spurious single pixel events in the data. The worst case run with 50000 spikes represents a factor of 33 higher than the expected levelof damage. In this case, the number of successful identifications had fallen to 1259. However, even with this extreme damage level, the attitude determination error had only increased to 0.045 pixels, or 7.3 arcseconds. This indicates that the main effect of proton spikes is to reduce the reliability of detection, while the attitude determination accuracy remains relatively unaffected.

5.2 Effects of degraded charge transfer efficiency

The second series of Monte-Carlo simulations examines the effect of star image smearing due to degradation in charge transfer efficiency. In this case the model was modified so as to shift the measured star centroid positions laterally by an amount which was linearly dependent on the CCD array coordinates.

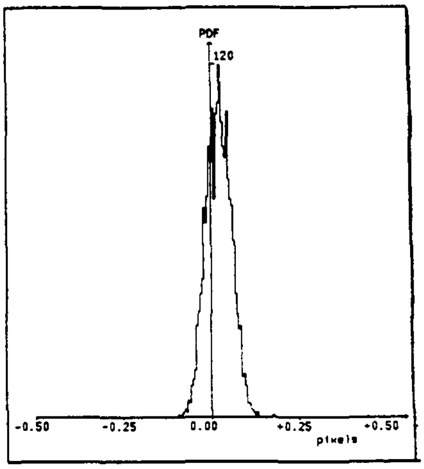

Figure 3 Performance with predicted CTI level

The results for the realistic level of smear are shown in figure 3. The number of successul identifications was 1984 out of 2000. This is virtually unchanged from the control run with no degradation.

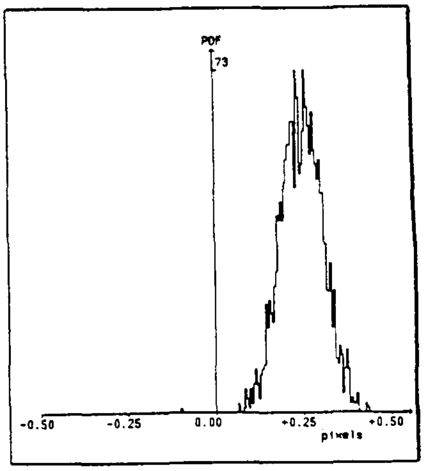

Figure 4 Effect of severe increase in CTI

The attitude determination error has increased from 0.035 pixels to 0.045 pixels, or 7.3 arcseconds. This small but significant reduction in accuracy would still be acceptable for a communications mission. In order to assess the margin a further run was carried out with an image smear of 10 times larger than the predicted value. This amounts to a centroid shift of 0.5 pixels at the furthest corners of the array.

The results, shown in figure 4, show a mean error of 0.257 pixels, as would be expected. Even with this large amount of shift, the number of successful identifications was 1982 out of 2000, illustrating that the main effect of smear is on the attitude error and not on the reliability of acquisition.

5.3 Combined effect at geostationary altitude

The final run was to estimate the effect of the simultaneous presence of realistic end of life levels of dark current, proton spikes, and image smear.

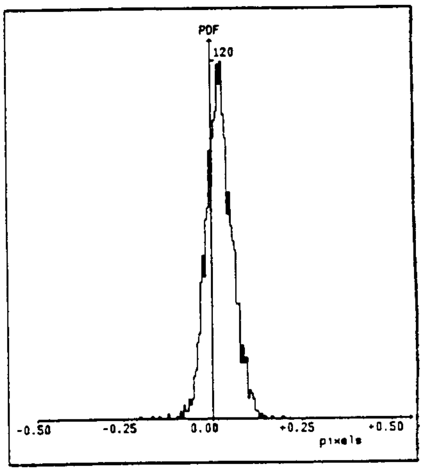

Figure 5 Predicted overall performance at End of Life

The results shown in figure 5 show that the success rate was 1959 out of 2000 and the attitude errror was 0.045 pixels or 7.3 arcseconds. These results show that satisfactory performance is still likely to be achieved at the end of a 15 year mission at geostationary altitude.

6. Conclusions

The overall impression to be gained from the results of the investigations is that a satisfactory sensor performance can still be achieved at the end of life of a geosynchronous communications mission. The greater effect on the reliability of acquisition is most likely to be caused by the presence of large number of pixels which have been damaged by proton collisions. However this would require a much greater level of radiation than the predicted value. and once acquisition has been achieved, the attitude determination accuracy is largely unaffected by the presence of the additional blemished pixels.

The degradation in charge transfer efficiency causes a smearing effect on the star spot image which has the greater effect on the spatial measurement accuracy. However the results show that there is little effect on the reliabilty of acquisition from this source. Also the centroid shift can be measured in flight and corrected.

When all the degradation effects are present at realistically predicted levels, the expected performance is still satisfactory at the end of mission life. The simulations carried out at artifically high levels of predicted radiation damage serve to show the performance margin, or to give an indication of what would occur during a mission of more intense radiation environment. This might apply to an interplanetary or other long duration mission.

7. Recommendations for further work

7.1 A tool for sensor development

Although very good reliability and accuracy is indicated by the existing results there is no doubt that reliability could be increased by further work. For example no use is currently made of the spare contiguous pixel group identified in the present software in case the triad contiguity tests reach the search bounds without success. A fourth group could be used as a health check to secure a highly reliable rejection of false triad identifications of which a few appear in each 2000 run sequence.

Other topics of value for future research include variable separation search bounds according to the separations catalogue density, removal of unsuitable star patterns from the tagged star and separations catalogues, logarithmic and/or correlator pre-processing of the video data in currently available hardware and an optimisation of the search bound parameters.

7.2 Improvements in radiation modelling

The simplified radiation models used in this paper leave some room for improvement and better data are continually becoming available as further work on CCD damage and radiation hardening is funded. A reexamination of the situation would be appropriate following the availability of any significantly updated CCD damage assessment.

7.3 "Software Hardening"

This self-contradictory expression has been invented to describe the developments of modifications to the processing algorithms which succeed in reducing the impact of radiation damage on sensor performance. One example already mentioned is the automatic identification and correction of pixel scale changes due to worsened CTI. A further example is the following:

When the effect of the really high proton spike levels is examined it becomes clear that, although the existing processing algorithms have been designed to reject single pixels classified as of signficant brightness in the initial thresholding, such pixels can ultimately flood out the useful data from the set of 256 brightest pixels currently employed. If the processing software is elaborated to generate a video gain-setting output to the threshold circuit prior to the ADC then the number of selected pixels can be adjusted in software and can be increased in circumstances where there is a flooding-out danger, without significantly increasing the processing time.

7.4 CCD versus Active Pixel Sensors (APS) over the next decade

Although current APS developments promise versatile hardened detectors with non-destructive readout, ultimately making the CCD obsolete, existing CCD technology has a lead of some 10 years The CCD sensor, on the basis of the predictions made in this paper, should have a further life of at least 10 years, probably more, bearing in mind the general reluctance of major programme managers to take on-board the risks associated with any new product. The work reported in this paper, and the suggested refinements, should remain of interest for most of this time.

When the APS detectors finally mature the work on pattern recognition algorithms and the tool for investigation of the disruptive effects of defects will remain applicable to the new sensor developments.

8. References

(1) A Wide-angle Autonomous Star Sensor for

Satellite use

Cope P, Crowden JB ,Priestley DM.

Matra-Marconi Space(UK)

2nd ESA International Conference on Spacecraft

Guidance Navigation and Control Systems

(2) Radiation damage evaluation of Loral CCDs for

the Visible IR Spectrometer (VIMS-V) on the

Cassini spacecraft

S.J. Watts, A. Holmes-Siedle, and

A. Mohammadzadeh. Brunel University

Brunel report No. BRU-CRD-95-4 10 August 1995

INTELLIGENT MODULAR STAR AND TARGET TRACKER - A NEW GENERATION OF ATTITUDE SENSORS

U.Schmidt, D.Wunder, E.Graf

Jena-Optronik GmbH, Prüssingstr. 41, 07745 Jena
Phone: (++49) 3641 200-0, Fax No. (++49) 3641 200 222
e-mail uwe.schmidt@djo-jena.de

ABSTRACT

Star sensors developed in the last years can be enhanced in terms of mass reduction, lower power consumption, and operational flexibility by taking advantage of improvements in the detector technology and the other analog/digital electronics components. The Jena-Optronik GmbH (DJO) is developing an Intelligent Modular Star and Target Tracker. Emphasis will be placed to increase the sensor adaptability to meet specific mission requirements.

There are some new features in the sensor design. The Intelligent Modular Star and Target Tracker shall generate positional information regarding a number of celestial targets or shall act as a navigation camera. The targets will be either stars or extended objects like comets and planetary objects, or both simultaneously.

The technical approach for the Intelligent Modular Star and Target Tracker will be presented in detail in the scope of this paper.

Because of the modular concept the sensor can be adapted to different mission requirements. One of the potential target missions is Rosetta, where star tracker as well as navigation cameras are required.

1. INTRODUCTION

The headline of this paper speaks about an intelligent modular star and target tracker as a new generation of attitude sensors. We have to answer the question: What's new on the herein presented sensor?

To come straight to the result, the new features are the low budgets referring to mass, volume and power at a high measuring performance, the modular concept and the flexible use because of the wide field of view design in connection with a high accuracy. Therefore the modular star and target tracker can be configured as a simple tracker up to an attitude determination sensor or a navigation camera.

The project, under which the development activities at DJO are running, is split into two phases; phase 1 which will conclude with the realisation of a fully detailed instrument design at the end of 1996 and phase 2 which covers the manufacturing and functional tests. The sensor will be available at the end of 1997.
The project is running under the ESA GSTP programme with the abbreviation SETIS - Stellar Extended Target Intelligent Sensor.

The aim of the development activities is to design, manufacture and test an upgraded and enhanced CCD star and target tracker based on modular design principles. Special attention is paid to autonomous attitude determination features.

Figure 1 shows the final mechanical outline of the sensor.

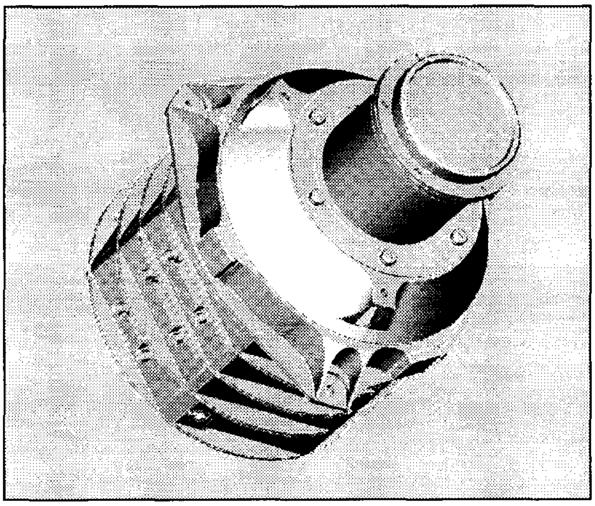

Figure 1: Mechanical outline of the sensor

The main design requirements were:

Field of View:	10° x 10°...20°...20°
Accuracy:	Noise ≤ 5.0 arcsec (2 sigma) Bias ≤ 5.0 arcsec (2 sigma)
Update Rate:	Attitude Determination ≥ 2Hz Single Bright Star Tracking 10Hz
Detector:	charge coupled device (CCD), frame transfer type, electronic shutter, anti-blooming, integrated Peltier cooler
Sensitivity Range:	-5.0mv up to the necessary lower limiting magnitude
Budgets:	Mass ≤ 3.0 kg Power ≤ 7.0 W
Size:	≤ 150x150x220 (L x W x H) [mm]

Proceedings Third International Conference on Spacecraft Guidance, Navigation and Control Systems, ESTEC, Noordwijk, The Netherlands, 26-29 November 1996, ESA SP-381 (February 1997)

Besides this standard star tracker requirements some special features were required which will become *design drivers* during the system analysis.

Firstly, the celestial objects to be tracked are stars as well as extended objects like planets, asteroids, comets etc.. These objects shall be simultaneously processed, which means tracking of already acquired targets and searching for new objects (e.g. appearing at the edge of the FOV) during one update period respectively CCD read-out interval. The number of celestial targets to be simultaneously tracked shall be up to 8 stars and/or up to 2 extended targets. Both, simultaneous track&search and star&extended target processing require a powerful hard-wired digital pre-processing for an on-line data reduction and object extraction.

Secondly, it is required that the sensor shall provide its line of sight in inertial co-ordinates. That means the sensor shall determine the attitude. Therefore an additional module was introduced, named „high level image data processing module". The attitude determination will be performed by the flight-proven DJO star pattern recognition algorithm using an internal guide star catalogue [1], [2].

2. DESIGN APPROACH

Due to the required wide field version with an FOV range from 10° x 10° up to 20° x 20° and the necessity to detect enough stars in all directions over the whole celestial sphere, the necessary limiting magnitude of the sensor can be evaluated. For this design approach a probability of 100% for a 3 star detection was assumed.

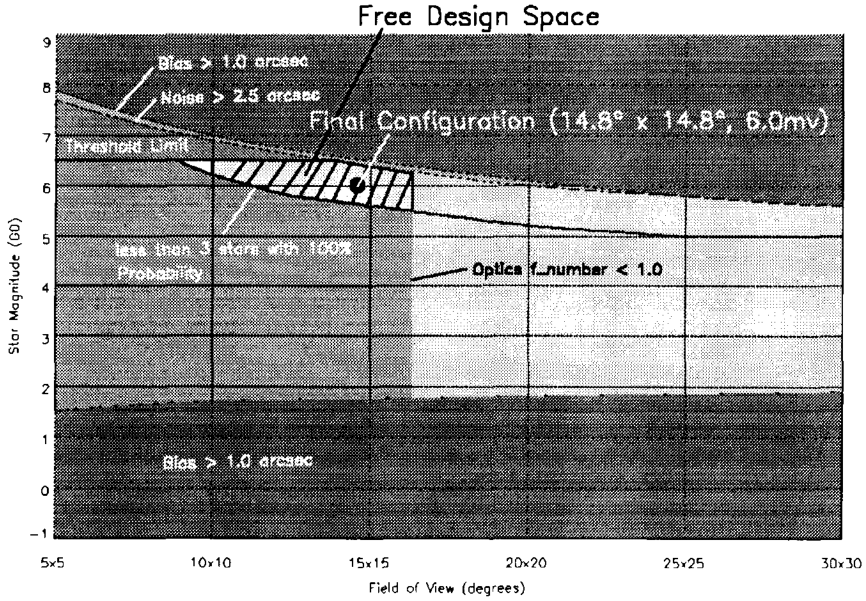

Figure 2: Design approach - Available free design space

Using a star catalogue and special S/W tools (e.g. which consider the real sensor instrumental magnitudes) the limiting magnitude can be calculated as a function of the FOV for a given number of stars and their corresponding detection probability [3]. Among other limitations figure 2 shows the described relation by the thick black line. Within the FOV range from 10° x 10° up to 20° x 20° the limiting star tracker magnitudes range from 6.2mv up to 5.2mv in order to detect in any direction 3 stars with 100% probability. This „3 star detection" line is also representative for a 99% probability of a 5 star detection.

The remaining free design space within the magnitude vs. FOV domain will furthermore be limited by the demanded accuracy and the minimum star detection threshold. The accuracy of 5.0arcsec (2sigma) in the noise and bias error forces a sufficient signal-to-noise ratio respectively star magnitude. Therefore the design space will be limited on the top by this reason (see fig. 2 noise and bias limit lines). The noise and bias behaviour within the magnitude vs. FOV domain was determined by a sensor simulation software tool which considers all signal processing steps from the star object itself up to the angle information.

In order to make a robust design the threshold limit for star detection has to be defined so that enough distance to the background noise floor is given. Furthermore, to distinguish a star from other false events like proton or shot noise, at least 3 coherent pixel signals shall appear above the detection threshold. Therefore the minimum detection threshold value is a further limitation for the remaining design space (see fig.2).

Last but not least the above mentioned necessary signal-to-noise ratio (to meet the accuracy) needs a minimum optical aperture at a given exposure (integration) time of 200ms. The diameter of the optics free aperture was therefore designed to 50mm. In connection with the FOV and the given detector area the resulting optics f_# can be calculated. By this reason a further limitation in the design space appears because of star tracker optics with a f_# less than 1.0 are not feasible. The corresponding boundary is also shown in figure 2.

At the end of this design approach the hatched area remains for a feasible sensor design. The final configuration of the sensor results in a FOV of 14.8° x 14.8° at a limiting magnitude of 6.0mv considering an exposure time of 200ms to reach the 5Hz update rate. Some other investigated approaches using a smaller CCD format like 384 x 288 pixels have shown that there remains no design space for achieving the required FOV/accuracy ratio with a feasible and robust design.

3. MODULAR DESIGN CONCEPT

The outline of the sensor is shown in figure 1. The sensor was designed axis-symmetric and mounted from the lens flange because this minimises the change of thermo-mechanical instabilities caused by thermal gradients and differential expansion. The electronic modules are mounted to the rear of the sensor mounting flange. Each of the module PCB's is housed in an axis-symmetric frame. These module frames can be configured as a stack. Therefore optionally electronic modules can be exchanged, added or replaced easily.

The basis module for all sensor applications is the CCD camera module placed right behind the CCD detector. The camera module includes 2 PCB's (see figure 3 PCB1 and PCB2). Whereby PCB1 is placed within the interface plate and PCB2 is mounted in a module frame and holds the ADC and housekeeping electronics. The electrical interface between PCB1 and PCB2 allows also a 2 box sensor design with an optical head and an electronics box.

The next module holds the image data pre-processing management unit and the sensor data interface. In the case of the current design approach the sensor data interface will be a MACS-Bus standard interface. This module performs the whole usual star tracker data processing up to the processed star co-ordinates in tan-values. In addition, some special functions are implemented in order to process also extended targets. The heart of this module is the powerful pre-processor management unit (PMU) which holds the whole data processing within an FPGA design, later on an ASIC design. The PMU will be explained in more detail in the next chapter.

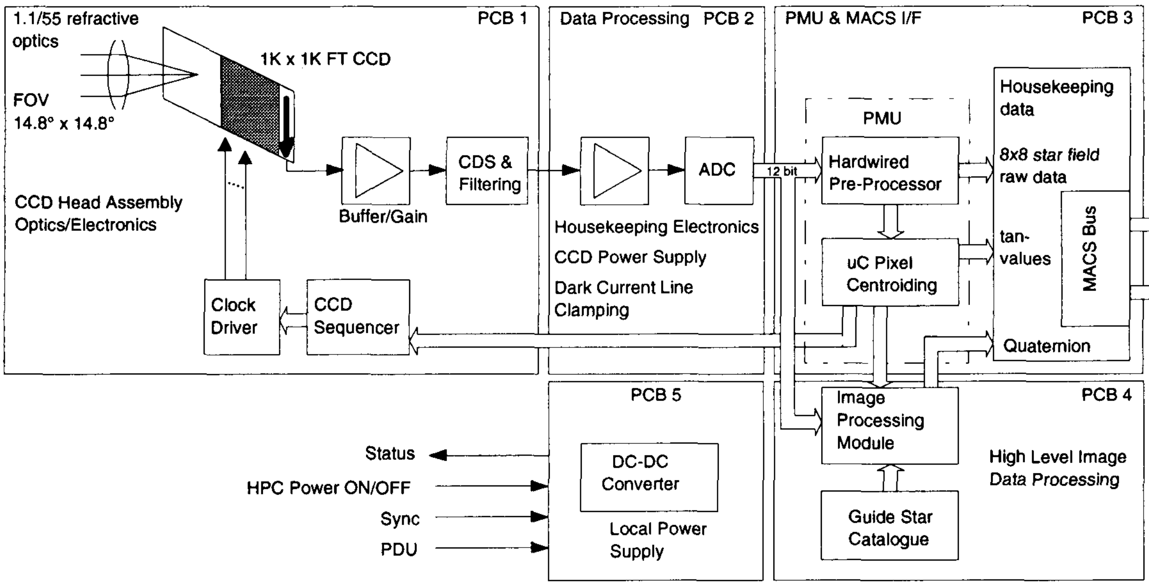
1.1/55 refractive optics
FOV 14.8° x 14.8°
1K x 1K FT CCD
PCB 1
CCD Head Assembly Optics/Electronics
Buffer/Gain
CDS & Filtering
Clock Driver
CCD Sequencer
Data Processing PCB 2
ADC
12 bit
Housekeeping Electronics
CCD Power Supply
Dark Current Line Clamping
PMU & MACS I/F
PCB 3
PMU
Hardwired Pre-Processor
uC Pixel Centroiding
Housekeeping data
8x8 star field raw data
tan-values
MACS Bus
Quaternion
A
B
PCB 5
DC-DC Converter
Local Power Supply
Status
HPC Power ON/OFF
Sync
PDU
PCB 4
Image Processing Module
Guide Star Catalogue
High Level Image Data Processing

Figure 3: Schematic sensor block diagram

The interface between the PMU and the sensor data interface allow also the connection to all other usual data interfaces (MIL1553, serial RS485, OBDH, etc.).

For completion of a simple star tracker only the power supply module has to be added to the module stack now. The power supply module finishes the module stack with a bottom housing plate.

For all additional high level image processing tasks (e.g. star pattern recognition, attitude determination, object tracking within extended targets, etc.) an image processor module was introduced. This module has direct access to the on-line image data flow and to the PMU output information (centroided stars). Therefore this module can be designed as frame memory necessary for a star camera application or as an attitude determination module using only the signal processor performance. In principal this module allows a lot of image processing tasks like filtering, object extraction, data compression etc. because of the frame memory/signal processor configuration.

The designed image processor module has taken into consideration the attitude determination capability with the first priority. Therefore a high performance signal processor was placed into this module with some data and code memory.

4. SIGNAL PROCESSING

The sensor signal processing can be divided in the CCD video signal processing and the digital signal processing.

The CCD signal processing will be performed by the following well known steps: signal decoupling, amplification, correlated double sampling, dark reference clamp and AD-conversion. The design goal to reach the 5Hz update rate forces a read-out frequency of 10MHz. On the other hand the required accuracy and dynamic range need a 12bit data resolution. These parameters especially in connection with the sensor power and mass budgets are marking a new quality in designing AOCS sensors with their high reliability requirements. The design solution which was found to achieve the above mentioned performance comply the referring ESA requirements.

The design of the digital processing electronics was one of the most difficult challenges during the sensor design activities. The already mentioned design drivers in the introduction require a powerful hard-wired digital pre-processing for an on-line star tracker related data reduction and object extraction.
Because of the limited time frame of 200ms (5Hz update rate) in conjunction with an image read-out time of approx. 120ms an on-line data processing is necessary. Figure 4 shows the digital data processing flow and figure 5 the corresponding sensor timing diagram.

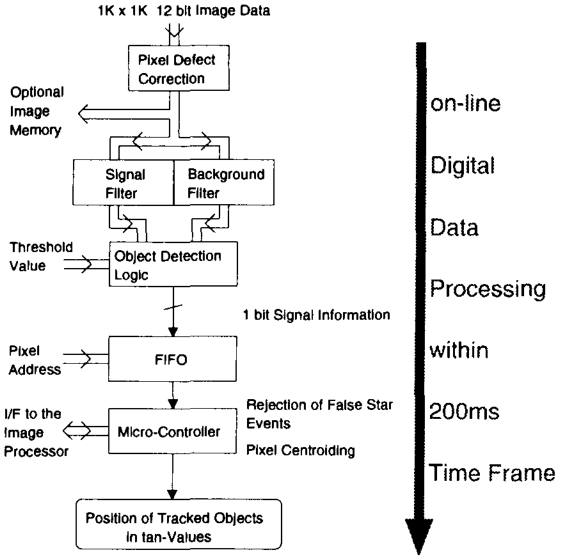
1K x 1K 12 bit Image Data
Pixel Defect Correction
Optional Image Memory
Signal Filter
Background Filter
Threshold Value
Object Detection Logic
1 bit Signal Information
Pixel Address
FIFO
I/F to the Image Processor
Micro-Controller
Rejection of False Star Events
Pixel Centroiding
Position of Tracked Objects in tan-Values
on-line
Digital
Data
Processing
within
200ms
Time Frame

Figure 4: Hard-wired digital data processing flow

The data processing flow shown in fig.4 is completely realised within an FPGA design which is described with VHDL tools.
At first the 12bit parallel image data will pass a pixel defect correction. A defect pixel can be replaced in 3 modes: 1. by the pixel value before, 2. by the value of its remaining pixel or 3. by the mean value of the pixel before and after it.
After the pixel correction logic the 12bit image data flow will be split in a filter logic and a frame memory interface which provides the image data to the optional image processor module. The digital on-line signal filtering performs an adaptive background value using an IIR filter and an FIR low pass signal filter. The outputs of both filters will be compared including a threshold value which will be added to the background value before the comparison. All filter parameters (coefficients) as well as the threshold value are controlled by the µ-controller.
Some precautions have to be done referring to the extended target processing within this filter structure. For example, in case of appearing an extended target within the FOV with an area of 10%FOV the adaptive background filter value is not allowed to adapt to the extended target grey levels, otherwise the extended target would not be proper extracted. By this reason some additional logic was included into the digital filter.

The object detection provides a binary information which extracts all objects from the background. Each object is stored in a FIFO with the corresponding address and some other necessary information as an object entry.

The µ-controller collects the object entries from the FIFO and separates false star events from valid objects. A star is proper detected when equal or more than 3 coherent objects appear. An extended object will be recognised when more than 9 (tbc) coherent objects appear.

Using the 12bit pixel values around the detected stars the µ-controller performs the centroiding with sub-pixel accuracy. The centroided position of up to 8 stars can be processed (tracked) simultaneously, meanwhile up to 32 stars can be monitored (acquired). That means a separation in an acquisition mode and a tracking mode usually in former star tracker designs is not further necessary. Now the search and track function will be performed simultaneously. New appearing stars and disappearing stars were monitored during each update period.

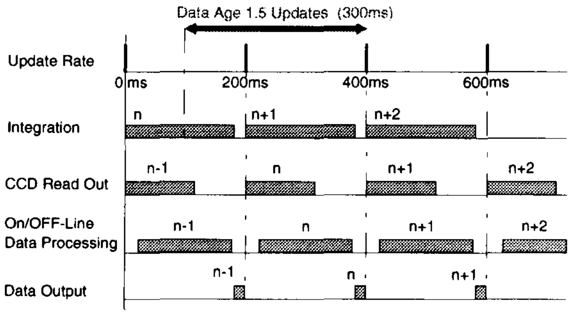
Data Age 1.5 Updates (300ms)
Update Rate
0ms
200ms
400ms
600ms
Integration
n
n+1
n+2
CCD Read Out
n-1
n
n+1
n+2
On/OFF-Line Data Processing
n-1
n
n+1
n+2
Data Output
n-1
n
n+1

Figure 5: Sensor timing diagram

The µ-controller starts its tasks (false star rejection, centroiding) when enough object entries are in the FIFO. Therefore the µ-controller is able to work during the image read-out. That means also that a short off-line processing will be necessary.

Using the described hard-wired signal processing the sensor output information can be provided at the end of the same frame in which the image was read out. Therefore the data age for the star tracker output

amounts to 300ms, starting in the middle of the integration period before (see also fig.5).
The attitude information will be processed within a further update period using a pipeline principal. By this reason the attitude information will have an age of 500ms and will be updated each 200ms.
The figures 6-9 show a simulated data processing flow using a real star image (acquired with the DJO „High Precision Star Sensor“) with an digitally overlaid fantasy extended object.

5. CONCLUSION

A modular star and target tracker with high performance and low budgets in terms of mass and power was designed at Jena-Optronik GmbH. The emphasis on modularity, both in terms of hardware and of software, will ensure that the sensor can be configured to meet a wide range of mission specific requirements, with minimal design changes. The sensor can be configured as a simple star tracker up to an autonomous attitude determination sensor.

All used parts and materials are available in a qualified status respectively qualifiable. Only materials and components with space qualification potential and with compliance to the relevant ESA standards were used.
By using the image processing module with a full frame memory the sensor can act as a navigation- or star camera. By changing the interface module all usual data interfaces are adaptable.

One of the potential target missions is Rosetta. Using the highest parts qualification level the sensor can also be used for commercial satellite projects which require a high reliability.

In parallel activities a low cost version of the sensor is under development for small satellite projects.

6. REFERENCES

[1] Elstner, C., Wunder, D.,
„Autonomous Attitude Determination Spacecraft Guidance Navigation and Control Systems“, ESA Workshop, ESTEC, Noordwijk, October 1992

[2] Elstner, C., Ratzsch, D., Skarus, W.,
Star Pattern Recognition Sensor of the ASTRO type,
„12th FAC-Symposium on Automatic Control in Aerospace“, Aerospace Control ‘92, Ottobrunn , Germany

[3] Abreu, R.,
Stellar Attitude Determination Accuracy with Multiple Star Tracking Advanced Star Tracker SPIE Vol.1949 Space Guidance, Control, and Tracking (1993)

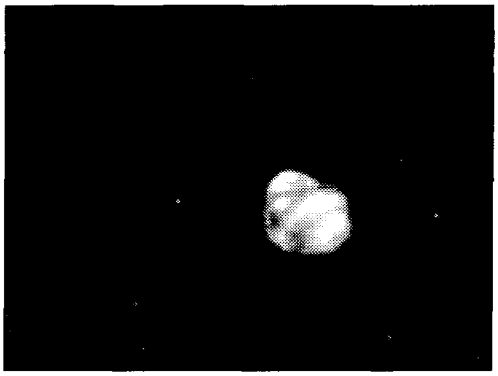

Figure 6: Real star image with an digitally overlaid fantasy extended object

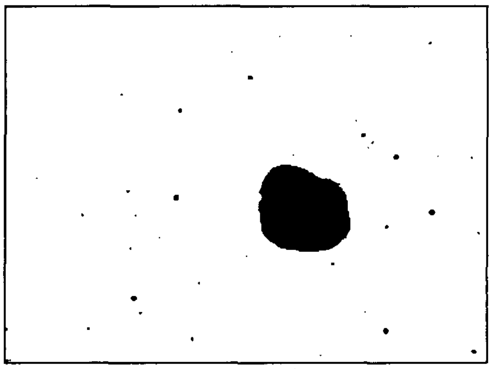

Figure 7: On-line processed binary object extraction with some remaining false star objects (proton or shot noise single pixel events)

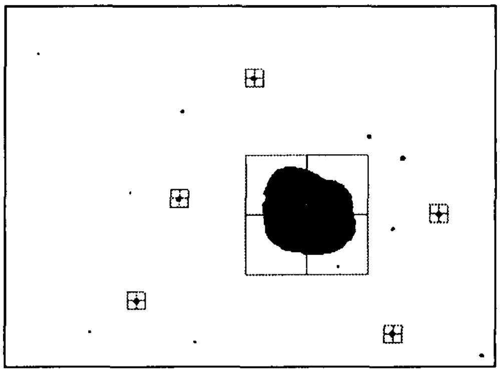

Figure 8: Tracked objects after rejection of the false star events; star tracker related output data age amounts to 300ms

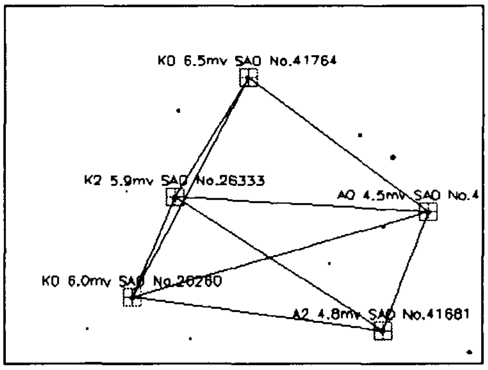

Figure 9: Identified stars and attitude determination using one additional frame period; attitude information data age amounts to 500ms

SESSION 3:
GPS SYSTEMS ASPECTS

Chairman: P. Silvestrin (ESA/ESTEC)

MOMSNAV

FIRST ANALYSIS OF GPS FLIGHT DATA FROM SPACE STATION MIR

S. Föckersperger[1], J.M. Fraile Ordóñez[1], O. Montenbruck[2] and E. Gill[2]

[1] Kayser-Threde GmbH, Wolfratshauser Str. 48, D-81379 Munich, Germany
Ph.: +49-89-72495-0, Fax: +49-89-72495-291
e-mail: sf@kayser-threde.de

[2] Germany Space Operations Center, D-82230 Wessling, Germany
Ph.: +49-8153-28-0, Fax: +49-8153-28-1349

ABSTRACT

For the first time, a GPS receiver has been placed onboard the Russian MIR Space Station. This receiver is an integral part of the high precision navigation package called MOMSNAV.

MOMSNAV has been developed to support the German MOMS-2P mission on PRIRODA, the earth sciences module of MIR, with Differential GPS (DGPS) orbit and inertial attitude information. It was launched together with PRIRODA on a Proton rocket on April 23, 1996. The off-line combined processing of GPS data from MOMSNAV and ground tracking stations is expected to provide MIR's position and relative attitude with an accuracy of approximately 5 meters and 10 arc seconds, respectively.

This paper will briefly describe the MOMSNAV system scientific background, its integration and initial operations. It will also discuss initial results obtained with MOMSNAV GPS flight data. The peculiar GPS satellite visibility conditions at the MIR station, and preliminary fast reconstructed orbits computed with MOMSNAV-only data will be reviewed.

1 INTRODUCTION

The Modular Optoelectronic Multispectral Stereo Scanner (MOMS-2P) is a second generation remote sensing instrument which was already flown in the German D2 mission on-board the Space Shuttle in 1993.

Based on the confidence gained with this successful mission, the German Space Agency (DARA) decided to fly the MOMS-2P camera on-board the Russian space station MIR's PRIRODA module, in a 18 months mission.

For the flight on-board PRIRODA and in order to enhance the scanner's capabilities, DARA decided to augment MOMS-2P with a navigation package which could provide the interested scientists and users with accurate position (GPS) and relative attitude information (the inertial sensors output angular and velocity increments). The German company Kayser-Threde GmbH was awarded a contract for the development of the all-new navigation package which was called MOMSNAV.

2 MOMSNAV RAISON D'ÊTRE

As already mentioned, MOMS-2P is an advanced high resolution three-linear spectral stereo scanner for earth observation from space. The purpose of the MOMS-2P mission is the provision of images for photogrammetry and thematic cartography. The modular optical system consists of five lenses while the digital imaging data is derived from eight sets of CCD sensors.

MOMSNAV was motivated by the fact that it is nearly impossible to determine the absolute orientation of the three-linear stereo images exactly by self-contained photogrammetric methods ([1] and [2]). Additionally, the position and relative attitude information can not be obtained from the navigation systems of the MIR station itself with the required accuracy.

The scientific requirements with respect to the accuracy are the following:

- Orbit accuracy: less than 5m (1-σ), to be achieved with Differential GPS (DGPS)
- Relative attitude acceleration (non-linearities): less than 10'' (1-σ)
- Attitude white noise: less than 1'' (1-σ)

The MOMSNAV navigation package does not provide itself orbit and attitude information directly with the required accuracy. The mission requirements for orbit and attitude will be achieved in off-line with the combined processing in differential mode of GPS MOMSNAV and ground based tracking stations data. A typical data take on-board PRIRODA amounts to only 5 minutes.

Proceedings Third International Conference on Spacecraft Guidance, Navigation and Control Systems, ESTEC, Noordwijk, The Netherlands, 26-29 November 1996, ESA SP-381 (February 1997)

3 MOMSNAV SYSTEM DESCRIPTION

MOMSNAV is integrated in the earth observation module PRIRODA of the Russian MIR Space Station. It consists of the following hardware components:

- two active dual antenna modules
- two redundant gyro packages
- one gyro electronic box with two redundant units
- MOMSNAV electronic box.

The first three items are mounted outside of the PRIRODA module whereas the last one is installed inside.

The inertial sensors and their electronic units were developed by the German company Litef GmbH, while the spaceborne GPS receiver Viceroy^{TM} was manufactured by Motorola GSTG from Arizona.

The main component in MOMSNAV is the electronic box manufactured by Kayser-Threde. It contains the data management system, a power control and distribution unit and, most important, the GPS receiver.

Figure 1 shows the electronic box with all the electrical and RF interfaces on its front side. Additionally, the aperture for the cooling fan is visible.

The GPS receiver is MOMSNAV kernel and the key to achieve the positioning accuracy required in the scientific mission of the MOMS-2P camera.

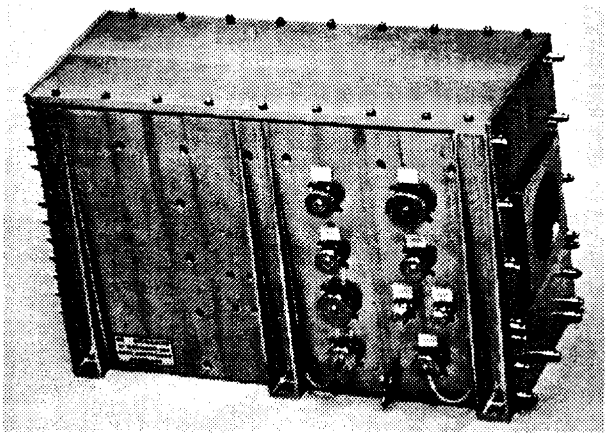

Fig. 1: MOMSNAV Electronic Box

The receiver can track GPS satellites at the L1 frequency and provides carrier and C/A-code phase measurements. It operates with two antennas simultaneously and has a total of 12 channels (each antenna is allocated to a single block of 6 channels). Though the Viceroy^{TM} GPS receiver is specially designed for its use in space missions (its parts are radiation tolerant, the dynamic limits have been increased as required, and the user interface is customised for operations in space), it is actually based on Motorola's low cost 6-channel GPS core receiver, which is widely used in land applications.

The receiver's carrier and code phase measurements accuracy levels have been verified at Kayser-Threde by means of inter-channel differences. The results obtained showed RMS errors of approx. 0.6 meters, and 2-7 mm in code and carrier phases, respectively.

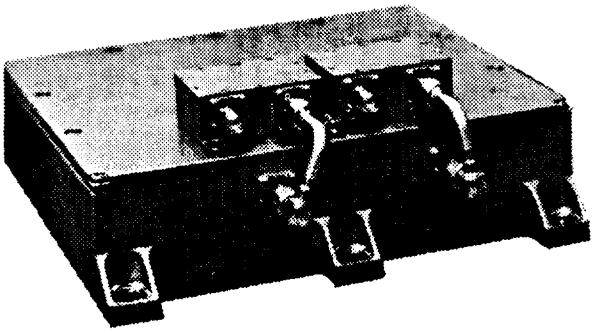

Fig. 2: Viceroy^{TM} GPS receiver

An important feature of MOMSNAV regarding its broad field of applications, is a last-minute modification performed upon request from ESA. Originally, it was not considered necessary to have real-time access to the GPS receiver raw measurement data since all data are stored on tape for subsequent dumping to ground stations.

However, following ESA's wishes, and in agreement with DARA, the electronic box was modified to add a RS-422 interface for external users which was a mirror reproduction of the own GPS receiver's interface. This enables users properly equipped with interfacing software, to command the receiver and to obtain measurement data in real-time on-board the MIR station.

This is one of the key issues that makes possible the European Space Agency's Relative GPS experiments for rendezvous and docking to be performed in the framework of the ATV Rendezvous Pre-development demonstration flights ([3]).

For the interested reader, [4] contains a more detailed technical description of MOMSNAV.

4 LAUNCH AND OPERATIONS

4.1 Integration, test and launch

A stand-alone full-scale functional test of MOMSNAV was performed at Kayser-Threde, using PRIRODA interface and telemetry/telecommand simulators provided by the Russian partners. After successful verification, MOMSNAV was transported to the Russian space company RSC-Energia near Moscow.

The second part of the acceptance took place at these facilities. After completion, MOMSNAV was handed over to RSC-Energia for integration into the PRIRODA module. A so called Complex Test was performed where the complete MOMS-2P system was tested including the

PRIRODA infrastructure. The first test period in Moscow lasted about four weeks. All equipment was subsequently transported to the Cosmodrome at Baikonour and the final series of system tests was performed there and lasted about two weeks. Finally, on April 23, 1996, PRIRODA, with MOMSNAV on-board, was launched with a Proton rocket, and docked to the MIR space station three days later. The second part of the MOMS system was launched with the PROGRESS M-31 on May 5th. The mounting of the MOMS optic unit with an Extravehicular Activity (EVA) took place on May 31st.

4.2 Mission Operation

The operational phase started with the Technical checkout phase. It started mid of June and lasted until end of September. First telemetry and telecommand links had been verified, then the complex MOMS-system was switched on piece by piece. All operations have been controlled under the responsibility of the German Space Operation Centre (GSOC) at Oberpfaffenhofen.

This initial operations phase was accompanied with a very busy period on-board MIR. The French-Russian MIR mission and a visit from the Space Shuttle took place in parallel to the MOMS-2P activities.

Since October the Commissioning Phase has started and the MOMS-system works on an almost day to day base. This phase will probably finish at the end of the year. Up to now several MOMS data takes have been dumped to the data processing centres. The scientific community is currently evaluating these data. First results are expected to be published in December, 1996.

4.3 Ground Segment

Two independent ways of transmission of MOMSNAV information are realised (see Figure 3). Generally three hours prior to a data take the system is activated and delivers GPS navigation solutions in the form of position and velocity data. with associated status messages (Housekeeping data) to the PRIRODA tape recorder. At subsequent contacts with a network of Russian ground stations, the PRIRODA telemetry data are transmitted via the BITS system to the Russian mission control centre at Kaliningrad for further distribution to GSOC. Due to the limitations of the tape recorder a maximum of 4 hours of MOMSNAV data can typically be collected per day. Independent from the PRIRODA telemetry data, camera data and associated MOMSNAV data, which include pseudorange and phase measurements are written to the MOMS tape recorder during the data take of typically five minutes. These science telemetry data are dumped via the BISU-PM system during the dedicated passes over the German DLR ground station at Neustrelitz or the Russian Obninsk station. The mean time for data reception from the MIR space station will be 7 min per day for each data processing center. At the reception station the data extraction, first level of data processing, archiving and data dissemination takes place.

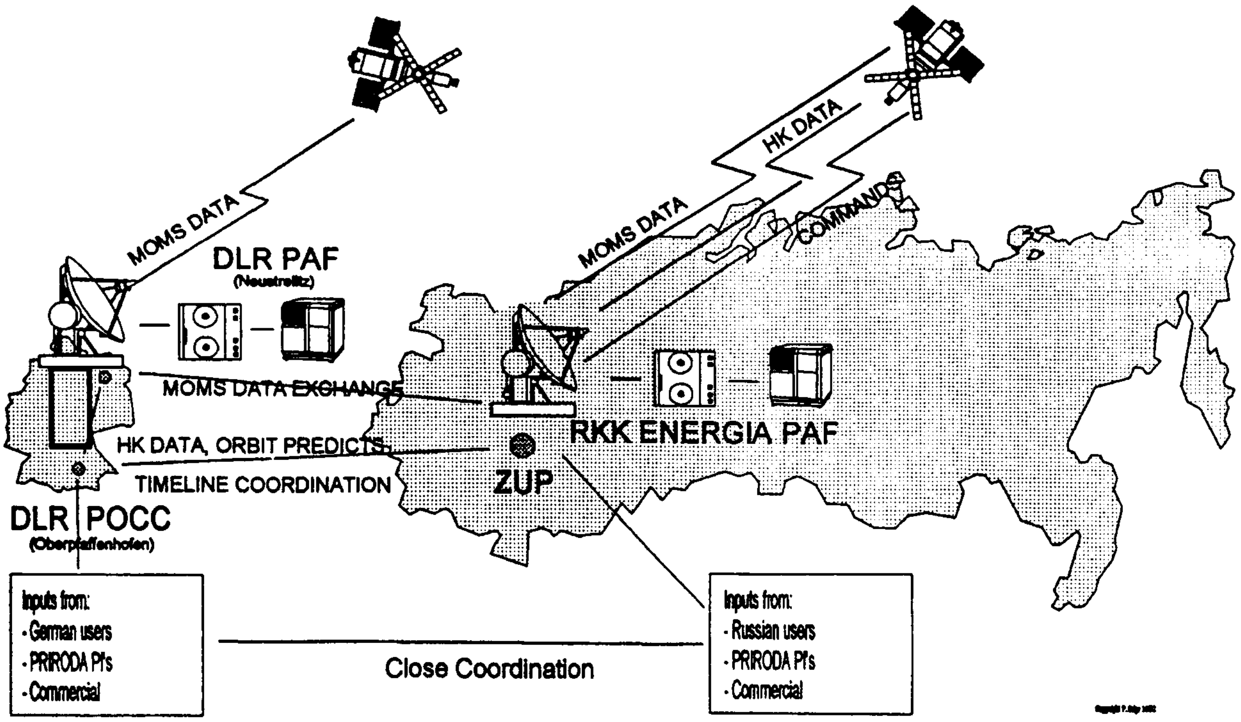

Fig.3: Ground Segment Scheme

5 PRELIMINARY ANALYSIS OF FLIGHT DATA

5.1 Satellite Visibility

One of the major concerns during the MOMS-2P mission design phase, was related to the visibility conditions of GPS satellites from the MIR space station. Initial preliminary analysis pointed out that this issue might be critical and as a consequence, it was decided to integrate in MOMSNAV a dual-antenna 12 (6+6) channel GPS receiver, and optimum antenna locations at the PRIRODA module were looked for.

The selected antenna configuration is such that the two GPS antennas are pointing towards fully opposite sides of the sky providing almost full sky coverage. An additional problem appears with the multitude of structures that are intrinsic parts of MIR and which cause significant signal blocking.

Once MOMSNAV design was completed and the antenna locations were selected, detailed mission analysis and visibility simulations were performed at Kayser-Threde. A summary of the results has been already published ([4]). In brief, the results indicated that as long as the MIR station is oriented in the MOMS-2P mission nominal attitude, MOMSNAV can be expected to track 6-8 GPS satellites most of the time. However, some drop-outs down to 3 satellites can not be excluded.

Experience shows surprisingly good agreement with the predictions made in the mission analysis. Figures 4 and 5 show the number of satellites tracked during two MOMS-2P data takes (during which, the MIR station was in the mission nominal flight attitude). Additional results for an approx. two hours-long data arc (with MIR in unknown attitude) are shown in Fig. 6.

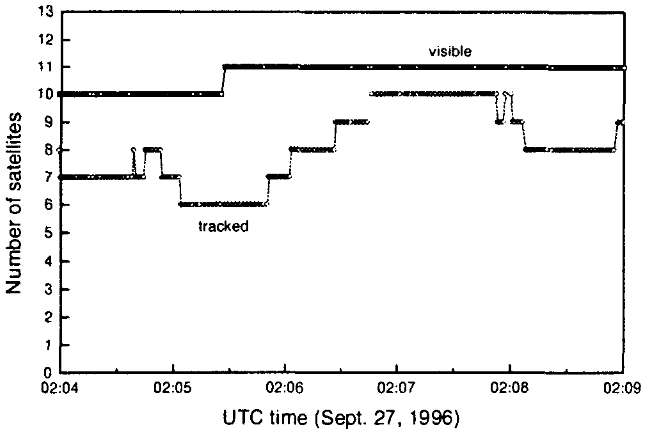

Fig. 4: Sat. visibility during data take on Sept. 27, 1996

In any case, if we take into account the environment which surrounds the GPS antennas, with numerous structures and solar panels, the visibility results can be regarded as very satisfactory.

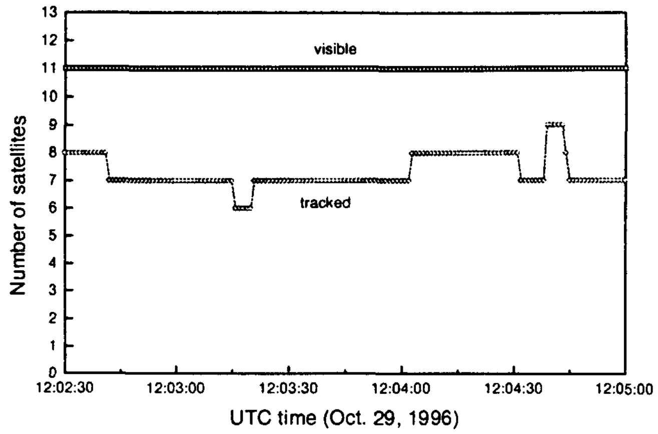

Fig. 5: Sat. visibility during data take on Oct. 29, 1996

5.2 GPS-based MIR Orbit Reconstruction

The German Space Operations Center (GSOC) is fully responsible for MOMS-2P mission operations. In the framework of this work, GSOC is computing fast and simple reconstructed orbits on a routine basis as a mission operations support tool, e.g. to re-initialise the GPS receiver's orbit after power down ([5]).

MOMSNAV GPS receiver provides position and velocity information of MIR. Although the absolute standalone position accuracy of approx. 100m may be sufficient for many scientific experiments, the provided navigation solution can experience interruptions caused by satellite visibility gaps and their associated signal reacquisition phases. In the case of the MOMS-2P mission, this may lead to image distortion well above achievable image resolution of typically 12-18m.

A solution for these limitations can be a simple least squares adjustment of GPS navigation data which takes into account the dynamical characteristics of the orbital motion of MIR. As a consequence, the resulting relative accuracy of the orbit solution will be given by the accuracy of the force model.

On the other hand, the absolute accuracy of the orbit solution crucially depends on the data arc were GPS navigation solutions are available. For short arcs, a minimum accuracy of 100m can be expected, which decreases to 10-20m for a one-day arc. For longer data arcs, the absolute position error approaches the relative position accuracy of 1m in the absence of systematic errors in the position solution.

GPS navigation solutions from MOMSNAV have been collected on a near-to routine basis during the mission commissioning phase. Usually the data update rate is 1s and the mean arc length has been 1.8 hours.

As a result of the mentioned orbit determination process, typical residual signatures are depicted in Fig. 6 for October 4, 1996. The data arc covers two hours and the sampling rate has been reduced to 1/15s. It can be observed that the majority of residuals stays well within a range of ±100m. Jumps in the residuals are commonly associated to changes in the configuration of tracked satellites. However, since the dynamics of the MIR station is rather high, the configuration changes quite rapidly and a direct correlation is difficult to prove due to the navigation filtering algorithm employed by the GPS receiver.

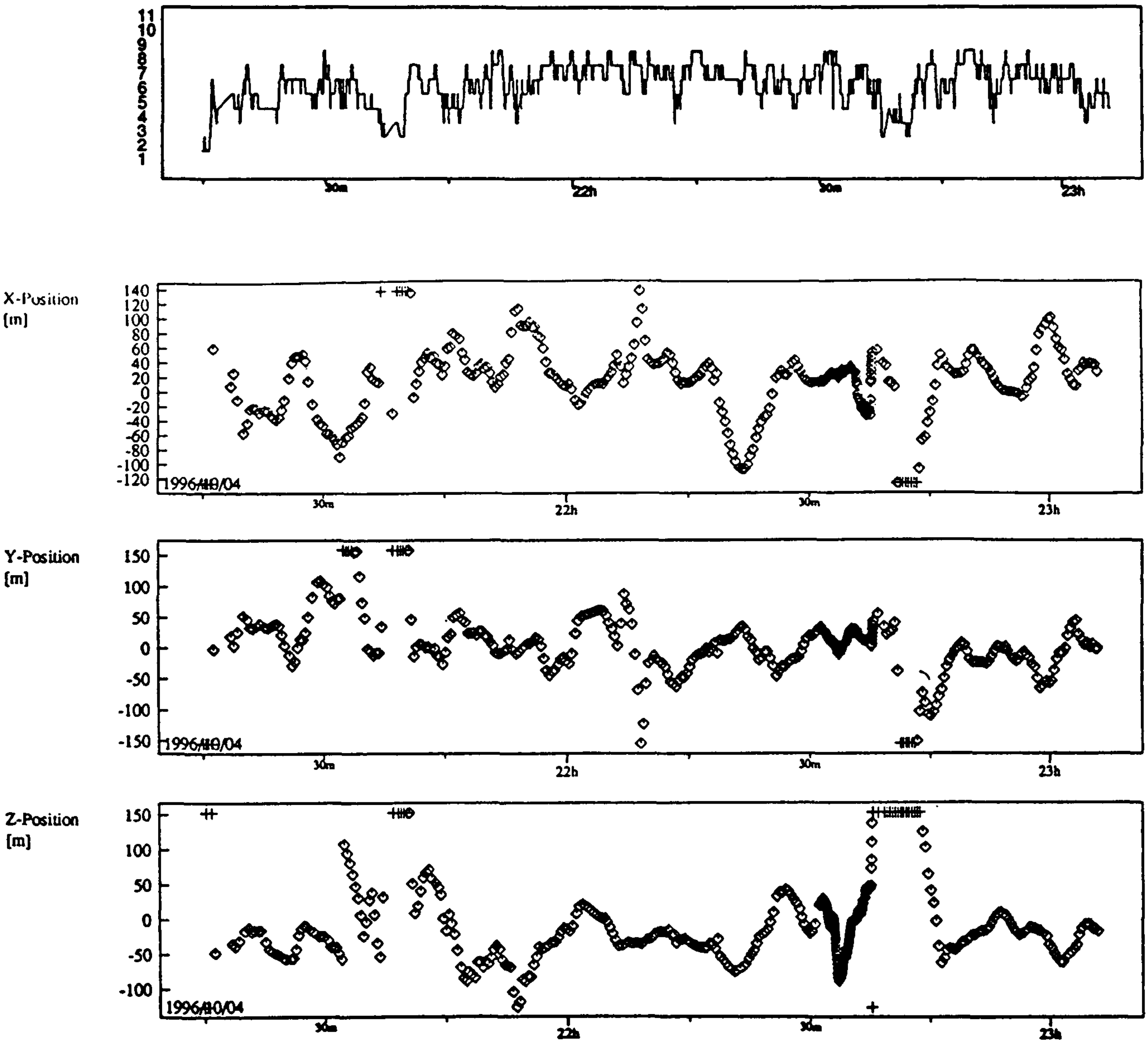

Fig. 6: Sat. visibility and residuals of GPS position fixes of MOMSNAV for October 4, 1996

6 DIFFERENTIAL GPS DATA PROCESSING

For the MOMS-2P mission, a detailed DGPS-positioning error analysis was performed in the early phase of the MOMSNAV development ([6]). The aim of that analysis was to assess the feasibility to achieve the requested position accuracy (5m, 1-σ) with the MOMSNAV concept available by that time. The results of our simulations and analysis showed that the required accuracy is achievable provided that:

- GPS data are processed in differential mode with several ground stations to eliminate Selective Availability's clock dithering errors,
- PDOP is approx. 2.1 (normally GPS data from 3 ground stations are to be processed simultaneously with MOMSNAV data),
- code phases are smoothed with carrier phases in order to reduce the observable's noise down to, at least, 0.4m,
- precise GPS satellite orbits are employed (e.g. from IGS, with accuracies of 0.04ppm)
- differential troposphere errors are held well below 1m
- differential multipath errors are below 1.5m
- differential ionosphere errors are reduced (to approx. 1-2 meters) by means of, for example, regional ionosphere models. This however, is only achievable when the ionosphere is under the effects of a low-medium cycle of solar activity.

Unfortunately, results from MOMSNAV real flight data Differential GPS processing are not available yet. The Geo-Forschungszentrum in Potsdam, Germany is responsible for the GPS data processing. Results of their investigations will certainly be published soon.

7 CONCLUSIONS

MOMSNAV, the navigation package of the MOMS-2P sensor on-board the MIR space station's PRIRODA module has been successfully integrated, launched and put into operation.

The MOMS-2P mission commissioning phase is near to completion and data are currently taken on a near-to routine basis. Large quantities of MOMSNAV GPS flight data have been already obtained and their processing is currently well under way.

From the operations point of view, the visibility conditions on-board the MIR space station are of special interest and have been analysed. The first results show good agreement with the analysis and the performance exceeds the expectations.

Additionally, the analysis of fast and simple reconstructed orbits has been briefly presented. They serve as a tool to support the mission operations, while at the same time they provide a valuable insight into the problems and advantages associated to the operational use of GPS on-board spacecrafts.

8 ACKNOWLEDGEMENTS

The work described has been funded by the German Space Agency DARA under Ref. No. 50 EE 9224 (Kayser-Threde GmbH) and 50 EE 9537 (GSOC).

Alfred Jansche's efforts and thorough work as system engineer along the lion's share of the MOMSNAV project is herewith very gratefully acknowledged.

9 REFERENCES

[1] Seige, P. and D. Meissner: *MOMS-02: An advanced high resolution multispectral stereo scanner for Earth observation.* Geo-Informations-Systeme, Vol. 6, No. 1, pp. 4-11; 1993.

[2] Ackermann, F.: *Das MOMS-02-Stereosegment: Ein hochgenaues System der digitalen Photogrammetrie.* Geo-Informations-Systeme, Vol. 6, No. 1, pp. 16-22; 1993.

[3] Lemke, N.; J.M. Fraile Ordóñez and P. Hofmann: *Relative GPS experiments during MIR'96 and ATV Rendezvous Pre-development Flight demonstration missions.* Proceedings of the 47th International Astronautical Congress, Beijing, China, Oct. 7-11; 1996.

[4] Föckersperger, S.; A. Jansche; N. Lemke and J.M. Fraile Ordóñez: *MOMSNAV, Location of the Russian Space Station MIR with Differential GPS (New Developments).* ESA WPP-071, Proceedings of the 2nd ESA International Conference on GNC, Noordwijk, The Netherlands, April 12-15; 1994.

[5] Montenbruck, O.; E. Gill and J.M. Fraile Ordóñez: *Orbit determination of the MIR Space Station using MOMSNAV GPS measurements.* Proceedings of the 20th International Symposium on Space Technology and Science, Gifu, Japan, May 19-25; 1996.

[6] Fraile Ordóñez, J.M.; A. Jansche and N. Lemke: *DGPS Positioning of the Russian MIR Station: Analysis of Visibility Conditions, Measurement Error Sources and Ground Requirements.* Proceedings of the 3rd International Conference on Differential Satellite Navigation Systems, London, United Kingdom, April 18-22; 1994.

A GPS-BASED ORBIT POSITIONING SYSTEM FOR THE EUROPEAN ARCHIMEDES MISSION

J. Potti
GMV S.A.
c/ Isaac Newton 11
28760 - Tres Cantos, Spain
Tel.: + 34 - 1 - 807 21 00
Fax: + 34 - 1 - 807 21 99
E-mail: jpotti@gmv.es

M. Bello
GMV S.A.
c/ Isaac Newton 11
28760 - Tres Cantos, Spain
Tel.: + 34 - 1 - 807 21 00
Fax: + 34 - 1 - 807 21 99
E-mail: mbello@gmv.es

A. Pasetti
ESA/ESTEC
P.O. Box 299
2200 AG Noordwijk, The Netherlands
Tel.: + 31 - 71 565 49 81
Fax: + 31 - 71 565 54 32
E-mail: apasetti@estec.esa.nl

ABSTRACT

Under the frame of a study contract funded by the European Space Research and Technology Centre (ESTEC), GMV has performed a thorough investigation on the orbit positioning of Archimedes, both the Orbit Determination and Orbit Control aspects, paying special attention to the possibility of using an on-board, autonomous orbit determination system based on GPS.

An Orbit Control algorithm for Archimedes has been defined resulting in an strategy requiring only groundtrack control with perigee manoeuvres. The individual optimisation of the initial set of orbital parameters for each spacecraft of the constellation allows removal of an active control of the eccentricity and angular parameters, thus minimising the propellant demands. The frequency and size of the orbit control manoeuvres can be chosen within a large range of values (45 to 100 days between two consecutive manoeuvres) with minimal impact in terms of the elevation over the service zones. The total required control ΔV for 10 years operational lifetime is of only 14 m/s per spacecraft.

Special attention deserves the GPS-based Orbit Determination system for which the study reveals that a single GPS antenna in nadir view connected to a low-cost GPS-receiver is the only hardware required by the proposed system. On software side, a simplified Kalman filter algorithm comprising a very low-cost dynamics model and simple techniques for attenuating the disturbing effect of ionosphere and selective availability is able to achieve an orbit location accuracy of approximately 100 m which is sufficient for the Orbit Control of Archimedes.

1. OVERVIEW OF ARCHIMEDES

The ESA experimental program Archimedes has the purpose of establishing the commercial viability and technical feasibility of high quality personal communication and sound broadcasting. The program consists of three to five experimental satellites to explore these challenges by the year 1998. In the context of the Archimedes program, HEO orbits are being investigated in detail for the distinctive merits in providing telecommunication service on regional or multiregional basis to zones located in the northern hemisphere. The feasibility of radio broadcasting and personal mobile services is based on the possibility of receiving the signal without blockage of the satellite line of sight. This is translated into the requirements of high elevation angles over wide areas. Recently the attention has been focused on the multiregional HEO orbits M-HEO(8) and M-HEO(16). In the case of the 8 hour orbit, a lower apogee altitude provides considerable power savings due to more favourable link geometry and also offers a considerable advantage in terms of orbit mass that can be delivered by a given launcher.

2. ORBIT DETERMINATION REQUIREMENTS

Communication missions are not very demanding on orbit determination requirements. For the Archimedes mission, an estimation of the required position accuracy may be derived as follows: the antenna onboard the satellite must be pointed at a fixed point on the Earth surface with an accuracy of 0.1 degree; this pointing error is made up of two components due to the attitude error and to the position error respectively. Allocating a position error contribution of 10%, and taking into account a duration of the active arc of ± 3 hours around apogee (M-HEO 8 hours orbit), an orbit determination requirement between 1.7 and 4.5 km is obtained. Therefore a 1σ position error of 1 km is considered for the Archimedes MHEO 8 hour orbit scenario.

3. GPS-BASED ORBIT DETERMINATION

3.1 General considerations

The approach which will has been followed in our analyses is to find out the minimal hardware configuration which allows on-board GPS-based orbit determination at the prescribed accuracy. For the case of Archimedes at M-HEO(8) the low demanding orbit determination accuracy allows to design an on-board GPS-based orbit determination system based on the use of a low-cost C/A code GPS receiver. Such GPS receivers provide pseudo-range, integrated Doppler (continuous carrier phase) and carrier phase only at the L1 frequency

Proceedings Third International Conference on Spacecraft Guidance, Navigation and Control Systems, ESTEC, Noordwijk, The Netherlands, 26-29 November 1996, ESA SP-381 (February 1997)

(L1=1,575.42 Mhz). The errors affecting the GPS observations are assumed being as follows:

Pseudo-range noise sigma	0.5 m
Doppler noise sigma at L1	1 mm
Initial value of the clock bias	0.0001 sec
Normalised clock frequency error	10^{-9} s/s
Normalised clock stability	-10^{-13} s^{-1}

With C/A-code GPS receivers ionosphere effects cannot be compensated on-board unless provisions were made for estimation the ionosphere refraction correction. On this respect it must be noted that:

- For the case where the satellite has a GPS antenna pointing in the zenith direction, then it can be demonstrated that above 1,000 Km the ionosphere refraction correction implies an additional error on GPS measurements of less than 1 meter, which can be neglected for practical purposes.
- For the case where the satellite has a GPS antenna pointing in the nadir direction, then it can be demonstrated that the ionosphere range error can attain values of 100 m which require implementation of some mechanism to overcome it. Several compensation methods have been discussed and it is proposed to use a method to reject ionosphere affected signals. This can be easily done by enlarging with 1,000 Km the size of the Earth; using this 1,000 Km constraint the ionosphere effects are almost null.

It must be noted that, being an on-board application, it is particularly important to minimise the hardware demands on-board the spacecraft. This means that the resulting algorithms should be simple enough to fit within the GPS receiver processor and, therefore, the on-board dynamics model shall be simple enough.

3.2 Observability Analysis

Due to the nature of the Archimedes orbit under consideration (see Figure 3-1), and assuming that the nominal S/C attitude is Earth pointing, both nadir-view and zenith-view location would bring GPS satellite signals within the GPS receiver antenna field of view. The advantage of the zenith-view antenna is that the ionosphere disturbing effect does not appear and that the GPS signals travel is shorter, thus, removing link budget problems; on the contrary, it provides worse visibility conditions as will be shown. For the nadir-view antenna, as discussed earlier, an on-board technique has been put in place to reject those signals which are suspicious of crossing the ionosphere. Therefore, ionosphere crossing signals are not considered as visible.

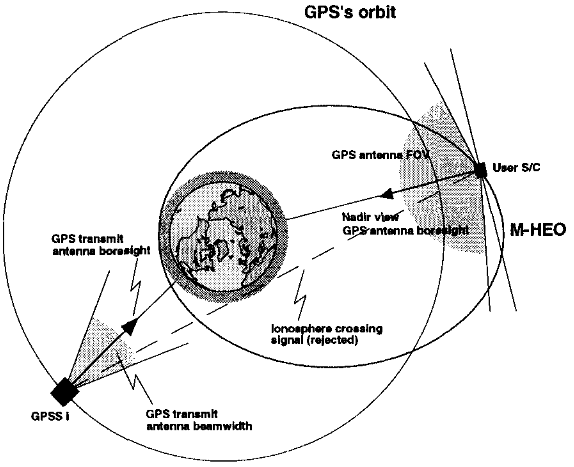

Figure 3-1: Geometry of the HEO mission scenarios and GPS constellation

Figure 3-2 and Figure 3-3 show the visibility charts where it has been assumed that the power level and signal-to-noise ratio of the GPS signals arriving at the GPS receiver are unconstrained. The issue of signal availability at required power levels will be discussed later

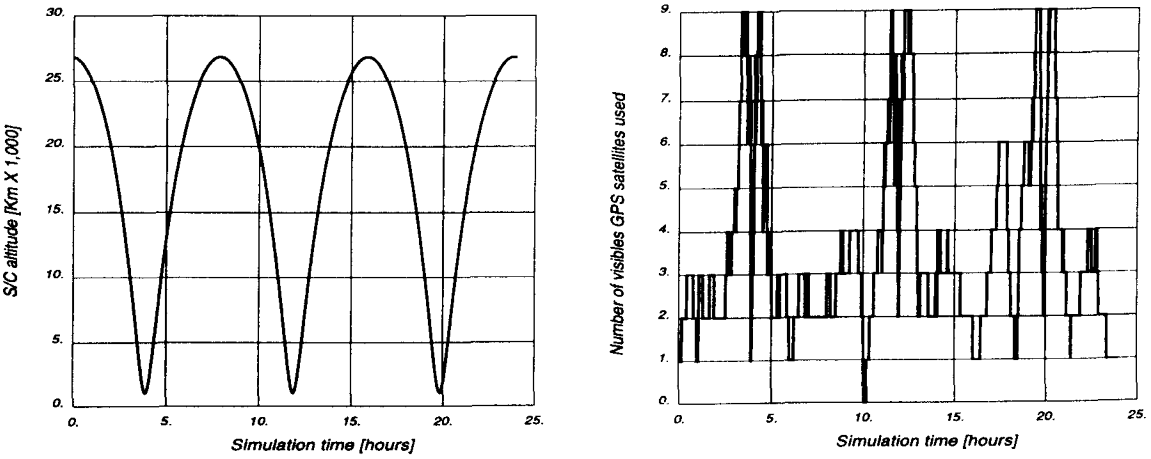

Figure 3-2: GPS observability charts from M-HEO(8); nadir-view antenna case

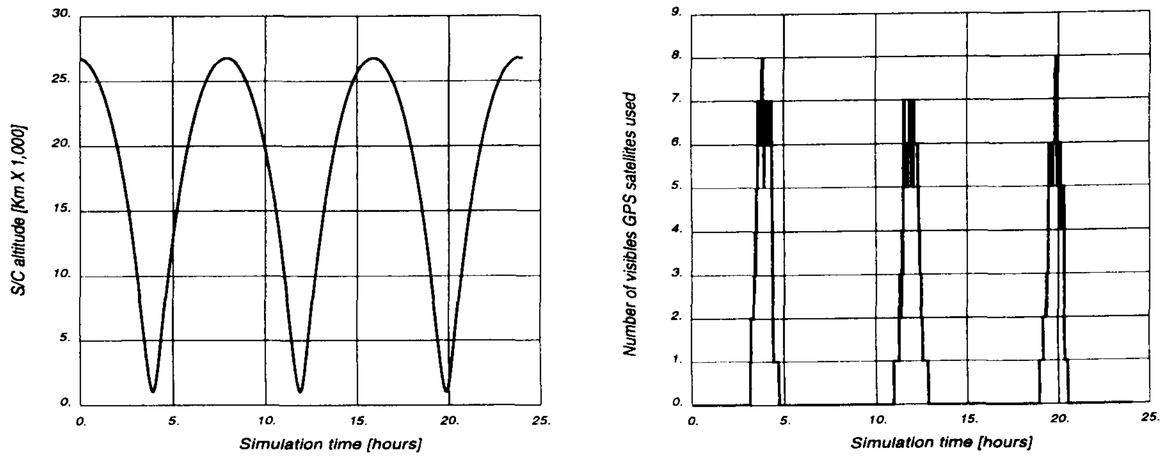

Figure 3-3: GPS observability charts from M-HEO(8); zenith-view antenna case

Analysis of these figures reveals that the zenith-view antenna case implies a large proportion of time with no visible satellite which could pose additional requirements in the quality of the on-board orbit dynamics model. In addition the nadir-view antenna provides a mean number of visible GPS satellite of 2.792, significantly higher than the 0.809 provided by the zenith-view case. It is therefore concluded that further investigations will concentrate in the nadir-view case; the zenith-view case is discarded.

3.3 Link Budget

GPS satellite signals power reception levels at Earth surface is -160 dBw as minimum (although current power levels are typically of about -154 dBw). Taking into account that in the case of an Archimedes satellite the signal travel can be significantly longer, geometric visibility does not imply signal availability at the required power levels.

Two parameters play an important role:

- The power level of the received GPS signals: commercial receivers are designed taking into account the minimum signal power level guaranteed by the USA DoD (-160 dBw). Due to the relatively large distance in this application it is likely that the received power level is less than that value.
- Most important yet is the received SNR of the GPS signals. While a weak signal can be amplified to reach the desired power level, nothing can be done if the contribution of the different noise sources is such that the overall SNR is less than the receiver sensitivity. From ref. [6], the minimum carrier-to-noise power density ratio for signal acquisition shall be of 38 dBHz whereas for signal tracking shall be of 34 dBHz (both measured at the LNA input).

Special attention deserves the antenna gain pattern of the GPS satellites. Ref. [3] provides a detailed picture of that pattern. Based on actual GPS signal levels, which are around 5 dB higher than specifications, it has been considered that the GPS satellites EIRP (in the maximum gain direction) is 30 dBw.

From ref.'s. [2] and [4] it is possible to derive the following formulation:

$$P_r = EIRP + L_t + L_s + L_b + G_r + L_a$$

$$C/N_0 = EIRP + L_t + L_s + L_b + G_r + L_a - 10\log_{10} T_s + 228.6$$

where (note that the term 228.6 corresponds to $10\log_{10} k$, where k is the Boltzmann's constant):

Pr	is the power level at the GPS receiver
$EIRP$	is the effective isotropic radiated power by the emitting GPS satellites in the maximum gain direction. Based on actual GPS signal levels, which are around 5 dB higher than specifications, it has been considered that the GPS satellites EIRP (in the maximum gain direction) is 30 dBw.
L_t	is the transmitter antenna gain loss with respect to the maximum gain direction. This term accounts for the antenna gain pattern of the GPS satellites. Ref. [3] provides a detailed picture of that pattern.
G_r	is the receiver GPS antenna gain in the maximum gain direction.
L_a	is the attenuation of the GPS signal when received from a direction different from the GPS antenna maximum gain. It is a function of the deviation of the incoming signal from the

maximum gain direction (zenith) and provided by the GPS receiver antenna manufacturer.

L_S is the free-space loss, given by

$$L_s = 20\log_{10}\left(\frac{\lambda_0}{4\pi d}\right)$$

where λ_0 is the wavelength (corresponding to L1 frequency) and d is the distance between the GPS-satellite and the GPS receiver

L_b encompasses other system losses like polarisation mismatch, etc.

T_S is the system noise temperature, significantly varying depending if the GPS receiving antenna is pointing at the Earth or not.

The above formulation allow us to calculate the resulting power level and associated SNR of every signal arriving at the GPS receiver. Computer simulations are performed with the aid of SOAP (refs. [1] and [5]) which comprises accurate GPS modelling (both for transmitters and receiver) including the issue of power level and signal-to-noise ratio of every measurement provided by the GPS receiver.

Simulations were performed to compute the effective observability charts when power level and signal-to-noise ratio constraints are put in place. Figure 3-4 corresponds to the visibility charts of previous section but now any GPS signal arriving at the GPS receiver with a signal-to-noise ratio below 38 dB is considered as not visible. As concerns the GPS receiver antenna it has been assumed a relatively low-cost antenna providing a gain in the maximum gain direction of 6 dB, with a usable beamwidth of 160 degrees and having a gain loss through the antenna field of view of up to 8 dB

Inspection of the these plots reveals that there is a significant loss in the number of GPS satellites observed at the required SNR level: the mean number of GPS satellites observed falls down to 1.480 (from 2.792 as described in previous section). However, the resulting visibility chart appears still promising to reach the specified OD accuracy requirement.

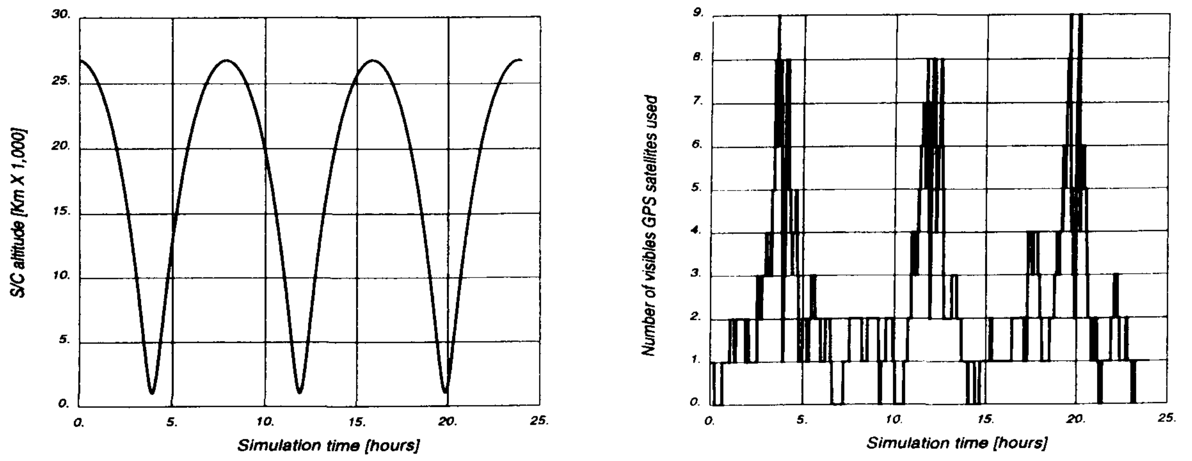

Figure 3-4: GPS observability charts from M-HEO(8) (nadir-view) with SNR > 38 dB

3.4 On-board Dynamic Model

Due to the fact that the GPS-based orbit determination algorithms are targeted to run on-board the spacecraft, there is a need for implementing a low-cost[1] dynamics model. Since the on-board estimation filter relies on both the measurements model and the on-board dynamics model to derive an optimum estimate of the spacecraft location, it is obviously deduced that the quality of the on-board measurement model is one of the driving factors of the orbit determination algorithm performances. This is particularly important in such orbital arcs where there is no available measurement as was discussed before.

Due to low demanding OD accuracy requirement for Archimedes, it has been selected an extremely simplified orbit dynamics model implementing only the Earth's gravity field model to the order and degree 2, i.e. the central gravity plus the J_2 and J_3 terms. The acceleration error of this model (compared to a state-of-the-art orbit dynamics model) is of approximately 5×10^{-5} m/s^2 when the spacecraft is near its orbit perigee and falls down to approximately 2×10^{-6} m/s^2 when the spacecraft is near its orbit apogee.

---

[1] Low-cost here refers to the requirements imposed by the selected dynamics model on the on-board processor in terms of memory requirements and CPU demands.

3.5 Analysis of OD Accuracy

A GPS-based estimation filter has been built to assess the performances of such a system in the selected HEO scenarios. Ref. [7] gives more details on the models and algorithms implemented. Here we simply remind the very fundamentals of the estimation technique employed:

- An extended Kalman filter is used to perform estimation of the following state vector:

  $$\vec{x}_{state} = \left\{ \vec{x} \quad \vec{v} \quad E_{clock} \quad \Delta T_B \quad \vec{b} \quad \vec{I} \right\}^T$$

  where $\vec{x}$ is the spacecraft position vector, $\vec{v}$ is the spacecraft velocity vector, E_{clock} is the normalised frequency of the GPS receiver clock, ΔT_B is the time bias of the GPS receiver clock, $\vec{b}$ is the range bias at each of the GPS receiver channels (note that these are modelled as 1st order Gauss-Markov processes, attempting to attenuate the disturbing effect of selective availability) and $\vec{I}$ is the Doppler integration constants at each of the GPS receiver channels.
- The previously stated orbit dynamics models is used for the purposes of on-board propagation of the position and velocity state vector components.
- Both pseudo-range and integrated Doppler measurements are processed in a sequential fashion to perform state vector update.

The simulation results obtained are shown in Table 3-1.

	RMS (m)	Maximum (m)
Along-track	61.270	216.785
Across-track	61.270	252.743
Radial	104.011	390.187
TOTAL	153.362	499.049

Table 3-1: GPS-based OD performances

3.6 Conclusions

From the above analyses it is shown that the following minimal hardware/software configuration allows to achieve the prescribed OD accuracy requirements:

- Hardware requirements:
  - A low-cost C/A code GPS receiver of at least 6 independent channels and able to acquire/track GPS signals which SNR is above 38 dB
  - A single GPS receiver antenna (having a field of view of 160 degrees, a gain in the maximum gain direction of 6 dB and a gain loss through the antenna field of view of up to 8 dB) with its boresight looking to nadir.
- Software requirements: an on-board GPS-based Orbit Determination filter (Kalman based) with the characteristics described at section 3.5 above.

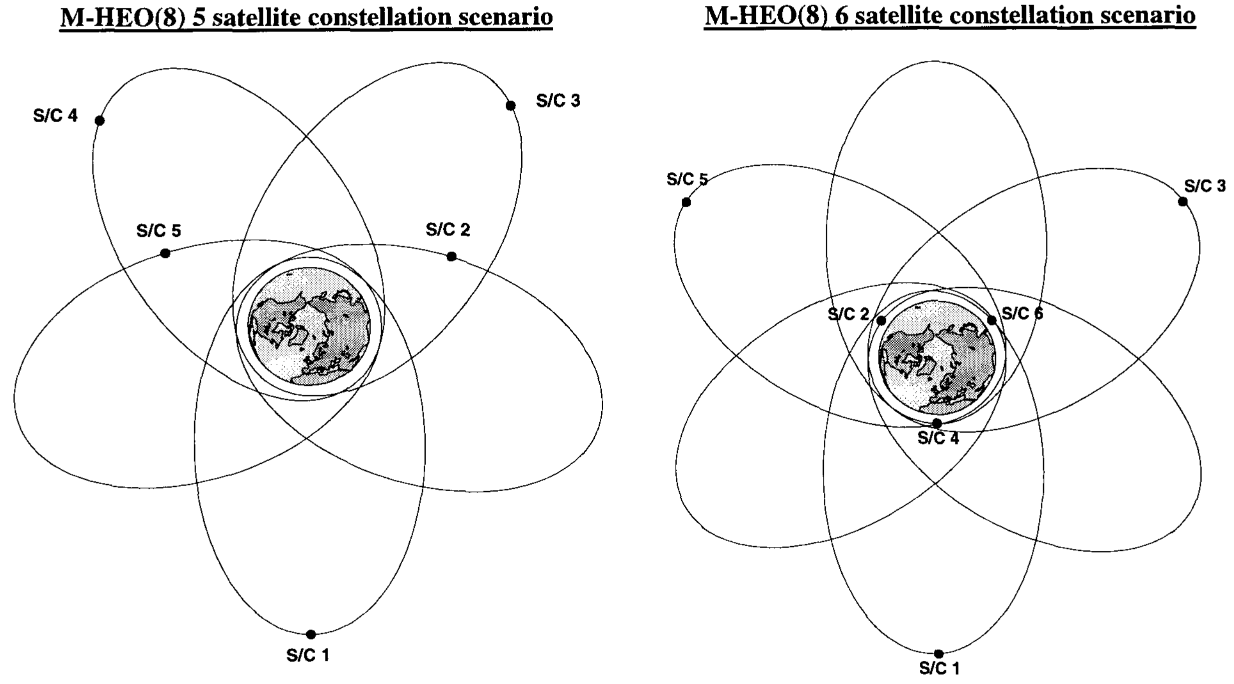

M-HEO(8) 5 satellite constellation scenario

M-HEO(8) 6 satellite constellation scenario

Figure 3-5: Archimedes satellite constellation scenarios

4. THE ORBIT CONTROL OF ARCHIMEDES

The problem of the orbit control was analysed not for a single satellite but for the whole constellation of 5 and 6 satellites which, it is expected, will be required for the Archimedes mission. The presence of a constellation adds complexity to the orbit control problem since it entails the need to control not only the absolute position of the satellite's orbital planes but also their relative position and synchronisation. A set of 22 cities in 3 different service zones has been chosen to define the constellation visibility acceptance criteria.

Five different orbit control strategies have been investigated which are depicted in the following.

4.1 Ground-track or semi-major axis control

The control of the ground-track (or semi-major axis control) is mandatory for this type of orbit. This is a low cost maintenance performed by perigee manoeuvres to increase the semi-major axis (period) of the orbit. The selected ground-track control strategy is based in defining a reference or optimum value of the apogee longitude as a function of the current value of the argument of perigee $\lambda(\omega)$ which is obtained through a thorough visibility acceptance criteria analysis. The natural evolution of the apogee longitude is to increase (East motion) due to the tesseral perturbation. At each perigee passage, the geographical longitude of the corresponding apogee over Europe is computed. If the difference between the actual apogee longitude λ and the reference value $\lambda(\omega)$ is greater then a given margin $\Delta\lambda$, then a ΔV manoeuvre at perigee is performed to increase the semi-major axis. The new (target) value of the semi-major axis is $a = a_{ref} + \Delta a$, where the reference semi-major axis a_{ref} is the theoretical value of the semi-major axis which provides an orbit with a 8 hour repetitive ground-track, taking into account the nodal regression. Since the regression of the nodes depends on the eccentricity and inclination of the orbit, then the reference semi-major axis is a function of those dynamic parameters. The increment of the semi-major axis Δa is a constant control parameter to increase the reference value such that a West motion is induced in the ground-track. The apogee longitude decreases down to a given minimum and then increases again due to the natural decrease of the semi-major axis.

4.2 Definition and performances of station keeping strategies

Station Keeping at the critical inclination: the first set of orbit control strategies is based on the selection of the critical inclination (63.435 deg) as the initial value of the orbital inclination for all the satellites of the constellation. The natural evolution of the argument of perigee as a function of its initial value shows that the initial optimum value is between 255 and 260 degrees. Higher values of this parameter would require effective control of the argument of perigee which is very expensive. The selected value for this study was of 260 degrees. The long-term evolution of the eccentricity for an Archimedes constellation shows two different perturbations:

- A 4.5 year periodic perturbation by lunisolar effects which is different for each satellite of the constellation.
- A secular variation due to resonant effect of the orbit control. This perturbation is similar for all S/C.

The nominal value of the eccentricity is 0.636 (perigee height of 1,000 Km). If the eccentricity is not controlled some satellites of the Archimedes constellation will re-enter into the Earth atmosphere before the end of the 10 years operational lifetime due to the secular perturbation. There are two ways to avoid this problem:

- to impose an eccentricity control (which may cost up to 200 m/s), or
- to select a lower value of the initial eccentricity (about 0.6) which is equivalent to having a higher value of the initial perigee height.

The 4.5 year eccentricity periodic perturbation imposes a differential node regression rate for each of the S/C of the constellation. This leads to a de-synchronisation of the constellation due to a large error on the relative position of the orbital planes. This problem can be corrected by the individual optimisation of the initial eccentricity for each satellite of the constellation.

A suitable station keeping strategy must cope with the problem of periodic (de-synchronisation) and the secular (perigee decay) eccentricity perturbations. Three different options have been analysed:

1. No eccentricity control:
   - The secular eccentricity perturbation is compensated by a lower initial value (0.6) of the eccentricity, which is equivalent to having a higher initial perigee height.
   - The periodic eccentricity perturbation is compensated by the individual optimisation of the initial eccentricity (perigee height) for each satellite (range of value between 1,500 and 1,800 Km).
2. Partial eccentricity control:
   - The secular eccentricity perturbation is compensated by control manoeuvres, 3 or 4 manoeuvres in 10 years are enough, which represent 82-112 m/s.
   - The periodic eccentricity perturbation is compensated by the individual optimisation of the initial eccentricity (perigee height) for each satellite (range of value between 1,000 and 1,200 Km).

3. Full eccentricity control:

- The secular and periodic eccentricity perturbations are compensated by very frequent control manoeuvres, up to 200 m/s in 10 years are needed.

Station Keeping at optimised inclination: it has been demonstrated that small variations of the orbital inclination (close to the critical) show a very good influence on the natural evolution of the argument of perigee. In particular, lower inclinations than the critical one, provide stability to the long-term evolution of the argument of perigee; initial orbital inclinations in the range from 62.2 to 62.8 degrees yield to an initial increase of the argument of perigee followed by a final decrease. Thus, selecting an initial value of the argument of perigee of 263 degrees, it is possible to find out an optimal initial inclination (of about 62.6 degrees) for each individual spacecraft for a given constellation such that the argument of perigee increases up to 277 degrees in the first period and than decreases down to the initial value after 10 years lifetime. Argument of perigee values under 270 degrees provide an increase of the eccentricity while higher values provide a decrease. This combination yields to an equilibrium between periods $\omega > 270$ and $\omega < 270$ degrees. The final result is that the secular perturbation of the eccentricity is cancelled and the argument of perigee is kept within ±7 degrees from its nominal 270 degrees.

A suitable station keeping strategy must then cope with the problem of the periodic (de-synchronisation) eccentricity perturbations. Two different options have been analysed:

1. No eccentricity control:

- The secular eccentricity perturbation is compensated by the optimisation of the initial orbit inclination according to the above proposed scheme.
- The periodic eccentricity perturbation is compensated by the individual optimisation of the initial eccentricity (perigee height) for each satellite (range of value between 1,000 and 1,300 Km).

2. Full eccentricity control:

- The secular eccentricity perturbation is compensated by the optimisation of the initial orbit inclination according to the above proposed scheme.
- The periodic eccentricity perturbation is compensated by very frequent control manoeuvres, up to 200 m/s in 10 years are needed.

Table 4-1 shows the ΔV budget of each strategy.

			Archimedes: 5 S/C constellation ΔV budget for 10 years mission lifetime				
			S/C 1	**S/C 2**	**S/C 3**	**S/C 4**	**S/C 5**
1	**Station Keeping at critical inclination**	No eccentricity control	8.648	7.966	6.916	6.742	7.881
2		Partial eccentricity control	82.27	112.2	111.5	85.12	86.06
3		Full eccentricity control	164.1	178.6	178.5	150.1	167.1
4	**Station Keeping at optimised inclination**	No eccentricity control	13.457	13.545	13.491	13.478	13.550
5		Full eccentricity control	169.79	188.32	192.73	169.33	181.11

Table 4-1: Orbit control ΔV budget for different station keeping methods and 5 S/C constellation

			Archimedes: 6 S/C constellation ΔV budget for 10 years mission lifetime					
			S/C 1	**S/C 2**	**S/C 3**	**S/C 4**	**S/C 5**	**S/C 6**
1	**Station Keeping at critical inclination**	No eccentricity control	7.687	6.914	5.926	5.464	5.782	7.000
2		Partial eccentricity control	85.75	85.37	110.7	84.13	84.16	85.31
3		Full eccentricity control	161.1	171.6	181.9	162.5	159.3	167.7
4	**Station Keeping at optimised inclination**	No eccentricity control	13.64	13.54	13.45	13.49	13.60	13.63
5		Full eccentricity control	170.2	185.4	196.3	177.3	173.7	181.9

Table 4-1: Orbit control ΔV budget for different station keeping methods and 5/6 S/C constellation

4.3 Selected station keeping strategy

The main characteristics of the 5 proposed orbit control options are summarised in Table 4-2, including the initial perigee height, the evolution of the argument of perigee, the initial inclination, manoeuvres at apogee, the total control ΔV and the required ΔV to inject the spacecraft from a parking orbit of 400 Km radius into the operational orbit. In a first selection, options 1 and 4 are preferred with respect to the remaining since they require only ground-track control manoeuvres at perigee. Eccentricity control is not required. The total ΔV required in 10 years is small compared to the station keeping options with eccentricity control. Option 4 is preferred with respect to option 1 due to the following reasons:

- The initial perigee heights of option 4 (1,000 to 1,300 Km) are lower than the corresponding to option 1 (1,500 to 1,800 K). Therefore, the injection ΔV from the 400 Km parking orbit is much smaller: 72-107 m/s compared to 130-164 m/s.
- The range of variation of the argument of perigee is closer to the nominal 270 degrees (263-277 degrees for option 4 while 255-260 for option 1). Therefore less interference with geostationary satellites are expected.

	CRITICAL INCLINATION			OPTIMISED INCLINATION	
	OPTION 1	**OPTION 2**	**OPTION 3**	**OPTION 4**	**OPTION 5**
	No eccentr. control	**Partial eccen. control**	**Full eccentr. control**	**No eccentr. control**	**Full eccentr. control**
Initial perigee height (Km)	1,500-1,800	1,000-1,300	1,000	1,000-1,300	1,000
Argument of perigee (deg)	260° → 255°	260° → 255°	260° → 255°	263° ↔ 277°	263° ↔ 277°
Initial inclination (deg)	63.435°	63.435°	63.435°	62.45°-62.65°	62.45°-62.65°
Manoeuvres at apogee ?	No	Yes (3-4)	Yes (frequent)	No	Yes (frequent)
Total control ΔV (m/s)	5-9	82-112	150-180	13.5	170-200
Injection ΔV (m/s)	130-164	72-95	72	72-107	72
Minimum elevation	GOOD	GOOD	VERY GOOD	GOOD	VERY GOOD

Table 4-2: Summary of Archimedes orbit control strategies

		Δa [Km]									
Δλ		**0.75**	**1.0**	**1.25**	**1.5**	**1.75**	**2**	**2.5**	**3**	**3.25**	**3.5**
±0.5°	Mean ΔV (m/s)	0.09	0.118	0.145	0.171	0.196					
	Time bet-mano. (days)	24	31	39	45	51					
	Total ΔV (m/s)	13.5	13.5	13.6	13.5	14.1					
±1.0°	Mean ΔV (m/s)					0.198	0.224	0.277	0.3		
	Time bet-mano. (days)					53	60	73	50		
	Total ΔV (m/s)					13.5	13.4	13.6	21		
±1.5°	Mean ΔV (m/s)								0.329	0.355	0.367
	Time bet-mano. (days)								87	93	88
	Total ΔV (m/s)								13.5	13.8	15

Table 4-3: Ground-track control parametric analysis

EUROPE				NORTH AMERICA				FAR EAST			
Δλ	**±0.5°**	**±1.0°**	**±1.5°**	Δλ	**±0.5°**	**±1.0°**	**±1.5°**	Δλ	**±0.5°**	**±1.0°**	**±1.5°**
Nicosia	48.0	47.1	46.7	**Vancouver**	54.0	53.9	53.1	**Hong-Kong**	30.6	30.6	30.2
Tunis	54.3	54.1	54.1	**Regina**	62.1	61.5	60.9	**Peking**	47.6	47.8	46.8
Porto	45.2	45.1	44.0	**Boston**	41.8	40.6	40.6	**Changchun**	56.9	57.0	56.3
Cork	51.5	50.5	49.9	**Quebec**	44.3	43.1	42.9	**Sapporo**	61.9	60.9	60.5
Edinburgh	53.9	53.6	53.0	**Miami**	35.1	34.4	34.1	**Tokyo**	55.1	55.0	55.0
Trondheim	53.5	52.8	52.3	**Corpus Christ**	45.5	45.3	45.2	**Tai-nan**	34.8	34.8	34.6
Leningrad	54.9	54.0	53.6	**Los Angeles**	46.4	46.5	45.7				
Moscow	53.9	53.1	53.0	**San Francisco**	46.8	46.7	45.9				

Table 4-4: Minimum elevations for different apogee longitude margins

4.4 Orbit control parametric analysis

The selected station keeping strategy incorporates a ground-track control which, as defined previously, is driven by two parameters:

- The margin of maximum deviation of the apogee longitude from the reference value (Δλ). A manoeuvre is performed if the actual deviation is greater than this value.

- The additional increment of the semi-major axis at the control manoeuvre (Δa) in order to induce a west motion on the ground-track and the corresponding decrease of the apogee longitude to correct the natural eastwards drift.

A sensitivity analysis has been performed with respect to these parameters and the results are shown in Table 4-3 and Table 4-4

Three different values of $\Delta\lambda$ have been considered: 0.5, 1.0 and 1.5 degrees. For each value, an increasing scan of Δa has been performed . This scan provides an optimum value (shadowed in Table 4-3) identified by a maximum value of the time between two consecutive orbit control manoeuvres. For an apogee margin of 0.5 degrees, the optimum semi-major axis increment is 1.5 Km, since higher values produce an increase in the total ΔV and a decrease of the time between manoeuvres. For an apogee margin the optimum semi-major axis increment is of 2.5 Km and for an apogee margin of 1.5 degrees, this is of 3.25 Km.

The minimum elevation analysis (Table 4-4) show that the frequency and size of the manoeuvres can be conveniently chosen within a large range of values without a significant penalty in terms of minimum elevation over the service zones.

5. REFERENCES

[1] Lear, W.M., "GPS Navigation for Low Earth Orbiting Vehicles", NASA, May 1987.

[2] Legido, J.M., Martínez-Olague, M.A., "Tracking of Geostationary Satellites with GPS, GPS-GEOTRACK, Phases 1 & 2 Final Report", Doc. No. GMVSA 2070/94, issue 1, July 1994.

[3] CNES, "Measurement of the RGIC Signal Code/Carrier Coherency with a GPS Receiver", Proceedings of the ION GPS-92, Alburqueque, New Mexico, USA, September 1992.

[4] Wertz, J.R., Larson, W.J. (ed.), "Space Mission Analysis and Design", Kluwer Academic Publishers, 1991.

[5] Potti, J., Peláez, A., "SOAP S/W User's Requirements Document", Doc. No. GMV/ODISHEO/SW/URD (GMVSA 2079/94), issue 01, August 1994. Study on Orbit Determination for Satellites at HEO (ODISHEO).

[6] Lecohier, G, "Archimedes Orbit Determination for the Tundra, Super Tundra and Molniya Orbit", Internal ESTEC Working Paper No. 1539, May 1989.

[7] Potti, J., Peláez, A. and Mora, E.J., "Detailed Definition of Orbit Determination Algorithms", WP-2000 Technical Note, Study on Orbit Determination for Satellites at HEO (ODISHEO), Doc. No. GMV/ODISHEO/TN/2000, issue 03, February 1995.

[8] Belló-Mora, M., GMV Contribution to Archimedes Phase A, "Station Keeping Strategies", WP-2000 Technical Note, Doc. No. GMVSA 2105/94, issue 1, October 1994.

RELATIVE GPS NAVIGATION DESIGN AND VALIDATION FOR ATV RENDEZ-VOUS

Hervé Marcille, Gérard Moreau, Virginie Pascal
Matra Marconi Space, 31 ave des Cosmonautes, 31402 Toulouse Cedex 4
Fax: (0)5.62.19.77.69; E-mail: *firstname.name*@tls.mms.fr

3rd ESA Symp. on Spacecraft Guidance, Navigation & Control Systems;
ESTEC, Noordwijk, November 25-28 1996

ABSTRACT

Through the ARP program (ATV Rendezvous Pre-development), ESA will demonstrate European mastering of the critical technologies involved in the achievement of autonomous rendezvous and docking of the future Automated Transfer Vehicle (ATV) to the International Space Station Alpha (ISSA). In the frame of this program, a GPS-based relative navigation system (RGPS) has been developed for use as the primary navigation reference for the long-range proximity operations (12 km to ~300 m). The baseline concept relies on a Kalman filter processing the data received simultaneously from two GPS receivers, one on ATV, and one on ISSA. Performance and robustness of the RGPS filter has been demonstrated by high fidelity simulations. Further validation of this RGPS concept has been performed in an open-loop test campaign carried out at ESTEC GPS-Lab (RGPS filter + actual ARP-GPS + NTC GPS stimulator). The next validation step shall be to process flight data obtained from the ARP-GPS during rendez-vous operations of STS 80 / ASTRO-SPAS. The very satisfactory results obtained in the frame of the above RGPS development and validation activities are presented in this paper.

1. INTRODUCTION

In 1994, the ATV Rendezvous Pre-development (ARP) program has been initiated by ESA in parallel to the ATV phase B in order to demonstrate Europe capability to master the key technologies involved in performing the ATV to ISSA orbital rendezvous (ref [2]), among which the relative GPS (RGPS) navigation technique. The ARP program includes the following elements and objectives:

- The rendezvous system pre-development (called ARP-Kernel with Matra Marconi Space as prime contractor).
- The development of a Rendezvous Sensor (RVS) by DASA JENA Optronik (ARP-RVS contractor).
- The procurement of a GPS receiver (ARP-GPS), by Laben (ARP-GPS contractor) based on the Laben/Loral Tensor^{TM}, which is used during ARP-Kernel activities for verification and demonstration of the relative GPS algorithms (ground tests and flight demonstration).

In the following, we shall focus on the RGPS navigation activities:

- Functional description of the RGPS navigation function, already detailed in [1].
- RGPS performance results from a high fidelity simulator.
- Results of the open-loop test campaign with the ARP-GPS receiver H/W.
- Expectations for the ARP Flight Demo 1 activities, i.e. RGPS post-processing of actual flight GPS data.

The activities undertaken in the frame of ARP-Kernel for the relative GPS aim at demonstrating with a full scale prototype that the RGPS is a relevant technology element for the automatic rendez-vous planned for the ATV.

2. RGPS FILTER DESCRIPTION

2.1 Operational conditions

The RGPS operations are triggered at about 12 km from the ISSA, once the ATV enters the ISSA communication range. This allows ATV to receive in real time the GPS data from the ISSA GPS receiver, through a local link. ATV absolute navigation/attitude estimation are already available, since they are needed for pre-Rendez-Vous operations. ATV and ISSA GPS receivers provide the GPS raw data at a 1 Hz rate, with a maximum latency of 2 sec (accounting for the local-Link delay). Both receivers operate on a single L1 frequency in C/A code, assuming Selective Availability active. During all the proximity operations, the ISSA is supposed to be a "co-operative target" in the sense that it does not perform linear control burns.

The performance requirements apply to the estimates of the relative position/velocity of the ATV with respect to the ISSA Local Vertical/Local Horizontal (LV/LH) frame. They are as follows:

position error	< 10 m (3σ)
velocity error	< 0.05 m/sec (3σ)

Proceedings Third International Conference on Spacecraft Guidance, Navigation and Control Systems, ESTEC, Noordwijk, The Netherlands, 26-29 November 1996, ESA SP-381 (February 1997)

2.2 RGPS filter functional description

The detailed functional description of the ARP-K RGPS filter is provided in ref[1]. Its basic principle is shown in Figure 2.2/1. It consists in using directly the differential GPS observables obtained by subtracting the target GPS raw data from the corresponding quasi-simultaneous chaser GPS raw data. This approach allows to cancel out directly the correlated errors that form the essential contribution to overall GPS performance systems (ionospheric delay, Selective Availability, ...). These data are then processed in the RGPS Kalman Filter fed in parallel by the available estimates of absolute navigation (from absolute GPS navigation filter) and attitude. The chaser control thrusts are taken into account in the RGPS dynamics propagator, based on a priori knowledge of the commanded accelerations (from the Control function).

The selected filter implementation is modular, separating the Absolute GPS navigation filter (needed throughout the mission) from the RGPS filter (needed only for Rendez-Vous operations). The latter filter only uses the output of the absolute filter for determination of the GPS satellites lines of sight. The obtained RGPS filter works with a relatively small state vector (8 states) made of:

- 3 relative position estimates*
- 3 relative velocity estimates*
- 1 relative clock bias estimate
- 1 relative normalized frequency error estimate

(*) relative position and velocity are expressed in the target Local Vertical/Local Horizontal (LV/LH) frame

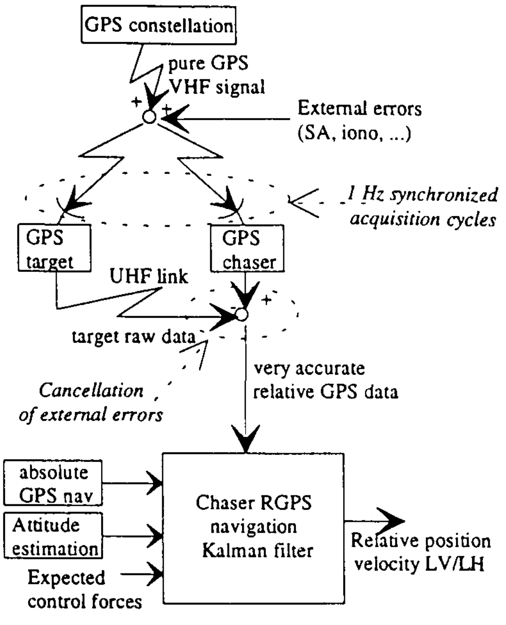
GPS constellation
pure GPS
VHF signal
+
+
External errors
(SA, iono, ...)
1 Hz synchronized
acquisition cycles
GPS
target
GPS
chaser
UHF link
+
-
target raw data
Cancellation
of external errors
very accurate
relative GPS data
absolute
GPS nav
Attitude
estimation
Expected
control forces
Chaser RGPS
navigation
Kalman filter
Relative position
velocity LV/LH

Figure 2.2/1 - Principle of RGPS navigation

The selected GPS observables are the pseudo-range and the carrier cycle count, primarily differentiated between chaser and target to obtain relative observables. The latter observables are directly back-differentiated to get a relative "delta-range" pseudo-measurement, treated as a relative velocity measurement. These data for the 4 best in view GPS satellites are processed in the RGPS filter according to the principle shown in Figure 2.2/2.

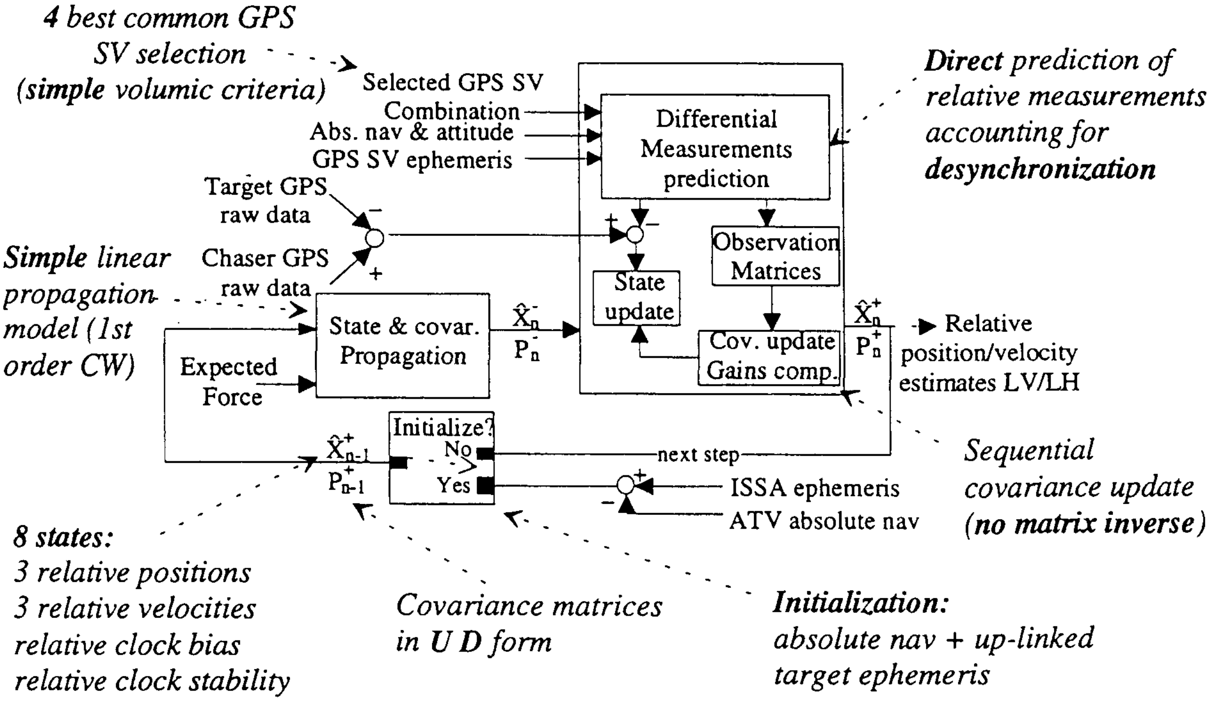
4 best common GPS
SV selection
(simple volumic criteria)
Selected GPS SV
Combination
Abs. nav & attitude
GPS SV ephemeris
Target GPS
raw data
Chaser GPS
raw data
-
+
Simple linear
propagation
model (1st
order CW)
Differential
Measurements
prediction
+
-
Observation
Matrices
State
update
Cov. update
Gains comp.
State & covar.
Propagation
Expected
Force
$\hat{X}_n^-$
P_n^-
$\hat{X}_n^+$
P_n^+
Relative
position/velocity
estimates LV/LH
Direct prediction of
relative measurements
accounting for
desynchronization
Initialize?
No
Yes
$\hat{X}_{n-1}^+$
P_{n-1}^+
next step
+
-
ISSA ephemeris
ATV absolute nav
Sequential
covariance update
(no matrix inverse)
8 states:
3 relative positions
3 relative velocities
relative clock bias
relative clock stability
Covariance matrices
in U D form
Initialization:
absolute nav + up-linked
target ephemeris

Figure 2.2/2 - RGPS filter functional description

3. RGPS PERFORMANCE EVALUATION

The RGPS algorithms described in §2 have been implemented full scale under the Xmath/SystemBuild™ environment in view of prototyping the actual on-board S/W by direct autocoding of the SystemBuild code into C code. In parallel, a high fidelity S/W model of the GPS measurement system has been developed for simulation purposes. It includes models of the GPS constellation, the navigation message interface, the GPS receiver model, and the space environment. This GPS S/W model has been used to feed the SystemBuild RGPS navigation model for open-loop performance evaluation.

The performance evaluation campaign has been carried-out based on a realistic rendez-vous scenario featuring a full Vbar approach (i.e. along the velocity axis). This corresponds to ~ 7000 sec, from 7 km to 300m relative distance. The input scenario was generated by the guidance/control ARP-K team (of DASA), based on highly representative dynamics and the actual prototype of guidance and control functions.

The GPS antenna configuration working assumption was very unfavorable for relative GPS navigation in term of GPS satellite common visibility from chaser/target. This situation lead to quite pessimistic results, where indeed 4 common GPS satellites were available only 60% of the time. Within the on-going ARP/ATV activities, the situation has evolved towards a much more favorable antenna relative configuration, as used for GPS-Lab testing (§4).

The GPS receivers measurement error figures are those specified for the ARP-GPS receiver i.e.: 10 m (3σ) pseudo range noise, and 6mm (3σ) carrier cycle count noise. In addition, all other effects independent from the receiver are included in the simulation (ionospheric delay, SA, ephemeris uncertainty, ...).

A Monte-Carlo analysis has been carried out based on 400 simulation cases, allowing to derive statistical performance indicators for the RGPS filter. These results are summarized in Table 3/1. This table contains two performance budgets, the first one corresponds to a "typical" GPS visibility scenario, i.e. the GPS global observability level encountered in 60% of the cases. The second budget covers more than 99% of the simulation cases, interpreted as a worst case visibility condition scenario.

With a more favorable antenna configuration, as the one more recently baselined for ARP-K (zenith pointing antenna, 75° half-cone angle, on both spacecraft), it is expected that the experienced GPS visibility will yield 3σ performances well within the typical budget of Table 3/1. Note also that the GPS constellation used for this evaluation was reduced by specification to a worst case of 21 operative GPS satellites, whereas 24 are nominally operating.

	Position error (3σ, m)			Velocity error (3σ, cm/sec)		
	X	Y	Z	X	Y	Z
Typical budget (average GPS visibility)	2.9	1.5	3.9	0.8	0.4	1.0
Worst case budget (worst case GPS visibility)	8.6	4.4	11.8	2.4	1.0	3.0
Specification	*10*			*5*		

Table 3/1 - RGPS statistical performance budget (with unfavorable relative antenna configuration)

The number of GPS satellites in common visibility has been averaged over the 400 simulation cases, to obtain the average time history of Figure 3/2. This illustrates the very challenging operating conditions of the RGPS filter in the frame of this analysis.

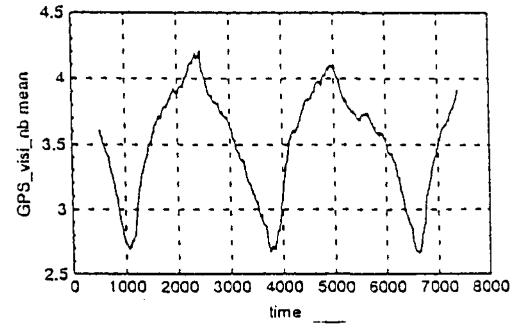

Figure 3/2 - Number of GPS satellites in common visibility (average over 400 runs)

The results of this performance evaluation has allowed to illustrate the need for a largest possible commonality of GPS antenna coverage between both spacecraft. Providing that this is correctly implemented, the obtained performance results are very satisfactory with respect to the desired accuracy for ATV Rendez-Vous operations.

4. GPS-LAB OPEN-LOOP TEST RESULTS

An open-loop test campaign has been carried out at ESTEC GPS-Lab, using the NTC GPS stimulator and a Demonstration Model (DM) of the actual ARP-GPS receiver. The primary objective of this campaign was to validate the GPS S/W model used for simulation with respect to both the GPS environment (comparison with GPS-Lab GPS system emulation) and the receiver modelling part (comparison with actual GPS output data). However, another interesting goal was to complement the RGPS filter validation by running it with actual GPS data. The principle of this test campaign is similar to the one used in ref[4].

The test set up is summarized in Figure 4/1. Since only one receiver is available, the GPS data acquisition is performed in two sequential runs, one for the chaser vehicle, one for the target vehicle. The trajectory of both vehicles are provided in open-loop, like in the navigation simulation of §3. The obtained GPS data from both runs are then stored and used to feed the RGPS filter model for performance evaluation and diagnosis. The obtained results are then compared with those obtained from an "all S/W" simulation as in §3. A number of intermediate result files are used for a thorough validation of the whole system, as described in Figure 4/1. For this test campaign, a single zenith antenna configuration was used for both vehicles, yielding correct GPS satellites common visibility conditions. All environmental parameters, and in particular the input signal to noise ratio at GPS feedline connection was tuned to the best estimate of actual space conditions. The only known limitation of this test environment is the lack of a realistic multipath model (lack of ATV realistic data to feed the available GPS-Lab model).

A number of single receiver test cases have been performed and allowed to validate thoroughly the GPS S/W model. Four test cases have been carried out for use in the RGPS filter, all conducted on the same reference full ATV Vbar approach described in §3:

- *RGPS1*: Nominal conditions
- *RGPS2*: Robustness to visibility holes by switching off gradually, then back on again the set of visible GPS satellites (10min of black-out).
- *RGPS3*: Increased level of ionospheric and Selective availability errors to check their cancellation in the RGPS filter.
- *RGPS4*: low input signal to noise ratio to provoke a high cycle slip rate.

All tests produced very satisfactory results for the RGPS filter both in term of performances and robustness. Indeed, the *RGPS1* nominal test lead to less than 2 m / 5 mm/sec relative position/velocity error, while all others remained within the typical budget of §3 in spite of the degraded measurement conditions imposed. The correlation with reference results obtained in the "All S/W" configuration of §3 is startling, as illustrated on Figures 4/2 & 4/3 (Nominal test case). These results allow to conclude to a very successful validation of both the RGPS filter algorithms and their simulation test environment.

In addition, several characteristics of the ARP-GPS receiver were identified through this campaign. Some erroneous data or behaviors of the receiver were detected (through RGPS rejection tests) and reported for further correction at receiver level. The pseudo-range measurement noise has been measured at less than 1.5 m 1σ, instead of 10m specified. The observed cycle slip rate in nominal conditions is of 1 per 500sec per channel, among which about 17% are detected and flagged by the receiver itself. With a degraded signal (*RGPS4* test), this rate increased to 1 per 30 sec per channel, with 82% detection probability at receiver level. In any case, all unflagged cycle slips were correctly rejected at the RGPS innovation rejection test level, with therefore no visible impact on the estimation performance.

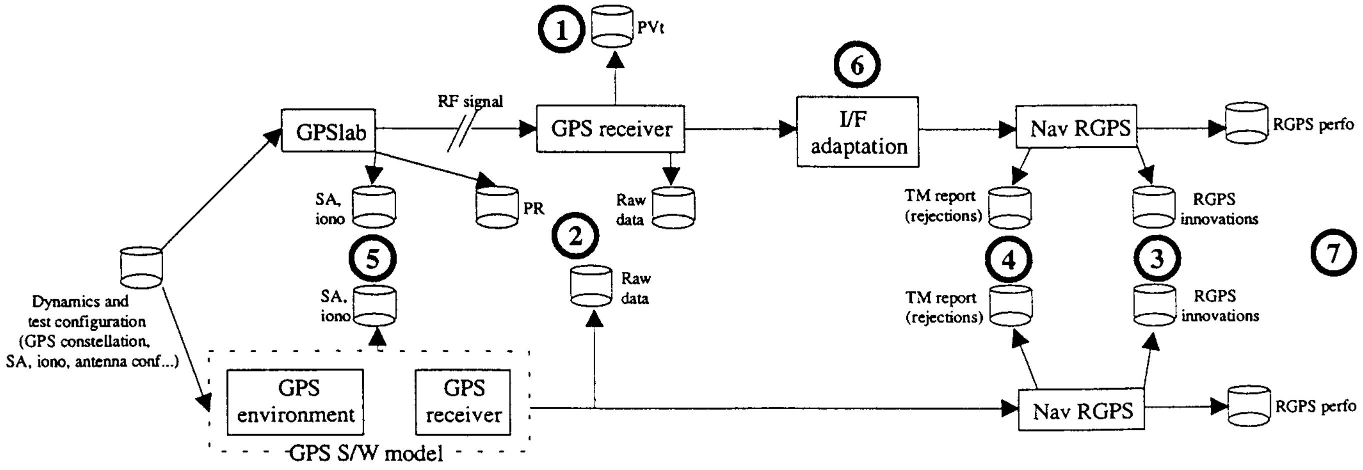

① Global behaviour of GPS receiver (satellite tracking, clock parameters, ...)

② - validation of S/W model (measurement, GPS system tracking)
- identification of GPS performance (pseudo-range, carrier cycle count)

③ GPS measurements performance identification (Pseudo-range &carrier cycle count accuracy, cycle slips, ...)

④ Identification of erroneous GPS data

⑤ Validation of S/W model : SA and ionosperic models

⑥ Check of output format / conversion

⑦ Validation of RGPS performance / robustness

Figure 4/1 GPS-Lab open loop test set-up and validation check points

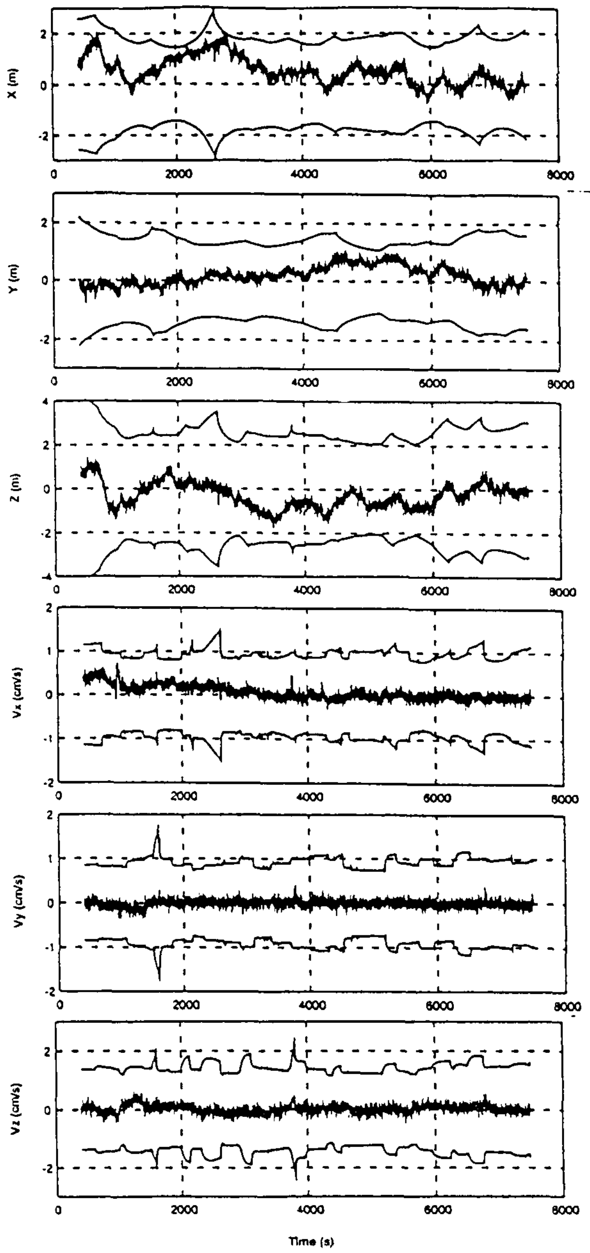

Figure 4/2 - RGPS1 performance results with the GPS S/W model (position/velocity in LV/LH frame)

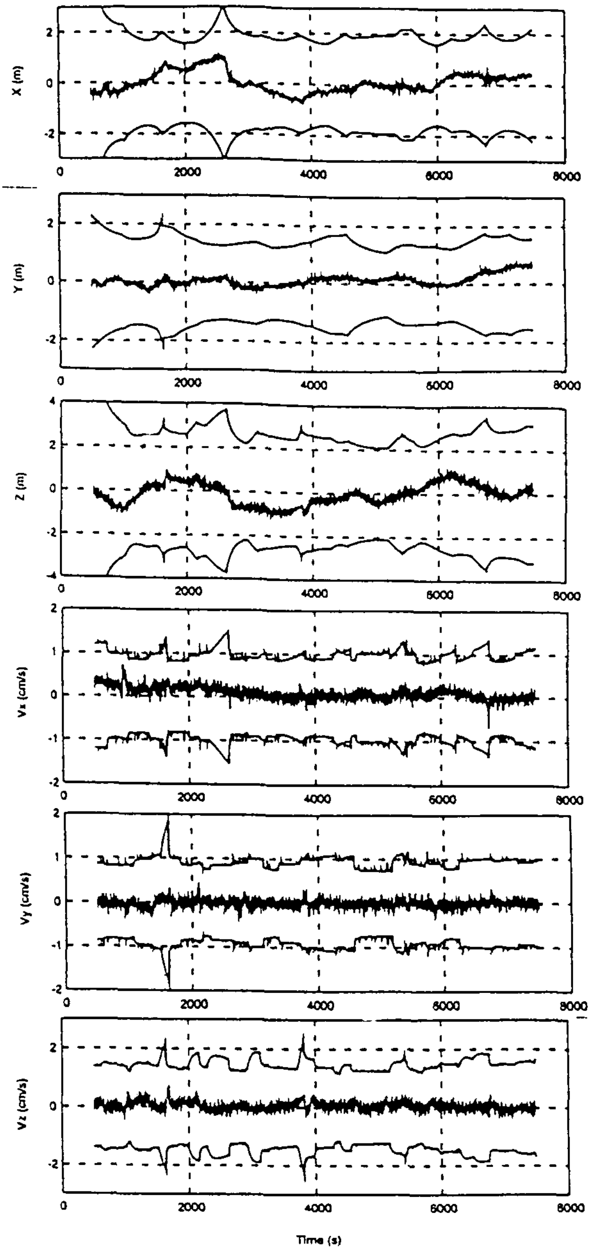

Figure 4/3 - RGPS1 performance results with the actual GPS data (position/velocity in LV/LH frame)

5. USE OF ACTUAL FLIGHT DATA

In the frame of the extended validation campaign of the ARP-Kernel project, three flight demonstrations are planned. The first one (FD1) relies on Shuttle flight STS 80 with launch planned on November 19, 96. The ARP-GPS flight model is mounted on a retrievable platform (ASTRO-SPAS) which is disposed from the Shuttle bay at beginning of mission, and retrieved 15 days later. The ARP experiment consists in operating the ARP-GPS receiver during both disposal and retrieval phases (featuring space Rendez-Vous conditions). The second receiver is the NASA Tans Quadrex (6 channels), which remains in the Shuttle bay throughout these phases. Actual GPS raw data from both receivers are recorded for on-ground post-processing with the RGPS algorithms. The relative navigation estimates obtained from the ARP-K RGPS filter will then be compared to best estimate relative trajectory available from several sources: by processing concurrently the accurate relative range/line-of-sight data from the shuttle "TCS" laser sensor, and through high accuracy DGPS orbit determination obtained from ESOC (ref[3]), that should provide a 30cm relative estimation performance.

The experienced flight conditions obtained in FD1 will of course differ from the baseline nominal ATV approach. In particular, both the Shuttle and ASTRO-SPAS will undergo wide angle attitude maneuvers during both disposal and measurement phases. This will lead to operate the GPS receivers with antenna boresights up to 90° from zenith, yielding temporary periods with very bad visibility conditions. However, both spacecraft will follow the same attitude profile in order to maximize the common visibility conditions. In addition, the expected control accelerations (to feed the RGPS propagator) shall be available only from inertial measurement, with a priori less accuracy than the propagation noise modeled in the ATV-adapted RGPS filter.

In order to predict the achievable performances, the FD1 disposal and retrieval phases have been evaluated on the RGPS S/W test bench, based on reference trajectories provided by NASA. The results are shown on Figure 5/1 & 5/2, where the retrieval phase is divided in two parts corresponding to the bad visibility conditions for the start of rendez-vous, and to the good zenith pointing situation of the end of the rendez-vous. The expected estimation errors are presented as the norm of the residual position/velocity errors, with the corresponding 3σ envelope. The peaks in the velocity error result from an accuracy of control forces inertial measurement beyond the expected on-board knowledge for ATV.

It is expected to obtain through this flight demo very useful data for a more thorough validation of the RGPS performance confronted to real space environment

REFERENCES

[1] M. Frezet, H. Marcille, J.M. Pairot, V. Pascal (MMS), H.Barré, M. Cislaghi, U. Thomas (ESA): *Relative GPS Navigation for ATV Rendez-Vous.* ION GPS Meeting, Palm Springs, Sept 12-15 1995.

[2] M. Cislaghi, U. Thomas (ESA), M. Lellouch, J.M. Pairot (MMS): *Development and Verification of Automated Rendez-Vous for ATV.* AIAA, 47th International. Astronautical Congress; Beijing, Oct 7-11, 1996.

[3] T.J. Martin Mur, J.M. Dow, S. Casotto, N. Bondarenco, J. Feltens, C. Garcia Martinez: *Use of GPS for Precise and Operational Orbit Determination at ESOC.* ION GPS Meeting, Palm Springs, Sept 12-15 1995.

[4] J.M. Legido, M.A. Martinez, R. Lucas: *Differential and Relative Navigation Results with a GPS Receiver for Space Applications.* Proceedings of ESA International Conference on GNC, Noordwijk, April 1994.

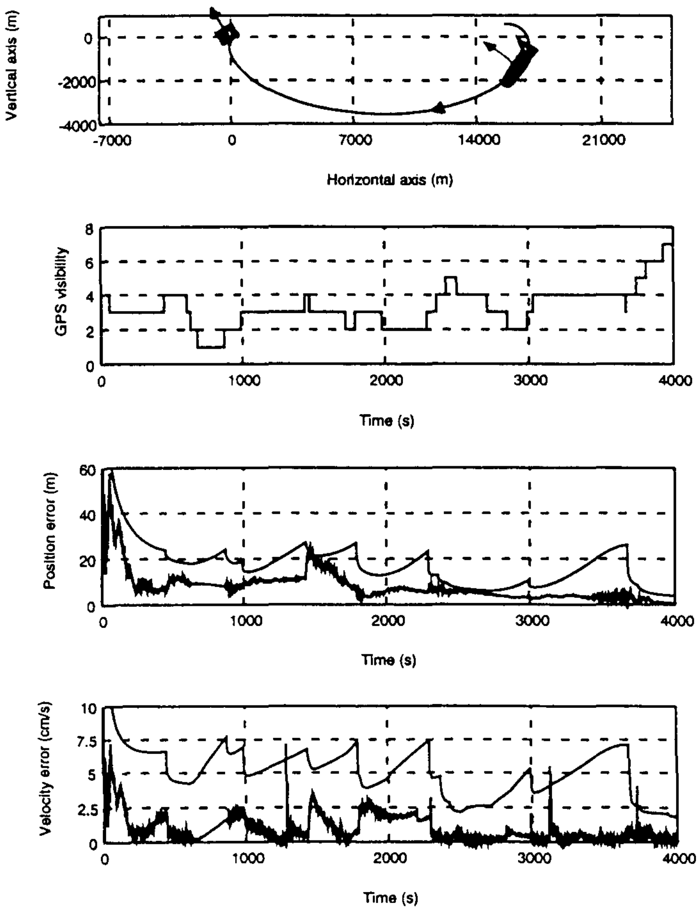

Figure 5/1 - RGPS expected results in FD1 Retrieval, first part (bad visibility conditions)

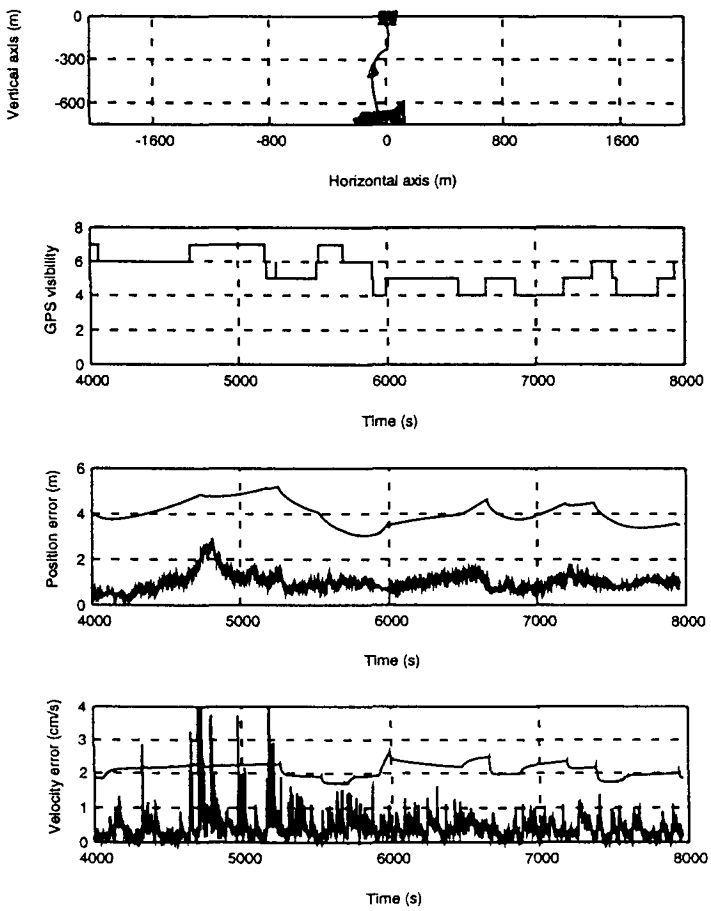

Figure 5/2 - RGPS expected results in FD1 Retrieval, 2nd part (good visibility conditions)

SESSION 4:
RVD

Chairman: W. Fehse (ESA/ESTEC)

ATV GNC DURING RENDEZVOUS

Josian Fabrega, Michel Frezet, Jean-Louis Gonnaud
MATRA MARCONI SPACE, 31, Av. des Cosmonautes, F-31402 TOULOUSE CEDEX 4 - FRANCE
Phone: (33) 5 62 19 63 27, Fax. : (33) 5 62 19 74 49, e-mail: firstname.name@tls.mms.fr

ABSTRACT

The Automated Transfer Vehicle (ATV) is the European logistic transfer vehicle designed to carry-out in-orbit replenishment missions to the International Space Station Alpha. One of the most challenging requirement for ATV is the autonomous on orbit RDV (RendezVous) capability with a manned station. ATV is the first vehicle to be developped in Europe to provide such a capability.

ATV program is currently in Phase B of its development. Phase C/D -including detailed design and construction of the first flight model- is planned to start in 1997 with a first flight planned for 2002.

This paper focuses on the major outcomes of the phase B for what concerns the determination of a baseline for the Guidance, Navigation and Control (GNC) functions of the ATV during its Rendezvous to the International Space Station Alpha.

0. INTRODUCTION

One of the cornerstones of the European contribution to the International Space Station Alpha (ISSA) program is the development and operations of an unmanned vehicle capable of in-orbit replenishment missions. This Automated Transfer Vehicle shall be capable of performing an automated rendezvous and docking to the ISSA, bringing along up to 10 metric tons of payload. An ATV flight is to take place every 12 to 18 months. During its attached phase on one of the docking port of the station, the ATV shall also provide sufficient thrust to perform the so called « reboost », raising the ISSA orbit altitude from 350 km to 450 km. The ATV is then to depart from the station and to perform an automated phasing and deorbit, leading to a destructive reentry in the atmosphere above the ocean.

The fully automated rendezvous and docking with the ISSA is one of the major breakthrough of the ATV program, as such missions have never been attempted in western Europe before. The autonomous rendezvous requires the implementation on-board the spacecraft of an accurate Guidance, Navigation and Control system. This system shall be designed to bring automatically and safely the ATV from an orbiting position far away from the station, down to the contact with the station docking port with a few centimeter accuracy. This paper presents the current baseline (Phase B status) for the definition of the GNC functions required for the ATV rendezvous.

1. OVERALL RENDEZVOUS STRATEGY

Figure 1 presents the nominal rendezvous strategy.

The ISSA is orbiting on a quasi-circular, 350 to 450 km altitude orbit. Its attitude is Earth pointed. The nominal docking of the ATV shall take place on the ISSA Russian segment, on a port aft of the station.

The ATV is first brought to a circular orbit below (about 2 km lower altitude) and about 20 km behind the station. This point is called S0. The ATV orbital rate being slightly higher than the one of the ISSA, the ATV catches-up his delay during a **Drift phase**.

A **Homing** transfer is then initiated in S1 to bring the ATV on the ISSA orbit, 2.5 km behind it. In this point S2, a station-keeping is performed, waiting for the ISSA and ground control to issue a clearance to proceed further.

A **Closing** transfer is then executed to bring the ATV to a point S3, 250 m behind the docking port. From there on, a **Final Translation** along the docking axis is performed until contact is made between the ATV and the ISSA docking mechanisms.

Withdrawal and **departure** are carried out by a reverse translation on the docking approach axis, followed by a thruster burn that brings the ATV on its phasing orbit in preparation for the deorbit maneuver.

Proceedings Third International Conference on Spacecraft Guidance, Navigation and Control Systems, ESTEC, Noordwijk, The Netherlands, 26-29 November 1996, ESA SP-381 (February 1997)

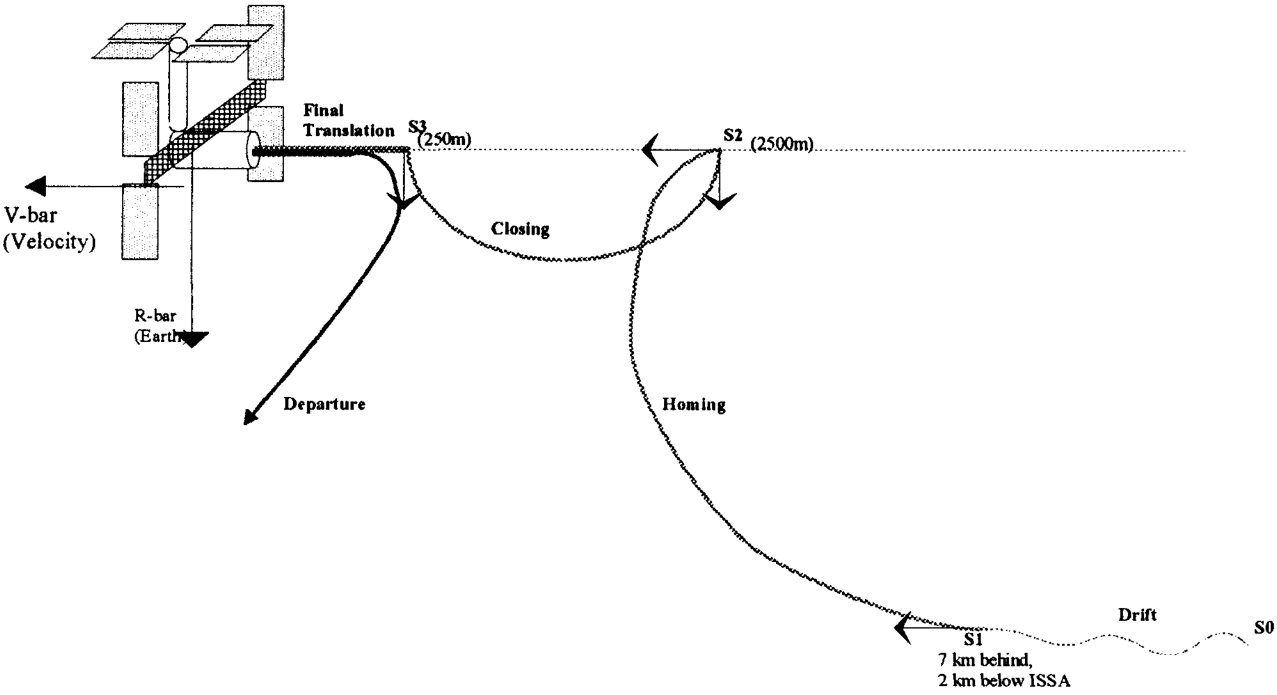
Final
Translation
S3 (250m)
S2 (2500m)
V-bar
(Velocity)
R-bar
(Earth)
Closing
Departure
Homing
Drift
S1
S0
7 km behind,
2 km below ISSA

Figure 1 - Nominal Rendezvous Trajectory

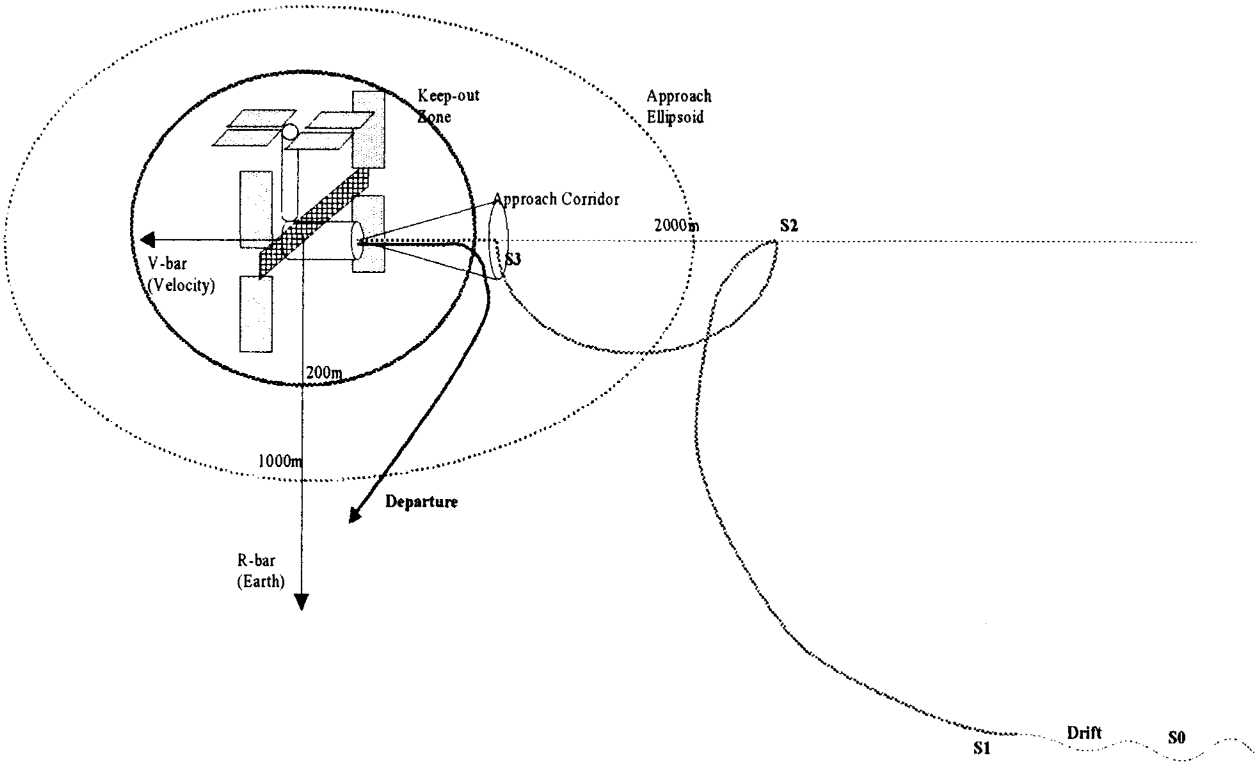
Keep-out
Zone
Approach
Ellipsoid
Approach Corridor
2000m
S2
V-bar
(Velocity)
S3
200m
1000m
Departure
R-bar
(Earth)
Drift
S1
S0

Figure 2 - ISSA Proximity Operations Flight Rules

2. ISSA PROX. OPS. FLIGHT RULES

The approach of a vehicle to the ISSA shall be carried out following pre-determined safety rules:

The **Approach Ellipsoid** is a 2km x 1km x 1km domain around the station. An incoming vehicle shall enter this approach ellipsoid only after having received a clearance to do so from the ISSA. The incoming vehicle shall be able to wait several hours before receiving the clearance to execute the maneuver (called **Approach Initiation**) that makes the spacecraft enter the Approach Ellipsoid. For ATV, the AI is performed in S2.

The ISSA is surrounded by a 200m spherical area called **Keep-out Zone**. No vehicle shall penetrate this volume, except within a conical approach corridor which is the only allowed way to achieve the approach to contact. The same corridor shall be followed to perform the departure.

The S3 point is a station-keeping point located therefore just outside of the keep-out zone. In S3, the GNC is switched to a more accurate navigation mean compatible with the stringent requirements of the approach corridor.

These flight rules are illustrated Figure 2.

3. NAVIGATION MODES DURING RENDEZVOUS

Figure 3 presents the successive use of the navigation means during the nominal rendezvous approach.

The orbital navigation of the ATV when free flying away from the station is based on an orbital navigation (orbit model) updated by GPS measurements. This navigation is referred to here after with the terminology Absolute GPS navigation (**AGPS**). Accuracy is typically between 70m and 160m, depending on coasting or boosted phase.

The homing and closing maneuvers, ending close to the station keep-out zone, require a higher accuracy navigation. The Relative GPS Navigation (**RGPS**) is used. See [1] for more details on the RGPS navigation. The RGPS navigation uses as an input a mix of GPS raw data from the ATV receiver and from the ISSA receiver. Thus, it can be activated only once a local radio link is established between the ISSA and the ATV. The range for the local link is 12 km.

The radio link contact is established during the drift between S0 and S1. RGPS navigation is initialized before reaching the S1 waypoint. The homing orbit transfer can be executed safely using the accurate RGPS navigation.

Depending on the ISSA crew field of view, the incoming ATV can be monitored during the end of the homing and during the closing.

The optical rendezvous sensor (**RVS**) is switched on in S3 to acquire the image of the retroreflectors placed in the vicinity of the ISSA docking port. Final translation is started only once RVS based navigation has converged.

Attitude estimation with respect to the local orbital frame is obtained by integration of gyropackages measurements. Earth pointed (belly to ground) attitude is maintained throughout the rendezvous, thus enabling continuous update of the absolute attitude estimation with Earth sensors and Sun sensors (out of eclipse) measurements.

4. COLLISION AVOIDANCE

The trajectories have been selected in accordance to the safety requirements of the ISSA. In any case where a wave-off and a mission abort is required, the ATV is in the position to execute either a **passive** or an **active** collision avoidance maneuver **(CAM)**

An active CAM consists in the activation of the ATV braking thrusters, giving a sufficient impulse to the ATV to go to a safe, collision-hazard free orbit. This is the case for example when braking and reversing the approach velocity during the final translation, thus reaching a departure trajectory (see Figure 4).

There are cases where the ATV is already naturally along a trajectory where, due to orbital coupling and air drag forces, a total propulsion cut-off would keep the ATV drifting away from the ISSA. In this case, the execution of a braking impulse is not required. This is the case for example when cutting the propulsion off after the S1 point has been missed. The ATV just drifts away and below the station (see Figure 4).

Mission resume after CAM execution is in any case to be initiated with ground support and control.

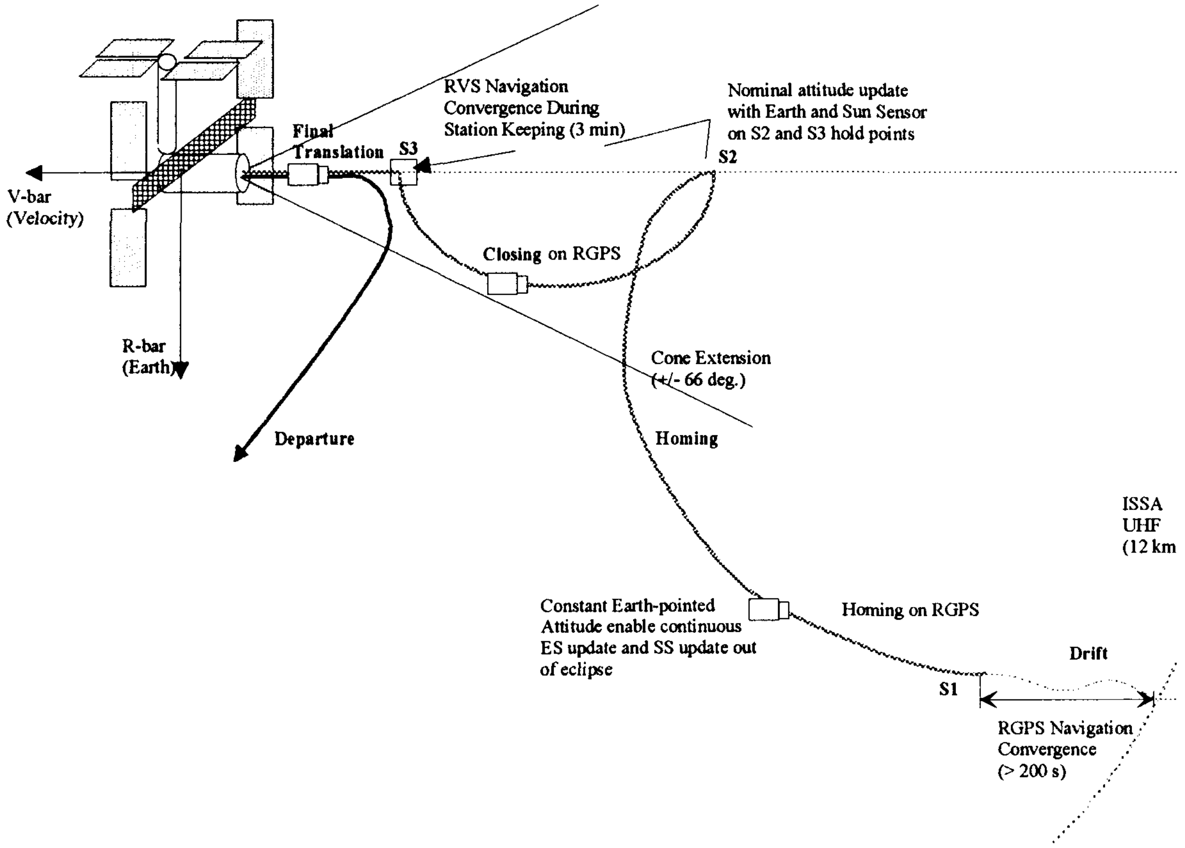
RVS Navigation
Convergence During
Station Keeping (3 min)
Nominal attitude update
with Earth and Sun Sensor
on S2 and S3 hold points
Final
Translation
S3
S2
V-bar
(Velocity)
Closing on RGPS
R-bar
(Earth)
Cone Extension
(+/- 66 deg.)
Departure
Homing
ISSA
UHF
(12 km
Constant Earth-pointed
Attitude enable continuous
ES update and SS update out
of eclipse
Homing on RGPS
Drift
S1
RGPS Navigation
Convergence
(> 200 s)

Figure 3 - Navigation modes during rendezvous phases

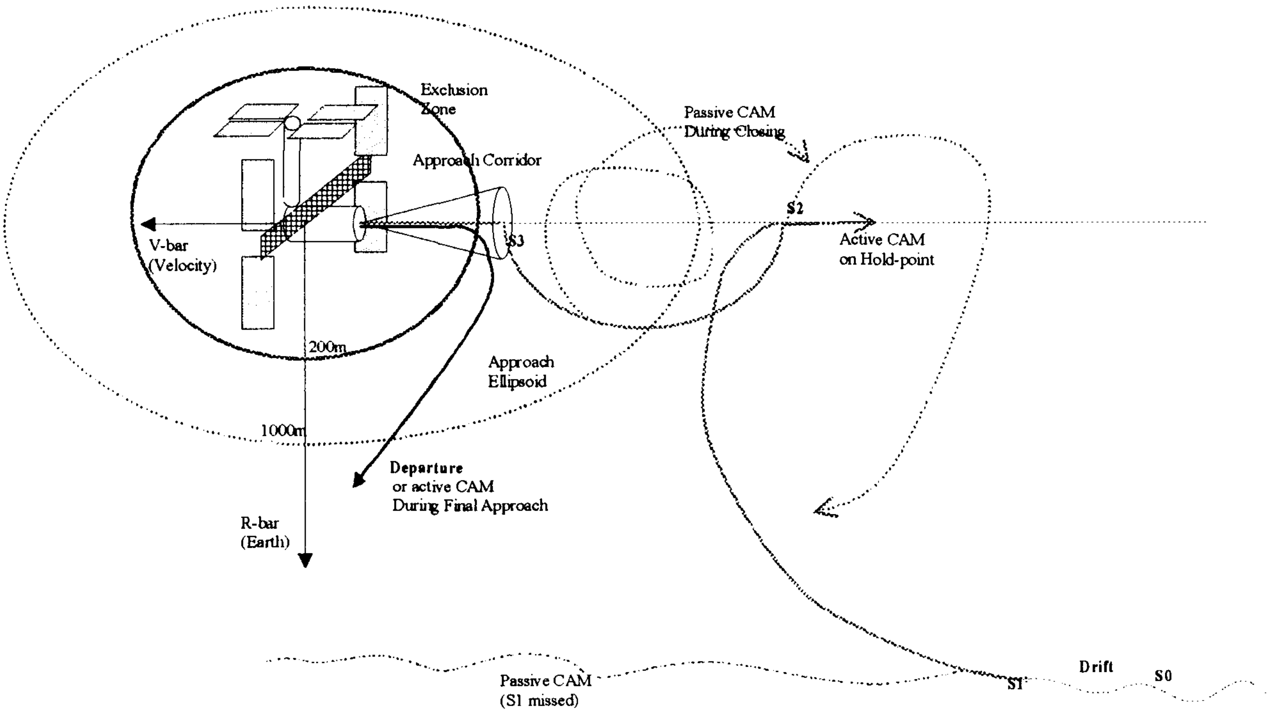
Exclusion
Zone
Passive CAM
During Closing
Approach Corridor
S2
S3
V-bar
(Velocity)
Active CAM
on Hold-point
200m
Approach
Ellipsoid
1000m
Departure
or active CAM
During Final Approach
R-bar
(Earth)
Drift
S0
S1
Passive CAM
(S1 missed)

Figure 4 - Illustration of some active/passive CAM cases

5. GNC_RV FUNCTIONAL ARCHITECTURE

The functional architecture of the ATV GNC for Rendezvous (GNC_RV) is based on separate, relatively independent Guidance, Navigation and Control functions, managed by a centralized GNC_RV manager function. Figure 5 provides an overall overview of the GNC_RV functional architecture.

The **GNC_RV manager** covers functions common for the Guidance, Navigation and Control: command and data handler (TM/TC), overall mission phases sequencing, etc...

The **Navigation** is in charge of the determination of an estimated absolute and relative position and velocity and attitude.

The **Guidance** is in charge of the generation of the nominal trajectory and of the impulses required to have the ATV follow the trajectory in an undisturbed environment.

The **Control function** provides forces and torques commands to compensate the deviations due to perturbations. Within the Control function, the Thruster Management Function (**TMF**) is in charge of the determination of the individual thruster ON/OFF command sequence to realize the commanded forces and torques.

Failure Detection, Isolation and Recovery (**FDIR**) is not centralized, but distributed in each functions. The general principle is to perform the FDIR operations at the closest possible point of the error/failure source, thus minimizing the risk of failure propagation. For example, corrupted measurements are detected and rejected an the input of the navigation function. Likewise, if a Mission Abort order is triggered at the level of the GNC_RV manager, the realization in the form of an active or passive CAM will be selected in the Guidance function.

The GNC modes are defined individually for each GNC function. This is to avoid to define a specific overall GNC mode for each change in a sub-function, which would lead to a prohibitive number of modes.

Table 5 presents the modes envisaged today for the functions.

It can be seen that a single Control mode can be used for a wide range of Navigation and Guidance modes.

It can also be noticed that the GNC functions modes changes do not always coincide with phases changes: RVS navigation is activated at the end of the Closing phase, and no change of Navigation mode is commanded for the phase switching to Final-Approach Phase.

6. NAVIGATION BASELINE

The ATV Navigation filter is based on a scheme involving state vector prediction, updated by external measurements (Kalmann filtering).

This scheme allow to achieve the required accuracy, as well as availability and continuity of the service in case of sensor failure.

Figure 6 presents the functional architecture of the Rendezvous navigation function.

6.1 Absolute Attitude Estimation

The absolute attitude estimation -estimation of the ATV angular position with respect to a Galillean reference frame- is required to be accurate to a level of 0.5 deg. to 0.8 deg. (3σ) during rendezvous.

The absolute attitude filter is based on:

- propagation with gyros (4 x 2-axes Dry Tuned Gyros)
- 3 hours autonomy in gyro propagation mode
- update with Earth Sensor (ES) and Sun sensor (SS):
    - * 3 axes quick update with ES and SS
    - * gyrocompassing mode with ES is possible (thanks to the ATV Earth pointed attitude) for a continuous update
    - * 2 ES units to ensure redundancy
    - * SS configuration: 3 self-redunded analog Sun Sensors, ensuring visibility without requiring dedicated spacecraft maneuver

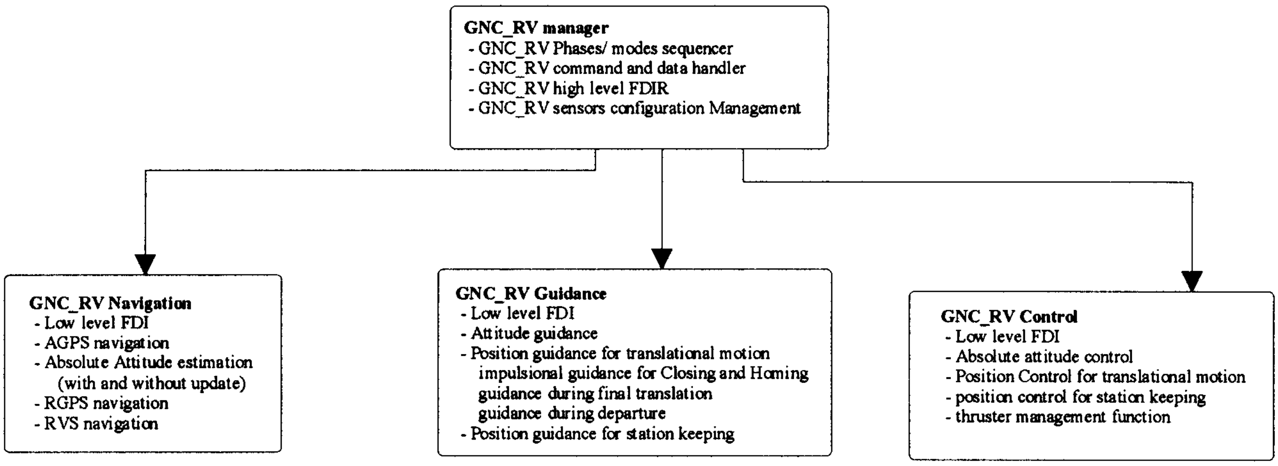
GNC_RV manager
- GNC_RV Phases/ modes sequencer
- GNC_RV command and data handler
- GNC_RV high level FDIR
- GNC_RV sensors configuration Management
GNC_RV Navigation
- Low level FDI
- AGPS navigation
- Absolute Attitude estimation (with and without update)
- RGPS navigation
- RVS navigation
GNC_RV Guidance
- Low level FDI
- Attitude guidance
- Position guidance for translational motion impulsional guidance for Closing and Homing guidance during final translation guidance during departure
- Position guidance for station keeping
GNC_RV Control
- Low level FDI
- Absolute attitude control
- Position Control for translational motion
- position control for station keeping
- thruster management function

Figure 5 - GNC_RV functional architecture

Mission Phase	Position Guidance	Attitude Guidance	Navigation Mode	Control Mode
Drift	S0 Drift	Constant Attitude	AGPS Mode	Far Range
			RGPS Mode	
Homing	S0 Drift			
	Homing Transfer			
	Station Keeping			
Closing	Closing Transfer			
	Station Keeping			
			RVS1 Mode	
Final_Approach	Forced Motion	Constant Attitude		Final Approach (One or Several modes TBD)
	Station Keeping TBC			
Last_Meter_App.	Forced Motion	Rel. Attitude	RVS2 Mode	
Attached	-	-	-	-
Departure	Earth Pointing Drift	Constant Attitude	RGPS Mode	Far Range
	Execute DeltaV			

Table 5 : GNC_RV functional modes

6.2. Absolute position/ velocity estimation

The Absolute Position navigation (AGPS) provides an estimate of the spacecraft position with respect to a Galillean reference frame. This estimation is required during rendezvous as an input to the Relative GPS navigation.

The AGPS navigation is based on:

- propagation with an orbital motion model, taking into account thrust commands for rendezvous maneuvers
- update with pseudorange and carrier phase GPS *raw data* (data not processed in the GPS receiver navigation filter)

The AGPS performances requested for RDV are typically :

- position ~ 80 m (3 σ)
- velocity ~ 0.8 m/s (3 σ).

6.3. Relative position/velocity estimation

The relative navigation provides the estimation of the relative position of the ATV with respect to the Space Station. Its accuracy is commensurate with the stringent requirements at docking. No requirement exist for the longer range navigation, but the RGPS navigation shall enable the safe approach and the target acquisition by the Rendezvous sensor.

- RGPS navigation: Model based on Euler-Hill equations for the relative flight (with ΔV commands) updated by the difference of ATV and ISSA GPS raw data **at the same date** (desynchronisation less than 0.1s) **from the same GPS satellite**. This requires AGPS navigation to determine the ATV to GPS satellite direction. It requires GPS raw data from ISSA to be transmitted by radio link.
- RVS navigation 1: Model based on Euler-Hill equations for the relative flight (with ΔV commands) updated by optical Rendezvous Sensor measurements: range and line-of-sight angles (azimuth and elevation).
- RVS navigation 2: Model of the relative motion of the ATV **docking port** with respect to the ISSA **docking port**, based on Euler-Hill equations for the relative motion of the center of mass of the two spacecraft (with ΔV commands and gyro attitude rates), updated by RVS measurements: range, line-of-sight, and relative attitude angles.
- Navigation for departure: based on RVS navigation 1 mode, followed by RGPS navigation
- RGPS navigation is in hot redundancy with RVS navigation for safety purposes. 2 GPS receivers are therefore in « backup » of 2 RVS, but the accurate automatic docking is not achievable based on RGPS navigation only.
- baseline update frequency for RGPS and RVS navigation is 1Hz (to be confirmed)

RGPS Navigation is presented more thoroughly in [1].

7. GUIDANCE AND CONTROL

The selected scheme for Homing and Closing transfers is an impulsional Guidance based on 2 boosts, each of an ½ orbit duration.

Quasi continuous control is used along the reference trajectory: this ensures the smoothing of the dispersions induced by the first Guidance burn, and limits the dispersions induced by the 2nd burn. Dispersions are reduced to maneuver uncertainties which are acceptable for the low level thrust. Delta-V values are about 0.6 m/s for Homing and Closing burns.

The H_2/H_∞ method for controller synthesis is used. (See [2] for more details). The same controller scheme is applicable for station keeping in hold points as well as for the trajectory control during orbit transfer.

For final translation and departure, a quasi continuous Guidance scheme with compensation of the lateral coupling forces is used. The same class of controller is used as for Homing and Closing (to be confirmed).

The Guidance and Control functional architecture is presented in the figure below.

8 - RENDEZVOUS GNC FDIR

The Failure Detection, Identification and Reconfiguration (FDIR) concept of the ATV Rendezvous GNC is based on the following main hypotheses applicable to the current Phase B.

- No independent simultaneous failures are to be considered.
- Active Collision Avoidance Maneuvers are to be used whenever necessary after the second failure. Ground control is then in charge of resuming the mission, using remotely the remaining ATV on-board capabilities.
- Only one software failure is considered to be covered. Safety is preserved after the software failure.

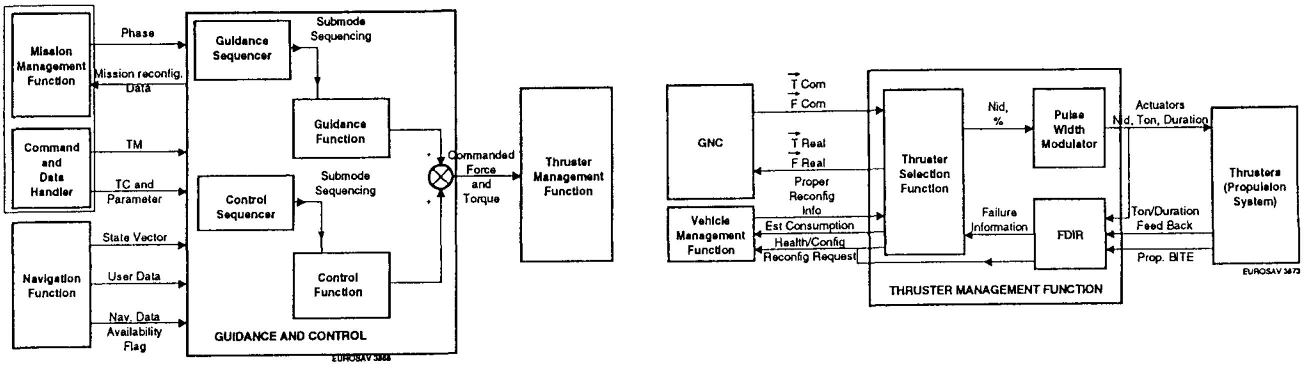
Mission Management Function
Phase
Mission reconfig. Data
Command and Data Handler
TM
TC and Parameter
Navigation Function
State Vector
User Data
Nav. Data Availability Flag
Guidance Sequencer
Submode Sequencing
Guidance Function
Control Sequencer
Submode Sequencing
Control Function
GUIDANCE AND CONTROL
Commanded Force and Torque
Thruster Management Function
EUROSAV 3868
GNC
T Com
F Com
T Real
F Real
Proper Reconfig Info
Vehicle Management Function
Est Consumption
Health/Config
Reconfig Request
Thruster Selection Function
Nid, %
Pulse Width Modulator
Failure Information
FDIR
THRUSTER MANAGEMENT FUNCTION
Actuators Nid, Ton, Duration
Ton/Duration Feed Back
Prop. BITE
Thrusters (Propulsion System)
EUROSAV 3873

Figure 6 - Rendezvous Navigation Functional Architecture

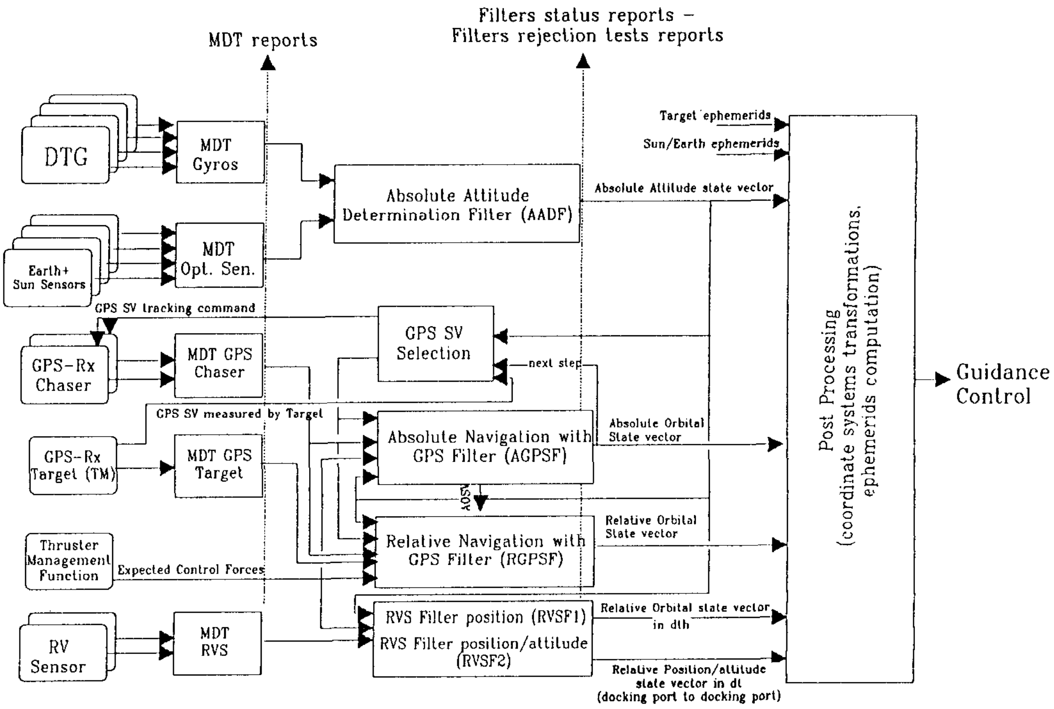
MDT reports
Filters status reports - Filters rejection tests reports
DTG
MDT Gyros
Earth+ Sun Sensors
MDT Opt. Sen.
Absolute Attitude Determination Filter (AADF)
GPS SV tracking command
GPS-Rx Chaser
MDT GPS Chaser
GPS SV Selection
next step
GPS SV measured by Target
GPS-Rx Target (TM)
MDT GPS Target
Absolute Navigation with GPS Filter (AGPSF)
AOSV
Relative Navigation with GPS Filter (RGPSF)
Thruster Management Function
Expected Control Forces
RV Sensor
MDT RVS
RVS Filter position (RVSF1)
RVS Filter position/attitude (RVSF2)
Target ephemerids
Sun/Earth ephemerids
Absolute Attitude state vector
Absolute Orbital State vector
Relative Orbital State vector
Relative Orbital state vector in dth
Relative Position/attitude state vector in dt (docking port to docking port)
Post Processing (coordinate systems transformations, ephemerids computation)
Guidance Control

Figure 7 - Rendezvous Guidance & Control Functional Architecture

Failure detection and identification is based on "analytical redundancy", that is the comparison of sensor measurements with measurements rebuilt from other on-board navigation filter output and from other equipment measurements. Test thresholds are to be tuned by extensive high-fidelity ground simulations to optimize detection sensitivity while minimizing the risk of false-alarms.

The active Collision Avoidance Maneuver is to be executed using tabulated thruster commands, with attitude control based on gyro propagation. Optionally, position estimation with relative and absolute motion model propagation can be used, but is not baselined currently.

The equipment redundancy scheme is the following :

- 4 2-axes DTGs on a common baseplate provide autonomous 2 failures detection, identification and reconfiguration.
- 2 GPS Receivers: 2 failures can be detected and isolated. After a second failure, ground can take over, possibly with TDRSS ranging (TBC).
- 2 Rendezvous Sensors: 2 failures can be detected and isolated. After a second failure, a CAM puts the ATV on a safe orbit and Rendezvous mission is aborted until ground control can recover.
- 2 Earth Sensors and 3 self-redunded analog Sun Sensors provide 2 failure tolerance detection and isolation capability with the help of self-secured gyro propagation. After 2 Sun Sensors failures, gyrocompassing mode with Earth Sensor is possible. After 2 Earth Sensors failures, only degraded update capability can be envisaged. In any case, after 2 failures during rendezvous, CAM can be activated based on gyro attitude.
- Propulsion configuration is such that the use of a Thruster Management Function optimization algorithm (see [2]) enables at least a one failure tolerance with respect to maneuvering capacity required for rendezvous, and at least a 2 failure tolerance for the execution of a safe active Collision Avoidance Maneuver.

9 - CONCLUSIONS

The Rendezvous GNC design has been shown as satisfactory with respect to the ATV System Requirements, both for performances and for robustness to failures and contingencies.

The current baseline for RDV_GNC depends on critical assumptions and data.

- Common GPS antenna orientation between ATV and ISSA
- functional « twin » (same raw data, same datation algorithm...) GPS receivers on ISSA and ATV
- requirements on docking conditions imposed by ISSA
- station dynamic conditions: currently ISSA attitude motion is within 1deg., 0.04 deg./s
- assumptions on common mode failures (sensor software, GNC software, simultaneous failures)

Very detailed quantitative data/results are complementary provided within proceedings [1] & [2], the reader is invited to refer to.

---

[1] Relative GPS Navigation Design and Validation for ATV Rendezvous, *V. Pascal, H. Marcille (Matra Marconi Space)*, 3rd ESA International Conference on Spacecraft Guidance, Navigation and Control Systems, Nov. 1996.

[2] ARPK GNC Design and Performances Evaluation for ATV Rendezvous, *JL. Gonnaud (MMS), M. Tsang (MMS), J. Sommer (DASA)*, 3rd ESA International Conference on Spacecraft Guidance, Navigation and Control Systems, Nov. 1996.

ARPK GNC DESIGN AND PERFORMANCES EVALUATION FOR ATV RENDEZVOUS

J.L. Gonnaud *, J. Sommer **, M. Tsang *

* MATRA-MARCONI SPACE, 31, Ave. des Cosmonautes, F-31402 TOULOUSE CEDEX 4
Phone: (33) 5 62 19 69 67, Fax. : (33) 5 62 19 77 69, e-mail: jean-louis.gonnaud@tls.mms.fr

** DAIMLER BENZ AEROSPACE AG Raumfahrt-Infrastruktur, Postfach 28.61.56, D-28361 BREMEN
Phone: (49) 421 539 4440, Fax. : (49) 421 539 4624 , e-mail: josef.sommer@erno.de

ABSTRACT

In the scope of the ATV Rendezvous Pre-Development Program Kernel activities (ARPK), MMS and DASA are developing a prototype of the Guidance, Navigation and Control software.

An integrated approach for the analysis, design and software implementation has been followed based on commercial Computer Aided Design tools: Xmath, Systembuild, Autocode™ .

This paper focuses on:

- the major trade-off used for the Guidance and Control design, based on H-infinity synthesis and Mu-analysis.
- the implementation of the selected concept in a Systembuild™ environment
- the methodology used to statistically derive a set of performance files covering the ATV flight envelope during rendezvous.

1. INTRODUCTION

The Automated Transfer Vehicle (ATV) is the European vehicle which will perform automatically replenishment missions to the International Space Station Alpha (ISSA). In order to secure the critical technical area of the high-accuracy, automated, in-orbit rendezvous, the European Space Agency has started the ATV Rendezvous Pre-Development Program (ARP), which includes sensor predevelopment activities and system activities conducted in the ARP Kernel (ARPK) program. The design and ground-testing of a prototype of the ATV on-board Guidance, Navigation and Control software -called Rendezvous Control software (RVC) in ARP- is one of the major objectives of ARP. Some of the other objectives include the development of ground test facilities, the development and in-orbit testing of both a Relative-GPS capable GPS receiver and an optical Rendezvous Sensor.

2. GNC DESIGN IN ARPK

The control of a spacecraft in its approach to dock to another spacecraft within very stringent dynamic conditions is inherently complex. It is the physical problem of controlling a 6 degree-of-freedom vehicle for which the axes are highly coupled. In particular, for example, the control of the relative position and relative attitude of the ATV docking port with respect to the ISSA docking port shall take into account the detrimental effect of an attitude motion of the ATV on the lateral offset of the ATV docking port with respect to the ISSA docking port.

Moreover, the missions the ATV has to cover are dealing with a wide range of cargoes, both for the "up" replenishment mission leg and for the "down" waste-disposal mission leg. The modular ATV-core + Cargo architecture does not provide either a very favorable propulsion configuration for a 6-degree of freedom vehicle, as all the thruster are grouped on the aft of the spacecraft (see Figure 1).

The sum of these constraints has led to the selection of modern Multi-Input Multi-Output (MIMO) control design methods. These methods are now supported by Computer Aided Design tools like Xmath™ or Matlab™.

3 - INTEGRATED APPROACH FOR GNC DEVELOPMENT

Once verified by the designers, in the second step of the verification process, the resulting GNC is to be implemented in the form of a prototype of on-board software code onto a breadboard of the ATV computer. This phase is the actual GNC-software prototype development and verification. In the ARP program, this prototype is to be tested in closed loop first in a simulated space environment,

Proceedings Third International Conference on Spacecraft Guidance, Navigation and Control Systems, ESTEC, Noordwijk, The Netherlands, 26-29 November 1996, ESA SP-381 (February 1997)

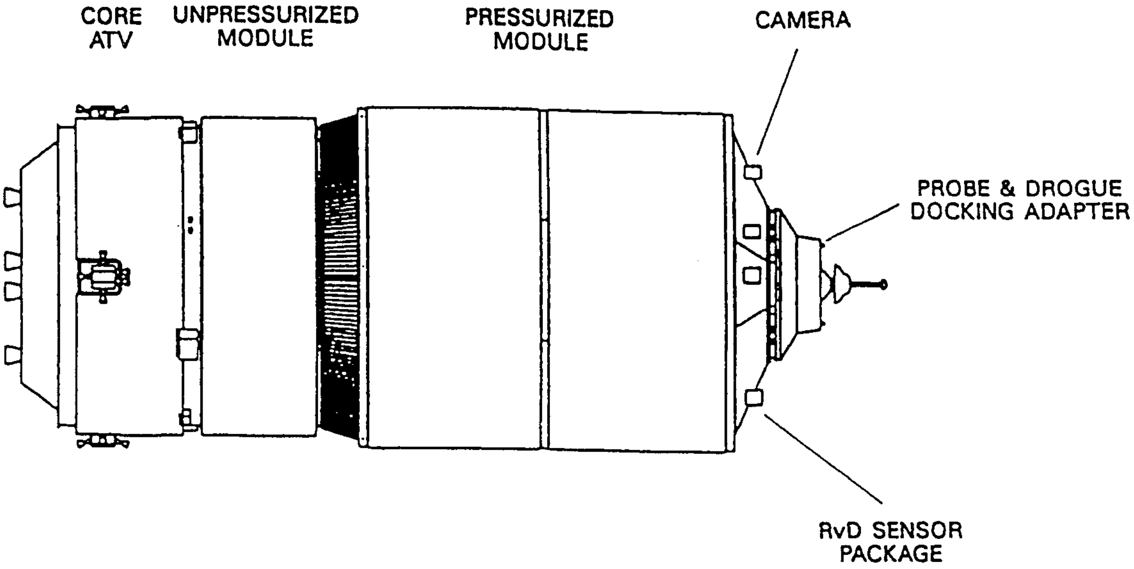

Figure 1 - ATV spacecraft configuration

then connected to actual navigation equipment like the GPS receiver or the Rendezvous Sensor. In the latter configurations, the navigation equipment will be stimulated by a complex test environment including for example a Nortel "GPS Flight Segment Simulator" or used in the large European Proximity Operation Simulator for validation in a realistic dynamic and lighting environment.

The step from the GNC design to the generation of on-board code prototype is classically performed through the writing of a detailed software specification in which all the GNC concepts are detailed in pseudo-code format. Recent development in Computer Aided Design tools have led to envisage other methods. An innovative approach for this second step of the verification is the use for the on-board software prototype of automatically generated code.

In order to explore the possible gains of the method, as well as to secure the development approach for the ATV, ESA and the industrial contractors have decided to experiment it in the case of the relatively large size ARPK GNC software. The Autocode™ tool that transforms the design blocks of Xmath™ Systembuild™ CAD tool into C-code was used for this project.

4 - NAVIGATION DESIGN

The ATV Navigation for rendezvous is based on the use of GPS in Relative GPS mode for the distance between 12km to 200 m of the ISSA. It is based on an optical rendezvous sensor for the final approach below 200m.

The RGPS navigation design is now completed and presented in details in [1]. Achievable performances have been obtained both with simulated environment and with the ARP GPS receiver. The integrated development approach with Systembuild-Autocode has not facilitated the design, mostly because the RGPS navigation is based on non-stationary Kalman filtering with large state (dimension 12 and over) vectors. Systembuild™ is primarily suitable for smaller, stationary systems. Nevertheless, integration of the large navigation system simulation software within the overall GNC in Systembuild™ was carried out succesfully.

The current baseline for ARP GNC sampling frequency is 1 Hz, allowing to use to a full extent in the navigation the data provided by the GPS receivers. Slower navigation rates are also investigated.

5 - GUIDANCE DESIGN

The Guidance function is the function that determines the nominal trajectory to be followed by the ATV and the set of feed-forward forces and torques required to have the ATV follow these trajectories. Guidance also implement the functionalities required for autonomous Failure Detection, Isolation and Recovery regarding trajectories, as well as for the observability and commandability of the trajectory by the ground. or the ISSA crew. Guidance parameters, like aim-points, pre-programmed Delta-Vs, and all the parameters that define the algorithms to be used, or the parameters needed to define the spacecraft nominal motion unambiguously, are stored internally in tables.

Starting from the ATV mission analysis, which defines the principles of the proximity operations of the ATV, an analysis has been performed to derive the expected performances.

The guidance scheme selected for all transfer phases is the impulsive transfer in 2 burns. This holds both for the Homing (orbit transfer), Closing (hop along the velocity axis) or ISSA fly-around to reach the point to final approach for berthing on the U.S. side of the station. Control is to be superimposed at the GNC sampling frequency all along the reference trajectory.

The current baseline for the final approach is a forced translation at a maximum velocity of 20 cm/s. Docking takes place with a nominal velocity of 5 to 20 cm/s, depending on the ATV mass. The withdrawal is to be ensured by an initial velocity of 6 to 10 cm/s, followed by a 1.4 m/s departure burn to leave the ISSA Approach Ellipsoid.

In any cases, the safety is ensured by a 2 failure tolerant Collision Avoidance Maneuver (CAM). The CAM can be a passive drift away in the area of the trajectory where no risk of collision exist: for example at the very beginning of the final approach or after the first closing burn.

Two steps have been carried out:

- an open loop feasibility analysis dedicated to algorithm definition, safety aspects and to the determination of preliminary timing and fuel budget.

- a closed loop performance analysis using a realistic environment, and sequentially first a simplified preliminary model of the Navigation and Control functions, then later when available the Control and Navigation functions. These tests were oriented toward the refinement of guidance parameters and the quantitative assessment of perturbation effects (air drag, propulsion errors due to MIB and thrust noise).

These steps have both been carried out in the Systembuild environment, on simple models first and finally on a larger scale "Functional Engineering Simulator" (FES)

(hold) point	reference	position [m]			description
		X	Y	Z	
V-bar approach to direct docking					
S0	ISS LVLH	undefined			on coplanar drift orbit behind and below the ISS, outside the SSCR
S1	ISS LVLH	will be calculated on board			start of homing, nominal position is 7212m behind and 2000m below ISS
S2	ISS LVLH	-2500	0	0	hold point, start of V-bar closing
S3	ISS LVLH	-250	0	0	hold point, transfer to RVS navigation
S4	ISS LVLH	entrance of Keep Out Zone			no hold point, CAM armed
S5	ISS LVLH ISS docking port	-70 40	0 0	0 0	hold point, transition to port-to-port control
S6	ISS docking port	0	0	0	docking port
R-bar approach to Berthing					
S0	ISS LVLH	undefined			on coplanar drift orbit behind and below the ISS, outside the SSCR
S1	ISS LVLH	will be calculated on board			start of homing, nominal position is 7212m behind and 2000m below ISS
S2f	ISS LVLH	-579.3	0	0	hold point, start of fly around
S3R	ISS LVLH	15.13	250	0	hold point, slew and transition to RVS navigation
S4	ISS LVLH	entrance of Keep Out Zone			no hold point, CAM armed
S5	ISS LVLH ISS berthing point	15.13 0	-5.6 40	56 6	hold point, transition to port-to-port control
S6	ISS berthing point	0	0	0	berthing point

Table 1 - Guidance function trajectory keypoints

In particular, the work performed resulted in the determination of a consistent set of tables covering the complete proximity operation scenario including provision for the management of planned contingencies. The work performed so far has focused on the RGPS based mission leg.

Accuracy performances are summarized in the section 8.

6 - CONTROL DESIGN

The Control function is in charge of the generation of the thruster commands needed to maintain the ATV on the preplanned trajectory and to compensate for the effect of the perturbations.

6.1 - MANEUVERING CAPACITY

The Reaction Control System of the ATV (see Figure 1) is based on the use of thruster pods grouped at the aft end of the spacecraft. Therefore, it is very difficult to generate pure forces or torques about the spacecraft axes, without creating side effects in forces or torques. This is especially true for the generation of lateral forces. This phenomenon is even more complex due to the large envelope allowed for the center of mass of the ATV cargo.

Another important constraint is the necessity to enable a full 6-degree of freedom maneuvering capacity, after any single failure. A single failure may yield the loss of one thruster. Thanks to the layout of the propulsion feeding links, a single failure will not impose the isolation -and loss- of the three thrusters of the same branch. Braking and escape capacity shall be guaranteed after any combination of two failures. Two successive failures may induce the loss of two or more thrusters.

The solution selected for ATV and prototyped in the ARP control software is based on the use of:

- "Off-modulation" of the thruster commands. A fraction of the nominal thrust capacity can therefore be achieved by selecting the adequate opening duration for each individual thruster during each control cycle.

- Selection of thruster opening times by the use of a linear optimization algorithm (simplex), that automatically determines for any combination of commanded forces and torques, the combination of thruster use that minimizes the propellant consumption.

This iterative algorithm converges to an acceptable solution in less than 20 cycles. The computer load imposed by such a complex algorithm is anyhow by far smaller than the computer load required by the Relative GPS Kalman filtering scheme.

Note that due to the non linear behavior of the propulsion system when too high forces and torques are commanded, a pre-saturation of the control commanded forces has been implemented in order to stay as much as possible in the linear range of use.

One additional peculiar aspect of such a propulsion system is its behavior when low thrust is commanded. Each individual thruster behaves with its own Minimal Impulse Bit (MIB), below which no thrust is generated. The linear optimization process to select the thruster does not take this into account. The resulting effect is:

- no limit cycle or discrepancy in the realized forces and torques when relatively high level commands are processed

- disturbances effect in all 6 degree-of-freedom axes may appear for lower level commands, including on axes where no command was sent !

If high accuracy remains a potential issue, at least propellant consumption can be minimized in the phases where accuracy is not of paramount importance (e.g. loitering station keeping), by implementing a "MIB saving technique" that sum up the successive non-executed commands until they reach a level compatible with their execution by the propulsion system.

The current ATV propulsive configuration (8x400N main engines, 20x200N RCS engines) has been found as satisfactory with respect to mission thrust needs. The impact of MIB on the accuracy performances for docking is still being investigated.

6.2 - CONTROLLER DESIGN METHOD

The attitude and position controller have been designed separately for the Relative-GPS based mission leg. A full 6-DOF controller is required for the final translation and docking based on Rendezvous sensor.

As recalled in section 2, the variety of missions to be fulfilled by the ATV has led to the selection of modern "Robust Control" design methods. Robust control design consists in designing a system not only for a given nominal system, but designing a system that guarantees the required stability and performances for a full set of systems that deviate from the nominal one by some level of uncertainties. For example, the robust control design enabled to design a single controller that can cope with an ATV with up to 25% variation in its mass and inertia.

Control design is performed in two steps.

- first the **synthesis** of the controller, that is the selection of control state vectors and the generation of the control gain structure and values

- then the **analysis** of the controller, that verifies the controller characteristics taking into account a wider range of uncertainties of the modelled system.

The synthesis was initially to, be performed on Xmath™, but the Matlab™ release of the Robust Control Toolbox appeared much more up-to-date when the design effort was initiated. H_2 and H_{inf} synthesis were used.

A step-by-step approach has been followed: first single-axis model, then multi-axis continuous model, finally multi-axis discrete controller. The attitude controller was directly designed in the discrete domain, because controller bandwidth was expected to be close to the sampling rate.

The analysis was carried out using μ-analysis, and it was checked that the generated controller was robust to the simultaneous presence of uncertainty sources. The following sources have been accounted for in the analysis:

- mass/inertia uncertainty up to 25%

- center of mass location shift (25%)

- uncertainty on feedforward guidance forces (up to 25%)

- uncertainty on navigation parameter: a typical navigation time-history was used after Fourier transform to represent this contribution

- maximum 2 second delay in the loop

- high frequency dynamic coupling modelled as high frequency unstructured uncertainties.

- spectral Fourier analysis of typical thrust history and slosh model (pendulum) history was used to derive the weighting functions modelling the contribution of the uncertainties coming from thruster selection and from slosh in tanks.

- MIB and saturation effect of propulsion, modelled as +/- 5Ns dead zone and +/- 120N saturation limit

Note that the control design by synthesis and analysis is an iterative process. Time domain simulations were also used to confirm the adequacy of the selection of the weighting matrices used for synthesis. The process was resumed from synthesis each time the analysis outlined a less than acceptable behavior.

The μ-analysis enabled to demonstrate a satisfactory behavior for a single controller for the whole RGPS based leg. A slower sampling rate has been investigated in this mission phase. Although performances remained acceptable in terms of accuracy, propellant consumption appeared to increase for a longer than 2s sampling rate. Accuracy performances are summarized in section 8.

Analyses are currently on-going for the final translation and docking.

7 - FLIGHT ENVELOPE VERIFICATION

The overall GNC elements implemented in Systembuild™ blocks can be used in closed-loop when connected with a software (C-code) simulating space environment. This results in the ARPK Functional Engineering Simulator (FES).

The FES is a relatively large simulation tool: about 10 Mbytes of code and 40 Mbytes of data. The use of Systembuild for such a large system is at the limit of the practical feasibility, in particular for the management and readability on the screen of workstations of large blocks with numerous input/output lines.

In the FES, the number of "superblocks" is about 200. Each superblock contains in average 6 blocks, but some contain up to 35. In average, the number of output per block is 20, but there exists a superblock with more than 200 output lines ! For the input lines, the average is closer to 10, but some contain up to 300 input lines ! Finally, the maximum number of superimposed layers of blocks in the FES, that is the number of levels in which a block is included in another block, is 12.

The relative complexity is illustrated by the figure 2 below that presents the implementation of the Control superblock.

It is important to note that Systembuild™ blocks simulations are necessarily interpreted. This tool can be used to derive a few simulations results, like for example the nominal and the worst case simulated missions. Nevertheless, it is too slow to be used efficiently in cases where a large number of simulations are required.

Nominal and worst case mission cases are not sufficient. For example, when an actual equipment like the Rendezvous sensor is used connected to the GNC in a nominal simulation scenario, the outcome of the simulation might well be:

- different from the nominal case, because the actual equipment did not strictly behave like the simulated equipment

- not as bad as the worst case.

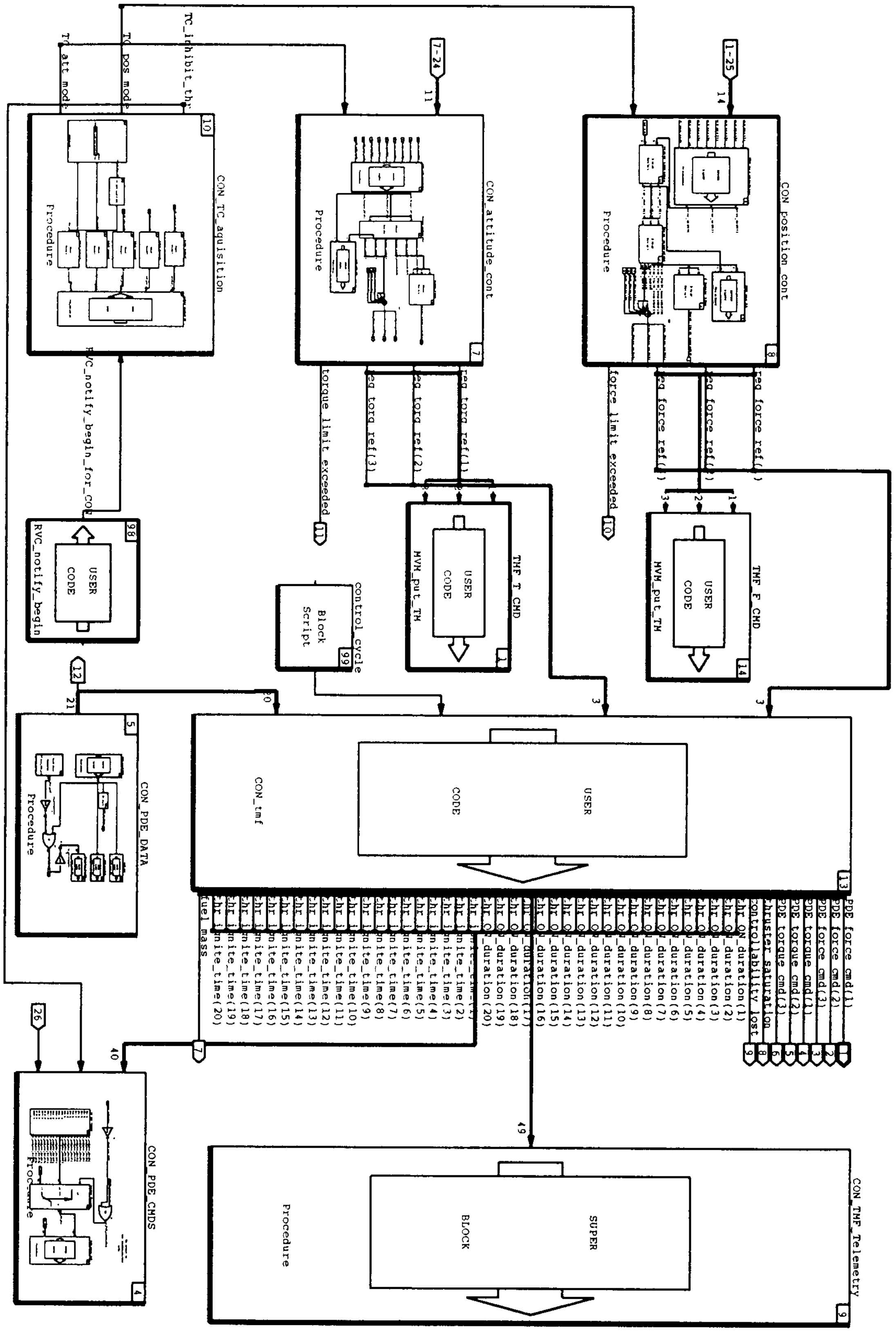
TC_inhibit_thr
TC_pos_mode
TC_att_mode
1-25
14
7-24
11
CON_position_cont
Procedure
8
CON_attitude_cont
Procedure
7
CON_TC_aquisition
Procedure
10
req_force_ref(1)
req_force_ref(2)
req_force_ref(3)
force_limit_exceeded
10
req_torq_ref(1)
req_torq_ref(2)
req_torq_ref(3)
torque_limit_exceeded
11
RVC_notify_begin_for_CON
1
2
3
THF_F_CMD
USER
CODE
MVM_put_TM
14
THF_T_CMD
USER
CODE
MVM_put_TM
1
98
USER
CODE
RVC_notify_begin
control_cycle
Block
Script
99
12
21
20
3
3
CON_PDE_DATA
Procedure
5
USER
CODE
CON_tmf
13
PDE_force_cmd(1)
PDE_force_cmd(2)
PDE_force_cmd(3)
PDE_torque_cmd(1)
PDE_torque_cmd(2)
PDE_torque_cmd(3)
thruster_saturation
controllability_lost
thr_ON_duration(1)
thr_ON_duration(2)
thr_ON_duration(3)
thr_ON_duration(4)
thr_ON_duration(5)
thr_ON_duration(6)
thr_ON_duration(7)
thr_ON_duration(8)
thr_ON_duration(9)
thr_ON_duration(10)
thr_ON_duration(11)
thr_ON_duration(12)
thr_ON_duration(13)
thr_ON_duration(14)
thr_ON_duration(15)
thr_ON_duration(16)
thr_ON_duration(17)
thr_ON_duration(18)
thr_ON_duration(19)
thr_ON_duration(20)
thr_ignite_time(1)
thr_ignite_time(2)
thr_ignite_time(3)
thr_ignite_time(4)
thr_ignite_time(5)
thr_ignite_time(6)
thr_ignite_time(7)
thr_ignite_time(8)
thr_ignite_time(9)
thr_ignite_time(10)
thr_ignite_time(11)
thr_ignite_time(12)
thr_ignite_time(13)
thr_ignite_time(14)
thr_ignite_time(15)
thr_ignite_time(16)
thr_ignite_time(17)
thr_ignite_time(18)
thr_ignite_time(19)
thr_ignite_time(20)
fuel_mass
1
2
3
4
5
6
8
9
7
26
40
49
CON_PDE_CMDS
Procedure
4
CON_THF_Telemetry
SUPER
BLOCK
Procedure
9

Figure 2 - Implementation of the Control function in Systembuild™

In this situation, only a statistical approach defining the expected acceptable performances in the nominal case can provide the answer whether the test is result is acceptable or not.

Likewise, for an efficient tuning of the Failure Detection Tests thresholds, such a statistical performance approach is mandatory. Finally, ESA GNC performance requirements are expressed in statistical terms (3σ performances).

In order to cover the need for statistical results, a GNC Statistical Simulator has been developed in the frame of ARPK. This simulator is fully coded in C, benefiting of the high execution speed of a compiled language. Some features (TM/TC handling...) of the Functional Engineering Simulator have not been modelled, as they were not considered relevant, whereas effort has been put on the possibility to cover the full ATV flight envelope by generating a large number of simulations input parameters distributed over a specified range. Storage and in-line statistical processing of simulations outcome is also an added feature. The core of the simulation control is derived from an existing structure developed in house for the simulation of attitude and orbit control system for Earth observation satellites.

Of course, in direct continuation of the ARPK experimental approach, automatically generated code has been widely used to produce the code of the on-board software elements in the Statistical Simulator. This minimizes the risks and allows to obtain code elements before they are available from the GNC software prototype for the ATV computer breadboard.

8 - CURRENT ASSESSMENT OF PERFORMANCES

This paper has been prepared as the ARPK program is not completed yet. In terms of performance assessment, GNC simulations have been performed on the Systembuild™ Functional Engineering Simulator, and are yet to be run on the Statistical Simulator. Only the RGPS based leg has been fully investigated so far. The second part of the ARP program, starting in the fall of 1996, will focus on the final approach and departure phases based on Rendezvous sensor navigation.

The results achieved so far are summarized in the table below:

	Required Accuracy	**Performances**
Position control (at 250m from ISSA)	12.5 m	7.3 m
Velocity control	-	5 cm/s
Attitude control	1 deg.	1 deg.

Table 2 - GNC performances (RGPS Phases)

9 - CONCLUSIONS

The GNC design and development carried out during the ATV Rendezvous Predevelopment program presents many innovative features.

- the integrated approach that uses the Computer Aided Design models to generate directly and automatically code to be used both in the prototype of the on-board software and in the statistical performances simulation facility. This approach has been applied on a large size control software prototype.

- modern "robust control" design techniques that provide a single control system applicable to many flight phases and to many configuration of ATV/cargo mass and inertiae.

- an innovative management of the thruster configuration to generate complex combination of forces and torques, that provide a sufficient thrust to complete the nominal mission in a degraded case after any single failure, as well as a 2-fault tolerant braking and wave-off capacity.

The successful advances achieved so far on the Relative GPS based phases of the ATV rendezvous will have to be complemented by the outcome of the detailed implementation of the GNC for the final translation and departure, yet to be carried out in the following activities of the ARPK program.

---

[1] Relative GPS Navigation Design and Validation for ATV Rendezvous, *V. Pascal, H. Marcille (Matra Marconi Space)*, 3rd ESA International Conference on Spacecraft Guidance, Navigation and Control Systems, Nov. 1996.

Rendezvous Strategy of the Japanese Logistics Support Vehicle to the International Space Station

K. Yamanaka

Guidance & Control Laboratory
National Space Development Agency of Japan
Tsukuba Space Center, 2-1-1 Sengen, Tsukuba, Ibaraki 305, Japan
Email : yamanaka.kouji@nasda.go.jp

Abstract

The National Space Development Agency of Japan (NASDA) has been studying an automated transfer vehicle for logistics support of the International Space Station. This vehicle, called the H-II Transfer Vehicle (HTV), will be launched by the H-IIA rocket which is an evolved version of the Japanese H-II rocket. After separation from the H-IIA rocket, the HTV performs a long-range rendezvous sequence which consists of phase, height and plane adjustment maneuvers. The long-range rendezvous sequence which has two elliptical intermediate orbits is being designed for the HTV. The long-range rendezvous uses GPS navigation. Near the Space Station, differential GPS navigation will be established for final approach to the Space Station. The HTV approaches the Space Station from below (i.e. R-bar approach). Laser radar navigation system will be used from a distance of 500m. At the Berthing Box, the HTV will be captured by the Space Station manipulator. The HTV navigation, guidance and control functions for proximity operations will be demonstrated in orbit by the rendezvous and docking experiments of the Engineering Test Satellite-VII (ETS-VII) which will be launched in 1997.

1. Introduction

The National Space Development Agency of Japan has been studying the automated transfer vehicle named H-II Transfer Vehicle (HTV) for the logistics support of the International Space Station. This paper describes the HTV rendezvous strategy to the International Space Station and also describes the HTV rendezvous guidance and control system.

HTV navigation, guidance and control functions necessary for the proximity operation will be demonstrated in orbit by the rendezvous docking experiments of the Engineering Test Satellite-VII (ETS-VII). These in-orbit experiments are also described.

2. H-II Transfer Vehicle

2.1 Mission Profile

The HTV is being designed to deliver 6-ton payloads to the Space Station. The HTV will be launched by the H-IIA rocket from Tanegashima Space Center. After separation from the H-IIA rocket, the HTV performs a long-range rendezvous sequence which consists of phase, height, and plane adjustment maneuvers. It arrives at the Space Station interface point and then starts to approach the Space Station under the Space Station Control Center operation authority. Finally, the HTV enters the Berthing Box in which the Space Station requires the HTV to stay and stop all actuators. The HTV will be grappled by the Space Station manipulator and berthed to the nadir port of the Space Station. After the HTV is berthed, payloads will be unloaded and disposables will be stored. The HTV will perform automatic departure from the Space Station, and destructive reentry with the disposal payload. (Fig. 2-1)

2.2 HTV Configuration

The HTV total weight at separation is about 13 tons. The HTV consists of the HTV Spacecraft and Logistics Carrier (Fig. 2-2). The HTV spacecraft is a 3.2m diameter, 2.0m long cylinder and weighs 4.0 tons including the propellant. Guidance and control equipment will be installed in the HTV Spacecraft.

Proceedings Third International Conference on Spacecraft Guidance, Navigation and Control Systems, ESTEC, Noordwijk, The Netherlands, 26-29 November 1996, ESA SP-381 (February 1997)

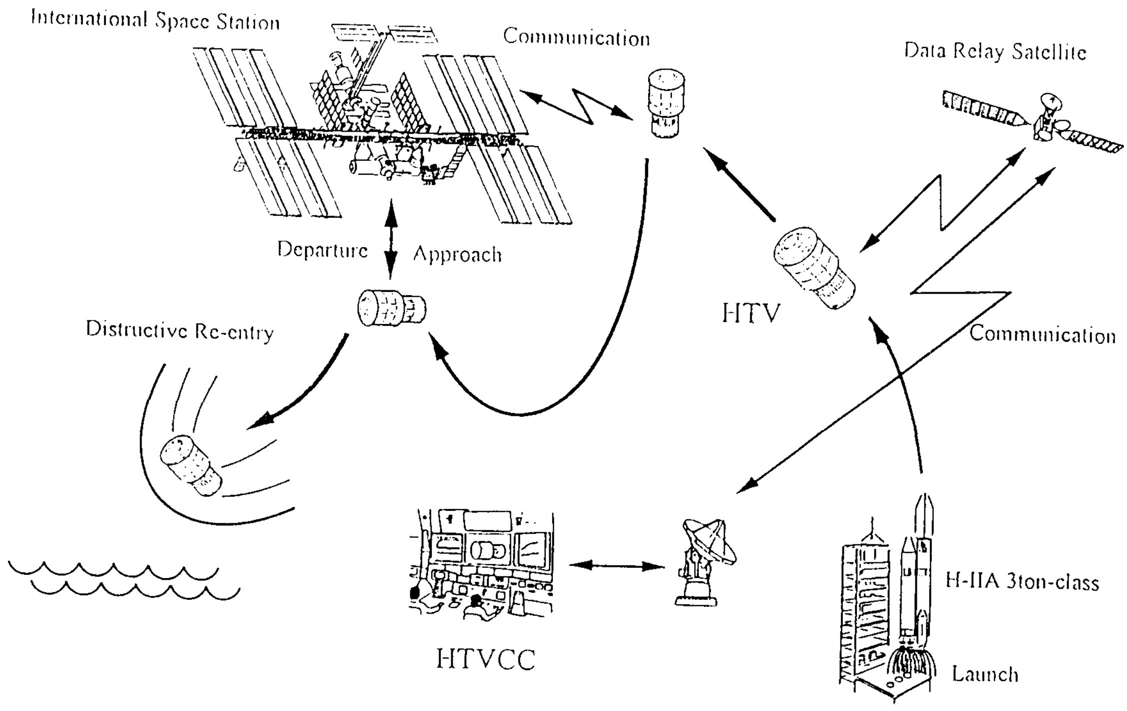
International Space Station
Communication
Data Relay Satellite
Departure
Approach
Distructive Re-entry
HTV
Communication
HTVCC
H-IIA 3ton-class
Launch

Fig. 2-1 HTV mission profile

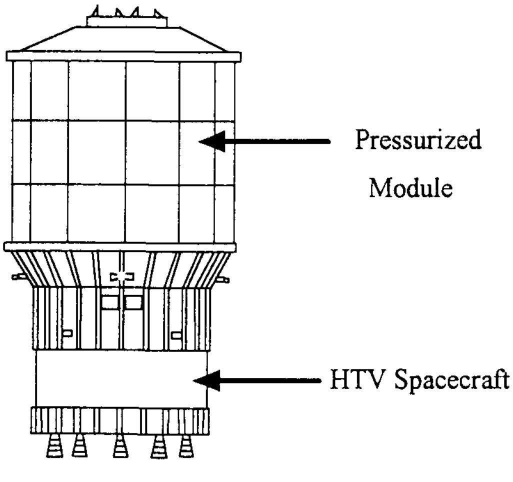
Pressurized Module
HTV Spacecraft

Fig. 2-2 HTV configuration

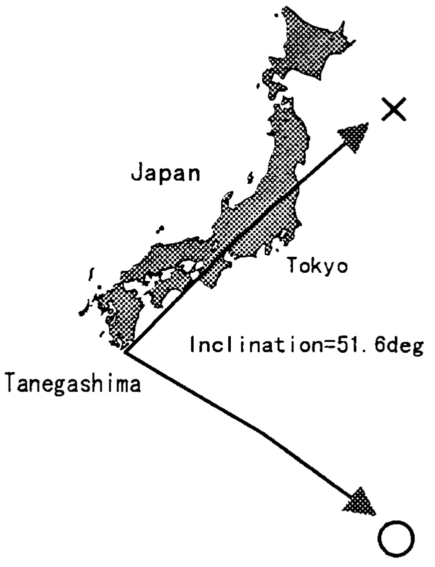
Japan
Tokyo
Inclination=51.6deg
Tanegashima
×
○

Fig. 3-1 Launch Direction

3. Launch Targeting

The H-IIA rocket launch site is located in Tanegashima island (30° 24'N,130° 59'E). This launch site will rotate under the Space Station orbit plane twice per day. Because of the launch safety constraints, however, only the south-ward launch (launch azimuth is greater than 90 deg) is possible (Fig. 3-1).

If the space station's orbit vector is given, the launch time of the HTV can be calculated. This calculation must consider nodal regressions of the Space Station and the HTV.

When the HTV conducts the rendezvous sequence, the orbit height of the HTV differs from that of the space station. This causes a difference of the nodal regression between the two spacecraft. The launch target plane must be biased a little from the real Space Station orbit plane for this reason. This bias is called nodal bias. If the phase angle between the HTV and the Space Station at separation is large, the HTV will be kept on a low altitude for a long time to reduce the phase angle rapidly and so the nodal bias becomes large. The reverse is also true. This relation is shown in Fig. 3-2. This figure shows the case where the Space Station altitude is 407km.

In this figure, initial phase angle means the phase angle between the Space Station and the

HTV at the HTV separation from the H-IIA rocket.

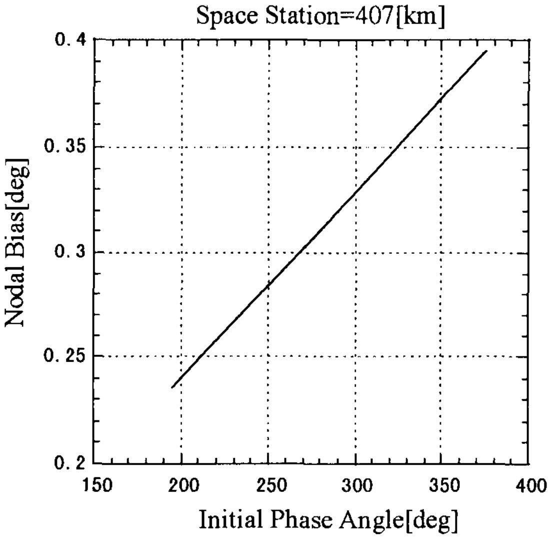

Fig. 3-2 Initial phase angle vs. Nodal bias

Figure 3-2 shows that the nodal bias is almost linear with respect to the initial phase angle. With this nodal bias the right ascension of ascending node of the target plane becames

$$\Omega_{SS} + \Delta\Omega$$

where Ω_{ss} is the right ascension of the ascending node of the Space Station and $\Delta\Omega$ is the nodal bias. Nominal launch time can be calculated by using this target plane.

If the launch time has been delayed from the nominal time by anomaly, the phase angle at the HTV separation becomes large and the node bias increases. On the other hand, the Space Station orbit plane regresses while the launch delay occurs. These two effects cancel each other. This relation is shown in Fig. 3-3. The increasing line shows the nodal bias and the decreasing line shows the regression of the Space Station ascending node. With this cancellation, the target plane can be fixed in inertial frame. The launch azimuth angle, however, must be changed according to the launch delay. The H-IIA rocket has a real time targeting function to change the launch azimuth angle automatically according to launch delay time.

Though the H-IIA rocket has a real time targeting function, the launch capability (possible launch mass) of the H-IIA rocket decreases with launch delay time. Figure 3-4 shows the launch capability of the H-IIA rocket. The launch window is being designed to 5min in order to prevent the decrease of the launch capability.

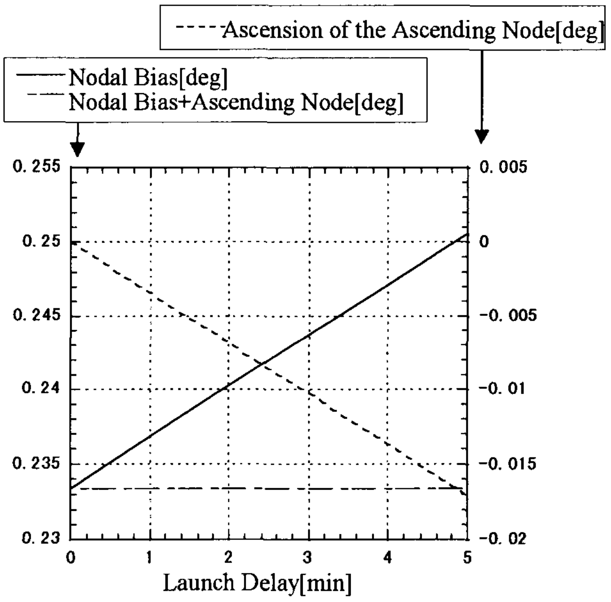

Fig. 3-3 Nodal bias + Ascending node

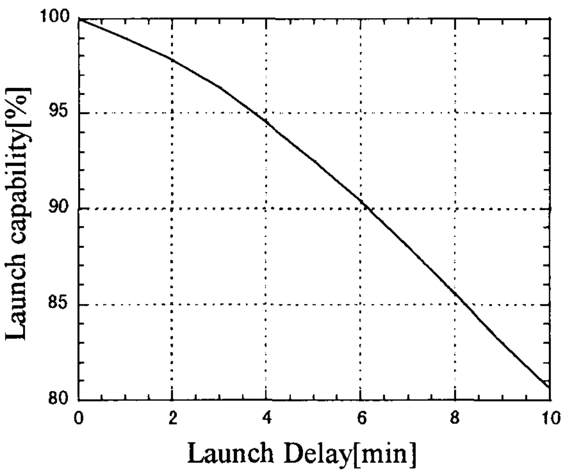

Fig. 3-4 Launch capability vs. Launch delay

4. Long Range Rendezvous Sequence

After separation from the H-IIA rocket, the HTV performs an orbit insertion maneuver by itself and reaches a 150km circular orbit. The HTV then performs the long-range rendezvous sequence which consists of phase, height, and plane adjustment maneuvers. Requirements for the rendezvous sequence are as follows:

- Phase angle, height difference and plane angle between the Space Station and the HTV must be reduced.
- Maneuver delay up to two revolutions must be recover.

- Important maneuvers must be monitored from the ground.
- Phasing capability must be greater than 180 degrees.
- Rendezvous time must be minimum.

To satisfy these requirements, a basic rendezvous sequence was designed as shown in Fig.4-1. In this sequence, "TI" means the Terminal phase Initiation point. Proximity operations begins from the TI point.

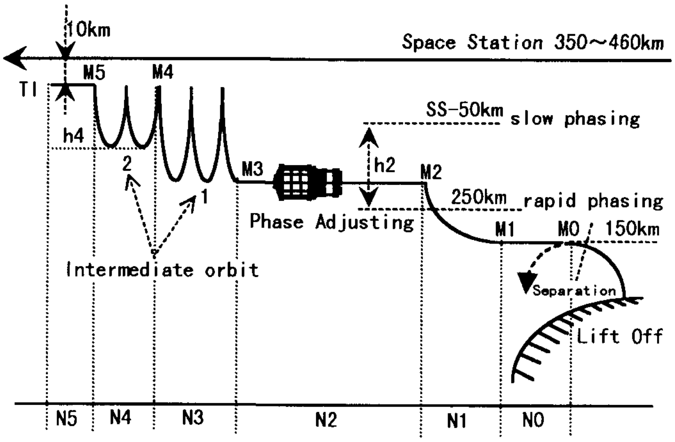
10km
Space Station 350~460km
TI
M5
M4
h4
2
1
M3
h2
M2
SS-50km slow phasing
250km rapid phasing
Phase Adjusting
M1
M0
150km
Intermediate orbit
Separation
Lift Off
N5
N4
N3
N2
N1
N0

Fig.4-1 HTV Basic Rendezvous Sequence

First, the phase angle between the HTV and the Space Station will be reduced mostly in a phase adjusting orbit whose height is selected properly depending on the initial phase angle. A plane change maneuver will be conducted in the end of this phase if necessary. After phase adjusting orbits, two intermediate elliptical orbits will be used to precisely adjust the phase angle and the height difference. These two intermediate orbits also provide margins for any previous maneuver failures. Each maneuver can be delayed up to two revolutions. The recovery plan is shown in Fig.4-2.

If the rendezvous sequence is designed to be able to compensate maneuver delay of up to two revolutions for each maneuver, the perigee height of the intermediate orbit 2 (h4 in Fig. 4-2) which minimizes the total rendezvous time can be calculated. As an example, Fig. 4-3 shows the rendezvous time when the Space Station altitude is 407km (220nm) and phasing altitude (h2) is 250km. In this case, the perigee of the intermediate orbit 2 (h4) is set to 375km. Intervals of each maneuver are shown in Table 4-1.

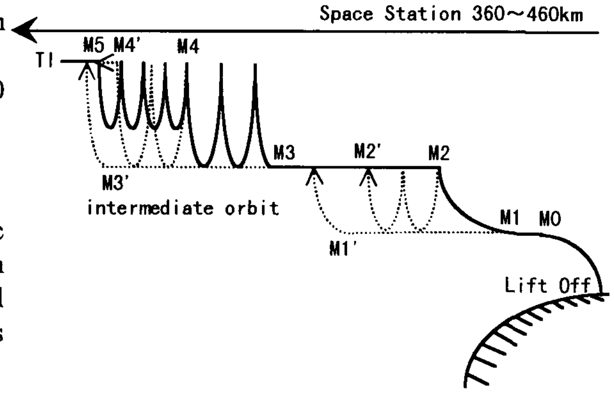
Space Station 360~460km
TI
M5
M4'
M4
M3
M3'
intermediate orbit
M2'
M2
M1'
M1
M0
Lift Off

Fig. 4-2 Recovery plan

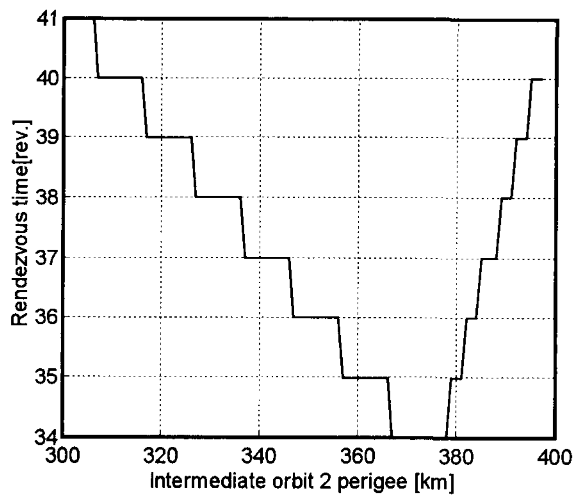

Table4-1 Intervals of each maneuver

N0	N1	N2	N3	N4	N5	Total
3	0.5	17	2.5	6	5	34

5. Proximity Operation

After phasing maneuvers and height raising maneuvers, HTV approaches TI. Proximity operation begins from the TI point. Figure 5-1 shows a proximity trajectory.

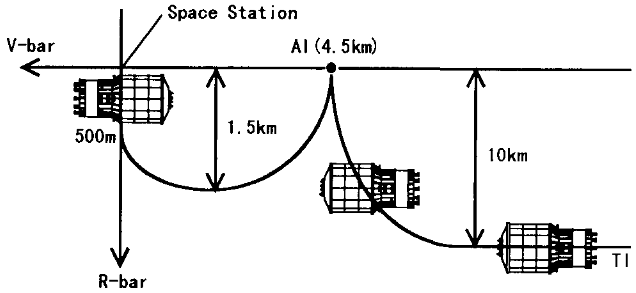
Space Station
V-bar
AI (4.5km)
500m
1.5km
10km
R-bar
TI

Fig5-1 Proximity trajectory

A communication link with the Space Station and the differential GPS navigation will be established at the AI point. From the AI point, the

HTV approaches the Space Station from below (i.e., R-bar approach). At a distance of 500m, the GPS based navigation is switched to the laser radar based navigation. At the Berthing Box, the HTV will be captured by the Space Station manipulator.

6. HTV Guidance and Control System

Figure.6-1 shows the HTV guidance and control system configuration. Besides the guidance and control computer, a control unit is provided for aborting rendezvous in an emergency. The Rendezvous Laser Radar (RVR) is used to measure the relative range and angle in the proximity area.

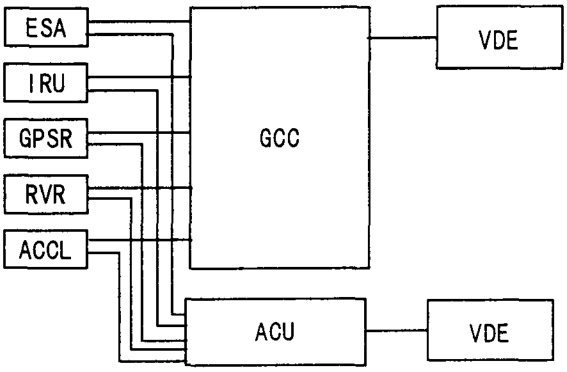

GCC : Guidance & Control Computer
ESA : Earth Sensor Assembly
IRU : Inertial Reference Unit
GPSR : GPS Receiver
RVR : Rendezvous Laser Radar
ACCL : Accelerometer
ACU : Abort Control Unit
VDE : Valve Drive Electronics

Fig. 6-1 HTV Guidance and Control System

The HTV guidance and control system will be developed based on the Engineering Test Satellite VII (ETS-VII) RVD system. Hardware specifications of the ETS-VII GPSR and the RVR are explained in the following section.

7. ETS-VII RVD Experiment

The ETS-VII Rendezvous and Docking (RVD) experiment was planned to verify the overall RVD system needed for unmanned spacecraft such as the HTV to perform an autonomous and safe RVD. The ETS-VII project was started in 1990, and the preliminary design review of the ETS-VII RVD system was completed in the fall of 1994.

7.1 Spacecraft Configuration

The ETS-VII consists of two spacecraft, a "Chaser" and a "Target". The in-orbit configuration of ETS-VII is shown in Fig. 7-1.

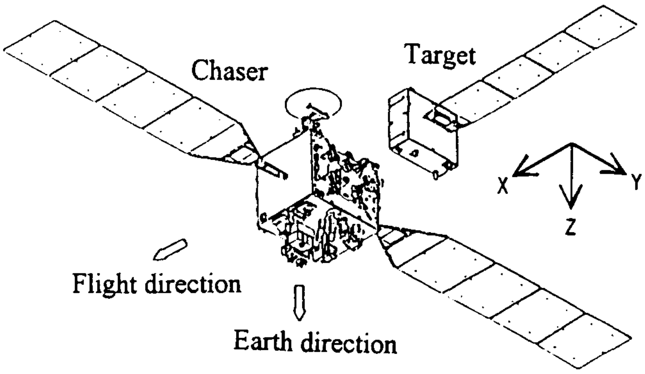

Fig. 7-1 ETS-VII Configuration

The ETS-VII is launched by an H-II launch vehicle into a parking orbit then ascends it's operational orbit (height =550km, inclination =35deg). RVD experiment operation is performed via a Japanese data relay satellite.

7.2 Flight Profile

The typical RVD flight is performed as follows (Fig. 7-2).

I. Chaser separates Target and retreats to TI (9km or 4.5km hold point).
II. Chaser approaches TF (500m hold point on V-bar or R-bar) using GPS differential navigation and Clohessy-Wiltshire (C-W) guidance
III. Chaser approaches VP (2m hold point) using RVR relative navigation and guidance along the reference trajectory.
IV. Chaser approaches the target satellite using Proximity Camera Sensor (PXS) relative navigation and 6 degrees of freedom control.
V. Chaser captures and docks the Target using docking mechanism.

In the ETS-VII RVD experiments, the basic approach path is a V-bar approach, but R-bar approach experiments will also be conducted (Fig. 7-2).

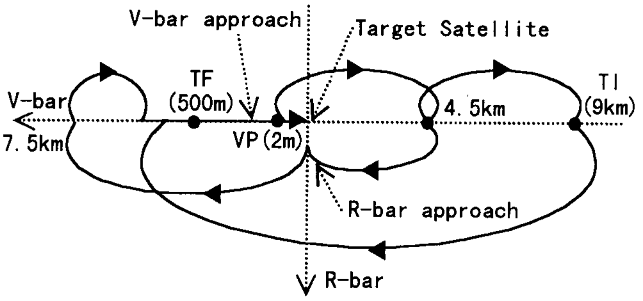

TI : Terminal Phase Initiation
TF : Terminal Phase Finalization
VP: Vicinity Point

Fig.7-2 ETS-VII flight profile

7.3 Navigation Systems

The typical ETS-VII RVD experiment is performed by using three navigation systems in accordance with the following RVD phases.

I. Relative approach phase (9km-500m)

In this phase, the GPS differential navigation is used to estimate the relative position and velocity. The navigation errors of GPS differential navigation are 20m for position and 5cm/sec for the velocity in the HILL's frame.

II. Final approach phase (500m-2m)

In this phase, the RVR relative navigation (including gyro and Earth sensor) is used to estimate the relative position and velocity in the HILL's frame. The accuracy of RVR navigation is 10cm in bias and 2cm in random.

III. Docking approach phase (2m-Docking)

In this phase, PXS relative navigation (including gyro and Earth sensor) is used to estimate the relative position, velocity, attitude, and angular rate.

Hardware specifications of the rendezvous sensors are as follows.

GPSR

The Chaser GPSR can perform differential navigation using a pseudo range based on the Target GPSR measurement data.

Relative navigation accuracy,
position (RSS, 3 σ) 20m
velocity (RSS, 3 σ) 5cm/sec
(GDOP<3)
Output frequency is 0.1 Hz

RVR

This sensor provides the range and Line Of Sight (LOS) angle (azimuth and elevation).

Range 0.3 to 660m
Field of view 8deg (cone angle)
Accuracy
Range : bias(0-p) 0.1m
: random(3 σ) 0.02m
Azimuth/elevation
: bias (0-p) 0.05 deg
: random(3 σ) 0.02deg
Acquisition time: within 10sec
Output frequency : 2Hz.

PXS

This sensor provides the relative position and attitude by measuring a 2D-CCD image of the three-dimensional marker.

Range 0.3 to 10m
Field of view 12deg (cone angle)
Accuracy
Relative position
X : bias(0-p) 2cm
Y,Z : bias(0-p) 0.5cm
Relative attitude
roll :bias(0-p) 0.05deg
pitch,yaw : bias(0-p) 0.02deg
Acquisition time :within 10 sec
Output frequency : 2Hz

ETS-VII will be launched in 1997.

Conclusion

The HTV is a Japanese automated transfer vehicle for logistics support of the International Space Station. Launch targeting, long-range rendezvous strategy, and proximity approach path were designed for the HTV. The HTV navigation, guidance and control functions for the proximity range will be demonstrated in orbit by the rendezvous and docking experiments of the Engineering Test Satellite-VII (ETS-VII) which will be launched in 1997.

Reference

1) T. Kato, T. Tanaka, T. Takahashi and H. Sasaki, "H-II Transfer Vehicle Study Status" AAS 95-584, pp 293-296

2)M. Mokuno, I. Kawano, H. Horiguchi and K. Kibe, "Development of ETS-VII RVD System -Preliminary Design and EM Development Phases-", AIAA GNC Conf., August, 1995, AIAA95-3357

3)D. J. Jezewski, et.al "A Survey of Rendezvous Trajectory Planning.", AAS91-505, pp1373-1396

REMOTE INTERVENTION IN AUTOMATIC ONBOARD GNC SYSTEMS

A. Vankov, A. Alyoshin, P. Chliaev
Gagarin Cosmonaut Training Centre, 141100, Star City, Russia
Phone: +7 -095-526-2511, Fax: +7-095-526-2612, E-mail: van@indy.gctc.rssi.ru

W. Fehse, F. Ankersen
ESA/ESTEC, P.O. 299, 2200 AG Noordwijk, The Netherlands
Phone: +31-71-65-3844, Fax: +31-71-65-5432, E-mail: wfehse@wk.estec.esa.nl

ABSTRACT

The paper reports on the results of a research and development activity on remote interaction concepts with automatic space vehicles during rendezvous operations. First an overview is given on contingency situations during the approach of automatic vehicles to a space station, on the onboard resources to overcome such situations and on the possibilities of remote intervention in automatic onboard GNC systems. The possibilities include various kinds of open loop and closed loop interactions. In order to investigate the various possibilities, a simulator has been built within the frame of the cooperation between the Gagarin Cosmonaut Training Centre and ESA/ESTEC, which allows a broad variety of approach strategies, contingency situations and a number of interaction methods to be simulated for a generic space station scenario. The scope and objectives of the simulator and the remote control concepts simulated are discussed and the corresponding operator interfaces are described. Typical displays are shown illustrating various interaction concepts and potential application of the results to the International Space Station (ISS) scenario are discussed.

1. INTRODUCTION

Manned Space Stations such as the Russian space station Mir and the planned ISS are serviced by manned and unmanned vehicles, e.g., Soyuz and Progress being in operation now for Mir and the Space Shuttle, Soyuz, Progress M and the Automated Transfer Vehicle (ATV) being planned for the ISS. In case of contingencies, the pilots aboard manned vehicles can react and make decisions according to the particular situation, whereas the automatic system of an unmanned vehicle can provide the proper answers to only those contingencies, the designers had thought of long before the vehicle became operational. It is, therefore, extremely important that human operators, whether on ground or aboard the manned target station, have access to the control system of an approaching unmanned vehicle, even if its automatic guidance, navigation and control system has been designed to be two failure tolerant. Two values are at stake: a) the safety of the crew inside the target station, and b) mission success, i.e. the investment made in the unmanned service vehicle, which is of the order of several 100 million $ including the launch cost.

In the Russian Space programme the need for remote control capabilities was ever present since the programme included the logistic re-supply of orbiting stations by unmanned vehicles in the 1970's. The first orbital station of the Salyut type was launched in 1971 and the first re-supply mission of the Progress spacecraft was successfully performed in 1978. Progresses still supply the Mir Station and, in a modified form, are planned to be used for the International Space Station.

Although the vehicle is fully automatic for nominal operations, remote control capabilities are indispensable and have been already used several times in contingency situations to save the mission. The Progress mission to Mir in September 1994 is one of the most vivid examples of this sort. During that flight, it was impossible to approach the station automatically. Therefore, the crew commander took over the control from the special post aboard the Mir Space Station and successfully performed the final translation to docking.

The remote control capabilities developed for Progress include continuous direct manual control of all 6 degrees of freedom by a cosmonaut in the target station or by a ground controller based on TV information, the command of individual thrust manoeuvres and initiate/inhibit commands for automatic modes.

The European Space Agency has started its research and development activities on remote control of unmanned vehicles with the emergence of the projects of the Columbus Free Flyer, which

Proceedings Third International Conference on Spacecraft Guidance, Navigation and Control Systems, ESTEC, Noordwijk, The Netherlands, 26-29 November 1996, ESA SP-381 (February 1997)

was supposed to rendezvous with the Space Station Freedom, and the European Spaceplane Hermes, which was supposed to visit the Free Flyer. After the suspension of these projects, as a result of political changes in Europe and the merger of the eastern and western space station programmes into the International Space Station, the ATV has become a part of the Western-European contribution. ATV is intended to participate in the re-boost and re-supply missions to the ISS. Remote control capabilities to be provided to the human operators in the Station and on ground are also indispensable for this vehicle to assure safety of the Station crew and mission success in case of contingencies during the automatic approach, which cannot be resolved by the automatic onboard system. The availability of such functions will increase both the mission success potential of the ATV and the safety of crew in the target station.

Because of similar interests in these matters, trajectory control/simulation groups at ESA/ESTEC and the Gagarin Cosmonaut Training Centre (GCTC) agreed in 1993 to establish a cooperative programme for the investigation and development of advanced remote control techniques.

In this paper, some results of the first two phases of this cooperative programme [1,2] are reported.

2. NEEDS AND POSSIBILITIES FOR REMOTE CONTROL

2.1. Contingency Situations During Proximity Operations of Unmanned Vehicles

Although the onboard systems of automated unmanned vehicles within the Space Station scenario must be single failure tolerant with respect to (w.r.t) all functions needed for success of the mission and two failure tolerant w.r.t. all functions essential for the crew safety, it is obvious that this build in failure tolerance can never cover all potential contingency cases.

Contingencies can be caused by external events, e.g., on the target station, by design mistakes which have not been uncovered during the qualification process or by manufacturing faults which have not been got rid of during the test and acceptance process.

Remote control techniques could help resolve the problem in a number of typical contingency situations during the approach, such as:

- the target station is temporary unable to receive the chaser vehicle;
- the approach needs to be stopped and the chaser vehicle be placed at a safe waiting position;
- the nominal trajectory needs to be modified for some reason, or a recovery trajectory has to be established as a result of a contingency;
- failure of the navigation function (sensor elements on chaser or/and target);
- failure of the automatic GNC function (thruster and thruster control function still being available);
- failure of all automatic functions (single thrusters can still be accessed by telecommand).

2.2 Possibilities of Remote Intervention in Automatic Onboard GNC Systems

The following four levels of intervention into the automatic onboard system are conceivable:

- high level intervention in phase/mode management and equipment assignment;
- intervention in the automatic GNC loop, i.e. in the navigation, guidance or control function;
- manual control, i.e. navigation, guidance and control performed in closed loop by a human operator;
- open loop intervention, i.e. human operator commands to provide discrete force/torque manoeuvres.

These levels of intervention are illustrated schematically in Fig. 1.

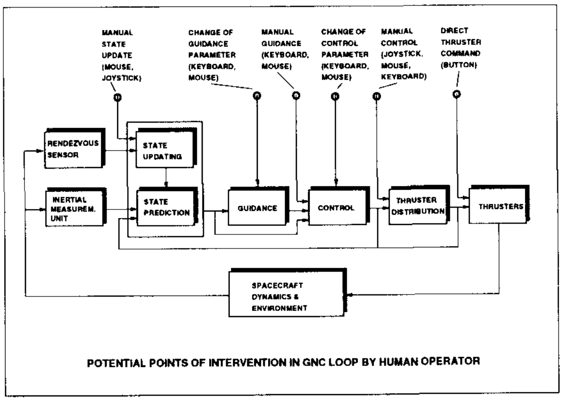
MANUAL STATE UPDATE (MOUSE, JOYSTICK)
CHANGE OF GUIDANCE PARAMETER (KEYBOARD, MOUSE)
MANUAL GUIDANCE (KEYBOARD, MOUSE)
CHANGE OF CONTROL PARAMETER (KEYBOARD, MOUSE)
MANUAL CONTROL (JOYSTICK, MOUSE, KEYBOARD)
DIRECT THRUSTER COMMAND (BUTTON)
RENDEZVOUS SENSOR
INERTIAL MEASUREM. UNIT
STATE UPDATING
STATE PREDICTION
GUIDANCE
CONTROL
THRUSTER DISTRIBUTION
THRUSTERS
SPACECRAFT DYNAMICS & ENVIRONMENT
POTENTIAL POINTS OF INTERVENTION IN GNC LOOP BY HUMAN OPERATOR

Figure 1: Intervention options

In case of a failure of the navigation function, the human operator (H-O) in the target station or on ground could take over the task of navigation based on TV information. The rest of the automatic GNC system remains in operation.

Concerning intervention in the guidance function, the H-O could command e.g.:

- change of start- and target points of 2 pulse manoeuvres,
- change of reference trajectory for continuously controlled manoeuvres,
- change of reference attitude.

In the third case (manual control), the H-O would replace the automatic GNC system and control the vehicle manually. As it is not feasible for the H-O in a closed loop control process to address each thruster individually, this type of intervention requires either that the thruster control function onboard is still operating or that the control algorithms for automatic thruster control are available in a computer at the human operator's control post in the target station or on ground.

2.3 Resources for Remote Control at the Station and on Ground

In order to be able to intervene in the GNC of the approaching spacecraft, the H-O needs to have at his disposal a number of resources concerning information and data, as well as command and control actions:

The following types of information would be useful:

- status of chaser vehicle:
  - state vector;
  - relative navigation data;
  - phase/mode status (GNC algorithm configuration);
  - GNC equipment configuration;
- state vector of target vehicle;
- status of communication links;
- TV/video images.

Video images are particularly important as a source of navigation information if relative navigation data and generally the state vector of the chaser vehicle are not available.

Image/graphics processing and display techniques available at the ground facilities and even in orbit have been improved considerably. Advanced remote control concepts, which were not foreseen a few years ago, can now be implemented. It is foreseeable that the resources for support functions such as computer generated graphics, image processing, high-speed prediction of the spacecraft trajectory and attitude, etc., will further be progressively increasing with time.

Command facilities will probably, in contrast, change much less. The main command tools are, and will remain to be, the computer keyboard and joysticks for direct manual control.

The most important constraints for all teleoperations are the communication links. Even if links to ground are redundant, they are subject to random interruptions due to atmospheric disturbances, shadowing, etc. Video links in addition require a large bandwidth which is not always available between space and ground but are much less of a problem between chaser and target.

For all the reasons described above, it was decided to concentrate the investigations on remote control schemes making use of advanced computers and man-machine interfaces including flexible displays, video- and artificial images and fast simulation techniques as described in the following chapter.

3. OBJECTIVES, SCOPE AND REFERENCE SCENARIO OF THE SIMULATOR DEVELOPED BY GCTC AND ESTEC

3.1 Objectives of Simulator

The purpose of this joint ESTEC-GCTC programme was to study the concepts and schemes for the remote manual control of rendezvous, docking and departure of an unmanned and nominally autonomous supply vehicle to/from a space station, in order to:

- improve safety and increase mission success probability in case of contingency and non nominal situations;
- contribute to the reduction of the onboard complexity of a vehicle which is non-recoverable.

In more detail, the objective of the activity was to develop, implement and test a prototype of a remote manual flight control system and of an according simulation of the spacecraft and operator environment to investigate:

- various levels of intervention by the human operator into the GNC loop in contingency situations;
- modification of the parameters defining the RVD trajectories and the GNC system behaviour;
- determination and correction of the components in the chaser state vector in non nominal situations using a camera and computer generated images;

- manual remote guidance and control of the chaser using video displays and virtual environment interface;
- man machine interface for decision making support including actions allowed for the human operator;
- prediction of the progress of events including identified non-nominal situations.

3.2 Scope of Simulator

The Remote Intervention Simulator includes the following functions:

- Dynamic simulation:
    - Onboard GNC functions;
    - Guidance functions for impulsive transfer, fly-around, straight-line approach, attitude hold and slewing;
    - Navigation functions with inputs from gyros, short and medium range rendezvous sensors and feedback of commanded forces;
    - Control functions according to above guidance functions for a vehicle similar to the ATV and thruster selection functions realised as look-up tables.
- Dynamics and environment:
    - modelling of spacecraft dynamics for an ATV-type vehicle in terms of mass, inertias and thruster type and locations, of disturbances such as atmospheric drag, and of sun illumination conditions.
- Simulation of support functions for the human operator:
    - Animation of chaser and target vehicle, simulation video pictures as seen from chaser or target video cameras;
    - Generation of virtual target picture for the manual state update;
    - Fast predictive trajectory simulation and the corresponding graphic user interfaces for data input and output (see chapter 4.3).
- Test operator control functions:
    - Windows for test set-up, scenario and test parameter definition;
    - Graphic user interfaces for manipulation of the simulation in terms of simulation speed, introduction of failure modes etc.

3.3 Reference Scenario

Since one of the objectives of the activity was to obtain generic results for remote control of unmanned vehicles in view of the needs of the ISS, the target spacecraft modelled is a space station with a structure similar to the ISS and the chaser spacecraft modelled is a vehicle similar to ATV presently under the development by the European Space Agency. The approach trajectory scheme used is similar to that presently defined for the ATV and described in [3]. A generalised illustration of the reference trajectories is presented in Fig. 2. Though the reference trajectory for a so-called V-bar approach is presented therein, R-bar approach was also given a special consideration during the study.

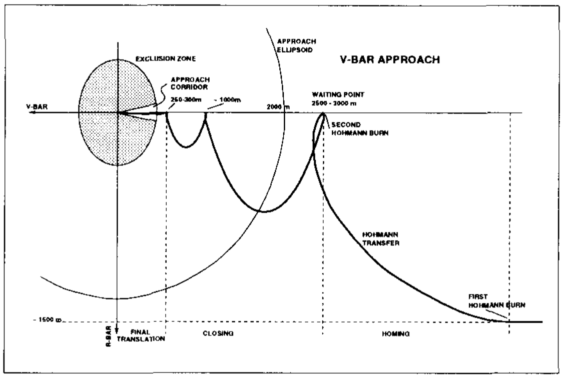

Figure 2 : Approach scenario (V-bar option)

After approaching on a drift orbit 1500 - 2500 m below the orbit of the Station, the chaser vehicle performs a Hohmann transfer to a waiting point on the orbit and at a distance of 2500-3000 m from the ISS. This point is outside the "Approach Ellipsoid" of the Station.

After permission by the Station to enter the above ellipsoid, one or more half-loop manoeuvres are performed. This subphase, called "Closing", ends at a distance from the target spacecraft of about 500 - 1000 m.

If the docking axis of the ISS is not aligned w.r.t. its V-bar (i.e., if it is pointing either in R-bar or any arbitrary direction), a "Fly-Around" manoeuvre is required, which will bring the chaser within a distance of 200 - 500 m of the target.

The "Final Translation" is the last subphase. During it, the chaser is approaching the ISS nominally on a straight line. This line has to be within a converging cone representing the allowable corridor, the centreline of which ends at the centre of the selected ISS docking port.

After each of the above mentioned subphases, "hold" or "waiting" points may take place on request of the H-O for checking procedures and mission re-planning in case of contingency situations.

The relative navigation sensor for all sub-phases until Final Translation will be Relative GPS (RGPS). From a range of less than about 250 m laser-based rendezvous sensors (RVS) will be used.

During the last part of the Final Translation, the trajectory of the chaser is not any longer passively safe. Therefore, a special collision avoidance manoeuvre (CAM) is necessary to abort the RVD mission in case of contingencies which cannot be resolved by the onboard system. This can be initiated automatically by the onboard system or commanded by the H-O.

In order to align thrusters and antennae according to needs, during each of the above subphases, the chaser may perform various slewing manoeuvres and will keep the required attitude between them.

During simulations, the data describing the chaser spacecraft was used in accordance with [4-6].

4. REMOTE CONTROL MODES AND OPERATOR INTERFACE IMPLEMENTED

4.1 Operator Intervention into the Automatic GNC

Various levels of intervention in the automatic GNC system have been addressed in chapter 2.2. The highest level concerns the intervention in the mission plan, i.e. the trajectory and attitude sequences, which involve also a change of the guidance parameters and of hardware and software functions required to support the various phase and modes. This all implies modifications of a so-called flight "baseplan" which is stored in the onboard computer. It is assumed that the baseplan defines as minimum:

- sequence of operations to be performed,
- conditions of completion of any operation,
- parameters describing each operation and reference trajectory,
- spacecraft onboard subsystems and equipment engaged.

The H-O is assumed to be allowed to provide changes of the:

- sequence of manoeuvres/modes, e.g.
  - transfer into another orbit,
  - angular manoeuvres;
- attitude stabilisation mode, etc;
- parameters defining each manoeuvre and/or its reference trajectory;
- GNC subsystem parameters (e.g., thresholds for stabilisation, maximum angular velocity, etc.).

It is envisaged that two levels of parameter modification may exist:

- the first level is related to the intervention of an astronaut in the target space station or a ground station controller,
- the second one implies the involvement of a GNC expert, who needs to be experienced concerning onboard guidance and control laws.

The following parameters are considered for modification at the first level:

- the required final chaser position/velocity w.r.t. the Space Station after the completion of each subphase,
- the frame (coordinate system) w.r.t. which the spacecraft is to be stabilised,
- the chaser attitude w.r.t. the selected frame,
- the type of the attitude stabilisation mode (rough, accurate, precise),
- the maximum duration of the manoeuvre (when applicable),
- parameters describing the exclusion zone around the Space Station,
- type of the Final Translation (selection of the appropriate option among the pre-determined ones),
- parameters describing the collision avoidance manoeuvre (namely, velocity increment and its direction w.r.t. the docking axis along with terminal conditions to acquire V-bar at the end of CAM).

Additional groups of parameters allowed for modification at the second level are related only to the Final Translation as the most critical subphase. They are:

- parameters defining the reference approach velocity profile and tolerances,
- parameters defining the profile of maximum allowable lateral position tolerances,
- parameters defining the profile of maximum allowable lateral velocity.

All the above mentioned possibilities have been implemented through a specially designed man-machine interface. The basic idea developed in this study is to provide the H-O with a tool allowing for the on-line creation of virtual environments and for operating therein to find the appropriate GNC strategy.

Virtual processes related to these environments, called "child processes", simulate the same model scenario (RVD), but may run in a "compressed" time as compared to real-time handling by the H-O. Also, the H-O may modify the parameters of RVD trajectory and the chaser GNC subsystem to try to improve the chaser performance if necessary. This is illustrated in Fig. 3.

One or more "child" processes may be initiated. Note, that the "parent" process needs not to be the basic real-time one, but it may also be any of the virtual processes, which has followed the basic one.

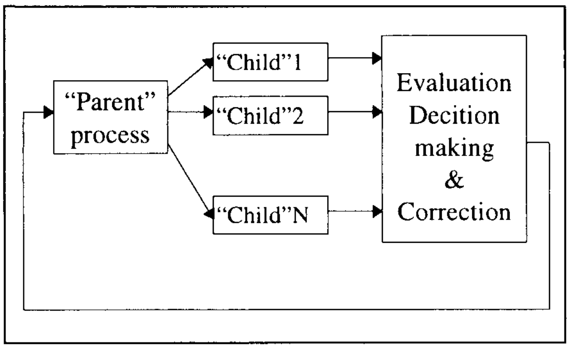

Figure 3: Search for the appropriate RVD baseplan

Theoretically, several generations of virtual processes may be created, but it would be obviously inconvenient for the H-O to work with many processes running simultaneously. It is important to note that interaction with any "child" process is provided in the same way as with any "parent" one.

The following "lines" of interaction between the operator and the software while controlling a spacecraft in a virtual environment have been implemented:

- run mode options,
- graphic user interface (GUI),
- modifiable parameters describing the reference trajectory and the chaser GNC subsystem

The following run mode options are available:

- Free run at "high" or "low" (default) speed: the process being controlled is running as fast as the processor and operating system allows (high), or with a predetermined time compression factor (low), e.g., 50 or 10 times faster than real time; the process runs up to the instant defined by the H-O and then stops thereat.
- Variable speed run: H-O explicitly controls the speed (time factor) using a virtual panel (slider).
- "Explorer" (ahead the parent process in real time): using this mode, H-O may anticipate the performance of the chaser and the progress of situation during the critical phases of flight (e.g., final translation to docking).

Both to control and monitor various generated processes, the H-O is provided with a flexible environment to build up an appropriate GUI. The main virtual panel is presented in Fig. 4.

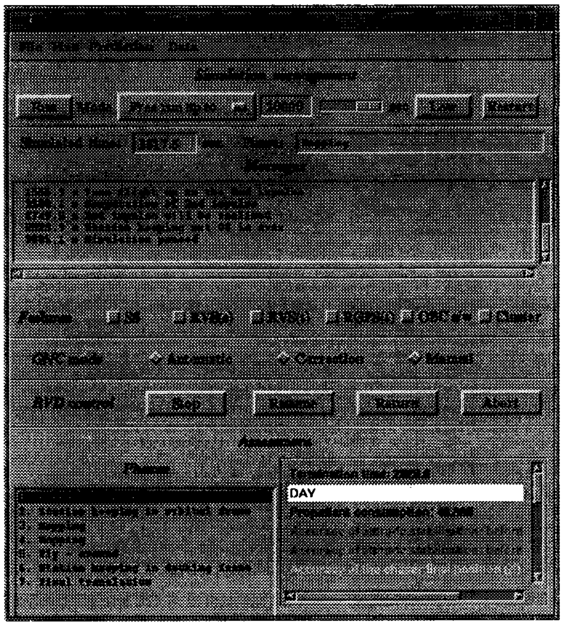

Figure 4: Main RVD simulation management panel

Fig. 5 represents an example of 2D-plot being rendered concurrently with the ongoing simulation process and 3D graphics.

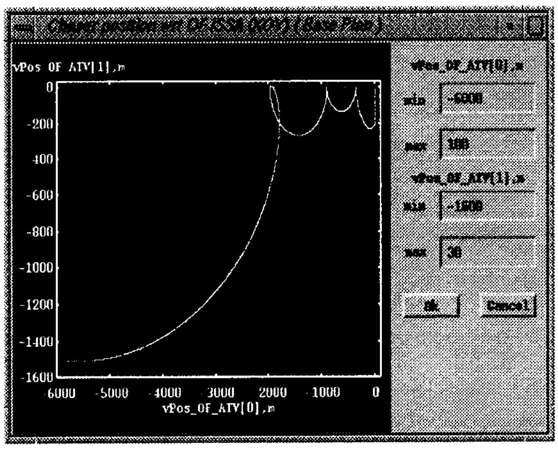

Figure 5: Example of RVD trajectory

To provide the H-O with the on-line support, an automatic assessment of predictive trajectories has been implemented. The following variables are used to provide the assessment of any trajectory (i.e. related either to "real" or "child" process):

- Trajectory and attitude errors,
- Fuel used up,
- Time deviation w.r.t. the Baseplan.

For any process there is a pull-down "assessment" menu. The user can choose the level of detail for an on-line analysis starting with a general information (notifying, e.g., that the above mentioned variables are within the predetermined tolerances) and ending with a time history for any selected variable.

Upon the completion of each subphase, each component of the error vector is assessed and represented by means of the background colour on the display, i.e. either excellent, good, satisfactory (warning), or bad (out of pre-defined tolerances).

Also, the following data is displayed:

- Instant of completion of the subphase being considered (termination time),
- Illumination conditions at that moment (day/night) with white/black background used accordingly,
- propellant consumed during this subphase.

The software simulating the remote manual flight subsystem described above and the ones described in the following chapters has been implemented on Silicon Graphics workstations and is able to run on any stand alone SGI IRIX 5.3 computer.

Simulations have shown that it takes a few minutes for the H-O to create any predictive virtual process, implement parameter changes, make it run and assess the results of prediction. The system is also expandable in terms of parallel work of several operators using a network of SGI workstations or a multi-processor system.

4.2 Manual State Vector Update Mode

A special kind of correction of the chaser motion may be used when the relative navigation fails, while the automatic control system is still available. This situation should be given special consideration, because it happened several times to the Russian transport spacecraft and e.g. because the relative GPS-based scheme proposed for ATV is new and only little experience in space will be obtained prior to the real mission. Also, this method can be used in case of a failure of the optical rendezvous sensor.

There exists an obvious opportunity to use the H-O as an image recognition "subsystem" (a task that humans can still do better than artificial intelligence systems). As a source of visual information, a TV-camera is assumed to be used, which is installed either onboard the chaser to be controlled (to monitor the Space Station), or in the target spacecraft/station (to monitor the approaching vehicle). Though a TV-image has no quantitative data, it may easily be complemented by a "virtual" environment.

In this case, the H-O has to compare two images of the reference object(s): the first one provided by the TV-camera and the second one generated by a computer. The operator's task is to match these images by varying the second one (i.e. by change of position, rotation, increase or decrease of size). Conceptually, an alignment of a "virtual environment" to the "real" world takes place here.

Because the computer generated image has all the necessary data such as range, line-of-sight angles, etc., when the pictures are matched, the above values can be entered into the GNC subsystem to update the state vector describing relative motion of the two rendezvousing spacecraft. Between two corrective updates, the spacecraft GNC subsystem uses a predictive model to compute its state vector. The procedure is aimed at the correction (error nullification) of the predictive model and must be periodically repeated as soon as the estimated uncertainty along any axis reaches the tolerance limit. This concept is a further development of the manual state update concept investigated in the ESA's RVD Pre-development Programme [9], in which the RVS target pattern instead of the overall spacecraft geometry was used as a reference.

In the simulation environment, this mode has been implemented with the additional feature that after a RGPS failure is detected, the chaser spacecraft automatically starts to perform a slewing manoeuvre in order to acquire the line of sight by the optical axis of the onboard TV-camera. Fig. 6 illustrates the proposed idea.

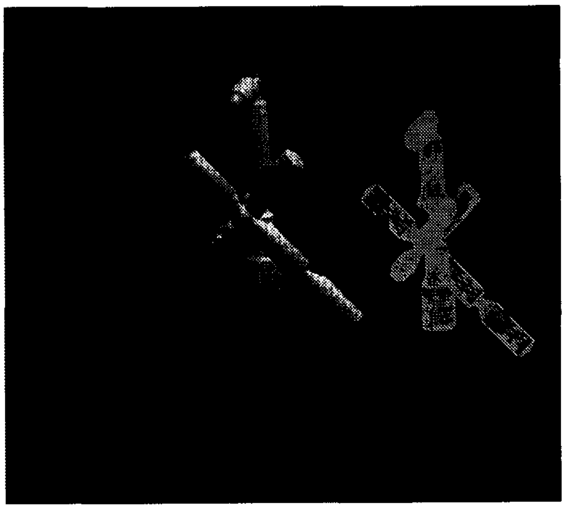

Figure 6: Correction of the relative state vector using virtual environment

Two computer-generated perspective images of the target spacecraft are presented therein. The first (solid-rendered) one represents the image of the Space Station provided by a TV-camera, while the second one (a wire-frame model) represents the "virtual" object. The latter model is mouse-driven in three directions (using two buttons). Simulations have shown that the operator can bring the above two images in coincidence in real time very effectively without any special training. The obvious advantage for the operator is that he can perform this task under various illumination conditions selecting the appropriate part of the Station and its elements.

It has been found during simulation runs that the operator is able to match the images very accurately. Typically at a distance of 250 - 400 m, the errors of spacecraft relative position determination were less than 5 m in the lateral plane and less than 10 m along the line-of-sight for a broad variety of illumination conditions. The above values are of the same order of accuracy that RGPS can provide. Determination of the relative velocity using this method resulted in errors of a few cm/s that is comparable with a "conventional" (non-relative) mode of GPS. Therefore, it has been decided to use the value of 3.5 cm/s accuracy of measurement provided by GPS as a worst case error available all over. All the above mentioned errors along with 5-min black-out period result in a final misalignment of less than 20 m after the completion of Fly-around. Assuming the distance of the beginning of Final Translation to be 200 m and field-of-view of Rendezvous sensors to be 15 degrees, the proposing method can help accomplish the Fly-around safely.

4.3 Predictive Manual Guidance and Control Mode

The manual control mode addressed in chapter 2.2 is the well-known method to replace the complete GNC system in case of failure by a human pilot. This is presently implemented e.g. as a backup system for the rendezvous of the Progress vehicles. The concept implies that the human operator is provided with appropriate displays and control sticks (typically, two ones) allowing for control of both translational and rotational motion. For the existing Russian transport spacecraft, the remote control post aboard the Space Station is equipped with the same instruments and control sticks as those being used onboard the Soyuz spacecraft. The latter implies the left handcontroller realising control of spacecraft translational motion and the right stick controlling the rotational motion. Both sticks have 3 degrees of freedom. Special force feedback helps the operator to feel the magnitude of the control input he is providing. The video image provided by a TV-camera is supported by fixed reticules in form of cross hairs and concentric squares, which provide the H-O with references for the estimation of the vehicle state relative to the target.

Conceptually, this is the most simple interface of direct manual control. Nevertheless, there are at least two effects which may drastically deteriorate the capability of man-in-the-loop to remotely control a spacecraft:

- time delays to do communication,
- slowness of reaction due to large mass/inertia and low control force/torque level.

The necessity for compensation of time delays in the control loop is one of the main problems arising for the remote control of aerospace vehicles. This delay is introduced by the time required for the signal propagation via "ground-space" and "space-ground" links and delays in the dedicated processing hardware. The typical value of the round-trip delay for the paths involving relay satellites is about 1.0-1.5 sec, whereas it is well-known that values of more than 0.3-0.4 sec lead to considerable difficulties in handling of space vehicles by the H-O. Moreover, the value of this delay may be variable if different paths for the signal propagation available along the orbit are used during the operations. Under such circumstances, if no special methods are used to compensate the delay, the human controller has to use a very primitive GNC strategy with quite simple control inputs. This may result in a considerable reduction of the total man-machine system performance.

The second problem often arises when a H-O tries to handle directly a heavy space vehicle with, on one hand, considerable mass and inertia and, on the other hand, relatively poor control forces and torques available. This case may be difficult for the H-O, as it does not fit his natural characteristics of reaction and thus may deteriorate his abilities to control the plant (because he has to permanently anticipate the progress of the situation). Moreover, values of time derivatives of the state vector components must not be beyond the thresholds of the human perception, and this requirement is not automatically met for "slow" space vehicles.

In both cases the involvement of a "virtual" simulation environment is highly desirable to improve the performance of this kind of man-machine systems.

To overcome the above mentioned problem, a new guidance and control scheme has been proposed and implemented. One of the main ideas is to provide the H-O with a "non-delayed" model of a dynamic system (plant) that can be used for the search of the control programme. It is based on the predictive GNC philosophy described in [7,8].

The Predictive Model (PM) simulates the process in a compressed adjustable scale of time, so in the predictive manual mode the H-O deals with the "virtual" plant that is not only free of time lag, but may also have improved handling qualities (the model may be more agile than the plant). Thus, if the H-O is involved in the loop, he/she starts controlling the model, so to say, in the "future". During the search, the operator every now and then commands special OK-marks, when he finds the process suitable. By that, the part of the control programme and reference trajectory that was found o.k., is then being realised at the proper period of time. The search for the optimal control command is arranged in an iterative process and the operator can repeat the attempt if he sees that a wrong or less effective command has been issued.

When an OK-mark is issued (e.g. by pressing a special button on the handcontroller or keyboard), the computer fixes the part of the program or/and trajectory that is determined at that moment. This part is then specially coded (to compress the data), transmitted to the vehicle and stored there. Conversely, if the H-O does not like the way he has controlled the "virtual" plant (i.e. he considers some previous command to be erroneous), he issues an another one - the "return" command. This returns the entire process to the instant and state vector that the system has had when the previous OK-mark has been issued. Given the relative slowness of motion during approach, the operator usually has enough time to provide several attempts (provided the virtual time is sufficiently compressed w.r.t. the real time) and his errors will influence the process through the reduction of this amount of time only.

A schematic illustration of the discussing methodology is presented in Fig. 7 for a two-dimensional control vector denoted by U(t) (time histories for state vector components are not presented for simplicity).

The proposed scheme also allows for a "brain-parallelism" to be implemented at the control site when several H-O's are simultaneously trying to find out the optimal control strategy and some supervisor chooses the best solution in accordance with pre-defined criteria.

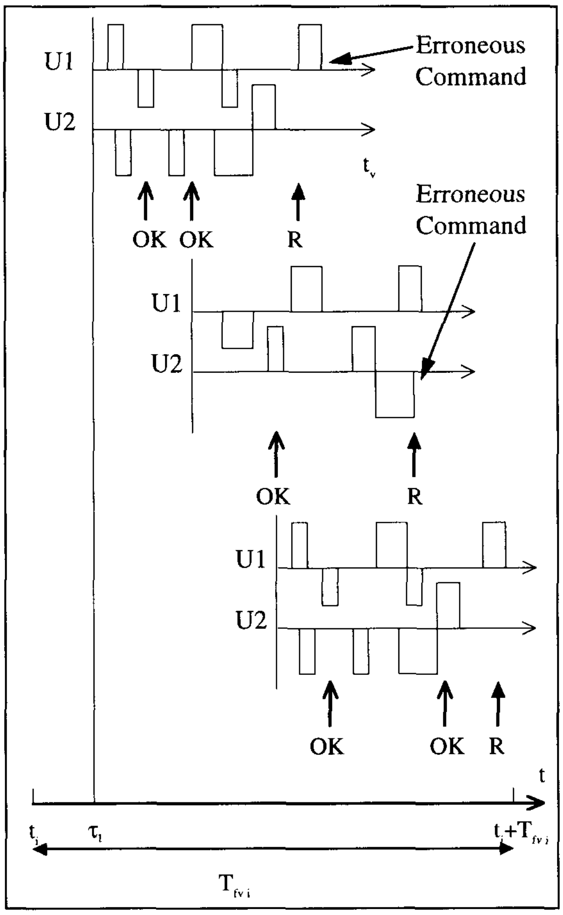

Figure 7: Predictive manual control

Computer simulations of this guidance and control mode have shown that the operator is able to control the spacecraft having the dynamic properties similar to those of ATV under the time compression factor equal 2 w.r.t. real time. Because of uncertainties in thruster parameters, it was impossible to let the H-O "go in future" far enough. Using thresholds of the order of docking contact tolerances (a few cm), it resulted in 20...30 sec of allowable period of prediction. Nevertheless, operator managed to be always ahead of real process and could return back in case of issuance a wrong command and its determination.

5. CONCLUSIONS

Various concepts of remote intervention in a GNC loop have been investigated, ranging from direct manual control until high level intervention in the automatic GNC system.

Two new original concepts of remote human intervention into the spacecraft GNC loop have been proposed. The first one is using the manual matching of a computer generated image with a real video image of the target to update the state vector in the navigation function of the automatic GNC system. The other concept is based on the virtual environment interface and predictive models simulating the spacecraft motion in a compressed time.

Depending on a contingency situation or failure occurred, the operator is allowed to provide:

- modifications of the flight plan and some parameters of the reference trajectory and onboard GNC subsystem,
- determination and correction of the spacecraft state vector superimposing a computer generated virtual picture on a video image provided by an onboard camera,
- remote control of a spacecraft in a virtual environment to alleviate negative impact of transport delay in the loop.

These modes have been implemented in a rendezvous and docking simulator. The simulator is a useful tool for studying next to the remote intervention concepts also various other issues, such as:

- automatic guidance and control laws,
- RVD scenarios and trajectories,
- graphical user interfaces.

Rendezvous and docking/berthing with the International Space Station by unmanned vehicles from different space powers will require increased supervision and remote interaction capabilities both from the Station and from ground. For this scenario, the remote intervention concepts described in this paper appear to provide important additional capabilities to counteract contingencies and to increase safety and mission success.

6. ACKNOWLEDGEMENTS

The authors are much indebted to

- B. Kryuchkov, the GCTC deputy chief, for his support within the CGTC to make this cooperative project possible,
- the ESTEC management for providing the financial basis for the joint programme,
- A. Vislotsky, a GCTC expert, for design and implementation of the thruster selection and fly-around algorithms which were used in the project,
- our colleagues from the ESTEC's Simulation and System Modelling Sections for providing valuable support in setting up the joint programme and in all matters concerning the use of the computer platforms at ESTEC.

7. REFERENCES

[1] Joint ESTEC-GCTC Research Programme on Advanced Control of RVD: Phase 1, Technical Note 3; October 17, 1994

[2] Joint ESTEC-GCTC Research Programme on Advanced Control of RVD: Phase 2, Technical Note 2; April 23, 1996

[3] W. Fehse: ATV-ISS RKA-NASA-ESA Technical Interchange Meeting Viewgraph presentation: Approach to and Departure from ISSA, Moscow, November, 1994

[4] ATV Rendezvous Pre-development (ARP) Kernel Control Design Specification Doc. ARPK-SP-RVC-1007-DASA, April 1995

[5] ATV Rider 6 - Configuration Review: ERNO-MMS Technical Note, 15 July 1993

[6] ATV Rider 6 - Study Synthesis: AEROSPATIALE Technical Note, 16 July 1993

[7] Vankov A.I.: Adaptive Control of Dynamic System Using Parametric-Group Forecast of its State. Automation & Remote Control, Plenum Press, 1990, No. 3, pp. 103-109

[8] Vankov A.I. and Alyoshin A.V.: Minimax Control of Spacecraft Rendezvous Under Uncertainties by Means of Predictive Models. Cosmic Research, Plenum Publish. Corp., 1993, v.31, No. 3, pp. 34-42

[9] Rendezvous & Docking System Pre-Development Programme, Final Report of ESA contract 8369/89/NL/JG Industrial Consortium lead by MMS, July 1993

SESSION 5:
MISSIONS I

Chairman: F. Tolivar (JPL, USA)

THE DESIGN AND DEVELOPMENT OF THE AOCS FOR THE XMM AND INTEGRAL SCIENTIFIC SPACECRAFT

D. Jukes and D.H.Parker

GNC Department, Directorate of Science and Radar Observation
Matra Marconi Space UK Ltd, PO Box 16, Bristol, United Kingdom
Phone: +44 117 900 6865, Fax +44 117 900 6853

ABSTRACT

The Cornerstone 2 mission in ESA's Horizon 2000 science programme is the XMM spacecraft, due for launch in 1999. The spacecraft is currently under development by an industrial team which includes MMS, which has the responsibility for the high pointing accuracy AOCS needed for the mission. The same service module is to be used for the second Medium science mission, INTEGRAL (International Gamma Ray Laboratory), to be launched in 2001.

Both missions are characterised by highly elliptical orbits: 48 hours period in the case of XMM (based on launch by a dedicated Ariane 5 and following a perigee raising manoeuvre), and 72 hours for the nominal INTEGRAL mission, which uses a Proton vehicle and a direct injection strategy. However, INTEGRAL must also be compatible with a launch on an Ariane 5 as an alternative.

This paper discusses the design of the AOCS for the two missions, describing both the common features, and the mission specific aspects. The basic concept draws on the heritage of the successful Hipparcos and SOHO programmes, but design drivers associated with the XMM mission lead to a more complex design. Solar illumination of the payload elements is a potentially mission-terminating event, and avoidance of this has strongly influenced the failure detection and correction philosophy.

Minimisation of rate sensor usage to ensure compliance with unit lifetime capability has also been a concern which has been given particular attention in developing the subsystem architecture. The extreme inertial characteristics of the X ray telescope payload and its more demanding pointing requirements in comparison with Integral have in most cases made the XMM mission the more challenging to the AOCS designer.

The paper describes the baseline equipment selection as well as the control system analysis work currently being undertaken. Subsystem budgets and some typical results from the XMM Phase C/D analysis campaign are presented.

1. INTRODUCTION

To provide a coherent long-term structure to its science programmes, the European Space Agency developed the Horizon 2000 concept, which comprises 4 major 'cornerstone' missions, beginning with SOHO/Cluster, together with a series of Medium missions. These latter, of which Huygens is the first, require a budget about half that of the cornerstones.

The second cornerstone was selected to be XMM, which will be launched on a dedicated Ariane 5 in 1999. Parallel phase A studies in 1992 of candidate Medium missions called PRISMA (a stellar seismology mission) and INTEGRAL (a gamma ray observatory) focused on re-using the XMM service module for the second medium mission. In both cases, the feasibility of this cost saving measure was demonstrated. In combination with the use of a Proton launch vehicle as part of a collaborative deal with the CIS, INTEGRAL was ultimately selected as the M2 mission.

Following a competitive tender, Dornier was selected as the Prime contractor for XMM, while Alenia was awarded the prime contract for INTEGRAL. Within the industrial team, the key importance of the attitude and orbit control subsystems lead to subcontracts being placed with MMS (Bristol) for the design and development of these elements of the spacecraft.

The MMS team at Bristol have been involved in the AOCS work on most previous ESA science missions, including GEOS, Ulysses, Hipparcos and SOHO. However, XMM and INTEGRAL represent major new technical and programmatic challenges.

2. THE XMM MISSION

XMM will be launched into a highly elliptical orbit with an apogee of 114 000 km above the Earth, and a perigee height of 242 km. The on-board hydrazine reaction control system (RCS) will raise the perigee to 7000km altitude, giving a 48 hour period. For radiation reasons, a 70 degree inclination is selected (apogee in the North) with Redu as the single ground station. Science operations are restricted to times above 40000km (again, as a result of radiation constraints), but this still allows 40 hours operation per orbit.

Proceedings Third International Conference on Spacecraft Guidance, Navigation and Control Systems, ESTEC, Noordwijk, The Netherlands, 26-29 November 1996, ESA SP-381 (February 1997)

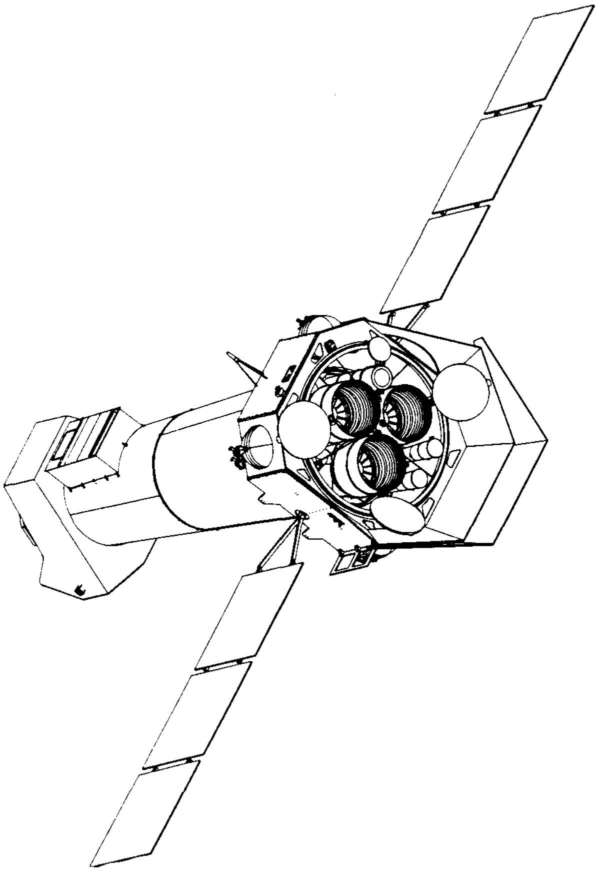

Figure 1: The XMM Spacecraft

Figure 1 shows the XMM spacecraft, whose layout is dominated by the 7m long carbon-fibre telescope tube. This connects the 1800 kg mirror support platform (MSP) from the 500kg focal plane assembly, where the detector instruments are mounted. The MSP supports three monolithic nickel x-ray grazing incidence mirror modules, an Optical Monitor instrument, plus the 2 star trackers of the AOCS. At launch, the payload units are protected by deployable doors. The solar arrays are of the 'deploy and fix' type. Thus, the spacecraft yaw axis is essentially sun-pointing, with slewing about this axis permitting complete sky-coverage over time.

Launch mass is 3900kg including contingencies and 485kg of fuel, making XMM larger than any previous ESA science spacecraft.

3. AOCS DESIGN DRIVERS

The AOCS for XMM must provide control for the spacecraft at all times following separation from the spacecraft, including:

- initial sun acquisition (ISA)
- before and after solar array deployment (SAD)
- perigee raising burns (Thruster Control Mode-TCM)
- slewing for scientific observations and prior and post thruster burns
- inertial pointing

Further, the need for tolerance to one failure in any part of the subsystem gives rise to a separate safe mode detection and control system. However, autonomous recovery following safe-mode entry is not required: the intervention of the ground station can be assumed.

The pointing requirements of the XMM payload are devolved into various elements, of which the requirements on the AOCS are only part. In particular, the thermo-elastic distortion of the telescope tube has been the subject of extensive study since Phase A. In order to ensure a rapid and uniform desorption of moisture from the tube, an unusual requirement of the AOCS is to permit a roll about the long axis at 180°/hour (Outgassing Manoeuvre Mode - OGM).

The AOCS level pointing requirements are summarised in Figure 2. Although the requirements are demanding, they are not as extreme as for previous MMS-built systems such as SOHO, where a very high performance sun sensor was needed to give sub-arc second pointing stability. However, other design drivers make the overall sub-system design much more challenging than SOHO.

Event	APE	AMA	Sun aspect angle
Sun acquisition	5°/5°/NA	NA	0°
3 axis acquisition	30'/30'/30'	30'/30'/30'	0°
slew manoeuvres	NA	50'/4'/4' for 20°/h	<± 20° (<± 40° for orbit raising)
delta-V	90'/15'/15'	30'/15'/15'	<± 20° (<± 40° for orbit raising)
stand-by	30'/30'/30'	30'/30'/30'	<± 20°
outgassing	60'/30'/30'	60'/30'/30'	<± 180° in YZ plane
safe attitude	8°/5°/NA	NA	0° except in eclipse

Note - values are in order X/Y/Z at 95% confidence

For fine pointing:

Axis	X	Y	Z
RPE (2 min)	2'	3"	3"
goals for 10s	2'	0.2"	0.2"

Figure 2: XMM Pointing Requirements

The spacecraft has a 3 day autonomy requirement (ground station outage). Because of the frequent slewing, combined with an extended design life of 10.25 years, reaction wheels are the primary actuator. This means that periodic off-loading via the RCS is needed. In fact, the spacecraft layout, inertial characteristics and orbit parameters give rise to substantial disturbance torques. Despite the use of large, 40Nms, reaction-wheels, off-loading is necessary on average twice per orbit (pre- and post perigee passage). Thus, although wheel off-loading is normally under ground supervision, a capability for autonomous wheel off-loading is also needed.

Although eclipses are of short duration (1.5 hours maximum) in comparison with the orbit period, the AOCS must accommodate their occurrence, including a failure during this period. The design of the AOCS is, however substantially complicated by two further constraints.

First, the FPA detectors are CCD based devices of extreme sensitivity. Exposure to direct sunlight could irreparably harm them. Thus, not only must the AOCS have a safe mode, it must be one which ensures that certain attitudes cannot occur, including the case where the failure has occurred in eclipse, but emergence into sunlight is imminent.

Second, several ESA spacecraft over recent years have suffered various forms of gyro failure (mechanical and electronic). Classically, gyros are used to provide rate signals in combination with absolute optical sensors (for example when slewing) or where a sun reference is not available for simple sun acquisition sensors to be used (e.g. in a failure detection/recovery mode). However, the problems with gyros have led to investigations into alternative approaches (e.g. the 1994 GMV/MMS study for ESTEC), and a general trend to reduce reliance on these devices. As the XMM mission necessarily demands very frequent slews, it was evident that reliance on gyros for the operational mission phases was to be avoided if possible.

4. OPTIONS STUDIED

For these reasons, a preliminary concept for the AOCS was established at the outset of Phase B which minimised the use of mechanical gyros. Within this concept, a number of options were considered:

1. for slews, the possibility of controlling on the sun (Z axis) and either 'star-hopping' on the yaw axis, or driving the yaw axes open loop using feed-forward momentum demands to the reaction wheels;
2. for safe mode in eclipse, the possibility of minimising gyro use by employing an Earth Centre Detector (ECD), or by spinning-up the spacecraft about the yaw axis to gyroscopically stabilise it;
3. for the outgassing manoeuvre, the possible use of the star tracker to derive 3 axis information by monitoring two well separated stars;
4. the use of low cost solid state Quartz Rate Sensors.

Although some of these solutions were in principle feasible, their complexity, equipment procurement problems or the impossibility of proving their performance led to the rejection of options 2,3 and 4. For the slew manoeuvres, the use of open loop slewing was selected. To minimise gyro usage then, the compromise solution was for almost all nominal operations (fine pointing, slewing, perigee raising and orbit maintenance) to not use gyros. However, operations in eclipse, pre-operational phases and following entry to safe mode *are* permitted to use gyros.

5. SUBSYSTEM CONCEPT

Figure 3 shows the AOCS configuration which has evolved. It comprises three distinct electronic units and a number of sensors and actuators.

For normal operations, prime and redundant high

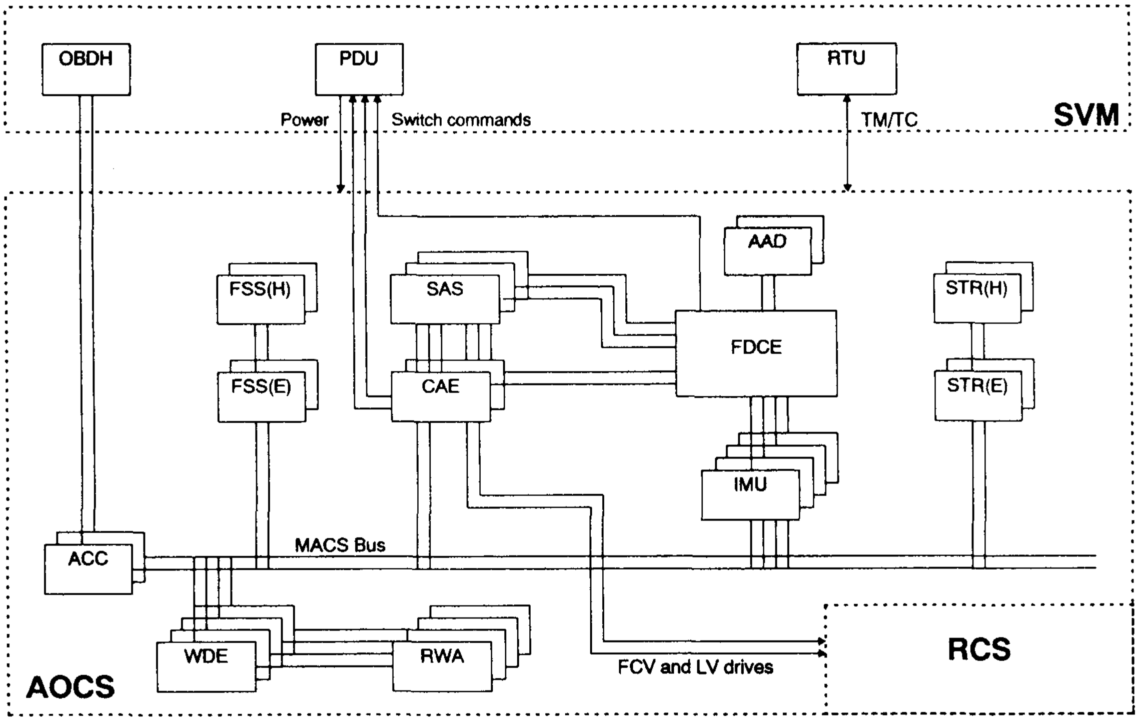

Figure 3: AOCS Block Diagram

accuracy star trackers (3°×4° FOV) are used for the Y and Z axis attitude measurement. The star trackers each use a microprocessor for switching and implementation of eight operational modes.

A digital fine sun sensor provides X and Y axis data, although only the X axis data is needed in the high accuracy science mode, for momentum dumping or in delta-V manoeuvres.

For initial acquisition and control in sunlit failure cases, analogue sun acquisition sensors (SASs) are used. SAS 1 is used for pitch and roll control in ISA, while SAS2/3 are used for failure recovery from any initial attitude prior to opening of the telescope doors. After ISA, SAS1 is also used for failure detection (roll/pitch).

Driven by the sun exclusion constraints, two optimised attitude anomaly detectors (wide and narrow FOV) within a single unit (the AAD) are used to signal pitch and roll axis anomalies.

Four two-axis dry tuned gyros provide rate sensing:

- in yaw, during ISA
- in roll for OGM and eclipse
- in roll, pitch and yaw for the ESAM (Emergency Safe Attitude Mode)
- for detection of 3 axis anomalous rates and attitudes *only* during non-nominal operations.

At the heart of the subsystem is the attitude control computer (ACC). This interfaces with the sensors and actuators via a MACS bus, and via the OBDH bus to the On Board Data Handling Subsystem. The ACC comprises fully redundant A and B halves within a common box. Each has a CPU core, DC/DC converters and the bus interfaces. The CPU is a MA31750 9 MHz microprocessor, providing 32k words ROM and 64k words RAM.

To interface with the analogue sun acquisition sensors, to provide control signals to the RCS and to power the analogue failure detection and correction electronics (FDCE), a separate Control and Actuation Electronics (CAE) unit is used. Again comprising redundant A and B branches, this is controlled via the MACS bus by the ACC.

The FDCE follows practice on previous MMS Bristol subsystems in comprising two functional modules. The failure detection electronics (FDE) monitors the failure criteria, each of which can be enabled or disabled independently. Should any of the monitored parameters exceed safe limits, the FDE signals the failure correction electronics (FCE) to initiate entry into the ESAM. In fact, ESAM comprises several sub-modes, depending on whether the failure is in sunlight or eclipse, and on how large the initial mis-pointing is. For sunlight conditions the SASs and gyros are used for initial rate reduction, followed by sun acquisition and yaw rate control. In eclipse the gyros alone are used to freeze the yaw axis attitude, and control rates about it.

The FDCE thus interfaces with those sensors and actuators used to detect failures and initiate ESAM (gyros, SASs, AAD and the RCS). As activation of the FDCE implies that a failure has already occurred, it is itself not redundant. However, the use of hard wired electronics provides a low risk, robust design solution.

The primary actuators are four ball-bearing reaction wheels, each providing up to 40 Nms storage and 0.2 Nm torque and driven by separate wheel drive electronics. Mounted in a tetrahedral layout, one wheel is held in cold redundancy to cope with a failure in any other unit.

The monopropellant RCS (the responsibility of BPD of Italy) provides orbit raising, orbit maintenance and attitude control functions using two sets of four thrusters. Each has a nominal thrust of 20N, but operate in a blow-down modes, giving delivered thrusts varying from 25N (BOL) to 6N (EOL).

Figure 4 provides a summary of the unit suppliers and the mass budget of the subsystem.

Unit	Supplier	Total Mass
ACC (1 off)	CRISA (E)	5.4 kg
CAE (1 off)	TERMA (DK)	7.6 kg
FDCE (1 off)	MMS (UK)	6.9 kg
Star trackers including electronics and baffle (2 off)	Officine Galileo (I)	22.2 kg
Fine Sun Sensors including electronics and thermal baffle (2 off)	Adcole (USA)	4.9 kg
AAD (1 off)	TPD (NL)	0.2 kg
SASs & baffle (3 off)	TPD (NL)	0.7 kg
gyro packages including mounting plates	SAGEM (F)	13.1 kg
reaction wheels including electronics and brackets (4 off)	MMS (UK)	41.0 kg

102 kg total

Figure 4: Subsystem Unit Data

6. ANALYSIS AND VERIFICATION

The fundamental operation of the digital controllers and sensors is at 2Hz, above the solar array flexure frequencies. Classical phase advance algorithms are used, implemented in difference equation form. Steady state errors are removed by integrators in wheel based modes.

As part of the design process, an extensive analysis campaign is under way. The purpose of the activity is to verify the performance of the various control modes against requirements, in the presence of worst case equipment imperfections and mode initial conditions.

Preliminary linear analysis of the controllers was undertaken using proprietary design tools, but the primary verification tool is an in-house developed simulator which allows non-linearities, mode switching and other detailed features to be correctly modelled. This simulator draws upon methods used in the SOHO project. Preparatory analysis is undertaken to identify worst cases to be investigated in simulation runs.

As an example, Figure 5 shows the roll, pitch and yaw angles resulting from the simulation of an eigenaxis slew. The net motion is equivalent to a 90° slew about the yaw axis followed by 40° about pitch. The slew rate is 90°/hr. Sensor quantisation and noise, wheel quantisation and friction, fuel slosh and array flexure are all modelled. To avoid excitation of fuel slosh , a sinusoidal acceleration profile is used, with a period three times that of the main slosh mode. At the completion of the slew, a star is visible in the field of view of the star tracker, allowing closed loop control to be regained.

To test the real hardware, and compare its performance with the simulation results, a dedicated test environment has been created, which will allow representative testing of the AOCS units and their interfaces. This AOCS Electrical Ground Support Environment (EGSE) will also be incorporated into the spacecraft level EGSE, to support system level testing by the prime contractor.

The AOCS EGSE is based on the ESA/NLR Test and Verification Equipment and is a deliverable assembly from the Dutch subcontractor. When combined with real sensor and electronic units, it will permit closed loop testing of the complete subsystem prior to delivery. Optical and inertial sensors will be electronically stimulated for closed loop tests, although open loop sign checks will involve optical or mechanical stimulation. As dynamic testing (for example on a motion rig) is neither practical nor cost-effective, the spacecraft response to actuator signals is simulated using a sub-set of the AOCS performance verification software, which is hosted within the AOCS test environment computer.

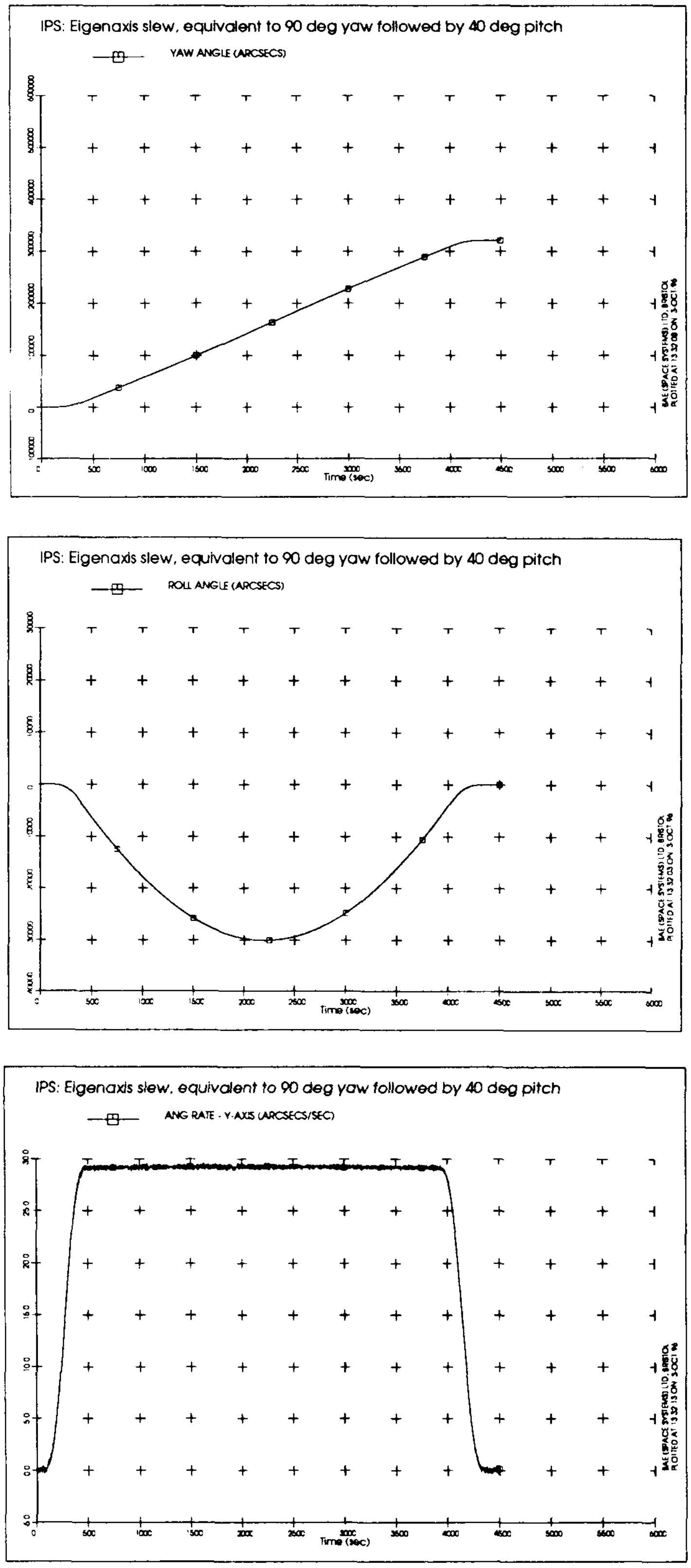

Figure 5: Large Angle Slew Manoeuvre

7. PROGRAMMATICS AND STATUS

Phase C/D (development and test) of the XMM programme began in March 1996 against a target delivery date of an Engineering Model (EM) subsystem (including all the electronic units and most of the sensors and actuators) in mid 1997, and delivery of the flight subsystem by early 1998. In comparison with previous programmes such as SOHO this represents a substantial schedule reduction for the design and development of a completely new AOCS. At present, the EM test set is beginning integration, with several key units already delivered to MMS.

8. INTEGRAL

As a follow-on project to XMM, INTEGRAL (Figure 6) is intended to maximise the re-use of subsystem units and design methods from the Cornerstone mission. However, many of the AOCS requirements are payload driven and INTEGRAL has to be designed to cope with two different launch vehicles and two different operational orbits. Thus the AOCS design and simulation activities have to be carried out separately from XMM to the same level of detail, even though the same sensors, actuators and electronic units are employed in the actual subsystem.

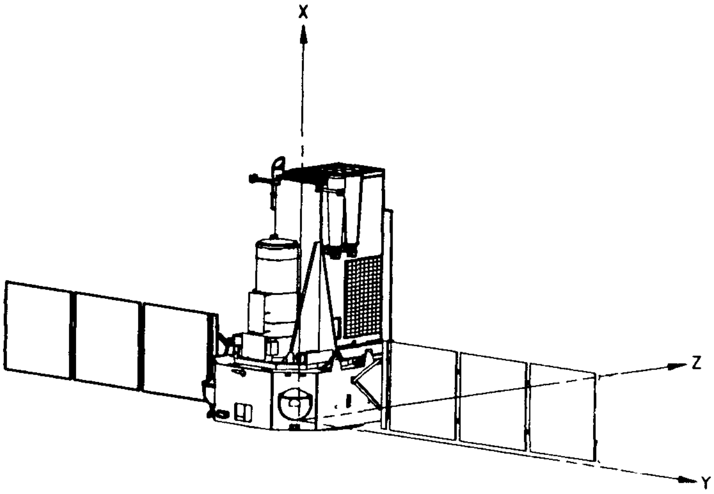

Figure 6: INTEGRAL

Some of the pointing requirements (Figure 7) are more relaxed than XMM, but slewing requirements are more demanding. The operational lifetime for sizing of consumables is 5 years. However, in comparison with XMM, the INTEGRAL spacecraft is more compact, so that although the launch mass is 3600kg, the inertial characteristics are quite different. For reasons of minimisation of plume impingement, the orientation of the thrusters is reversed with respect to XMM, and a different failure detection and correction logic is being considered.

Despite the changes, the contracted price of the Integral AOCS is about half that of XMM.

Event	APE	AMA	Sun aspect angle
Sun acquisition	7.5°./7.5°/NA	NA	0°
3 axis acquisition	45'/45'/45'	45'/45'/45'	0°
slew manoeuvres	NA	4.5'/1.5'/ 1.5'	<± 40° ± 5° for roll
delta-V	7.5°/7.5°/2.25°	45'/22.5'/22.5'	<± 40° ± 5° for roll
fine inertial pointing	15'/5'/15'	3'/1'/1'	<± 40° in YZ plane
safe attitude	5°/5°/NA	NA	0° except in eclipse

Note - values are in order X/Y/Z at 95% confidence

For fine pointing mode:

Axis	X	Y	Z
RPE (1000s)	1'	0.3'	0.3'

Figure 7: INTEGRAL Pointing Requirements

9. CONCLUSIONS AND OUTLOOK

XMM and INTEGRAL represent a further extension of the MMS-UK experience with high performance science mission attitude control systems. In the future it is hoped to report more fully on the progress of the AOCS development programme, including the advanced test environment which has been developed with NLR, and also on the unique features of INTEGRAL.

Looking to the future, next generation astronomy missions such as FIRST (Far-Infra Red Sub-millimetre Telescope) will combine the ultra high performance pointing characteristics of SOHO with the orbit and slewing features of XMM. MMS is studying the use of more advanced AOCS sensors and architectures which will give spacecraft such as FIRST the required low noise payload environment, while reducing subsystem complexity and lowering ground station costs through greater autonomy.

ACKNOWLEDGEMENTS

The authors are pleased to acknowledge the contributions to this paper of the entire XMM and Integral AOCS teams.

THE GN&C DESIGN OF THE NEW EARTH OBSERVING SYSTEM COMMON SPACECRAFT

Thomas P. Nosek

TRW Civil and International Systems Division
Redondo Beach, CA
Phone 310-813-3634 Fax 310-812-0513
e-mail tom.nosek@trw.com

ABSTRACT

The new Earth Observing System (EOS) common spacecraft is designed to serve as a common bus for the EOS mission payload complements - the PM, AM, and Chemistry missions. EOS missions view the Earth from sun-synchronous, 705 km altitude, near polar orbits; each of the three missions carries a different complement of instruments which collect a wide variety of information on the Earth's atmosphere, oceans, and climate.

The spacecraft must accommodate potential instrument design, or even instrument complement, changes during the life of the program without requiring significant design change in the spacecraft itself. The EOS GN&C system primary requirements stem from the variety of instruments carried, each of which has distinct requirements for pointing accuracy, pointing knowledge, and for pointing stability over a variety of time intervals. The payload instruments also contribute significant torque disturbances which strongly influence pointing performance of the whole spacecraft. The design of the GN&C system considered spacecraft flexibility, mounting accuracy and measurement of the instruments, and the influence of spacecraft disturbances such as reaction wheels and antenna slews. The design meets all of the instrument requirements. Attitude control is provided by reaction wheels, with excess momentum dumped through magnetic torque rods. Attitude determination is stellar inertial. Navigation is provided by on-board propagation of ground-based state vectors. Safe and survival modes complement the fine pointing and delta-V modes used in normal operation.

1. INTRODUCTION

The EOS program features three satellite mission payloads - the PM, AM, and Chemistry missions instrument complements - designed to provide a comprehensive set of measurements on the Earth's environment. Satellites will be launched at 6 year intervals, providing very large sets of data for study by environmental scientists. The design of the first of the series (AM 1) was done by GE (now part of Lockheed Martin); this Atlas-launched satellite is scheduled for launch in 1998. Following the award for that satellite, NASA elected to request a design which could be launched on a medium size booster - the Delta launcher was selected. A Delta launch required a reduction in size of the satellite and innovative approaches to instrument packaging and deployment.. A further requirement was that the satellite bus be common in design for all three EOS missions - that is, a common structure and essentially common subsystems, with flexibility to accommodate different instruments with different performance requirements.

TRW was awarded the contract for the EOS common bus in 1995, for the PM 1, Chemistry, and AM 2 missions. The first launch (PM 1) is scheduled for December, 2000. The program has gone through a System Configuration Audit, and will have Preliminary Design Review in April, 1997. Figure 1 shows the common bus configured for the PM mission. There is substantial international content in the spacecraft, including reaction wheels supplied by a German company and the solar array from Fokker Space in the Netherlands.

The GN&C subsystem is fully common to all three missions, in spite of the fact that each of the missions has a different instrument payload (and hence instrument torque disturbances) and different point pointing accuracy, knowledge, and stability requirements. The GN&C design features stellar-inertial attitude determination, backed up by earth sensors for maintenance of attitude in safe modes. Momentum control and spacecraft pointing is provided by four reaction wheels; magnetic unloading through torque rods limits buildup of momentum in the reaction wheels. The hydrazine reaction control system is used during initial injection to complete the orbit

Proceedings Third International Conference on Spacecraft Guidance, Navigation and Control Systems, ESTEC, Noordwijk, The Netherlands, 26-29 November 1996, ESA SP-381 (February 1997)

period and inclination control, and the GN&C system provides control of the reaction jets to maintain stability during this phase of flight. Ephemeris determination onboard is provided by propagation of ground-determined orbit state, which is periodically uplinked to the spacecraft.

The GN&C design was constrained to cost targets, and emphasized low risk through use of flight proven components. Modelling techniques were employed to determine the contributions of structural deformation, instrument mounting flexibility, and control system operation to overall instrument pointing performance. Control design parameters were varied to reach a design with sufficient stability and performance over the entire range of mass properties associated with the three mission configurations. This commonality feature is a key element of the EOS program, but requires careful analysis of all three mission configurations to verify that a common design can meet all three sets of requirements. Since the GN&C subsystem is processor-controlled, a reliable fault management approach is necessary: the design includes techniques to verify processor performance, sensor performance, attitude accuracy and stability, and to make a safe fail-over to backup units in the event of an anomaly.

Fault detection and management software protects spacecraft health and safety; redundant components make the design operable against single faults, with ground commanded reconfiguration. Each of the on-board processors (there are a total of four) has a backup and are linked by a 1553 data bus. 1553 sub-busses connect the processors to sensors and actuators; the GN&C processor runs all attitude control functions.

2. GN&C REQUIREMENTS

Although all three EOS missions are in the same orbit, the payload instruments differ; hence, the GN&C pointing accuracy and knowledge requirements differ significantly by spacecraft. The instruments have a widely varying range of disturbances, which complicate the job of designing a common attitude control and pointing design. A requirement in the subsystem design was to achieve commonality in design for all three missions in hardware, and as far as possible, in software.

The GN&C subsystem maintains the spacecraft in a three axis stabilized, zero-momentum, earth pointing orientation during the normal science mode. Additional modes to perform delta-V orbit adjust maneuvers, calibration maneuvers, and safe and survival states are provided.

Significant portions of the instrument pointing accuracy and knowledge requirements are allocated to mounting of the instruments on the spacecraft (and measuring the alignment after mounting) with the remaining pointing allocated to GN&C and structural deformation in orbit (primarily due to thermal effects). With these factors considered, the pointing allocations to GN&C were divided into frequency ranges of bias, or very low frequency, drift, and jitter as follows (in arc seconds):

Frequency Range	Accuracy	Knowledge
Bias	18	17
Drift	35	24
Jitter	3	3

To determine pointing in an earth-fixed frame, and to index the location of the instrument fields of view on the ground, a navigation accuracy requirement of 500 meters is imposed.

The GN&C subsystem is additionally responsible for pointing the solar array to the Sun, and pointing the medium gain antenna to a selected TDRS spacecraft for communication with the ground. The ephemerides of four TDRS spacecraft are carried on board, and with the knowledge of spacecraft position and attitude, the proper pointing commands to TDRS are computed and used to control the bi-axis gimbal at the base of the antenna. A safe mode and a survival mode are required to preserve the spacecraft during any anomalies, either in the GN&C subsystem itself or in other areas. Finally, the GN&C subsystem must maintain control during firing of the hydrazine engines used for orbit adjustment.

The design challenge was to meet all mission requirements simultaneously with the same basic GN&C subsystem design, while achieving adequate margin to protect against surprises in the instrument disturbance magnitudes or frequency content. Further design goals of low weight and low cost, coupled with use of flight proven components added to the mix of requirements.

3. GN&C SUBSYSTEM DESIGN

The GN&C subsystem design (Figure 2) used flight proven equipment where possible, integrated into a subsystem architecture based on the TRW Advanced Bus development program. The Advanced Bus program had built up an avionics test laboratory with engineering models of the electronics units, and the subsystem designers capitalized on the design work already performed.

Table I describes the primary GN&C modes of operation: after initial acquisition of the earth following separation from the launcher, the spacecraft will transition to the normal, fine point mode for science operations, where it will spend the bulk of its life in orbit. Periodic delta-V maneuvers to remove drag effects on the orbit, and to maintain inclination if required, are done in an inertial hold mode using the hydrazine thrusters. The earth mode acts as a transition between acquisition modes and fine pointing, and also serves as the safe mode if stellar-inertial reference is lost or suspect. If a significant anomaly threatens the power safety of the spacecraft, a sun pointing mode is the highest level of safety: the spacecraft points to the Sun with the solar array fixed for maximum electrical power.

The actuators and sensors communicate through a 1553 data bus with the ACS processor; the ACS processor communicates with three other processors (Figure 3) on a primary 1553 data bus. Each of the four processors is dual redundant; the Data Handling processor acts as the bus master. The ACS processor handles the attitude control and ACS safe mode control software. This was done to keep the spacecraft under positive attitude control even if data bus problems should interrupt communications with the master processor, or the master processor should fail and switch to its redundant unit. This design, which would put the spacecraft into safe mode in case of bus or master processor problems, would interrupt science operations to some extent (the attitude control accuracy in safe mode is not as good as in science mode) but would preserve the spacecraft in a local level attitude with safe operation of the power subsystem and the ACS subsystem. Recovery to normal science mode operation once the fault has been corrected will then be rapid and simple.

The primary sensors for accurate attitude determination are the two stellar trackers mounted on the spacecraft upper surface. The stellar trackers have an 8 x 8 degree field of view, can track up to 6 stars at one time, and provide one input to the spacecraft's attitude determination Kalman filter. The other input is from the inertial reference unit; a single unit, internally redundant uses four hemispherical resonance gyro. The attitude determination Kalman filter estimates spacecraft attitude and rate, plus gyro bias. An initial calibration on orbit which included the stellar tracker-to gyro axis alignment will be run to verify the alignment parameters which may have been subject to shifts across launch.

With an update rate of once per 30 seconds, the estimated attitude determination accuracy at the stellar inertial reference base is 5.3 arc seconds. However, transferring this attitude knowledge to the base of each instrument involves calculation of the structure rigidity, structural motion due to disturbances, and the alignment of each instrument on the spacecraft (in addition to shifts through the launch environment and on-orbit thermal effects. All of these factors were estimated to reach the final pointing budget for each instrument.

Analysis of the spacecraft body thermal and bending effects show that the attitude knowledge at the base of each instrument is better than 60 arc seconds throughout the mission.

4. TESTING AND SIMULATION PLANS

The Software Development & Validation Facility (SDVF) Figure 4) is an engineering model testbed which includes both hardware and software to accurately emulate the onboard spacecraft environment. The SDVF provides a complete software development environment. In the SDVF, the GN&C subsystem electronic units are tested in concert with the flight software and the other elements of the spacecraft avionics subsystems.. GN&C sensors and actuators will, in general, be represented by simulators: the GN&C avionics units such as the Valve Drive Electronics and Wheel Drive Electronics will be actual engineering models. Operation of the GN&C subsystem will be tested, including operation during anomaly modes and simulated equipment failures, to verify the operation of all of the GN&C modes and interaction with the other elements of the spacecraft.

5. GN&C PERFORMANCE

The attitude control system performance was evaluated through simulation. Figure 5 shows the performance of the attitude control design over a time interval of about 5.5 hours: the goal of 25 arc seconds in pitch and yaw and 10 arc seconds in roll, is met satisfactorily. Figure 6 illustrates a typical speed profile of one of the four reaction wheels while maintaining the fine point mode.

Navigation requirements are set by the need to determine position for transformation of instrument pointing lines of sight into earth fixed coordinates. The 500 meter accuracy, principally intrack, introduces about 15 arc seconds of uncertainty into the coordinate transformation to the earth fixed frame. Designers considered various approaches to on-board navigation; the current design uses an on-board propagated state vector initialized by a ground uplinked state based on periodic tracking through the TDRS data relay satellites.

6. CONCLUSION

The GN&C design of the Earth Observing Spacecraft satisfies all of the separate instrument requirements for pointing accuracy and knowledge using a set of actuators and sensors common to all three instrument complements in the EOS program. Redundancy in key components yields a 6 year life reliability of approximately 0.98 and secure safe and survival modes protect the spacecraft in event of anomalies within GN&C or in other subsystems. The launch of the first spacecraft in the series, PM 1, will occur in December, 2000, providing scientists with a comprehensive data set on the Earth's environment at the start of the 21st century.

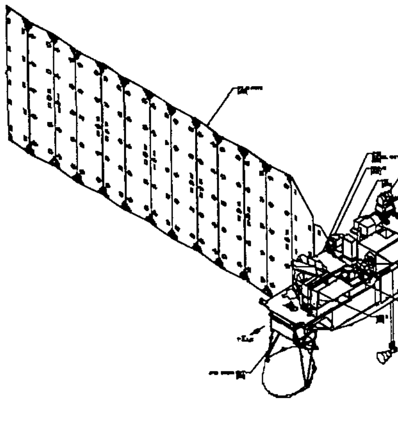

Figure 1

The EOS Common Spacecraft

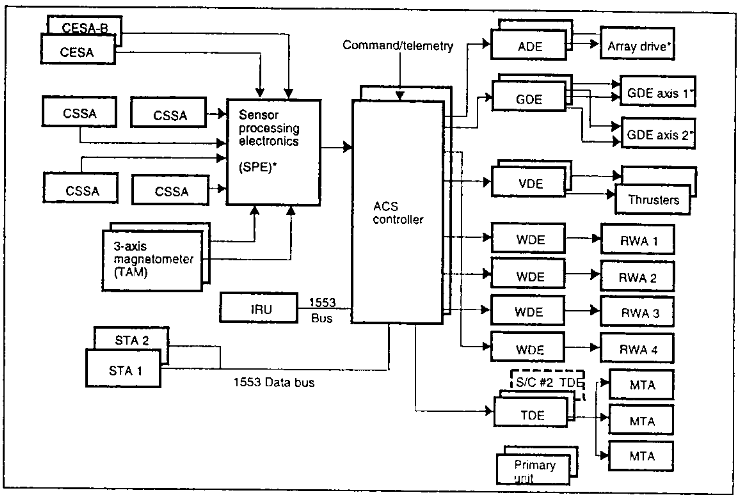

Figure 1.7-2. GN&C Block Diagram

Figure 2

Mode	Function	Implementation
Fine point (Normal)	Precision earth pointing for science operations	Stellar-inertial attitude determination reaction wheel control with magnetic unloading
Inertial hold (Delta V)	Attitude hold during ΔV for maneuver and post-deployment	IRU attitude reference thruster attitude control
Earth Mode	Earth-referenced attitude for safe mode and test checkout and readiness for transition to normal mode	Earth sensor attitude reaction wheel/mag torquer unload
B-dot	Anomaly recovery mode from arbitrary attitudes if earth reference lost	Magnetometer measurement of earth's field, rate of change control law, torque rod control with reaction wheels
Sun-pointing	Survival mode-direct transition from normal mode or via earth mode if fault triggers activate. Assure power safety	Coarse sun sensors and reaction wheels with magnetic unloading. Continuous sun pointing with rotation around LOS to sun
Post-deployment sun acquisition	Thruster controlled post-deployment mode used if earth reference lost	Coarse sun sensors and thruster control for lost in space recovery at deployment. Subsequently disabled

Table 1 - GN&C Modes

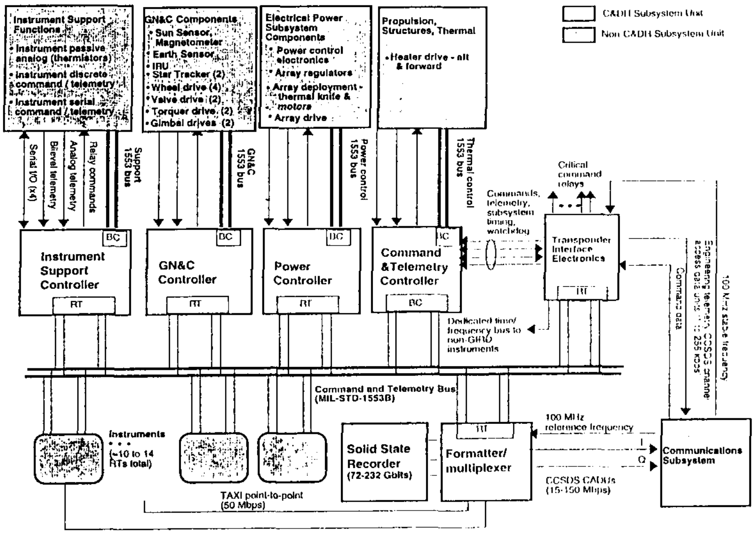
Instrument Support Functions
• Instrument passive analog (thermistors)
• Instrument discrete command / telemetry
• Instrument serial command / telemetry
GN&C Components
• Sun Sensor, Magnetometer
• Earth Sensor
• IRU
• Star Tracker (2)
• Wheel drive (4)
• Valve drive (2)
• Torquer drive (2)
• Gimbal drives (2)
Electrical Power Subsystem Components
• Power control electronics
• Array regulators
• Array deployment - thermal knife & motors
• Array drive
Propulsion, Structures, Thermal
• Heater drive - aft & forward
C&DH Subsystem Unit
Non C&DH Subsystem Unit
Serial I/O (x4)
Bilevel telemetry
Analog telemetry
Relay commands
Support 1553 bus
GN&C 1553 bus
Power control 1553 bus
Thermal control 1553 bus
BC
Instrument Support Controller
RT
GN&C Controller
Power Controller
Command &Telemetry Controller
Commands, telemetry, subsystem timing, watchdog
Critical command relays
Transponder Interface Electronics
Dedicated time/frequency bus to non-GIRD instruments
Command data
Engineering telemetry, CCSDS channel access data units 1 to 255 kbps
100 MHz stable frequency
Command and Telemetry Bus (MIL-STD-1553B)
Instruments
• • •
(~10 to 14 RTs total)
Solid State Recorder (72-232 Gbits)
Formatter/ multiplexer
100 MHz reference frequency
I
Q
CCSDS CADUs (15-150 Mbps)
Communications Subsystem
TAXI point-to-point (50 Mbps)

Figure 3

Data Bus and Processor Configuration

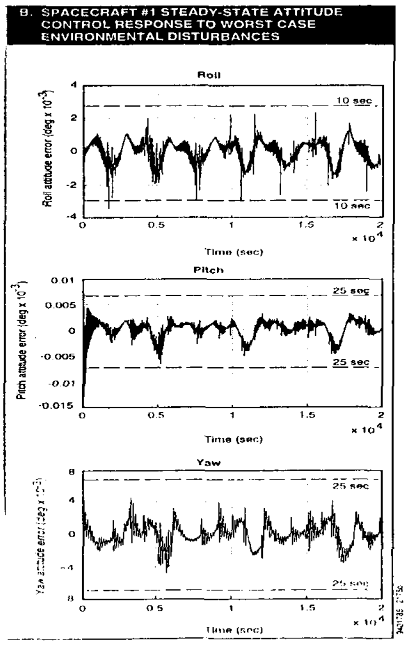

Figure 5 - Attitude
Control Accuracy

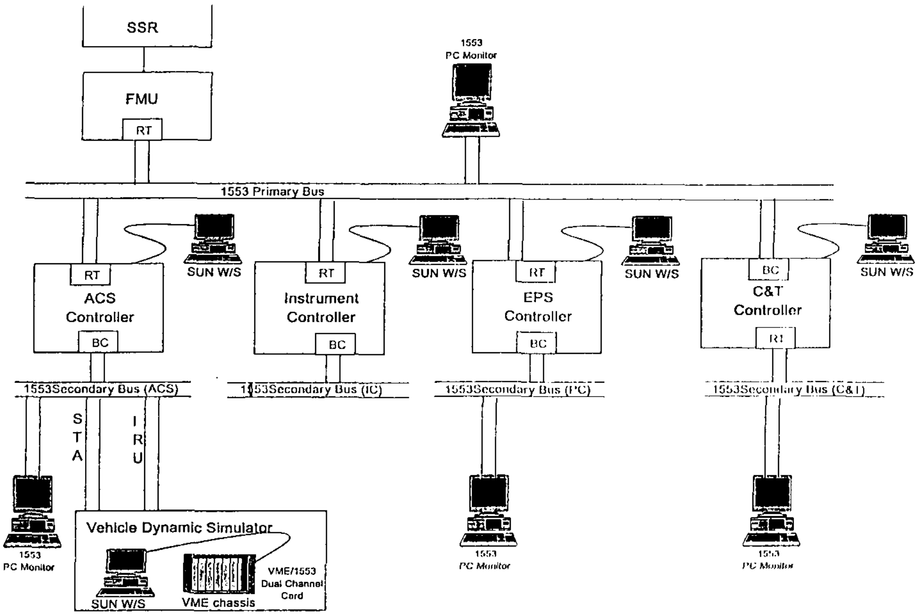
SSR
FMU
RT
1553 PC Monitor
1553 Primary Bus
SUN W/S
ACS Controller
BC
Instrument Controller
EPS Controller
C&T Controller
1553Secondary Bus (ACS)
1553Secondary Bus (IC)
1553Secondary Bus (PC)
1553Secondary Bus (C&T)
S T A
I R U
Vehicle Dynamic Simulator
VME chassis
VME/1553 Dual Channel Card

Figure 4

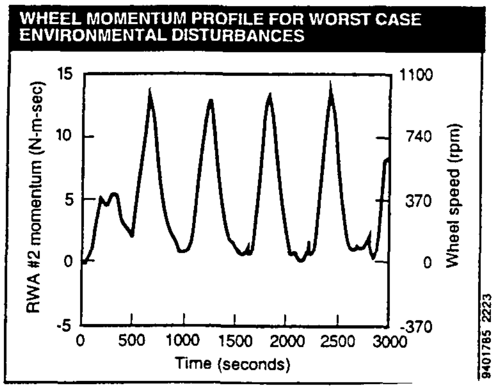

Figure 6 - Reaction Wheel
Speeds

ATTITUDE AND ORBIT CONTROL SYSTEM FOR MULTIMISSION SPACECRAFT PLATFORM

Michel SGHEDONI, Jean Luc BEAUPELLET, Jacques BUSSEUIL, Francis DOUILLET

AEROSPATIALE Espace et Défense, 100 boulevard du Midi, B.P. 99, 06322, Cannes La Bocca, FRANCE.
Phone: (33) 4.92.92.76.40., Fax: (33) 4.92.92.33.40.

ABSTRACT

The French generic satellite platform PROTEUS, initiated by CNES (French National Agency) is defined as a low cost small satellite, operating in low Earth orbit and able to perform various missions without major specific adaptations. The different types of missions considered are : inertial or Solar pointing, Earth, Anti-Earth Pointing or Nadir pointing.

AEROSPATIALE has been selected by CNES to lead the development of the PROTEUS platform.

After an overview of the key requirements, this paper describes the Attitude and Orbit Control System of the generic platform now developed. The System approach used by AEROSPATIALE has allowed to define an AOCS using the same equipment, the same on-board software and also the same control mode architecture for all specified missions. The AOCS is designed around the three key components: one star tracker, a 3 axes gyro package and a set of reaction wheels. Use of them in all AOCS modes (except one), allows to minimise their number. Only five modes are used: Star Acquisition Mode, Normal Operation Mode, Orbit Correction Mode with 4 thrusters for large ΔV maneuvers, Orbit Correction Mode with 2 thrusters for fine ΔV adjustments and Safe Hold Mode. The Safe Hold Mode (SHM) which maintains a Sun-pointing attitude, uses low authority sensors and actuators providing good robustness to the satellite system. In parallel of the PROTEUS program, AEROSPATIALE has already tested SHM on a 3 axes-table dynamic bench.

This paper also describes some aspects of the development logic taking into account the schedule and cost constraints of the PROTEUS program.

This AOCS design and also the whole platform system is well adapted to a large range of altitude and orbit inclinations. It also allows pointing performance independent of missions and orbital conditions.

1 - INTRODUCTION

End of 1995, the French national agency CNES (Centre National d'Etudes Spatiales), has issued a Request For Proposal (based on previous analyses performed during 1994) to the French space companies to define a 3-axes stabilised minisatellite platform. The name of the project is PROTEUS (Plate-forme Reconfigurable pour l'Observation, les Télécommunications Et les Utilisations Scientifiques).

This platform has to be easily adaptable to a large range of missions :

- missions with orbit altitude and inclination variables : 500 to 1400 km and inclination upper than 15°,
- missions requiring all the pointing possibilities : Earth pointing, inertial or solar pointing,
- missions with a great flexibility for launcher choice : all low orbit launchers in the range of 500 kg,
- missions requiring installation of different payloads.

A second aim of the project is to develop a low cost platform.

This paper describes the technical solution proposed by AEROSPATIALE for the Attitude and Orbit Control System (AOCS). It satisfies all the multimission requirements with a minimum of adaptation. Platform architectural choices keep a great simplicity for the concept, and using robust technologies guarantees a low cost for the global system.

2 - MISSIONS

The multimission platform PROTEUS is by definition compatible with a large range of low Earth orbit missions such as: Earth Observation, Telecommunication and Scientific missions. These missions can be classified in two groups with regard to the type of pointing accuracy they require: Earth, anti-Earth or Nadir pointing and inertial or solar pointing.

All these missions are on CNES responsibility and management (in particular arrangements in case of international cooperation).

The PROTEUS platform has to be compatible as close as possible with four main missions specified by CNES: JASON, COROT, SAMBA and TROPIQUES. These missions are the first four most probable missions that the French Space Agency has selected for the design of PROTEUS.

These missions are very different both in the payload and the orbital characteristics. These characteristics are given in the next table and a short description of each mission is presented hereinafter.

	JASON	COROT	SAMBA	TROPIQUES
altitude (km)	1336	600/900	820	1000
inclination (deg)	66	89/91	99	15
solar angle w.r.t. orbit plane	continuously evolving	continuously evolving	sun synchronous 90°	*in range* ± 38°
orbit correction required	yes	yes	no	no

Table 2-1 : Orbit characteristics

Proceedings Third International Conference on Spacecraft Guidance, Navigation and Control Systems, ESTEC, Noordwijk, The Netherlands, 26-29 November 1996, ESA SP-381 (February 1997)

JASON : The JASON mission main objective is to furnish high accurate altimeter measurements to continue the previous French-American Topex/Poseidon mission intended to study ocean motions and sea level variation. Understanding of ocean dynamics is very important to get knowledge of the Earth climate.

COROT: The COROT mission is stellar seismology study. From continuous observation during a long period of the intensity variation of radiance emitted by not mature stars, one can deduce characteristics of internal structure of these objects. A secondary objective is the observation of planet Jupiter. Accuracy of the three axes inertial pointing is demanding to separate target variations and control sensors errors.

SAMBA : The Astronomical SAMBA mission is the measurement of the 3 Kelvin black body radiance fluctuation. These observations will give information about density fluctuations of the early universe responsible for today's structures in the universe. A quasi-total coverage of the sky will be performed by an anti-Earth pointing payload. This mission uses a polar orbit.

TROPIQUES : The mission is not totally finalised today but the main scientific objective is the study of water variation and energy exchange in the atmosphere in the tropical latitude over several different time scales. For Earth pointing, this mission uses a quasi-equatorial orbit.

3 - AOCS REQUIREMENTS

Typical key requirements specified by CNES for PROTEUS' platform are resumed in the following table:

pointing accuracy attitude knowledge	pointing axis : 0.05° (3σ) around pointing axis : 0.15° (3σ)
pointing bias	< 0.05° (3σ) all axis
pointing stability	7e-4°/s (3σ) in 0-1Hz band

Table 3-1 : Normal Mission Mode accuracy

Several major constraints had to be considered for the AOCS design :

- no use of propulsion in survival mode,
- to design a system compatible with a large range of orbit inclinations, in particular quasi-equatorial orbits,
- to avoid (except in transient motions) crossing of sensitive payload line of sight and Sun line direction,
- In Normal Mission Mode, AOCS has to accept an evolutionary attitude bias lower than 10° to point to Nadir, to follow a ground trace or to point to Earth poles,
- Large angle maneuvers (180°) have to be realised in less than 10 minutes.
- the required reliability of all these missions are not the same: for instance a high level is required for JASON and a lower for the other missions. This constraints all the satellite system and especially the choices for AOCS.

4 - CONTROL ARCHITECTURE

Mission pointing applications drive the sensor suite to ensure adequate information to the controller in order to maintain pointing requirements. Earth pointing missions could make use of earth sensors and sun sensors while stellar and inertial missions would be better served with star trackers. All LEO applications may be accommodated by GPS attitude determination however GPS attitude determination developed knowledge is limited.

Trade issues and system considerations led to our proposed PROTEUS sensor definition. The objective was to develop a sensor configuration which was capable of satisfying all mission applications with minimal change between missions, within defined cost constraints and with a potential for future evolution to maintain or increase performance at reduced cost.

To accommodate the broad range of missions, a zero-momentum three axis stable control architecture was selected. In this architecture, actuation is performed by reaction wheels with magnetic momentum management. As a consequence, all types of pointing are possible :

- inertial pointing,
- Earth pointing,
- Nadir pointing with or without yaw steering maneuver.

Any required orbit maneuvers are performed by hydrazine thrusters. With this selection of controller, sensors which provide attitude information for spinning satellites were rejected. Attitude sensing in this controller could be either mission specific, using sensors related to the mission purpose, or generic for all missions. Our objective was to maintain the same sensor suite over the complete mission set, if possible.

Three type of sensor architectures were evaluated :

- Earth sensor, Sun sensor, gyro;
- Star trackers, gyros;
- GPS, gyros.

The conclusions of our trade study are:

- The controller architecture which best supports the mission set is a stellar inertial design,
- The Earth sensor/Sun sensor option does not provide accuracy and ease of operation for the total mission set,
- The GPS solution for attitude determination is not mature enough at this time but may provide an alternative for future missions,

The star tracker solution was selected as the attitude determination sensor because it provides the best performance and cost approach at this time.

From system considerations not developed in this paper, our 3-axes stabilized platform uses a two solar array architecture and a four hydrazine thruster concept for the orbit correction. With a total mass (including payload) of 500kg, our platform has main inertia close to 270, 200, 400 Kg.m^2.

The spacecraft axes (Xs, Ys, Zs) are such that Xs is the launcher axis and generally the payload (antenna, telescope, altimeter...) axis, Ys the solar array axis.

5 - EQUIPMENT

Our PROTEUS design uses a stellar inertial controller with control algorithms based on quaternion feedback. The design approach and the components were selected to accommodate multiple mission scenarios with minimal change to either the control hardware or software. Except in the survival mode, the key components in this design are the gyro and the star tracker.

On the first mission spacecraft, a GPS receiver for attitude determination purpose will be used on-board as an experiment.

In table 5-1 is provided a summary of the components with typical performance and development/qualification status after the first step of selection. A brief description of the application for the components follows.

Component	Performance Parameters	Heritage
Gyro (GYR)	- SF: 0.05 arc-sec/bit - fine range: 2 ^{o}/sec - bias stability: 0.1 ^{o}/hr - SF stability: 1000 ppm	flown
Star Tracker (STR)	- accuracy: 15 arc-sec (3σ) - range: 0.6 ^{o}/sec - magnitude: 2 - 7 - FOV: 22 ^{o} x 18 ^{o}	being qualified
Coarse Sun Sensor (CSS)	- output: analog - coverage: 4 p - accuracy: 3 ^{o} plus albedo	flown
Magnetometer (MAG)	- range: 1 gauss - output: analog - sensitivity: < 4 mgauss	being qualified
Reaction Wheels System (RWS)	- torque: 0.075 Nm - momentum: 8 Nms - digital tachometer	flight qualified
Magnetic Torquer Bars (MTB)	- linear dipole: 60 Am^2 - residual: 0.7 Am^2	flown
Thrusters (THU)	- force: 1 N - fuel: hydrazine	flight qualified
Processor (PRO)	- 1 MIPS DIAS - RAM: 256 Kbytes - ROM: 64 Kybtes	new design
GPS	- att. det.: 0.3° (3σ) - position: 100 m - velocity: 2.5 m/sec	in development

Table 5-1: ADACS Components

Gyro : The baseline gyro consists of three two-axes gyros and electronics. This gyro technology has extensive flight experience by many vendors. Due to the significant utilization throughout the PROTEUS control modes, a fully redundant implementation was selected. Gyros are mounted in an orthogonal configuration on the spacecraft; thus they provide redundant measurements on the three orthogonal spacecraft axes. This sensor is the baseline error sensor for all modes except for the survival mode.

Star Tracker : Except for the JASON mission, a non-redundant configuration using one star tracker is baselined. A large FOV star tracker was selected which results in reduced star gaps and in better knowledge resolution about the tracker boresight. The star tracker provides absolute attitude measurements used in the Kalman Filter to correct spacecraft pointing and gyro bias errors during normal and orbit adjust modes.

Coarse Sun Sensor : The CSS consists of 8 analog solar cells mounted on the spacecraft to provide 4-pi sterradian coverage in a non-redundant implementation. The analog solar sensors provide current output approximately proportional to the cosine of the sun angle with respect to the solar cell normal. Pitch and Yaw axes sun sensors each use 4 of the solar sensors. These sensors, along with the magnetometers, are the control sensors in the survival mode and are used to provide initial attitude determination during the stellar acquisition process.

Magnetometer : The baseline PROTEUS design uses a non-redundant implementation. Redundancy is provided for JASON or other long life missions to improve reliability. This component provides measurements of the local Earth magnetic field which is used during survival mode and initial attitude determination. In addition, it is used during star acquisition mode to provide momentum management control signals. To ensure a proper Earth magnetic field measurement, magnetic torquer bars will not be commanded during measurement (no spacecraft developed field).

Reaction Wheels : A four reaction wheel implementation mounted in a pyramidal configuration, as shown in Figure 5-2, is used for PROTEUS. This configuration will be used for JASON or other long life and high reliability missions. Other missions will use the same pyramidal mounting arrangement with only three flown wheels. Thus, the control algorithm of reaction wheels will be unchanged from mission to mission. Missions with only three wheels will use the back-up three wheels controller developed for a failed wheel condition when the four wheel implementation is flown. All the four reaction wheels will operate simultaneously for JASON to avoid attitude errors due to wheel zero-speed crossing. This problem would occur if only three wheels were used.

Magnetic Torquer bars : Magnetic torquer bars with redundant coils are baselined. This component design has flown many times and can be purchased as a standard product. During non-survival modes, one set of coils on these bars provides the actuation for reaction wheel momentum management. During survival mode, the other set of coils is used for spacecraft control actuators. Magnetic torquer bars are sized for the survival mode which require more torque than the momentum management application.

Thrusters : Four thrusters (1N BOL and 0.25 N at EOL) are located and oriented as shown in Figure 5-2. These thrusters are used to provide delta-V actuation in either a four thrusters mode or a two thrusters mode. Four thrusters are only used early in the mission for large delta-V maneuvers. When all four thrusters are used, an off-pulsing controller provides attitude control capability. When only two thrusters are used, roll torque is countered by reaction wheel commanding; pitch and yaw torques nominally cancelled are also regulated with wheels.

GPS : This component is not part of the baseline control sensor complement; however it will be flown on JASON as an attitude determination experiment. Pending performance results, future missions may use GPS attitude determination instead of the star tracker derived attitude determination. JASON will operate the GPS experiment during all modes and the ground will have the data to compare with the baseline attitude determination algorithm. Performance assessment can then be made by ground staff.

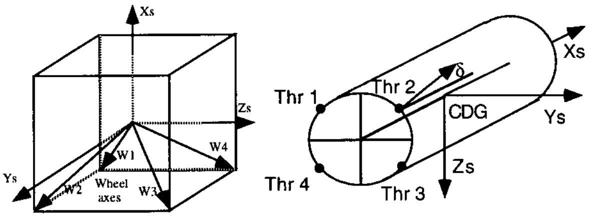

Figure 5-2: Wheel and thruster implementation

To also enhance applicability to future missions, in our implementation, space is reserved for adding redundant components, which can be accommodated on a mission-by-mission basis, to support missions with higher reliability and/or longer life requirements.

6 - DESCRIPTION OF OPERATIONAL MODES

6.1 - Mode Definition

PROTEUS has five (+one) distinct operational modes which are specific to various stages of the mission:

- LUM - Launch Mode
- STAM - Star Acquisition Mode
- NOM - Normal Operations Mode
- OCM4 - Orbit Correction with 4 Thrusters
- OCM2 - Orbit Correction with 2 Thrusters
- SHM - Safe Hold Mode

Each mode uses a prescribed subset of the hardware suite to accomplish the required performance objectives. Equipments used according to modes are shown in Table 6.1.

	LUM		STAM		NOM		OCM4		OCM2		SHM	
status	ON	OFF	ON	OFF	ON	OFF	ON	OFF	ON	OFF	ON	OFF
GYR		X	X		X		X		X		X not used	
STR		X	X		X		X		X			X
CSS		X	X		X not used		X not used		X not used		X	
MAG		X	X			X		X	X		X	
RWS		X	X		X		X not used		X		X	
MTB		X	X		X		X not used		X		X	
THU		X		X		X	X		X			X
PRO		X	X		X		X		X		X	
GPS		X	X experiment		X experiment		X experiment		X experiment		X experiment	

Table 6.1 : Hardware Utilization

A brief functional description of each mode, including the attitude determination and control algorithms used, presents how the hardware is employed, and the performance objectives.

LUM - Launch Mode. The AOCS is completely unpowered during launch.

SHM - Survival (and Attitude Acquisition) Mode. SHM is activated in case of detection of an anomalous condition or hardware failure, and also to acquire the initial attitude after separation from the launcher. SHM brings the spacecraft -X axis to the Sunline and damps inertial rates so that the solar arrays can generate electrical power and gives a starting point for acquiring attitude knowledge. The SHM control laws first damp the inertial body rates by using the MTB as magnetic brakes to dissipate any initial kinetic energy of the body. Then the spacecraft rotates to the Sunline by torquing with the MTB. A gyroscopic stiffness created by spinning the RW at a constant speed serves to hold the spacecraft on the Sunline regardless of the environmental torque disturbances or even at night. After successful completion of SHM, the ground can command transition to STAM.

STAM - Star Acquisition Mode. The objective of STAM is to acquire stars in the STR and to improve sufficiently both attitude determination and control in order to initiate Normal Operation Mode. STAM begins with the spacecraft approximately on the Sunline with moderate attitude and attitude rate errors. Wheels are initially commanded to rate damp the spacecraft using GYR data. Attitude knowledge then is initialized thanks to the Sun and Magnetic field vectors measurements using the MAG and CSS. Subsequent measurement are collected and processed over a period of time by a Kalman filter in order to improve the knowledge of attitude and body rate. When the attitude knowledge has reached a sufficient precision, the spacecraft is commanded to slew to a predetermined acquisition guide star field. Visible stars in the STR field of view are downlinked to the ground for positive verification before being incorporated in the Kalman filtered attitude knowledge solution. When the filter has converged sufficiently on the star vectors, the ground can command transition to Normal Operation Mode.

NOM - Normal Operation Mode. NOM is the mode in which all scientific missions are performed. The spacecraft is inertially stabilized using the RW, while attitude knowledge is maintained to the arcsecond level by Kalman filtering STR and GYR data. Attitude control is then facilited by sending a series of time tagged quaternion commands to the control laws which simply slave the spacecraft attitude to follow the current command. The Controller software is made generic by using the same commanded quaternion algorithms for both Earth pointing and Celestial pointing missions, thus software interfaces are standardized and simplified. To point to an inertial fixed target, the quaternion command is held constant, and similarly, to point relative to the Earth, the quaternion command is made to evolve with time. During NOM, excess momentum accumulated in reaction wheels due to external disturbance torques is dissipated magnetically using the MTB.

OCM4 - Orbit Correction with 4 Thrusters. OCM4 is used to generate large ΔV adjustments on the order of meters to tens of meters per second. In this mode, thrusters are used for both propulsion and attitude control (wheels are not used). Precise attitude determination is obtained identically to NOM, with the GYR used for precision control with periodic updates from the STR when stars are available. The nominal condition for 4 thrusters is to be fired continously until the control logic detects an attitude error, whereupon the THU are off-pulsed to generate a restoring torque.

OCM2 - Orbit Correction with 2 Thrusters. OCM2 is used for fine ΔV adjustments on the order of centimenters down to millimeters per second. In this mode, two thrusters are fired continuously and reaction wheels are used to maintain attitude. Attitude determination also uses the STR/GYR Kalman filter.

6.2 - Mode Transitions

Modes are logically organized to facilitate a prescribed progression of mission operations. Transitions between modes can be either automatic or by telecommand (TC) as dictated by mission doctrine. The mode architecture, logical dependencies, and transitions are shown in Figure 6-2.

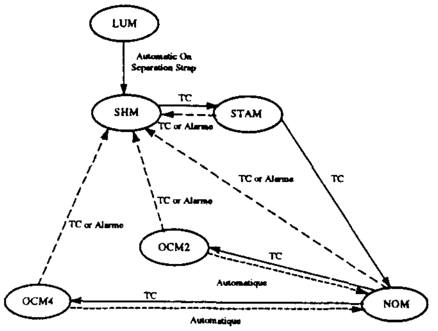

Figure 6.2 - Mode Transition Logic

7 - SIMULATION RESULTS

All the operational modes have been simulated to evaluate their performances. Some simulations applied to JASON mission are presented in this section.

Star Acquisition Mode. Figure 7-1 shows the overall attitude determination quadratic error over 4 orbits with the assumption of perfect control. After an initial period of convergence lasting about 2 orbits, the filter settles to a steady state error of about 0.25°. The settling time is mainly governed by the convergence of the gyro bias estimates.

Orbit Correction Mode with 4 thrusters. With the assumption of a perfect attitude knowledge and constant disturbance torques (due to thruster misalignment and unbalances and COG uncertainty), solar array bending modes, non cylindrical inertia tensor, figure 7-2 shows attitude angles and rates.

Survival Mode. Figure 7-3 shows over 8 orbits, the angles between Sun direction and the three spacecraft axes (-Xs, Ys, Zs) and the day/night durations as a function of time. Initial angular rates of 2, 5, 3 deg/s, worst case of 10 deg error on CSS due to albedo effect, 10^{-4} Nm constant disturbance torque added to gravity gradient, non diagonal inertia tensor are the actual simulation conditions.

In day time, pointing of -Xs (opposite of payload L.O.S) toward the sun direction is better than 30°. In eclipse period, attitude depointing occurs because of disturbance torques, but is quickly reduced when in day time.

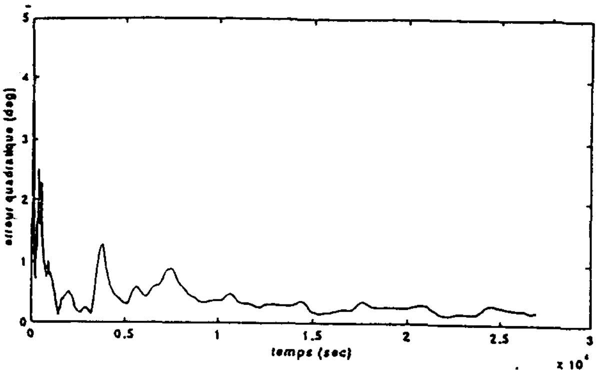

Figure 7-1: STAM : overall quadratic error.

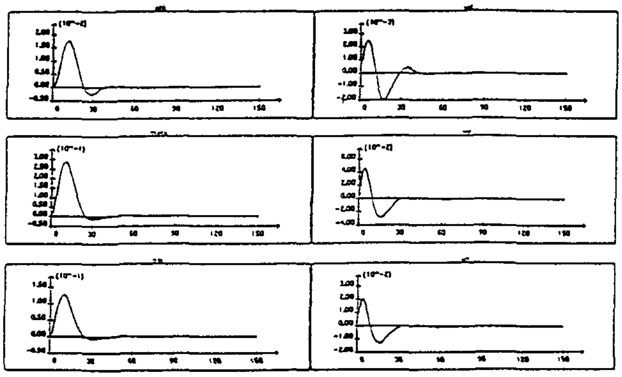

Figure 7-2: OCM4 : attitude and rates.

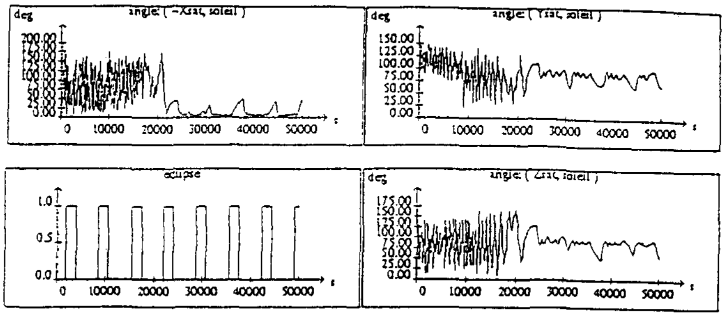

Figure 7-3: SHM - S/C axes w.r.t. Sun direction.

8 - PERFORMANCE

A system error budget was generated to determine the overall capability of the PROTEUS attitude control system design. Error sources were categorized into static, dynamic low frequency, and dynamic high frequency where :

Static Errors : RSS of fixed errors (biases and alignment errors) and launch shifts.

Dynamic Low Frequency Errors : RSS of time varying errors caused by disturbances with frequency within the controller bandwidth.

Dynamic High Frequency Errors : RSS of time varying errors caused by disturbances with frequencies above the controller bandwidth.

The expected PROTEUS pointing performance in arc-seconds for the various mission types is summarized in Figure 8-1.

	Earth Pointing			**Stellar, Inertial**		
	Roll	**Pitch**	**Yaw**	**Roll**	**Pitch**	**Yaw**
Static Errors	60.22	60.22	60.22	7.14	7.14	7.14
Dynamic Low Frequency Errors	62.34	81.24	62.34	62.34	81.24	62.34
Dynamic High Frequency Errors	2.45	5.48	2.45	2.45	5.48	2.45
Total System Pointing Error Budget	**125.01** 0.035°	**146.94** 0.041°	**125.01** 0.035°	**72.44** 0.02°	**94.25** 0.026°	**72.44** 0.02°

Figure 8-1. PROTEUS Error Budget in Arc-seconds

9 - AOCS DEVELOPMENT APPROACH

9.1. Development Logic.

9.1.1. Assumption for development.

An AOCS is defined by three main components: the equipment units, the on-board software and the interfaces.

- Equipment was presented in the previous section.
- At the level of software, the concept for the platform is to have only one centralised computer (CCTD) so the AOCS software is imbeded in it.
- All the equipment have a specific interface with the computer.

The subsystem verification approach must show how is qualified the proposed concept : which specifications are relevant, which models have to be used and which tests have to be performed. This logic is written in order to give a high level view of the tasks to be performed and how they are combined.

9.1.2. Specifications.

There is no direct notion of subsystem for a low cost, generic platform like PROTEUS. In particular there is no specific requirement for the AOCS but for the system. These specifications on which the system will be designed and tested are of 4 types:

- the platform specification, which is normally limited at the start of a project to a performance specification,
- the design specification : the full design will be included in the AOCS software specification, the so-called User Requirements Definition (URD).
- the interface specification : this specification can indeed be shared over all unit specifications and the S/W specification.
- the verification specification : this is in fact the test plan used to validate the design.

9.1.3. Equipment development.

Philosophy for development and unit qualification is as follows:

- an Engineering Model for all equipment not already fully qualified on previous programs,
- a Qualification Model if an EM has been developed,
- a Preliminary Flight Model for all unit with an unchanged design w.r.t their qualification and with only new PROTEUS environmental levels,
- a Flight Model for all recurring equipment.

In order to respect the low cost objective, it is very important to limit new unit development to the maximum extent, and off-the shelf units shall be preferred if compatible with design and requirements.

9.1.4. Software development.

As part of this verification approach, it is essential to freeze the AOCS design as soon as possible and to avoid as far as possible design changes at a late stage.

Such changes are in all projects the cause for large delays: this explains why the URD is quasi-frozen in the middle of phase B to allow an optimal design of the software architecture.

9.2. Test approach.

9.2.1. Test philosophy.

Taking into account the schedule and cost constraints of the PROTEUS program , the test philosophy must be established such that the number of tests is limited and performed as early as possible but also such that the design and performance specifications are sufficiently covered.

The computer is the heart of the system. Its functions and interfaces must be available and tested as soon as possible. Other equipment are not specific to the PROTEUS program and one of the criteria for their selection is their state of qualification, as a consequence if modifications are required for interfacing, they will occur on the computer.

9.2.2. Tests at equipment level.

Function of the state of qualification and complexity for interfacing, an Engineering Model fully representative of unit functions and interfaces could be provided by the manufacturer. The most sensitive sensor is the star-tracker because of the large data flow it exchanges with the computer and the fundamental role it has in the AOCS. As a consequence very early in the program, testing of its interface will take place.

9.2.3. Tests at system level.

Tests with the Computer Engineering Model.

The first subsystem tests will start once a first version of the AOCS S/W is loaded in the computer EM. These tests will be performed in closed loop, the loop being closed in the test computer where the satellite dynamics will be simulated, as well as the sensors and actuators and the satellite environment. The same simulator as the one used for the subsystem design set-up will be used.

The test definition will be included in the test plan and will cover all AOCS modes, functional interfaces, transitions, FDIR (Failure Detection and Isolation Recovery) features, etc.

Tests with the Computer and AOCS equipment Engineering Models.

The aim of these tests is to validate the electrical interfaces between computer and equipments. Each equipement is connected to the computer and electrically stimulated by its own test equipment. These are open loop tests. In this sequence are also performed polarity tests (end to end) to save time in preparing the tests for the Flight Model.

Tests with AOCS Flight Model units.

To reduce cost, these tests are very limited. They will be included in the Integration operations, including check of the electrical interfaces, and polarity test between sensors and actuators. Dynamic Bench Tests (DBT) using a three-axes table are not proposed for PROTEUS system validation. The utility of such tests is to verify transient behaviour of some sensors and their consequences on AOCS functionality and performance. Reasons not to proposed DBT are as follows :

- a long time period can be necessary to perform these tests which is not compliant with low cost,
- a stimulator of a large field of view star tracker compliant with a three axes table constraints has a complex implementation, not very representative of reality and rather expansive,
- all the On-Board Software can be changed and loaded during the flight. As a consequence if filtering or data processing are required, it can be done easily.

10 - CONCLUSION

The PROTEUS Attitude and Orbit Control System design complies with many low Earth orbit mission requirements. The baseline PROTEUS design is based on the use of qualified components, whenever possible, in a cost effective implementation employing minimal redundancy. The AOCS design uses the flight proven stellar-inertial architecture which is inherently suited to the broad range of missions proposed for PROTEUS. The number of AOCS modes is significantly reduced and as a consequence the mode logic is very simplified.

ATTITUDE AND ORBIT CONTROL SYSTEM DESIGN FOR X-RAY ASTROPHYSICS SPACE OBSERVATORY ASTRO-E

Keiken Ninomiya, Tatsuaki Hashimoto

Institute of Space and Astronautical Science,
3-1-1,Yoshinodai,Sagamihara,229,Japan
Phone:+81-427-51-3977,Fax:+81-427-59-4260,E-mail: ninomiya@nnl.isas.ac.jp

Ken Maeda (NEC Corp.,Japan)

Tetsu Saitoh, Asami Genba, Masahiko Akisue (NEC Aerospace Systems Ltd.,Japan)

ABSTRACT

'ASTRO-E' is the Japan's fifth astrophysics satellite to be launched in the beginning of 2000. The satellite carries a new X-ray telescope of a high spatial resolution, thus a notably precise attitude control is required for the satellite to make full use of the telescope capability. The attitude determination system of the satellite uses microcomputer based strapdown system which combines data from a pair of star trackers, a fine digital sun sensor, and an inertial reference unit for use in on-board Kalman filtering. The attitude control system employs 3-axes momentum bias stabilization system which uses as actuators four skew arranged momentum wheels as well as three magnetic torquers. In this paper, the design policies of ASTRO-E attitude and orbit control systems which have the following unique features are described together with the system design results:

1. An autonomous, highly operable attitude determination system implementing on-board star identification algorithm.
2. Initial attitude and orbit acquisition maneuver compatible to M-V launch vehicle restrictions.
3. A unique safe-hold attitude control scheme employing hybrid bias momentum system.
4. An effective anomaly detection system which optimized function assignment between hardware and software.
5. A new magnetic control law in the operational control phase [Ref. 1], which can suppress a high level attitude disturbance effectively.

Keywords:
Attitude Control; Bias Momentum; Multi-Wheels; On-board star identification; Hybrid bias momentum; Momentum Management

1. INTRODUCTION

The Japan's fifth astronomy satellite 'ASTRO-E' is a high-throughput X-ray observatory scheduled for launch in early 2000 (see Figure1 for satellite overview and coordinate systems). The observatory will be injected into near-circular, 550km mission altitude orbit with the B.O.L weight of 1.6 tons. It carries both soft and hard X-ray telescopes which aim at a highly precise measurement of location of unknown X-ray radiation sources at the deep-most place in space. A high spatial resolution of measurement is realized by extending this telescope's X-ray mirror in orbit to get a long focal length(4.75m). The high resolution, on the other hand, requires the telescope line-of-sight direction (Z_B axis) to be pointed at the observed target with a correspondingly high accuracy of 0.2 arcmin(3σ). Moreover, a rather stringent specification is set for attitude stability during observation so as to suppress attitude fluctuations in 8 seconds to within 0.1 arcmin(3σ), in order to avoid degradation of telescope image. In addition, the inertial direction of the telescope line-of-sight vector must be determined with an even higher accuracy of 0.1 arcmin(3σ) to meet needs for post-flight measurement data evaluation.

The observatory is requested to have enhanced attitude maneuvering capabilities also compared with previous missions [Ref. 2] to utilize the limited operational life more effectively. These are; rapid maneuver capability (maximum 0.2deg / sec) and accurate post-maneuver attitude acquisition performance (attitude settling time :within 10 minutes after end of maneuver). To satisfy these mobility requirements, the attitude control system is equipped with 4 skewed momentum wheels.

The attitude control system of ASTRO-E employs several notable designs specifically developed to meet above challenging requirements. Among those, the operational mode attitude control system implements a new magnetic control law briefly described below. As a consequence of telescope body exten-

---

Proceedings Third International Conference on Spacecraft Guidance, Navigation and Control Systems, ESTEC, Noordwijk, The Netherlands, 26-29 November 1996, ESA SP-381 (February 1997)

sion, the satellite acquires an incommensurately big moments of inertia as compared with ordinary inertia to mass ratio. This results in generation of an extraordinarily large gravity gradient torque acting on the satellite. The peak value of accumulated angular momentum per orbital revolution reaches as large as 30Nms (see Table 1 for satellite inertia properties dependent on in-orbit configuration and Table 2 for resulting attitude disturbance). To cope with this situation, our new magnetic control method [Ref. 1] first abstracts the secular (i.e.,orbital mean) component out of the full excess momentum, based on the estimation of the gravity-gradient torque. The magnetic torquers are then excited so that only this secular momentum is dumped into space instead of full momentum dumping. This strategy eliminates needless excitation of magnetic torquers and consequently can reduce necessary magnetic torquer size considerably. Application of this technique to operational mode attitude control system thus brings a substantial improvement of the magnetic control efficiency over conventional systems. For ASTRO-E, the magnetic torquer with only 75% capacity of the conventional ones is estimated as enough for complete momentum management.

The magnetic control law described above, however, cannot be used during safe-hold control mode because necessary orbital information may not be available during the period. Instead, the safe-hold control system rotates the satellite body about the Y_B axis at a constant spin rate to avoid an excessive angular momentum accumulation due primarily to gravity gradient torque. This is done by utilizing a bias angular momentum which had been stored in four momentum wheels and had been controlled to point the sun direction in the operational control mode. The thermal and power survivability conditions during the safe-hold control mode can be met by aligning the bias momentum direction (body Y_B axis, also solar paddle plane normal direction) to the sun vector and then keeping the attitude with magnetic control.

In the following the orbit and attitude maneuver sequence in the initial attitude acquisition phase is briefly described. First the satellite will be injected into an elliptic orbit of apogee height 550km and perigee height about 200km using M-V launch vehicle, with the spin rate of 5 rpm imparted subsequent to the attitude change maneuver performed by the vehicle's third stage. Thereafter several perigee-up ΔV maneuvers are executed to finally acquire the 550km mission altitude orbit, keeping the initial spin rate of 5 rpm. The worst case mission analysis shows that there exists a situation where the satellite must execute ΔV maneuver immediately at first apogee after orbit injection in order to avoid reentering into the atmosphere by the previous injection errors. Considering these circumstances, the spin-axis attitude during ΔV maneuvers is so chosen that the subsequent initial attitude acquisition maneuver can be securely achieved using limited satellite resources. The whole orbit and attitude maneuvers to be conducted in the initial orbit and attitude acquisition phase are actuated with RCS (Reaction Control System) which uses hydrazine as propellant.

2. SYSTEM DESCRIPTION

Figure2 shows the AOCS Component Block Diagram.

The inertial reference unit (IRU) is composed of two units, IRU-SA and IRU-SB. IRU-SA contains four single-axis FRIGs while IRU-SB contains a single axis FRIG. The input axis direction of each constituent gyro is appropriately allocated to give a fault-tolerant measurement. Thus, a possible failure occurring in any one of the five gyros can be covered by the remaining three normally functioning gyros, with error sensitivity value of angular rate measurement as low as 2 or below (provisional design).

The satellite carries two fine sun sensors (FSS) based on the failure analysis at anomaly. One is used for monitoring attitude anomaly in the operational control mode, while the other is used for safe-hold control.

Each of the two star trackers (STT) uses a two-dimensional CCD device as a star direction detector and can track stars up to 6.5-th visual magnitude within 5deg by 10deg FOV. It permits a notably fine attitude sensing with the accuracy of 3arcsec(3σ) random error and 7arcsec(3σ) bias error. A big design effort was dedicated to fix the FOV allocation of the two STTs under limited freedom severely restricted by the possible interference with other on-board equipments. The FOV allocation criteria adopted were ;

- The allocation geometry should not result in the attitude determination error sensitivity value exceeding 2.0.
- The time period during which star sensing is active using both STTs concurrently with X-ray telescope measurement should be, at the shortest, longer than 55% of the total X-ray observation period.

To reduce the effect of the in-orbit variation by thermal distortion of mechanical alignment between STTs and IRU as much as possible, the STTs and IRU were installed on a common structural panel.

Four identical momentum wheels (MW), each with angular momentum storage capacity of 50Nms and with maximum reaction torque of 0.03Nm, are installed about satellite Y_B axis in a skew-symmetrical configuration with each rotor spin axis inclined by 20deg from the satellite $X_B Z_B$ plane. This inclination angle was employed taking into consideration both the maximum maneuverable range of the satellite attitude in the operational control mode and the angular momentum storage capacity in the safe-hold control mode.

Three magnetic torquers, each capable of generating maximum magnetic moment of 250ATm^2, are installed in a orthogonal triad configuration.

3. INITIAL ATTITUDE AND ORBIT ACQUISITION

Figure3 shows the Initial Sequence of Events.

The M-V launch vehicle terminates its third stage burn at a possible lowest altitude to maximize the payload mass to be placed into initial target orbit. This makes the resulting satellite orbit with an intended apogee height of 550km(the value depends on the satellite mass) but with a rather low perigee height of 200km preserving the injection altitude. Thus, should the worst case error of orbit injection using the third stage rocket be resulted, the perigee height has to be raised up as soon as possible immediately after injection. To meet this need, ASTRO-E acquires, prior to orbit injection, an attitude necessary for perigee-up ΔV firing, given 180deg rotation maneuver about the orbit normal by the third stage motor, as well as 5rpm spin rate to stabilize its attitude. Then the satellite carries out a simple anomaly check by monitoring the angle between the spin-axis and the sun vector using a FSS.

If the spin-axis attitude is judged as normal, the satellite executes a first ΔV maneuver (30m/s) using four 23N thrusters. The satellite executes five ΔV maneuvers in all within five days to finally acquire the 550km mission altitude circular orbit. During this period both the nutation control and the spin-axis direction control are carried out as needed using 3N thrusters. After the orbit acquisition maneuvers are successfully completed, the satellite is rate-dumped using RCS thrusters to a spin rate as low as 0.5rpm where the start up of IRU gyros are available. Then the satellite is nearly completely despun with rate damping control and initiate sun acquisition. When it is successfully done, the solar paddles are deployed and momentum wheel run-up is started. After the completion of wheel run-up, the satellite is finally handed over to operational mode control.

4. ONBOARD ATTITUDE DETERMINATION

Figure4 shows the functional block diagram of onboard attitude determination system. The system employs a Kalman filter-based strapdown scheme combining measurement data of two STTs and IRU. The resetting type Kalman filter, often used in astronomical missions, is employed here too in order to effectively estimate both satellite attitude angles and gyro drift rate errors. The angular velocity measurement data obtained by IRU gyros are integrated by up/down counter at 32Hz sampling to calculate the satellite attitude. These integrated small attitude rotation angles are then transformed to equivalent q parameters set for computational efficiency. Each STT is capable of acquiring and tracking up to 10 stars within its FOV simultaneously, among which the most appropriate 3 stars are chosen for use in attitude reference. Nearly 20 stars to be observed by STTs at a target satellite attitude are listed up in advance by the ground control center and their inertial directions stored in a star sub-catalogue. The catalogue is then commanded up to the satellite prior to actual star measurement. When several stars are observed within STT FOV, the onboard computer refers already received star catalogue to identify those stars. If the identification is performed, the computer solves the obtained measurement equations necessary to update satellite attitude by a typical Kalman filter processing. The onboard star identification technique stated above greatly enhances both autonomy and operability of attitude determination system. Specifically, it permits a reliable attitude determination even in a case where a relatively large attitude error remains immediately after an attitude maneuver which is caused by gyro scale factor error. Because the speed of Kalman filter convergence is strongly dependent on the updating period of STT measurement data, it is set to 2 seconds for ASTRO-E, a rather short period, to improve the convergence performance.

5. STEADY STATE ATTITUDE CONTROL

Figure5 shows the block diagram of steady state (operational mode) attitude control system. The operational mode control system is organized from;

- pointing control system which uses four momentum wheels as main actuator to perform fine attitude pointing
- maneuver control system which controls various attitude acquisition maneuvers given attitude determination result and target attitude
- angular momentum management system (magnetic control system) which manages magnetic torquer operations

The pointing control system enforces the satellite attitude to rapidly converge to a specified target attitude and keeps it thereafter using a classical PID wheel control law. A fast response is realized by using IRU gyros as primary sensor for attitude and angular velocity measurements. The control system is designed to have an enough stability margin against injurious effects such as solar paddle flexible dynamics and sloshing motion of liquid helium contained in some mission instruments.

The gyro-coupling effect which is caused by dynamical interaction between the bias angular momentum of four momentum wheels and body angular velocity generated during maneuver control is canceled out by the decoupling control law shown in the figure. The pointing control law calculates needed wheel control torque along each body axis independently. They are then distributed to each of four wheels according to wheel distribution law to form wheel control command.

Each wheel is equipped with a tachometer feedback loop which controls the rotor rotational period, instead of instantaneous rotor speed, to a target value. This makes use of the fact that the period can be measured very accurately using a high frequency clock. However, the measurement of rotor period naturally requires certain time span needed for a complete rotor revolution, and this fact makes it difficult to retain a sufficient stability of control system when the rotor speed is very low. This problem is resolved by modifying the loop so that a torque command can be given directly to the wheel without using tacho-loop when the rotor speed is down to a critically low value.

The maneuver control system outputs angular velocity commands of attitude acquisition maneuver to the pointing control system. The maneuver is executed as an Euler axis-Euler angle type rotation maneuver based on the calculations using attitude determination result and the commanded target attitude. The control system employs the q parameter-based attitude representation scheme throughout to realize singularity-free attitude maneuvers.

6. CONTINGENCY STRATEGY

The safe-hold control is activated in case of contingencies of the attitude control system. The purpose of this control mode is to acquire and maintain the attitude which satisfies the survival condition of the satellite. The design concept of this control scheme is described below.

1. To satisfy the system requirements on the safe-hold attitude control;
    - From the power and thermal condition, the angle between the solar paddle normal and sun direction needs to be less than 30deg.
    - According to the consideration on the control system reliability and the contamination to the mission instruments, it is not allowed to adopt the RCS as actuators for this control.
    - Basically, any one failure of attitude components should not cause fatal situation.
2. To realize the stable and reliable attitude control;
    - This control scheme should have enough capability to suppress the large external disturbance torque.
    - The transition from the steady state control mode to safe-hold mode should be dynamically stable. [*Ref.* 3]
    - The safe-hold control should be operated without ground support at least more than three weeks.
3. To detect the abnormality by reliable error detection;
    - An anomaly should be detected by simple hard-wired logic and careful software logic. These two error detection systems act complementary each other.

As mentioned above, this satellite has large gravity gradient torque. Therefore there is a severe difficulty in the safe-hold control system design. The most important point in the system design is to select the safe-hold attitude which reduces the disturbance torque. The result of gravity gradient disturbance analysis shows that a "constant" spinning around Y_B axis (4 rpo is enough) attitude is suitable for this mode, because of its disturbance cancellation effect and simple control logic.

To achieve the stable slow spin, there are three subjects which should be considered. The first subject is how to control the satellite body rate at 4 rpo. We adopted a conventional rate control logic around Y_B axis with the active nutation damping by two wheels. Although this control utilizes wheels, the factor of activating the safe-hold mode may be the failure of one wheel. Therefore, the selection of wheels for this mode is important in the redundancy strategy, and also from the point of angular momentum reconfiguration. By stopping two opposite wheels including a wheel which may fail, the discharged angular momentum from these wheels is expected to rotate satellite body at 4 rpo. The second subject is how to satisfy the stability condition of dual spin dynamics.

The simplest method is to spin satellite with stopping all four wheels. Unfortunately, however, Y_B is a principal axis of intermediate moment of inertia so this satellite cannot spin stably around Y_B axis. Therefore, the hybrid bias-spin scheme (we tentatively named) is adopted as safe-hold attitude. In this scheme, the angular momentum is shared with satellite body and the selected pair of wheels. By introducing wheel bias momentum, the dynamics stability is excellently improved. The third subject is angular momentum management. This is performed by using a three axes magnetometer and three magnetic torquer. The control scheme simply eliminates the excess angular momentum by driving magnetic torquers with bang-bang manner.

7. CONCLUSION

The attitude control system of the astrophysical space observatory ASTRO-E is outlined. This control system is well adjusted for astronomy observation mission requirement and current launch vehicle interface. Especially, star identification scheme of the attitude determination system, a unique safe-hold attitude control method, initial attitude and orbit acquisition maneuver which is compatible to M-V launch vehicle restriction are the notable features of this control system. Now the prototype model of this control system is under development, and it is expected to confirm the effectiveness of this attitude control system.

REFERENCES

1. K.Ninomiya, H.Iida, *A New Approach to Magnetic Angular Momentum Management for Large Scientific Satellites*, SPACEFLIGHT DYNAMICS, Toulouse, June 1995, pp.623-643
2. K.Ninomiya, M.Uo, K.Maeda, T.Saitoh, *Attitude Control System of The X-ray Observatory ASTRO-D*, 11th IFAC WORLD CONGRESS, Tallinn 1990, Vol.1,pp.101-106
3. K.Ninomiya, J,Kawaguchi, K.Maeda, *Stability Analysis of ASCA Safe-Hold Dynamics*, ISAS 3rd Workshop on Astrodynamics and Flight Mechanics, 1993, pp.206-211

Table 1: Mass Property and Orbit

Total Weight	1.6t (at B.O.L.)
Moment of Inertia [kgm^2]	(4163, 3814, 901)
Orbit	550km Altitude Circular Orbit (after perigee-up maneuver)

Table 2: External Attitude Disturbances

		Gravity Gradient	Solar Radiation	Aero Drag	Magnetic Residual	Total
Accumulated Angular Momentum [Nms/rev]	X	16.0	3.3	1.7	0.2	20.2
	Y	18.0	0.0	0.9	0.1	17.0
	Z	25.0	0.0	2.3	0.3	4.4

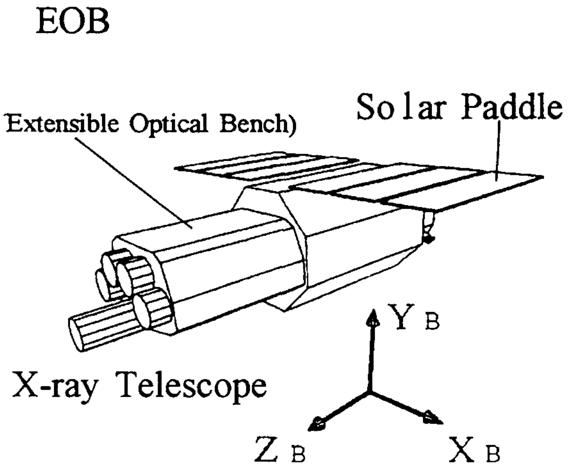
EOB
Extensible Optical Bench)
Solar Paddle
X-ray Telescope
Y B
Z B
X B

Figure 1: Outline of ASTRO-E

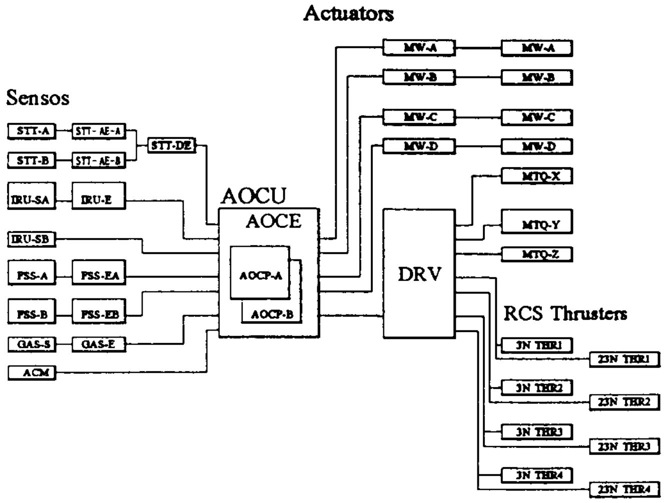
Actuators
Sensos
STT-A
STT-AE-A
STT-B
STT-AE-B
STT-DE
IRU-SA
IRU-E
IRU-SB
PSS-A
PSS-EA
PSS-B
PSS-EB
GAS-S
GAS-E
ACM
AOCU
AOCE
AOCP-A
AOCP-B
DRV
MW-A
MW-A
MW-B
MW-B
MW-C
MW-C
MW-D
MW-D
MTQ-X
MTQ-Y
MTQ-Z
RCS Thrusters
3N THR1
23N THR1
3N THR2
23N THR2
3N THR3
23N THR3
3N THR4
23N THR4

Figure 2: AOCS Component Block Diagram

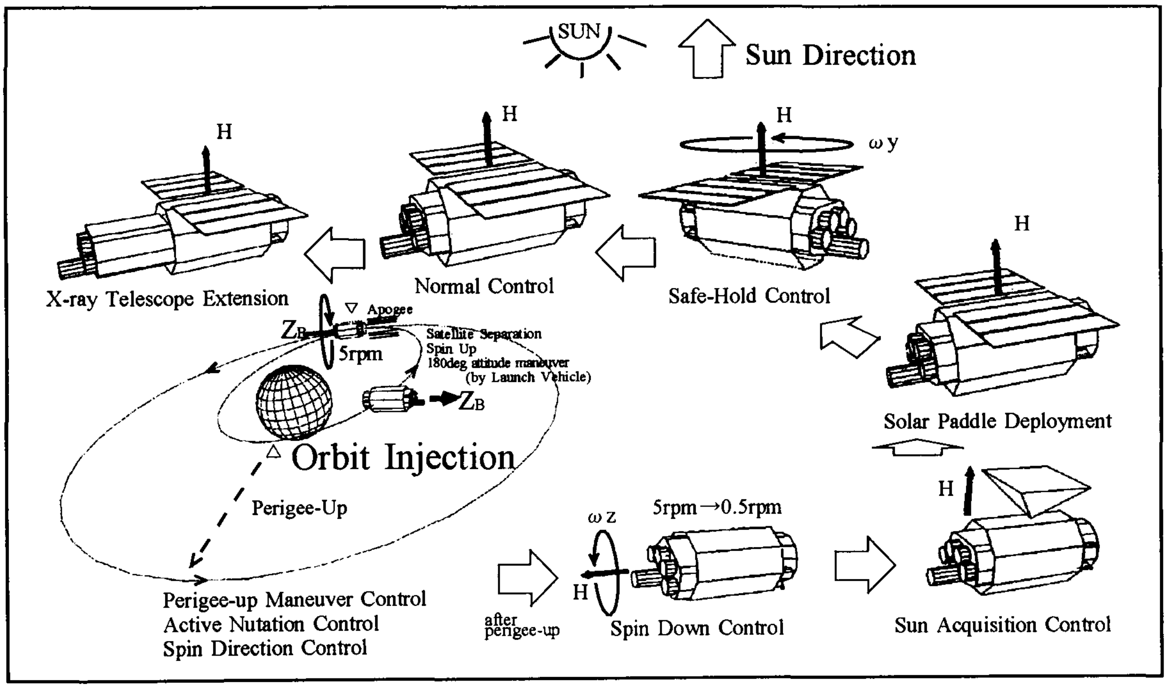
SUN
Sun Direction
H
X-ray Telescope Extension
Normal Control
ω y
Safe-Hold Control
Solar Paddle Deployment
Apogee
Satellite Separation
Spin Up
180deg attitude maneuver
(by Launch Vehicle)
5rpm
ZB
Orbit Injection
Perigee-Up
Perigee-up Maneuver Control
Active Nutation Control
Spin Direction Control
after perigee-up
ω z
5rpm→0.5rpm
Spin Down Control
Sun Acquisition Control

Figure 3: Initial Sequence of Events

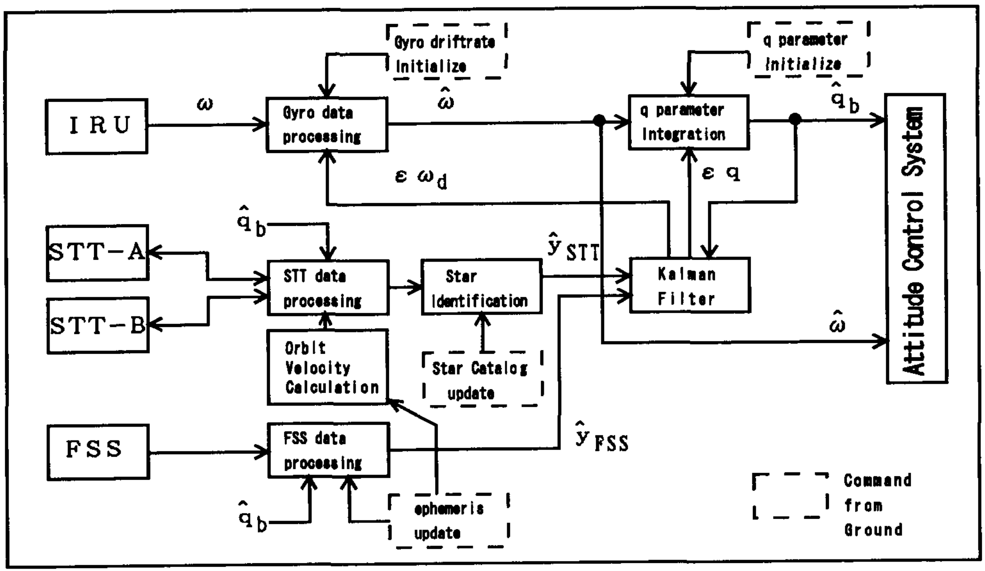
Gyro driftrate Initialize
q parameter Initialize
IRU
ω
Gyro data processing
ω̂
q parameter Integration
q̂b
ε ωd
ε q
q̂b
STT-A
STT-B
STT data processing
Star Identification
ŷ STT
Kalman Filter
Attitude Control System
Orbit Velocity Calculation
Star Catalog update
ω̂
FSS
FSS data processing
ŷ FSS
q̂b
ephemeris update
Command from Ground

Figure 4: ADS Functional Block Diagram

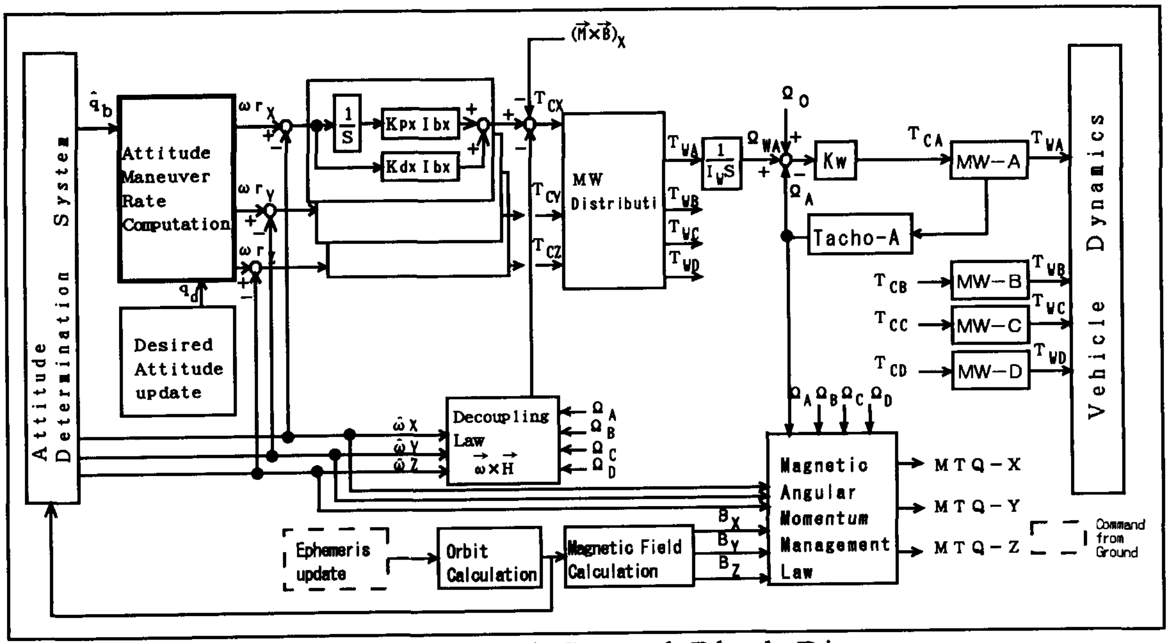
Attitude Determination System
q̂b
Attitude Maneuver Rate Computation
ω rX
ω rY
ω rZ
qd
Desired Attitude update
1/S
Kpx Ibx
Kdx Ibx
(M×B)X
TCX
TCY
TCZ
MW Distribution
TWA
TWB
TWC
TWD
1/IWS
ΩWA
Ω0
ΩA
Kw
TCA
MW-A
TWA
Tacho-A
TCB
MW-B
TWB
TCC
MW-C
TWC
TCD
MW-D
TWD
Vehicle Dynamics
ω̂X
ω̂Y
ω̂Z
Decoupling Law
ω×H
ΩA
ΩB
ΩC
ΩD
ΩAΩBΩCΩD
Magnetic Angular Momentum Management Law
MTQ-X
MTQ-Y
MTQ-Z
Command from Ground
Ephemeris update
Orbit Calculation
Magnetic Field Calculation
BX
BY
BZ

Figure 5: Normal Control Block Diagram

SESSION 6:

RE-ENTRY

Chairman: S. Strandmoe (ESA/ESTEC)

NAVIGATION, GUIDANCE AND CONTROL OF THE ATMOSPHERIC RE-ENTRY DEMONSTRATOR

G. Pignié, P. Clar, E. Ferreira, L. Bouaziz, J. Caillaud
AEROSPATIALE, Espace & Defense
66 Route de Verneuil, B.P. n°2, 78133 Les Mureaux Cedex, FRANCE
Fax: 33 1 34 92 19 99
e-mail: gerald.pignie@espace.aerospatiale.fr
philippe.clar@espace.aerospatiale.fr

ABSTRACT

The Atmospheric Re-entry Demonstrator (ARD) is a flight demonstration project initiated by the European Space Agency (ESA) to consolidate technological knowledge for the development of future manned re-entry vehicles. Aerospatiale is the prime contractor for ARD, and is in charge of the whole ARD GNC and Flight Software development

The A.R.D. is an unmanned capsule-like vehicle scheduled to be launched on a Ariane 5 flight from Kourou in French Guyana. After a flight of three-quaters of an orbit, the ARD will perform a guided re-entry ending with a final deceleration phase under parachutes and a splash-down in the Pacific Ocean. The ARD's main objective is to acquire flight data for improving predictions of re-entry phenomena and thus reducing the design margins for future vehicles.

After a brief profile of the ARD's mission this paper will focus on the development of the guidance, navigation and control (GNC) algorithms. For each algorithm, the main design guidelines will be stated, the general principles given. The essential characteristics are the following:

Navigation: This algorithm is based on an inertial navigation algorithm updated by GPS measurements. It also uses an altitude estimate constructed from the longitudinal acceleration measurements, and a drag model. Special care has been taken to insure performance robustness.

Guidance: This algorithm is of the Apollo-Shuttle type. As no angle of attack modulation is possible, it commands only the lift vector orientation to control the vertical projection of the lift, in order to follow a drag versus velocity profile. The guidance algorithm must limit the maximum thermal flux and the maximum load factor encountered during re-entry while optimizing splashdown accuracy.

Control: A seven thrusters architecture is used to control the capsule attitude and to carry out the guidance orders. This algorithm is based on a classical state feedback control law and a state estimator. The tunning of the control law has been chosen to maximize control efficiency at low Mach number where the ARD is dynamically unstable.

Then the global performances of the algorithms are shown, using Monte-Carlo simulation results.

INTRODUCTION

The Atmospheric Re-entry Demonstrator (A.R.D.) program has been initiated by the European Space Agency (ESA) in order to prove Europe ability to design and build a re-entry capsule with a limited budget and within a short time. Such a project will allow to validate Europe's know-how in re-entry flight and to acquire a large set of data (on the atmospheric characteristics, the aerodynamic behaviour, the thrusters efficiency...), in order to ease the design of future manned space vehicles,. The A.R.D. is an Apollo-like shape guided re-entry capsule, using as much as possible Ariane 5 avionics equipments (On Board Computer, Inertial Measurement Unit,...). The general sketch of the A.R.D. is shown in figure 1.

Copyright © 1996 by AEROSPATIALE. Published by ESA with permission.

Proceedings Third International Conference on Spacecraft Guidance, Navigation and Control Systems, ESTEC, Noordwijk, The Netherlands, 26-29 November 1996, ESA SP-381 (February 1997)

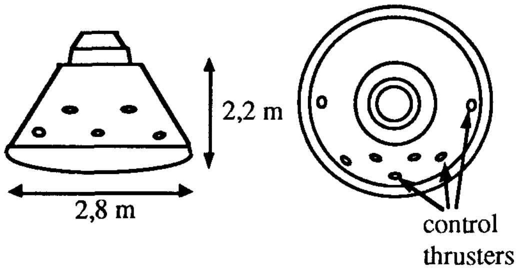

Figure 1

The A.R.D. experiment is scheduled to be carried out in 1997. Figure 2 presents its typical mission profile and the four different flight phases (launch phase, ballistic phase, re-entry phase, descent phase).

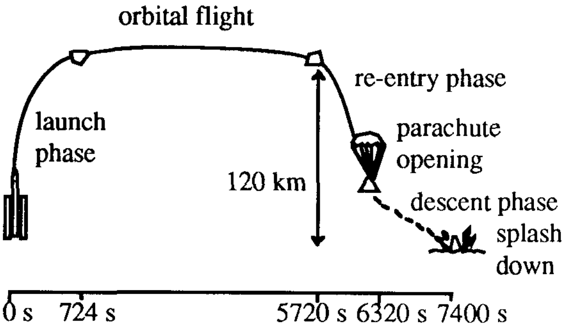

Figure 2

The A.R.D. navigation algorithm, which is described in the first part of this paper, is based on I.M.U. measurements and designed to cope with each phase characteristics. One of the main purposes of the A.R.D. experiment is to conceive and implement GNC algorithms that enable a landing accuracy of 100 km (3 σ). One shall quote that no link with the Ariane 5 on board computer has been implemented, in order to launch the capsule exactly as a usual payload. Because of I.M.U. defects, a pure classic inertial navigation algorithm is unable to guarantee the required accuracy. So, the basic navigation algorithm has to be updated by external measurements. These measurements may be provided by an on board G.P.S. receiver. As the A.R.D. mission has to be successful even in case of a G.P.S. failure, a scheme to update the basic navigation algorithm has been conceived. This peculiar updating method uses altitude pseudo-measurements, called D.D.A. (for Drag Derived Altitude) and computed using an estimate of the non-gravitational acceleration and aerodynamic and atmospheric models.

During reentry, the guidance law, described in the second part, is of the Apollo-Shuttle type[2] : control of the instantaneous vertical L/D ratio as a function of drag and velocity. These principles were retained but some improvements were brought, particularly concerning the derivatives computation and the ranging technique. The vertical guidance logic is based on the tracking of a reference trajectory, which is updated at each guidance step. The steering parameter is the L/D ratio projected in the vertical plane. The activation of roll reversals is used for the lateral guidance in order to remain within an azimuth corridor.

During reentry the capsule is always statically stable ($C_{m\alpha} < 0$), dynamically stable in hypersonic and supersonic domain, but with a very weak damping ratio ($C_{mq} < 0$), and is unstable below Mach number 1.2 ($C_{mq} > 0$). So, the objective of the attitude control function is to damp the angle of attack and sideslip angle at their natural trimmed values and to control the lift orientation (the aerodynamic bank angle), in the direction computed by the guidance algorithm. The maximum rate of the aerodynamic bank angle is 15°/s.

The control law is based on a linear model and a state feedback design. The feedback gains are computed by locating the eigenvalues and the eigenvectors of the system in order to yield a reasonable closed loop behaviour. The state vector is obtained using an asymptotic Kalman estimator with the measurements issued by the IMU and the navigation algorithm. Due to uncertainties on the CoG location, body shape and aerodynamic coefficients, the natural trimmed angle of attack and sideslip angle are unknown. So the natural way is to have only an angular rate control. Nevertheless, to improve the stability margin of the closed loop we will see that it is interesting to allow an angle of attack and sideslip angle feedback. So we will perform an on board estimation of the trimmed angle of attack and sideslip angle. The description of this control algorithm is the matter of the third part of this paper.

NOMENCLATURE AND CONVENTIONS

m	vehicle mass
A, B, C	roll, pitch and yaw inertia
S	reference area
l	reference length
V	vehicle velocity relatively to the Earth
Q	dynamic pressure

g	gravity
ϕ	thermal flux
ρ	air mass per unit volume
z	altitude
r	vehicle to the Earth center radius
U_l, U_m, U_n	roll, pitch and yaw RCS torques
p, q, r_1	roll, pitch and yaw angular rates
α	angle of attack
β	sideslip angle
γ	aerodynamic flight path angle
χ	aerodynamic azimuth
μ	geometric bank angle
μ_a	aerodynamic bank angle
C_D	drag coefficient
C_Y	lateral coefficient
C_L	lift coefficient
C_A	axial force coefficient
L	lift force
D	drag force
Cl	aerodynamic roll torque coefficient
Cm	aerodynamic pitch torque coefficient
Cn	aerodynamic yaw torque coefficient
C_q	heat flux coefficient

$$\text{We denote:}\begin{cases} C_{u,v} = \dfrac{\partial C_u}{\partial v} & \text{for } v \in \{\alpha, \beta\} \\ C_{u,v} = \dfrac{V}{l}\dfrac{\partial C_u}{\partial v} & \text{for } v \in \{p, q, r\} \end{cases} \qquad (1)$$

The conventions used concerning the angles, the trihedra and the aerodynamic coefficients are the classical ones used for flight dynamics.

We just remind here that the vehicle trihedron (O, X, Y, Z) is such as:

O is the capsule cone apex,

X is the revolution axis directed towards the shield,

Z is such as the plan (X, Z) contains the desired CoG location. The direction of Z is chosen so that the CoG has a negative component on the Z axis.

Y completes the trihedron

The geometric bank angle is representative of the Z direction with regard to the vertical.
The aerodynamic bank angle is representative of the lift direction with regard to the vertical.

NAVIGATION ALGORITHM

The basic navigation algorithm provides estimates of the A.R.D. position and velocity in the reference inertial equatorial trihedron Teq (see figure 3). It is based on I.M.U. measurements and a gravity model. During the phases when the A.R.D. is submitted to an important non-gravitational acceleration (launch, re-entry and descent phases) an usual inertial algorithm integrating the I.M.U. measurements (similar to the Ariane 5 algorithm) is used. But, during the ballistic phase the non-gravitational acceleration can be neglected with regard to I.M.U. defects. Therefore, it has been chosen not to take into account the I.M.U. measurements during this ballistic phase.

at launch date :

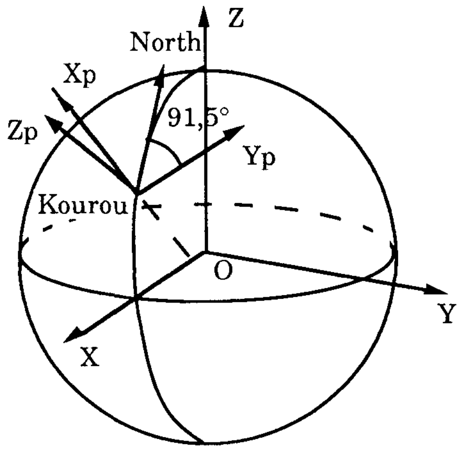

O,X,Y,Z : Teq
K,Xp,Yp,Zp : Tp

Figure 3

Inertial algorithm

The navigation outputs are :

-$\vec{X}$: the A.R.D. position in Teq

-$\vec{V}$: the A.R.D. absolute velocity in Teq.

They are computed using the Ring Laser Gyros I.M.U. measurements (supplied by the I.M.U. software, at high frequency in the platform trihedron Tp). As I.M.U. measurements are quantized with a LSB of 0,04572 m/s, a correction of half a LSB is done to prevent the navigation estimates from being biased.

The complete inertial navigation algorithm is based on a second order integration algorithm in frame Teq. Simulations have shown that a gravity model truncated at the J2 Earth potential harmonic, and a navigation frequency of 1,4 Hz, are enough to cope with the A.R.D. requirements (they induce an error lower than 0,2 m/s on the velocity at the jettisoning).

However, A.R.D. navigation has been implemented with a time mesh of 0,72 s.

Ballistic algorithm

The previous inertial algorithm is not adapted to the ballistic phase as the integration of I.M.U. defects during more than 5000 s would generate a very poor accuracy on the position and velocity estimates. Therefore, a specific algorithm that ignores I.M.U. measurements has been implemented. Ariane 5 studies have proven that such an algorithm is efficient as long as the average non-gravitational acceleration is smaller than the accelerometer bias.

Nevertheless, at this stage, such an algorithm would not take into account the forces due to control activity during the ballistic phase. As most thrusters activations are too brief to be detected by the I.M.U. (because of the quantization), an algorithm that would only use velocity increments during the control activation is not valid. A good compromise is to include an open-loop propulsion model to take thrusters activations into account.

The ballistic navigation algorithm is presented hereunder :

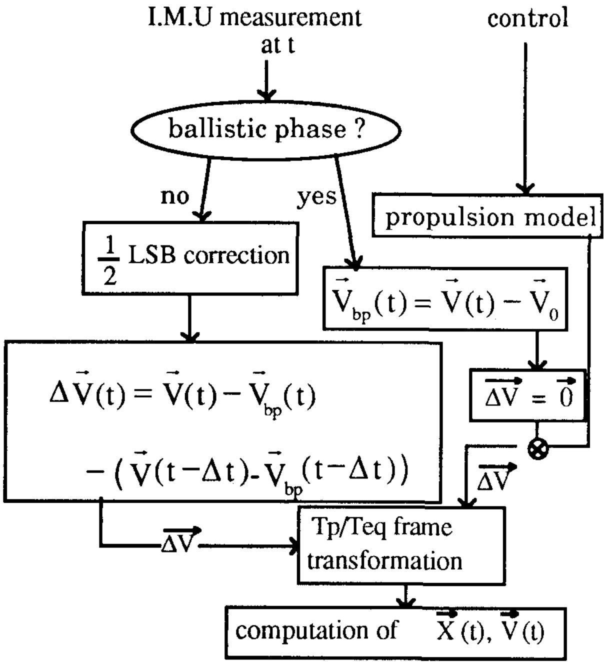
I.M.U measurement at t
control
ballistic phase ?
no
yes
propulsion model
$\frac{1}{2}$ LSB correction
$\vec{V}_{bp}(t) = \vec{V}(t) - \vec{V}_0$
$\vec{\Delta V} = \vec{0}$
$\Delta\vec{V}(t) = \vec{V}(t) - \vec{V}_{bp}(t) - (\vec{V}(t-\Delta t) - \vec{V}_{bp}(t-\Delta t))$
$\vec{\Delta V}$
$\vec{\Delta V}$
Tp/Teq frame transformation
computation of $\vec{X}(t)$, $\vec{V}(t)$

where :

$\vec{V_0}$ is the sum of velocity increments at the beginning of the ballistic phase,

$\vec{V_{bp}}$ is the sum of velocity increments observed during the ballistic phase.

Simulations have proven that the error bred by the residual drag in high atmosphere and the gravity model truncation error have a negligible impact on the navigation accuracy.

Moreover, this algorithm has been secured thanks to an alarm : if the I.M.U. measurements observed during the ballistic phase are abnormally high (because of a thruster leak for instance), the navigation switches back to an inertial algorithm.

G.P.S. measurements

G.P.S. measurements provide both position (altitude, longitude, latitude) and relative velocity (in the [North, West, Vertical] trihedron) with regard to the WGS84 geoide.

The G.P.S. measurements accuracy expected (with at least 4 satellites available) ranges from 176 to 400 m at 2 σ, in position, and 2 to 2.5 m/s at 2 σ, in velocity, depending on the altitude configuration.

G.P.S. measurements are to be used by the navigation algorithm during the orbital and the re-entry phases. They will be interrupted because of the black-out phenomenon, roughly between 90 and 42 km altitude.

For the sake of simplicity (because of the short delays of development) and robustness, it has been chosen to use G.P.S. measurements only to re-initialize the navigation (i.e. no sophisticated updating gains are needed). However, extensive simulations were performed to prove that such an updating model does not induce a major accuracy loss compared to a complete hybridation and fits the A.R.D. landing accuracy requirements (see chapter 4).

In order to improve the navigation robustness (in case of G.P.S. receiver failure, jamming...), G.P.S. measurements are taken into account only if :

- they fulfil the receiver auto-tests (at least 4 satellites available, measurement data verification),
- they are consistent with the current navigation estimates.

G.P.S. measurements are delivered with a maximum delay of 0,2 s. A specific processing has been developed to take this delay into account. Its implementation uses the measurement datation that is provided by the G.P.S. receiver.

D.D.A. pseudo-measurements

The Drag Derived Altitude (D.D.A.) is a pseudo-measurement of the altitude obtained thanks to aerodynamic and atmospheric models and the estimated non-gravitational acceleration. This pseudo-measurement is especially dedicated to update the navigation algorithm in case of a G.P.S. failure. In this chapter the principle, accuracy and implementation of D.D.A. measurements are described.

The A.R.D. longitudinal non-gravitational acceleration verifies :

$$\Gamma = \frac{1}{2\,m} \rho S V^2 C_A \qquad (2)$$

If one has an atmospheric model and assumes that atmospheric density evolution is locally exponential, one may write :

$$\rho = \rho_0 \exp\left(-H(z).z\right) \qquad (3)$$

where:

H(z) is the local atmospheric coefficient

ρ_0 is the sea level atmospheric density.

which leads to, locally around z (H constant) :

$$z = \frac{1}{H} \ln\left(\frac{2\,m\,\Gamma}{\rho_0 S V^2 C_A}\right) \qquad (4)$$

Thanks to this model, a "pseudo-measurement" of the altitude is available:

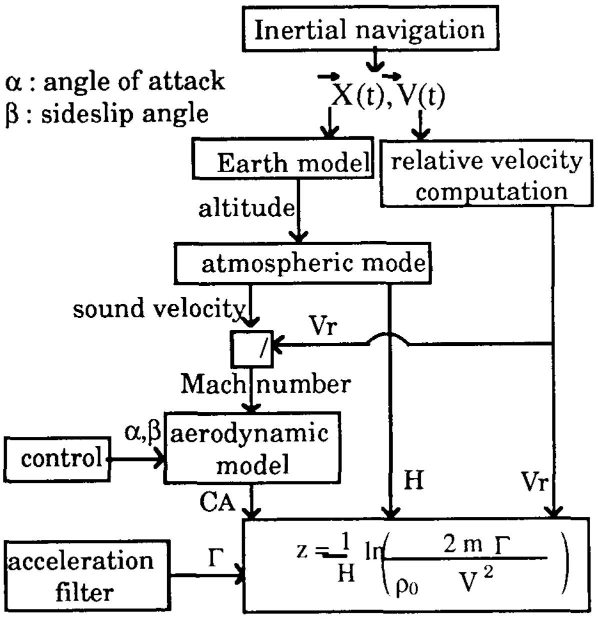
Inertial navigation
α : angle of attack
β : sideslip angle
$\vec{X}(t), \vec{V}(t)$
Earth model
relative velocity computation
altitude
atmospheric mode
sound velocity
Vr
/
Mach number
control
α,β
aerodynamic model
CA
H
Vr
acceleration filter
Γ
$z = \frac{1}{H} \ln\left(\frac{2\,m\,\Gamma}{\rho_0 \quad V^2}\right)$

The maximum error on the D.D.A. measurement is mainly due to the uncertainties on the atmospheric and aerodynamic models and the errors of the inertial navigation. It appears that D.D.A. measurements have the best accuracy between 70 and 30 km altitude : at lower altitudes the wind velocity is too important with regard to the A.R.D. velocity, and at higher altitudes no significant acceleration can be estimated.

The D.D.A. accuracy can be improved by carrying out a sequence of several D.D.A. measurements as described in figure 4.

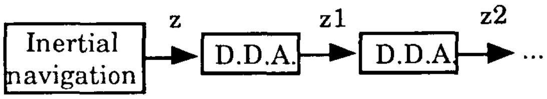
Inertial navigation
z
D.D.A.
z1
D.D.A
z2
...

Figure 4

Simulations have shown that the best D.D.A. measurement accuracy between 70 and 30 km altitude is ± 2,5 km. Figure 5 presents the evolution of D.D.A. accuracy with regard to the number of D.D.A. iterations. It shows that the optimal number of iterations to compute a D.D.A. measurement is 3 with respect to both computation burden and accuracy.

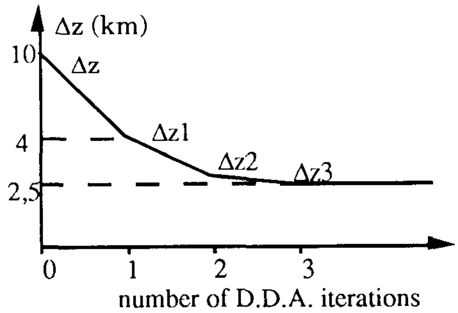

Figure 5

Finally, the D.D.A. enables a confinement of the altitude accuracy and requires very few operations to be computed.

For the D.D.A. updating implementation, a Kalman filter is chosen to compute the D.D.A. measurements updating gains. But, as A.R.D. computer limitations are not in favor of an on board Kalman gains computation (that would require to propagate the covariance matrix as described in reference ^{1}), pre-calculated gains have been determined to cover the envelope of possible trajectories.

These gains are computed on the nominal trajectory by propagating the covariance matrix of a state model including the position, the velocity and all the I.M.U. major defects. We

- a constant flux phase at the beginning of the reentry when the flux reaches its maximum values,
- a constant drag phase around the altitude of 40 km when the load factor is maximum.

They are chosen by taking margins from the specified limitations : about 35 % for the constant flux phase and about 30 % for the constant drag phase. These margins ensure the vehicle remains within the acceptable limits.

Additional profiles are defined to connect these profiles (cubic drag with respect to velocity phases) and for the terminal phase a linear profile of drag w.r.t velocity is chosen The reference trajectory may be then represented on figure 7:

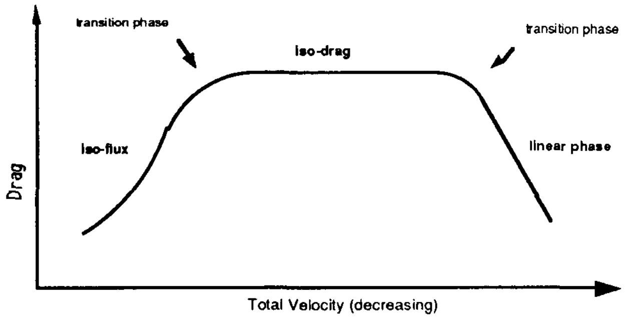

Figure 7

where, in fact the profiles are depending on the total velocity : $V_{tot} = \sqrt{V^2 + 2\,g\,z}$

GUIDANCE METHOD

The guidance principle is based on a reference trajectory tracking, typically on a drag versus velocity (or total velocity) profile.

With some approximations valid for small flight path angle re-entries (for ARD $\gamma_0=-3°$), one can formulate the open-loop control for a given drag-velocity profile. This is described below.

$$\text{Since}\quad D = \frac{1}{2}\rho S C_D V^2,\ \frac{\dot{D}}{D} = \frac{\dot{\rho}}{\rho} + 2\frac{\dot{V}}{V}$$

where $(\dot{\ })$ means derivative w.r.t time.

If we suppose a local isotherm atmosphere (with H_0 a constant atmospheric coefficient) :

$$\rho = \rho_0 e^{-\frac{z}{H_0}} \Rightarrow \frac{\dot{\rho}}{\rho} = -\frac{\dot{z}}{H_0} \Rightarrow \dot{z} = -H_0\left[\frac{\dot{D}}{D} + 2\frac{D}{V}\right]$$

$$\text{So}\quad \ddot{z} = -H_0\left[2\frac{\dot{D}}{V} + 2\frac{D^2}{V^2} + \frac{\ddot{D}}{D} - \left(\frac{\dot{D}}{D}\right)^2\right]$$

If we assume now the flight-path angle remains small during the reentry, and a spherical earth (constant earth radius) :

$$\dot{z} \approx V\gamma \Rightarrow \ddot{z} = V\dot{\gamma} + \dot{V}\gamma$$

$$\text{Since}\quad V\dot{\gamma} \approx L_v + \frac{V^2}{r} - g \quad (\text{with } L_v = L\cos\mu : \text{vertical lift}),$$

The reference projection of the lift-to-drag ratio, product of the lift-to-drag ratio and the cosine of the bank angle is then assessed as :

$$\overline{\left(\frac{L_v}{D}\right)} \approx \frac{g}{\overline{D}}\left(1 - \frac{V^2}{r\,g}\right) - H_0\frac{\ddot{\overline{D}}}{\overline{D}^2} + H_0\frac{\dot{\overline{D}}}{\overline{D}}\left(\frac{\dot{\overline{D}}}{\overline{D}^2} - \frac{3}{V}\right) - 4H_0\frac{\overline{D}}{V^2} \quad (6)$$

Ranging technique

This reference profile is updated at each guidance step : the algorithm computes the vehicle down range offset by comparing the current estimated range-to-go and the nominal one. The ranging logic consists in computing the magnitude of an updated drag reference profile in order to null this offset. With the approximation of small flight-path angle reentry, the correction of the current reference drag value is inversely proportional to the down range offset. A main advantage of this, is that drag derivatives w.r.t velocity admit the same correction from the nominal value (these derivatives are needed for open loop command computation). So, the desired command drag profile is written:

$$\overline{D} = \frac{1}{K}\overline{D_{ref}}$$

where the coefficient K is defined as :

$$K = \frac{\text{estimated current range-to-go}}{\text{tabulated nominal range-to-go}}$$

The range R, for small flight path angle, may be determinated using the formula:

$$R = -\int \frac{m\,V\,dV}{D}$$

but, actually, more complete models are used in the algorithm.

Enslavement law

In order to track the reference profile, the drag and the vertical velocity are enslaved. A classical P.I.D. (Proportional-Integrator-Derivated) control is used. The computed command is the vertical projection of the lift-to-drag ratio written :

$$\left(\frac{L_v}{D}\right)_c = \overline{\left(\frac{L_v}{D}\right)} + k_1\delta\left(D-\overline{D}\right) + k_2\,\delta\left(V_z-\overline{V_z}\right) + k_0\int \delta\left(D-\overline{D}\right) \qquad (7)$$

The gains k_0, k_1 and k_2 are computed by locating the three eigenvalues (one real and two complex) of the system. The final vertical steering variable, which is the absolute value of the commanded bank angle is finally obtained by the expression :

$$\cos\mu_c = \frac{\left(\frac{L_v}{D}\right)_c}{\left(\frac{L}{D}\right)} \qquad (8)$$

Lateral logic

Once this absolute value of the commanded bank angle is defined, its sign must be chosen: this is the purpose of the lateral guidance. The sign is determined in a way to keep the velocity direction within a pre-defined corridor around the line of sight: when this direction goes out the limits, a roll reversal is commanded. For the ARD mission, the corridor is defined constant from the beginning down to the end of the capsule reentry phase. A roll reversal is commanded when the estimated azimuth angle exceeds the deadband limits. The azimuth error is the angle $\Delta\psi$ defined as:

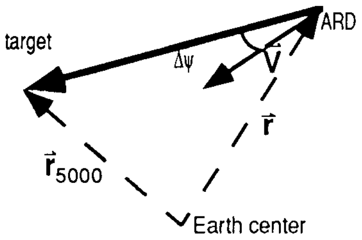

Figure 8

RE-ENTRY CONTROL LAW ALGORITHM

LINEAR MODEL OF THE VEHICLE BEHAVIOUR

At the control law time scale, the latitude, longitude, radius and the velocity are nearly constant and we may neglect the Earth rotation on the flight path angle and azimuth evolution. As yaw, pitch and roll axes are close to the principal axes of inertia of the capsule, the behaviour of the vehicle can be summarized with the following systems:

$$\begin{cases} \dot{\gamma} = \left(\frac{g}{V}-\frac{V}{r}\right)\cos\gamma + \frac{QS}{mV}\left(C_L\cos\mu - C_Y\sin\mu\right) \\ \dot{\chi} = \frac{QS}{mV\cos\gamma}\left(C_Y\cos\mu + C_L\sin\mu\right) \end{cases} \qquad (10)$$

$$\begin{cases} \dot{p} = \frac{QSl}{A}C_l - \frac{C-B}{A}qr_1 + \frac{U_l}{A} \\ \dot{q} = \frac{QSl}{B}C_m - \frac{A-C}{B}pr_1 + \frac{U_m}{B} \\ \dot{r}_1 = \frac{QSl}{C}C_n - \frac{B-A}{C}pq + \frac{U_n}{C} \end{cases} \qquad (11)$$

$$\begin{cases} \dot{\alpha} = \frac{q\cos\beta - p\cos\alpha\sin\beta - r_1\sin\alpha\sin\beta - \dot{\chi}\cos\gamma\sin\mu - \dot{\gamma}\cos\mu}{\cos\beta} \\ \dot{\beta} = p\sin\alpha - r_1\cos\alpha + \dot{\chi}\cos\gamma\cos\mu - \dot{\gamma}\sin\mu \\ \dot{\mu} = p\cos\alpha\cos\beta + \left(q-\dot{\alpha}\right)\sin\beta + r_1\sin\alpha\cos\beta + \dot{\chi}\sin\gamma \end{cases} \qquad (12)$$

The trimmed sideslip angle is not equal to zero because of the dissymmetries of the vehicle (CoG offset on the transversal axis) but its value remains low (lower than 3° in the case of the ARD). So it is licit to make the following assumption, in equation (12):

$$\begin{cases} \cos\beta = 1 \\ \sin\beta = 0 \end{cases} \qquad (13)$$

The objective of the control law is to stabilize the capsule closed to its trimmed position and to enable the lift orientation maneuver, in the direction defined by the guidance law. This maneuver is done with a angular rate less or equal to 15°/s. So the angular rates are low and we can neglect the gyroscopic torques in the model, with respect to the aerodynamic and RCS torques. With these approximations, equations (11) and (12) become:

- longitudinal behaviour

$$\begin{cases} \dot{\alpha} = q - \frac{QS}{mV}C_z + \left(\frac{g}{V}-\frac{V}{R}\right)\cos\gamma\cos\mu \\ \dot{q} = \frac{QSl}{B}C_m + \frac{U_m}{B} \end{cases} \qquad (14)$$

- lateral behaviour:

$$\begin{cases}\dot\beta = p\sin\alpha - r_1\cos\alpha + \dfrac{QS}{mV}C_Y + \left(\dfrac{g}{V} - \dfrac{V}{r}\right)\cos\gamma\,\sin\mu \\ \dot p = \dfrac{QSl}{A}C_l + \dfrac{U_l}{A} \\ \dot r_1 = \dfrac{QSl}{C}C_n + \dfrac{U_n}{C} \\ \dot\mu = p\cos\alpha + r_1\sin\alpha + \dfrac{QStg\gamma}{mV}\left(C_Y\cos\mu + C_L\sin\mu\right)\end{cases} \qquad (15)$$

Then we linearize the systems (14) and (15) at the desired value α_c, β_c, μ_c, p_c, q_c, r_{1c} . For the lateral motion (15), in order to decouple lateral modes, we consider the angular rates $\bar p$ and $\bar r$ expressed on the velocity trihedron:

$$\begin{cases}\bar p = p\cos\alpha + r_1\sin\alpha \\ \bar r = p\sin\alpha - r_1\cos\alpha\end{cases} \qquad (16)$$

We introduce the offset variables:

$$\begin{cases}\Delta\alpha = \alpha - \alpha_c \\ \Delta\beta = \beta - \beta_c \\ \Delta\mu = \mu - \mu_c\end{cases} \qquad \begin{cases}\Delta\bar p = \bar p - \bar p_c \\ \Delta q = q - q_c \\ \Delta\bar r = \bar r - \bar r_c\end{cases} \qquad (17)$$

and the pitch (in body trihedron) coefficients:

$$\begin{cases}Z_\alpha = -\dfrac{Q\,S}{m\,V}C_{L\alpha} \\ M_\alpha = \dfrac{Q\,S\,l}{B}C_{m,\alpha} \\ M_q = \dfrac{Q\,Sl^2}{B\,V}C_{m,q}\end{cases} \qquad (18)$$

also the yaw (in velocity trihedron) coefficients:

$$\begin{cases}Y_\beta = -\dfrac{QS}{m\,V}C_{Y\beta} \\ N_\beta = -\dfrac{QSl}{C}\left(C_{n\beta}\cos\alpha - \dfrac{C}{A}C_{l\beta}\sin\alpha\right) \\ N_{\bar r} = \dfrac{QSl^2}{V}\left(\dfrac{C_{nr_1}}{C}\cos^2\alpha + \dfrac{C_{l,p}}{A}\sin^2\alpha\right) \\ N_{\bar p} = \dfrac{QSl^2}{V}\left(-\dfrac{C_{nr_1}}{C} + \dfrac{C_{l,p}}{A}\right)\sin\alpha\cos\alpha \\ U_{\bar r} = \dfrac{U_l}{A}\sin\alpha - \dfrac{U_n}{C}\cos\alpha\end{cases} \qquad (19)$$

and the roll (in velocity trihedron) coefficients:

$$\begin{cases}L_\beta = \dfrac{QSl}{A}\left(C_{l\beta}\cos\alpha + \dfrac{A}{C}C_{n\beta}\sin\alpha\right) \\ L_{\bar p} = \dfrac{QSl^2}{V}\left(\dfrac{C_{l,p}}{A}\cos^2\alpha + \dfrac{C_{nr_1}}{C}\sin^2\alpha\right) \\ L_{\bar r} = \dfrac{QSl^2}{V}\left(\dfrac{C_{l,p}}{A} - \dfrac{C_{nr_1}}{C}\right)\sin\alpha\cos\alpha \\ U_{\bar p} = \dfrac{U_l}{A}\cos\alpha + \dfrac{U_n}{C}\sin\alpha\end{cases} \qquad (20)$$

We can neglect the effect of the lift rotation on the evolution of the sideslip angle and the bank angle. The lateral model can be written:

$$\begin{bmatrix}\Delta\dot\beta \\ \Delta\dot{\bar r} \\ \Delta\dot\mu \\ \Delta\dot{\bar p}\end{bmatrix} = \begin{bmatrix}Y_\beta & 1 & 0 & 0 \\ N_\beta & N_{\bar r} & 0 & N_{\bar p} \\ 0 & 0 & 0 & 1 \\ L_\beta & L_{\bar r} & 0 & L_{\bar p}\end{bmatrix}\begin{bmatrix}\Delta\beta \\ \Delta\bar r \\ \Delta\mu \\ \Delta\bar p\end{bmatrix} + \begin{bmatrix}0 \\ U_{\bar r} \\ 0 \\ U_{\bar p}\end{bmatrix} \qquad (21$$

The longitudinal model is described by:

$$\begin{bmatrix}\Delta\dot\alpha \\ \Delta\dot q\end{bmatrix} = \begin{bmatrix}Z_\alpha & 1 \\ M_\alpha & M_q\end{bmatrix}\begin{bmatrix}\Delta\alpha \\ \Delta q\end{bmatrix} + \begin{bmatrix}0 \\ 1/B\end{bmatrix}U_m \qquad (22)$$

So the model which describes the pitch mode, is linear. The lateral model, which describes the yaw and roll modes, is also linear but the yaw and roll modes are coupled. Nevertheless, the coupling terms are not the main effect on the lateral behaviour of the vehicle (small damping terms), and so they can be neglected. Hence, we obtain two second order uncoupled models to describe the yaw and roll modes:

$$\begin{bmatrix}\Delta\dot\beta \\ \Delta\dot{\bar r}\end{bmatrix} = \begin{bmatrix}Y_\beta & 1 \\ N_\beta & N_{\bar r}\end{bmatrix}\begin{bmatrix}\Delta\beta \\ \Delta\bar r\end{bmatrix} + \begin{bmatrix}0 \\ U_{\bar r}\end{bmatrix} \qquad (23)$$

$$\begin{bmatrix}\Delta\dot\mu \\ \Delta\dot{\bar p}\end{bmatrix} = \begin{bmatrix}0 & 1 \\ 0 & L_{\bar p}\end{bmatrix}\begin{bmatrix}\Delta\mu \\ \Delta\bar p\end{bmatrix} + \begin{bmatrix}0 \\ U_{\bar p}\end{bmatrix} \qquad (24)$$

CONTROL LAW

Control Law Structure

The design of the pitch, yaw and roll control law is done with a classical method of state observer and state feeedback control.

We want the command such that the 3 modes (pitch, yaw and roll) remain almost uncoupled. So the structure of the control law is given by:

$$\begin{cases} U_m = K_\alpha(\alpha - \alpha_c) + K_q(q - q_c) \\ U_{\bar{r}} = K_\beta(\beta - \beta_c) + K_{\bar{r}}(\bar{r} - \bar{r}_c) \\ U_{\bar{p}} = K_\mu(\mu - \mu_c) + K_{\bar{p}}(\bar{p} - \bar{p}_c) \end{cases} \tag{25}$$

The gains feedback are onboard computed by locating the eigenvalues of the model (22), (23) and (24) in order to have the desired closed loop behaviour (pulsation and damping ratio) for each mode.

The aerodynamic coefficients C_L, C_D, $C_{m,\alpha}$, $C_{n,\beta}$ etc... which define the model are computed onboard using an aerodynamic behaviour model of the vehicle, as a function of the Mach number altitude, and total angle of attack.

At last, we compensate the gyroscopic torques which have been neglected to obtain the model. The expression of the pitch, yaw and roll RCS torques is then:

$$\begin{cases} U_m = K_\alpha(\alpha - \alpha_c) + K_q(q - q_c) + (A-C)\, p\, r_1 \\ U_n = C\left(-U_{\bar{r}} \cos\alpha + U_{\bar{p}} \sin\alpha\right) + (B-A)\, p\, q \\ U_l = A\left(-U_{\bar{r}} \sin\alpha + U_{\bar{p}} \cos\alpha\right) + (C-B)\, q\, r_1 \end{cases} \tag{26}$$

Commanded Attitudes and Angular Rates

The commanded angular rates p_c, q_c, and r_{1c}. are obtained expressing that when the vehicle has reached its commanded attitude, the angular rate of the vehicle trihedron is equal to the angular rate of the aerodynamic trihedron.

The commanded angle of attack and sideslip angle α_c, β_c, are the trimmed ones which are *a priori* unknown. As we know that the vehicle flies at its trimmed angle of attack and sideslip angle, we may use the estimated α_m and β_m which are a good estimation of the trim angles, provided we filter the high components frequency of these two signals. So the dynamic of α_c and β_c is a low frequency dynamic, and then it does not spoil the dynamic of the state feedback.

The guidance order is the aerodynamic bank angle while the state variable is the bank angle. The offset between these 2 bank angles is due to the fact that the body plan (X, Z) is not a symmetry plan, mainly due to a CoG offset on the Y axis.

Obviously, the offset between the 2 bank angles has a low frequency dynamic. Also, in the phase where the guidance is efficient, the RCS induced forces are small with regards to the aerodynamic forces and the wind velocity is negligible with regards with the capsule velocity $\vec{V}$. Hence, if we denote $\vec{\Gamma}_m$ the non gravitationnal acceleration obtained with the accelerometers measurements, we can consider that the acceleration due to the lift is:

$$\vec{\Gamma}_{m,L} = \vec{\Gamma}_m - \left(\vec{\Gamma}_m . \vec{V}\right)\vec{V} \tag{27}$$

The direction of this acceleration enables us to have a measurement of the offset $\delta\mu_c = \mu_{a,m} - \mu_m$

The way to control the aerodynamic bank angle is to filter this offset measurement between the aerodynamic and geometric bank angle with a high time constant filter and then, using this estimated offset, to translate the guidance aerodynamic bank angle order into a geometric bank angle order.

Opening Duration of the RCS Thrusters

The opening duration of the RCS's thrusters is function of the RCS torques computed by the control law and the RCS's architecture. Each thruster can achieve a thrust which depends on the inner tank pressure (blow-down system). An onboard model allows to compute the inner tank pressure and the thrust level.

The RCS is composed of seven thrusters which can achieve, in a first approximation, pure torques in the vehicle axes. So each opening thruster duration is easily computed to preserve, on each axis, the torque impulse computed by the command law. If a duration is lower than T_{MIB}, it is set equal to zero.

Implementation

- angle of attack and sideslip modes

As the trimmed values of the angle of attack and sideslip angle are unknow, the natural way to adjust the gains feedback is to impose the closed loop pulsation equal to the opened loop pulsation in order to make the gains K_α and K_β equal to zero. Then the only parameter to adjust the control law are the damping ratios. But this natural way is not the best one from a stability margin point of view, and more precisely for the time delay margin . Actually, to improve the delay margin one has to reduce the closed loop pulsation. The smaller the closed loop pulsation is, the less sensitive the system towards the delay in the loop is and so, the better the delay margin is.

- roll mode

The roll closed loop is adjusted, in order to respect the guidance specification, of a time response lower than 3s.

STATE ESTIMATOR

The function of the state vector estimator is to build the state vector (α, q, β, r, p, μ).

The state vector estimator is based on the classical Kalman scheme. Using simplification assumptions, the systems can be easily integrated, and we obtain an analytical expression of the prediction.

We denote $X_{k/k}$ the estimation of X ($X\in\{p, q, r, \alpha, \beta, \mu\}$)at the step k et $X_{k+1/k}$ its prediction at the step k+1. The available measurements at the date k+1 to update the prediction of the state variable prediction $X_{k+1/k}$ are the attitude measurements, from which we can derive pseudo-measurements of the angle of attack $\alpha_{m,k+1}$, the sideslip angle $\beta_{m,k+1}$ and the geometric bank angle $\mu_{m,k+1}$.

With the approximation:

- $\cos\beta \approx 1$,
- influence of $(q - \dot{\alpha}) \sin\beta$ may be neglected,

And if there is no torque and no force, we get:

$$\begin{cases} q = \dot{\alpha} - \dot{\mu} \sin\beta \\ p = \dot{\beta} \sin\alpha + \dot{\mu} \cos\alpha \\ r = -\dot{\beta} \cos\alpha + \dot{\mu} \sin\alpha \end{cases} \quad (28)$$

One can show that in order to update the prediction $q_{k+1/k}$ of the pitch rate one needs only a gain on the pseudo-measurement $\alpha_m + \mu_m \sin\beta$.
In the same way, to update the prediction $r_{k+1/k}$ (resp. $p_{k+1/k}$) of the yaw (resp. roll) rate one needs a gain on the pseudo-measurement $-\beta_m \cos\alpha + \mu_m \sin\alpha$ (resp. $\beta_m \sin\alpha + \mu_m \cos\alpha$). Hence, the update of the prediction may be reduced to the simple model:

$$\begin{cases} p_{k+1/k+1} = p_{k+1/k} + k_p\left((\beta_{m,k+1} - \beta_{k+1/k})\sin\alpha + (\mu_{m,k+1} - \mu_{k+1/k})\cos\alpha\right) \\ q_{k+1/k+1} = q_{k+1/k} + k_q\left((\alpha_{m,k+1} - \alpha_{k+1/k}) + (\mu_{m,k+1} - \mu_{k+1/k})\sin\beta\right) \\ r_{k+1/k+1} = r_{k+1/k} + k_r\left(-(\beta_{m,k+1} - \beta_{k+1/k})\cos\alpha + (\mu_{m,k+1} - \mu_{k+1/k})\sin\alpha\right) \\ \alpha_{k+1/k+1} = \alpha_{k+1/k} + k_\alpha(\alpha_{m,k+1} - \alpha_{k+1/k}) \\ \beta_{k+1/k+1} = \beta_{k+1/k} + k_\beta(\beta_{m,k+1} - \beta_{k+1/k}) \\ \mu_{k+1/k+1} = \mu_{k+1/k} + k_\mu(\mu_{m,k+1} - \mu_{k+1/k}) \end{cases} \quad (29)$$

where the update is entirely defined with 6 gains.

RESULTS

The GNC algorithms have been validated, using both a very complete 6 dof numerical simulator and a real time/real elements simulator (derived from Ariane 5 ISF simulator), with an extensive set of simulations; in order to show global performances of the GNC algorithms, we provide some Monte -Carlo simulation results. The uncertainties taken into account are:

-ARD injection point (position and velocity),
- aerodynamic model (torques and forces),
-mass model,
-RCS performances (Isp, delay, pressure),
-atmosphere model (temperature, density, wind, wind gradients and gusts)
-IMU defects (biases, scale factors, non orthogonalities, alignement error, ...)
-GPS measurement (bias, delay, noise, failure modes, availability).

We may summarize the main results in the following table:

	mean value	standart deviation	min. value	max. value
ϕmax (kW/m2)	960	20	900	1000
Nmax (g)	4.5	0.004	4.4	4.5
lon.offset (km)	15	17	-25	+60
lat. offset (km)	10	16	-40	+50

The longitude and lattitude offset show a splash-down accuracy much better than the objective and the constraints are well controlled.

For one of these simulations, we provide a set of figures related to the guidance function: altitude (Fig. 9), velocity (Fig. 10) and flight path angle (Fig. 11) compared to the one on the updated profile. We present the evolution of the heat flux (Fig. 12), the load factor (Fig. 13), the commanded bank angle (Fig. 14) and drag profile (Fig. 15). The guidance function is desactivated below Mach 2 because of its inefficiency at low Mach number, and the bank angle is set to zero.

Then the figure 16 to 21 present the evolution of the control state vector For the angle of attack (AOA), side slip angle (SSA) and the bank angle we compare the actual value with the commanded one. The bank angle is well controlled to the value commanded by the guidance. Between the real and commanded AOA and SSA there is a bias due to the wind, but nevertheless the real AOA and SSA are well controlled to their trimmed value. The transient phase on the AOA and pitch rate at the end of the simulation is the consequence of the opening of the chutes.

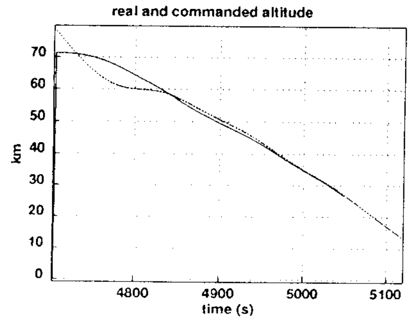

Figure 9

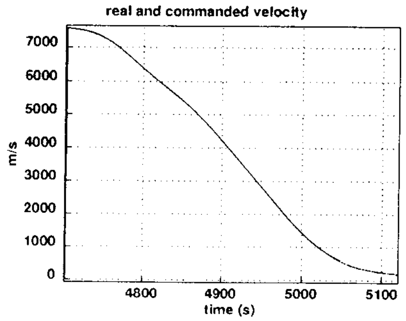

Figure 10

Valeur estimée ········· Valeur Réelle

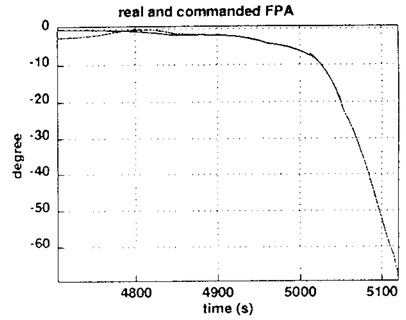

Figure 11

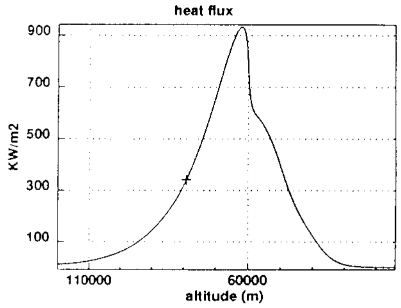

Figure 12

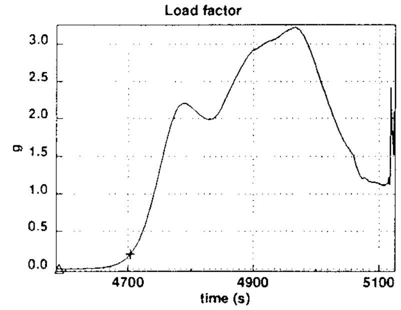

Figure 13

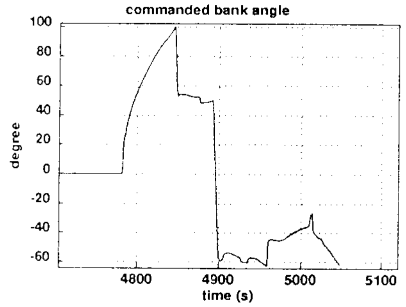

Figure 14

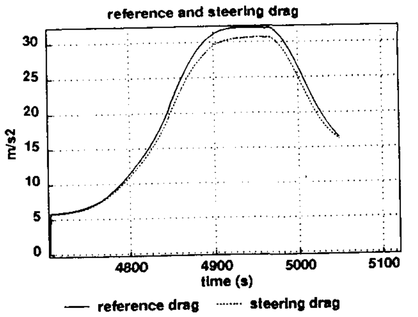

Figure 15

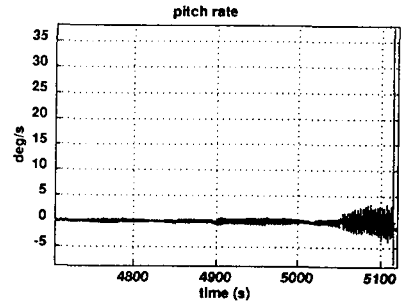

Figure 19

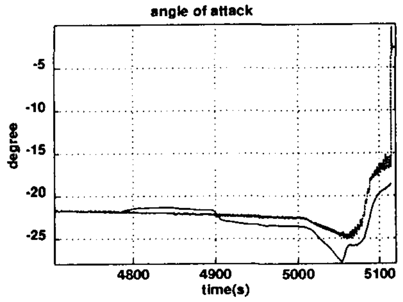

Figure 16

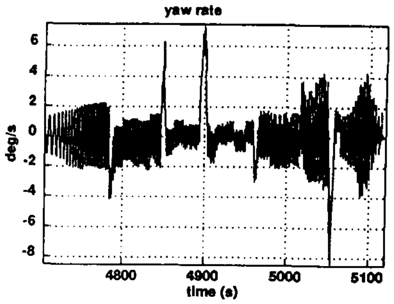

Figure 20

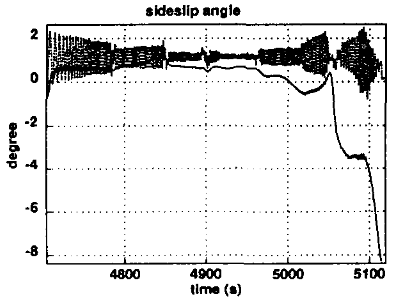

Figure 17

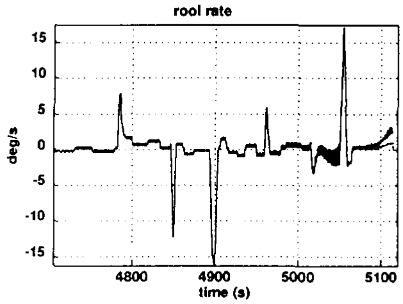

Figure 21

——— Valeur Commandée ············ Valeur Réelle

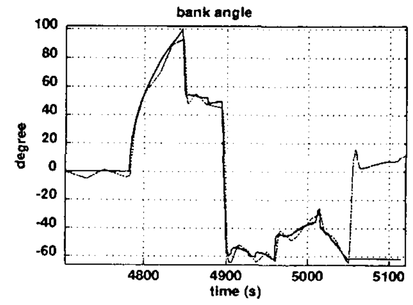

Figure 18

REFERENCES

[1] N. M. Montez, M. F. Madden, "Space Shuttle orbiter descent navigation", AIAA, CP 82-1563, 1982.

[2] Harpold, J.C., Graves, C.A., "Shuttle Entry Guidance", Journal of the Astronautical Sciences, Vol. 27, N° 3, 1979, pp. 239-268.

[3] L. Bouaziz, P. Delaux, "Navigation Algorithm of the ARD", AIAA GNC-96-3754, 1996.

[4] G. Pignie, L. Bouaziz, P. Delaux, H. Kebci, F. Trinquard, "Parachute Opening Triggering Algorithm of the ARD", AIAA GNC-96-3755, 1996.

REENTRY AND AEROASSISTED TRANSFER TRAJECTORY OPTIMAL CONTROL: THE GRADIENT RESTORATION ALGORITHM

M. Belló Mora
Grupo de Mecánica del Vuelo SA, Isaac Newton 11, PTM Tres Cantos, 28760 Madrid, Spain
Tel:+34-1-807 2139, Fax:+34-1-807 21 99, e-mail:mbello@gmv.es

G. Dutruel-Lecohier
WMM/ESTEC(ESA), P.O. Box 299, 2200 AG Noordwijk, The Netherlands
Tel:+31-71-565 3760

1. ABSTRACT

This paper presents the solution of the atmospheric re-entry and aeroassisted transfer trajectory optimisation by using a very robust indirect optimal control method: the Gradient Restoration algorithm. This method (developed by A. Miele and the staff of the Aero-Astronautics Group of Rice University in Houston) is a very robust algorithm to solve the multiple point boundary value problem associated to the optimal control problem.

A very flexible software tool has been generated to solve all type of reentry and aeroassisted transfer optimisation problems. This program has been integrated in the RATT (Reentry and Atmospheric Transfer Trajectories) software tool which has been developed under ESA Contract (ESTEC).

Solutions for atmospheric re-entry and aeroassisted transfer are presented. The performance of this optimisation method is demonstrated by comparison with with direct control programs: TOP, TROPIC and PROMIS.

2. INTRODUCTION

The Re-entry and Atmospheric Transfer Trajectories (RATT) software is an integrated flexible S/W assembly for simulation, optimisation and covariance analysis of re-entry and atmospheric transfer trajectories. This software tool has been developed from end'89 until mid'95 by an industrial team leaded by GMV with Dornier and MATRA Marconi Space acting as subcontractors under ESA contract (WMM/ESTEC).

Each RATT package is an independent program. The Common User Interface (CUI) as the overall shell allows a menu-guided communication between the operator and the flight dynamics S/W, which includes the following sub-assemblies:

- **3 degrees of freedom Flight Dynamics**
- **6 degrees of freedom Flight Dynamics**
- **Trajectory Optimisation**
- **Sensitivity and Covariance Analysis**

The trajectory optimisation part of the previous version of RATT comprises three different methods:

- A non-linear programming optimisation TOP (NPSOL, derived from the NAG library) together with a direct collocation method (Hermite polynomials) for the dynamic solver.
- The TROPIC, and,
- The PROMIS optimisation packages, produced by DLR Oberpfaffenhofen.

Those packages are based on direct methods which treats the optimisation problem in the discrete time domain. In order to complement the trajectory optimisation module, an indirect optimal control method has been implemented by GMV to solve the problem in the continuous time domain. The selected method is the Gradient Restoration algorithm.

3. OPTIMAL CONTROL METHODS

There are two types of optimal control methods:

- **Indirect Methods**: they are based in the calculus of variations approach (or the Pontryagin's principle) to the optimal control problem. They introduce an adjoint vector and the Hamiltonian, leading to a two point boundary value problem (TPBVP), where the control variables are eliminated by means of an optimality condition. The consideration of path constraints

Proceedings Third International Conference on Spacecraft Guidance, Navigation and Control Systems, ESTEC, Noordwijk, The Netherlands, 26-29 November 1996, ESA SP-381 (February 1997)

leads to Multiple Point Boundary Value Problem (MPBVP).

An interesting indirect method was presented by Miele, Pritchard and Damoulakis [11] in 1970, it is called the Sequential Gradient Restoration Algorithm. This is a very robust method which is extended in several publications by Miele in 1973 [19], Henning and Miele in 1973 [6], Miele, Damoulakis, Cloutier and Tietze in 1974 and Miele again in 1975 [12]. The implementation of general boundary conditions is published by Gonzalez and Miele in 1978 [3], and the conjugate gradient version is presented by Heideman and Levy in 1975 [5]. This algorithm has been extensively used in aerospace vehicle problems, in particular Miele, Mohanty, Venkataraman and Kuo [13] and [14] have applied the Gradient Restoration in 1982 to solve minimax problems. Optimal aeroassisted transfer trajectories have been computed by Miele and Venkataraman [15] in 1984, Miele and Basapur [16] in 1985 and Miele, Basapur and Lee [17] in 1986.

- **Direct Methods**: those algorithms avoid the transformation to the two point boundary value problem, they use Non Linear Programming Techniques (NLP solvers or constrained parameter optimisation) on the original problem. The direct methods perform a discretization of the control variables or both control and state variables and compute directly the state variables and hence the performance index and the constraints. The problem is then stated as a constrained minimisation and standard parameter optimisation routines can be applied.

  One of the most important direct methods is the collocation. In this algorithm both control and state variables are parameterised in the discrete grid of time above presented. Hargraves and Paris proposed in 1987 [4] to approximate the state vector by piecewise Hermite interpolation by cubic polynomials. This method, extended by C. Jänsch [10], is the base of the software package TROPIC. The trajectory optimisation program (TOP) which is included in the actual version of the Reentry and Atmospheric Transfer Trajectories (RATT) is also based in the direct collocation method (S. Jallade [8]). A direct method was developed by Bock and Plitt in 1984 [2] and extended by Schnepper [9], it introduces a multiple shooting structure into the parameterised optimal control problem. An extension of this algorithm is the base of the program PROMIS which has been successfully applied to aerospace trajectory optimisation.

The direct optimisation programs TOP, TROPIC and PROMIS have been implemented in the original RATT software for the 3 DoF reentry and aeroassisted transfer trajectories. The obtained trajectories are in general sub-optimal due to the discretization. The global aim of this study is the introduction into the RATT software of a complementary 3 DoF trajectory optimisation module based on indirect methods that leads to continuous optimal trajectories.

4. SELECTION OF THE INDIRECT OPTIMAL CONTROL METHOD

Taking into account that our objective is the solution of the reentry and aeroassisted transfer problem for a wide range of different cases (several cost functions and constraints), the efficiency parameters which play an important role in this selection process are the robustness of the algorithm, the "setup time" and the capability of numerical generation of the switching structure information. The Gradient Restoration algorithm has above defined characteristics and it has been successfully used for the optimisation of Hermes type reentry trajectories in reference [1]. The Gradient-Restoration Algorithm has in addition the following advantages:

- It presents the most general formulation:
  - The functional to be minimised contains:
    - An integral part over the path (integrated heat rate).
    - A function of the initial state vector (de-orbiting manoeuvre).
    - A function of the final state vector (cross or down range).
  - The initial and final state vector may have:
    - A given value (altitude and velocity at the TAEM).
    - A free value (TAEM heading angle).
    - Satisfy a set of relations (latitude and longitude at the entry point).
  - All kind of constraints may be applied by using suitable transformations:
    - State inequality constraints.
    - State equality constraints.
    - Problems with bounded control.
    - Problems with bounded state.
- The Gradient-Restoration is an algorithm suitable to be implemented in a modular way. The optimal control modules are independent of the functional modules which define each particular problem. This allows many different problems to be treated with a minimum change in

the functional modules. Maximum down range, cross range or minimum integrated heating over the trajectory can be computed with a small change in the cost function module.

- An important property of this algorithm is that it produces a sequence of feasible suboptimal solutions; the functions obtained at the end of each cycle satisfy the constraints to a predetermined accuracy. Therefore, the values of the functional corresponding to any two elements of the sequence are comparable [3].
- The Gradient-Restoration Algorithm has been extended by adequate transformations techniques to solve minimax problems [13] and [14]; in particular, approximate solutions to minimax optimal control problems for aeroassisted orbital transfer have been computed using this technique [15], [16] and [17].

The drawback of this algorithm is the slow convergence rate close to the final solution. The tolerance in the optimality penalisation function must be carefully selected in order to avoid the computation of a very large number of cycles.

5. CONSTRAINED OPTIMAL CONTROL PROBLEM

Let t denote the independent variable, and x(t), u(t) and P the dependent variables. The time t is a scalar, the state x(t) is a vector of dimension n, the control u(t) is a vector of dimension m and the parameter P is a vector of dimension p. The state x(t) is partitioned into vectors y(t) and z(t), defined as follows: y(t) is a vector of dimension a including those components of the state that are prescribed at the initial point, and z(t) is a vector of dimension b including those components of the state that are not prescribed at the initial point (a + b = n).

With the above descriptions, the optimal control problem with general boundary conditions may be stated as follows:

Minimise the functional

$$I = \int_0^1 f(x,u,P,t)dt + [h(z,P)]_0 + [g(x,P)]_1 \quad (1)$$

with respect to the state x(t), the control u(t), and the parameter P which satisfy the differential constraints :

$$\dot{x} = \phi(x,u,P,t), \qquad 0 \le t \le 1 \qquad (2)$$

the boundary conditions

$$y(0) = given, \qquad (3)$$

$$[w(z,P)]_0 = 0, \qquad (4)$$

$$[\psi(x,P)]_1 = 0, \qquad (5)$$

and the non-differential constraints

$$S(x,u,P,t) = 0, \qquad 0 \le t \le 1 \qquad (6)$$

In the above equations I, f, g, an h are scalar, the function ϕ is an n-vector, the function w is a c-vector, the function ψ is a q-vector and the function S is a k vector.

From calculus of variations, the problem can be recast as that of minimising the augmented functional

$$J = I + L \qquad (7)$$

subject to the constraints defined in equation 2 to 6. The functional L is defined as

$$L = \int_0^1 [\lambda^T(\dot{x} - \phi) + \rho^T S]dt + (\sigma^T w)_0 + (\mu^T \psi)_1 \quad (8)$$

where $\lambda(t)$ is an n-vector variable Lagrange multiplier, $\rho(t)$ is a k-vector variable Lagrange multiplier, σ is a c-vector constant Lagrange multiplier and μ is a q-vector constant Lagrange multiplier. Integrating by parts, the functional may be expressed as

$$\begin{aligned} L &= \int_0^1 (\dot{\lambda}^T x - \lambda^T \phi + \rho^T S)dt + \\ &\quad (-\lambda^T x + \sigma^T w)_0 + (\lambda^T x + \mu^T \psi)_1 \qquad (9) \end{aligned}$$

The functions x(t), u(t), P and the multipliers $\lambda(t)$, $\rho(t)$, σ and μ must satisfy the feasibility equations 2 to 6, and the following necessary conditions for optimality:

$$\dot{\lambda} - f_x + \phi_x \lambda - S_x \rho = 0, \qquad 0 \le t \le 1 \quad (10)$$

$$f_u - \phi_u \lambda + S_u \rho = 0, \qquad 0 \le t \le 1 \quad (11)$$

$$w(z,P)_0 = 0, \qquad (12)$$

$$\begin{aligned} &\int_0^1 (f_p - \phi_p \lambda + S_p \rho)dt + \\ &(h_p + w_p \sigma)_0 + (g_p + \psi_p \mu)_1 = 0 \qquad (13) \end{aligned}$$

$$(-\gamma + h_z + w_z)_0 \;=\; 0, \tag{14}$$

$$(\lambda + g_x + \psi_x \mu)_1 \;=\; 0. \tag{15}$$

As the state vector x(t) is partitioned into an a-vector y(t) and a b-vector z(t), the multiplier vector λ(t) is partitioned into an a-vector β(t) and a b-vector γ(t).

The differential system above defined is in general nonlinear, approximated methods are employed to find a solution iteratively; if the norm squared of a vector v is defined as

$$N(v) = v^T v \tag{16}$$

then, the constraints error R can be written as

$$\begin{aligned} R \;=\; & \int_0^1 N(\dot{x} - \phi)dt + \int_0^1 N(S)dt \\ & + N(w)_0 + N(\psi)_1, \end{aligned} \tag{17}$$

and the error in the optimality conditions Q is given by

$$\begin{aligned} Q \;=\; & \int_0^1 N(\dot{\lambda} - f_x + \phi_x \lambda - S_x \rho)dt + \\ & \int_0^1 N(f_u - \phi_u \lambda + S_u \rho)dt + \\ & N[\int_0^1 (f_p - \phi_p \lambda + S_p \rho)dt + \\ & (h_p + w_p \sigma)_0 + (g_p + \psi_p \mu)_1] + \\ & N(-\gamma + h_z + w_z \sigma)_0 + \\ & N(\lambda + g_x + \psi_x \mu)_1 \end{aligned} \tag{18}$$

an approximated solution is obtained if

$$R \leq \varepsilon_1, \qquad Q \leq \varepsilon_2 \tag{19}$$

where ε_1 and ε_2 are small, preselected numbers.

6. GRADIENT RESTORATION ALGORITHM

The Gradient Restoration algorithm has been developed by A. Miele and the staff of the Aero-Astronautics Group of Rice University, Houston (Texas). The technique is a sequence of two-phase cycles, composed of a gradient phase and a restoration phase [11]. The gradient phase involves one iteration and is designed to decrease the value of a functional, while the constraints are satisfied to first order . The restoration phase involves one or more iterations and is designed to force constraint satisfaction to a predetermined accuracy, while the norm squared of the variations of the control, the parameter, and the missing components of the initial state is minimised [12].

The stepsize of the gradient phase is determined by a one-dimensional search on the augmented functional J, while the stepsize of the restoration phase is obtained a one-dimensional search on the constraint error R. A time normalisation is used in order to simplify the numerical computation. If the actual final time τ is free, it is regarded as the first component of the parameter vector P to be optimised.

The gradient phase is only started when the error in the optimality conditions Q is bigger than the preselected number ε_2; it involves one iteration and is designed to decrease the value of the functional I or the augmented functional J, while the constraints are satisfied to first order.The restoration phase is started only when the constraint error R is bigger than ε_1; it involves one or more iterations, each designed to decrease the constraint error R, while the norm squared of the variations of the control u(t), and the parameters P and z(0) is minimised.The restoration phase is terminated whenever the constraints are satisfied to a predetermined accuracy given by ε_1.

A complete gradient-restoration cycle is designed so that the value of the functional I decreases, while the constraints are satisfied to the required accuracy both at the beginning and at the end of the cycle. Finally, the algorithm is terminated whenever inequations 19 are satisfied simultaneously.

Each gradient or restoration phase involves the solution of a simplified boundary value problem which is solved by using a forward integration scheme in combination with the method of particular solutions [18].

The present algorithm can be started with nominal functions x(t), u(t) and P satisfying 3 and violating none, some or all of conditions 2 and 4 - 6. If the nominal functions are such that the constraint penalisation R is bigger than the preselected limit, the algorithm starts with a restoration phase, otherwise a gradient phase is started.

At the end of a gradient phase of any cycle, the constraint error R must be computed, if it is bigger than the selected tolerance, a restoration phase is started. Otherwise, the restoration phase is bypassed, and the next gradient phase of the algorithm is started.

After a restoration phase is completed, the functional I is computed, if it is less than the previous phase, the next cycle of the sequential gradient-restoration algorithm is started. If not, the stepsize of the previous gradient phase is bisected, and a new restoration phase is started.

For the restoration phase taken individually, convergence is achieved whenever the penalisation function R is less than the selected tolerance ε_1. For the sequential gradient-restoration algorithm taken as a whole, convergence is achieved whenever inequations 19 are satisfied simultaneously.

7.FORMULATION OF THE REENTRY AND AEROASSISTED TRANSFER TRAJECTORY OPTIMISATION PROBLEM

The optimisation problem for the Reentry and Aeroassisted Orbit Transfer trajectories may be defined as follows: given an initial orbit and a prescribed final conditions, obtain the adequate de-orbit and re-orbit parameters, angle of attack (α) and bank angle (μ) profiles between the entry and exit point of the sensible atmosphere such that a given cost function is minimised and a set of path and boundary constraints are satisfied.

The resulting trajectory shall satisfy the dynamics equations of motion of a vehicle within the atmosphere of a rotating celestial body.

The optimal angle of attack and bank angle profiles are only required in the trajectory section within the limits of the sensible atmosphere. The optimal control problem is formulated then between the atmospheric entry point and the final point for reentry or the atmospheric exit point for the AAOT case.

State, Control and Parameter Variables

The independent variable is the normalised time χ. The classical variables of the state vector (dimension 6) are the following:

- 3 for the position:

  r radius

  θ_L longitude

  ϕ_L latitude

- and 3 for the velocity:

  V velocity modulus,

  γ path angle, i.e., the angle between $\vec{V}$ and the local horizontal.

  Ψ heading angle, i.e., the angle between the local parallel and the projection of $\vec{V}$ on the local horizontal.

The control vector u (dimension 2) defined in the previous RATT optimisation software consists on:

- the angle of attack (α),
- and the bank angle (μ).

These two control variables are subject to constraints corresponding to the manoeuverability domain of the vehicle. These constraints are expressed by:

$$\begin{array}{lll} \forall\, t, & \alpha_{min} \leq \alpha(t) \leq \alpha_{max} & \mu_{min} \leq \mu(t) \leq \mu_{max} \\ \forall\, t, & \dot{\alpha}_{min} \leq \dot{\alpha}(t) \leq \dot{\alpha}_{max} & \dot{\mu}_{min} \leq \dot{\mu}(t) \leq \dot{\mu}_{max} \end{array}$$

The minimum and maximum bounds of the angle of attack and bank angle are automatically taken into account by the optimisation method by replacing those variables by two new auxiliary variables: η and ζ. Those auxiliary variables are defined as follows:

$$\alpha = \frac{(\alpha_{max} + \alpha_{min}) + (\alpha_{max} - \alpha_{min}) \sin \eta}{2}$$

$$\mu = \frac{(\mu_{max} + \mu_{min}) + (\mu_{max} - \mu_{min}) \sin \zeta}{2}$$

In order to consider the limits on the minimum and maximum value of the angle of attack and bank angle derivatives and to guarantee a smooth control, the following transformation of variables is performed:

- Two new control variables u(1) and u(2) are selected. They are related to the auxiliary variables η and ζ according to the expressions:

$$\frac{d\eta}{d\chi} = \dot{\eta}_{max} \sin u(1) \qquad (20)$$

$$\frac{d\zeta}{d\chi} = \dot{\zeta}_{max} \sin u(2) \qquad (21)$$

where $\dot{\eta}_{max}$ and $\dot{\zeta}_{max}$ are the maximum permissible values of the auxiliary variables derivatives $\dot{\eta}$ and $\dot{\zeta}$. They are obtained by imposing an upper limit to the maximum modulus of the angle of attack and bank angle derivatives:

$$\dot{\eta}_{max} = \frac{2t_f}{(\alpha_{max} - \alpha_{min})} \dot{\alpha}_{max} \tag{22}$$

$$\dot{\zeta}_{max} = \frac{2t_f}{(\mu_{max} - \mu_{min})} \dot{\mu}_{max} \tag{23}$$

- The state vector x is augmented with two new components (dimension n = 8), which are the auxiliary control variables η and ζ, directly related to the control angles α and μ. The new state vector x has the following components:
  - Non dimensional radius r or altitude h
  - Geographical longitude θ
  - Geographical latitude ϕ
  - Non dimensional Velocity modulus v
  - Flight Path angle γ
  - Heading Angle Ψ
  - Auxiliary control variable η
  - Auxiliary control variable ζ

This transformation of state and control variables guarantees that the minimum and maximum value of the angle of attack and bank angle and its derivatives satisfy the constraints imposed by the manoeuverability domain of the vehicle along the whole atmospheric pass.

Differential Equations (Function ϕ)

The differential equations (function ϕ in the Gradient Restoration Algorithm formulation) to be satisfied by the state, control and parameter variables are the reentry and AAOT kinematic and dynamic equations expressed in spherical coordinates system with the velocity expressed in the flight path coordinate system.

Boundary Constraints

Initial Conditions (Function w)

The initial point for this formulation is the entry point in the sensible atmosphere. The following cases are considered:

- Direct input of initial conditions
- De-orbit by one manoeuvre
- De-orbit by two manoeuvres

Final Conditions (Function ψ)

The final conditions which have been implemented for the RATT indirect optimisation problem are the following:

- Reentry Problem: The following final conditions may be prescribed by the user:
  - final altitude or final radius,
  - final geographical longitude,
  - final geographical latitude,
  - final velocity,
  - final path angle and/or
  - final heading angle.
- AAOT Problem: The first component of the final constraints vector ψ is the condition that the final radius is the upper limit of the sensible atmosphere. For the remaining components, the following alternatives are presented:
  - Re-orbit by one manoeuvre
  - Re-orbit by two manoeuvres

Path Constraints (Function S)

The most important path constraints are the minimum and maximum value of the angle of attack and bank angle and the minimum and maximum value of its time derivatives. They are imposed by the manoeuverability domain of the vehicle. The transformation of state and control variables presented in this section guarantees that above path constraints are satisfied along the atmospheric trajectory path.

Additional path constraints correspond to the structural and heat load limits of the vehicle. The heat load limits are of two types: the maximum allowed heat flux and the maximum allowed total absorbed heat. The structural load limits correspond to the maximum allowed dynamic pressure and the maximum allowed load factor.

Above list of inequality path constraints are transformed into equality path constraints by adding an auxiliary control variable u(i) such that:

$$S(i) = P_{max} - P - u(i)^2 = 0 \tag{24}$$

The control vector is augmented with auxiliary variables in a number which is equal to the number of considered path constraints. However, the fact that some of above constraints do not explicitly depends on the control variables induces some numerical instabilities in the Two Point Boundary Value problem solver of the Gradient Restoration Algorithm. This is solved by formulating those constraints as minimax penalty function to be added to the cost function.

Cost Functions (Functions f, g and h)

Direct Reentry

Four different cost functions are considered:

downrange: $-\theta(tf)$
crossrange: $-\phi(tf)$
total absorbed heat: $\int_o^{T_f} \frac{C_q}{\sqrt{R}} \sqrt{\rho}\, V^3\, P(\alpha)\, dt$
total de-orbit ΔV

Aero-Assisted Orbital Transfer (AAOT)

The basic cost functions are:

$$J = \sum_i \Delta V_i$$

$$J = \cos\left(i(t_f) - i(t_o)\right)$$

A linear combination of above is also considered.

8. OBTAINED RESULTS

Horn Test Case

This test case is a direct Earth reentry trajectory in the equatorial plane with minimum integrated heat flux. It is based on a test case of Horn (reference [7], 1989). The cost function is the integrated heat load. The following boundary constraints are considered:

initial: $h = 122.$ km
$v = 10.49948$ km/s
$\gamma = 5.75^o$
final: $\Theta_L = 13.77^o$
$h = 22$ km
$v = 0.327$ km/s
$\gamma = -26^o$

The evolution of the optimum angle of attack is a smooth and continuous function(Figure 3). The optimum angle of attack proposed by Horn (Figure 4)

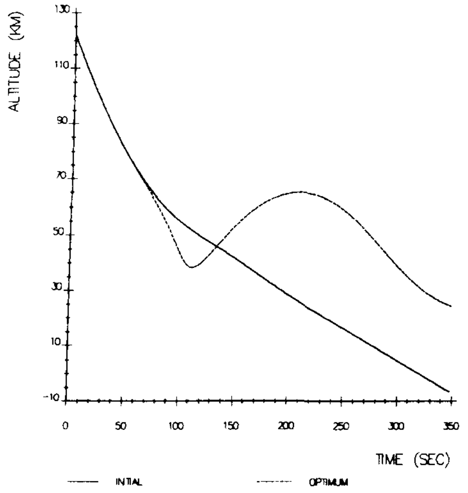

Figure 1: Horn Test Case: Altitude (km).

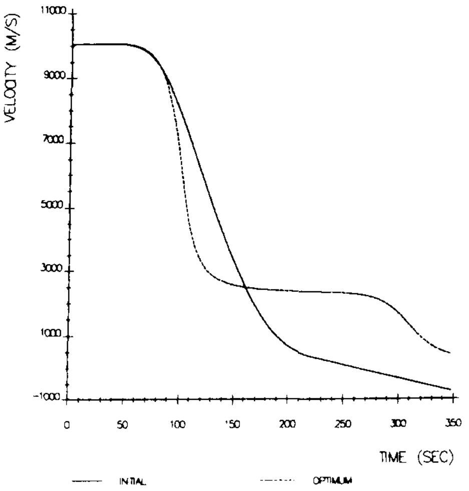

Figure 2: Horn Test Case: Velocity (m/s).

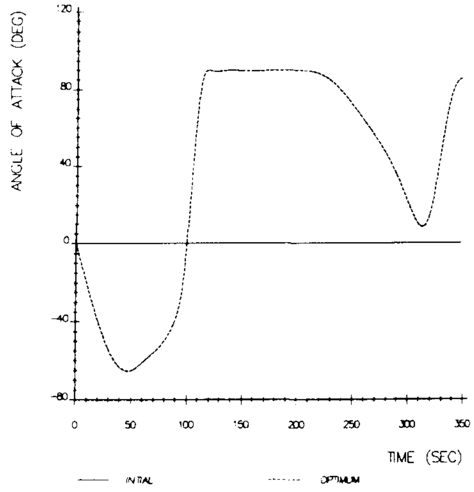

Figure 3: Horn Test Case: Angle of Attack (deg).

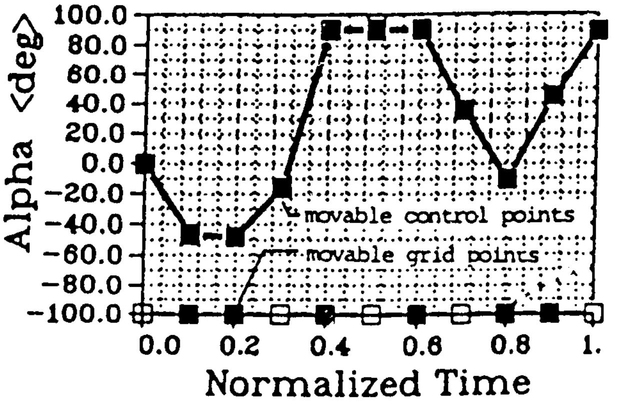

Figure 4: Horn Test Case: Angle of Attack (deg) proposed by Horn.

is very close to the solution obtained with this indirect method. The total duration is 347.7 seconds and the obtained value of the integrated heat load is 5054 Jul/cm2, better than the TOP minimum value (5093 Jul/cm2).

0.0.0.1 Test Case ACRV

The ACRV is the emergency capsule of the Space Station Freedom; it is in charge of taking the crew back to the Earth in case of serious problem on board the station. This vehicle has an Apollo shape. The reentry optimisation problem consists in minimising the integrated heat rate along the trajectory with an imposed final crossrange of 85 km. The ACRV test case is a direct reentry with boundary constraints in the final altitude (7 km) and cross range (85 km). The equilibrium angle of attack (25 degrees) is supposed to be constant, it corresponds to a constant L/D ratio of 0.3. The unique control variable is the bank angle. The initial state is defined as follows:

- altitude: 120 km
- longitude: 0 deg
- latitude: 0 deg
- velocity: 7487 m/s
- path angle: -1.7 deg
- heading angle: 0 deg

The total reentry duration is about 460 seconds and the obtained value of the total absorbed heat integrated along the trajectory is about 3100 Jul/cm2. This value is better than all the previous run of this test problem with TOPOP (3362

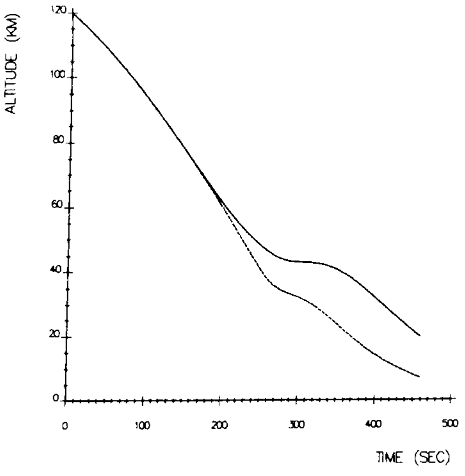

Figure 5: Test Case ACRV: Altitude (km).

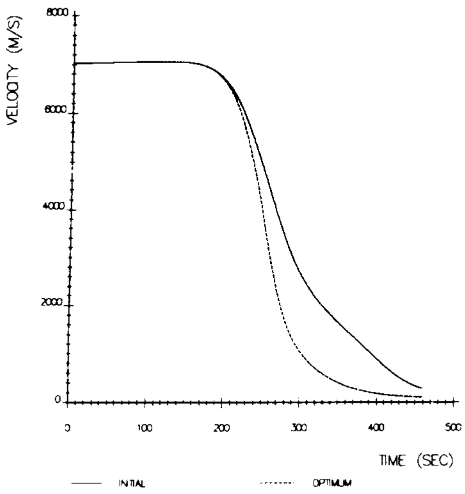

Figure 6: Test Case ACRV: Velocity (m/s).

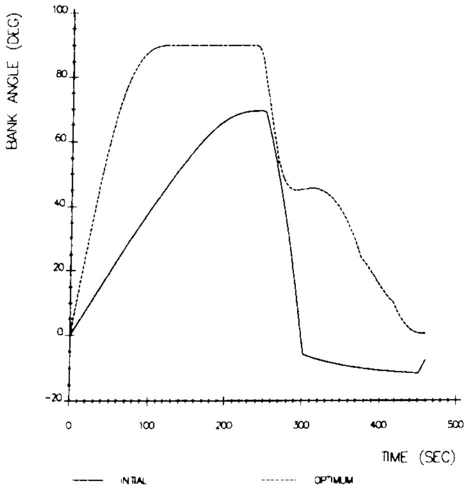

Figure 7: Test Case ACRV: Bank Angle (deg).

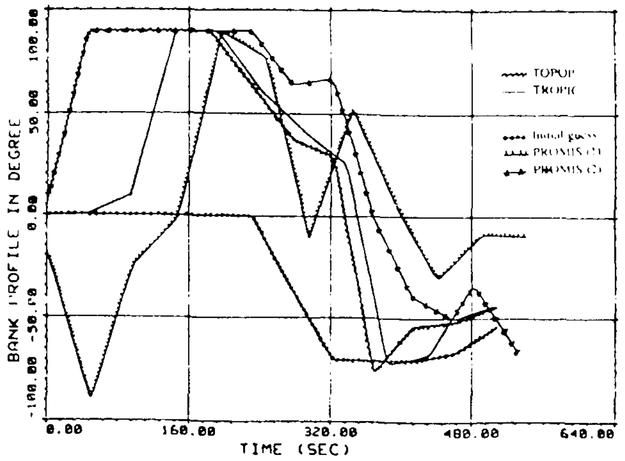

Figure 8: Test Case ACRV: Optimum Bank Angle (deg) by PROMIS, TOPOP and TROPIC.

Jul/cm2), TROPIC (3376 Jul/cm2) and PROMIS (3395 Jul/cm2). Only PROMIS starting from the optimum TOPOP provides a value which is similar (3176 Jul/cm2) but higher than the minimum obtained with the Gradient Restoration. The evolution of the optimum bank angle is presented in Figures 7.

0.0.0.2 Test Case AFE: Aeroassisted Flight Experiment

This test case is a full 3D GEO to LEO non coplanar transfer with minimum ΔV. It is based on the Miller, Wang, Lee and Zhao (1989) test case for the Aeroassisted Flight Experiment (AFE) with one re-orbit manoeuvre. The cost function is the total required ΔV. The boundary constraints are:

initial: $h = 121.92$ km
$v = 10.31$ km/s
$\gamma = -4.49^o$
$\Theta = -134.52^o$
$\Phi = -4.49^o$
$\Psi = -28.13^o$
final: $h = 329.7$ km
$v = 7.708$ km/s
$\gamma = 0^o$
$\Psi = -28.45^o$

The angle of attack is kept constant (17 degrees), the only control variable is the bank angle. The obtained optimum trajectory presents the following parameters:

- Δ V: 72.05 m/s (72.04 m/s in Miele et al),
- Integrated heat load: 12,314 J/cm^2,

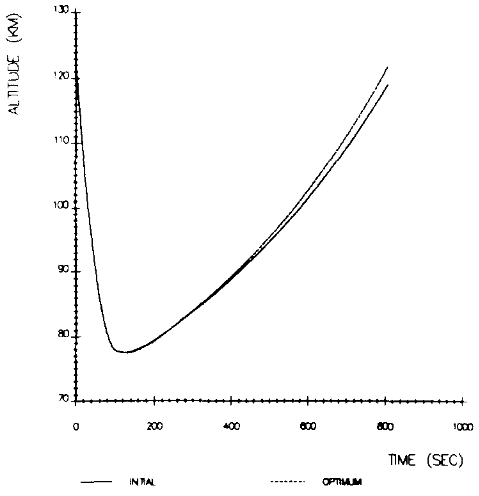

Figure 9: AFE Test Case : Altitude (km).

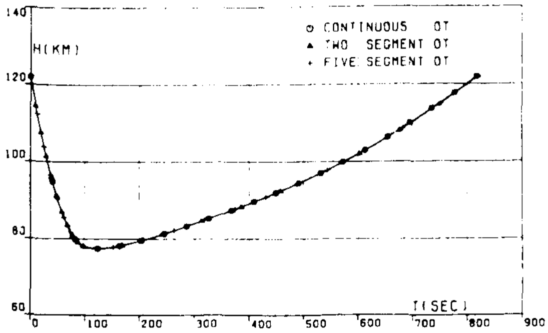

Figure 10: AFE Test Case : Altitude (Miele).

- Duration of atmospheric flight: 817.7 seconds (817.6 in Miele),
- Maximum heat rate: 53.4 W/cm^2 ,
- Maximum load factor: 0.03 ,
- Maximum dynamic pressure: 1205 Pa (1174 in Miele).

9. CONCLUSIONS

The following conclusions can be derived:

- The Gradient Restoration algorithm is a very powerful indirect method for reentry and AAOT trajectory optimisation problems.
- The obtained optimal solutions are characterised by a smooth variation of the control.
- All the boundary and path constraints and the differential equations are satisfied.

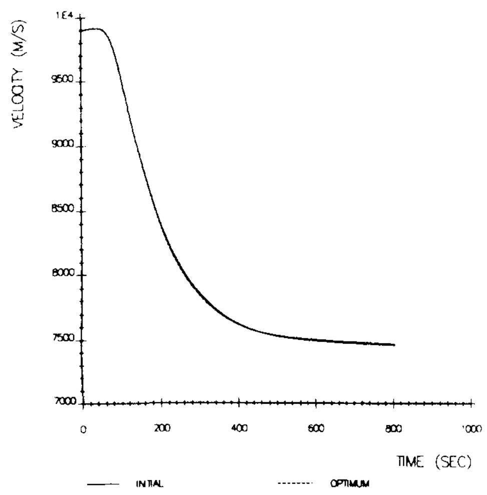

Figure 11: AFE Test Case : Velocity (m/s).

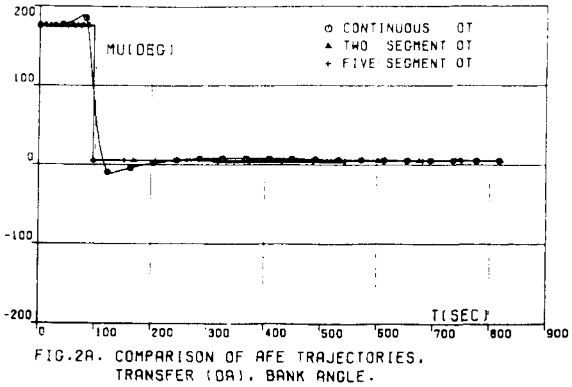

Figure 14: AFE Test Case : Bank Angle (Miele).

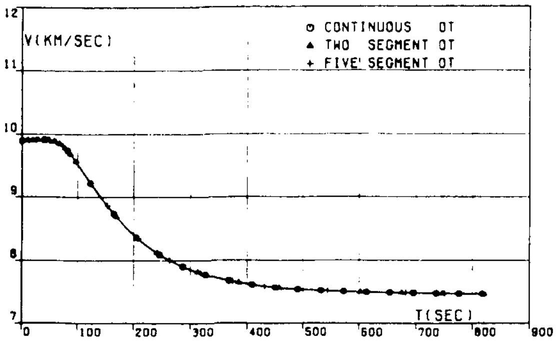

Figure 12: AFE Test Case : Velocity (Miele).

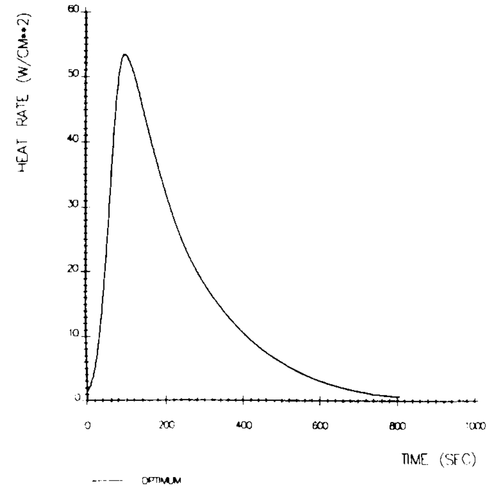

Figure 15: AFE Test Case : Heat Rate.

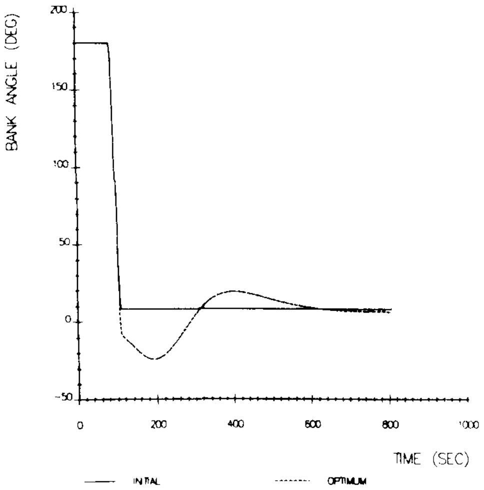

Figure 13: AFE Test Case : Bank Angle (deg).

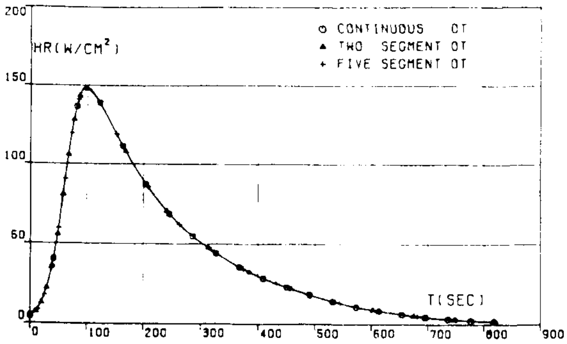

Figure 16: AFE Test Case : Heat Rate (Miele).

- The obtained value of the cost function is better than the corresponding to the previous run of the alternative direct optimisation methods.
- The main disadvantage of this method is that some path constraints are incorporated as penalty cost functions where the user must monitor the value of the corresponding multiplier factor.
- An additional disadvantage is the low convergence rate close to the final optimal solution.

References

[1] Belló Mora M., **Optimal Control of Atmospheric Reentry Trajectories**, Doctoral Thesis, Flugmechanik Institut, TU Braunschweig, April 1991.

[2] Bock, H.G., Plitt, K.J. **A Multiple Shooting Algorithm for Direct Solution of Optimal Control Problems** Proc. of the 9th World Congress of the IFAC, Budapest, Jul 2-6, 1984

[3] Gonzalez, S. and Miele, A. **Sequential Gradient Restoration Algorithm for Optimal Control Problems with General Boundary Conditions**. Journal of Optimisation Theory and Applications: Vol 26, No. 3, 1978.

[4] Hargraves, C.R., Paris, S.W. **Direct Trajectory Optimisation Using Non Linear Programming and Collocation** Journal of Guidance and Control, Vol 10, No. 4, 1987.

[5] Heideman, J.C., Miele, A. **Sequential Gradient Restoration Algorithm for Optimal Control Problems**. Journal of Optimisation Theory and Applications, Vol 15, No. 2, 1975.

[6] Henning, G.R., Miele, A. **Sequential Gradient Restoration Algorithm for Optimal Control Problems with Bounded State**. Journal of Optimisation Theory and Applications, Vol 12, No. 1, 1973.

[7] Horn, K. **Solution of the Optimal Control Problem Using Software Package STOMP** Proc. of the 8th IFAC Workshop on Control Application of Non Linear Programming and Optimisation, Paris, June 7-9 1989

[8] Jallade S., **Numerical Methods of Optimisation. Output of WP 415**, Reentry and Atmospheric Transfer Trajectories Software, ESA/ESTEC Noordwijk/NL, Contract No. 7766/88/NL/MAC, 30th July 1990.

[9] Jänsch, C., Schnepper, K., **Trajectory Optimisation and Guidance of Aerospace Vehicles. Part II: Optimisation Methods** Carl-Cranz Gesellschaft e.V., Course DR 4.04, Oberpfaffenhofen June 1991.

[10] Jänsch, C., Paus, M., **Aircraft Trajectory Optimisation with Direct Collocation using Movable grid points** Proceedings of the 1990 American Control Conference, pp 262-267, San Diego, May 1990.

[11] Miele, A., Pritchard, R.E., and Damoulakis, J.N. **Sequential Gradient Restoration Algorithm for Optimal Control Problems**. Journal of Optimisation Theory and Applications: Vol 5, No. 4, 1970.

[12] Miele, A. **Recent Advances in Gradient Algorithms for Optimal Control Problems**. Journal of Optimisation Theory and Applications: Vol 17, No. 5-6, 1975.

[13] Miele, A., Mohanty, B.P., Venkataraman, P. and Kuo, Y.M. **Numerical Solutions of Minimax Problems of Optimal Control, Part 1**. Journal of Optimisation Theory and Applications: Vol 38, No. 1, 1982.

[14] Miele, A., Mohanty, B.P., Venkataraman, P. and Kuo, Y.M. **Numerical Solutions of Minimax Problems of Optimal Control, Part 2**. Journal of Optimisation Theory and Applications: Vol 38, No. 1, 1982.

[15] Miele, A., Venkataraman, P. **Optimal Trajectories for Aeroassisted Orbital Transfer**. Acta Astronautica Vol. 11, No. 7-8, pp 423-433, 1984.

[16] Miele, A., Basapur, V.K. **Approximate Solutions to Minimax Optimal Control Problems for Aeroassisted Orbital Transfer**. Acta Astronautica Vol. 12, No. 10, pp 809-818, 1985.

[17] Miele, A., Basapur, V.K., Lee, W.Y. **Optimal Trajectories for Aeroassisted Noncoplanar Orbital Transfer**. IAF-86-229, 37 Congress of the IAF Oct 4-11, 1986 Innsbruck, Austria.

[18] Miele, A. **Method of Particular Solutions for Linear, Two-point Boundary Value Problems**. Journal of Optimisation Theory and Applications: Vol 2, No. 4, 1968.

[19] Miele, A. **Gradient Methods in Optimal Control Theory. Optimisation and Design**. Edited by M. Avriel, M.J. Rijckaert, D.J. Wilde Prentice Hall, Englewood Cliffs, New Jersey 1973

Analysis of a CTV Reentry Navigation Concept

H. Malthan, J. M. Fraile-Ordóñez, M. Krischke
Kayser-Threde GmbH, Wolfratshauser Str. 48, D-81379 München
Phone: (++49) 89/72495-0, Fax No. (++49) 89/72495-291
e-mail: mn@kayser-threde.de

ABSTRACT

In the planned operation of the International Space Station an essential element is the transport of men to the station and from the station to earth. For this function the crew transfer vehicle (CTV) was proposed by ESA. In the DASA led German team for Phase A Kayser-Threde was responsible for the CTV navigation. In the frame of this work the GPS/INS based reentry navigation of the crew module (CM) has been examined, analytically and by simulations, with the main emphasis given to the flight phases from propulsion module separation until the radio blackout and during blackout until reacquisition of the GPS signal. The state estimation process in the first phase after separation and the free inertial accuracy in the blackout phase will be described and requirements for the navigation system deduced therefrom.

The applicability of GPS technology on-board of CTV faces a number of important limitations and critical issues. For example, the visibility of GPS satellites from antennas located on the structure of such a conical shaped capsule is far from optimal. Other critical issues are related to the capsule's long operation periods of time in a 'dormant' status while docked at the Space Station (age of GPS almanac, time and position initialization, time-to-first-fix after emergency separation, etc.). Furthermore, another essential point in the performance of the GPS subsystem is the reacquisition of the GPS satellites signals after the radio blackout experienced by the capsule during re-entry.

In this paper, a detailed discussion and analysis of the mentioned critical issues will be presented. Additionally, the results of some preliminary-in-nature simulations with a GPS satellite signal simulator and a spaceborne GPS receiver will be shown and briefly discussed.

1. INTRODUCTION

For the transport of men between the planned International Space Station (ISS) and earth the Crew Transfer Vehicle (CTV) was proposed by ESA. In the DASA led German team for Phase A Kayser-Threde was responsible for the CTV navigation. The navigation concept was based on the usage of GPS and GPS/INS respectively. The main topics of this study were

- the evaluation of the achievable attitude accuracy
- the navigation performance
- critical items with respect to the GPS usage onboard of CTV
- the identification of sensor combinations suited for the relevant tasks.

This paper concentrates on the second and the third point. Attitude accuracy will be discussed only as far as the navigation performance is involved.

In the second section the reentry environment is described. Then the specific GPS related problems encountered in case of a forced quick separation from the station are discussed in Section three.

A critical point in the GPS based reentry is the signal loss in the so-called blackout phase due to the plasma formation in the vicinity of the reentry vehicle. The navigation performance from this point depends on the navigation performance of the Inertial Navigation System (INS) as well as on the time needed for GPS signal reacquisition after blackout.

The INS based navigation performance and its dependence on the INS accuracy and the initial errors is discussed in section four. The GPS performance during the reentry trajectory and after blackout in particular have been analysed through simulations using a GPS signal simulator and a spaceborne receiver. These simulations are described in the fifth section. The conclusions are given in Section 6.

2. MISSION SCENARIO

Ground Track and Altitude of a typical reentry scenario are given in Figs. 1 and 2. The trajectory starts from an initial orbital flight at an altitude of about 400 km and an inclination of 51.6°. At a specified time, a de–orbit boost is performed and the capsule (crew module CM) is separated from the RPM (Resource and Propulsion Module). At an altitude of 120 km the atmospheric re–entry begins. The capsule will be guided back to the earth's surface along a pre–specified trajectory.

Proceedings Third International Conference on Spacecraft Guidance, Navigation and Control Systems, ESTEC, Noordwijk, The Netherlands, 26-29 November 1996, ESA SP-381 (February 1997)

The trajectory shown is based on data, which have been provided by DASA at study time. Although some optimization is still to be done, it is expected, that the trajectory is representative and that no significant changes will result from updated versions. The total duration between deboost manoeuvre (re-entry start) and parachute opening is 3300 seconds.

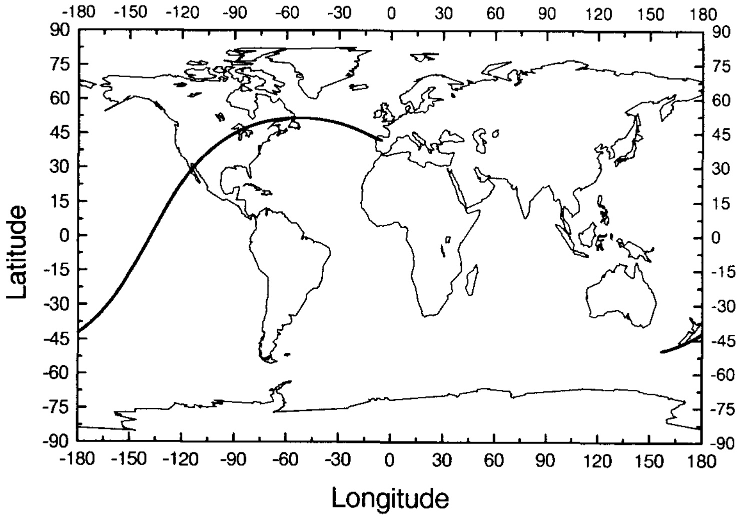

Fig. 1 CTV Ground Track

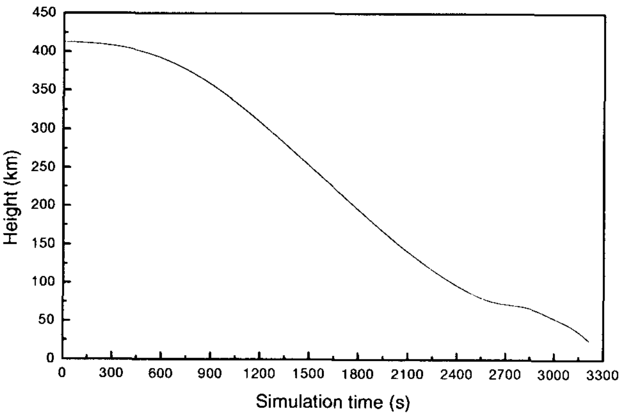

Fig. 2 CTV Altitude

Critical requirements with respect to navigation stem from the fact that in case of a quick (rescue) departure from the station the position shall be available within 23 minutes. The landing accuracy required is of 6 and 9 km for CTV and CRV (rescue variant of CTV) respectively.

3. GPS INITIALIZATION

A critical issue in the GPS usage onboard of CTV is related to the capsule's long operation periods of time in a 'dormant' status while docked at the Space Station. Therefore neither valid GPS satellite position and time nor receiver position and velocity are generally known at start time of the navigation system.

Certainly, the ISS will use GPS as the main positioning means. Thus, GPS receivers will be present on–board the station. The initialization of CTV's GPS receiver in the normal departure case can therefore use the GPS–derived ISS's position and the existing interfaces to the capsule. In this way, it can be expected that CTV's GPS receiver will be initialized with a position affected by only about 150 m error.

In principle, this seems straightforward. However, special attention should be paid to the way that initialization is performed.

The optimal way to initialize CTV's GPS receiver would be transferring the following information from the ISSA's receiver to CTV's (assuming that CTV's receiver is able to accept all that information): GPS satellite constellation almanac, GPS ephemeris for all visible satellites, receiver location as orbital parameters in GPS ephemeris format and GPS time.

In these conditions CTV's GPS receiver would be able to perform a hot–start whose duration is estimated to be far shorter than one minute by most GPS receivers.

In the quick departure case however, the optimal CTV's GPS receiver initialization just described can not be applied. In this case it can not be assumed that the information transferred from the ISS be reliable; actually, not even the existence of such transfer can be assumed. In principle, CTV's receiver will be powered on during the three minutes of ingress of crew in the capsule.

Therefore, the conditions encountered by CTV's GPS receiver in the quick departure case can be summarized as follows:

- GPS time not known accurately (several seconds error) ,

- no current GPS satellite constellation almanac available (the available one can be up to three months old),
- no ephemeris of visible GPS satellites available, and
- no accurate information on receiver's location available (available information can be erroneous by up to several hundred kilometers).

In this conditions, it is arguable whether CRV's GPS receiver will get a position fix within the required 23 minutes following separation from ISS. For example, once the receiver has acquired a first satellite, it will need 12.5 minutes of continuous tracking to decode a complete GPS almanac. CTV's rotational dynamics contribute to the complexity of the situation by reducing the continuous tracking period.

Four feasible alternatives have been identified, each of them offering advantages and disadvantages. The decision on which one to choose will surely depend on the availability of power at CTV during its stay docked to ISSA in dormant mode. The different alternatives are the following:

1. CTV's GPS receiver stays powered on during the whole period of time in which the capsule stays docked in dormant mode
2. CTV's GPS receiver is powered on for about one hour regularly every day during the whole period of time in which the capsule stays docked in dormant mode
3. Automatic daily storage of GPS satellite constellation almanac and ISSA orbital data (as derived from the operating ISSA GPS receiver) into a memory location of the VTC, or
4. CRV's GPS receiver is accurately initialized from ground immediately after separation from ISSA.

Among the possible problems are an increased power consumption, an increased receiver operational time (in the worst case exceeding its nominal life time) or high complexity. Weighting the different pro and con's the third alternative was finally recommended as most appropriate.

The third alternative offers a series of key advantages, with the only potential important disadvantage, that the receiver's time initialization might be not accurate enough. The receiver's oscillator could be powered by a miniature back–up battery during the capsule's dormant periods, but whether this is enough to keep the GPS receiver synchronized to GPS time (within very few seconds of error) or not still needs assessment (it depends heavily on the characteristics of the crystal oscillator, on the temperature gradients which it experiences, etc.). In negative case, a method to keep CTV synchronized to GPS time in order to allow for the accurate time initialization of the GPS receiver needs to be found. More detailed information related to the usage of GPS onboard of CTV is to be found in [4].

4. ATMOSPHERIC REENTRY INCLUDING RADIO BLACKOUT

The atmospheric re–entry flight begins at an altitude of about 120 km , about 2400 sec after the beginning of the de–orbitation boost. From this re–entry start point down to landing, the on–board navigation system has to provide to the guidance and control system the estimation of the capsules attitude, position and velocity.

With regard to navigation this phase may be separated into three parts, the first being the time from deboost until radio-blackout, the second during blackout and the third determined by the GPS signal re-acquisition process. The re-acquisition process will be described in Section 5, so that we concentrate here on the first two parts of the reentry phase.

Based on simulations using a GPS satellite signal generator and described below (Section 5), it is expected that also during the re–entry increasingly dynamic phase the GPS information is essentially available without interruption. Therefore the optimal determination of the flight path based on GPS and INS data can continue until the radio black–out occurs. In this time navigation accuracy is mainly determined by the GPS system.

During radio blackout on the other hand navigation is solely due to the INS, with the accuracy determined by the INS accuracy, the flight dynamics and the initial conditions at entrance into the blackout phase.

The CTV navigation performance during the reentry phase has been studied in analyses and simulations. The main point of interest was the evaluation of the INS free inertial performance in this highly dynamic flight phase and how well initial attitude errors may be estimated during the time when GPS is still available. The latter is of special importance, since it is assumed that after separation from RPM the CM has no absolute attitude sensor onboard for initialization of the attitude angles. Instead the attitude angles from the RPM have to be transferred to the CTV before separation. An initial accuracy of 0.5 degrees is assumed. This is due to measurement accuracy as well as due to the mechanical tolerances between the two modules.

For the analysis a covariance analysis simulation was performed using an integrated 34 state Kalman filter. The filter processes the inertial data together with the GPS raw data. Code pseudo ranges and doppler data have been assumed as GPS observations. The basic assumption to be verified is that the residual attitude errors may be estimated by the filter if the dynamics is high enough. This is achieved by velocity and position matching in the dynamic phase before entrance into blackout.

	'low frequency'	'high frequency'
Amplitude/ m (1σ)	15	5
Periode/s	3000	200
Correlation Time/s	3000	200

Tab. 1 Parameters of SA-Model (2nd Order Markov)

The simulations are based on the actual trajectory described in Section 2. The trajectory starts after the deboost manoeuvre and is characterised by the deceleration at the beginning with a duration of about 550 s and a long free flight phase until the atmosphere reentry. The final reduction of altitude/velocity occurs in a relatively short time. The blackout is assumed to start and end at a given thermal load. For the simulation this limit has been selected to 300 kW/m². This seems to be a rather pessimistic assumption , leading to a shorter time for attitude improvement and a late reacquisition. At the end of the blackout phase a time of 30 s has been added to allow for reacquisition of the GPS position and velocity. This results in an effective blackout (no GPS available) between 82 and 48 km (T=2530.. 3060 s). The high dynamic phase before blackout lasts about 500 seconds.

	Class 1	Class 2
Gyro Bias [deg/h]	0.5	0.01
Gyro Random Walk [deg/√h]	0.2	0.005
Scale Factor [ppm]	1000	100
Misalignment [mrad]	1.0	0.1
Accel-Bias [mg]	1.0	0.1
Scale Factor [ppm]	1000	100
Misalignment [mrad]	1.0	0.1

Tab. 2 INS Accuracies

With respect to GPS it is assumed that up to the beginning of the blackout phase the GPS signal (at least 4 satellites) is available. Regarding the accuracy it was assumed that only C/A code precision is available during the mission, with the SA-degradation switched on. The SA-induced error was modelled as a second order Markov process. Two different types have been examined, a more low frequency part and a high frequency part. The relevant parameters are shown in Tab. 1. The reduced GPS performance is one of the differences w.r.t earlier studies [3].

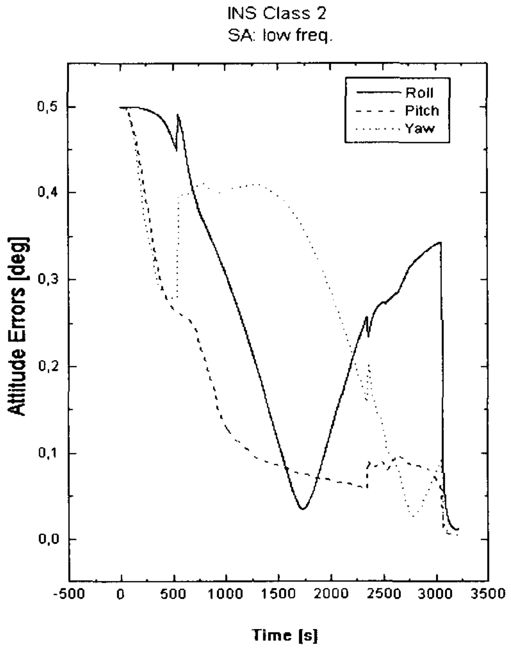

Fig. 3 GPS/INS Attitude Errors

Two classes of INS's have been considered. The one is the medium to low accuracy class (Class 1), which is representative for aided attitude and reference systems, the other is the high to medium accuracy class (Class 2) capable for free inertial navigation over longer times. The errors assumed are given in Tab. 2.

The simulations and their results will be described in the following.

In the phase before blackout the main attention is on the residual attitude errors. With regard to the Class 2 system only a rather marginal improvement was found. A better situation is apparent for the class 2 INS system. Fig. 3 shows the attitude errors for the low frequency SA-model.

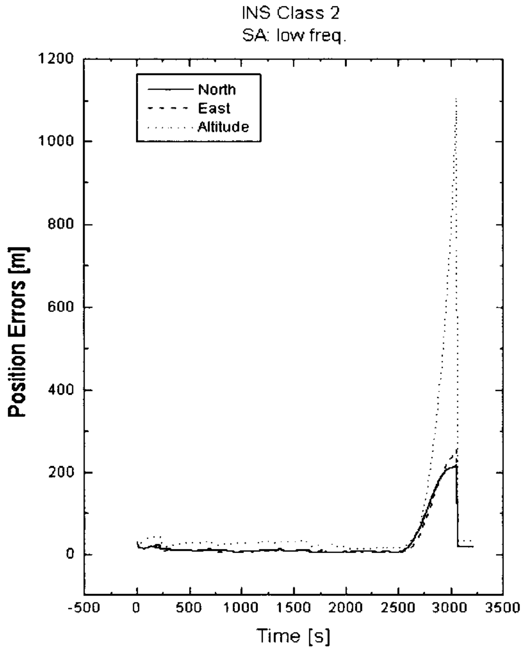

Fig. 4 GPS/INS Position Errors

Here some of the errors are already reduced during the initial deceleration. This INS type is not only better for itself, but allows also the Kalman filter (because it 'knows' about the INS performance) to concentrate on the initial attitude error which is the dominant one at this time.

During blackout the aim is at the position error in the free inertial mode, due to the residual initial and instrument errors. For the class 1 INS the latitude and longitude errors are in the 2 km range, the altitude error is about 4 km and might be critical. The error build up is nevertheless relatively moderate and indicates that the systematic INS errors have been estimated to a good amount. One should remember that the main error sources in this class of instuments are determined essentially by the day-to-day repeatability, which can be calibrated online as long as GPS is available.

The INS class 2 results (Fig. 4) are much better. This is expected, since these systems should be accurate enough, also if not aided. If a high-grade INS is used, sufficient accuracy seems achievable even in case that the reacquisition fails. This has to be verified if necessary.

The reacquisition is very fast in all cases and brings the attitude and position errors down to negligible values. Both types of data will be significantly better than the pre-blackout data. The position errors at the end of the black–out phase together with the expected velocity errors can be used for an extrapolation of the errors until landing.

In conclusion the results confirm that the concept of the integrated GPS/INS system is valid also in this application even if the degradation due to SA is being taken into account. Although at this time no requirements exist yet with respect to the attitude and position accuracy at the end of radio blackout, it can already be said, that the attitude accuracy will be no problem in any case. As far as the position is concerned, the decision what type of INS to chose has to be deferred until the relevant requirements are known. The existing data are very promising in any case. Nevertheless, the trend is to use a better (type 2 class) INS equipment. The performance assumed are well state of the art, so that no problems are expected from this side.

5. RE-ACQUISITION AFTER BLACKOUT

The most critical topic in CTV navigation during the atmospheric re–entry phase is the GPS receiver's capability to re–acquire the GPS satellites signals after the radio black–out has concluded. In the simulation described above it had been asumed that there will be a 30 s acquisition time. In general, a receiver's capability to re–acquire signals after a prolonged loss–of–lock depends on two separate parts: the accuracy of the re–initialization, and the receiver's GPS signal search strategy.

The previous section analyzed the position and velocity errors that build up during the free inertial operation. This error magnitude is to be expected for the receiver's re–initialization error after the radio black–out.

The influence of these initialization errors on the re-acquisition time depends heavily on the signal search strategy implemented in the receiver's firmware. That strategy is certainly very different from receiver to receiver and can surely be optimized for an application like CTV's. We at KT are very familiar with the Motorola Viceroy™ spaceborne receiver and its GPS signal search strategy [6]. This receiver is in no way specially designed to be used in an atmospheric re–entry mission and therefore can be regarded exclusively as an example of how "things can be done", though not as an example of how "things have to be done" in CTV. In any case, it will be shown that although the Viceroy's search strategy is not optimized for high g's environments, it would already work reasonably well in CTV.

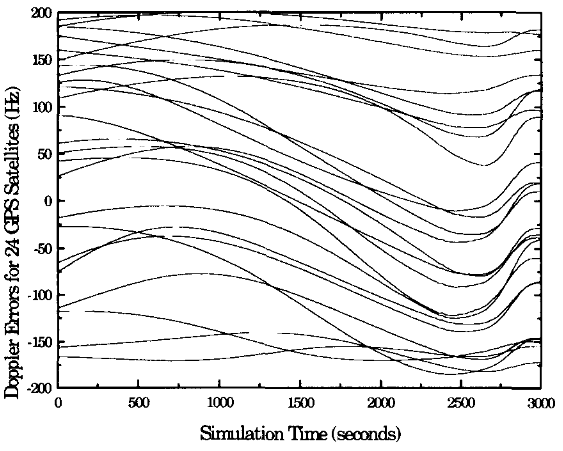

Fig. 5 Results of Doppler Error Analysis

During the radio black–out, it is expected that the GPS receiver will loss lock to all satellites for about 400s. After this interruption, the receiver will be re–initialized with the position and velocity information delivered by the INS. This situation corresponds to the so–called *hot–start* in which, the receiver is synchronized to GPS time to a high accuracy and has available in its memory newest GPS almanac data as well as satellite ephemeris data from all satellites which were tracked until the begin of the black–out. This knowledge allows for much more accurate doppler predictions in the signal search process than a normal warm-start: the quality of the estimated doppler is the key to fast signal acquisition.

In the case of the Viceroy receiver for example, if the estimated doppler for the satellites to be tracked is less than 500 Hz in error from the actual doppler the TTFF will be typically 24 seconds with a 90% probability of being 30 seconds or less. If the estimated doppler is more than 500Hz in error, the receiver starts a frequency search about the estimated frequency in 400Hz steps. This search is performed with first a positive doppler offset and then a negative one. Each 400Hz step takes approximately 24 seconds to perform a two code search for both the positive and negative doppler. Therefore, every 400Hz of error in doppler adds additional 24 seconds to the acquisition time.

So if we take this as a potential valid example, the question that arises is how accurate the position and velocity re-initialization after the black–out has to be in order to guarantee that the estimated doppler has less than 500Hz in error.

In order to provide an answer to the last question, doppler errors in CRV/CTV's application have been investigated in the following way: for the CTV re–entry trajectory we computed the doppler shifts experienced by the signals from all 24 GPS satellites (making no distinction of whether the satellites were visible or not). Then we degraded CRV/CTV trajectory introducing errors of 30km in every position and of 20m/s in every velocity component and re–computed the doppler shifts (according to the previous section, these errors are far larger than the ones expected to affect the receiver re–initialization using INS information). Finally, both doppler estimates were compared in order to get doppler shift estimation errors caused by the degradation in position and velocity information. The results of this analysis are shown in Fig. 5.

It can be clearly seen in Fig. 5 that the estimated doppler shifts are in error of max. ±200Hz when the navigation errors are according to the conditions above mentioned.

The important conclusion of this doppler error analysis for this CTV Phase A Study is that the re–acquisition time needed by the GPS receiver after black–out can be expected to be about 24 seconds with 90% probability of being 30 seconds or less, as long as the frequency search strategy is similar to the one used in the Viceroy receiver. The missing not estimated 10% of probability will appear whenever the code is missed in the frequency search. This can eventually happen even if the estimated doppler finds itself within the first 500Hz search window. CTV's GPS receiver firmware should be designed to minimize the probability of missing the code when searching in the right doppler window.
Of course, different strategies optimally adapted to CRV/CTV's mission can be developed and implemented which should deliver improved performance.

As a complement to the analyses just described simulations have been performed using an GPS signal simulator in combination with a spaceborne GPS receiver.

The signal simulator (Northern Telecom (UK)) provided 10 channels of C/A–code on the L1 frequency at one single RF output. The output was splitted feeding the dual antenna input of the receiver.

The GPS receiver was a Viceroy spaceborne receiver already mentioned. It is a low-cost L1 C/A-code, dual antenna, 12 (6+6) channel receiver, and was based on a commercial core design originally developed for the SEASTAR small satellite program.

The scenario characteristics can be briefly summarized as follows:

- CTV trajectory as as given above, duration approx. 3300 sec.
- GPS satellite constellation: actual 25 satellite constellation as derived from the almanac for GPS week 836
- SA effects simulated
- GPS satellite signal power level modeled as a function of distance between user satellite and GPS satellite.

During the simulation a GPS satellite signal black-out was simulated between 80 and 60 km altitude (corresponding to seconds of simulation 2556 and 2935), the number of "visible" GPS satellites during that interval was therefore zero.

The results of the simulations performed can provide a valuable insight on the applicability of GPS technology for CTV navigation. However, it is important to note that the Viceroy GPS receiver was not specified to be used in the dynamic conditions which will be encountered during a CTV re-entry mission thus causing it to perform far worse during the simulations than it can be expected should the correct receiver be used. Significant limitations of the Viceroy receiver include for example:

1. Maximum specified dynamics: 2g (during the simulations it tracked satellites at higher g's): this can have an important negative impact on the accuracy of the navigation results.

2. Re-initialization only with position information possible after loss of track in black-out (the receiver could not be re-initialized with additional velocity information): this has a decisive impact on the required satellite re-acquisition time after black-out. Of course, no re-initialization with the navigation results potentially available from a simulated INS was possible.

3. Inability to track satellites whose signal Doppler shift falls within the ±3 kHz range: this has an impact on the number of tracked satellites.

The simulation results are shown in Fig. 6. The number of simulated GPS satellites and the actually tracked ones by the GPS receiver are given. Please note the simulated radio black-out. The geometry factor PDOP (as calculated from the set of satellites tracked by the receiver) is also plotted. Navigation results are only reliable as far as the PDOP factor has a value below 6.

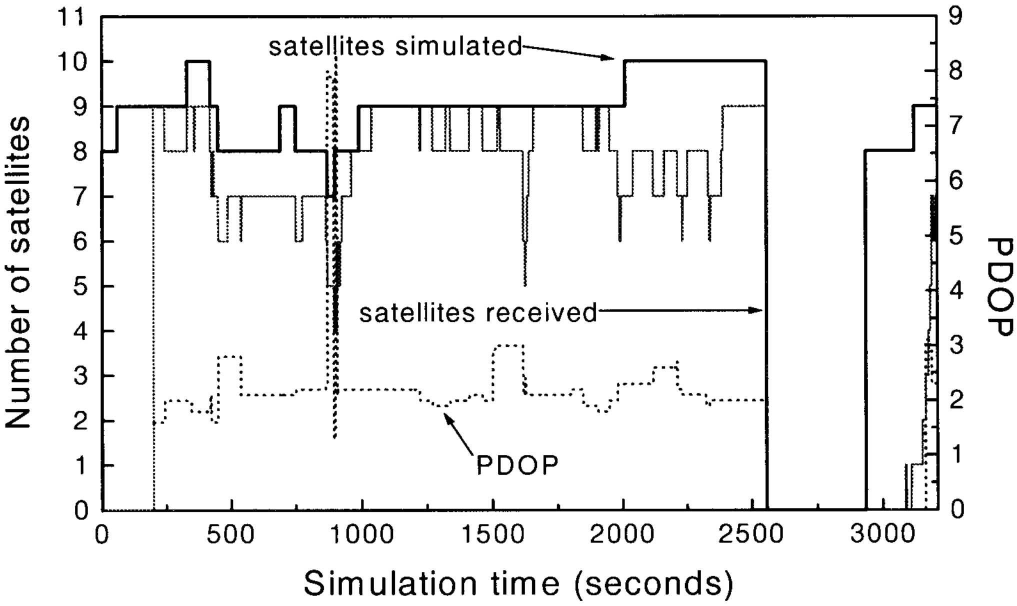

Fig. 6 Simulated and Tracked Satellites

It is interesting to observe that despite the mentioned receiver re-initialization limitation, the GPS receiver still managed to re-acquire up to 7 satellites after the black-out (although with a very long delay).

The altitude, position and velocity errors (receiver-computed vs. simulated) proved to be very large however. This is very probably due to the simulated high dynamics and the suspected limitations of the receiver's navigation filter which was designed to deal with maximum accelerations of 2g.

6. CONCLUSIONS

Re-entry navigation essentially based on GPS and INS has been analyzed and shown to be feasible. Possible problems have been identified in case of a quick departure from ISS, since without special cares timely positioning is in question. Different solutions have been proposed. During blackout intelligent (Kalman-) filter algorithms will provide sufficiently accurate navigation, even in case of relatively low initial attitude accuracy and GPS Selective Availabilty switched on. A medium accuracy INS may be accurate enough, preference is given to higher accurate systems however. Finally it has been shown by analyses and simulation that tracking of a sufficient number of satellites during the re-entry flight and a sufficiently short re-acquisition time for the GPS signal after blackout can be expected. The GPS receiver should be optimized however with regard to the flight dynamics and the initialization possibilities.

7. REFERENCES

[1] CRV/CTV Phase A Workshop 2.
Handout at Workshop No. 2 in Turin,
April 11–12; 1995.

[2] CRV/CTV Phase A Spacionics Architecture Workshop.
Handout at workshop in Turin,
February 28th; 1995.

[3] HV–TN–11X1–016–DASA
CTV Phase 0 Study
Overall Predesign Report
Issue 1; 29.04.94.

[4] HV - TN - 2100 - 012 - DASA
CRV/CTV Phase A Study
Reentry Trajectory Guidance and Navigation
Issue; 19.06.95

[5] Smith, C.A. and K.W. Graves:
Sensitivity of GPS Acquisition to Initial Data Uncertainties.
NAVIGATION: The Journal of the Institute of Navigation, Spring 1985.

[6] Motorola GSTG:
Viceroy GPS Receiver, Software Interface Document
Rev. XC; 27.03.95.

PARAFOIL TECHNOLOGY DEMONSTRATOR OBC DEVELOPMENT

– a successful exercise in timely and low-cost development –

Paul H. van Rossem, Fokker Space BV, currently director of Van Rossem Timeware
Tempellaan 18, NL-3721 VH Bilthoven, the Netherlands
tel: +31 30 220 4006, fax: +31 30 220 3858, p.h.van.rossem@timeware.nl

Pieter G. Beerthuizen, Jos B. Geerdes, Fokker Space BV
Newtonweg 1, NL-2333 CP Leiden, the Netherlands
tel: +31 71 524 5000, fax: +31 71 524 5999
p.beerthuizen@fokkerspace.nl, j.geerdes@fokkerspace.nl

Uwe Soppa, Hans Strauch, Daimler-Benz Aerospace
Hünefeldstraße, D-28059 Bremen, Germany
tel: +49 421 539 5191, fax: +49 421 539 5726
uwe.soppa@erno.de, hans.strauch@erno.de

Geert Jan Dekker, Rob Udo, Netherlands Aerospace Laboratory NLR
Anthony Fokkerweg 2, 1059 CM Amsterdam, the Netherlands
tel: +31 20 511 3113, fax: +31 20 511 3210
gjdekker@nlr.nl, robudo@nlr.nl

ABSTRACT

The Parafoil Technology Demonstrator is an ESA feasibility study towards the controlled precision landing of a Crew Transfer Vehicle using a large parafoil. The demonstration will consist of the automatic landing of a test vehicle with a total mass of 3200 kg. DASA (Daimler-Benz Aerospace) is the prime contractor for the demonstrator and also designed the GNC software; Fokker Space its subcontractor responsible for the electrical architecture, the GNC subsystem and final Assembly, Integration and Test (AIT). This paper focuses on the GNC On-board Computer development which was partially subcontracted to NLR (the Dutch National Aerospace Laboratory).

The development approach was dominated by a short development time and by using low-cost solutions. This required great flexibility both from the development team as well as from the hardware and software being used. For this reason an unconventional development approach was taken, based upon very early interface specifications and heavy use of simulators.

The paper will discuss this successful development approach, especially from a system engineering point of view. We will follow the decisions taken and evaluate the consequential results.

1. INTRODUCTION

Late 1994 DASA approached Fokker Space with a request for a quotation for an On-board Computer (OBC) for the Parafoil Technology Demonstrator project (PTD). The purpose of this project is to demonstrate the feasibility of a controlled landing of a Crew Transfer Vehicle using a large parafoil. The demonstration will involve several droppings of the vehicle with a dummy load from an aircraft at altitudes ranging from 2 to 5 km and a total weight varying from 1600 to 3200 kg. The task of the OBC is twofold: it must (1) establish a precision landing of the test vehicle and (2) it must perform extensive measurements concerning parafoil and environment interactions.

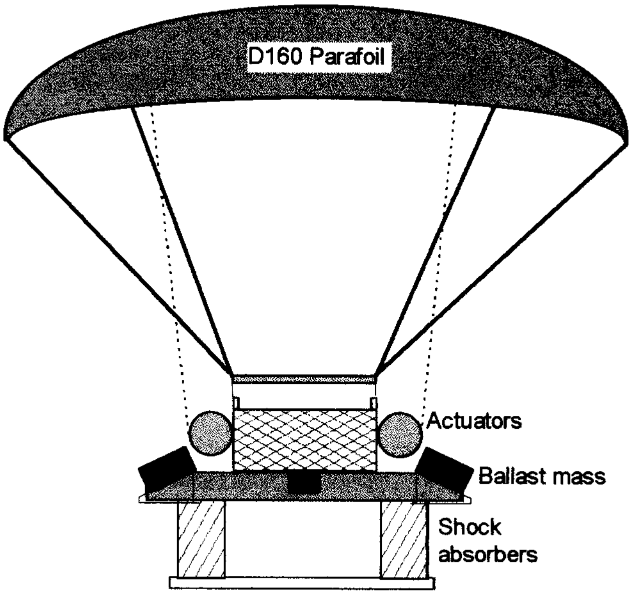

Figure 1: Test Vehicle in Flight Configuration

Therefore the OBC, together with various sensors and actuators, implements a GNC system with extensive telemetry. The primary sensors are a differential GPS (Global Positioning Satellites) subsystem, an inertial attitude reference system, laser altimeter and wind- and temperature sensors. The primary actuator is a dual-winch servo-controller to control the parafoil. Two mutually redundant telecommand links allow remote control from a ground-based manual input device, in case of control failures, or premature dropping of 1600 kg of steel ballast and deployment of an uncontrolled emergency parachute.

Proceedings Third International Conference on Spacecraft Guidance, Navigation and Control Systems, ESTEC, Noordwijk, The Netherlands, 26-29 November 1996, ESA SP-381 (February 1997)

2. PROPOSAL PHASE

From the requirements study it became immediately obvious that the driving requirements were in fact constituted by limiting conditions, such as development time and cost. Therefore we concluded that a conventional development approach, based upon a waterfall model as in ESA's PSS standards [1], would not work. We decided to concentrate on the following possible solutions:

- reuse of existing hardware and software ("horizontal" reuse, [2]),
- reuse of selected hardware and software throughout the project ("vertical" reuse),
- use of low-cost equipment and tools,
- reuse of concepts and ideas,
- several threads of parallel development, immediately from the start of the project,
- minimize the number of documents, but provide detailed technical specifications,
- assign high priority to specification and verification of interfaces,
- establish reliable and fast data connections between the development teams.

Fortunately, the prime contractor's and ESA's attitude towards this proposed alternative development approach have been very cooperative, notwithstanding the fact that this concerned flight hardware, although an unmanned demonstration.

The search for existing hardware and software (*horizontal reuse*) revealed that NLR exploited a highly modular, airborne telemetry system, used for Fokker-60 and other aircraft testing. This is a 68040-based µ-computer with various configurable sensor units. Its software is based upon the pSOS+ real-time kernel, extended with drivers for the various available sensors. The main reason to select this system was its timely availability, including most of the software and its easy configurability. Therefore the OBC hardware and system software was subcontracted to NLR. Due to the specific requirements of this project, no existing reusable application software could be found. The NLR telemetry system however provided enough spare capacity to extend it with such control software. Another advantage with the NLR system was that it could be rented off-the-shelf from NLR, thereby saving considerable cost.

The idea of reuse of hardware and software within various stages of the project (*vertical reuse*) resulted in the reuse of a single System Check-out Equipment (SCOE) during testing, validation and as a ground station without modifications. Furthermore simulator software was heavily used at various instances in the project, as described below.

An investigation of possible parallel threads of development provided the following candidates:

1. the Application Software (ASW), further divided into:
   1a. GNC algorithms and
   1b. parafoil dynamics models,
2. the Basic Software (BSW), consisting of:
   2a. the operating kernel, and
   2b. drivers,
3. the OBC Hardware configuration (HW).

Recent experience with SAX and ISO satellites (rsp. a joint Italian-Dutch project, [4], and an ESA project) learned that such parallel software developments, each assigned to a different team, are only beneficial if the interfaces can be frozen at the most detailed level at a very early stage. Therefore it was decided not only to write an Interface Specification, but include also right from the start the coded interface files (in the form of "C" header files) and a set of additional coding rules (such as using ANSI "C" [3], and other more specific conventions). The purpose of these arrangements was to provide a sound technical contract between the partners, allowing the parallel developments without the usual programmatic dependencies.

Our experience with the SAX satellite furthermore learned that the availability of simulators, used as stubs or drivers for missing software and hardware modules, was a valuable asset for the independent development teams. Thereto an OBC simulator would have to be built, implementing the exact functionality of the interfaces defined in the interface specifications. This would allow verification of designs and to validate partial developments. If such a simulator of OBC hardware, sensors and operating system could be made available to the prime contractor at the start of their application software coding cycle, it would for instance be possible to develop the complete ASW on the local development system and transfer it only in a final stage to the target system for integration and testing. This allows to run the same ASW, without additional coding effort, both on the development system as well as on the target system.

To save further on cost it was decided to use low-cost development tools, such as PCs and already available compilers and other tools. Except for reused, existing software, almost all software development for flight software, simulators and SCOE could be done on PCs. Although the "C" compilers available at DASA, Fokker Space and NLR were all three of a different brand, this seemed not to impose a problem because of the established coding rules.

To allow for easy, reliable and fast data exchange of ideas, documents and program sources and binaries it was decided to establish unrestricted Internet connections for E-mail and FTP (File Transfer Protocol) between the development teams.

3. ARCHITECTURE

3.1 Electrical Architecture – The general electrical architecture of the OBC subsystem is shown in figure 2. This illustrates all hardware / software interfaces of the OBC. On the left side the various off-the-shelf sensors are shown: a differential GPS, a standard airborne attitude and heading reference system, laser altimeter, wind sensors, temperature sensors and housekeeping data from various sources, including feedbacks. All are linked to a data acquisition unit and then translated into a single Pulse Code Modulation (PCM) stream. This stream is sampled by the OBC as input to its control loop software, saved on an on-board solid state recorder and also sent in parallel to the ground for monitoring.

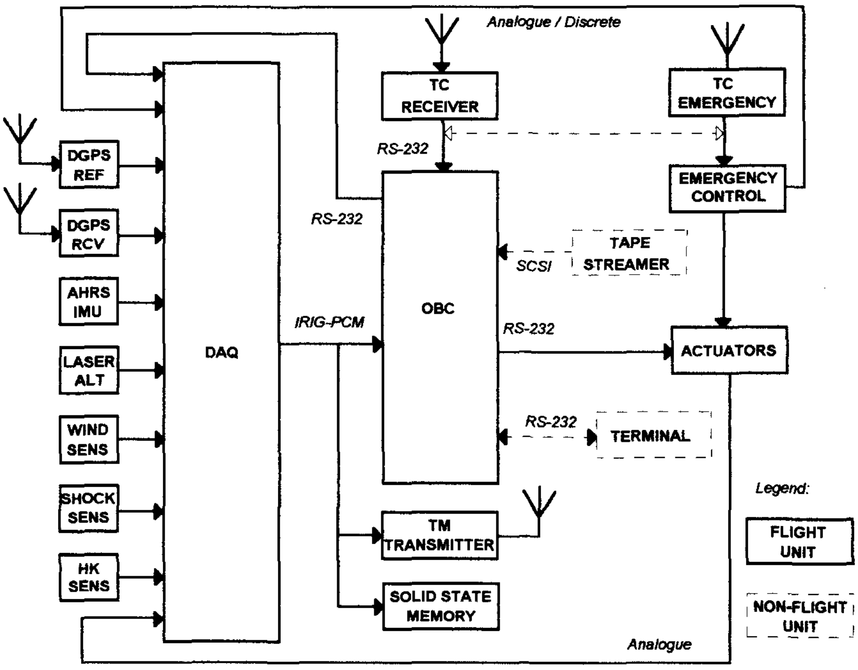
Analogue / Discrete
TC RECEIVER
TC EMERGENCY
RS-232
EMERGENCY CONTROL
DGPS REF
DGPS RCV
AHRS IMU
LASER ALT
WIND SENS
SHOCK SENS
HK SENS
DAQ
RS-232
IRIG-PCM
OBC
SCSI
TAPE STREAMER
RS-232
ACTUATORS
RS-232
TERMINAL
TM TRANSMITTER
SOLID STATE MEMORY
Analogue
Legend:
FLIGHT UNIT
NON-FLIGHT UNIT

Figure 2: PTD OBC Electrical Architecture

The OBC processor is based upon a VME architecture with a Motorola 68040 µprocessor. The tapestreamer is only used for software loading, the terminal is used for health monitoring and entering of wind parameters just prior to dropping the system from an aircraft. The TC receiver and TC emergency links can be used for commanding the unit in-flight, including completely manual override of parafoil control or ignition of an emergency sequence, using pyrotechniques for dropping the ballast and deploying a backup parachute.

3.2 System Software Architecture – The software architecture of the OBC software is illustrated in figure 3. It shows the logical software layering of the software components (in a simplified view of reality).

The Application Software (ASW) tasks run on top of the OBC platform, consisting of computer hardware and interfaces plus Basic Software (BSW). The task of

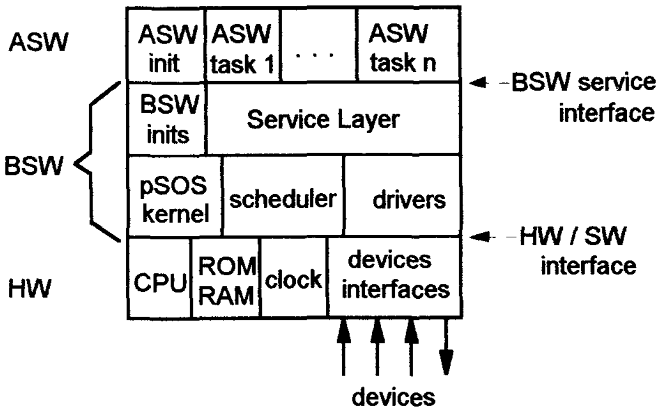
ASW
BSW
HW
ASW init
ASW task 1
. . .
ASW task n
BSW inits
Service Layer
pSOS kernel
scheduler
drivers
CPU
ROM RAM
clock
devices interfaces
devices
BSW service interface
HW / SW interface

Figure 3: OBC Logical Architecture

the BSW is to provide a single Service Access Point (SAP) interface to the ASW, thereby hiding implementation details from the ASW and providing the platform independent services that the ASW requires.

The Basic Software consists of the following items:

1. pSOS+ multi-tasking operating system kernel,
2. Off-the-shelf drivers for the interfaces to sensors, actuators, TM/TC link, tape streamer, and ASW housekeeping data.
3. Initialization functions,
4. Service Layer, providing the SAP services to the ASW, and allowing equivalent interfaces to the flight OBC and to the OBC simulator,
5. A scheduler which cyclically activates the periodical GNC algorithms at predefined moments inside the control cycle.

3.3 Interface Specification – The interface between the BSW and the ASW is defined in the On-Board Computer Basic Software Interface Control Document (BSW ICD). This interface specification describes the protocols and data formats of all interactions between the Application Software and the Basic Software. The document also services as an interface contract between DASA and Fokker Space/NLR. Thereto it was necessary to make it a very detailed specification, including "C" header files. This ICD, together with the OBC simulator based upon it, and its availability to all three partners involved in the software development, greatly contributed to a reliable development.

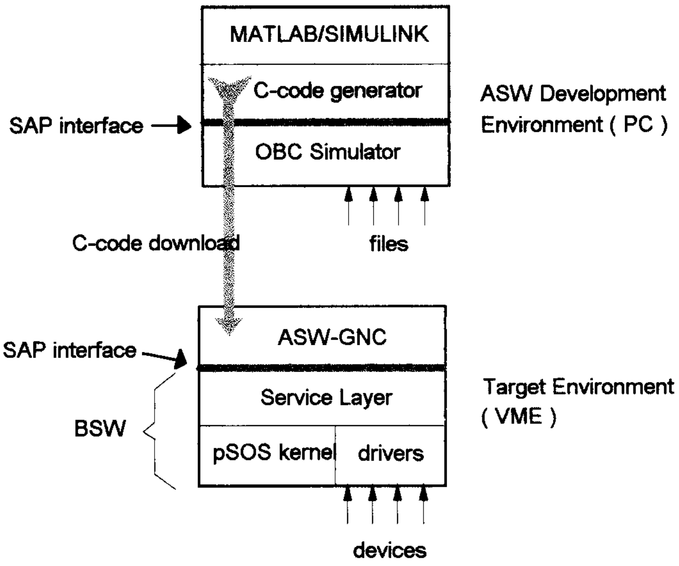
MATLAB/SIMULINK
C-code generator
SAP interface
OBC Simulator
ASW Development Environment (PC)
files
C-code download
SAP interface
ASW-GNC
Service Layer
BSW
pSOS kernel
drivers
Target Environment (VME)
devices

Figure 4: SAP Interfaces for BSW and Simulator

3.4 Target Computer Simulator – A Target OBC Simulator emulates the complete OBC hardware and BSW at the level of the BSW ICD.

This WINDOWS-based simulator is written in "C" and is used both by BSW and ASW teams to verify proper behavior of their software. It is used as part of the ASW development environment to test the following items:

- All interfaces between BSW and ASW (Service Access Points);
- The ASW functionality in open-loop configuration;
- The ASW functionality in closed-loop configuration;
- Provide a preliminary assessment of the OBC performance in terms of CPU load.

Figure 4 illustrates the Service Access Point (SAP) interface provided by the OBC simulator in the ASW module test environment and the SAP interface provided by the BSW in the target environment. The protocols for both SAP interfaces are the same, although their implementation and usage is completely different for both environments.

Special provisions allow to add additional ASW-level tasks that simulate environmental conditions. These tasks communicate through dedicated service calls with the simulator to dynamically obtain actuator output values and preset sensor values. No special interfaces with the flight ASW are necessary, allowing equivalent ASW on simulator and flight units.

3.5 **Application Software Architecture** – To allow for easy replacement of real ASW tasks by simulations, both on the development system as well on the target system, the multitasking architecture as shown in figure 5 was developed and implemented, using two different priority levels. The higher priority level may pre-empt the lower level; tasks within the same priority level are non pre-emptive. The boxes shown here generally represent a software task which is - in the scope of the PTD project - a parameterless procedure executed by the real time scheduler with a user defined rate. Communication between tasks is only done via the data buffers, represented here by bubbles. The memory allocated to the buffers is administrated by the BSW such that the BSW is in control of read / write access and can solve potential conflicts resulting from the parallel execution of the two priority cycles.

The tasks and buffers drawn with thick lines are provided by the BSW and can be accessed by the ASW using the SAP interface syntax which is identical on target and simulator platforms. Therefore, the ASW can be transferred to the target system without any additional code adaptations.

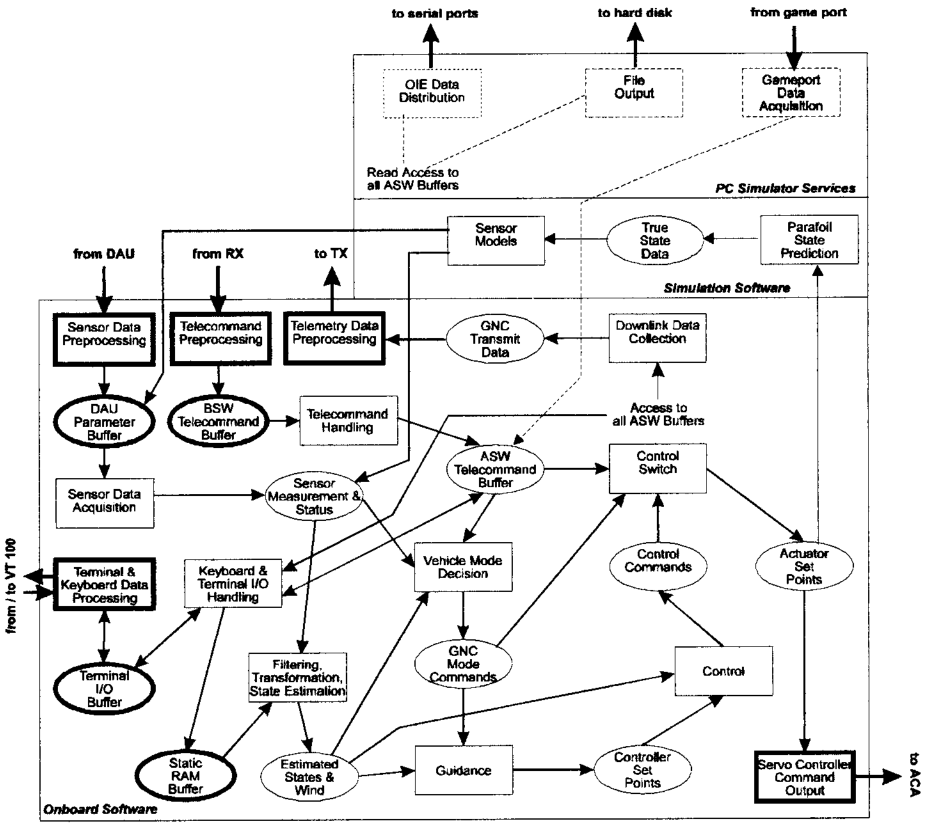
to serial ports
to hard disk
from game port
OIE Data Distribution
File Output
Gameport Data Acquisition
Read Access to all ASW Buffers
PC Simulator Services
Sensor Models
True State Data
Parafoil State Prediction
Simulation Software
from DAU
from RX
to TX
Sensor Data Preprocessing
Telecommand Preprocessing
Telemetry Data Preprocessing
GNC Transmit Data
Downlink Data Collection
DAU Parameter Buffer
BSW Telecommand Buffer
Telecommand Handling
Access to all ASW Buffers
ASW Telecommand Buffer
Control Switch
Sensor Data Acquisition
Sensor Measurement & Status
from / to VT 100
Terminal & Keyboard Data Processing
Keyboard & Terminal I/O Handling
Vehicle Mode Decision
Control Commands
Actuator Set Points
Terminal I/O Buffer
Filtering, Transformation, State Estimation
GNC Mode Commands
Control
Static RAM Buffer
Estimated States & Wind
Guidance
Controller Set Points
Servo Controller Command Output
to ACA
Onboard Software

Figure 5: PTD application software architecture

4. SIMULATOR USAGE

4.1 Role of Simulators - Within the PTD project, simulations played an essential role in GNC algorithm development, mission management concept implementation, pilot training, software integration tests, and post flight analysis. The idea of 'rapid prototyping' in terms of a short turnaround cycle between GNC design, development, and implementation was translated into the requirement to minimize the manual coding activities. This was also regarded as essential due to the allocation of the tasks to different engineering teams within the project consortium. Consequently, the software transfer concept presented in figure 6 has been applied.

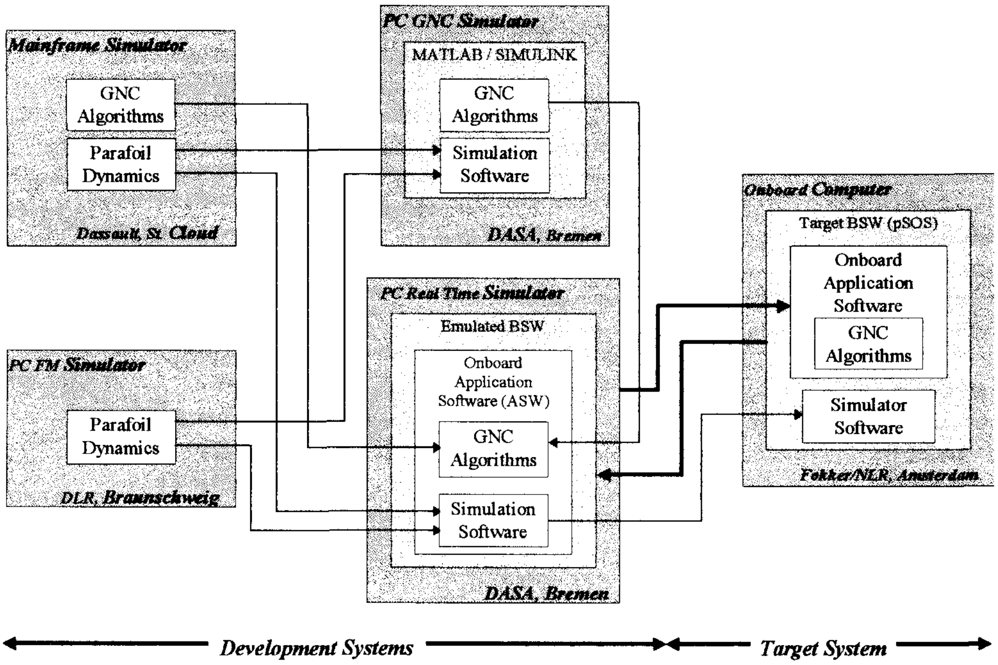
Mainframe Simulator
GNC Algorithms
Parafoil Dynamics
Dassault, St. Cloud
PC GNC Simulator
MATLAB / SIMULINK
GNC Algorithms
Simulation Software
DASA, Bremen
PC Real Time Simulator
Emulated BSW
Onboard Application Software (ASW)
GNC Algorithms
Simulation Software
DASA, Bremen
PC FM Simulator
Parafoil Dynamics
DLR, Braunschweig
Onboard Computer
Target BSW (pSOS)
Onboard Application Software
GNC Algorithms
Simulator Software
Fokker/NLR, Amsterdam
Development Systems
Target System

Figure 6: Software transfer during development and integration activities

The parafoil dynamics models have been extracted from existing simulators shown on the left hand side. These models have been provided in FORTRAN and were translated to ANSI-C using an automatic conversion program. Without any modification, these models could be reused on all platforms. This also applies to the GNC algorithms provided by Dassault Aviation.

An alternative solution for the GNC algorithms was applied at DASA using the MATLAB control toolbox for controller design and SIMULINK for simulations (a MATLAB extension). The full nonlinear parafoil model was used for design verification. It has to be noted that the test strategy for the software must take into account the special character of the PTD project: as the knowledge of the parafoil dynamics increases with the number of flights, the models and control algorithms may be modified after each flight.

The core of the simulation tools is the so called 'real time simulator' built on top of the OBC simulator. Although multitasking is obviously not possible on a DOS PC, real-time execution could be enforced using the DOS system clock which made the simulator applicable for interactive piloting as well.

For the AIT activities it was considered useful to add a closed-loop simulation capability to the target system application. Therefore, the simulation tasks shown at the top of figure 5 are also part of the ASW to be transferred. On the target system, these tasks will be deactivated during the OBC boot sequence only when running in flight mode. The multi-tasking architecture of the system provided for an easy addition of such simulation tasks. Moreover, interactive simulation and analysis capability was required from the PC simulator. Thereto an additional layer of PC simulation services was provided with access to interactive control devices and hard disk storage capabilities not available on the target system. This part of the ASW is exempted from the transfer (dotted lines).

4.2 Results of this Approach – In line with the timeline established during the proposal phase, the system software and application software, hardware and software interfaces were agreed one month after the start of the project. Six weeks later the PC-based OBC simulator (GNC hardware and system software) was up and running and could then be used for the complete application software (guidance and navigation) development. This development approach proved to be of great value during the whole course of development.

Well within another 3 months a first pre-integration of the OBC hardware (excluding a few units), system software and major parts of the application software took place on a laboratory model of the target system. This integration took less than one day to verify proper interface protocols and furthermore validated the PC-based OBC simulator and thus increased the confidence to the development approach and the software transfer process.

Subsequently, the ASW was usually transferred from DASA to NLR using E-mail. Due to the strict application of the coding standards and the portability of the

ASW interfaces, the software transfer only consists of an automatic cross compilation and loading via a tape streamer.

The only problems occurring during the ASW integration to the target system were related to parameter inconsistencies between the BSW and the ASW which could only be detected as soon as real hardware (e.g. the actuator assembly) became involved. Some other system anomalies resulted from incorrect wiring. Due to the fact that the same ASW could be run on a PC and the target system it was always rather easy to isolate the source of a problem. Since motion animation of the test vehicle was impracticable, the simulation capability of the ASW has proven to be very useful for these tests.

5. CONCLUSIONS

The ASW development approach applied for PTD has proven to be practicle even for a distributed development team. Introducing the BSW as interface layer in order to separate hardware and software development, gave the teams a large design flexibility and the possibility to test the system very early using laboratory mockups. It also greatly simplified the communication between the interdisciplinary engineering teams avoiding costly misunderstandings.

Especially the combination of an early interface specification with a simulator built according to that specification, together with the possibility to run that OBC simulator on various platforms, has been proven to be very useful. This incremental development approach was felt far more effective than the common waterfall model with extensive design documentation, that has to be iterated again and again, usually lagging far behind the actual design status and thus causing many interface inconsistencies.

This approach would not have worked without the direct communications between the various teams, either in the form of temporary co-locations, or in the form of Internet connections used for the easy, fast and reliable exchange of ideas, textual and graphical specifications and program sources and binaries.

A prerequisite for the established informal and flexible development approach is however certainly the early delegation of responsibilities and corresponding mutual trust between the various development teams. This is an important and many times difficult factor in the ESA context of space projects, spanning so many different cultural backgrounds.

Furthermore, this flexible development approach would probably never have been allowed for a real space project. We strongly feel however that specific aspects could however be implemented there as well, without compromising quality and safety. This concerns the use of an incremental approach instead of the waterfall model, and more direct informal communications at a technical level than is usually seen in ESA projects.

6. REFERENCES

[1] ESA Software Engineering Standards, PSS-05-0, issue 2.

[2] Guerin and Laue: “Commonality - A keyword for the Groundsegment Infrastructure”, ESA Bull. 1992 (72, Nov.), pp. 88-93.

[3] H. Schildt: “The Annotated ANSI C Standard, ANSI/ISO 9899-1990”, ISBN 0-07-881952-0.

[4] G.J. Dekker, E. Kesseler: “Product Assurance for the Development of the SAX AOCS Application Software”, ESA Prod. Ass. Symposium and Software Product Assurance Workshop, ESA SP-377, May 1996, pp. 283-289.

SESSION 7:
INSTRUMENT POINTING AND DRAG FREE

Chairman: P. Vuilleumier (ESA/ESTEC)

POINTING SYSTEM CONCEPT FOR SOLAR INSTRUMENTS LOCATED ON THE INTERNATIONAL SPACE STATION TRUSS

Th. BLAIS
A. DEFENDINI

MATRA MARCONI SPACE FRANCE
31 avenue des Cosmonautes
31044 TOULOUSE CEDEX 4

Phone : (33)5.62.19.70.73 Fax : (33)5.62.19.73.03
Phone : (33)5.62.19.77.02 Fax : (33).5.62.19.78.97
e.mail : thierry.blais@tls.mms.fr
e.mail : ange.defendini@tls.mms.fr

ABSTRACT

This paper presents the results of the work performed for the specification and the conceptual design of a pointing system dedicated to solar instruments accommodated on the International Space Station (ISS) truss structure. The ISS characteristics in terms of attitude variation and environment (micro-vibrations) are presented. Performance requirements of the pointing system in terms of angular range required to follow the relative motion of the Sun, pointing accuracy and stability required to fullfil the instrument need are introduced. A CD ROM video, generated by CAD modelling under the SYSTEMA environment developped my MATRA MARCONI SPACE, illustrates the pointing system mission and operations on ISS. This tool simulates the evolution of the payloads fields of view and their possible masking by ISS elements (Solar Array, etc).

Several pointing mechanism architectures were compared. The main functions and components of the prefered configuration, hereafter called "standard cardanic configuration", are presented. Among them, the launch locking device (LLD) was identified as a critical element, since a relocking mechanism is required for returning the payload down to Earth. The implementation of LLD ensures high performances achievement but leads to significant extra-cost. A cost-effective option, without LLD, has therefore been investigated. The drawback are reduced pointing performances. System budgets are compared for both concepts: with our without LLD.

1. INTRODUCTION

In 1995, the European Space Agency initiated a study related to the physical accommodation of a set of reference payloads on the Express Pallet Adapter (EPA) and to the definition of their integration process.

1.2. Express Pallet Adapter

Up to 4 Express Pallets can be accommodated on the starboard truss of ISS through the Payload Attach System (see figure 1). Two of these Express Pallets are zenith oriented, the other two being Earth pointing. This offers multidirectional viewing capacities and covers the whole spectrum of applications. Each of these Express Pallets is capable of accommodating 6 Express Pallets Adapters (see figure 2). The major characteristics of the Express Pallet Adapter are given in the following table.

Parameter	Express Pallet Adapter
Payload mass	225 kg
Size	1.60 m x 0.86 m (10 cm adapter height)
Height limitation	70 cm (TBC)
Thermal Interface	Passive
Power Interface	2.5 kW @ 120 V or 28 V DC
Data Interface	Mil-STD 1553B ; RS 422 /485 Ethernet (TBD) Analog ; Discrete ; High Rate data (Optical link)
Telemetry	payload data requested through Payload Interface Adapter PIA

1.1. Payloads grouping

The reference payloads which are foreseen by ESA to be installed on Express Pallet Adapters are of several types:

- solar instruments requiring tracking of the Sun,
- astronomy instruments
- environmental instruments
- a space exposure biology facility

Such a variety of instruments present a wide range of characteristics and peculiarities when looking into their detailed accommodation.

A grouping is composed of mutually compatible instruments sharing common mission requirements and which can be accommodated together on the same

---

Proceedings Third International Conference on Spacecraft Guidance, Navigation and Control Systems, ESTEC, Noordwijk, The Netherlands, 26-29 November 1996, ESA SP-381 (February 1997)

Express Pallet Adapter. A preliminary analysis led to the selection of 8 groupings for deeper analyses.

The major constraints encountered for the grouping of solar experiments are related to pointing and stability requirements at interface level. Solar instruments are mounted on the support plate of the pointing system. In addition to the instruments, a Sun Sensor installed on the plate to control the pointing direction. A solar grouping installed on the pointing system is presented on figure 4. The pointing system mechanically interfaces both with the support plate and the Express Pallet Adapter.

2. ANALYSIS OF THE SOLAR INSTRUMENTS MISSION

2.1 Kinematics Requirements

When installed on board ISS, solar instruments require a compensation of two angles to follow the Sun:

- a derotation angle which compensates for the orbital motion of the station around the Earth: ±30° for 15 minutes of observation, ±40° for 20 minutes, ±60° for 30 minutes. The derotation rate is about 4° per minute i.e. 1mrd/s,
- an indexation angle which accounts for the rotation of the ascending node and of the rotation of the Earth around the Sun. A ±75° compensation is required to be able to follow the Sun during a complete year. The indexation rate is approximately 5° per day, i.e. 1µrd/s.

Figure 3 illustrates the rotation of the Sun in an ISS reference frame. The variations of the indexer angle over one year are in the range [-80° ; 80°]. A "reasonable" pointing system design takes into account a limited range. In fact, ISS structural members, and in particular the Russian Solar Arrays, can generate a more or less important masking of instruments fields of view depending on the position of the Sun (indexer angle). To avoid such effects a canted indexer with a range of -20°/+60° has been preferred instead of a centred indexer.

To validate the kinematics of the pointing system, the geometry of the ISS, including all the mobile parts such as solar arrays, was modelled with a MMS concurrent engineering software environment : SYSTEMA. The pointing mechanism candidate configurations were modelised too. A large number of cases was analysed by simulation (rotation during one orbit, seasonal effects) to visualize the Sun visibility. The more demonstrative results are recorded on a CD-ROM which provides user friendly interfaces and easy-to-understand simulation results.

2.2. Pointing System Operational Modes

The Sun tracking is the main purpose of the mechanism with regards to the payloads operations. Additional modes are necessary to complete the overall mission. The main operational modes of the pointing system are illustrated hereafter.

- ***Wait***. The wait mode is active between two observation periods. It corresponds to a set of angular positions (0, 0) pointing towards Nadir. This position provides maximum clearance with regards to EVA and Servicing operations. It is a safe configuration and the system can remain as long as necessary in that position without endangering neither the payload nor the pointing system, in terms of mechanical, electrical and thermal conditions. In case of electrical supply switch off, the mechanism ensures no motion and remains in wait position.
- ***Rallying***. The rallying mode is activated before an observation period. The trajectory definition takes into account the ISS attitude knowledge and the ephemerids. The trajectory to be followed is defined with respect to the EPA frame and is executed in local position/velocity control loop. It ends in a fixed position, waiting for the Sun detection by the Sun sensor.
- ***Centering***. When the Sun rises in the Sun-sensor Field of View, a relative pointing error signal is generated by the Sun sensor. Within few angular degrees, the pointing system zeros the Sun sensor error signal by generating commands towards the pointing mechanism actuators. At the end of "Centering", both the pointing accuracy and the pointing velocity stability requirements are fulfilled, consistent with the tracking mode.
- ***Tracking***. It provides all the dynamical, pointing, electrical and thermal conditions necessary for the nominal utilisation of the payloads. Scientific data are delivered by the payloads and stored by the payload control unit. The tracking is performed during 20 min typically, requiring 80° operational derotation angle. This angle ensures no interference of the payload by the ISS elements. At completion of tracking, the mechanism control is switched from Sun pointing to velocity zeroing with respect to an ISS related frame.
- ***Back rallying***. When the pointing mechanism velocity is nulled, a rallying trajectory is executed, starting from the "end of tracking final point" to the "wait" location. The trajectory is defined in terms of position/velocity profiles ensuring proper rallying towards the "wait " point.

The mode definition aims at reducing as far as possible the number of modes. The purpose is to limit the complexity of the control software. One shall take care of the sequencing logics which may become huge in relationship with the ISS environment : operations definition, operators authority, task planning including EVA activities and robotics.

3. ANALYSIS OF POINTING SYSTEM REQUIREMENTS

3.1 Pointing and Stability Requirements

The pointing system supports a set of payloads. As indicated at the beginning of the paper, each payload has its own set of requirements (power, sequencing, pointing).

Based on a payload grouping, an enveloppe of pointing requirements was issued. The reference groupings considered during the study leads to the following pointing requirements :

- absolute pointing requirement : better than ± 0,1° (1σ) between the actual Sun direction and the payload Line of Sight (LOS) ;
- pointing stability. Two different sets of stability requirements were considered :
  - . *option 1* : $\leq \pm$ 6" (1σ) over 2 seconds
  - . *option 2* : $\leq \pm$ 50" to 200" (1σ) over 2 sec
- no pointing requirement around the Sun direction was arisen by the payload designers ; a value of less than 0,6 dg over 10s typ. was considered as acceptable. This value is consistent with the rotation around the Sun direction without specific control around this axis.

3.2. Analysis of Pointing Requirements

When considering a set of payloads, the integration accuracy and long term effects (thermo-elastic, hydro-elastic when applicable) participate to the absolute pointing performances. A set of frames was defined, allowing to point out the possible sources of error and to establish a preliminary pointing budgets. The contributors are the Sun sensor bias, the mounting accuracy of the elements on the mobile plate, the internal error between the payload mounting plate and the payload actual pointing direction. Additional errors are due to the mechanism components characteristics and to the control law performance : both bias and transient errors were considered. The pointing accuracy requirement has been identified has being not too critical.

3.3. Analysis of Stability Requirements

The pointing stability requirement can be translated into a frequency template where the maximum amplitude of a monochromatic motion of the pointing direction is given as function of the frequency. At high frequency, a given motion magnitude of the P/L LOS has more severe effects in terms of stability compared to low frequency motion. Special care shall be taken at frequency above 1 Hz.

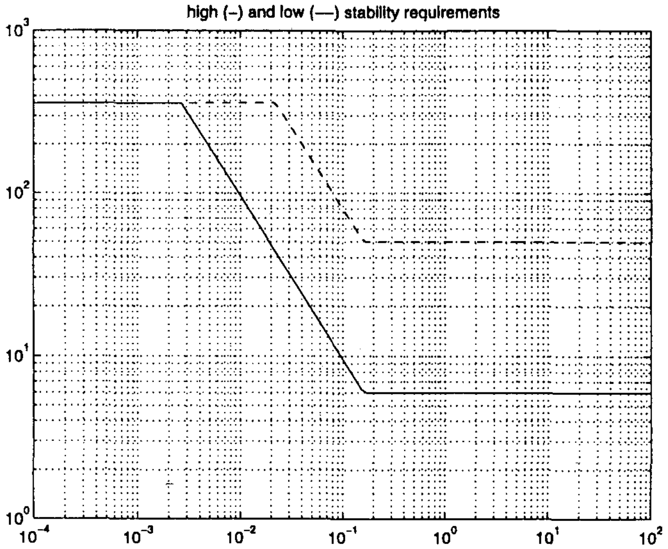

Pointing stability requirement

This stability requirement has to be compared to the disturbances generated by the ISS at pointing system interface level. The available literature dealing with the ISS generated disturbances was reviewed. The main sources of linear accelerations are pointed out by NASA to be the Crew, the US On-orbit Segment and the Russian Solar Arrays (see figure below). The disturbance magnitude is assessed by between DC and 10 Hz. No data are provided about the disturbance level above 10 Hz..

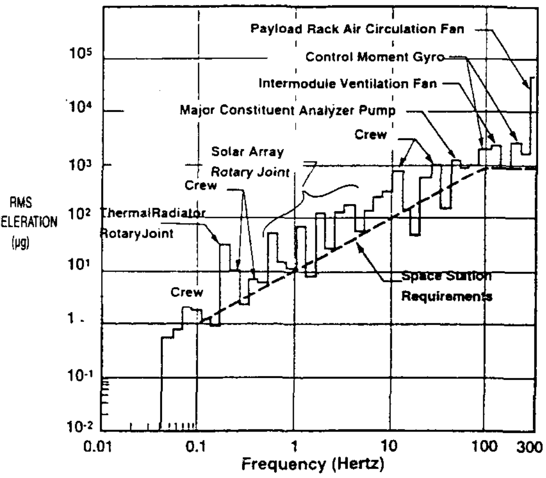

High frequency disturbances (vibrations and sporadic impulses) of the microgravity environment

The linear displacement generated at Express Pallet level are illustrated below.

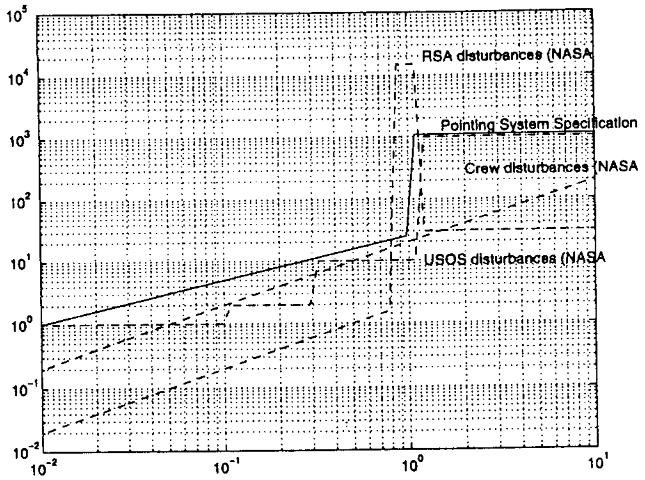

For simplicity sake, an enveloppe of the template was considered in terms of ISS interface specification for the pointing system design. This enveloppe does not incorporate completely the effect of the RSA around 1 Hz. It was considered that this data needs to be confirmed before to be taken into account in the interface specification. Only "reasonable" disturbance level was considered around 1 Hz, in consistency with the template above and below this frequency region.

An other design driver is the level of micro-vibration generated by the ISS environment at EPA level in terms of *rotational jitters*. No data could be found in the literature. As the isolation properties of the pointing system should be consistent with the rotational jitter, this type of data shall be provided by NASA. Without the associated template, it is difficult to perform any mechanism conceptual activities.

In order to over come this lack of information, MMS used a simplified model of the ISS dynamical behaviour. This model allows to translate the micro-gravity data provided by NASA into rotational jitters magnitude versus frequency. The resulting template was considered preliminary. The engineering approach followed is based on a robust pointing system concept, featuring sensitivity to the ISS dynamical interface as low as possible. Special emphasis was put for derivating mechanism design requirements in terms of static balancing, rotational stiffness, eigen frequencies and associated mode shapes, "magnification" factors. These parameters were determined to match the isolation requirements and to provide sufficient margins consistent with the interface specification uncertainties.

4. POINTING SYSTEM CONCEPTUAL DESIGN

4.1. Simplicity constraints

The overall cost of the pointing system development aimed at being minimised. Complex architectures were illiminated when possible, focusing on pointing system alternatives as simple as possible. One cost driver is the Launch Locking Device (LLD) ; the cost of which being usually of the same order of magnitude as the mechanism itself. Furthermore, dedicated isolation equipments were not privileged compared to simpler design alternatives. The combination of dedicated isolation device - passive or active - with the implementation of LLD appeared to be too expensive.

4.2. Pointing system overview

Geometrical and kinematical analyses were completed on various mechanism candidate configurations. Sensitivity to micro-vibration disturbance was assessed. The configuration featuring the best quotation after trade-off is sketched hereafter.

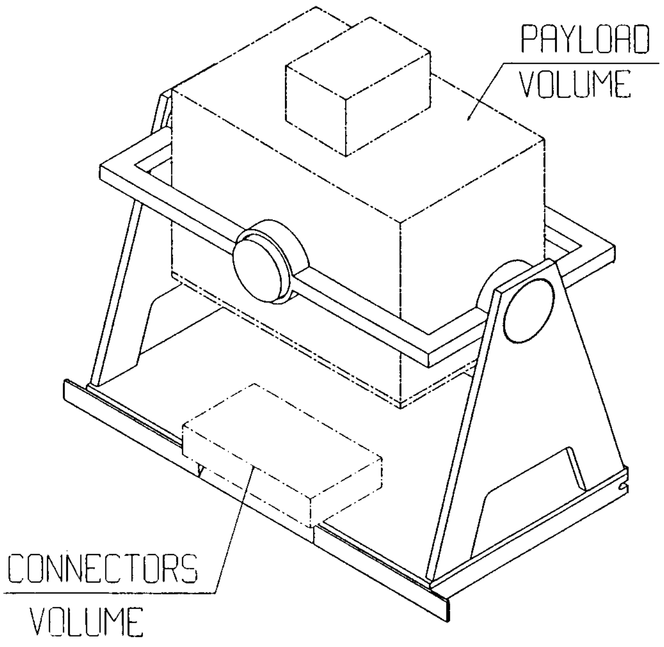

This configuration provides maximum clearance and maximum room for the accommodation of the payloads on the mobile plate. A sun sensor is located with the payload set and is used to close the control loop. Possibility to implement a cost-effective sun sensor was analysed. A good candidate is the LIASS sun sensor (see figure 5).

For the mechanism motor drive and sensor proximity electronics, the possibility to accommodate a recurring hardware was investigated. A cost-effective candidate is recalled figure 6. It was developed in the frame of a European programme.

4.3. Control architecture

The pointing system control is embedded in the centralised Payload Control Unit (PCU). This architecture takes benefit of the computation capabilities provided by the PCU, requiring no additional computer for the pointing system control. The dedicated electronics : motor drive, joint sensors and Sun sensor acquisition functions are located on PCBs plugged inside the PCU cabinet. Two main control modes are proposed :

- *angular control loop* using the mechanism hinge sensors for rallying and Sun detection modes. The corresponding microgravity disturbances - rotational jitters - rejection capabilities are not significant but are sufficient with respect to the requirements.

- *Line of Sight (LOS) control in closed loop* in tracking mode. The two axes of the mechanism are driven from the Sun sensor outputs. The microdisturbances generated by the ISS at EPA level can be rejected in an efficient way, combined with the low mechanical sensitivity provided by the mechanism concept.

5. MECHANISM MAJOR CONSTRAINTS : TRANSPORTATION AND INSTALLATION AT ISS

Transportation is made by the National Space Transportation System (NSTS - Shuttle). The nominal way is that the adapter is locked inside the Dry Cargo Carrier (DCC), which itself is installed on the Unpressurized Logistics Carrier (ULC) which interfaces with the Shuttle Cargo Bay. Adapters can also be transported while mounted on the Express Pallet, which also interfaces with the ULC.

For ESA groupings the method of transportation is not fixed yet. The NSTS will be berthed to ISS by the Space Station Remote Manipulator System (SSRMS) about 48 hours after its launch (TBC) . The cargo bay will be open and the Express Pallet Adapter (or even the Express Pallet with some EPAs) will be transferred to its final destination by ISS robotics (combination of SSRMS and Special Purpose Dexterous Manipulator SPDM). The duration of transportation and installation from launch to final position may last up to 72 hours (TBC).

The criticality of these operations lies in the thermal conditioning of instruments since, up to now, no power seems to be available either in the cargo bay, or when transported by SSRMS/SPDM (with a potential exception when the Mobile Base System supporting the SSRMS/SPDM is stationary).

In launch phase, the quasi-static loads are : 4g. Safeguard atmospheric re-entry features 8g. Sine and random are not specified. In addition, vibration magnification is indicated by NASA to be dependent on the location in the NSTS cargo bay. A specific constraint is coming from the ISS utilisation : the payload set and the pointing mechanism shall be returned to Earth. Re-entry conditions in the cargo bay shall be withstood by the mechanism.

Two extreme design approaches are therefore :

- either utilisation of a Launch Locking and Re-entry Relocking Device (relockable LLRRD), which is an expensive device.
- or without locking device. This approach is more risky and the launch constraints implicate severe mechanism design drivers.

In both cases, the mass of payload implemented on the pointing system is in the range [120 ; 200 kg].

When considering performance and development costs, the definition of the launch and the re-entry environments - including magnification - are critical aspects. It was stressed out that the environmental specification needed to be refined to secure the mechanism development.

6. PERFORMANCES BUDGETS

To go further in the design-to-cost approach, two mechanism concepts were investigated :

- high performance (option 1) featuring more demanding requirements but implicating more expensive developments.
- limited performance (option 2) ; the requirements relaxation being an opportunity to introduce cost savings.

The feasibility of both options had been established during the study. The major differences between the two options were:

- a launch locking and relocking device was mandatory for the "high" performance pointing system, whereas for the "low" performance pointing system this system could probably be replaced by a rotational blocking device at hinges level. Nevertheless this would have to be confirmed by deeper analysis when the shuttle and ISS environments are better specified,
- the high performance pointing system necessitates a digital sun sensor whereas the "low" performance pointing system can include an analog sun sensor.

Achieved performance and budgets for both options are summarized in next table. For *option 1* (high performance pointing system) the stability is directly affected by the ISS disturbances. Static unbalance is a major contributor, combined with the effect of mechanism structural magnifications at eigen frequencies. For *option 2* (reduced performances), more severe constraints apply to the guidance components due to the fact that they have to withstand the launch loads. The internal mechanism noises become the most significant contributors, in association with the noises of the Sun sensor (in that case the Sun sensor is cheaper but features higher noises).

	"High " Performance Option	" Low " Performance Option
Pointing Accuracy	Ensured by Sun sensor and alignments stability	
Achieved Pointing Stability	±7.4 arcsec over 2s (1σ)	±43 arcsec over 2s (1σ)

The mass budget for both options was assessed and is quite similar (50 kg). This result can be explained by the fact that the mechanism mass saved by implementing a LLRRD is counterbalanced by the extra-mass of the LLRRD itself. For various payload groupings, the overall mass budget exceeds by 130 kg the EPA specification (225 kg).

Since then two major actions have been completed to fit the mass allocation:

- reduction of instruments mass to 80 to 120 kg (by deletion of one instrument),
- iteration on the frequency response requirement of the pointing system (reduction of the first eigenfrequency)

After iteration on the pointing system definition, a new mass budget was established in compliance with EPA mass requirements, leading to a total mass of instruments of 110 kg.

The advantages of each option can be pointed out. The stability performance achievable with the option 1 is compatible with the more stringent requirements. The mechanism design can be optimised considering the orbital constraints ; sensitivity to the definition and the specification of the launch environment is very low.

Conversely, the feasibility of a mechanism without LLRRD seems possible, but remains very sensitive to the launch environment specification. A cost effective Sun sensor - LIASS - allows to fulfil the option 2 requirements.

7. DEVELOPMENT PLAN

The assumption is that the development and integration programme for external payloads will start January 97 and will end December 2000 with the delivery of integrated EPA flight units at KSC.

This development plan is based on 3 major steps:

- system analyses covering all aspects common to the various groupings, aiming at specifying all support equipment and at establishing an Interface Requirement Document based on the selected payloads and groupings. This phase will be completed by a System Requirement Review (SRR). Interface specifications of the mechanism with regards to the EPA on the one hand and on the Payload on the other hand are of high importance.

- analytical integration which is mainly dedicated to specific groupings analyses and writing of ICDs

- physical integration which is dedicated to the integration and testing of the different models: a Mechanical and Thermal Model (MTM) of an integrated EPA, an Engineering Model (EM) to validate the data handling and power interfaces between the EPA and the instruments, 3 flight models corresponding to the 3 selected groupings.

The support equipment and the pointing system will have a parallel development flow compatible with the outputs of integration (specification) and with the delivery dates of the various models.

8. CONCLUSIONS

The implementation of external payloads was assessed using the preliminary information available concerning the Express Pallet utilisation. Potential groupings of external payloads load to the establishment of a set of requirements, consistent with each payload needs. Combining the P/L stability requirements and cost aspects, two pointing systems are proposed in response to the two different sets of requirements.

In the course of the pointing system and mechanism analysis, two areas appeared to be major design drivers :

- ISS dynamic disturbances assumptions, concerning translational and furthermore angular jitters (magnitude versus frequency) : need to be defined by NASA,

- Shuttle launch environment and dependency on the location inside the cargo bay. Establishment of interface specification is mandatory.

Cost-effective mechanism designs are very sensitive to these requirements and could not be compatible with stringent environments.

Open points resulting from the current - uncertain - knowledge of the design and capabilities of the Express Pallet are identified. This will have an impact on both the future selection, development and grouping of payload instruments and associated pointing system.

To overcome the uncertainties and proceed with the mechanism design, two classes of requirements were issued and two different mechanism concepts were proposed accordingly. Due to schedule and budget constraints, complex architecture with expensive equipment were avoided. In that respect, gyrometers, accelerometers, passive - and furthermore active - isolation system were disregarded. Special care is then necessary concerning static and dynamic balancing and vibrations structural magnification. The implementation of an expensive LLRRD is pending to the requirements ; it would be mandatory for stringent environmental conditions. The utilisation of off-the-shelf components was deeply investigated. A promising approach is based on the implementation of equipments with minimum non-recurrent cost : analog sun sensor, actuators, angular sensor, acquisition & drive electronics, taking benefit of previous developments.

For MMS, low cost/high stability pointing system is an area of special interest. In order to consolidate early the feasibility of such a system, MMS developed a partial breadboard - one axis - during 3Q96 ; various applications are addressed, including the ISS payload pointing mechanism. The results obtained in terms of noises and stability are very promising.

In the mean time, dedicated breadboard and phase C/D activities were initiated by ESA, with industrial rules. The critical items described herebefore will have to be solved by the selected team, allowing to consolidate the pointing system design. At last, the utilisation of 3D modelling was very powerful, allowing to verify the adequacy of the mechanism kinomatics ; consistency between payload pointing requirements - angular range - and the ISS elements was reviewed in a user-friendly way.

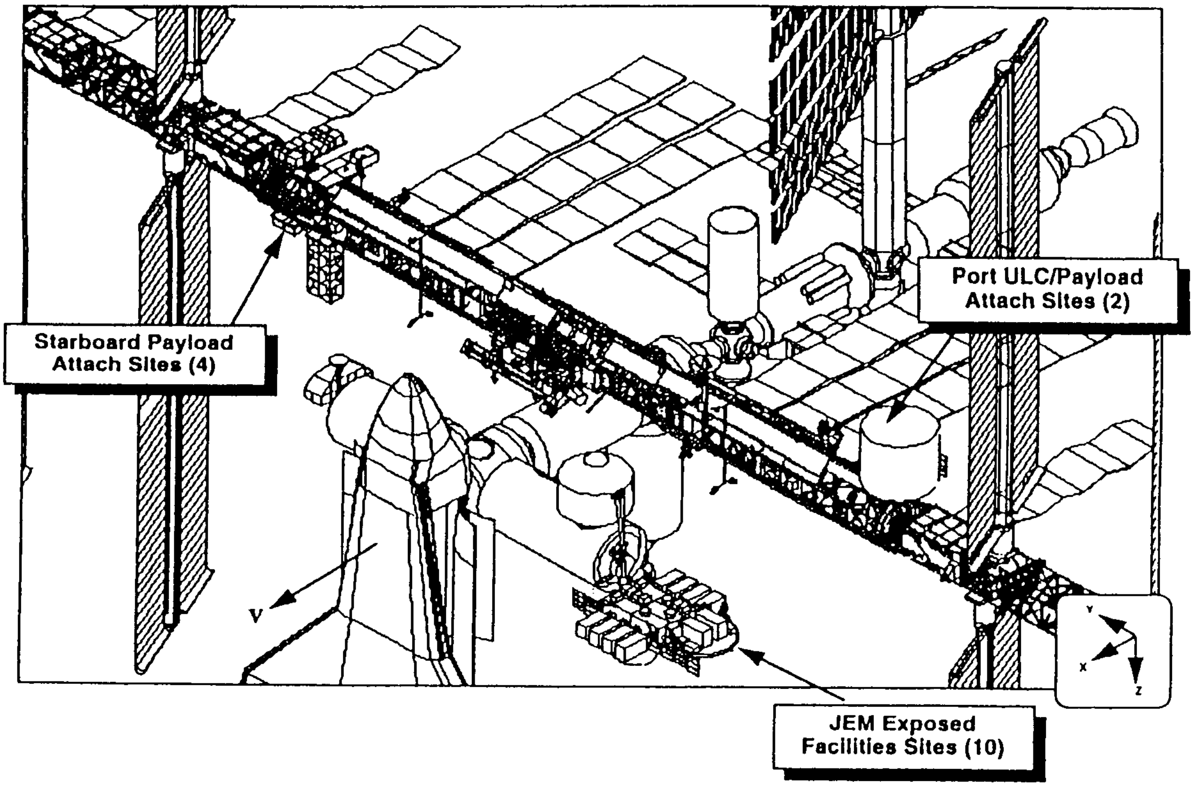
Starboard Payload
Attach Sites (4)
Port ULC/Payload
Attach Sites (2)
V
Y
X
Z
JEM Exposed
Facilities Sites (10)

Figure 1 : Locations of External Accommodation Sites on the International Space Station

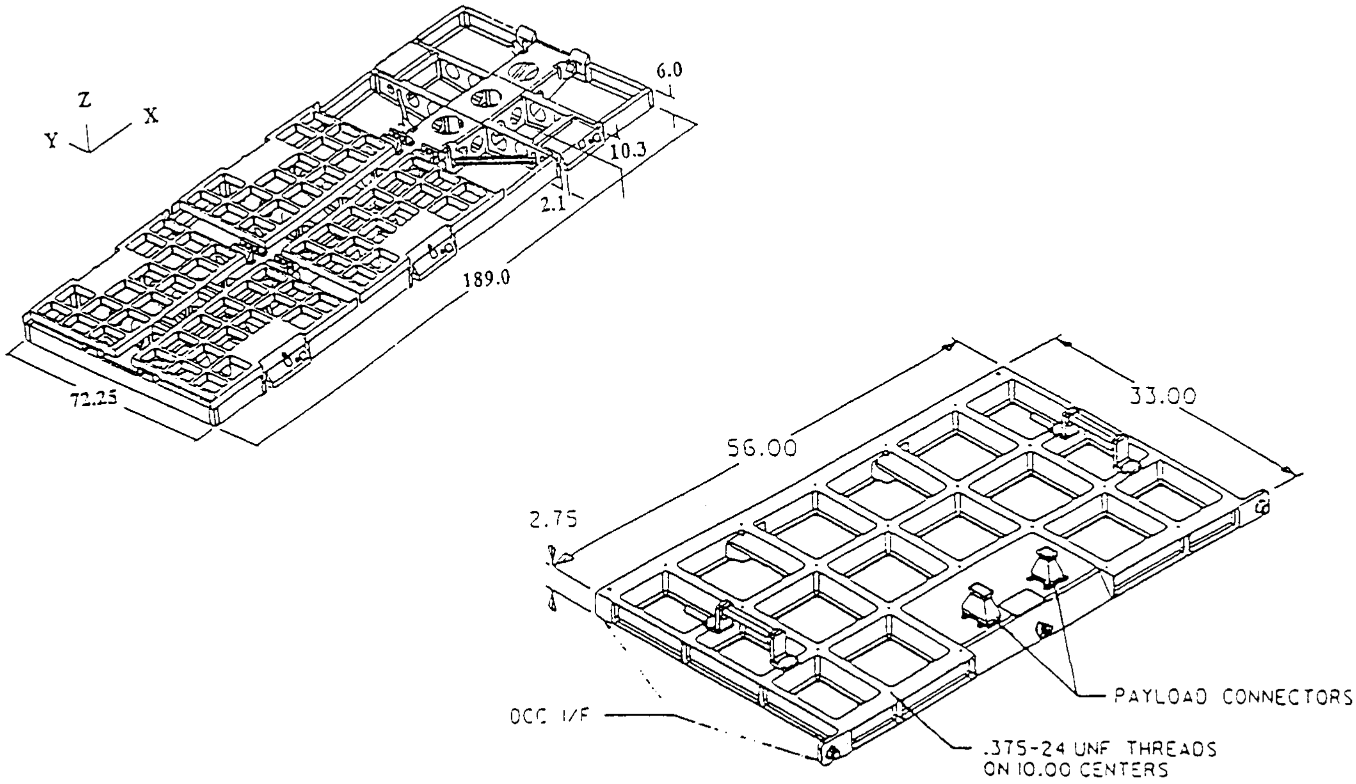
Z
Y
X
6.0
10.3
2.1
189.0
72.25
33.00
56.00
2.75
OCC I/F
PAYLOAD CONNECTORS
.375-24 UNF THREADS
ON 10.00 CENTERS

Figure 2 : Express Pallet Adapter Configuration with 4 adapters mounted (left) and Express Pallet Adapter (right) all dimensions in inches

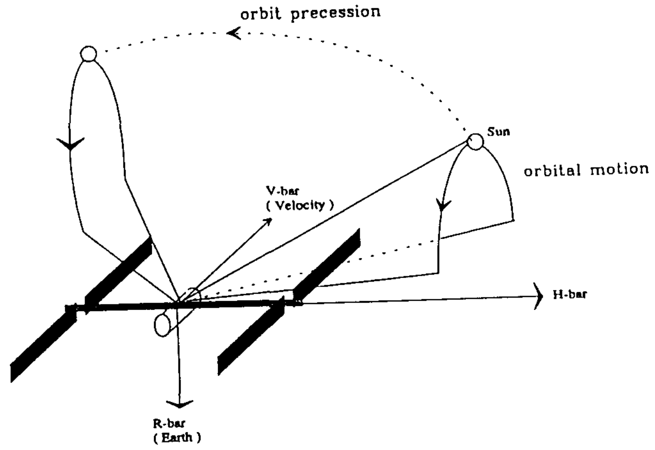
orbit precession
Sun
orbital motion
V-bar
(Velocity)
H-bar
R-bar
(Earth)

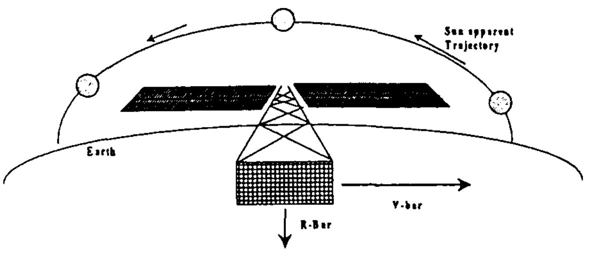
Sun apparent
Trajectory
Earth
V-bar
R-Bar

Relative motion compensated by the derotating function

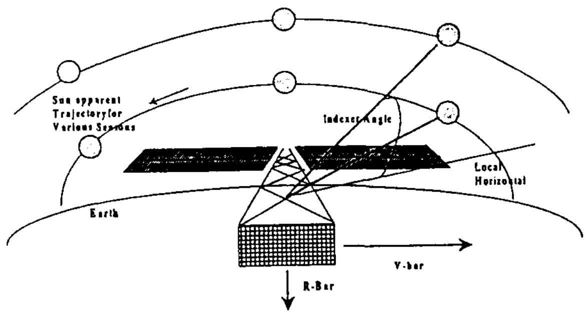
Sun apparent
Trajectoryfor
Various Seasons
Indexer Angle
Local
Horizontal
Earth
V-bar
R-Bar

Relative motion compensated by the indexer function

Figure 3 : Relative motion of the Sun in an ISS frame

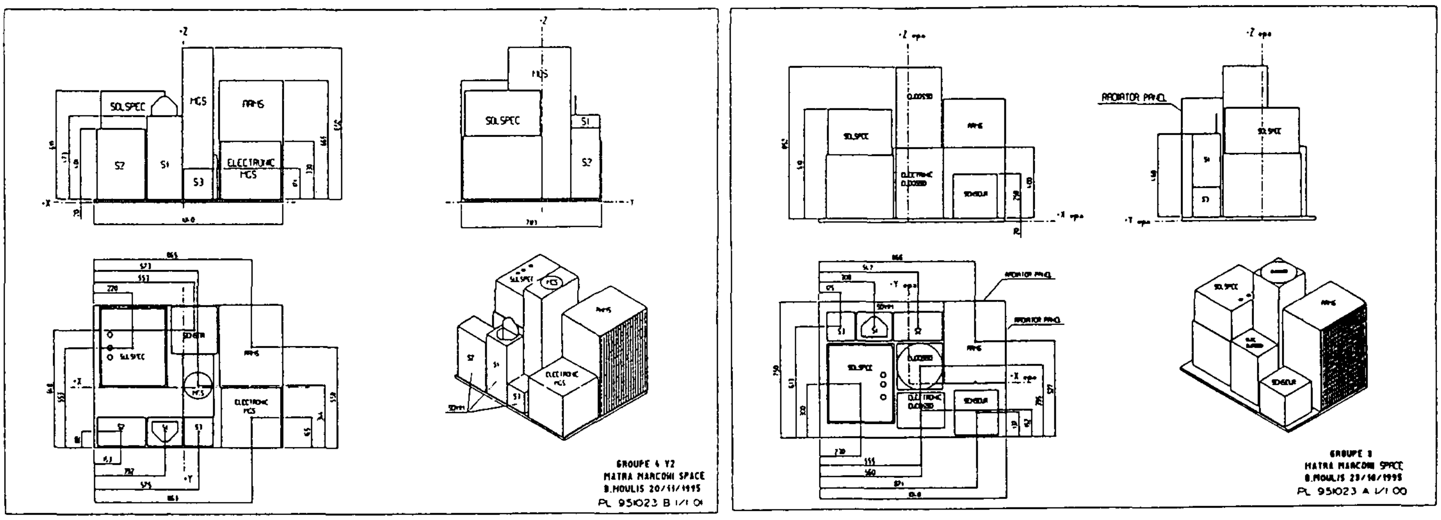
SOLSPEC
MCS
ARMS
S2
S1
S3
ELECTRONIC
MCS
GROUPE 4 Y2
MATRA MARCONI SPACE
B.HOULIS 20/11/1995
PL 951023 B 1/1 01
RADIATOR PANEL
SOLSPEC
ARMS
GROUPE 3
MATRA MARCONI SPACE
B.HOULIS 23/10/1995
PL 951023 A 1/1 00

Figure 4 : Solar grouping accommodated on the pointing system

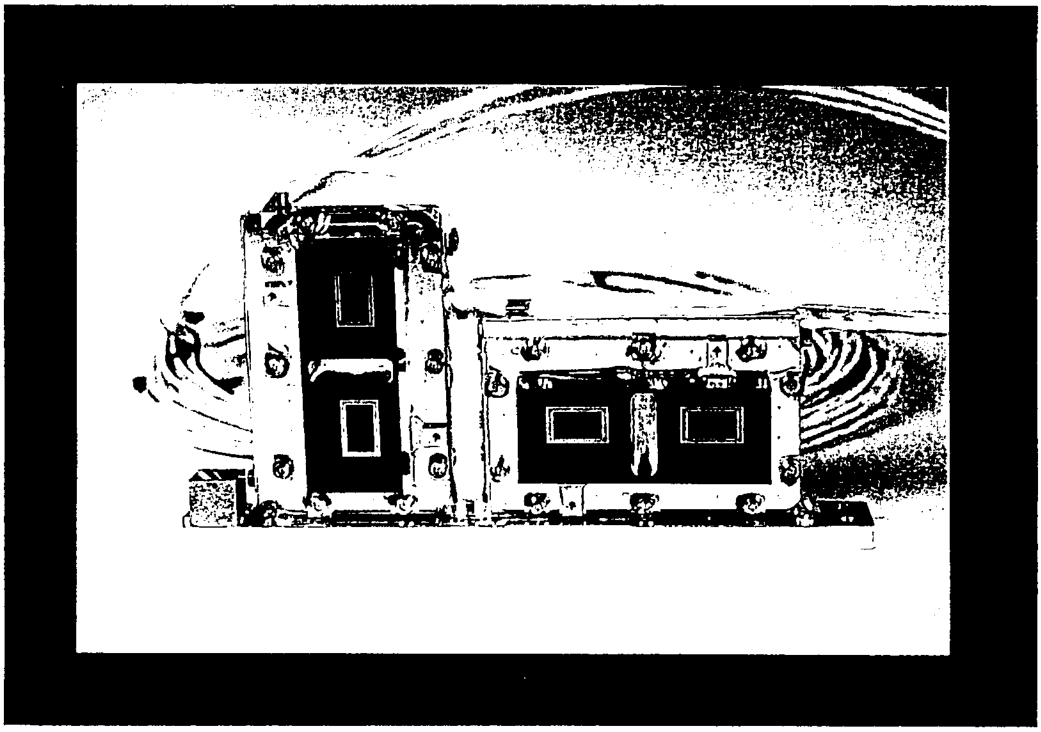

Figure 5 : LIASS Sun Sensor

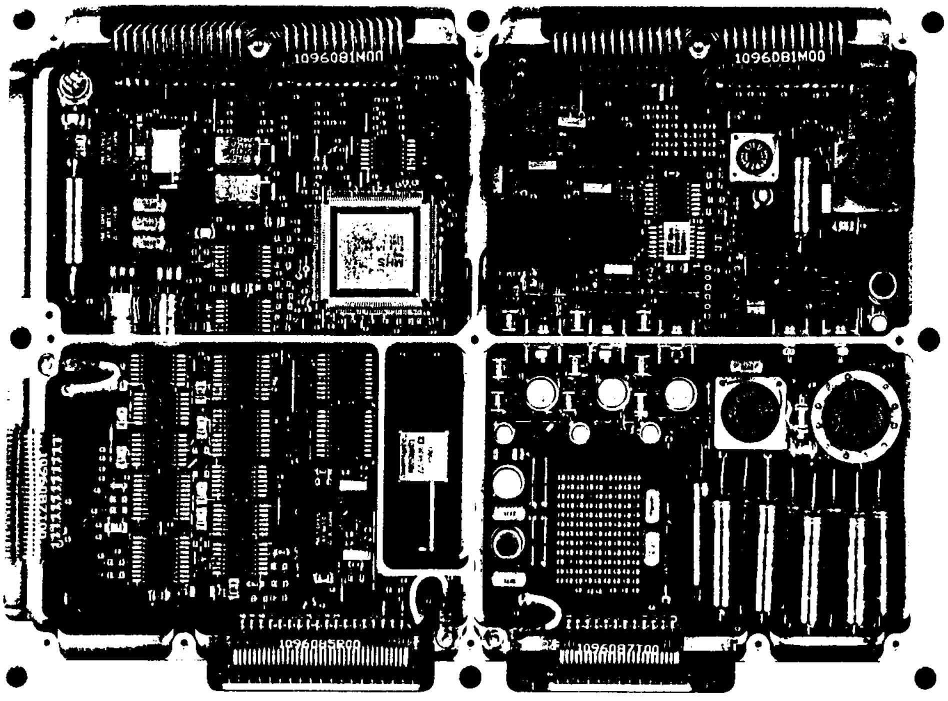
1096081M00
1096081M00
1096085R00
1096087T00

Figure 6 : Motor Drive and sensor proximity electronics

HEXAPOD POINTING SYSTEM

R.Trucco, P.C.Galeone**, F.Pepe**

* ALENIA SPAZIO S.p.A. , Corso Marche 41, 10146 Turin, Italy
Tel.: + 39 11.7180.944 Fax: + 39 11.7180.098 e-mail: fpepe@to.alespazio.it
** ESA-ESTEC Keplerlaan 1, 2200 AG Noordwijk,The Netherland
Tel.: +31 71565.4967 Fax: + 31 71565.6603 e-mail: pgaleone@estec.esa.nl

ABSTRACT

This paper presents a description of an Hexapod pointing system designed for a specific application. The system requirements, scenario and performances for the particular application are summarized in the paper, together with the main kinematics, mechanical and electronic aspects.
Actually, ALENIA Spazio is Prime Contractor, in the frame of an ESA phase B contract, for the definition of an Hexapod pointing system, for the SAGE III experiment, and for the manufacturing and testing of a Development Model.
The SAGE III experiment performs the mapping of the mesosphere, stratosphere and troposphere aerosol and gas distribution, using the solar and lunar occultation measurement techniques.
This instrument will provide global long term measurement of atmospheric composition relying on Hexapod to compensate the ISS attitude errors with respect to the Local Vertical. SAGE III will be one of the Earth Observing System (EOS) experiments in the frame of *"Mission to Planet Earth"* NASA program.
The Hexapod, from a structural point of view, is an isostatic mechanism based on six independent linear actuators, interconnected with a lower and upper mounting plates. The Hexapod allows 6 d.o.f. control for positioning and alignment of the upper mounting plate where the payload is rigidly mounted.
The paper summarizes the output of the kinematic analysis outlining the main results in terms of motion strategies, kinematic algorithms and working envelopes, both when in normal conditions and when degraded due to an actuator failure.
The possibility to upgrade the Hexapod pointing system, by including the capability of dynamic compensation of the attitude rate error generated by the Space Station is also considered. The paper introduces the dynamic characteristic of the Hexapod system together with the results of the simulation activity performed with the aim to predict the DM performances.
The presentation will give more technical details on the control design solutions that have been analyzed, and implemented into the Development Model together with the preliminary results of the test activity on the DM.

1 INTRODUCTION

The Space Station will give to the scientfic community the big opportunity to explore the space environment and to observe the Sun, the Earth and the Stars from outside the Earth atmosphere.
The Space Station is a Laboratory that presents, in general, a good base for a big variety of payloads, even having different or conflicting requirements.
In nominal conditions the ISS is characterized by a large inclination of the orbit (51.6 deg) and by an attitude close to LVLH during the TEA (Torque Equilibrium Attitude) mode.
The Station fullfils the great part of the experiments requirements, but few specific kinds of instruments have pointing requirements that impose the use of a pointing system.
ESA has indentified, for the Space Station, two pointing systems: Coarse Pointing Device (CPD) and Hexapod. While the first, devoted to Solar/Astronomy observation payloads, requires a coarse accuracy (1 deg) over a big range (± 40 deg), the second, dedicated to SAGE III, can be used to point with an accuracy of ±30 arcsec over a shorter range (±10 deg).
Alenia Spazio, as prime contractor with ADS and Gavazzi Space in the frame of Hexapod phase B study, have designed an Hexapod pointing system suitable to SAGE III and they have also manufactured a DM.
The Hexapod pointing systems are very practical when small angular displacements, but many degrees of freedom are to be exploited. On ground based telescopes such systems are used to accurately control five degrees of freedom of the primary or secondary mirrors.
In principle, with appropriate actuators strokes, a payload can be arbitrarily positioned and oriented in space above the base plane of the mechanism, which means that any degree of freedom of the rigid body can be controlled indipendently. Even if the linear displacements of the payload may not require control, this extra capability of the mechanism can be useful if mutual position of two payload must be controlled, or if sufficient clearance must be guaranteed, or in order to optimize the coverage of the allowed operative envelope, or as intrinsic redundancy capability in case one actuator fails.

Proceedings Third International Conference on Spacecraft Guidance, Navigation and Control Systems, ESTEC, Noordwijk, The Netherlands, 26-29 November 1996, ESA SP-381 (February 1997)

The achievable pointing range depends on various geometrical and mechanical parameters.

Two basic configurations can be adopted: one with the instrument mounted abovc the Hexapod upper plate; the other with the instrument partially inside the Hexapod mechanism, mounted on a flange joined to the actuators. The first configuration has for sure no interference between payload and actuators, but the second solution is more compact.

From a dynamic point of view, the actuators must control the upper platform motion in order to keep the target image as stable as possible. This can be achieved only if the platform moves smoothly and the six strokes are commanded individually but coordinated.

This capability is useful in case of tracking requirement. Figure 1 presents Hexapod/SAGE III configurations.

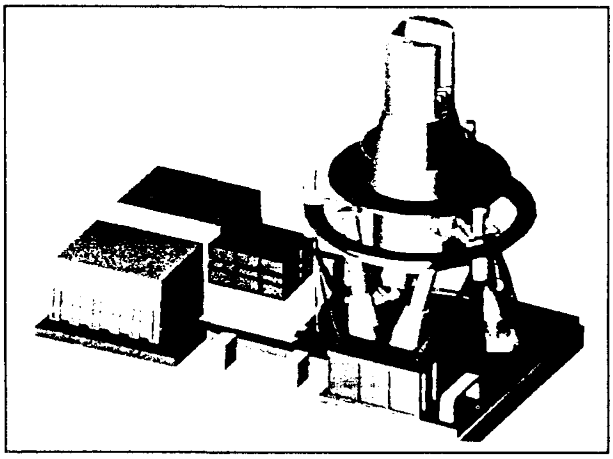

Fig. 1: Hexapod

2 HEXAPOD FOR SAGE III

Actually a development activity is addressed to define a pointing system for the SAGE III experiment. This payload has beed designed, and is now under manufacturing, by NASA Langley Research center, to map high stratosphere and troposphere areosol and gas distribution. It will be one of the EOS experiments in the frame of *"Mission to Planet Earth"* NASA program.

SAGE III is the fifth orbital atmospheric monitoring system based on Earth-limb extinction technique: solar radiation is measured during sunrise and sunset at wavelengths from 0.29 to 1.55 microns.

The measurement of sun radiation with the interposition of an atmosphere screen allows the analysis of atmospheric gas.

SAGE III main components are the sensor assembly and the electronic box. The sensor assembly, depicted in figure 2, can be rotated with respect to ISS truss, and positioned in the required attitude with respect to the proper reference frame, by Hexapod pointing system.

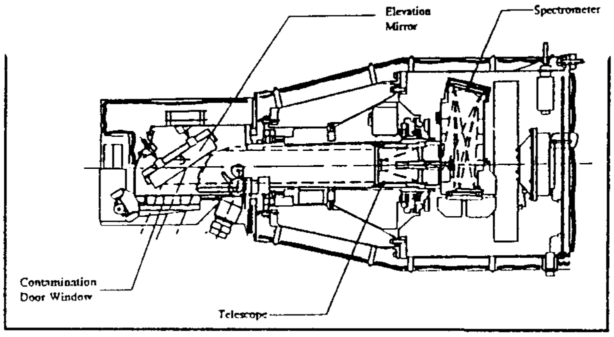

Fig. 2: SAGE III

During each orbit SAGE III will perform from two to four measurements: two with Sun light and one or two exploiting the Sun light reflected by the moon (if achievable).

For most time during each orbit the instrument remains in stand-by conditions and then it executes the scanning motion by itself, provided that at the beginning of each observation phase it has been correctly pointed toward the Nadir direction.

Azimuth rotation of the whole upper part of SAGE III (telescope and spectrometer) is driven by its own sun/moon sensors so as to maintain the vertical direction of the elevation scanning motion. SAGE III tilt mirror scans the sky in the rising sun (or moon) direction at a speed of 15 arcmin/sec, inverting its motion when source boundaries are crossed. Furthermore, direct view of light source without the interposition of the atmosphere is performed for sensor calibration.

The SAGE III characteristics, together with the ISS constraints, become design guidelines and requirements for the Hexapod pointing system.

The scope of the Hexapod pointing system is, hence, the compensation of the ISS attitude errors, prior to starting the SAGE III observation periods.

The composite Hexapod/SAGE III is accommodated on the ISS Nadir Pointing Express Pallet by means of an Express Pallet Adapter. Figure 3 displays Hexapod/SAGE III on the Express Pallet Adapter.

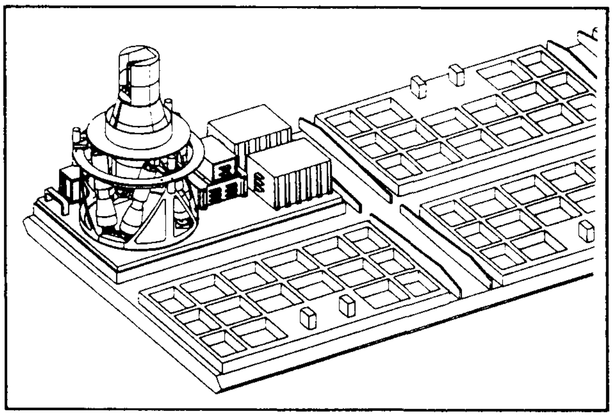

Fig. 3: Express Pallet

3 HEXAPOD REQUIREMENTS

The Hexapod principal requirements are contained in the following table.

DESCRIPTION	REQUIREMENT
* Pointing accuracy	± 30 arcsec (between lower and upper platform)
* Pointing stability	0.0035 deg/s (during the event - without motion)
* Pointing range	± 8 deg
* Pointing rate	1.2 deg./s
* Payload accommodation	SAGE III
* Maximum height	Max 1.0 m (target)
* Mass	M = 70 kg
* On-orbit lifetime	5 years
* Launch vehicle	NSTS

4 HEXAPOD MECHANICAL AND AVIONIC CONFIGURATIONS

The Hexapod Pointing system is composed by six electromechanical linear actuators disposed along the inclined sides of three trapezia, between the upper and the lower platforms; one of the two platforms is fixed to the carrier while the position of the other is defined by the length of the six linear actuators.
A dedicated off-loading device has been foreseen in order to support the launch loads.

The following mechanical interfaces are defined:

- interface to SAGE III sensor assembly: a flange is introduced in the SAGE III sensor assembly design, which interfaces with the Hexapod upper platform.
- interfaces with the EPA: the Hexapod lower platform and the electronics units interface with the adapter plate.

In particular the Mechanical assembly is composed of:

- Upper platform, providing mechanical interface for the SAGE III Payload. The configuration considers a body mounted flange.
- Six linear actuators with relevant interfaces and joints.
- Lower platform, providing mechanical interface with the EPA
- Off-Loading device, providing mechanical support for the loads due to the launch environment and giving mechanical support to the environmental control devices (heaters and MLI).
- Multi-Layer Insulation, covering all six legs and heaters to provide the necessary protection from the severe space thermal environment.

The Hexapod avionic configuration is driven by the main system requirements and well established configuration and functions:

- * Six Linear actuators servo control;
- * Operational modes and relevant configurations management;
- * Power conversion, protection and distribution to electrical equipment;
- * Commands/data handling;
- * Anomalies Detection and Isolation capability;
- * Ground operational interfaces and communication management;

The Hexapod avionic configuration is reported in fig. 4.

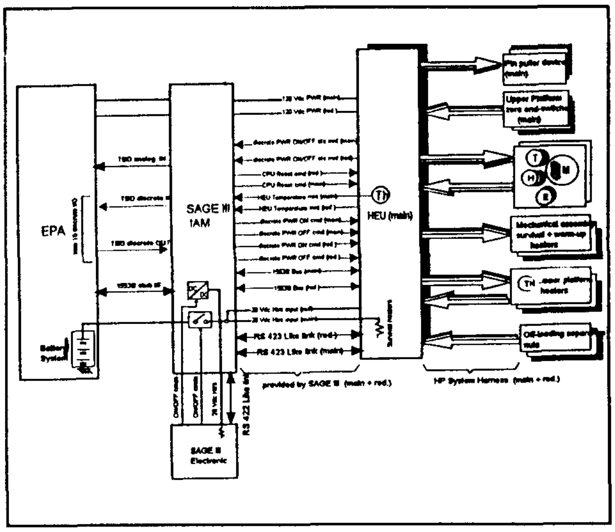

Fig. 4: Hexapod Avionic Configuration

In particular the Electronic assembly is composed of:

- Hexapod Electronic Unit (HEU), providing the power conversion and distribution, command and data handling to/from ISS and SAGE III and linear actuators commanding and control.
- Heaters and Thermostats, providing the necessary power and relevant control to maintain a suitable temperature range.
- Sensors and Electrical Devices, providing temperature measurement, actuators zero position measurement, off-loading device separation command.
- Actuator control SW, executing the kinematic algorithms, generating the actuator commands and performing actuators positioning control.
- Modes management SW, providing the configuration management, anomaly detection and reporting and data communication management.

5 OPERATIONS AND MODES

The operational approach of the composite SAGE III/Hexapod can be summarized as follows:

- Hexapod receives the attitude and position informations from the ISS GPS (updated every second), and it is able to correct the attitude moving the upper platform toward the Nadir. The Hexapod corrections are performed on the basis of a SAGE III command/data (information from SAGE III to Hexapod of the starting of the observations and correction offsets).
- The ISS attitude errors are compensated by Hexapod before starting of SAGE III measurements while, during solar or moon occultations, Hexapod is fixed.

The system modes of the Hexapod can be summarized as follows and reported in figure 5:

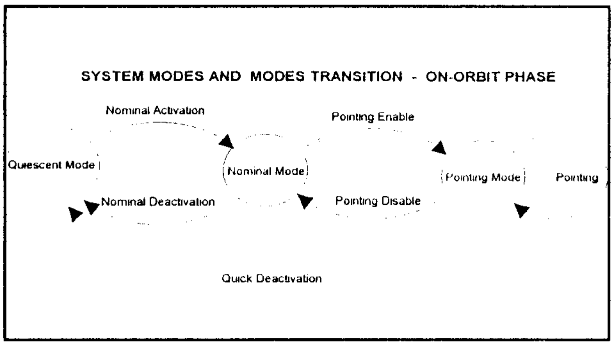

Fig. 5: Hexapod Operational Modes

* Quiescent Mode. It is a passive mode, only survival heaters can be powered on, if necessary. This mode supports nominal and contingency operations: it is the mode before activation and check out, after deactivation or after any unrecoverable contingency. This mode supports reconfiguration and exchange.

* Nominal Mode supports nominal operations and it is entered as soon as Hexapod is activated from ISS. The capabilities provided are: power distribution, heat provision, nominal commands and data handling, anomalies detection and isolation, attitude determination, data exchange with SAGE III, periodic check, S/W uploading/downloading from Ground Center.

* Pointing Mode is the only mode that supports the actuation of the Hexapod in order to achieve the appropriate pointing. The capabilities provided are: power distribution, heat provision, nominal command and data handling, anomalies detection and isolation, attitude determination, data exchange with SAGE III, linear actuator zeroing, pointing.

6 KINEMATIC AND DYNAMIC CHARACTERISTICS

The Hexapod, from a kinematic point of view, is an isostatic mechanism based on six independent linear actuators. It is composed by one body (Upper plate/ SAGE III) having 6 degrees of freedom, and six extendable legs with 3 d.o.f. each. The system is hence kinematically defined by 24 variables.

The upper plate has six dof, but for SAGE III utilization the interest is in particular addressed to the two rotational degrees of freedom: roll (X) and pitch (Y).

It has to be noted that the same attitude can be reached with different actuator lengths. The problem is solved fixing a suitable center of rotation (C.o.G.).

The kinematic model of Hexapod is reported in figure 6. The Hexapod pointing system can be conveniently modeled in a three-dimensional space by means of 18 vectors: six defining the lower platform joints, six the upper platform ones (each group of vectors is fixed and constant with reference to the relevant platform) and six, defining the linear actuators, variable in direction and magnitude.

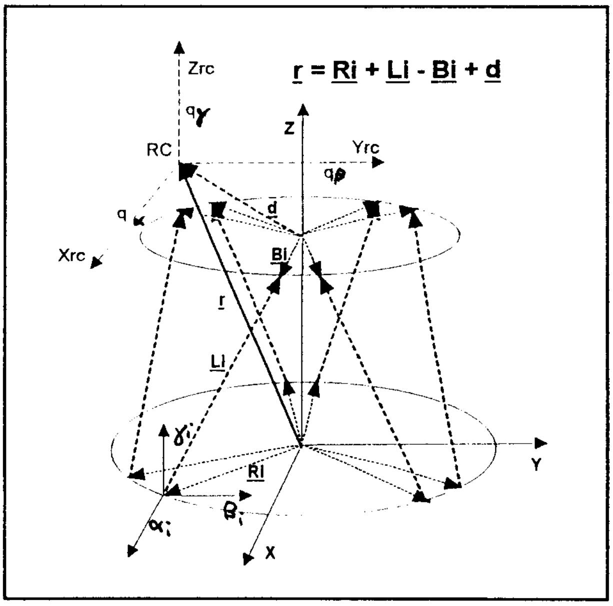
Zrc
$\underline{r} = \underline{Ri} + \underline{Li} - \underline{Bi} + \underline{d}$
q_γ
Z
RC
Yrc
q_β
q
d
Xrc
Bi
r
Li
γ_i
Ri
β_i
α_i
X
Y

Fig. 6: Hexapod Kinematic Model

The solution of the kinematic problem consists in translating the desired attitude into the legs length (inverse kinematic) or viceversa to determine from the legs length the upper platform attitude (direct kinematic). The direct and inverse kinematic algorithm can be derived considering the legs reference axes and relevant equations. The legs are characterized by three equations (x,y and z directions), representing the kinematic constraints between the lower plate, the legs length and the upper plate.

From this set of 18 kinematic constraint equations

(algebric but not linear), the direct and inverse kinematics algorithms are finally derived.
The algorithms are based on the Newton-Raphson method to find the root of a system of non linear equations.

The kinematics algorithms are expressed in a parametric way in terms of:

- Radius of the circle were the equivalent hinges of the lower actuator joints are placed;
- Distance between the plane of the actuator joint lower hinges and the Hexapod fixed platform;
- Angle between two consecutive hinges on the lower platform;
- Radius of the circle were the equivalent hinges of the actuator upper joints are placed;
- Distance between the plane of the actuator joint upper hinges and the Hexapod movable platform;
- Angle between two consecutive hinges on the upper platform;
- Actuator length at zero stroke;
- Position of the center of rotation with respect to the Hexapod movable platform.

These parameters could be changed accordingly to the best way of describing the Hexapod geometry with the only condition to be a complete set able to define uniquely the Hexapod geometry.
The input for the inverse kinematic algorithm is the desired attitude (Nadir) projected in the lower platform Reference Frame while the output are the six actuator displacements.
The direct kinematics allows to calculate the Hexapod movable platform angular position for a given set of six actuator lengths. This type of calculation, needed at the power on or after a reset, could also be useful to evaluate the effects of thermal-induced displacements of the actuator on the Hexapod pointing accuracy.

6.1 Constraint equations

Each of the 18 constrain equations states the position of the Upper plate (X, Y and Z direction) going through the six legs. The constraints using the trascendental (non-linear) function look like the following equation:

$$q_x = R1_x + L1[\sin\beta_1 \cos\gamma_1 + \cos\beta_1 \sin\alpha_1 \sin\gamma_1] - B1_x \cos q_\beta \cos q_\gamma + B1_y(\sin q_\alpha \sin q_\beta \cos q_\gamma - \sin q_\beta \cos q_\gamma + B1_z(\sin q_\gamma \sin q_\alpha + \cos q_\gamma \sin q_\beta \cos q_\alpha)] + d_x$$

In condensed form can be rewritten as:

$$C_j(L_i, \alpha_i, \beta_i, q_x, q_y, q_z, q_\alpha, q_\beta, q_\gamma) = 0$$

$j=1,2..18$ Number of the constraints
L_i Leg length $(i=1,2..6)$
α_i Leg attitude $(i=1,2..6)$
β_i Leg attitude $(i=1,2..6)$
$q_{x,y,z}$ Rotation center position
$q_{\alpha,\beta,\gamma}$ Rotation center attitude

The complete Jacobian matrix is obtained deriving analytically the 18 equations w.r.t the 24 variables:

$$J = \begin{vmatrix} J_{11} & J_{12} & \cdots\ J_{1,n} \\ J_{21} & J_{22} & \cdots\ J_{2,n} \\ \cdot & \cdot & \cdots\cdots \\ J_{n_c,1} & J_{n_c,2} & \cdots\ J_{n_c,n} \end{vmatrix} \qquad J_{ij} = \partial \frac{C_i}{\partial q_j}$$

$n_c = 18$: number of constraint equations
$n = 24$: number of variables (d.o.f.)
$i = 1,2, .. n_c$ Number of Constraints
$j = 1,2, .. n$ Number of d.o.f.

6.2 Direct and Inverse complete solutions

The constraint equations allows several solution depending on the choice about free (independent) coordinates and dependent coordinates. Hereafter the main approaches are illustrated together with the algorithms suitable to solve the specific problem.
The Direct and Inverse Kinematics are defined solving, through Newton-Rapson method, the system identified by the following equations:

$$J \cdot \delta \mathbf{x} = -C(\mathbf{x}_{old})$$

$$\mathbf{x}_{new} = \mathbf{x}_{old} + \delta \mathbf{x}$$

In these cases the Jacobian is a square matrix obtained selecting the proper 18 columns among the 24 of the Jacobian matrix already presented:
The unknown variables for the direct kinematic are in the vector as follows:

$$\mathbf{x}^T = (\alpha_1, \beta_1, \alpha_2, \beta_2, \alpha_3, \beta_3, \alpha_4, \beta_4, \alpha_5, \beta_5, \alpha_6, \beta_6, \ldots\ q_x, q_y, q_z, q_\alpha, q_\beta, q_\gamma)$$

while the unknown variables for the inverese kinematic are in the vector as follows:

$$x^T=(L_1,\alpha_1,\beta_1,L_2,\alpha_2,\beta_2,L_3,\alpha_3,\beta_3, \dots$$
$$L_4,\alpha_4,\beta_4,L_5,\alpha_5,\beta_5,L_6,\alpha_6,\beta_6)$$

The inverse kinematics can be used to find the viewing space compatible with the physical boundary conditions ($429 \leq Li \leq 499$) of the Hexapod mechanism. For example it is interesting to know the maximum rotation around the X (roll) and Y (pitch) axes keeping fixed the Center of rotation position and attitude around z axis.
The hypothesis in this case is to use upper plate attitude (q_α, q_β) as varying parameters and to know the following fixed quantities: the position and the Z-axis attitude of the Rotation center (q_x, q_y, q_z, $q_\gamma = 0$).
The resulting viewing space is depicted in figure 7.

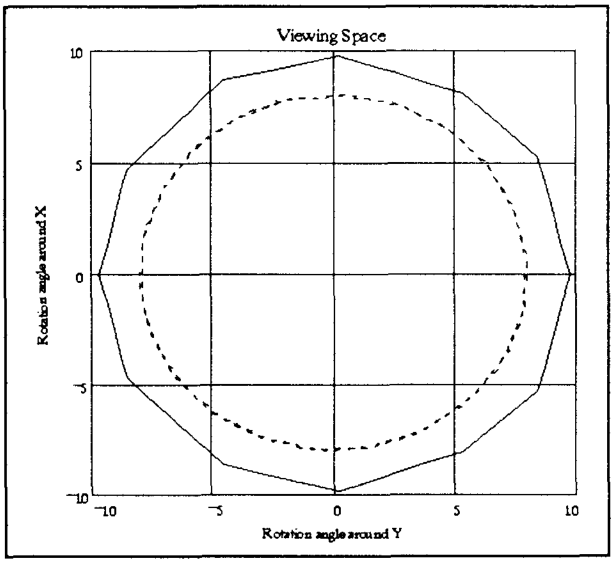

Figure 7: Viewing space

6.3 Undetermined Kinematic

The undetermined kinematic is suitable to find solutions, having constraints both on the leg length and on the upper body attitude. The main difference with respect the direct and inverse kinematics is that the number of constraints is minor (or greater) than six.
For example this algorithm is able to characterize the viewing space associated with a leg length fixed (without constraints on the upper plate position/attitude). In this case the Jacobian is characterized by a non squared matrix. The approach in this case shall use the Singular Value Decomposition (SVD) tecnique in order to determine within the family of solutions that one that minimizes the norm of the solution vector.

$$J\cdot\delta x=(U\cdot w\cdot V^{T})\delta x=-C(x)$$

An example of dependent variables is given in the following vector:

$$x^T=(L_1,\alpha_1,\beta_1,L_2,\alpha_2,\beta_2,L_3,\alpha_3,\beta_3,L_4,\alpha_4,\beta_4, \dots$$
$$L_5,\alpha_5,\beta_5,\alpha_6,\beta_6,q_x,q_y,q_z,q_\gamma)$$

The hypothesis in this case is to use the upper plate attitude (q_α, q_β) as varying parameters and to know one fixed leg length (L_6 = 429, 464, 499 mm).
In order to keep the length of the free leg within the physical boundary conditions ($429 \leq Li \leq 499$) the following equations relevant to these additional constraints have been added to the Jacobian.

$$L_i=L_0+35\cdot\sin(\theta_i)$$

The resulting viewing space is depicted in figure 8.

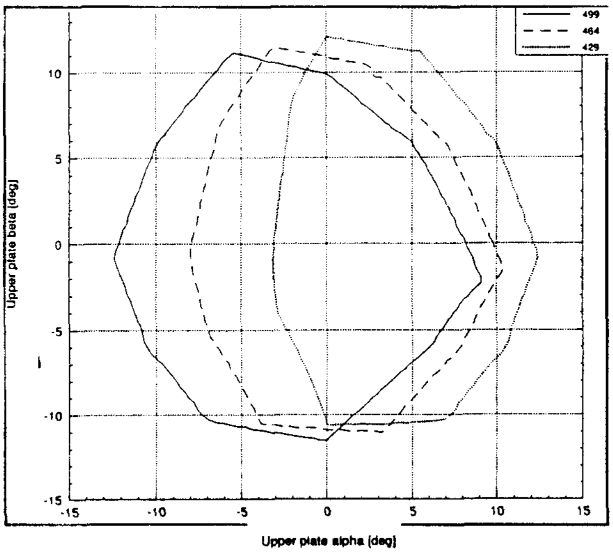

Figure 8: Undetermined kinematics - Viewing space

6.4 Linearized (Closed) Form Algorithm

It is possible to define kynematic algorithms able to convert small changes of the independent variables in approximated variation of the dependent variables. The Taylor expansion method takes profict by the use of the already known Jacobian matrix. This approach is suitable for every consistent set of variables (for "small variations"), but is very useful when for fast motion, real time computation is needed.
The following formule show a potential application of this algorithm very useful for the stability compensation.

$$\begin{vmatrix}L_1\\L_2\\L_3\\L_4\\L_5\\L_6\end{vmatrix} = \begin{vmatrix}\overline{G}_{1,1} & \overline{G}_{1,2} & \dots & \overline{G}_{1,6}\\ \overline{G}_{2,1} & \overline{G}_{2,2} & \dots & \overline{G}_{2,6}\\ . & . & \dots\dots & \\ \overline{G}_{6,1} & \overline{G}_{6,2} & \dots & \overline{G}_{6,6}\end{vmatrix} \cdot \begin{vmatrix}q_x\\q_y\\q_z\\q_\alpha\\q_\beta\\q_\gamma\end{vmatrix}$$

$$\delta x_{dep} = -[\bar{G}]_{6,6}\,\delta x_{indep}$$

$$[\bar{G}]_{6,6} = \mathrm{subspace}([G(x_0)]_{18,6})$$

$$[G(x_0)]_{18,6} = [J(x_0)]^{-1}{}_{18,18}[J(x_0)]_{18,6}$$

x_{dep} = $(L_1, L_2, L_3, L_4, L_5, L_6)$
x_{indep} = $(q_x, q_y, q_z, q_\alpha, q_\beta, q_\gamma)$
x_0 = linearsation point
$J^{-1}(\mathbf{x}_o)$ = inverse of the Jacobian in $\mathbf{x}_o$
$J(\mathbf{x}_o)$ = part of Jacobian not inverted
(function of indep. variable)

In order to assess the error due to the use of the approximated solution a rotation of 1 deg has been used as input in the two different algorithms (complete/reduced). These computations gives results different for amount lower than 0.1%.

6.5 Hexapod Control Loops

Hexapod system, from a control point of view, is characterized by:

- an external loop, closed or open depending on the configuration (attitude sensor position);
- six position closed loops to control the legs length.

The Hexapod control architecture is shown in figure 9. The control architecture has six inner position closed loop, one for each motor, and an outer loop computing the reference command for each actuator. In general it can be the payload to drive Hexapod toward the required direction. For SAGE III, however, the pointing angles are computed on the basis of the attitude information coming from the Space Station GPS.

The attitude control loop works, on demand, for a short period of time just before the SAGE III acquisition event starts. During the remaining part of the orbit the attitude information coming from the GPS is used for the attitude determination task.

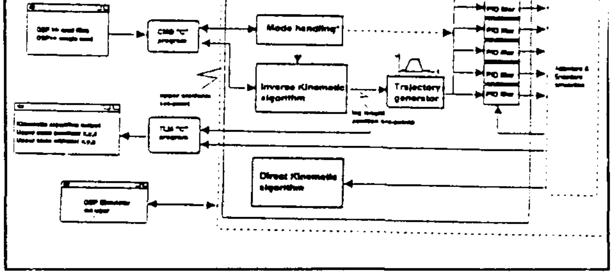

Fig. 9: Control Architecture

6.6 Actuator Control Loop

The six Linear Actuators servo control have a central role in the Hexapod design because the system performances are strongly driven by the actuators control and accuracy.

The control is now implemented following two different but complementary strategies:

1) For large motion through a position driven Proportional, Integral, Derivative (P.I.D.) algorithm with predefined time history, which provides optimal acceleration and velocity profile.
   This approach offers the advantage to be simple and guarantees both the final accuracy and the optimisation of actuator motors performance.
2) For the stability compensation using a position driven Proportional, Integral, Derivative (P.I.D.) algorithm with feedforward compensation in order to have the best performances in terms of tracking capability.

The different implementation of the control algorithms (PID with and without feedforward) have been evaluated in order to optimize the following design parameters:

- frequency bandwidth
- control loop stability
- torque profile
- final accuracy
- tracking capability

Each actuator control loop is independent from the other (allowed by the fact that the mechanism is isostatic), but anyway the control strategy is based on a coordinate motion of the 6 legs.

6.7 DCAP Dynamic Model

The dynamic model is devoted to analyse the stresses on Hexapod during the reentry phase in case of failure of the locking mechanism and then being freely moving under the effects of the reentry acceleration.

A dedicated DCAP model of the Hexapod system, put under different cases of reentry accelerations, has been set up, in order to assess the most severe load conditions on the Hexapod legs and off loading device.

The main effects that have been considered in the Hexapod model are:

- forces due to the leg hard stops;
- forces exchanged between the off loading device and the legs;
- viscous effects acting on the actuator motors;
- reduced inertia of the actuator motors w.r.t the Hexapod upper plate;
- friction effects on the screw lead due to the nut preload.

Hexapod DCAP model is constituted by:

- a rigid body BO1 representing the lower plate of HP locked to EP;
- a rigid body BO2 representing the u.p. of HP having 6 d.o.f. w.r.t. BO1;
- 4 DCAP devices for simulating each HP leg accounting for:
  - LEx1: viscous damper;
  - LEx2 and LEx3: lower and upper hardstops;
  - LEx4: effects of the reduced inertia of the electric motors;
- 3 DCAP jet actuators acting on the centre of mass of BO2 along the X, Y aand Z axes for simulating the effects of the reentry accelerations.

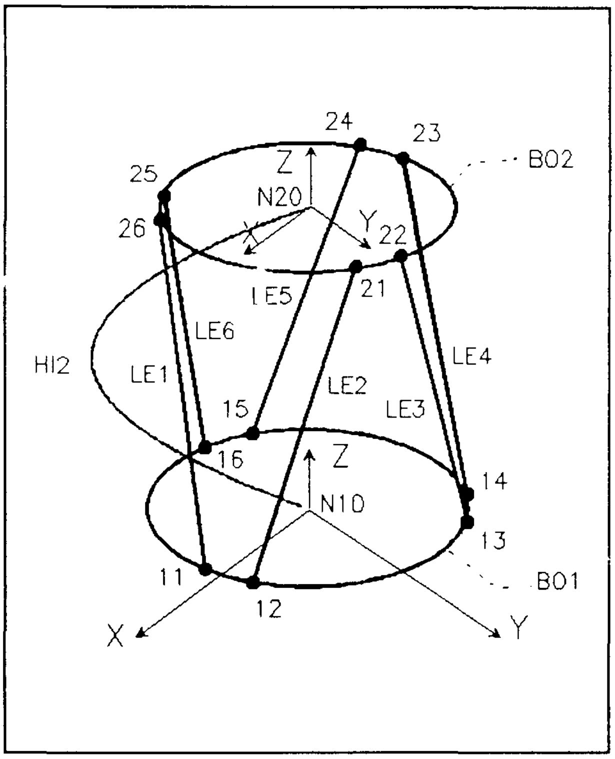

Fig. 10: Hexapod DCAP model

7 DEVELOPMENT MODEL ACTIVITIES

In the frame of Hexapod phase B, it is foreseen the design, procurement, manufacturing and test of a Development Model (DM) which is representative of the functional performances.

The Hexapod DM is addressed to:

* prove that, under ambient conditions, the Hexapod is able to provide the requested performances in terms of pointing accuracy, pointing range, pointing rate and stability.

* Full End to End verification of the control law and kinematic algorithms chain.

* Pointing accuracy and pointing range verification by comparison with external reference.

* Pointing rate verification.

* Verification of the stability performance to assess if HP pointing system is able to perform an active compensation of disturbances even if it is not longer a requirement.

The DM is depicted in Figures 11 and 12.

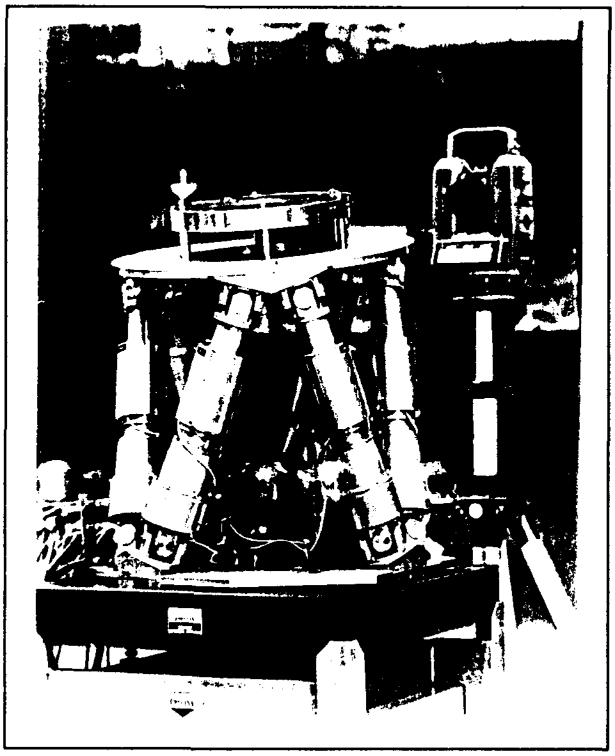

Fig. 11: Hexapod Development Model

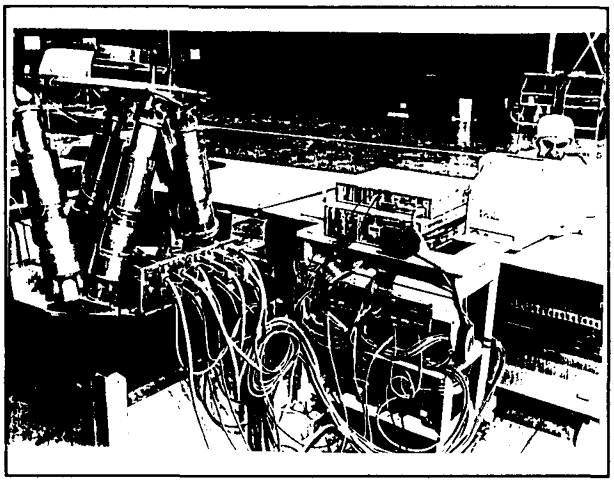

Fig. 12: Hexapod Development Model

DRAG-FREE & ATTITUDE CONTROL SYSTEM FOR THE GRAVITY EXPLORER MISSION

L. VAILLON, C. CHAMPETIER

MATRA MARCONI SPACE France
31, rue des Cosmonautes, 31077 TOULOUSE, FRANCE
Tel: (33) 05 62.19.61.39, Fax: (33) 05 62.19.78.97

ABSTRACT

This paper presents the feasibility analysis of the Drag-Free and Attitude Control System (DFACS) for the Gravity Field and Ocean Circulation Explorer Mission (GOCE) whose objective is to produce high resolution global measurements of the Earth gravity field. The payload, mainly composed of a gradiometer, basically an assembly of ultra-sensitive accelerometers to measure gravity gradients, must be flown in extremely quiet dynamic environment, both in translation and rotation. Two DFACS concepts are investigated in parallel in connection with the specific performance and implementation constraints of the two candidate payload technologies, a room temperature and a cryogenic instrument. In both cases, Drag-Free Control (DFC) is performed along the velocity axis only in order to compensate for the main aerodynamic drag force (DC component and fluctuations up to gradiometer MBW (Measurement Bandwidth, 5 to 100 mHz) upper limit. RF ion thrusters with high thrust throttlability and fast response time validated by tests are baselined for drag compensation to largely reduce the required propellant mass. For attitude control, the gradiometer is used to provide a 3-axis high accuracy measurement of angular accelerations. This reference is combined with an absolute attitude reference given in one concept by a wide field-of-view medium accuracy star tracker and in the other by a Sun sensor plus a magnetometer. The actuators are also different for the two mission concepts, impulsive nitrogen thrusters for the room-temperature instrument, and proportional thrusters using the helium boil-off gas from the payload cryostat for the other. Reaction wheels are also considered as an alternate solution, with preliminary assessment of the impact of microvibrations induced by the wheels on the payload measurements.

Key words:

Drag-Free Control, Attitude Estimation and Control, Electric Propulsion, Gravity Field

LIST OF ACRONYMS

AMCS	Attitude Measurement & Control System
DFC	Drag-Free Control
DFACS	Drag-Free & Attitude Control System
GOCE	Gravity Field & Ocean Circulation Explorer Mission
GPS	Global Positioning System
LOS	Line Of Sight
MBW	Measurement BandWidth
MIB	Minimum Impulse Bit
MM1	Model Mission 1 (Room-temperature capacitive gradiometer)
MM2	Model Mission 2 (Cryogenic inductive gradiometer)
PHT	Proportional Helium Thruster
RW	Reaction Wheels

INTRODUCTION

The Gravity Field and Ocean Circulation Explorer Mission (GOCE) is one of the candidate missions for implementation in the ESA Earth Explorer programme. The objective of the mission is to produce high resolution global measurements of the Earth gravity field (accuracy of 2 mgal (2 10^{-5} m/s^2) RMS and ground spatial resolution better than 100 km), leading to improved geoid and gravity models for use in a wide range of scientific applications. The data set for gravity field reconstruction is the combination of measurements of the local gravity gradient using a spaceborne gradiometer and satellite-to-satellite tracking (SST) by GPS/GLONASS receiver. SST will provide large scale information on the gravity field, corresponding to signal frequencies below about 5 mHz. The gradiometer will provide complementary data on the small scale fluctuation of the gravity field, in a frequency range from 5 to 100 mHz.

Two very different mission concepts are investigated in parallel. The first one relies on the ARISTOTELES heritage and features a room-temperature gradiometer based on six electrostatic accelerometers installed on an ultra-stable structure. The second one is based on an integrated supraconductive gradiometer bathed in a cryostat filled with superfluid helium, a technology developed for relativity test missions like Gravity Probe B (USA) and STEP (ESA).

The payload gradiometer must be flown in extremely quiet dynamic conditions, both in translation and rotation, to

---

Proceedings Third International Conference on Spacecraft Guidance, Navigation and Control Systems, ESTEC, Noordwijk, The Netherlands, 26-29 November 1996, ESA SP-381 (February 1997)

prevent corruption of the tiny gravity fluctuation signals to be detected. The required nearly perfect zero-g environment (nano-g RMS typically) is actually achieved by drag-free control of the satellite, i.e. fine compensation of linear and angular disturbance accelerations in the 5 - 100 mHz frequency range, the so-called measurement bandwidth (MBW). Within one of the two pre-phase A studies, led by ALENIA SPAZIO, MATRA MARCONI SPACE was in charge of the design of the Drag-Free and Attitude Control System (DFACS).

1. GOCE MISSION CONCEPTS OUTLINE

The selection of mission parameters is the result of a system-level trade-off analysis performed during the first phase of the definition study. The main parameters necessary for the understanding of the DFACS analyses are summarised below.

The GOCE orbit is a 6h-18h Sun-synchronous circular orbit, so that the S/C Y-axis, aligned with the orbit normal, is pointed close to the Sun. This allows to place the S/C in stable thermal and power conditions without rotating solar panels. The nominal altitude is set to 270 km as a compromise between experiment sensitivity and aerodynamic drag magnitude. The satellite is Earth-pointed, (Z-axis pointed towards the Earth centre and X-axis aligned with the S/C velocity) since any other pointing mode results in excessively stringent attitude stability requirements. Moreover, Earth pointing simplifies DFACS design since the main drag force is fixed in the satellite frame and because attitude sensor implementation is easier.

For both mission concepts, the minimisation of the along-track cross section (to reduce aerodynamic drag) results in a tapered shape of the spacecraft body (1 x 1 m cross section and 3 m length), for a satellite mass of about 1000 kg. Because of the fixed orientation relative to the Sun (close to Y-axis), the solar arrays are body-mounted with fixed wings in the XZ plane. Two mission concepts are investigated, corresponding to the two candidate gradiometer technology:

- Model Mission 1 (MM1) features the room-temperature capacitive accelerometers developed by ONERA on the basis of the ARISTOTELES heritage. The gradiometer is composed of six three-axis accelerometers implemented on a high stability structure (see figure 1). Three-axis diagonal gravity gradient measurements are obtained by difference between the outputs of the accelerometers along their separation line, other outputs combinations are being used to measure satellite linear and angular accelerations about the three axes. The baseline length (separation between a pair of accelerometers) is set to 0.5 m.

- Model Mission 2 (MM2) is built around the cryogenic gradiometer proposed by OXFORD Instruments (UK) based on the supraconductive inductive sensing technology. The gradiometer is an integrated instrument (figure 2) providing direct measurements of gravity gradients and satellite linear and angular accelerations about the three axes. The whole instrument is housed in a cryostat filled with 100 litres of superfluid helium in order to maintain the very low temperature (2° K) necessary to operate the superconducting detection circuits. To fit in the cryostat the MM2 instrument must be more compact, with a reduced baseline (0.12 m), but the loss of sensitivity is largely compensated by the increased measurement resolution.

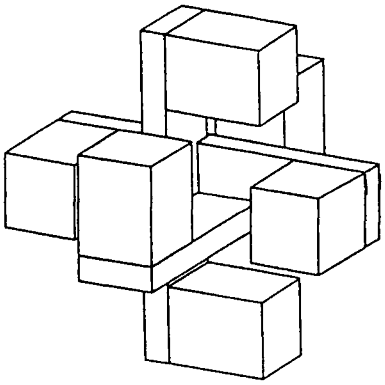

Figure 1. Capacitive gradiometer (MM1) configuration

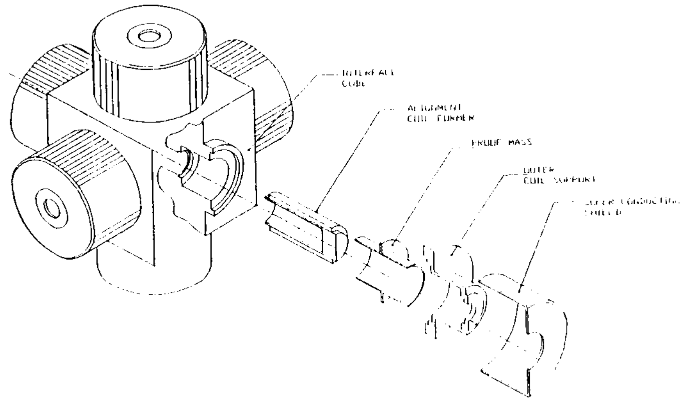

Figure 2. Cryogenic gradiometer (MM2) configuration

Gradiometer performance is basically defined by two parameters, the intrinsic resolution of the acceleration gradient measurement and the coupling coefficients expressing the fraction of satellite dynamics that couples into the measurement. Indeed, because of the imperfections of the gradiometer (scale factor mismatch, sensitive axes misalignments and test mass offsets from true sensitive axis), satellite linear and angular motions, the so-called « common-mode acceleration », corrupt the differential acceleration induced by the local gravity gradient. The expected performances of the two candidate technologies are summarised in figure 3. It can be seen that the cryogenic instrument is about one order of magnitude more sensitive, at the price of an increased complexity.

Gradiometer technology	Non-cryogenic (MM1)	Cryogenic (MM2)
Instrument expected sensitivity (EU/√Hz)	5 10^{-3}	4 10^{-4}
Rejection of linear acc.	10^{-5}	10^{-7}
Rejection of angular acc.	3.10^{-5}	10^{-6}
Mission performance target (EU/√Hz)	1.4 10^{-2}	1.1 10^{-3}

NB: 1 EU = 1 Eötvös Unit = 10^{-9} s^{-2} (acceleration gradient)

Figure 3. Performances of the two instruments

2. DRAG-FREE & ATTITUDE CONTROL REQUIREMENTS

The top-level requirement is the accuracy objective for gravity gradient measurements in the MBW (0.005 to 0.1 Hz). The selected approach is to match this requirement with the expected resolution of the considered gradiometer technology, so as to achieve a good balance between errors from the platform and the instrument. This allows a fair comparison of the two model missions as a compromise between mission scientific interest and cost. As a result the overall performance requirements are more stringent for MM2 since the cryogenic instrument is more sensitive.

The requirements derivation follows a classical top-down approach: the detailed expression of the measured differential acceleration for each axis of the gradiometer allows to identify the various error sources, and an allocation of the mission performance objective is realised. The error contributors can be arranged in five classes (figure 4), of which three are directly related to satellite control.

Measurement error origin	Involved Item
S/C linear acceleration	Drag-Free Control
S/C absolute pointing	Attitude Estimation & Control
S/C attitude stability in MBW	Attitude Estimation & Control
Gradiometer resolution	Gradiometer technology
Gradiometer thermo-elastic distortions	Gradiometer structural design & thermal control

Figure 4 Major error contributors to gradiometer measurements

Since the gravity gradients to be measured are very small quantities, even very low coupling levels (as defined in figure 3) combined with standard spacecraft microgravity environments would result in excessive measurement errors. For this reason, the platform dynamics, both in translation & rotation, must be controlled in the MBW. The resulting requirements, summarised in figure 5, are expressed as spectrum levels in the MBW for consistency with the scientific objective.

Error terms that can be compensated for by post-processing of the gravity gradient measurements are distinguished from those that have to be cancelled at spacecraft level. This allows to largely relax the pointing stability requirements, and at the same time to minimise the constraints set on platform design. In particular, the very stringent requirements on the attitude stability about the orbit normal (Y) are not to be achieved at satellite level.

Satellite absolute pointing is also constrained to avoid an excessive error when transporting the measurements from the satellite frame to an Earth reference. Nevertheless, the absolute pointing requirements are much less severe than the attitude stability requirements (see figure 5) and corresponds to standard medium accuracy pointing needs.

Gradiometer technology	Non-cryogenic (MM1)	Cryogenic (MM2)
Acceleration ($m/s^2/\sqrt{Hz}$)	$1.0\ 10^{-7}$	$2.0\ 10^{-7}$
Absolute pointing	0.1° (X&Z) 2.5° (Y)	0.1° (X&Z) 0.2° (Y)
Angular rates knowledge ($rad/s/\sqrt{Hz}$)	X&Z: $3.4\ 10^{-6}$ Y: $4.2\ 10^{-9}$	X&Z: $9.6\ 10^{-7}$ Y: $3.4\ 10^{-10}$
Angular acc. control ($rad/s^2/\sqrt{Hz}$)	$2.4\ 10^{-7}$	$5.6\ 10^{-7}$

Figure 5. DFACS requirements summary

3. DRAG-FREE CONTROL SYSTEM DESIGN

The needs for drag-free control (DFC) are first determined by comparison of the disturbance acceleration induced by aerodynamic drag fluctuations in the MBW. The air drag, by far the dominating disturbance source at the considered low altitude (270 km) was modelled by ALENIA SPAZIO (ref. [2]) with the ESABASE software using MSIS density and wind models. Random short term drag fluctuations were modelled using a recent model of density fluctuations (ref. [3]). From the time history and the spectrum of the computed drag forces shown in figure 6, the following conclusions can be drawn

- the X-drag force dominates the Y-drag by a factor of 20 and the vertical component (Z) is quite negligible. DFC is definitely not necessary on the Z-axis and DFC analyses have shown that it is also not requested on the Y-axis. Therefore DFC has only to be performed along-track (X), which largely simplifies DFACS design.

- the spectra of the drag variations in the MBW have a similar shape and can be modelled with an 1/f envelope for DFC requirement derivation.

The DFC rejection needs in the MBW are derived as the ratio between the requirement on the residual acceleration spectrum level (derived in section 2) and the drag disturbance spectrum. Because of its 1/f decay, the most stringent rejection requirements are observed at the lower limit of the MBW (see figure 7). In the MBW, the 20 dB/decade rejection profiles are obtained with standard control schemes, but the resulting control bandwidth is rather large, about 0.5 Hz for MM1 and 0.1 Hz for MM2. Since solar panels are body mounted, the frequency of the first flexible mode is quite large (17.4 Hz), so control-structure interaction is not a concern.

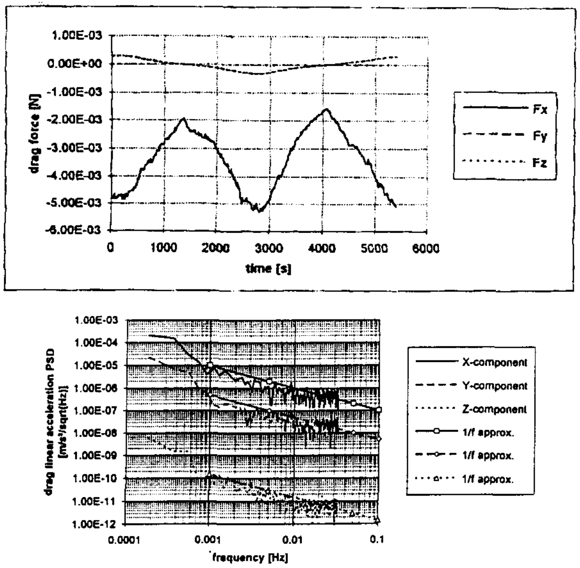

Figure 6. Drag disturbance forces (from [2])

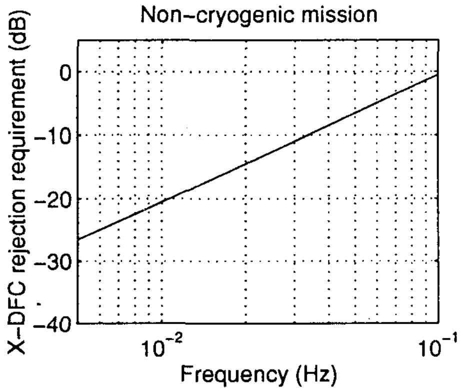

Figure 7. DFC Rejection needs for MM1 (worst case)

There is no specific need to control drag fluctuations below the MBW, except for the average drag force, which shall be compensated in order to prevent the decay of orbit altitude. This orbit maintenance function is generally performed in a periodically activated mode to restore the nominal orbit altitude. For the GOCE mission, this would imply periodic interruptions of gravity measurements collection, since the disturbances induced by the firing of the orbit maintenance thrusters would be excessive. In order to avoid such an unacceptable degradation of mission performance, continuous orbit maintenance has been selected both MM1 & MM2 concepts: DFC and orbit maintenance are realised with the same thrusters whose thrust is modulated to compensate for drag variations up to MBW upper limit.

The selection of thrusters for DFC& orbit maintenance, being one of the cost & design driver for the platform, was the result of an important trade-off activity. Electric propulsion with thrust modulation was finally retained for both mission concepts, since it combines the high fuel efficiency required because of the very low altitude (270 km) flown by GEM and the possibility to finely compensate for satellite linear accelerations.

As the result of phase 1 trade-offs (see ref. [2]), three different types of electric thrusters can be figured for drag compensation (see figure 8):

- FEEP (Field Emission Electric Propulsion), developed at Centrospazio (Italy) delivers low thrust with a high accuracy both in pulsed and proportional modes.

- "RF ion propulsion", specifically developed by PROEL (Italy) for drag-free applications, with nominal thrust level from 1 to 10 mN and built-in throttling capability

- "Conventional ion propulsion", developed for application to the North/South station-keeping of geostationary satellites, represented in Europe by the RIT-10 (MBB/Germany) and the UK-10/T5 (MMS-UK) thrusters.

	FEEP thrusters	RF ion thruster (PROEL)	Conventional ion thruster
Nominal thrust	< 1 mN	1 to 10 mN	10 to 20 mN
Specific impulse	> 6000 sec	3000 sec	3000 sec
Specific power	> 60 W/mN	30 W/mN	30 W/mN
Propellant mass	< 3 kg/year	6 kg/year	6 kg/year
Peak power	< 350 W	170 W	170 W

Figure 8. Candidate electric propulsion systems

The selection between these different thrusters is dictated by the selected altitude, for a best fit of the nominal operating thrust and the average drag level. Indeed, the fuel efficiency (specific impulse) and the power efficiency (specific power, ratio of the peak power to the realised thrust) of a given thruster are largely degraded when it is not operated close to its nominal thrust. For the selected 270 km altitude, the average thrust to be delivered by each of the two ion thrusters is 2.8 mN. Therefore conventional ion thrusters are far too large (10 to 20 mN). FEEP thrusters could be used in clusters, but the key issue is then the power demand. Therefore, the recommended thruster technology is the intermediate size RF ion thruster from PROEL. The thrust modulation performances of this thruster were shown to be adequate through an extensive test programme running in parallel with the system definition study.

The orbit is autonomously determined on-board with the GPS receiver part of the payload. The average thrust level is continuously adjusted to cancel out the measured orbit decay. This allows to compensate for the DC drag component and the first harmonics of the orbit rate. For measurement of higher frequency drag fluctuations the GPS data is complemented with the drag-free reference given by the common mode output of the gradiometer, i.e. 3-axis measurement of the satellite accelerations.

4. ATTITUDE DETERMINATION

The required absolute attitude estimation accuracy is relatively modest, 0.1 deg. on X & Z axes and 1 deg. (resp. 0.2°) about the Sun line (Y-axis) for MM1 (resp. for MM2). At the opposite, high accuracy measurement of the attitude jitter in the MBW are necessary for post-processing of the gradiometry data and not achievable with standard attitude sensors. For this reason, attitude determination is based on the hybridisation of the angular acceleration measurements from the gradiometer and the absolute attitude reference given by a set of classical sensors. This approach is quite similar to the classical "gyro-stellar" hybridisation scheme: the angular acceleration reference from the gradiometer is used to propagate the attitude reference between the updates from the classical sensors. Since the gradiometer measurements provide a very low noise attitude reference over a wide frequency range (typically a few mHz to a few Hz), the recurrence of the classical attitude sensors updates can be quite long (up to a few hundreds of seconds). This actually allows to average the sensors outputs over long periods, resulting in a drastic reduction of the sensor noise contribution (at least by a factor of 10). The absolute attitude determination performance is then driven by the systematic errors (biases) of the attitude sensors.

Candidate medium accuracy sensors for absolute attitude determination have been extensively traded-off, resulting in the following baseline selection:

- for MM1, new generation low weight & power consumption digital Sun sensors (like Jena Optronik FSS or TPD/TNO DSS) are baselined. Such sensors are currently under development but should be available by the time of the S/C development. For sensing about the Sun line, a magnetometer is proposed to minimise cost & complexity, possibly replaced by an Earth sensor if performances are found too marginal during detailed design phases. The same sensors are used for the initial attitude acquisition, which largely simplifies the ACMS design.

- for MM2, a wide field-of view, medium accuracy star tracker is recommended, because a higher pointing accuracy is requested. With detection of at least two stars, a 3-axis attitude determination is then possible.

The gradiometer is used to provide a 3-axis high accuracy measurement of angular accelerations. For the capacitive instrument (MM1), angular acceleration estimates are obtained by double differences on the gradiometer outputs about transverse axes (acceleration measurements normal to the baseline vectors). A detailed model of accelerometer errors has been used to evaluate through time simulation the achievable relative attitude determination accuracy. The resulting simulation results, provided as the estimation error spectrum in the MBW are shown in figure 9. For all axes, the resolution of the angular acceleration measurements is in the range of 2.10^{-8} deg/s^2 RMS in the MBW. Such accuracy is largely sufficient to fulfil the attitude determination requirements about the X & Z axes, but does not allow to meet the very stringent requirements about the Y-axis. This is however no a critical issue, since the corresponding error term can be removed by post-processing of the gradiometry data using the fact that the gravity tensor is traceless. For the cryogenic instrument (MM2), angular accelerations are directly measured by dedicated superconductive circuits of the integrated gradiometer, with a similar expected accuracy. Therefore fine attitude determination for data post-processing is not seen as a critical point for the mission.

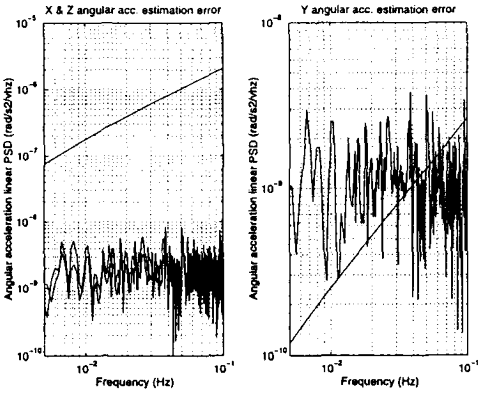

Figure 9 Angular acceleration estimation error compared to attitude knowledge requirements

5. ATTITUDE CONTROL

The disturbance torques analysis has demonstrated that the fluctuations in the MBW result in an attitude jitter compatible with the satellite pointing stability requirements. Therefore attitude control can be limited to the compensation of low frequency disturbance torques, in order to achieve the medium accuracy absolute pointing requirements (0.1 deg. typically, as shown in section 2). This largely simplifies actuator selection for attitude control, even if the payload definition results in different type of actuators in the two mission concepts.

For MM1, impulsive nitrogen thrusters are selected for their simplicity and demonstrated reliability in order to perform long-term attitude control of the platform through periodic actuations. A simulation of the cycle limit control using the 20 mN Nitrogen thrusters flown on HIPPARCOS has been set up to assess the attitude cycle characteristics: 200 sec average duration corresponding to about 20,000 thruster actuations over the 18 month mission. A key point was then to assess the dynamic disturbances induced by thrust pulses that could potentially corrupt the gradiometry measurements in the MBW. The dynamics parameters output of the long-term control simulations were fed into the detailed model of the gradiometer and the measurement was computed. The resulting error spectrum in the MBW is compared to the platform attitude stability requirement in figure 10, showing that the dynamic disturbances induced by thruster impulses are not critical. Finally, it was checked that the saturation of the capacitive sensors of the accelerometers during thrust impulses are also not critical for the mission, since only about 1% of the gravity gradient measurements are lost.

For MM2, the same actuators are in principle applicable, but the best approach is to use the helium boil-off gas from the payload cryostat as propellant in dedicated proportional thrusters (otherwise the expelled helium would be the largest source of disturbance torques). The proposed proportional helium thrusters (PHT) are derived from those developed for Gravity Probe B NASA mission and foreseen for the STEP mission. Such thrusters are basically composed of a magnetically driven poppet controlling the exhaust flow rate from the cryostat (see figure 12) providing thrust levels in the mN range with a relatively low specific impulse (150 sec). The thrust modulation can be very smooth, with a 1 μN typical resolution and a 10 Hz bandwidth, making such thrusters excellent candidate for fine DFC. The major limitation is due to the small control authority, driven by the available helium flow rate, itself determined by the heat leaks of the cryostat. For the GOCE instrument, the helium flow rate is estimated to 0.6 mg/s, equivalent to only 0.8 mN thrust in a single direction. It is therefore crucial to optimise thrusters implementation on the platform according to the spatial distribution of the disturbance torques to provide sufficient control authority margins. Optimisation results have demonstrated good flow rate margins (30 %), allowing if necessary to extend attitude control in the MBW to improve the error budget.

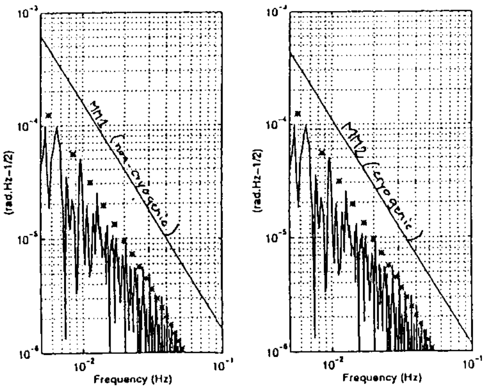

Figure 10. Spectrum of dynamic disturbances induced by thrust impulses in the MBW

Finally, attitude control with reaction wheels was considered as an attractive alternative to thruster-based strategies. Indeed, reaction wheels are widely used on fine pointing platforms, providing a large control authority and allowing fine attitude control in the MBW. Reaction wheels were not baselined for GOCE because such rotating devices are known to generate high frequency microvibrations, likely to be unacceptable for the acceleration sensitive payload. An attempt was made in parallel to the main study to measure the acceleration levels induced by a reaction wheel in the low frequency MBW of GOCE. Despite of the difficulty to measure very tiny acceleration levels at such low frequencies, the experimental characterisation conducted by ALENIA Spazio (Turin) succeeded to demonstrate that the reaction wheel disturbances are not critical in the MBW. However, this characterisation did not assess the effect of reaction wheel microvibration frequency conversion through gradiometer non-linearity and aliasing caused by data sampling. If the impact of non-linear response of the accelerometers is quite difficult to assess without dedicated analysis and experimentation, orders of magnitude can be produced for aliasing through gradiometer data sampling. Measurements at MMS on the SOHO flight model ball-bearing reaction wheels (0.1 Nm, 40 Nms) have demonstrated radial forces at wheel rate of typically $F_0 = 1$ N at 100 Hz, proportional to the frequency squared. Considering the accelerometer as a second-order lowpass filter with a 20 Hz cut-off frequency, the induced high frequency attenuation compensate for the frequency dependence of the wheel disturbance force. The level of the high frequency harmonics in gradiometer measurements is therefore independent of the wheel rate. It is evaluated for the coincidence of an harmonic disturbance with a flexible mode, for a structural damping ratio of 0.005:

$$\delta a = 4.10^{-3} \text{ m/s}^2 \text{ for } f > 20 \text{ Hz}$$

This harmonic disturbance is about five orders of magnitude larger than the signal to be detected in the MBW (100 dB dynamic range). It shall be efficiently removed from the accelerometer measurements before sampling to prevent corruption through aliasing. Such an attenuation requires to implement a third-order anti-aliasing filter with a cut-off frequency of 0.2 Hz. Effects of gradiometer non-linearities will not be solved with anti-aliasing filters, so the only reliable solution is to dynamically decouple the gradiometer from the vibrating platform using low frequency suspension systems. Such passive isolation systems based on elastomeric materials are well known at MMS and high performances (40 dB rejection above 50 Hz) have been demonstrated within the ESA TRP "Very High Pointing Accuracy AOCS" study (ref. [4]).

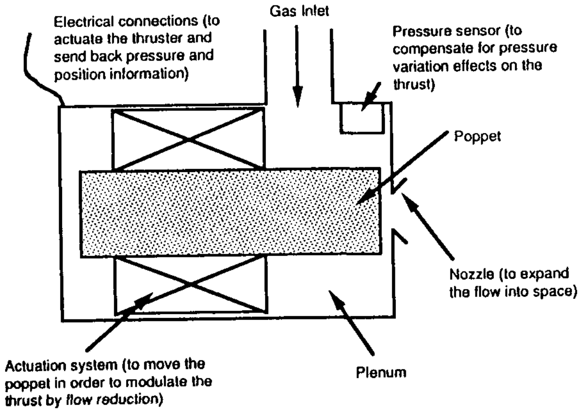
Electrical connections (to actuate the thruster and send back pressure and position information)
Gas Inlet
Pressure sensor (to compensate for pressure variation effects on the thrust)
Poppet
Nozzle (to expand the flow into space)
Actuation system (to move the poppet in order to modulate the thrust by flow reduction)
Plenum

Figure 11 Schematic principle of a PHT

CONCLUSION

This paper has presented the preliminary definition of the Drag-Free and Attitude Control System (DFACS) for the GOCE mission, as performed during the assessment study aimed at the selection of the candidate missions for the ESA Earth Explorer Programme. The major achievement is the demonstration of the feasibility of a DFACS concept fulfilling the challenging mission requirements while keeping system cost & complexity within reasonable limits. This has been made possible first by a thorough derivation of DFACS requirements from scientific objectives and second by the maximum use of validated actuation & sensing hardware. A specific DFACS design has been proposed to best address the characteristics of each mission concept, with the objective to match the DFACS performance to the expected sensitivity of the considered instrument. The resulting systems differ in performances, as they will differ in cost and complexity, but this will be further traded-off with the scientific achievements. The major open point is the applicability of reaction wheels, a quite appealing alternative to the proposed thruster-based attitude control: additional analysis and experimental work is necessary to assess the impact of frequency conversion of reaction wheel disturbances in the gradiometer measurement bandwidth.

ACKNOWLEDGEMENTS

The work presented in this paper was performed in the pre-phase A study for the Gravity Explorer mission under the ESA direction of MM. P. L. SILVESTRIN, M. AGUIRRE and A. TOBIAS. The study was led by ALENIA SPAZIO, with Mr R. TRUCCO as study manager and Mr A. ANSELMI as technical officer.

REFERENCES

1. L. Vaillon

Gravity Explorer Mission System Study: Baseline Drag-Free & Attitude Control System Concepts, MATRA MARCONI SPACE, ref. 260/LV/NT/17.96, June 1996

2. A. Anselmi

Gravity Field & Ocean Circulation Explorer Mission & System Design Report, ALENIA SPAZIO, ref. GEM/RP/AI/0002, August 1996

3. M. P. Hickey

A Simulation of Small Scale Thermospheric Density Variations for Engineering Applications, NASA Contract Report 4605, May 1994

4. L. Vaillon & al.

Passive & Active Microvibration Control Systems for Very High Pointing Accuracy Space Systems, Proceeding of the 3rd ESA International GNC Conference, Nov 1996

SESSION 8:
ANALYSIS I

Chairman: Th. Lange (DLR, Germany)

MIMO CONTROL FOR 6DoF RELATIVE MOTION

E.J. Mora
GMV S.A.
c/Issac Newton 11
28760-Tres Cantos
Madrid, Spain
Tel.:+34-1-807-21-00
Fax.:+34-1-807-21-99
E-mail: emora@gmv.es

J.B. Serrano
GMV S.A.
c/Issac Newton 11
28760-Tres Cantos
Madrid, Spain
Tel.:+34-1-807-21-00
Fax.:+34-1-807-21-99
E-mail: jbserrano@gmv.es

F. Ankersen
ESA/ESTEC
P.O. Box 299
2200 AG Noordwijk
The Netherlands
Tel.:+31-71-565-3865
Fax.:+31-71_565-5419
E-mail: finn@wk.estec.esa.nl

ABSTRACT

This paper describes the detailed investigations on control matters regarding simultaneous translational and rotational 6 degree of freedom relative motion between two spacecraft with an arbitrary pointing. The controller design and analysis have been based on modern Multi-Input Multi-Output (MIMO) control methods, which have two clear advantages: first, the controller can be designed such the stability and robustness of the system are ensured and, second, the controller characteristics can be analyzed using the powerful state-of-the-art MIMO tools.

After reviewing different MIMO control design techniques, four were selected as the most promising ones, trying to cover, as much as possible, the complete spectrum of possible MIMO techniques: Pole-placement and LQG/LTR as representative of the "classical" MIMO techniques and H_∞-Synthesis and μ-Synthesis as the state-of-the-art MIMO design techniques. For the investigations, the ATV-ISSA RVD mission was selected as baseline. This paper describes the application of these MIMO design techniques to two representative GNC modes, covering different motions (forced approach and station keeping), references (with respect to the target local orbital frame and docking frame) and target attitudes (Earth pointing, Sun-pointing).

1. INTRODUCTION

The study of automatic Rendezvous and Docking (RVD) and the development of the associated technology had been initiated in Europe in the beginning of the eighties in expectation of future European Space programs including mating of two or more spacecraft. However, in the past ESA studies on RVD and manoeuvring, the emphasis for the GNC design has been concentrated on Guidance and Navigation, without spending too large effort on the Control matters. It is however necessary to investigate the control aspects in more depth as well as to perform an analysis of the complete feedback loop, which so far could not be done properly due to the lack of detailed control design.

Past studies have been concentrated on designing controllers assuming decoupled components of the RVD system. However, the importance of the coupling between the trajectory and the attitude components is clear from the corresponding equations of motion, the presence of certain disturbances (e.g., plume impingement, parasitic forces and torques) and the proper geometrical coupling between both components. Therefore it would be of special interest to include this coupling effect during the design process.

The design problem facing the control engineer can be described as achieving the best trade-off between a set of performance requirements and a set of constraints on system performance. Generally speaking, some performance requirements will be imposed and they should be achieved in the presence of constraints (i.e., actuators limitations, sensor operational constraints such as field-of-view, safety considerations, final conditions,...) and uncertainties on the system, namely, on the dynamics, actuators and sensors.

In general, designing control systems using conventional analytical methods involves iterative design analyses that are costly in time and manpower. These classical techniques are often misleading in evaluating system stability and robustness concerning model inaccuracies. Previous designs of the control function of the GNC for RVD missions have been made selecting one or more operational points and guaranteeing robustness to parameter variations by designing large single-loop stability margins and evaluating the design through simulation. Recent developments in control system design provide the theoretical mathematics required for optimizing the controller design and evaluating stability and robustness to simultaneous parameter uncertainties. Using new methods for characterizing uncertainties, controller robustness properties may be evaluated, reducing the number of design conditions analyzed.

Proceedings Third International Conference on Spacecraft Guidance, Navigation and Control Systems, ESTEC, Noordwijk, The Netherlands, 26-29 November 1996, ESA SP-381 (February 1997)

2. PROBLEM CHARACTERIZATION

2.1. Reference mission

The **International Space Station Alpha** (ISSA) is selected as target spacecraft. Its orbit is circular of 460 km altitude and 51.6° inclination. Two reference attitudes are considered: Earth pointing and Sun pointing. The attitude deviations with respect to the reference one are modelled, for simulation purposes, by means of Fourier series: no detailed characterization of the target attitude control is performed.

The **Automated Transfer Vehicle** (ATV) is selected as chaser spacecraft. It is assumed to be composed of the ATV core + Unpressurized Cargo Carrier + Payload. According to the GNC modes description, three reference attitudes are considered: Earth pointing, Sun pointing and target pointing. For the purposes of the study and due to the high impact of the flexibilities in the attitude control performances, two flexible solar arrays have been added to the ATV nominal configuration. The tank configuration is composed of four tanks of 0.65 m diameter (assumed spherical). A detailed characterization of the ATV surfaces was performed in order to compute the aerodynamic perturbing actions.

The reaction control system which is used for orbit and attitude control consists of 20 hot gas thrusters of 200 N thrust level. The thruster selection and thrust on-times computation is performed by means of an optimization algorithm which minimizes the fuel consumption and takes into account the thruster state history in order to reduce the thruster valve duty frequency. The high value of the Minimum Impulse Bit (5 Ns) together with the thrust errors and thruster mounting misalignments led to very high undesired forces and torques.

On the other hand, the chaser navigation equipment is assumed to be composed by a GPS receiver, a RV sensor, Earth sensors, Sun sensors and gyros.

The **GPS receiver** provides the relative chaser-target position and velocity estimates coming from a RGPS navigation concept. It is applicable for relative distances greater than 300 meters. While the **RV sensor** provides two different measurements: relative position measurements for chaser-target distances lower than 300 meters and relative attitude measurements for distances lower than 40 meters.

2 Earth sensors and **2 Sun sensors** are required due to the different chaser ATV reference attitudes. Finally, **3 gyros** provide attitude rate information along three body-directions.

2.2. GNC modes characterization

Two representative GNC modes, covering different motions, references and target attitudes, have been used to demonstrate the application of the MIMO design techniques for the 6DoF Relative Motion in a RVD scenario: RSK02 and IAPP01 (the investigations for some other GNC modes can be found in Ref.[1]).

The **RSK02 GNC mode** is a R-bar station keeping to an Earth pointing target. The chaser is controlled with respect to the target docking frame (typically, referred to as E_{DT}-frame), located at the target docking port. The chaser is target pointed and the chaser rotational control is also performed with respect to E_{DT}-frame. The chaser relative state (both translational and rotational) is obtained from the RV sensor measurements. The coupling between orbit and attitude is due to the geometrical coupling, the sensor information, the plume impingement and the effect of the parasitic forces and torques. The relative distance between chaser and target is 40 meters and the maximum allowed position and attitude deviations are (3σ criteria): 3 m and 1 m along approach and transverse axes, respectively, and 1° about all the axes, relative to the target motion.

The **IAPP01 GNC mode** is an inertial forced approach to a Sun pointing target. The translational approach is performed with respect to the theoretical target docking frame (E_{DTH}-frame), located at the target docking port and assuming the nominal target orientation. The chaser is target pointed and the chaser rotational control is performed with respect to the E_{DTH}-frame. The relative position is obtained from the RV sensor measurements whereas there is no information on the relative attitude with respect to the target: attitude information is obtained from Earth and Sun sensors and gyros. The coupling between orbit and attitude is due to the proper geometrical coupling, the plume impingement and the effect of the parasitic forces and torques. The relative distance between chaser and target is from 300 to 40 meters and the maximum allowed position and attitude deviations are (3σ criteria): 5 m and 1° at the GNC mode entry, and 3 m and 1 m along approach and transverse axes, respectively, and 1° about all the axes at the GNC mode exit.

3. MIMO CONTROL DESIGN TECHNIQUES

3.1. General

A review of the a-priori candidate MIMO control techniques was performed. Hints on the different control techniques were provided in order to pre-select the most promising techniques to be used for MIMO controllers for 6DoF relative motion in rendezvous missions. The candidate MIMO control design technique were the following:

- **Robust Control**: H_2-Synthesis, H_∞-Synthesis and μ-Synthesis
- **Linear Quadratic Control**: General Cost Function-Synthesis, LQ Minimax-Synthesis and LQG/LTR-Synthesis.
- **Modal Control**: Pole-placement (several candidates were analyzed), Eigenstructure Assignment Techniques (several candidates were analyzed) and Multivariable Nyquist-like Techniques.

For the selection of the MIMO design techniques, several factors were taken into account such as the goodness of the performances of the resulting controller (in terms of command following, disturbance rejection and low sensitivity to sensor noise), the existence of dedicated procedures for such design techniques within the selected commercial tool (MATRIX$_X$ Product Family) and covering as much as possible all those groups. The selected MIMO Control Design Techniques for being applied to the 6DoF relative motion were the following: H_∞-Synthesis, μ-Synthesis, LQG/LTR synthesis and Pole-placement.

For each of these MIMO techniques, the design procedures were structured into a design methodology, which can be split is two major stages: first, the formulation of the control design problem (in terms of the nominal plant model, uncertainties model and control requirements) and, second, the controller design itself, which includes the iterative process in order to obtain the optimum compromise between performance and stability considerations by fulfilling the system constraints.

3.2. H_∞-Synthesis

The MIMO nominal plant is modelled in the state-space form as follows:

$$\begin{aligned} \underline{\dot{x}} &= \tilde{A}\underline{x} + \tilde{B}_1\underline{q} + \tilde{B}_2\underline{u} \\ \underline{p} &= \tilde{C}_1\underline{x} + \tilde{D}_{11}\underline{q} + \tilde{D}_{12}\underline{u} \\ \underline{y} &= \tilde{C}_2\underline{x} + \tilde{D}_{21}\underline{q} + \tilde{D}_{22}\underline{u} \end{aligned} \qquad (1)$$

where $\underline{x}$ is the system state vector, $\underline{u}$ is the control vector, $\underline{y}$ is the measurements vector, $\underline{q}$ is the vector of references, disturbances and noises and $\underline{p}$ is the critical performances vector.

The extended MIMO plant model (see Figure 1) is computed by pre- and post- multiplying the nominal plant model by the input and output weighting transfer functions: $\underline{e} = W_{out}\,\underline{p}$ and $\underline{q} = W_{in}\,\underline{w}$ (note that the control actions have been included within the performance vector, $\underline{p}$). Then, the inputs/outputs of the resulting MIMO plant model are normalized. The input weighting functions are driven by the size and signature (frequency behaviour) of the external disturbances whereas the output weighting functions constitute the tuning parameters and they are used to characterize the desired control performances.

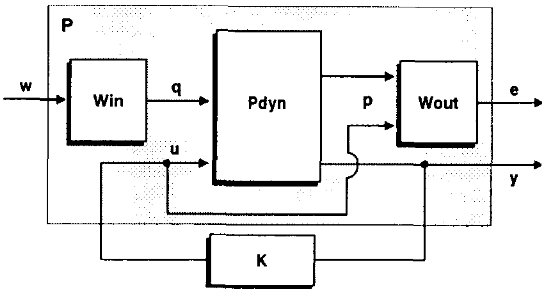

Figure 1.- H_∞-synthesis model for controller design.

Once the H_∞-assumptions are verified, the objective of the H_∞-methodology is to find a stabilizing controller K, such that the infinity norm of the closed-loop transfer function $H_{ew}(s)$ from $\underline{w}$ to $\underline{e}$ is minimized. The solution of this problem cannot be computed directly. However, an iterative scheme, the so-called γ-iteration (Ref.[2]), can be used to find solutions arbitrarily close to the optimal. This iterative approach consists of finding stabilizing compensators which guarantee

$$\| H_{ew}(s) \|_\infty = \sup_\omega \sigma_{\max} \left[H_{ew}(j\omega) \right] < \gamma \qquad (2)$$

Once the stabilizing controller has been designed, the closed-loop transfer function G is obtained (see Figure 2). The following analyses can be performed: nominal performances, by analysing the maximum singular values of the transfer function H_e and the stability and performance robustness (for structured uncertainties, Δ $\sigma_{max}(\Delta) < 1$), by verifying the fulfilment of the conditions $\|\mu(G_{11}(s))\|_\infty < 1$ and $\|\mu(G(s))\|_\infty < 1$, respectively, where μ is the Structured Singular Value.

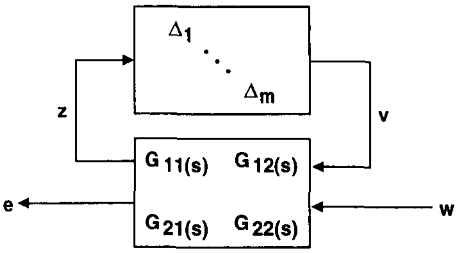

Figure 2.- H_∞-Synthesis model for stability and performance robustness analysis.

3.3. μ-Synthesis

The design process for the μ-Synthesis starts from the same plant model as the H$_\infty$-Synthesis. After building the extended plant model (pre- and post- multiplying by the input and output weighting functions) and after including the effect of the uncertainties into the plant model, it yields:

$$\begin{aligned}\underline{\dot{x}} &= A\underline{x} + B_1\begin{bmatrix}\underline{v}\\ - \\ \underline{w}\end{bmatrix} + B_2\underline{u}\\ \begin{bmatrix}\underline{z}\\ - \\ \underline{e}\end{bmatrix} &= C_1\underline{x} + D_{11}\begin{bmatrix}\underline{v}\\ - \\ \underline{w}\end{bmatrix} + D_{12}\underline{u} \qquad (3)\\ \underline{y} &= C_2\underline{x} + D_{21}\begin{bmatrix}\underline{v}\\ - \\ \underline{w}\end{bmatrix} + D_{22}\underline{u}\end{aligned}$$

where $\underline{x}$ is the system state vector, $\underline{u}$ is the control vector, $\underline{y}$ is the measurement vector, $\underline{w}$ is the vector of "normalized" commands, disturbances and measurement noises, $\underline{e}$ is the vector of "normalized" critical performance signals, $\underline{z}$ and $\underline{v}$ are the output and input vectors for modelling the effect of the uncertainty in the system.

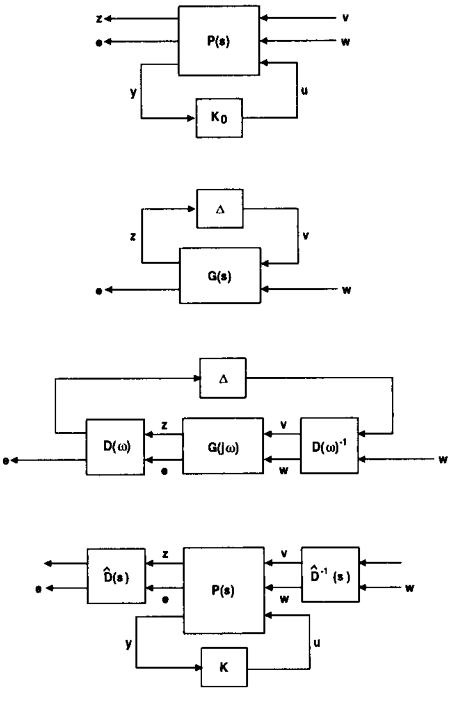

Figure 3.- μ-Synthesis: D-K iteration.

Once the H$_\infty$-assumptions are verified, the objective in the μ-synthesis methodology (Ref.[4]) is to design a controller which minimizes the upper bound to μ (Structured Singular Value) for the closed loop system:

$$D(s)L_l(P(s),K(s))D(s)^{-1} \qquad (4)$$

where $L_l(P(s),K(s))$ is the closed-loop system transfer function and $D(s)$ is a frequency dependent scaling matrix. The approach usually followed for solving the μ-synthesis problem is the so called **D-K iteration** technique: the approach is to alternate between finding $K(s)$, to minimize the expression (4) for a fixed $D(s)$, and then to find a minimizing $D(s)$ for a fixed $K(s)$ (this latter step is conducted point-by-point in frequency with a different constant D matrix result for each frequency point).The μ analysis of the closed-loop system is unaffected by the D-scales. However, the H$_\infty$ design problem is strongly affected. The D-K iteration procedure is illustrated schematically in Figure 3.

Once the stabilizing controller has been designed, the closed-loop transfer function is obtained (see Figure 2). The following analyses can be performed: nominal performances, by analysing the maximum singular values of the transfer function H_e and the stability and performance robustness (for structured uncertainties, Δ, $\sigma_{max}(\Delta)<1$), by verifying the fulfilment of the conditions $\|\mu(G_{11}(s))\|_\infty < 1$ and $\|\mu(G(s))\|_\infty < 1$, respectively.

3.4. LQG/LTR

The MIMO nominal plant is modelled in the state-space form as follows:

$$\begin{aligned}\underline{\dot{x}} &= A\underline{x} + B\underline{u}\\ \underline{y} &= C\underline{x}\end{aligned} \qquad (5)$$

where $\underline{x}$ is the system state vector, $\underline{u}$ is the control signals vector and $\underline{y}$ is the vector of sensor measurements.

The approach to be followed consists of two major steps: first, the design of the LQR Controller, and second, the design of a Kalman Filter in such a way that the stability and robustness characteristics of the LQR controller (designed previously) are recovered.

The LQR controller is designed such that it fulfils the imposed performance and robustness requirements and it minimizes the cost functional

$$J = \int_0^\infty (\underline{x}^T Q_0 \underline{x} + \underline{u}^T R_0 \underline{u})dt \qquad (6)$$

The excellent stability and robustness characteristics of the LQR design are degraded when a Kalman Filter is inserted into the feedback loop (in order to obtain a LQG controller) if it is not performed via the Loop Transfer Recovery (Ref.[5]). The goal of the LTR is to recover the LQR properties in the LQG design: the Kalman filter state estimator is designed selecting a filter recovery parameter q which recovers the LQR frequency-domain characteristics over the frequency range of interest. The Kalman filter is designed by using a modified noise intensity (state vector noise matrix):

$$Q = Q_0 + q^2 B B^T \tag{7}$$

Once the controller has been designed, the closed-loop transfer function is obtained and the following analyses can be performed: nominal performances, by analysing the maximum singular values of the sensitivity function and the stability robustness (for structured uncertainties, Δ, $\sigma_{max}(\Delta)<1$), by verifying the fulfilment of the conditions $\|\mu(G_{11}(s))\|_\infty < 1$.

3.5. Pole-placement

Strictly speaking, the pole-placement technique is not an unique technique but a group of design techniques, all of them based on finding a controller which leads to a closed-loop system with certain target poles. Thus, there is a great variety of pole-placement techniques, depending on the method used in order to design such a controller. Among them, one based on the use of a linear quadratic regulator (LQR) has been selected due to the fact that it gives a robust system by guaranteeing adequate stability margins.

The design process for the Pole-placement starts from the same plant model as the LQG/LTR. However, prior to the controller design, it is needed to analyze in detail the system performance and stability specifications with the purpose of defining the desired closed-loop poles. This is one of the major drawbacks of this pole-placement design technique due to the absence of reliable criteria for selecting them, carrying-out in most of the cases an heuristic approach.

Together with the selection of the closed-loop poles, the designer must choose the relative importance of every pole in the general cost function. This is performed by means of the pole weighting parameters, V_i, which expresses the contribution of every pole to the error in the cost function.

The approach followed consists of two major steps: first, the design of the LQR Controller in order to achieve the desired closed-loop poles, and, second, the design of a Kalman Filter. The LQR design is performed by means of an iterative process in order to minimize the cost function (Ref.[7]):

$$J = \sum_{i=1}^{n} [V_i \, (\lambda_{d,i} - \lambda_{a,i})^2] \tag{8}$$

where V_i is a positive weighting parameter for the poles, $\lambda_{d,i}$ is the i^th^ desired pole, and $\lambda_{a,i}$ is the i^th^ achievable pole from LQR controller design.

Once the controller has been designed, the closed-loop transfer function is obtained and the following analyses can be performed: nominal performances, by analysing the maximum singular values of the sensitivity function and the stability robustness (for structured uncertainties, Δ, $\sigma_{max}(\Delta)<1$), by verifying the fulfilment of the conditions $\|\mu(G_{11}(s))\|_\infty < 1$.

4. MIMO PLANT LINEAR MODEL

4.1. General

Roughly speaking, the linear model corresponding to a generic plant is composed by the linear formulation and by the uncertainties model. The linear formulation is derived from the high fidelity (and, probably, non-linear) model by simplifying, linearizing or removing certain terms. Then, the uncertainties model is in charge of taking into account in the resulting linear model such aspects not covered by the linear formulation and which might have an impact in the control performances.

The high complexity of the 6DoF Relative Motion RVD scenario makes convenient to obtain the associated linear model in a component-oriented way, that means, to build the high level MIMO plant linear model by connecting adequately the MIMO linear models (linear formulation and uncertainties model) corresponding to the different components of the RVD scenario: orbit and attitude dynamics, chaser equipment (sensors and actuators) and the performance drivers (for control design purposes).

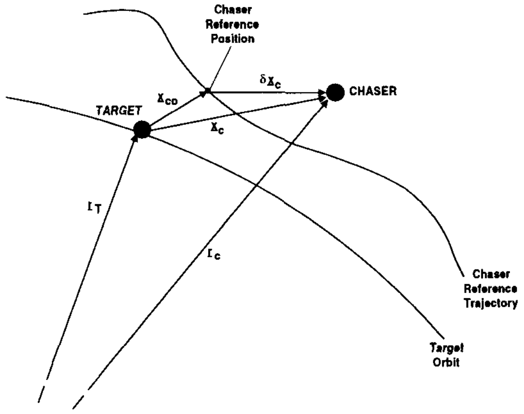

Figure 4.- Reference and deviation relative orbit state vectors.

Concerning the **linear formulation**, the methodology followed has been based on splitting the relative chaser state (orbit and attitude) in two contributions (see Figure 4 for the orbit state). The reference relative state (orbit and attitude), which corresponds to the state which would have the chaser in absence of disturbances ($\underline{x}_{C0}$). And, the deviations relative state (orbit and attitude), which is the difference between the real chaser relative state and the reference one ($\delta\underline{x}_C$).

By introducing this state vector decomposition in the non-linear/linear high fidelity formulation and, then, after manipulating them, two different formulations are obtained: one corresponding to the relative reference state and the other one to the deviation relative state. The second formulation is intended to build the MIMO plant linear model for control design purposes whereas the first one is used to obtain the feedforward control actions (forces and torques) and the sensor reference outputs.

The **uncertainties model** is in charge of covering those aspects not included within the linear formulation such as non-linear effects, parameter variations, unmodeled dynamic effects or known dynamics which are handled as uncertainties to simplify the resulting linear model. Two types of uncertainties can be considered.

- Unstructured Uncertainty. The uncertainty is expressed in terms of a specific single perturbation: several sources of uncertainty are described with a single perturbation which is a full matrix with the same dimensions as the plant.
- Structured Uncertainty. The individual sources of uncertainty are identified and represented directly (see Figure 5): there is no need to lump them together. The uncertainty is, then, described in a structured manner by identifying the sources and locations of uncertainty in the system: these perturbations (unmodeled dynamics, non-linear effects, parameter variations, ...) may correspond to model parameters, actuator uncertainty and measurement uncertainty.

However, the designer should not necessarily describe the uncertainty as rigorously as possible. Rather, we should take an "engineering approach" and describe the uncertainty only as rigorously as necessary. After analysing the features of the plant model under study, was concluded the convenience of using structured uncertainties. This was motivated basically by the difficulty of lumping all the effects into a single uncertainty (unstructured), without adding excessive conservativeness, due to the different nature of the possible sources of uncertainties and to the complexity of the 6DoF Relative Motion plant. This is in line with that component-oriented general philosophy.

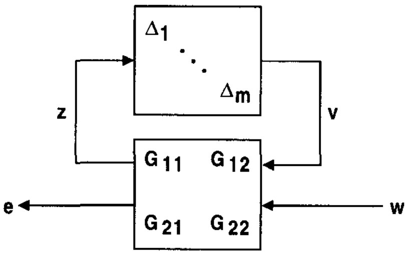

Figure 5.- Structured uncertainty (Δ-block) model.

4.2. Nominal linear models

Linear models without uncertainty description were developed for all the components of the 6DoF Relative Motion plant model for controller design purposes: relative orbit dynamics (Clohessy-Wiltshire equations of motion), relative attitude dynamics (including linear models for the flexible perturbing effects due to two flexible modes), chaser sensors (GPS receiver, RV sensor, Earth sensor, Sun sensor and gyros) and control performance drivers. As an example, Table 1 summarizes the nominal linear model corresponding to the RV sensor.

4.3. Perturbed linear models

From the analysis of the performances of the nominal linear models corresponding to the different components of the MIMO plant modes, several sources of uncertainties were identified, some of them covering mismodellings coming from the linear formulations and

$$\begin{bmatrix} \delta\rho \\ x_0\delta\alpha \\ x_0\delta\beta \end{bmatrix} = \begin{bmatrix} \delta x_{DC} \\ \delta y_{DC} \\ \delta z_{DC} \end{bmatrix} = -\left[L_{DCH,GT}\right]\begin{bmatrix} \delta x_{GT} \\ \delta y_{GT} \\ \delta z_{GT} \end{bmatrix} - 2\left(\left[L_{DCH,GT}\right]\underline{x}_{0/GT} \times\right)\delta\underline{q}_C + \left[A_C\left(\underline{x}_{OT,ODT/DT}\right)\right]\left(\delta\underline{q}_C - \delta\underline{q}_T\right)$$

$$\left[\delta\theta_x \;\; \delta\theta_y \;\; \delta\theta_z\right]^T = 2\left(\delta\underline{q}_C - \delta\underline{q}_T\right)$$

$L_{DCH,GT}$	Transformation matrix between E_{DCH}-frame and E_{GT}-frame
$\delta x_{GT}, \delta y_{GT}, \delta z_{GT}$	Components of the orbit deviation state vector w.r.t. E_{GT}-frame
$\underline{x}_{0/GT}$	Reference relative orbit state vector w.r.t. E_{GT}-frame
$\delta\underline{q}_C, \delta\underline{q}_T$	Chaser and target attitude deviation with respect to the reference one
$\underline{x}_{OT,ODT/DT}$	Target docking frame centre position vector w.r.t. OT and expressed in E_{DT}
A_C	Auxiliary matrix, 2 by the skewsymmetric matrix

$$A_C(\underline{\omega}) = \begin{bmatrix} 0 & -2\omega_z & 2\omega_y \\ 2\omega_z & 0 & -2\omega_x \\ -2\omega_y & 2\omega_x & 0 \end{bmatrix}$$

Table 1.- RV sensor nominal linear model (relative position and attitude measurements)

some others covering the effect of variations of certain parameters: Chaser mass (3%), inertia (3%) and characteristic flexible frequencies (5%) (parametric). In addition, ITCU actuators errors, including the undesired forces and torques due to the thruster arrangement (dynamic at the plant input) and Nominal RVS range measurement, to extend the applicability of the developed RVS linear model (parametric at the plant output), were included.

Then, the perturbed linear models were obtained from the computation of the variations of the state-space system matrices with respect to each uncertain parameter and from the compilation of such variations into an extended linear model (see Figure 6), pre- and post-multiplied by two constant matrices L and R (function of the uncertain parameter variation ranges).

Then, this methodology was applied to all the MIMO plant components affected by those uncertainties, i.e., relative orbit and attitude dynamics, perturbing effects due to flexibilities, actuators and RendezVous sensor, in order to obtain their perturbed linear models.

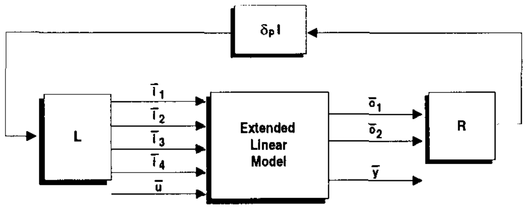
δpl
L
$\bar{\iota}_1$
$\bar{\iota}_2$
$\bar{\iota}_3$
$\bar{\iota}_4$
$\bar{u}$
Extended Linear Model
$\bar{o}_1$
$\bar{o}_2$
$\bar{y}$
R

Figure 6.- Extended perturbed linear model.

4.4. High level MIMO plant linear models

The major difference between the different control design techniques, on what concerns to the MIMO plant model, comes from the variables whose minimization will be achieved by the controller to be designed: for the robust control design techniques (H_∞- and μ-Syntheses), the performances vector $\underline{e}$ is minimized whereas for the LQG/LTR and Pole-placement control design techniques, the state vector $\underline{x}$ is minimized. It implies that special effort will be required to include within the MIMO plant model state vector those performances drivers whose minimization is intended. Taking into account these considerations, three wide purpose MIMO plant models have been implemented (see Figures 7 to 9).

5. DESCRIPTION OF THE DESIGN/ SIMULATION TOOL

5.1. General

All the aspects about the MIMO plant linear models and MIMO Control Design Techniques (mentioned in Sections 3 and 4) have been implemented in a software tool, named MIMOTOOL S/W, for the design and detailed performance evaluation of MIMO controllers for a RVD scenario. Then, this software tool supports the complete loop to be performed by the designer: first, controller design (by modelling adequately the plant and by using a certain control design technique) and, second, detailed performance assessment of the designed controller.

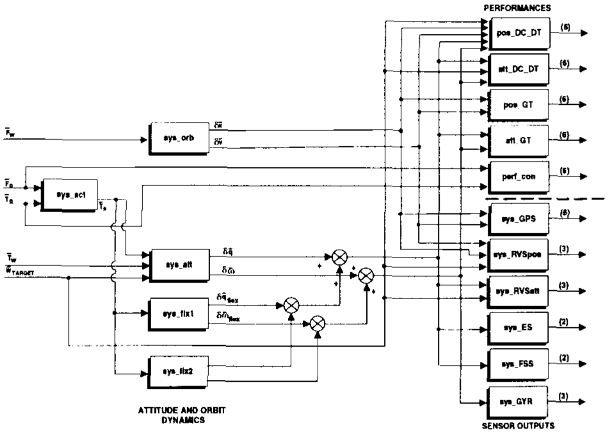
PERFORMANCES
pos_DC_DT
att_DC_DT
pos_GT
att_GT
perf_con
sys_GPS
sys_RVSpos
sys_RVSatt
sys_ES
sys_FSS
sys_GYR
(6)
(3)
(2)
$\bar{F}_w$
sys_orb
$\delta\bar{x}$
$\delta\bar{v}$
$\bar{F}_a$
$\bar{T}_a$
sys_act
$\bar{T}_s$
$\bar{T}_w$
$\bar{w}_{TARGET}$
sys_att
$\delta\bar{q}$
$\delta\bar{\omega}$
sys_flx1
$\delta\bar{q}_{flex}$
$\delta\bar{\omega}_{flex}$
sys_flx2
ATTITUDE AND ORBIT DYNAMICS
SENSOR OUTPUTS

Figure 7.- plant_rvd1 high level decomposition.

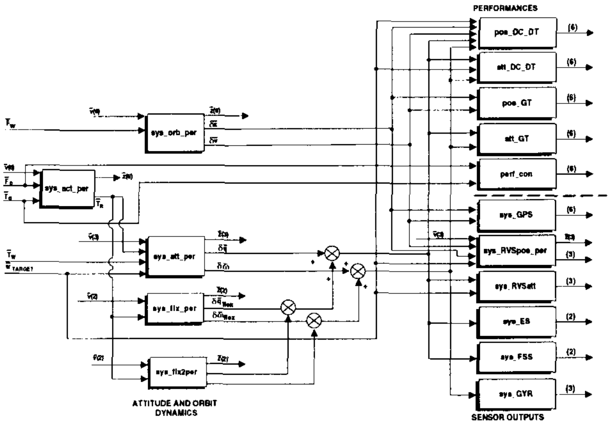
PERFORMANCES
pos_DC_DT
att_DC_DT
pos_GT
att_GT
perf_con
sys_GPS
sys_RVSpos_per
sys_RVSatt
sys_ES
sys_FSS
sys_GYR
sys_orb_per
sys_act_per
sys_att_per
sys_flx_per
sys_flx2per
ATTITUDE AND ORBIT DYNAMICS
SENSOR OUTPUTS

Figure 8.- plant_rvd2 high level decomposition.

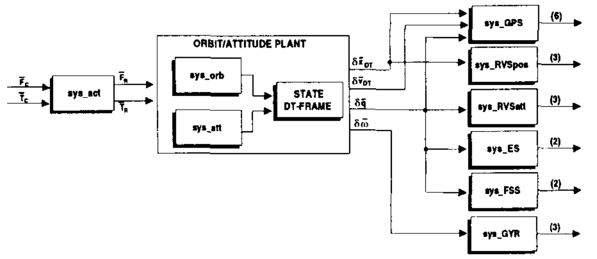
ORBIT/ATTITUDE PLANT
sys_orb
sys_att
STATE DT-FRAME
sys_act
$\bar{F}_c$
$\bar{T}_c$
$\bar{F}_a$
$\bar{T}_a$
$\delta\bar{x}_{DT}$
$\delta\bar{v}_{DT}$
$\delta\bar{q}$
$\delta\bar{\omega}$
sys_GPS
sys_RVSpos
sys_RVSatt
sys_ES
sys_FSS
sys_GYR
(6)
(3)
(2)

Figure 9.- plant_rvd3 high level decomposition.

The MIMOTOOL S/W has been implemented under the Xmath™ and SystemBuild™ development environment. It is basically composed by Xmath™ script files which are in charge of performing automatically the different computations required for the controller design and performance evaluation. In addition to them, a high fidelity 6DoF Relative Motion simulation model implemented in SystemBuild™ is invoked by the corresponding Xmath™ script files for the detailed performance assessment of the designed controller.

Four high level functional modules can be identified in the MIMOTOOL S/W (see Figure 10). The **INITIALIZATION module** which is in charge of setting the Xmath data which define the GNC mode to be run. The **BUILD module** which computes the MIMO plant linear models for controller design and linear performance analyses purposes. The **DESIGN module** (detailed in Section 5.2). And, finally, the **SIMULATION module** (detailed in Section 5.3).

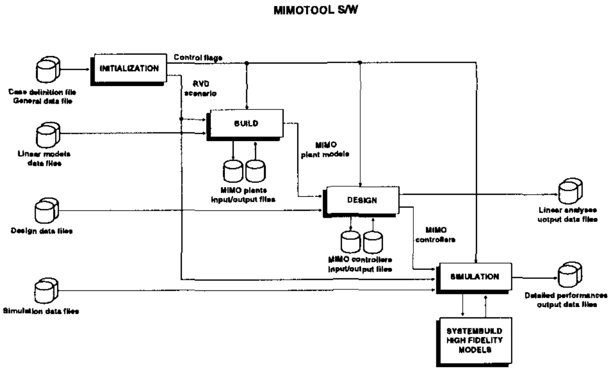
MIMOTOOL S/W
INITIALIZATION
Control flags
RVD scenario
Case definition file
General data file
BUILD
Linear models data files
MIMO plant models
MIMO plants input/output files
DESIGN
Design data files
Linear analyses uotput data files
MIMO controllers
MIMO controllers input/output files
SIMULATION
Simulation data files
Detailed performances output data files
SYSTEMBUILD HIGH FIDELITY MODELS

Figure 10.- MIMOTOOL S/W functional modules.

5.2. Design Facility

The Design Facility of the MIMOTOOL S/W is in charge of designing the MIMO controller and of carrying-out its performance evaluation by means of linear analyses tools. Four MIMO Control Design Techniques are considered: H_∞-Synthesis, μ-Synthesis, LQG/LTR and Pole-Placement. Figure 11 shows the modular decomposition of the Design module corresponding to the H_∞-Synthesis.

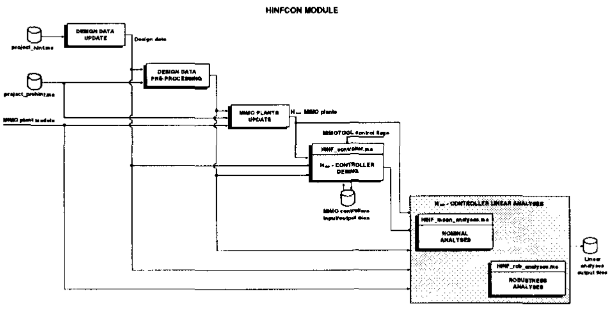
HINFCON MODULE
DESIGN DATA UPDATE
Design data
DESIGN DATA PRE-PROCESSING
MIMO PLANTS UPDATE
MIMO plant models
MIMOTOOL control flags
HINF_controller.ms
H∞ - CONTROLLER DESIGN
MIMO controllers input/output files
H∞ - CONTROLLER LINEAR ANALYSES
NOMINAL ANALYSES
ROBUSTNESS ANALYSES
Linear analyses output files

Figure 11.- H_∞-Synthesis modular decomposition.

5.3. Simulation Facility

The Simulation Facility is in charge of carrying-out the detailed performance evaluation of the designed controller. For that purpose, a high fidelity model of the RVD scenario has been implemented in SystemBuild™, providing a great confidence about the degree of realism of the simulation results. This high fidelity model includes (see Figure 12) the dedicated modules (SystemBuild SuperBlocks) in charge of simulating in detail the relative chaser-target orbit and attitude dynamics and kinematics, external and internal (fuel sloshing and solar array flexibilities) disturbances, chaser actuators, chaser sensors (GPS Receiver, RV sensor, Earth sensor, Sun sensor and gyros), chaser Intelligent Thruster Control Unit (ITCU). A dedicated module is in charge of computing the feedforward and the feedback (MIMO controller) control actions.

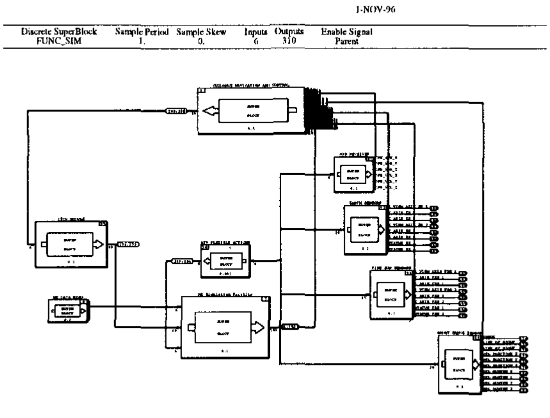
1-NOV-96
Discrete SuperBlock
FUNC_SIM
Sample Period
1.
Sample Skew
0.
Inputs
6
Outputs
310
Enable Signal
Parent

Figure 12.- Simulation SystemBuild™ model.

6. MIMO CONTROLLER DESIGN AND PERFORMANCE EVALUATION

6.1. General

For the MIMO controller design of the reference case under consideration, two aspects need to be considered: first, the relatively high undesired forces and torques, mainly due to the high MIB (5 Ns), and, second, the presence of the solar array flexibilities (intentionally added to the ATV spacecraft nominal configuration). Both facts impose lower and upper limits to the resulting control bandwidth, respectively. The lower limit comes from the need of reducing the orbit and attitude excursions due to the undesired forces and torques and, hence, a fast response controller would be desirable. On the other hand, the upper limit comes from the presence of the solar array flexibilities which would make conveniently (if they are considered as external disturbances) the limitation of the manoeuvrability at those frequencies.

On the other hand, aspects such as the sensor measurement errors (composed mainly by bias and random terms) and the target attitude deviations (for those GNC modes where the control is performed with respect to the E_{DT}-frame) must be considered during the controller design.

For the H_∞-Synthesis, the design parameters were the feedback control actions (size and frequency behaviour) and the frequency behaviour of the state performances. From the preliminary designs, the inconvenience of including the flexibilities in the MIMO plant model for the H_∞-controller design due to the excessively high sensitivity of the resulting controller with respect to uncertainties in the values of such characteristic frequencies was recognized (low robustness). Then, those effects were handled as external disturbances.

For the μ-Synthesis, in addition to the H_∞-Synthesis design parameters, the format of the D-scaling matrices was considered as design parameter. The flexible modes are included within the MIMO plant model. The use of constant D-scaling matrices (null fitting order) was found as optimum because it provides good robustness properties without increasing the state dimension of the controller (w.r.t. the H_∞-one).

For the LQG/LTR, the design parameters were the level of the feedback control actions and the recovery factor. Higher recovery factors lead to better robustness features but, however, the resulting control bandwidth is enlarged (possible impact in the closed-loop performances due to the presence of flexible appendages).

For the Pole-placement, the design parameters were the desired closed-loop poles, the level of the feedback control actions, the closed-loop poles weighting coefficients in the cost function and the format of the weighting matrices for the LQR design.

6.2. IAPP01 GNC mode

For this GNC mode, different performance requirements are applicable at GNC mode entry and exit (300 m and 40 m of relative distance chaser-target). On the other hand, the RVS measurements error budget is also varying with the relative distance. After analysing both facts, it was concluded that the most stringent control scenario correspond to the GNC mode entry. Four MIMO controllers have been designed, one for every MIMO design technique.

Concerning the nominal performances, the μ-controller has lower control actions (see Figure 13) in the frequency interval corresponding to the flexible modes considered (0.083 and 0.24 Hz) whereas the performances are slightly poorer in terms of speed of response and disturbance rejection capabilities than the other MIMO controllers (see Figures 14 and 15). The closed-loop responses of the nominal system to a constant load disturbance (Figure 14) present non-zero steady states for all the MIMO controllers because no explicit integral terms have been included in their design. However, concerning the stability and performance robustness, the μ-controller has shown that its performances are much less sensitive to variations in the uncertain parameters in comparison with the other MIMO controllers. By comparing the other three controllers, it can be noted that H_∞- and LQG/LTR-controller show similar behaviour in terms of performances and robustness whereas the Pole-controller present much degraded performances.

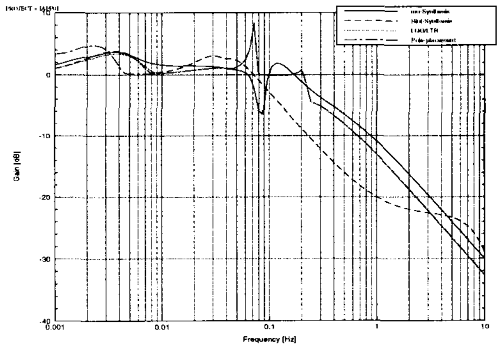

Figure 13.- Maximum singular values of control actions/disturbances transfer function.

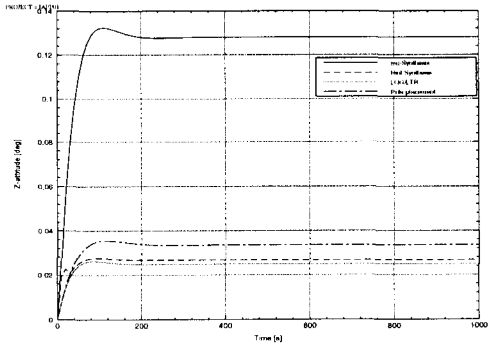

Figure 14.- Closed-loop response of a constant load disturbance of 5 Nm. Nominal system.

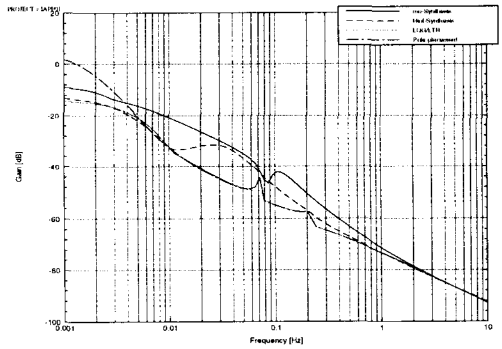

Figure 15.- Maximum singular values of performances/disturbances transfer function.

6.3. RSK02 GNC mode

In this GNC mode the coupling between orbit and attitude motions is higher than the existing in the

IAPP01 GNC mode because the chaser is controlled with respect to the E_{DT}-frame.

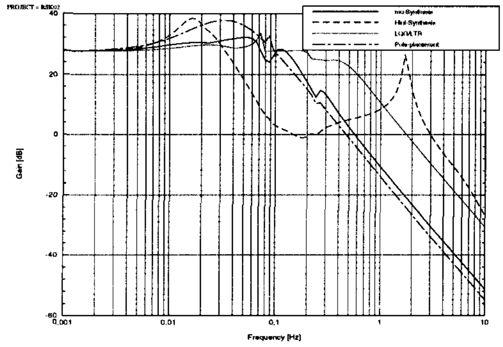

Figure 16.- Maximum singular values of control actions/measurement noises transfer function.

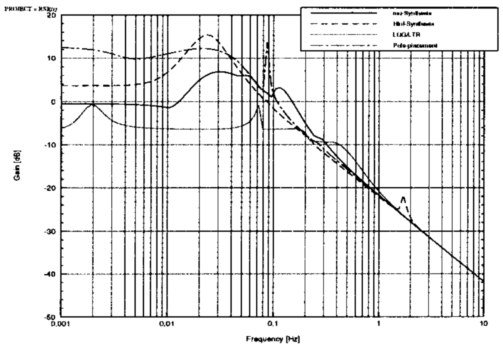

Figure 17.- Maximum singular values of performances/measurement noises transfer function.

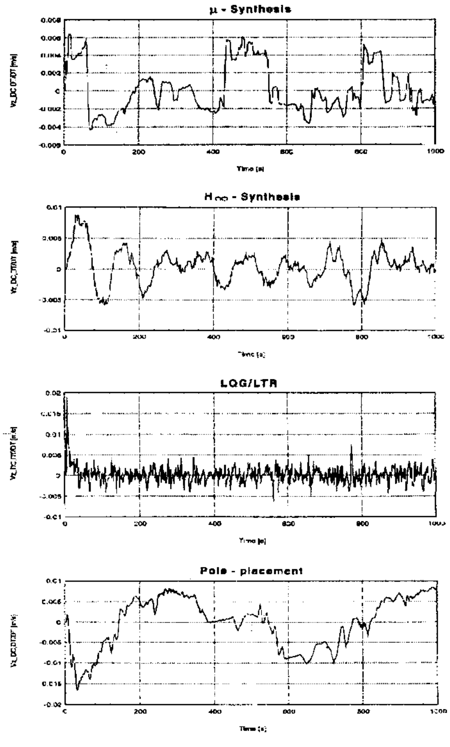

Figure 18.- Velocity performances. Non-linear model.

The considerations mentioned for the GNC mode IAPP01 are also applicable in terms of the speed of response and noise rejection capabilities associated to the μ-controller if compared with the LQG/LTR-, Pole- and H_∞-ones (see Figures 16 and 17 where the maximum singular values of the transfer functions with respect to the measurement noises are plot). Figure 18 show the velocity control performances (from the detailed performance evaluation) along one transverse axis for those controllers. Two important aspect must be remarked: first, the different signature of those performances which denotes the better noise rejection capabilities of the μ-controller and, second, the poorer performances of the Pole-controller which indicates the difficulty of achieving the desired performances.

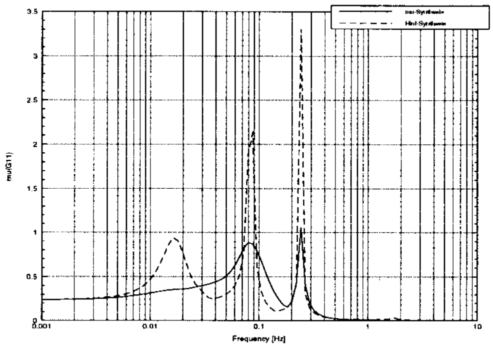

Figure 19.- Stability robustness. Reference uncertainties boundaries.

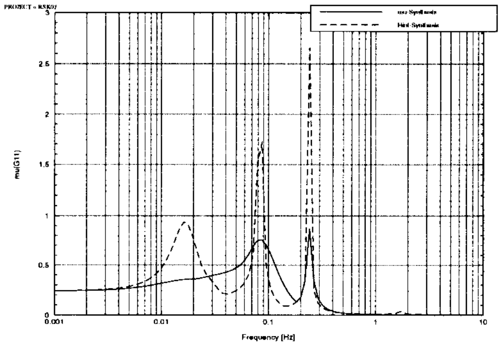

Figure 20.- Stability robustness. Reduced flexible mode uncertainty (4%)

Concerning the robustness properties, the μ-controller present better stability and performance robustness than the H_∞-controller, in terms of the range of the uncertain parameter values for which the closed-loop system is stable and fulfils the imposed performance requirements. Figure 19 shows the stability robustness results obtained from the μ-analysis. The peaks correspond to the flexible mode frequencies (0.083 and 0.24 Hz). From that Figure, the H_∞-controller allows the closed-loop system stability for a quite limited range of values of the uncertain parameters (about one third of the considered uncertainty boundaries) whereas, for the μ-controller, the closed-loop stability robustness is assessed for practically all the boundaries considered (note that the maximum value of $\mu(G_{11})$ is equal to 1.05). If the range of variations is reduced (e.g., considering variations of the flexible mode frequencies of 4%), the μ-analysis shows the fulfillment of the closed-loop stability robustness for the μ-controller (see Figure 20).

7. SYNTHESIS AND RECOMMENDATIONS

Four controllers have been designed for two representative GNC modes of a RVD scenario by using the most promising MIMO Control Design Techniques: H_∞-Synthesis, μ-Synthesis, LQG/LTR and Pole-placement.

The μ-controllers have shown better robustness properties and an adequate handling of the perturbing effects due to the solar array flexibilities and, hence, its use would be strongly recommended when flexibilities might have a strong impact in the control performances. Furthermore, the H_∞-Synthesis and LQG/LTR have shown good disturbance rejection capabilities (mainly the undesired forces and torques). The presence of solar array flexibilities might impose the degradation of the system performances because of the sensitiveness of the resulting controller to such disturbances. And, finally, the achievement of the desired performances (nominal and robustness) by using the Pole-placement MIMO Control Design Technique is rather difficult due to the high number of design parameters: desired closed-loop poles and weighting coefficients. This increases significantly the design tasks.

These conclusions can be extended to a generic Attitude and Orbit Control System (AOCS) design where the presence of flexibilities might have a relevant impact on the control performances.

ACKNOWLEDGEMENTS

The work described in this paper has been performed by GMV under ESA Contract No.9982/92/NL/JG (WO12) on MIMO Control for 6DoF Relative Motion.

REFERENCES

[1] Serrano Martínez, J.B. and Mora Castro E.J.: *MIMO Control for 6 Degree of Freedom Relative Motion. Final Report.* RVD-MIMOCO-GMV-FR. GMVSA 2191/96. Issue 1. November 1996.

[2] Doyle, J.C.; Glover, K.; Khargonekar, P.P. and Francis, B.A.: *State-Space Solutions to Standard H_2 and H_∞ Control Problems.* IEEE Transactions on Automatic Control, Vol. 34, No. 8, August 1989, pp. 831-847.

[3] Doyle, J.C. and Stein, G.: *Multivariable Feedback Design: Concepts for a Classical/Modern Synthesis.* IEEE Transactions on Automatic Control, Vol. AC-26, No. 1, February 1981, pp. 4-16.

[4] Balas, G.J.; Packard, A.K. and Harduvel, J.T.: *Application of μ-Synthesis Techniques to Momentum Management and Attitude Control of the Space Station.* AIAA Paper 91-2662.

[5] Stein, G. and Athans, M.: *The LQG/LTR Procedure for Multivariable Feedback Control Design.* IEEE Transactions on Automatic Control, Vol. AC-32, No. 2, February 1987, pp. 105-114.

[6] Liebst, B.S. and Robinson, J.D.: *A Linear Quadratic Regulator Weight Selection Algorithm for Robust Pole Assignment.* AIAA paper 91-2604, 1991.

[7] Chen, W.Z. and Levan, N.: *Design of Robust Linear Quadratic Controller with dynamic compensators.* AIAA paper 91-2603. 1991

H_∞ TECHNIQUES : FROM RESEARCH TO INDUSTRIAL APPLICATIONS

B. Frapard, C. Champetier

Matra Marconi Space, 31 Avenue des Cosmonautes,
31402 Toulouse Cedex 4, France
fax : (33.)5.62.19.78.97
benoit.frapard@tls.mms.fr, calixte.champetier@tls.mms.fr

ABSTRACT

As industry displayed an increased maturity in the 80's, spacecraft manufacturers were faced with new challenges. New projects were increasingly demanding in terms of performances as the systems got more complex at the same time. Traditional automatic control practices for space systems were then revisited : they needed to adapt to the design of systematic, robust and high performance control systems on-board modern space vehicles.

Initiated in the early 90's under the sponsorship of the Centre National d'Etudes Spatiales (CNES), Matra Marconi Space's investigations concentrated on the new emerging techniques of robust control design. Space engineering heritage led to an approach formulated in the frequency domain, the now well known « H_∞ » techniques. Continuous research activities were then conducted, most of them motivated by new projects under development at Matra Marconi Space : drag-free control for Aristoteles, motor harmonics active suppression for SPOT Mark II platforms, LOS jitter control for pointing applications, in particular the GOMOS and SILEX instruments, attitude control during manoeuvres for the new generation of telecommunication platforms, the Eurostar 2000+ and 3000 bus.

The diversity of the control problems addressed, together with a firm industrial orientation steered toward early achievements, and an original and generic set of tools. This work resulted in successful applications, that are in their terminal phase of industrial development, functional and integrated tests for the GOMOS instrument and SILEX terminals, prototype and development tools for SPOT5, ENVISAT, and the telecommunication platforms. Unique results were also obtained in the field of active vibration control for space structures.

1. MOTIVATION

MATRA MARCONI SPACE was first confronted to the limits of traditional approaches for its Eurostar 2000 generation of telecommunication. These platforms are made of a central body, two large antennas, together with two long flexible solar arrays on opposite sides, rotating with respect to the Earth pointing central body at a rate of one rotation per day.

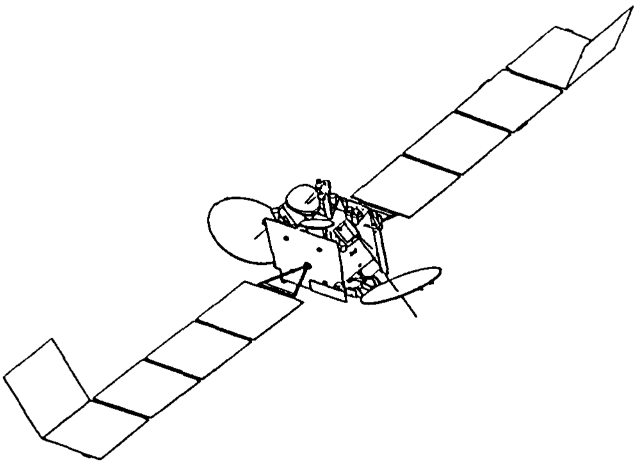

Figure 1 - The Eurostar 2000 Platform for Satcoms

In normal operation (or normal « mode ») the spacecraft evolves in a weakly disturbed environment that requires low control authority for the geocentric attitude preservation, the arrays being rigid in the control bandwidth. This normal mode is operated through solar sailing. Alternatively, during the periodic orbit maintenance manoeuvres, the spacecraft is transitorily submitted to thrusters induced disturbance torques that require some 1 to 10 Nm control authority to limit depointing below some 0.1 degrees. The large solar arrays can no more be assumed to be rigid in the frequency band where the control system has to be active. The low damping, shifting frequency modes with high resonant peaks of the large rotating solar panels led to design a stiff filtering solution, where the control filter was designed to present an attenuation of -60dB in the frequency range of the solar array flexibilities. Under this constraint, the design of the control filter tried to optimise the control gain to limit attitude transients at the start of the manoeuvre operation.

Proceedings Third International Conference on Spacecraft Guidance, Navigation and Control Systems, ESTEC, Noordwijk, The Netherlands, 26-29 November 1996, ESA SP-381 (February 1997)

- ◊ adapted to rapid optimisation of performances, under constraints of robustness on parameters variations
- ◊ capable to address « flexible structure control », formulation in the frequency domain

All these requirements converged towards the consideration of the emerging field of robust control design, or the so-called H∞ Techniques.

3. DEVELOPMENT OF THE MATRA MARCONI SPACE H_∞ PLATFORM

Background & MATRA MARCONI SPACE Research Orientations

Research activities on the robustness issue for control systems gained momentum in the 80's. It culminated with the algebraic setting that embedded H_2/LQG and H_∞ in a common optimisation frame and the associated state-space solution (Ref.[1]). Time domain and frequency domain approaches, traditionally separated, were brought together. The fundamental engineering tool of stability margins was formalised, enlarged to fit with general multivariable systems, addressing parametric, structured or non-structured, constant or time-varying uncertainties.

Early achievements in H_∞ application demonstrated the need for some methodological guidelines, to give sense to the somewhat mathematical abstract existence conditions. The standard problem (Ref.[1]), while enlarging the possibilities to formalise a control problem closer to the physical needs, tended to be a more complex approach than the comparatively simplistic LQG procedure, because of the intricate multi-objective, complete performance versus cost versus constraints optimisation problem provided by the standard problem and the associated H_∞ solver.

Simplified versions of the standard problem were then proposed to help access to this new formalism : the well-known MSC or Mixed Sensitivity Configuration (Ref.[2]) is an example of this tendency. It offered a frequency domain approach of multi-variable control design, close to traditional engineering approaches. Its direct application on space platforms proved however to be unfeasible, being unable to handle the rigid body dynamics, thus not satisfying existence conditions.

The Standard Compensation Configuration (Ref.[3,4]) offered an alternative approach. Steering from LQG practices, it offered a variational approach, close to the differential game approach to optimal control, providing direct ways to ensure physically the existence conditions. However, the robustness criteria lost its « stability margin » direct interpretation, and the difficulty in associating physical requirements to mathematical criteria made it practically unapplicable. In particular, loop shaping specifications of performances in the frequency domain were difficult to address.

The co-prime factor approach (Ref.[6]) is certainly a more elaborated and complete setting for simplifying the formulation of performance needs and mastering robustness, with a generic methodology suited to most existing systems. However, the independent control of individual criterion is lost, and the procedure of optimisation is global, with no performance index, clearly separated from the design constraints, to optimise. In addition, the loop-shaping procedure involved an increased complexity in the augmented system that produced high order control filters.

The following table summarises the different characteristics that were retained for the development of the MATRA MARCONI SPACE H_∞ platform, and the adequation of these candidate formulations.

Criterion / Method	Robustness explicit formulation	Separation constraints vs perf.	Generic approach (rigid body)	Loop Shaping criteria
MSC	☒	☒	☐	☒
SCC	☐	☐	☒	☐
Coprime	☒	☐	☒	☒
GOAL	☒	☒	☒	☒

The general ambition was then to develop a methodology that would support the main advantages of the existing settings while eliminating their shortcomings. The research approach was strongly directed towards industrial applications, supported by the most demanding control systems under development at Matra Marconi Space.

Research at MATRA MARCONI SPACE

Initiated in the early 90's under the sponsorship of the Centre Nationale d'Etudes Spatiales (CNES) (Ref.[5]), Matra Marconi Space's investigations concentrated on deriving a practical methodological setting for the formulation of a control design problem in the standard form, suited for the use of H_∞ solvers provided in commercial packages, such as Matlab or MatrixX. This methodological setting is realised/supported by a set of specifically developed software tools, and constitutes the so-called « H_∞ platform » at Matra Marconi Space.

The requirements or ambitions for this platform are summed up hereafter

- ◊ formulate explicitly and with no conservatism the robustness constraints : in other words, preserve the gain and phase margin approach widely adopted by control engineers,
- ◊ support the classical formulation of performance objectives in the frequency domain, in other words « loop-shaping » types of specification,
- ◊ separate performance objectives (to optimise) from design constraints (to fulfil) : to be able to operate GainMP type of optimisation with the filtering constraint frozen and the control gain increasing to its optimum,
- ◊ separate explicitly the different kinds of performance objectives, time response, disturbance rejection, noise transmission, command authority control, for a true management of the multi-objective functional at the user level,
- ◊ be suited to space platforms, in particular deal with free motion dynamics, systems with delays, poorly known and low damping flexible modes.

The development of this platform was performed in a continuous process (Ref.[7,8]), still on-going, working on new control problems submitted by projects under development at Matra Marconi Space to adapt, complete and validate it for new practical needs. One original feature in most of these developments was the existence of a « classical » solution, either derived by hand, issued from numerical solvers (such as GainMP) or from other techniques (LQG). The H_∞ setting was then developed and evaluated for its adequation to the given control problem, its capacity to increase performances, and also the evolution in the design process it implied : genericity, time reduction for the generation of the control filter coefficients, insertion in the analysis-design & validation cycle for the elaboration of on-board control filters.

The « Astrolab » Package

The resulting H_∞ platform was progressively enlarged to support other functionality in the analysis, design & validation cycle of an industrial project (Ref.[9,10,12,13])

- ◊ order reduction and discretisation,
- ◊ implementation structure optimisation (numerical truncature and round-off errors)
- ◊ robustness analysis for uncertain, low damping flexible structures
- ◊ non linear simulation and parametric sensitivity analyses

The result is the « Astrolab » package. It consists in a whole set of integrated modular tools to support the control design process, taking advantage of the modern computer-efficient and user-interactive CACSD facilities as Matlab or MatrixX. Astrolab provides a generic set of tools to ease the access to state-of-the-art algorithms in the field of automatic control, a GUI interface for direct use of a specific tool with no previous knowledge required, a standard platform to accept future extensions.

Astrolab comprises some 35 commands for general purposes, 35 commands for graphics management and data post-processing, 35 commands and block diagrams for control design and analysis, 50 commands and block diagram for the H_∞ environment itself. Such an environment appears today as of direct necessity to monitor multi-parametric optimisation, and take full advantage of the capacity of H_∞ and other advanced techniques in the field of automatic control for design and analysis of multi-variable uncertain systems.

4. APPLICATION TO EUROSTAR

We give as an example the solution to the Eurostar design problem introduced in section 1.

The stiff filtering constraint is formalised through a shaping filter that tightly encompass all resonant peaks produced by varying the flexible parameters in their uncertainty interval, as well as making the solar arrays rotate. This filter is approximated by a 4th order stable filter to serve as a weighting function to a loop-shaping procedure. (See figure 3)

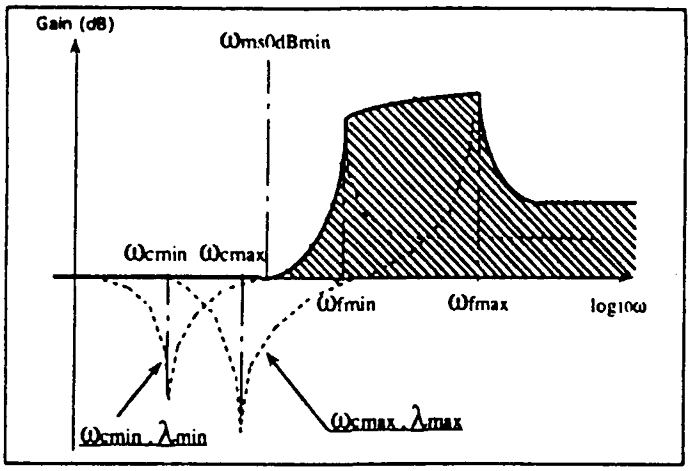

Figure 3 - Envelop of Peak Resonant Modes

This loop-shaping procedure is completed by the performance specification in terms of control gain in the frequency bandwidth, as well as the generalisation of the 6dB/30° stability margins for robustness.

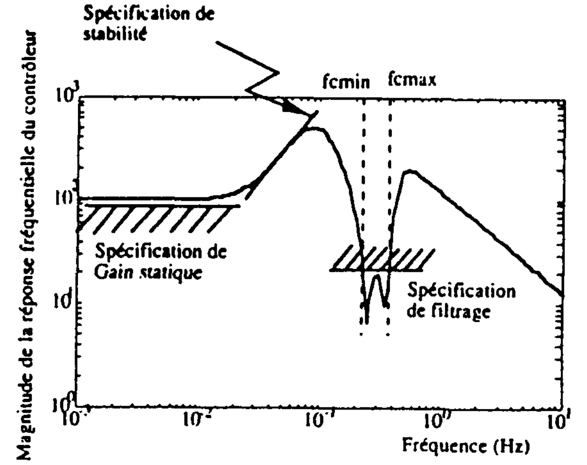

Figure 4 - Illustration of the Loop-Shaping specifications

The actual performance requirements are expressed in the time domain : the attitude transient overshoot, the settling time and the static error to a step entry in disturbance torque. These criteria are indirectly addressed through the weighting functions of the augmented system of the loop-shaping procedure. These functions are parameterised and a complete sensitivity analysis allows to make use of the remaining unused degrees of freedom to approximate the actual requirements. A numerical optimisation procedure takes the place of the traditional gamma-iteration to complete the sub-optimal H_∞ solver.

The result is illustrated in figure 5. On the left-hand axis is displayed the settling time, on the right-hand axis the attitude transient overshoot. The horizontal axis displays the static gain, the direct criterion for GainMP optimisation. The H_∞ solution is not provided as a unique solution but instead as a family of acceptable controllers, all respecting the design constraints, while optimising a complex performance index. The display of this family of solutions is striking, as it provides directly the degradation in settling time as the static error is reduced, or the asymptotic behaviour of the transient overshoot amplitude as the static gain is increased. In comparison, the GainMP solution (or « a » particular solution obtained through the parametric optimiser) appears as a single solution with no alternative, that presents a degraded settling time for a given attitude overshoot, for a fixed, non maximum static gain.

The controller obtained is a SISO 10th order filter. It is reduced by inspection to a 7th order filter equivalent to that obtained with the fixed structure parametrically optimised GainMP solution. Consequently, the H_∞ design was derived to fit with the on-board software requirements, and the evolution in design tools had no impact on the resulting AOCS architecture, software complexity and validation approach.

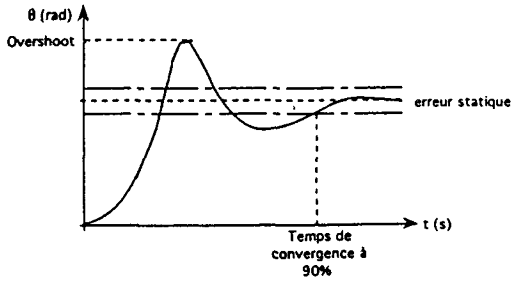

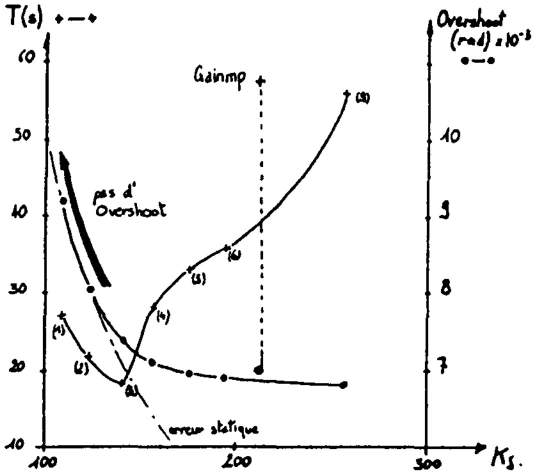

Figure 5 - H_∞ Family of controllers for the Eurostar application

As a consequence, H_∞ optimisation has been capable on this single control problem to increase performances in comparison to a numerically optimised controller. It displays a true capacity for managing high level trade-offs by providing a whole family of optimised controllers, thus displaying the physical conflicts underlying this particular control problem, giving back to the designer the physical insight he would have benefited from if the problem had been handled by hand.

To summarise the Eurostar application case, and illustrate some of the key features of the Matra Marconi Space H_∞ platform, this design approach features

- ◊ a SISO design, with loop-shaping specifications. Performances in the time domain are addressed through numerical optimisation based on the parametrisation of the LS specifications.
- ◊ The solution is made of a whole family of optimised, acceptable controller to serve the purpose of high level trade-offs.

- ◊ The performance of the H_∞ design is improved by 20 to 40% in comparison to the GainMP design, according to the performance criterion retained for comparison.
- ◊ The H_∞ design procedure is fast, a few seconds CPU time, and fully automated inside Astrolab
- ◊ The formulation of the optimisation problem is generic, and can be easily adapted to other problems ; in particular, the GOMOS and SILEX applications are directly derived from the original Eurostar formulation.
- ◊ This control solution is currently used as the nominal design tool for the whole family of Matra Marconi Space platform Eurostar 2000+.
- ◊ It is generally adapted for the attitude control of spacecraft during orbit manoeuvres : the most recent application is the control of the Delta-V manoeuvres for the ROSETTA interplanetary mission (Figure 6).

5. STATUS ON INDUSTRIAL APPLICATIONS AT MATRA MARCONI SPACE

The following table summarises the main programs developed or under development at Matra Marconi Space that have benefited from the Astrolab control design platform. Some of these applications were motivated by the absence of any other solution, due to some stringent requirements : it was the case for the Aristoteles project, now cancelled, but still exemplary in that prospect. Other applications benefited of Hinf design early in the design process, the modern design tool being hence developed first for its rapidity of adaptation to changes in configuration, in modelling assumptions, in system specifications. Eventually, a set of modern design tools are now completed for industrial use on family of well identified problems, ensuring the memorisation of engineering expertise, ease of use and drastic reductions in the development time.

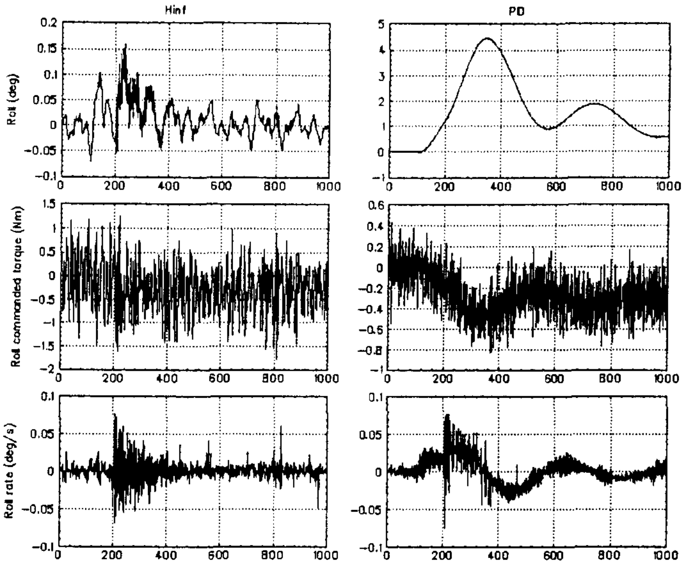

Figure 6 - AANT - ROSETTA Delta-V Manoeuvres

Application	Objective	Characteristics	Industrial Status	Hinf Design procedure qualification
Aristoteles	drag-free control	Loop shaping SISO system	Program cancelled	Demonstrated the feasibility of the concept
GOMOS	telescope pointing control	Dist. Rejection Delayed system Noise transmission	Final Integration and Validation tests	Nominal use from preliminary design up to final tuning
SILEX	line of sight jitter suppression	low sampling to bandwidth ratio high performances	Industrialisation phase completed	Nominal use for control law tuning Improved performances by a factor of 2
SPOT MkII	solar array drive mechanism active control	Decentralised control harmonic suppression bandpass control loops interactions	Standard P/F for LEO Earth observation	Standardised industrial tool for future Earth obs. P/F Gain of 20% wrt SPOT3-4
Eurostar	attitude control in manoeuvres	4th order stiff filt time step response monitoring	Standard P/F for GEO Telecom Satellites	Standardisation on-going Performances improved by 20 to 40% Nominal use on current systems under developt
	attitude control in normal mode	multivariable limited observability noise transmission		Reduced control design cycle by a factor of 2 to 10 Robustness enhancement Under qualification for industrial use
Vibration control	active control of smart structure for vibrations isolation	dense flexible modes signature spill-over vibration active control 10kHz real-time control	Laboratory tests	Integrated design procedure 20-30dB attenuation in the 50 to 200Hz capability demonstrated on real-time tests experiments

6. CONCLUSIONS

The diversity of the control problems addressed, together with a strong industrial orientation steered toward early achievements, and an original and generic set of tools. This work resulted in successful applications, that are in their terminal phase of industrial development, functional and integrated tests for the GOMOS instrument and SILEX terminals, prototype and development tools for SPOT5, ENVISAT and operational use for the telecommunication platforms. Unique results were also obtained in the field of active vibration control for space structures.

We intend to continue research in this field where many technical achievements of practical value are still to be expected. Automatic control in a modern perspective has been confirmed as a major axis for industrial research.

ACKNOWLEDGEMENTS

We gratefully acknowledge the support of the Dynamics and Automatic Control Department of CNES, led by M. Ph. Marchal for the development of some of the techniques and tools presented in this paper.

Some of the work on these new techniques was performed in the frame of on-going collaborations with research laboratories. We would like to thank in particular M. Zasadzinski from LARAL at Nancy, and J.F. Magni and M. Gauvrit from CERT in Toulouse.

REFERENCES

[1] J.C. Doyle, K. Glover, P. Khargonekar and B. Francis, "State Space Solution to Standard H_2 and H_∞ Control Problems", IEEE Trans. on Automat. Contr., AC-34, 8, pp. 832-847, Aug. 1989.

[2] M.G. Safonov and R.Y. Chiang , "CACSD Using the State-Space L_∞ Theory - A Design Example", IEEE Trans. on Automat. Contr., AC-33, No. 5, pp. 477-479, May 1988.

[3] S.D. O'Young, I. Postlethwaite, D.W. Gu, « A treatment of jw-axis Model Matching Transformation Zeros in the Optimal H2 and H_∞ Control Designs », IEEE Trans. On Automat. Cont., may 1989.

[4] I. Postlethwaite, J.L. Lin, D.W. Gu, « A classical Loop Shaping Approach to Robust Performance », ECC 1991

[5] C. Champetier, E. Desplats, P. Pelipenko, « Modern Control Techniques for Spacecraft AOC/GNC Systems », 1st Int. ESA Conf. on GNC Systems, 1991

[6] D. Mc Farlane and K. Glover, "Robust Controller Design Using Normalised Coprime Factor Plant Descriptions," in Lecture Notes in Control and Information Sciences, Springer Verlag, 1989.

[7] B. Frapard, S. Leballois, C. Champetier, "H_∞ Techniques for Spacecraft Control", sept. 1993, proc. 2nd Int. Conf., Cranfield.

[8] B. Frapard, P. Van Troostenberghe, "H_∞ Design for Satellite Attitude Control", Proc. 2nd Int. ESA Conf. on GNC, Apr. 94

[9] M. Zasadzinski, L. Caramelle, M. Darouach, B. Frapard, C. Champetier, « Frequency Weighted Closed Loop Balanced Controller Reduction using Normalised Coprime Factors Descriptions » ACC, Seattle, Aug. 1995

[10] B. Frapard, M. Zasadzinski, L. Caramelle, M. Darouach, C. Champetier, « H_∞ Controller Order Reduction Techniques based on Normalised Coprime Factors for Space Control Systems on-board Implementation », 3rd ECC, Rome, Sept. 1995

[11] B. Frapard, S. Fritz, « Contrôle d'un Satellite à Appendices Flexibles », Colloque Sup'Aéro Infautom, Toulouse, 1996

[12] B. Frapard, M. Zasadzinski, L. Caramelle, M. Darouach, C. Champetier, « Techniques de Réduction d'ordre H_∞ pour l'implantation à bord de véhicules spatiaux », Journées Automatique et Aéronautique et Spatial, Toulouse, Feb. 1996

[13] M. Gauvrit, J.F. Magni, B. Frapard, C. Champetier, « Méthodes d'Analyse de Pire-Cas Paramétriques : Application au Contrôle d'Attitude de Satellites Flexibles », Journées Automatique et Aéronautique et Spatial, Toulouse, Feb. 1996

[14] R.Y. Chiang, M.GM Safonov, « Robust Control Toolbox », The Mathworks, Inc., Natick, MA, 1992

CONTROLLER DESIGN FOR RVB WITH A HERA TYPE MANIPULATOR

H. Strauch†,Th. Görlach†,F. Ankersen‡

†Daimler-Benz Aerospace, Space Infrastructure, Bremen, Germany
‡ESTEC, Noordwijk,The Netherlands
e-mail: hans.strauch@erno.de, thomas.goerlach@erno.de, finn@wk.estec.esa.nl

ABSTRACT

The paper describes the application of the H_∞ design and μ-synthesis technique for the development of a robust controller for a HERA type manipulator used for berthing. Emphasis is put on showing that this recently established multivariable design technique can, in a straightforward way and in a comparatively short time, produce a controller, which can very well compete and improve with a classically designed regulator. This is illustrated by comparison with the control law used for the Shuttle manipulator.

Keywords: H_∞ design, μ-analysis technique, μ-synthesis, robot arm control , ERA, SRMS

1. Introduction

Manipulator arms like ERA or the Shuttle Remote Manipulator System (SRMS) are typically designed for moving masses which are small compared with the base of the arm, i.e. HERMES or the Shuttle. When using such arms for berthing with large payloads (which have masses and inertias of about the same order of magnitude as the base of the robot arm), the kinematic and dynamic couplings and the large changes of the matrix of inertia of the composite demands for a more complex control law.

Usually the structure of the controller for the arm is a simple independent joint control which sometimes is, in an ad hoc way, augmented by a compensation for the coupling (like SRMS). A further influence, which is often neglected, is the operation of the attitude control during the arm motion,i.e. arm control and attitude control are regarded as independent in the design.

The paper describes the design of multi-input/multi-output (MIMO) control laws which treats the composite, i.e. chaser, target and arm, as one plant. The equation of motion of this plant is not only coupled but also includes non-linear terms (via centrifugal forces). The aim was to design a control law which is sufficiently robust against the large parameter variations and can therefore work without a gain scheduling scheme.

The variation of the matrix of inertia during the operation of the arm was modeled with an appropriate weighting function for the H_∞ design. Other uncertainties and unmodelled non-linearities are characterized with a weighting function for additive errors. The performance specification is expressed in the weighting for the sensitivity S and the complementary sensitivity function T, where $S = (I + GK)^{-1}$, $T = (I + GK)^{-1}$ and GK is the open loop transfer function. The control law uses the RVD sensor and the Inertial Measurement Unit as inputs and it commands torques for controlling the joint angle and the composite attitude and motor currents for controlling the joint angles.

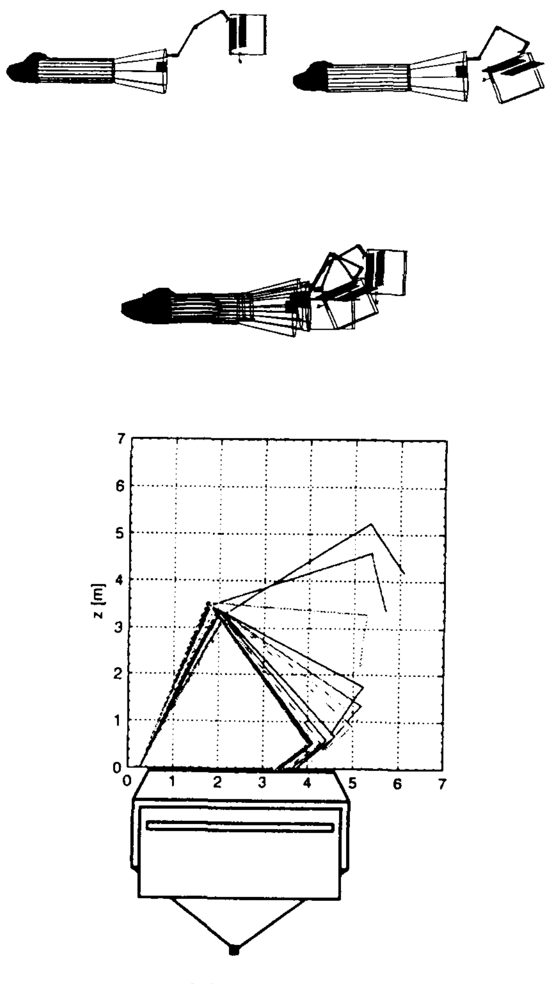

Figure 1: HERMES/EURECA berthing and the arm movement: Top: Initial and final position, Middle: Summation, Bottom: Movement to scale, $(0,0)$ at arm base

Proceedings Third International Conference on Spacecraft Guidance, Navigation and Control Systems, ESTEC, Noordwijk, The Netherlands, 26-29 November 1996, ESA SP-381 (February 1997)

It can be shown that the H_∞ design and μ-analysis technique can be used relatively straightforward for a problem as sketched above. Only a few iterations were necessary for designing a controller which meets the specifications (tested in the non-linear simulation environment). In some aspects the controller slightly outperformed the classically designed one, used for the Shuttle arm (adapted for HERA). This is an interesting result since the classical one is quite complex due to compensations made for the MIMO coupling effects. Because the H_∞ design inherently takes the MIMO structure of the plant into consideration, no ad hoc measures as in the classical case are necessary. The used design technique proved feasible at least at study level when a quick estimation of the achievable performance is of interest.

The paper also describes the modelling of the chaser, target and arm motion in the XMATH/Systembuild environment and presents one example of the simulation results for the berthing of HERMES/EURECA.

2. Problem Statement

The figure 1 shows as an example the berthing of HERMES and EURECA. Note that the third subfigure illustrates the change of the attitude of the composite during the berthing process (attitude control switched off).

Comparing the RVB problem with the usual way to design the controller of a manipulator arm the following can be stated:

- Usually the payloads which are handled by the robot arm are small compared to the mass and inertia of the spacecraft which carries the arm. Therefore it is justified to treat the attitude control and arm control loop as independent. In our case it is obvious that with a large payload the attitude and arm control interact. The question is how severe the coupling influences the stability of the overall loop and whether improvements can be gained with a combined control law which takes the coupling into account.
- A further classical simplification at the design of a manipulator control law is to assume that the moments of inertia as seen by the individual joints are constant and mainly determined by the motor drive mass. Technically this assumption is justified by the high gear ratio which reduces the apparent load seen at one joint. With the high payload masses this is no longer valid. Figure 2 illustrates this effect.

Therefore the goal is to design a controller which explicitly takes into account the coupled nature of the attitude as well as of the robot dynamic. A second aim was to derive a control law which was robust enough to cope with the time varying nature of the problem without recourse to a gain scheduling scheme. (A gain scheduling was undesirable due to higher complexity when it comes to the realization of the software.) The μ synthesis technique was selected as a promising design candidate for this task (see [Ref. 1]). The multi-variable character of the problem is a further rational behind the μ technique, since it is a design technique which is fully rooted in a MIMO framework thus automatically taking into account the coupling of the states.

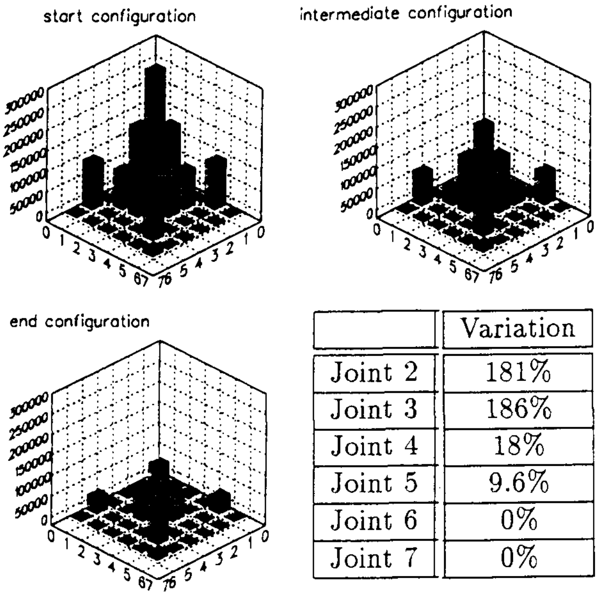

	Variation
Joint 2	181%
Joint 3	186%
Joint 4	18%
Joint 5	9.6%
Joint 6	0%
Joint 7	0%

Figure 2: Variation of the composite mass matrix $[kgm^2]$, and the moments of inertias [%]

The steps to derive the μ-controller are as follows:

1. A linear model of the plant has to be derived. Although the μ approach makes much fewer simplification than it is done at the classical approach, it is still a linear approach while the plant is truly non-linear. The common approach to fully work with the non-linearity of the plant is state-feedback linearization (see [Ref. 2]). Although this approach is often tried in academic research very few industrial implementations are reported.
2. Often a model reduction must be performed in order to achieve an acceptable controller dimension.
3. The plant uncertainties have to be modeled as internal feedback loops where the loop is closed by a bounded perturbation $|\Delta| \leq 1$ (see figure 3

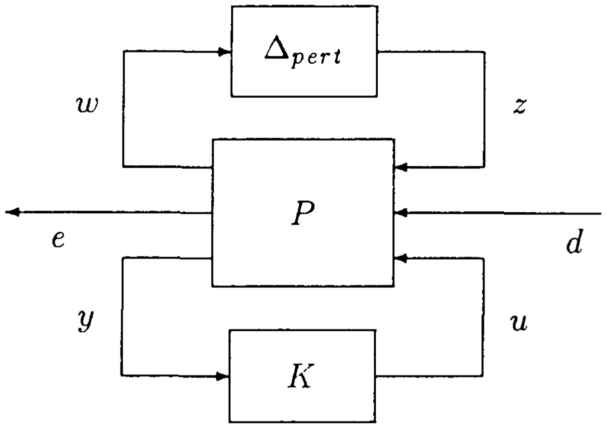

Figure 3: General Framework of the μ design

and 6). The task of the modellisation essentially means to find an inner Δ loop and the appropriate frequency weighting , which is sufficiently representative for the uncertainty.

4. The performance requirements must also be transformed into a frequency weighting at the appropriate point in the plant model. This is done by specifying appropriate weighting on the sensitivity function S and T.
5. Principally the controller synthesis is then straightforward. However, since the modellisation of uncertainties and performance contains some ad hoc decisions, generally the process is iterative. This is most often true if the performance requirements are very ambitious and thus contradict robustness requirements or constraints due to the inherent plant dynamic.

3. Plant Model

Principally there are two different approaches in modelling the complex dynamic of a manipulator arm: A numerical approach (see [Ref. 3]) where the differential equation of motion is set-up by a Newton-Euler algorithm or a symbolic approach (see [Ref. 4]) where the potential and kinematic energy is specified in appropriate generalized coordinates and the equation of motion directly follows from differention of the Lagrange equation. The latter approach has the advantage that, after a heavy computational burden at the first step, the subsequent simulation does not pose any numerical problems. The first solution technique demands for a clever implemention of the mathematics but allows easy incorporation of flexibilities specified in a finite element setting (e.g from NASTRAN).

Our model is based on a Newton-Euler formulation for the manipulator arm delivered as a FORTRAN code by the Canadian company SPAR, which was responsible for designing the Shuttle arm. As mentioned above the integration of the equation of motion demands for various special precautions in implementing the mathematics of integration. Therefore the standard routine as provided by Systembuild cannot be used. Above mentioned FORTRAN code, which included its own integration, was incorporated into Systembuild as a User Code Block. Since this block is regarded as a pure algebraic block, a linearization by the methods provided by Systembuild will not generate a linear model needed for the design. It was necessary to treat the FORTRAN code (plus the dynamics of the actuator and sensor added on Systembuild level) as a black box for system identification procedure.

Since system identification is not the topic of this paper we will only briefly present the results to such an extent as needed for the controller design. However, the effort of achieving a model for such a complicated system and its importance for the design should be stressed.

Figure 12 (see last page) presents the Systembuild blockdiagram of the plant. The block labeled SPARDYN7 contains the FORTRAN code which models the manipulator (including HERMES as a rigid body). The blocks MOTOR and GEARBOX contain models for the electrical and mechanical drive of the joints. Note the block JOINT-CONTROLLER which contains an inner control for the motor speed. The controller to be designed commands the motor speed for each joint and the torques for the composite (input number 8:10 at the SPARDYN7 block).

This block was subject to an identification procedure with commands for torque and motor velocity as input and the joint angle and HERMES attitude as output. Initial, intermediate and final manipulator position were used as a nominal operating point around which torques and motor velocities were stochastically applied to excite the plant. The estimated transfer function matrix has 9 inputs and outputs. The general structure of the transfer function matrix is illustrated by presenting the following submatrix: one output (y attitude) and seven input (6 manipulator velocity , y torque). Figure 4 shows the resulting 7 transfer functions.

The solid curve shows the main component: y-attitude versus y-torque. It has the expected form of an integrator (the notch must be attributed to the sampling). A truly decoupled problem would show

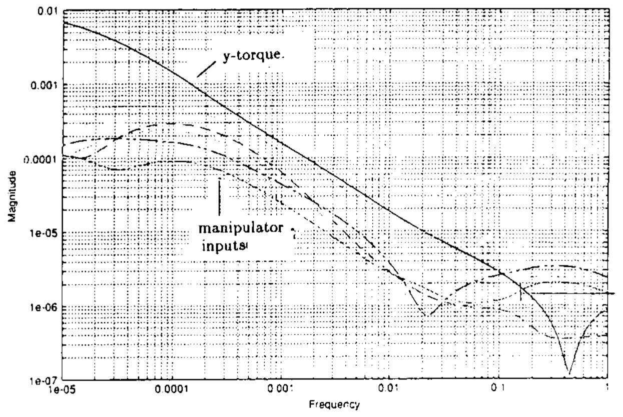

Figure 4: Bodeplot of a submatrix of the transfer function matrix, y-attitude/y-torque, joint commands

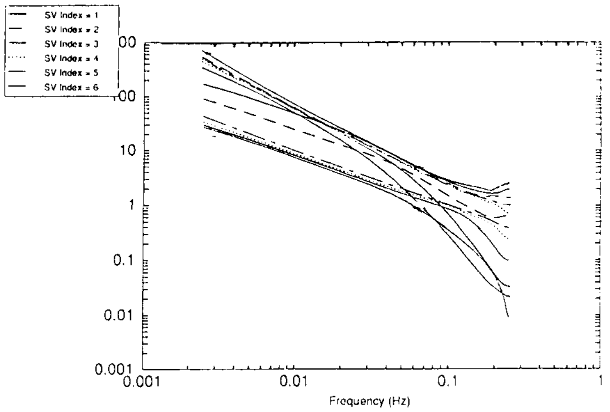

Figure 5: Singular value plot of the transfer function matrix at two operating points: top - initial point, bottom - final point

no influence of the manipulator commands to the attitude. In fact the resulting transfer functions are one order of magnitude below the main one. However, in a certain range of frequency one manipulator curve is only a factor of two away.

All other transfer functions of the full matrix have a similar structure: the integrator type behavior for the main diagonal element of the matrix and coupling from axes of at least a factor two smaller. This illustrates why the independed joint control approach is principally successful: even in our case with the very heavy payload the system only starts to become coupled.

Also of importance is the plot of the singular values for two operating points as shown in figure 5. This figure illustrates the time varying, i.e trajectory dependent, nature of the linear model. The upper group of the singular values is the identified plant for the intermediate point, while the lower group represents the final point of the trajectory. It will be of importance when it comes to modelling the uncertainty of a 'nominal' model used for the design. The difference in the transfer functions can be captured by an weight which models the uncertainty in the μ framework.

4. Controller Design

The μ controller design technique demands beside the nominal plant a couple of weighting functions which models the uncertainty and performance requirements. We will demonstrate this for the modeling of the uncertainty due to plant variations when the arm moves from the initial to the final point. Figure 5 shows the multiplicative weight corresponding to the singular value plot of figure 7.

The uncertainty at the low frequency is selected as 600 %. Note that we did not select the maximum difference between the upper singular value of the maximum curve of figure 5 and the lower singular value of the minimum curve. It seems reasonable to use a mean difference which is between the two maximum singular values of the two curves. From 0.02 Hz the error is assumed to be less than 10 % corresponding to the fact that the intermediate singular value of figure 5 is within the range of the upper/minimum range of the final configuration. This plant uncertainty can be modeled as a multiplicative delta block (see figure 6).

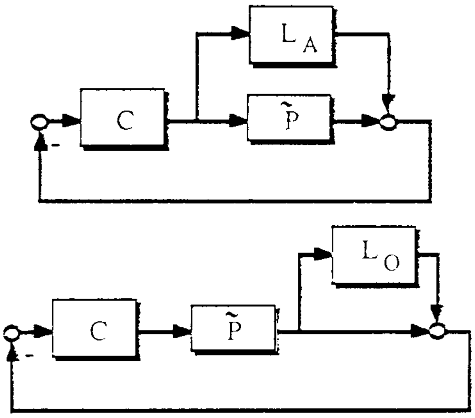

Figure 6: Multiplicative L_O and additive input weighting L_A (from [6])

For the additive perturbation we do not have such a strong justification. Since it should model the general uncertainty toward the higher frequency end, we select it in the same order of magnitude as proposed in the various papers (see [Ref. 5] or see [Ref. 6]).

The next step is to express the performance requirements in terms of the sensitivity and complementary

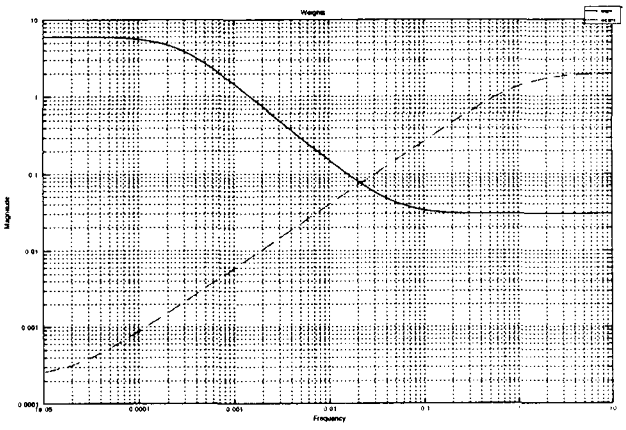

Figure 7: Multiplicative and additive Weighting Functions

sensitivity function. This shall not be described in detail (see [Ref. 6] for a general discussion) and in fact it demands for some trial and error checking the achieved closed loop behavior with the simulator.

After modelling the nominal plant and the perturbations in the above described way the μ synthesis is a straight forward mathematical procedure. Figure 8 shows the singular value plot of the final controller. The dominating upper curves which are closely together corresponds to the main elements of the transfer function matrix, i.e (joint 1 - speed command 1, etc). The lower curves are due to the interaction, i.e due to the multivariable character of the plant.

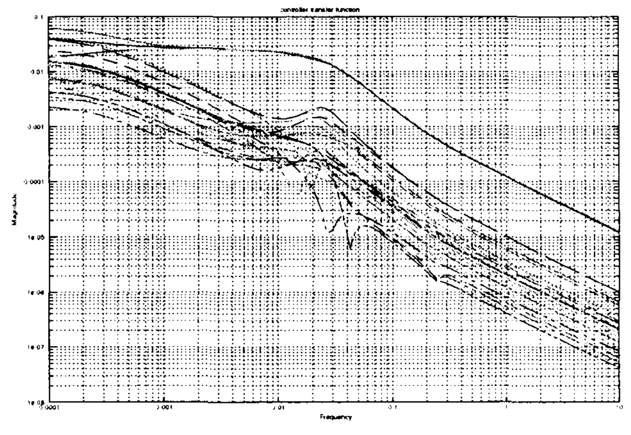

Figure 8: Singular Value Plot of the final Controller (first μ iteration)

It can clearly be seen why the independent joint control scheme principally works, since also the μ design generated a relative decoupled design. It is also interesting to display figure 9 which shows the first step, i.e the H_∞ design. This controller is much more coupled than the one from figure 8. This is illustrated by the fact that the upper group of singular values which belong to the main diagonal, i.e joint i - command i, is quite close to the off-diagonal elements around a frequency of $0.05[rad/sec]$.

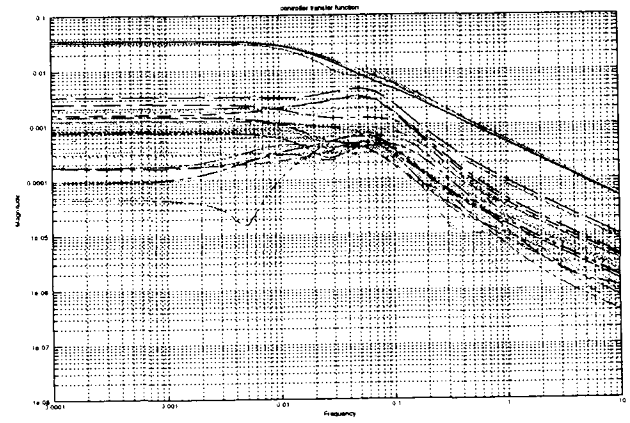

Figure 9: Singular Value Plot of the first Controller (H_∞ step)

The μ analysis showed that the test, i.e $\mu < 1$, was violated for this controller (see figure 10). The controller from figure 8 is the one generated in the first μ synthesis step achieving $\mu \sim 0.4$ (see figure 11).

This result confirms conventional wisdom that the independent joint control used in robotics is quite robust in practice. (Note that this remark only concerns the fact that the controller is decoupled. The μ synthesis also provides definite answers for the gain and time constants of the controllers, while in conventional control these figures are often based on engineering feeling).

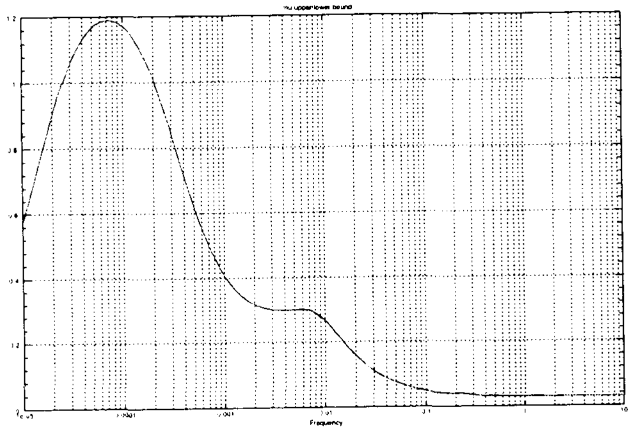

Figure 10: μ Analysis of the H_∞, i.e first step in μ design

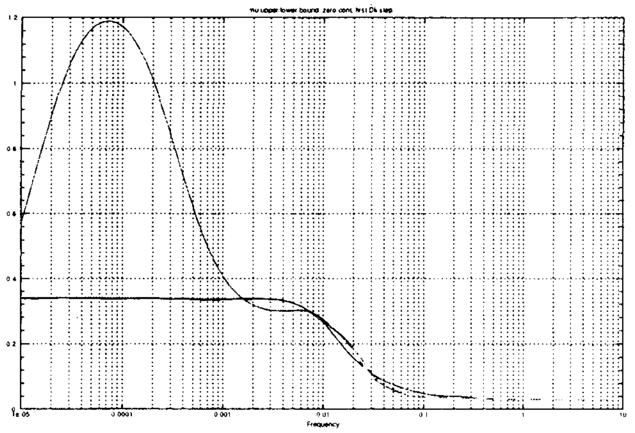

Figure 11: μ Analysis of the first μ synthesis controller

5. Performance Analysis

Finally a simulation run is shown in figure 14. Note that the full non-linear program (flexibility, saturation, friction, sensor noise, etc) is used. The classical control, i.e the controller used for the Shuttle arm (modified by SPAR accordingly) in combination with a conventional attitude HERMES control law is shown.

The achieved performance after sufficient settling time is comparable. Note however the much faster overall control time which can be achieved by the μ controller. This is due to the fact that the indepent joint control scheme used by the classical control law does not allow a high bandwidth. (Actually some measures against coupling are also introduced in the Shuttle law. However, they are minor ones more intended to avoid derivation from a ideal trajectory, which would irritate the astronauts when using the arm for manipulation of smaller objects).

The difference in attitude is due to the fact that the HERMES control law uses a wide deadband (2 deg) for avoiding excitation of the arm motion, while the μ controller is a purely linear controller. The deadband works more as a switch-on and off device.

6. Conclusion

It could be shown that the μ synthesis procedure can be used to design a controller for a fairly complex system. With a mathematically straightforward procedure it was possible to achieve a comparable performance (even better for the operation time and in accuracy for some components of the state vector) within the limited scope of an ESTEC study.

Still there remain questions when it comes to a realization of the controller within a fully operational setting: E.g the need of an anti integrator wind-up scheme forces one to extract poles with $s = 0$ from the state-space realization. Practical considerations often demand for a structure where the differential action acts only on the filtered measurement but not on the controller error (in order to avoid excitation due to set-point changes).

Regardless of this, it has been shown that the μ synthesis is at least useful to access the achievable performance with a limited level of effort and gives valuable theoretical hints why classical schemes are working.

REFERENCES

1. A. Packard and J. Doyle. The complex structured singular value. *"Automatica"*, 29(1), January 1993.
2. J-J. E. Slotine and W. LI. *Applied Nonlinear Control.* Prentice Hall International, 1991.
3. M. W. Spong and M. Vidyasagar. *Robot Dynamics and Control.* John Wiley & Sons, 1989.
4. S. M. Megahed. *Principles of Robot Modelling and Simulation.* John Wiley & Sons, 1993.
5. Huibert Kwakernaak. Robust control and H_∞-optimization - tutorial paper. *Automatica*, 29(2), March 1993.
6. M. C. Morari and E. Zafirou. *Robust Process Control.* Prentice Hall, 1989.

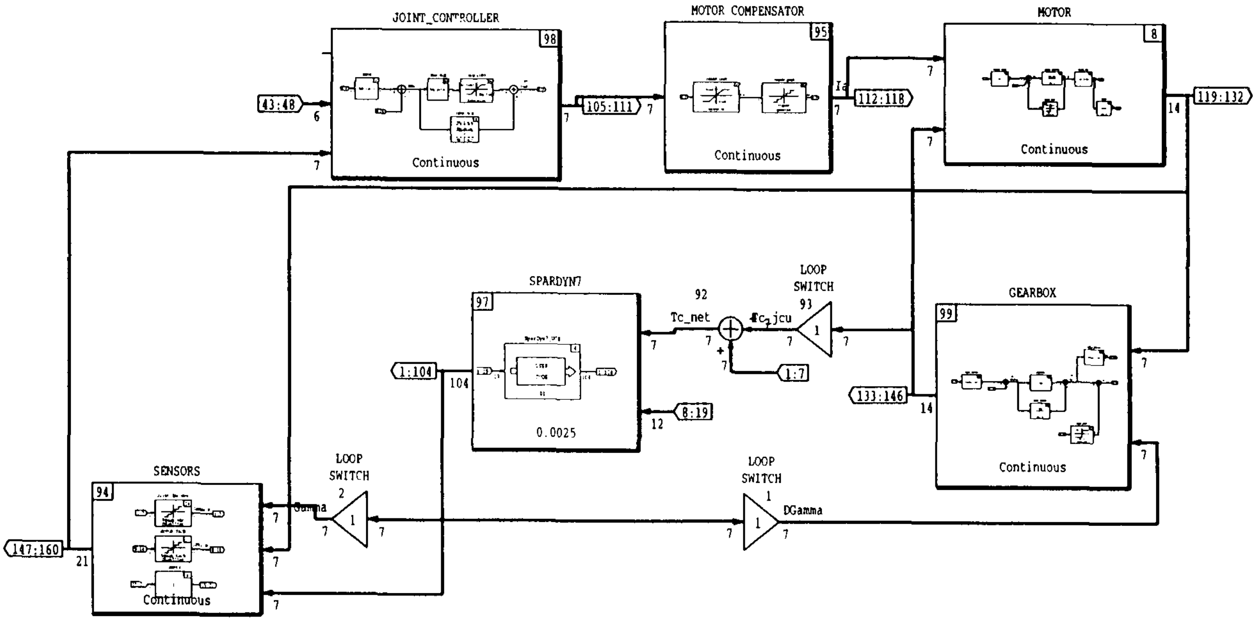
JOINT_CONTROLLER
98
Continuous
MOTOR COMPENSATOR
95
Continuous
MOTOR
8
Continuous
43:48
105:111
Ia
112:118
119:132
SPARDYN7
97
0.0025
92
Tc_net
Tc_jcu
LOOP
SWITCH
93
1:104
104
8:19
12
1:7
133:146
14
GEARBOX
99
Continuous
SENSORS
94
Continuous
147:160
21
LOOP
SWITCH
2
Gamma
LOOP
SWITCH
1
DGamma

Figure 12: Systembuild blockdiagram of the plant model

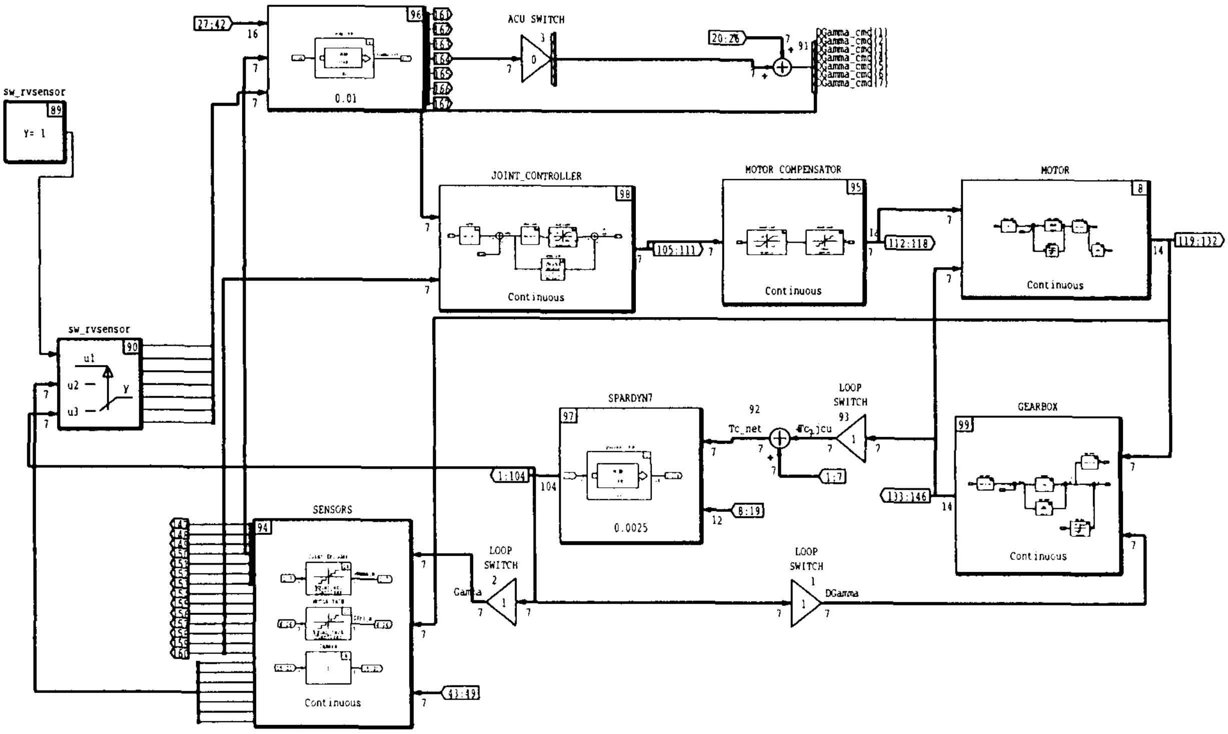
27:42
16
96
0.01
ACU SWITCH
3
0
20:26
91
DGamma_cmd(1)
DGamma_cmd(2)
DGamma_cmd(3)
DGamma_cmd(4)
DGamma_cmd(5)
DGamma_cmd(6)
DGamma_cmd(7)
sw_rvsensor
89
Y= 1
sw_rvsensor
90
u1
u2
u3
y
JOINT_CONTROLLER
98
Continuous
MOTOR COMPENSATOR
95
Continuous
MOTOR
8
Continuous
105:111
112:118
119:132
SPARDYN7
97
0.0025
92
Tc_net
Tc_jcu
LOOP
SWITCH
93
1:104
104
8:19
1:7
133:146
GEARBOX
99
Continuous
SENSORS
94
Continuous
43:49
LOOP
SWITCH
2
Gamma
LOOP
SWITCH
1
DGamma

Figure 13: Controller Structure

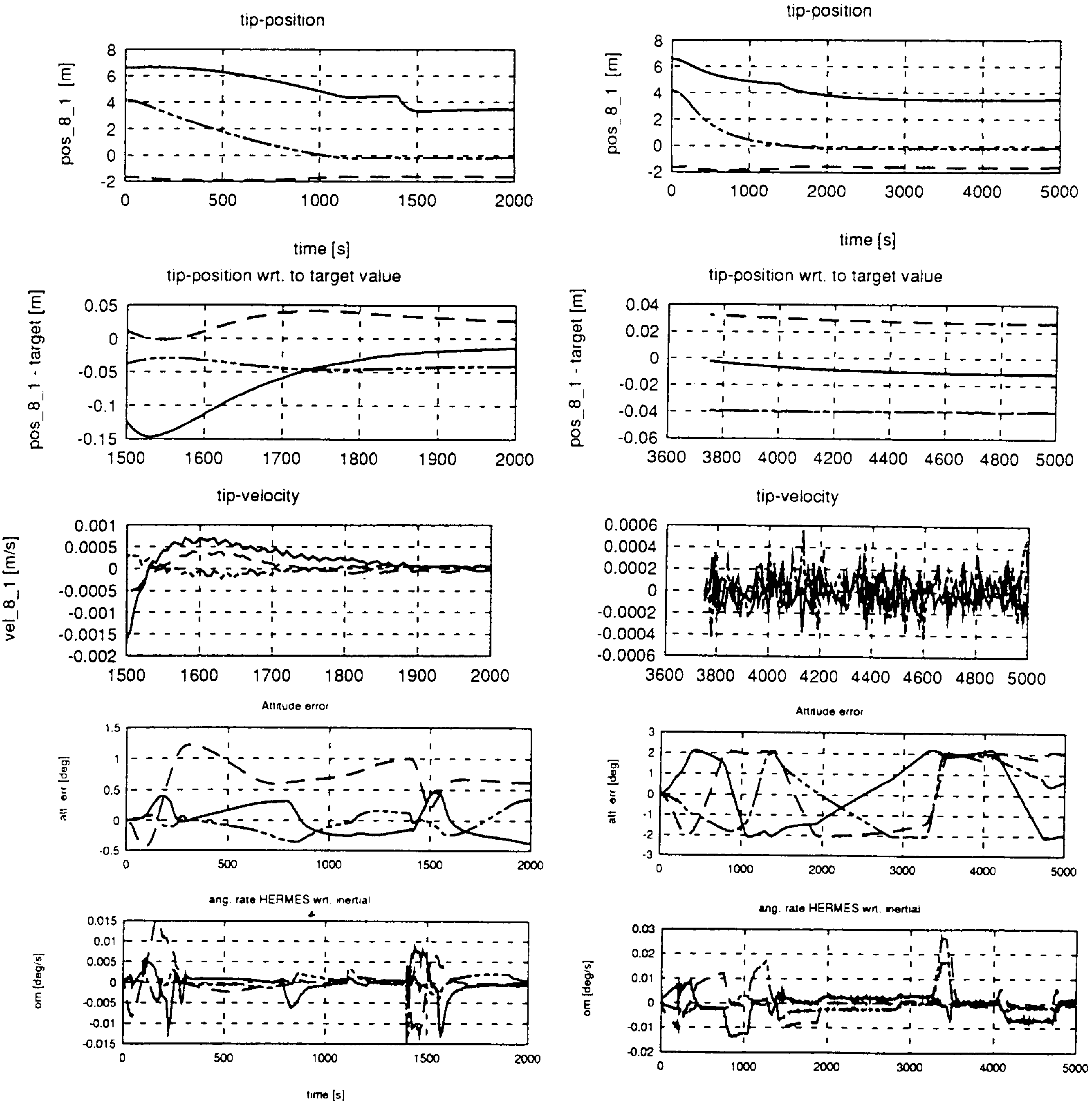

μ controller

Eureca deployed arrays

no plume, no sloshing, flexible

classical control

Figure 14: Simulation Result

Robust Attitude Control of a Telecommunication Satellite: a L.M.I. Approach

R. DRAI, M. BORDIER
Ecole des Mînes de Paris, C.M.A., B.P. 207
Valbonne, France
email = rdrai@cma.inria.fr

M. MAYER
Aérospatiale, Espace et Défense Cannes la Bocca, France

November 27, 96

Abstract

We present an application of the concept of extended dissipativity to the attitude control of a deformable satellite of the SpaceBus family düring an acceleration maneuver.
The mechanical model retained consists for the pitch axis of two pendulum sloshs and one flexible modes, for the filling ratio considered the dynamic interaction between propellant and the spacecraft rigid body motion is unstable and we show how a Linear Matrix Inequalities approach together with the notion of dissipativity can be used as a tool for analysis of such phenomenom and in fact suggests a solution in terms of an 'extended' Low and High Authority Design.

Keywords: attitude control, robustness, linear matrix inequalities

1 Introduction

Robust control of Large Space Structures has suscited a lot of research during the two preceding decades.
To this respect, it has been a privileged field of application of the progress of robust control including those concerning H_∞ techniques.
The main goal of this paper is to show how the framework of Linear Matrix Inequalities (L.M.I.) can be used in analysis and robust control of spatial structures with special emphasis on the attitude control of a deformable spacecraft during a station keeping maneuver.
The specifities of Large Space Structures are well-known :
Practical considerations implies the use of reduced order models in order to describe complex structures.In particular modal truncation can lead to observation or control spillover.
The unpreciseness of prelaunch 1 g measurements has as a consequence important parametric uncertainties and moreover Large Space Structure are intrinsically characterize by a very low natural damping For these reasons most 'modern control' techniques such as L.Q.G. or L.T.R. cannot be applied directly to these systems in order to obtain robust controllers.

Proceedings Third International Conference on Spacecraft Guidance, Navigation and Control Systems, ESTEC, Noordwijk, The Netherlands, 26-29 November 1996, ESA SP-381 (February 1997)

Despite its well-known advantages in terms of robustness H_∞ control shares the same defect with the preceding approachs since it is also basically a 'model-based' design which rely on the knowledge of the system parameters to tune the state estimator []. As an illustration since usual singular value analysis is oriented toward high frequency unstructured pertubations in phase and gain, a H_∞-based control design can be overduly conservative when directly applied to flexible structures: In fact it is well known that a if 'small-gain description' of uncertainties is judicious for neglected dynamics and sensor/actuator effects, it is inapropriate for parametric/modal uncertainties.

In particular the ignorance of the phase information present in most flexible structures is largely responsible of the conservatism of H_∞ when applied to such structures.

Positivity and LAC/HAC Design:

For flexible structures a powerful technique that takes account phase information and garantees stability in presence of significant modeling uncertainties is the positive real approach.

Inherited from networks theory and widely used in adaptative and non-linear control, the notion positivity is closely linked to dissipativity and energy concepts.

Roughly speaking Positive Real Systems can described as systems that do not generate energy

In the context of L.S.S. the exploitation of this physical property has lead naturally to the so-called Low Authority Control/High Authority Control design which is based on the classical scheme of a two level controller.

The LAC /HAC can be shortly described as follows:

> the first control which is usually a a collocated velocity feedback is closed on the structure in order to actively damp the most critical flexible modes.
>
> the expected effect is to attenuate model errors and to prepare subsequent control design of the lowest (possibly rigid) modes.

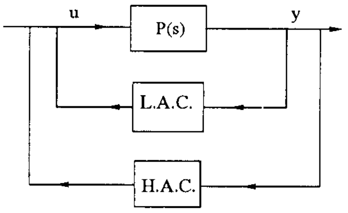

Figure 1: *Two level architecture of LAC/HAC design*

2 SpaceBus Station Keeping Maneuver

The equations of motion of the simplified model of fig.2 are (neglecting damping):

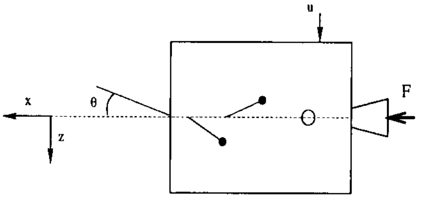

Figure 2: *Pitch-axis dynamics of SpaceBus during an Acceleration Maneuver*

$$M\ddot{\eta} + K\eta = bu$$

$$\text{with}:\ M = \begin{pmatrix} J & \delta & \delta_1 & \delta_2 \\ \delta & m & 0 & 0 \\ \delta_1 & 0 & m_1 & m_2 \\ \delta_2 & 0 & m_2 & m_3 \end{pmatrix}$$

$$K = \begin{pmatrix} 0 & 0 & \Omega_1^2 & \Omega_2^2 \\ 0 & \Omega^2 & 0 & 0 \\ 0 & 0 & \Omega_1^2 & 0 \\ 0 & 0 & 0 & \Omega_2^2 \end{pmatrix},\ b = (1 \quad 0 \quad 0 \quad 0)^t$$

$$\text{and}\ :\eta = (\theta \quad q_{flex} \quad q_{slosh1} \quad q_{slosh2})^t.$$

The main important point here is that:

$$K \neq K^t.$$

It can nevertheless be shown that the familiar notion of 'structural modes' can be here preserved: the examination of the eigenvalues of the matrix $M^{-1}K$ shows that the above equations described in fact a so-called 'pseudo-conservative' system.

The examination of the root locus for the transfer function

$$g(s) = \frac{\dot{\theta}(s)}{u(s)} = \frac{J^{-1}}{s} + \sum_{i=1}^{3} \frac{k_i s}{s^2 + 2\xi_i \omega_i s + \omega_i^2}$$

reveals that for the filling ratio considered the above system is no longer positive:

one can clearly see that the pole/zero alterning is lost and that the negativity of residue k_2 implies that a positive rate feedback can have a destabilizing effect.

It must be clear that from the control engineer point of view this feature has some important consequences, in particular the classical LAC/HAC design must be adapted.

The next section will provide a convenient framework to cope with the presence of such an 'in the loop mode', a feature generally encountered in non collocated system.

3 Dissipativity

Supply Rates and Storage Functions: We first review some well-known facts concerning second order mechanical systems.

Consider:

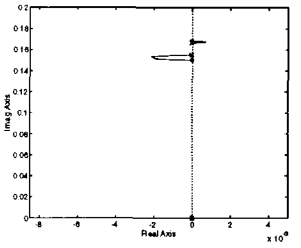

Figure 3: *Unstable interaction between rigid body and sloshing mode*

$$M\ddot{\eta} + (D + G)\dot{\eta} + K\eta = bu$$

with : $M = M^t > 0$, $D = D^t$,
$G = -G^t$, $K = K^t > 0$, $y = b^t\dot{\eta}$
where the matrices D and G describe respectively damping and gyroscopic effects.

Let E denote the total mechanical energy of the structure, it is readily seen that along all trajectories of such *hamiltonian*, linear mechanical second order systems we have:

$$\frac{dE}{dt} \leq u^t y$$

This simple fact explains why for colocated flexible systems a positive rate feedback

$$u = -Ly\ ,\ L = L^t > 0$$

is sufficient to insure stability
(c.f. the pioneering works of Gevarter, Martin, Canavin).

It also leads to the following generalization due to J.C. Willems [1]:

A system with input u and output y will be said dissipative w.r.t. the *supply rate*
$p(u\,,y) = (y^t\,u^t)\begin{pmatrix} Q & N \\ N^t & R \end{pmatrix}\begin{pmatrix} y \\ u \end{pmatrix}$
if there exists a *storage function*

$E : R^n \longrightarrow R_+$ s.t.:

$$\int_0^T p(u\,,y)\,dt \geq E(x(t)) - E(x_0)$$

$$\forall\, T \geq 0 \;,\; \forall u \in L^2_+$$

Examples of supply rates:

- . Positive real systems: $p(u\,,y) = y^t u$
- . H_∞-norm bound systems: $p(u\,,y) = \gamma^2 u^t u - y^t y$
- . Sector-bounded systems: $p(u\,,y) = -ab\,u^t u + (a+b)\,y^t u - y^t y$

LMI and Frequential Characterization of Dissipative systems :

A general dynamical system $(A\,,B\,,C\,,D)$ minimal is dissipative w.r.t. $p(u\,,y) = (y^t u^t)\begin{pmatrix} Q & N \\ N^t & R \end{pmatrix}\begin{pmatrix} y \\ u \end{pmatrix}$ i.f.f.:
$\exists\; P = P^t > 0$ such that:

$$\begin{pmatrix} \mathcal{A} & \mathcal{B} \\ \mathcal{B}^t & \mathcal{C} \end{pmatrix} \geq 0$$

with:
$\mathcal{A} = C^tQC - (PA + A^tP)$
$\mathcal{B} = C^t(QD + N) - PB$
$\mathcal{C} = R + N^t + D^tN + D^tQD$

This result which admits as special cases the well-known Positive and Bounded Real Lemmas has a frequential counterpart:
if $Q \leq 0$, it also equivalent to:

$$(G^*(j\omega)\;\; I)\begin{pmatrix} Q & N \\ N^t & R \end{pmatrix}\begin{pmatrix} G(j\omega) \\ I \end{pmatrix} \geq 0$$

Note that for SISO systems the preceding test has an obvious interpretation in terms of Nyquist plot for each of the three examples of supply rates given.

An Asymptotic Stability Result:

Let's mention finally the following result in which, paraphrasing J.C. Willems, much of the work on feedback stability has culminated.
If $G_1(s)$ is dissipative w.r.t. $p_1(u\,,y)$ and $G_2(s)$ *strictly* dissipative w.r.t. $p_2(u\,,y)$ and $p_1(\,,\,)\,,p_2(\,,\,)$ verifying:
$\alpha p_1(u,y) + \beta p_2(-y,u) \leq 0$ for some real constants α and β.
Then the following closed-loop sytem is asymptotically stable:

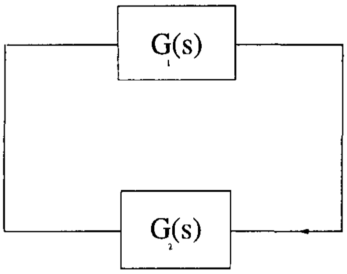

Figure 4: *A general stability result*

This theorem admits as special cases the small gain and passivity theorem.

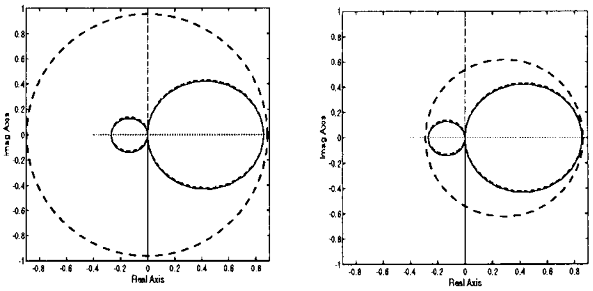

Figure 5: H_∞ *and sector characterization of the slosh dynamics*

4 Application to SpaceBus S.K.M.

We now turn to show how the preceding concepts can be used for the attitude control of SpaceBus during a Station Keeping Maneuver.

Considering fig.5 it appears first that a sector bounded characterization of the slosh dynamics is clearly 'tighter' than a H_∞ one.

This simple observation despite its crudeness is in fact a good illustration of the usual conservatism of H_∞ techniques when applied directly to most structural systems.

The examination of the Nyquist plot for SISO systems and/or the resolution of the associated LMI for the multivariable case will provide us a general method in order to deal with the unstable slosh interaction observed above.

More precisely the preceding considerations suggests an 'extended' LAC/HAC design for generic pseudo-conservative sytems that can be presented as an alternative to the already existing engineering practice resting mostly on phase and gain stabilization, cf [].

Indeed for this example, the fact that the Nyquist plot representing slosh dynamics is included in a circle of diameter [a,b] centered on the real axis is equivalent to:

$Herm\,(G^*(j\omega) - aI)(G(j\omega) - bI) \leq 0$

$\Leftrightarrow G(s) \in Sect\,[a\,,\,b]$.

And thus by virtue of the general stability result the choice of any: $K(s) \in Sect\,[-\frac{1}{b}, -\frac{1}{a}]$ will ensure stability.

Of course in presence of both sloshs and flexible modes the preceding reasonning can be adapted in a obvious manner.

One can recognize in the above approach a strong reminescence of the classical circle criterion except that here the context is purely linear and that generalization to MIMO systems is immediate.

5 Conclusions

We have shown how the notion of dissipativity can be used in order to quantitavely characterize a defect of positivity in a simple one-axis mechanical model of SpaceBus and how in fact the very same notion suggests a robust control design strategy.

We conclude by indicating some of the possibilities concerning the design of controllers verifying the appropriate sector conditions, in the case of static velocity feedback it resumes in an obvious limitation the gain, we also have encouraging results concerning synthesis of dynamic L.Q.G.-type controllers in which the weighting matrices are chosen in order that the resulting controller verifies the appropriate sector conditions.

References

[1] Willems, J.C. Dissipative Dynamic Systems,
in Archive for Rational Mechanics and Analysis, Part I-II, vol. 45, pp. 321-351, pp. 352-353 (1972)

[2] Joshi M.J./ Maghami P.G.
Robust Dissipative Compensators for Flexible Spacecraft Control,
IEEE Trans. Aerospace Electronic Systems, vol. 28, July 1992,

[3] Gupta, G. /Joshi, M.S.
State space Characterization and Robust Stabilization of Dissipative LTI Systems,
American Control Conference 1995

[4] Bals/Goh/Grubel
Tuning Analytical Synthesis Techniques via Multiobjective Optimization for a Two-feedback-loop Control of Flexible Space Structures
Second International Conference on GNC, Noordwijk, April 1994

SESSION 9:
GPS HARDWARE

Chairman: J.-L. Gerner (ESA/ESTEC)

LOCALISATION OF SPACECRAFT WITH MULTISTANDARD GPS/GLONASS/RA RECEIVER

Christian Mehlen*, Manuel Toledo Lopez, Christian Müeller*****

* **SEXTANT Avionique (Valence - France)**
** **GMV (Madrid - Spain)**
*** **CIR (Neuchatel - Switzerland)**

Abstract

While the use of on-board GPS receiver is today well-established for localisation and attitude determination of orbiting spacecraft, the interest of multistandard GPS/GLONASS/RA receiver is still to be discussed.

SEXTANT Avionique, GMV and CIR have completed the design, development and test of a multistandard receiver prototype for ESTEC. The receiver processes the L1 C/A signals from GPS, GLONASS and regional augmentation satellites, in order to improve availability, integrity and accuracy of localisation.

This paper presents an analysis related to the use of Multistandard receiver versus GPS-only receiver, for spacecraft localisation. It also discusses the architecture and performances of a multistandard receiver and presents some test results from real measurements on ground.

1. Introduction

Two satellite navigation systems are currently operational: the American GPS/NAVSTAR and the Russian GLONASS. ESA, in close cooperation with relevant international organisations, is developing the concept of a civil Geostationnary regional augmentation (RA), which will permit to achieve inter-operability between GPS and GLONASS and to improve the integrity and accuracy issues.

In this frame, SEXTANT Avionique with GMV and CIR has developed for ESTEC in 1995/1996 a multistandard receiver prototype able to process GPS, GLONASS and RA signals. ESTEC will use this receiver prototype for the conduction of field tests during the RA development.

Although the primary interest of multistandard receiver is for terrestrial and aircraft applications which require a high level of integrity and availability, we can consider its use for spacecraft localisation, in replacement of GPS-only receiver. For this purpose, it is necessary to review the advantages of navigation with a multistandard receiver, to discuss the specific problems related to the design of multistandard receiver and to evaluate the added complexity.

2. Interest of multistandard navigation

The first improvement is in the field of the navigation availability due to the very best redundancy of navigation satellites and the resulting improvement in the geometry of the constellation observed by the receiver (see Ref. 4). There is a great increase of the availability for horizontal and vertical navigation with the aiding of GLONASS to GPS, and a small additional increment due to additional GEO satellites. The Figures 1 and 2 are an example of the portion of time having available HDOP and VDOP values below the thresholds indicated in the horizontal axis. The increment in availability has as result the increment of the continuity in navigation performances and in failure detection and isolation capability.

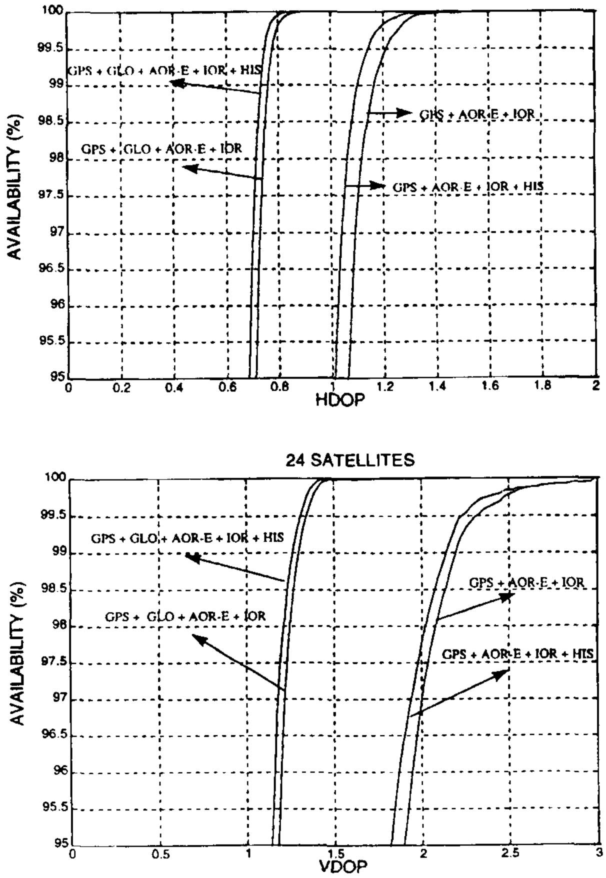

Figure 1 et 2

Proceedings Third International Conference on Spacecraft Guidance, Navigation and Control Systems, ESTEC, Noordwijk, The Netherlands, 26-29 November 1996, ESA SP-381 (February 1997)

Although the continuity is a very valuable characteristic in aircraft navigation, the requirements are weaker in satellite orbit determination using filtering methods considering satellite orbital model. Such filtering methods allow the navigation with few satellites in view, and include integrity mechanisms (see Ref. 1, 2 , 3 for GPS-only orbit determination).

Nevertheless, the better GDOP and the augmentation of the in-view NSs will significantly improve the accuracy of the localisation, especially for high-altitude orbits. The accuracy will be also improved when considering that the GLONASS satellites have no selective availability. The main error source are in the broadcasted ephemeris, satellite clock bias, and ionospheric error.

Low-Earth orbiting spacecraft will also take benefit from the RA broadcasted information from the GEO satellites (integrity data and ranging corrections relative to the GPS, GLONASS, RA NSs). The ranging correction provides separated slow clock and ephemeris correction, fast clock correction (GPS only), and ionospheric correction. The broadcasted ionospheric correction is dedicated to terrestrial and aircraft user, and cannot be used for orbital application. The fast clock correction has a short validity time, and has to be considered carefully for use on a spacecraft. The slew clock and ephemeris correction is useful because its validity period is long and allows its temporary use outside of the area of coverage of the GEO satellite. The slow correction provides a real advantage with GLONASS satellites, because it allows to correct all the GLONASS error sources, (excepted ionospheric contribution).

An other improvement is related to the interference mitigation. The GPS C/A signal is spread in a 1 MHz bandwidth around 1575.42 MHz, the GLONASS signals are distributed in a 15 MHz bandwidth around 1610 MHz. Therefore it is unlikely that an interference signal could disturb the two bandwidths. This is a significant advantage for aircraft and terrestrial applications. The interest is lower for orbital mission because the interference signals are generated by the spacecraft itself (on-board RF transmitter, harmonics of digital signal) and can be identified and corrected by adequate filtering and shielding technics before the mission.

The conclusion about the interest in using a multistandard receiver in Satellite Orbit Determination over using a GPS-only receiver is that the availability and integrity of the navigation solution are strongly improved while the accuracy can be improved to different levels, depending on how is computed the navigation solution (GLONASS-only, GLONASS + RA, GPS + RA, GPS + GLONASS + RA). Accuracy at the level of meters are expected to be obtained using GLONASS satellites with associated RA correction.

But in order to reach these performances the multistandard receiver has to cope with several sources of complexity over a GPS receiver. Beside the obvious fact that each of the systems have to be fully implemented in the receiver (GPS/GEO and GLONASS), there are also the problems derived from the necessity to combine these systems.

3. Combination of GPS and GLONASS Systems

The joined processing of GPS type measurements and GLONASS measurements requires to deal with a relationship between both systems. GPS and GLONASS are two independent self-contained and self-consistent systems. Each of them has its own coordinate and time system, with different features. The GPS system uses the WGS-84 datum and as time reference the GPS time which is steering around UTC (USNO) without the leap seconds since 1980. The GLONASS system uses currently the PZ-90 datum and as time reference the GLONASS time which is free drifting but related to UTC (SU).

The definition of a coordinate transformation between WGS-84 and PZ-90 is a difficult task. The formal description of the respective ECEF coordinate frames are self-consistent, and without any connection to be used as a basis for determining the transformation. Even if the formal definitions were identical, this fact would not have ensured that the coordinates of a point as determined by measurements from both systems will be identical, simply because each coordinate frame is implemented by adopting the coordinates of two independent and autonomous sets of stations. There has been recently several estimations of the transformation between both systems (Ref. 5 and Ref. 6). They have been based on orbit determination of the GLONASS satellites in WGS-84 and comparing the result with the ephemeris broadcasted by the GLONASS satellites. The Multistandard Receiver prototype implements the values provided by the MIT (see Ref. 5).

The time systems have to be also linked in order to perform a joined processing of GPS and GLONASS measurements. Both systems have a similar structure of the time reference. Each satellite has its own clocks which are related to the clocks of the respective Master Control Stations. Each of the Master Clocks are related to the respective national UTC time standards, which are related to the mean UTC in different ways. These GPS and GLONASS time systems are slowly drifting each other at a relative rate of few meters per day. This fact is used in the navigation algorithms of the receiver which have to estimate the bias between the receiver clock and the GPS AND GLONASS time systems.

These filters are considering a simplified model where the offset between both systems is constant, although it is being estimated continuously.

4. Processing of GPS/GLONASS/RA signals

The processing of the GPS/GLONASS/RA signals in the receiver in order to provide code and carrier measurements requires some strong modifications in the hardware of a GPS-only receiver.

For the RF/IF section of the receiver, two architectures can be considered: either to process the whole GPS/GLONASS bandwidth through a single RF/IF path, or to process separately GPS and GLONASS through two independent RF/IF paths in order to get the best resistance to external interference signals. An intermediate solution has been implemented in the multistandard receiver prototype : The RF front end in common to GPS/GLONASS, and the IF sections are separated for GPS and GLONASS. It provides a good compromise between hardware complexity and resistance to external interference signals.

The digital processing of the GLONASS signal requires the implementation of one high-quality frequency-programmable baseband converter per satellite channel, in order to select the carrier frequency dedicated to each GLONASS satellite.

The multistandard receiver is characterised by its number of channels, ie the number of satellites which can be tracked simultaneously in parallel. In the multistandard receiver for ESTEC, all the implemented channels are identical and can be programmed to track either GPS, GLONASS or RA satellite.

The general architecture of the multistandard receiver is shown in figure 3.

The processing of the RA GEO signals has no direct impact on the hardware because they use the same code and frequency as GPS. It requires some extra software computation power in order to demodulate and decode the RA data at 500 bit/s with VITERBI encoding.

5. GPS/GLONASS interchannel bias

The RF and IF sections of radio-navigation receivers include some passeband filters, which are used to mitigate the effect of interference and noise. The effect of these RF/IF filters on the interchannel bias is bigger in GLONASS-only receiver or GPS/GLONASS receiver than in GPS-only receiver, because each satellite has a different carrier frequency which is affected by a different group delay inside the filters. A compromise has to be found between the rejection of interference and the group delay variation. The figure 4 shows the interference rejection applicable to the multistandard receiver prototype. The figure 5 shows the group delay of the RF/IF filters of the multistandard receiver prototype. Variations larger than 50 nsec (15 meters) can be observed from one GPS or GLONASS satellite to the other.

An other source of interchannel bias is related to the multipath which are generated in the cable between the antenna and the receiver, or inside the receiver due to unperfect line matching. Figure 6 shows the typical group-delay ripple due to antenna/receiver mismatch. The ripple is 2 nsec peak-to-peak, which cannot be neglected when considering localisation accuracy at the level of meters.

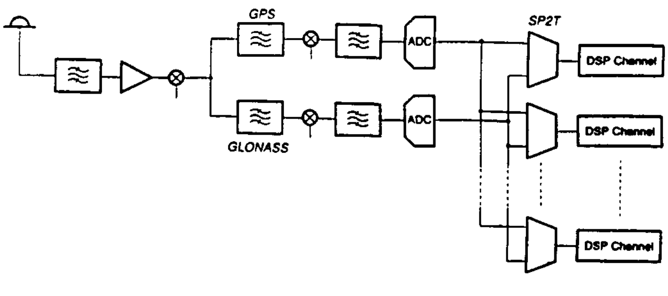

Figure 3 - Hardware architecture

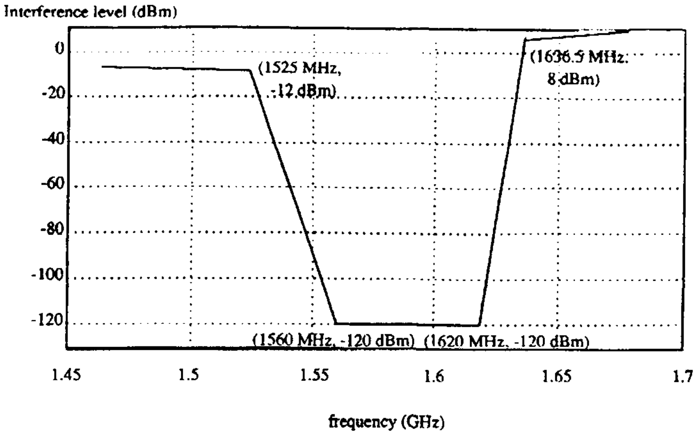

Figure 4 - Interference rejection

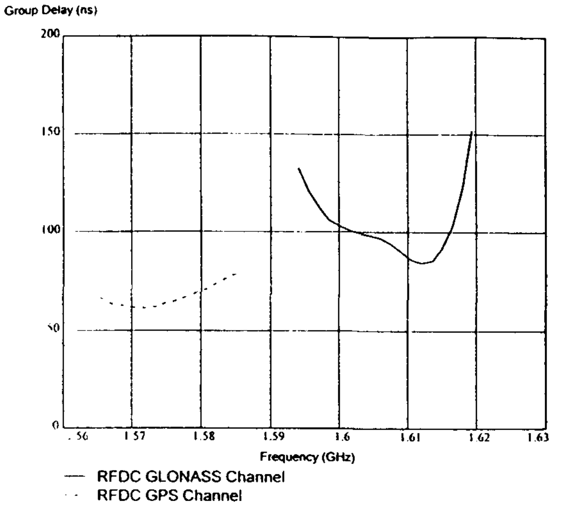

Figure 5 - Receiver group delay due to RF/IF filters

A first way to reduce the interchannel bias is to perform a calibration in factory. Then the receiver software can correct the measurements with the use of a calibration table. The remaining error will be caused by temperature variation and aging drift of the hardware filters, and will be in the order of a few nsec, depending on the quality and price of the filters.

The method implemented in the multistandard receiver prototype is different and consists in continuously monitoring and correcting the inter-channel bias. For this purpose, the receiver includes an autocalibration system, which consists in an internal GPS/GLONASS-like signal generator which is coupled with the RF input of the receiver and is controlled by the computer of the receiver. This allows a periodic, accurate and non-disturbing measurement of the group delay. The figure 7 shows a typical measurement of the interchannel bias of the multistandard receiver prototype. This is a plot of the difference between the pseudorange measurements from two synchronised satellites, the one at GPS frequency, the other at GLONASS frequency k = 20, when the receiver is connected to a dual-channel GPS/GLONASS RF simulator. The mean value is the interchannel bias and is below 1 nsec.

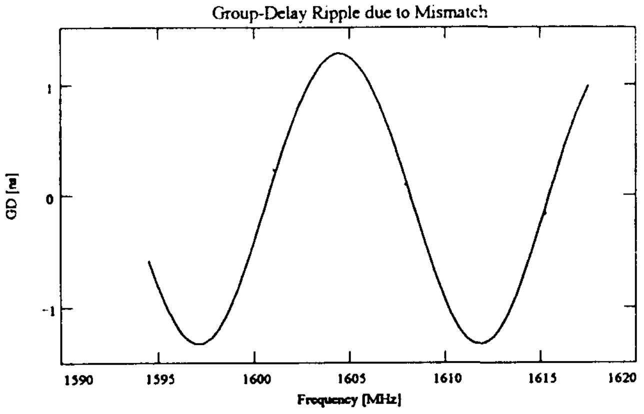

Figure 6 - Group-delay ripple due to mismatch

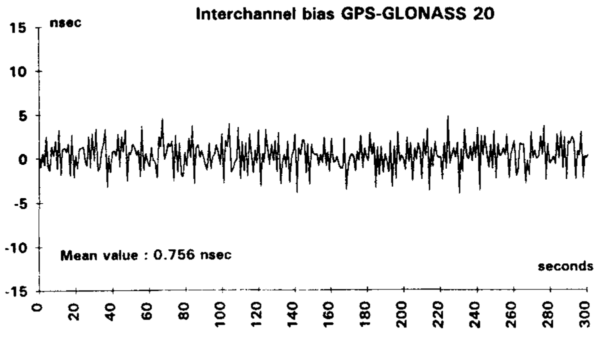

Figure 7 - Interchannel bias measurement between GPS channel and GLONASS 20 channel

6. Description of the multistandard receiver prototype

The multistandard receiver prototype has "All-in-view" capability. It has 30 parallel multistandard channels: 14 are software-configured for GPS and RA satellites, 14 are software-configured for GLONASS satellites, 2 are allocated to the internal autocalibration system. The receiver provides simultaneous position, velocity, acceleration and time determinations using the navigation systems independently or combined. Five different navigation solutions are implemented: only GPS, only GLONASS, GPS and GLONASS, GPS and RA and, in a preliminary design, the fully integrated navigation solution including GPS, GLONASS and RA signal. All these navigation solutions are provided with indications of the integrity and reliability of the achieved solution. The integrity is based on RAIM technics or RA information, depending on the respective navigation solution.

The complete receiver prototype is shown in figure 8, and consists in:

- a GPS/GLONASS antenna and associated GPS/GLONASS preamplifier.
- a signal-processing unit (SPU). This is an equipment of 3 kg developed jointly by SEXTANT Avionique and CIR. The equipment includes all the RF, IF and digital processing ressources for the parallel tracking of 30 multistandard satellite signals, with associated autocalibration system. It provides code and carrier measurements and demodulated data for each tracked satellite.
- a receiver processing unit (RPU), which is hosted in a personal computer. The RPU software has been developed by GMV and has in charge all the real-time processing of the measurements transmitted by the SPU ; position/velocity/ acceleration/time computation, integrity monitoring, control of the SPU channels, I/O and display functions.

At the rate of 2 Hz, the RPU receives raw pseudorange and carrier phase measurements from the SPU. System-Corrected measurements are obtains with estimations of the NS clock errors, ionospheric and tropospheric delay errors and Earth rotation effect, using received satellite ephemeris and almanac data. Other errors considered are the receiver clock errors, estimated with the navigation filters. The obtained system-corrected measurements are then processed in a set of extended Kalman Filters using the Navigation Satellite Systems in different combinations, as many as user required navigation solutions. Depending on the measurement combinations, the Kalman Filters state vectors are different, but all of them estimate the position, velocity and acceleration of the receiver antenna. A satellites management function performs also satellite selection, ephemeris and almanac messages decoding, and computation of aiding data for the SPU tracking loops.

Indicators of the integrity of the different Position/Time solutions are computed by two different procedures: Receiver Autonomous Integrity Monitoring (RAIM), and using RA Geostationnary Integrity information.

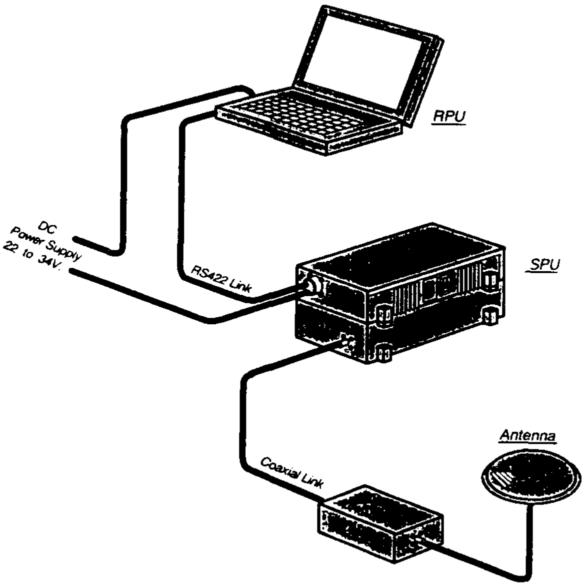

Figure 8 - Multistand receiver prototype

7. Integrity of the navigation solution

The reliability of the navigation solutions is determined by Integrity Monitoring algorithms. The navigation solutions using GPS and GLONASS measurements incorporate RAIM technics. When RA signal is used, the integrity relies on the broadcasted information, but using RAIM technics as back-up checking.

The RAIM algorithm has been designed to fulfil airecraft requirements of GPS as supplemental system. In case of detection of failure in one of the navigation satellites, the implemented process is called Partial Identification (see Ref. 7). Instead of trying or waiting until the identification of a unique satellite, the two most likely failed satellites are rejected from the navigation. This allows to reduce the probability of misidentification and the rejection can be done early in the exclusion process. This procedure also allows to keep in use as much as possible satellites with the subsequent benefits for the navigation accuracy. The RAIM algorithm was modified to work when GPS and GLONASS satellites are combined in the same navigation solution. The differences of coordinate frames and time has been carefully considered to keep the failure detection and identification capability.

The integrity based on RA information uses the currently preliminary designs of the RA signal specification and receiver architecture. The health of the satellites is read in the RA messages. With the healthy satellites, a bounded estimation of the horizontal position error is computed and it has to fulfil the requirements imposed in the flight phase.

8. Some results

The figures 9 to 14 show the horizontal and vertical error of one static point using GPS-only measurements, GLONASS only measurements, and GPS + GLONASS measurements. They have been obtained with real measurements on ground. The accuracy of the GPS + GLONASS solution is near ± 10 m horizontal and ± 20 m vertical.

9. Conclusion

Significant improvements in the real-time accuracy and integrity of the localisation are expected to be obtained when using multistandard receiver for spacecraft navigation.

The difficult issues in the design of a multistandard receiver have been discussed, and the architecture and main characteristics of the multistandard receiver prototype for ESTEC have been presented.

References:

1. Potti, Carmona, Bernedo, GMV S.A. ; Silvestrin, ESA/ESTEC; "An Autonomous GNSS-Based Orbit Determination System for Low-Earth Observation Satellites", Proceedings of the 1995 International Technical Meeting on GPS, Inst. of navigation.

2. Potti, Bernedo, GMV S.A. ; Pasetti, ESA/ESTEC, "Applicability of GPS-based Orbit Determination Systems to a Wide Range of HEO Missions", Proceedings of the 1995 International Technical Meeting on GPS, Inst. of Navigation.

3. Martin, Dow, Bondarenco, ESA ; Casotto, Padova ; Feltens, Gmbh ; Garcia, GMV S.A., "Use of GPS for Precise and Operational Orbit Determination at ESOC", Proceedings of the 1995 International Technical Meeting on GPS, Inst. of Navigation.

4. Misra, Bayliss, Lafrey, Pratt and Muchnikk, MIT ; "Receiver Autonomous Integrity Monitoring (RAIM) of GPS and GLONASS", Navigation, Vol. 40, No. 1, Spring 1993.

5. Misra, Abbot, Gaposchkin, MIT ; "Integrated use of GPS and GLONASS: Transformation between WGS-84 and PZ-90", Proceedings of the 1996 International Technical Meeting on GPS, Inst. of Navigation.

6. Rossbach, University FAF Munich ; Habrich, Institute of Applied Geodesy; Zarraoa, DLR-DFD Neustrelitz ; "Transformation Parameters Between PZ-90 and WGS-84", Proceedings of the 1996 International Technical Meeting on GPS, Inst. of Navigation.

7. Grover Brown, Iowa State University ; Kraemer, U.S. DOT ; Nim, Volpe NTSC ; "A Partial Identification RAIM Algorithm for GPS Sole Means Navigation", Proceedings of the 1994 International Technical Meeting on GPS, Inst. of Navigation.

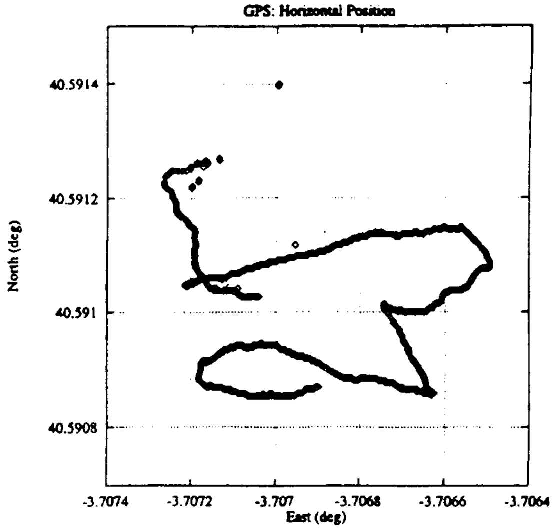
GPS: Horizontal Position
North (deg)
40.5914
40.5912
40.591
40.5908
-3.7074
-3.7072
-3.707
-3.7068
-3.7066
-3.7064
East (deg)

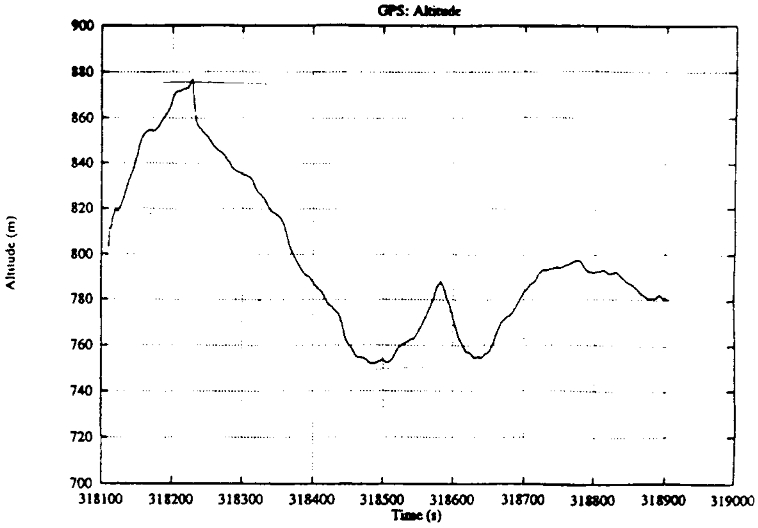
GPS: Altitude
Altitude (m)
900
880
860
840
820
800
780
760
740
720
700
318100
318200
318300
318400
318500
318600
318700
318800
318900
319000
Time (s)

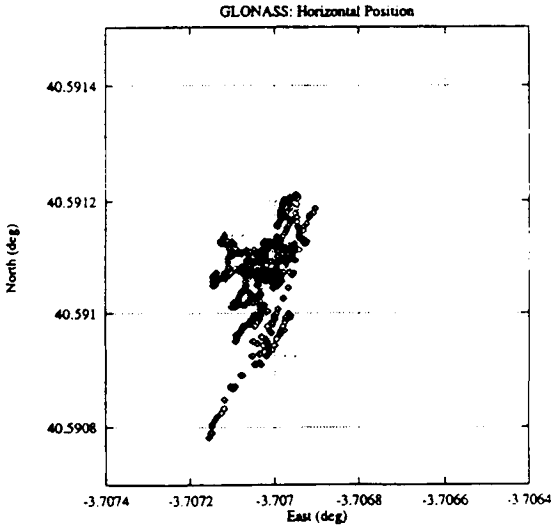
GLONASS: Horizontal Position
North (deg)
40.5914
40.5912
40.591
40.5908
-3.7074
-3.7072
-3.707
-3.7068
-3.7066
-3.7064
East (deg)

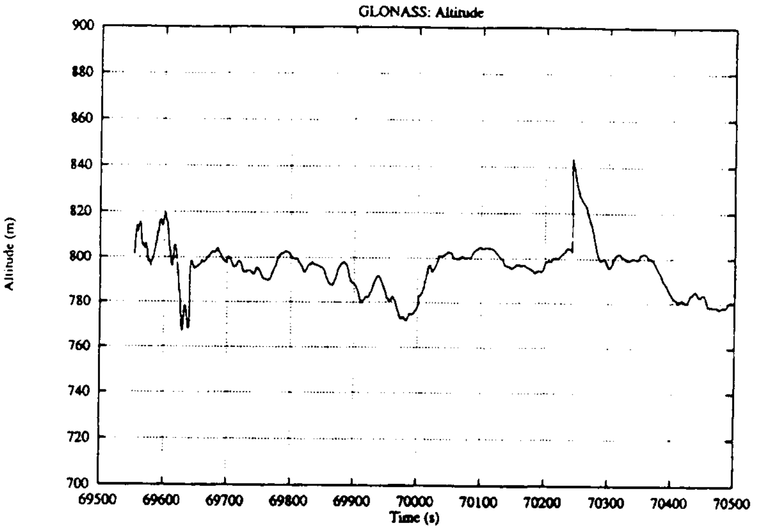
GLONASS: Altitude
Altitude (m)
900
880
860
840
820
800
780
760
740
720
700
69500
69600
69700
69800
69900
70000
70100
70200
70300
70400
70500
Time (s)

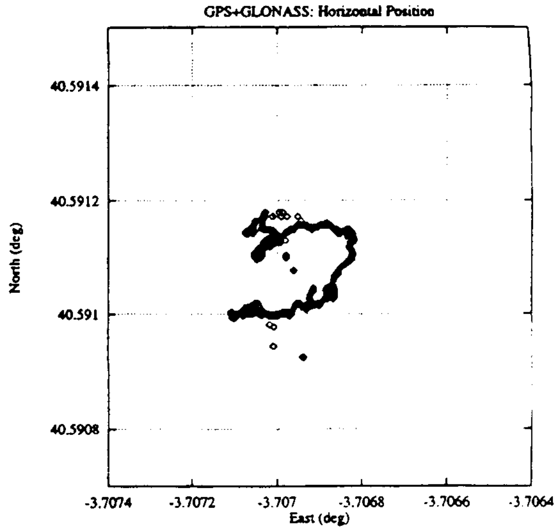
GPS+GLONASS: Horizontal Position
North (deg)
40.5914
40.5912
40.591
40.5908
-3.7074
-3.7072
-3.707
-3.7068
-3.7066
-3.7064
East (deg)

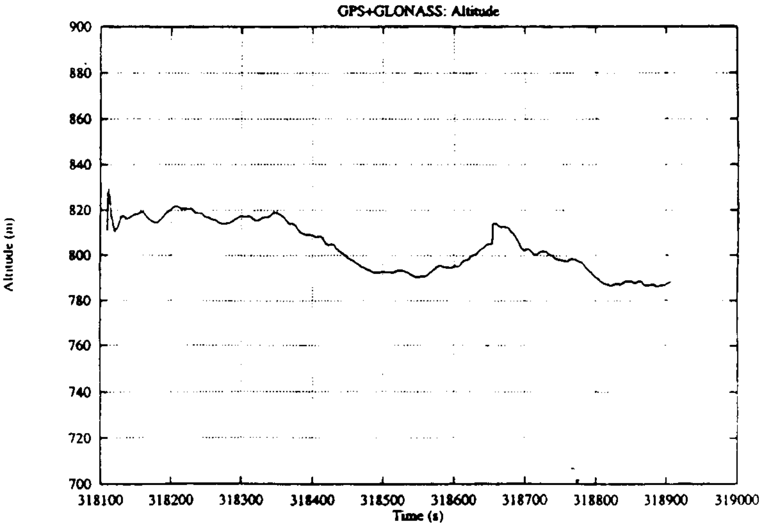
GPS+GLONASS: Altitude
Altitude (m)
900
880
860
840
820
800
780
760
740
720
700
318100
318200
318300
318400
318500
318600
318700
318800
318900
319000
Time (s)

Acronyms :

ADC:	Analog-to-Digital Converter
GDOP:	Geometric Dilution of Precision
GEO:	Geostationnary
HDOP:	Horizontal Dilution of Precision
IF:	Intermediate frequency
NS:	Navigation satellite
RA:	Regional Augmentation
RAIM:	Receiver autonomous Integrity monitoring.
RF:	Radio-frequency
RPU:	Receiver Processing Unit
SPU :	Signal Processing Unit
UTC (SU):	Universal Time Coordinated by Soviet Union
UTC (USNO):	Universal Time Coordinated by United State Navy Observatory.
VDOP:	Vertical Dilution of Precision
WGS:	World geodetic system

THE GPS AT GTO EXPERIMENT

Lieutenant P Coulson Royal Navy, N P Shave

Defence Evaluation and Research Agency, Space Department, DERA Farnborough, Hants, GU14 0LX, UK
Phone: (++44) 1252 394223 Fax: (++44) 1252 396310
E-mail: P_Coulson@scs.dra.hmg.gb

ABSTRACT

The NAVSTAR Global Positioning System (GPS) is a satellite based navigation aid owned and operated by the United States Department of Defence (US DoD). The system is designed for the positioning and navigation of terrestrial and near terrestrial users. The system has been successfully used by a number of experimenters for the navigation of Low Earth Orbit (LEO) Satellites [1].

Many advantages can be perceived if a GPS Receiver is operated on Geostationary satellites. A number of theoretical studies suggest this is feasible [2,3], but uncertainties currently exist regarding GPS signal strengths at geostationary altitudes. The GPS at GTO Experiment (GAGE) intends to fly a dual frequency GPS sampling device into Geosynchronous Transfer Orbit to resolve these uncertainties.

This paper examines the reasons for pursuing the experiment, introduces the overall plan for the mission, including a broad description of the hardware involved, and presents the expected GPS satellite visibilities resulting from recent simulation work.

1. INTRODUCTION

NAVSTAR GPS is based upon a constellation of 24 satellites at an orbital altitude of approximately 20,200 km. Navigation is achieved by answering the three fundamental questions: where, at what time and at what speed ? This is realised in GPS through the reception of signals from a minimum of four GPS satellites. These signals are transmitted on two frequencies designated L1 and L2, directed towards the earth.

A Geostationary Earth Orbit (GEO) satellite would be positioned above the GPS constellation, at approximately 36,000 km altitude, and would therefore rely on signals from satellites facing the opposite side of the earth [Figure 1]. The large Free Space Loss involved in these geometries means that approximately 2 satellites would be visible to a geostationary satellite at any one time [2]. This reduced visibility implies the need for non-conventional algorithms for position determination. Should GPS satellite side lobe signal strengths prove adequate the number of satellites available increases dramatically and would enable four satellite fixing to be achieved.

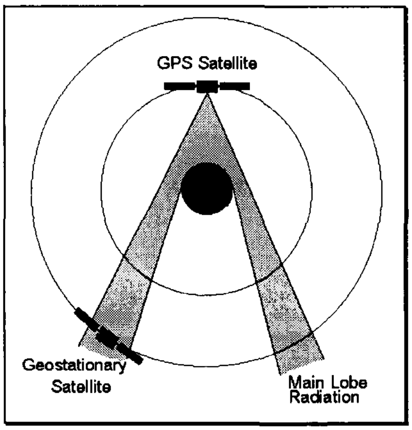

Figure 1: GPS Receiver in GEO

Whilst feasibility studies suggest that orbit determination of geostationary spacecraft through GPS is possible, they highlight uncertainties regarding GPS signal strengths at these altitudes and recommend a flight test to resolve these uncertainties [2]. GAGE is the response to these recommendations.

2. BENEFITS OF USING GPS AT GEO

Provision of a GPS receiver on a geostationary spacecraft would lead to the availability of positional information and GPS system time. These two features of GPS could result in significant advantages for the spacecraft operator, payload and end user. This paper focuses on the military implications and advantages of the use of GPS on geostationary communications satellites, but many of the potential applications outlined below could be equally relevant to civil satellites.

Onboard orbit determination could aid a ground station with satellite station keeping through avoiding the need

Proceedings Third International Conference on Spacecraft Guidance, Navigation and Control Systems, ESTEC, Noordwijk, The Netherlands, 26-29 November 1996, ESA SP-381 (February 1997)

for regular radio ranging. Orbit determination accuracy similar to that available with current ranging techniques is considered feasible [2]. This would lead to significant cost savings and less dependence on overseas tracking stations. Reducing the need for large (and expensive) tracking sites raises the prospect of small, mobile ground stations which would be difficult to counter detect making the ground segment more secure from attack.

Alternatively, all station keeping could be performed on the spacecraft with little or no operator input. This would enhance all the benefits highlighted above whilst further increasing system availability in the event of loss of ground segment. Of course, this places considerable responsibility on the space segment and therefore represents a higher risk: the need for safety critical anomaly detection and spacecraft safe mode is implicit.

The on-board availability of GPS system time could have a number of interesting applications. These are based on the requirement for 'open system' or 'absolute' time rather than closed system timing which may use accurate on-board clocks with probably lower risk and cost. Potential applications include:

a. The synchronization of TDMA transmissions using an open loop system, eliminating the need for a reference station and reference bursts.

b. Synchronizing terminals in an orthogonal frequency hopping communications network, increasing system autonomy and reducing the management task of a centralised accurate time source.

c. Providing system time to a number of geographically discrete sensors in a Geolocation system.

d. Aiding link acquisition in a long sequence CDMA communications system.

e. Providing tracking information for narrow beam, EHF communications.

For payload applications GPS system time may not be available continuously, depending on the level of GPS satellite visibility (which will be determined by GAGE). However, GPS could provide a periodic update to synchronize the on-board clock. Initial research [2] suggests that GPS could provide an accuracy of approximately 900 nanoseconds (3σ) for a geostationary satellite using the Precise Positioning Code (P-Code).

3. EXPERIMENT DESCRIPTION

GAGE is a collaborative project between the United Kingdom's Defence Evaluation and Research Agency (DERA), which is an agency of the UK Ministry of Defence, NASA's Jet Propulsion Laboratory (JPL) and the US DoD.

The GAGE mission aim is to understand and confirm any contribution that the use of GPS may make to the operation of future missions beyond the GPS constellation. In order to achieve this goal it is essential that the availability of GPS signals at the altitudes of interest is fully understood.

A sampling device developed by JPL will be flown on STRV 1c (see section 4) into GTO. On orbit, GAGE will sample the RF environment within the GPS frequency bands at intervals and for durations determined by an adapting experiment schedule. Each sample will consist of noise in which any GPS signals present at the sample location will be embedded. The quantized signals will be stored in memory within the experiment prior to downlink to the STRV ground station at Lasham, England, for subsequent analysis. This analysis will consist of observable extraction (pseudorange, signal strength, Doppler shift) followed by orbit determination. The system will use both L1 and L2 frequencies and P(Y) codes will be available offering potentially better accuracy than a C/A code only system, but perhaps more importantly enabling the cancellation of ionospheric variation of group delay.

A simple system architecture is shown in Figure 2. The sampling device, known as Bitgrabber, will have two modes of sampling: Acquisition Mode 1 will be the primary mode and sample at 40 MHz utilizing both L1 and L2 signals; Acquisition Mode 2 will sample at 2 MHz making use of the C/A Code on L1 frequency only. In both cases in-phase (I) and quadrature (Q) channels will be sampled for a specified duration (in the range of 2 milliseconds to 400 milliseconds). The maximum sampling frequency is selected to enable Nyquist sampling out to the first sidelobe of the P(Y) code chipping rate. Each sample will be quantized using one bit, i.e. a simple threshold. The entire data set for a number of samples will be held in the Bitgrabber internal store.

Several antennae arrangements were considered, the final decision was a single patch antenna in preference to a four element array. It was considered that the less directive beam pattern would reduce the pointing requirements placed on the spacecraft by GAGE, at the expense of reduced antenna gain. The antenna will be located on the edge of one of the spinning faces (with

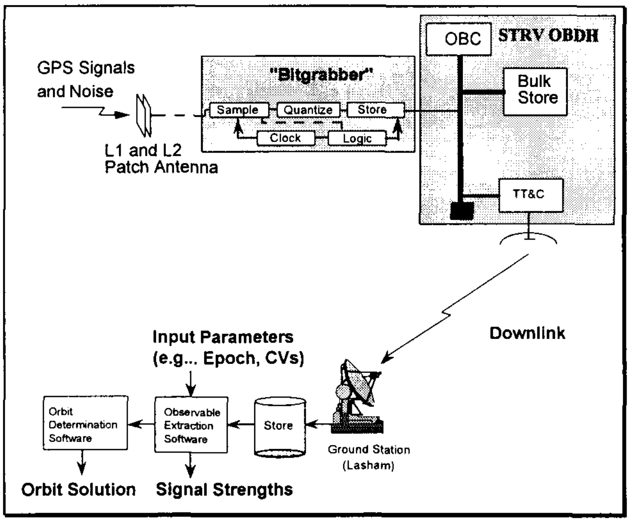

Figure 2: System Schematic

the spin vector parallel to the orbit normal). Bitgrabber will require triggering at the desired epoch for a certain sample duration when the receive antenna is pointing in the correct direction with respect to the GPS constellation. The epoch at which Bitgrabber is triggered will be determined by the altitude of current interest and the moment which is likely to present the best geometry for high visibility of GPS signals. Essentially there are three altitudes of interest and these are referred to as altitude Bins [Figure 3]. Bin 1 is the region of primary concern at altitudes corresponding to geostationary orbits. Bin 0 is for calibration purposes, since this is a well characterized region in terms of GPS signal strength; it will also be useful for providing accurate fixes of STRV position aiding orbit solving and prediction of vehicle position later on in the orbit. Bins 2 and 3 correspond to altitudes around the GPS constellation height. It is hoped that this will yield information regarding antenna side lobe strengths.

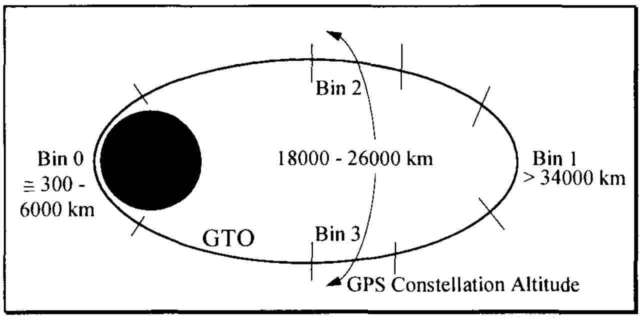

Figure 3: Altitude Bins

The duration of a sample will be under experimenter control and range from 2 ms in Bin 0 to a maximum of 400 ms in Bin 1. The longer sample durations bring about a number of benefits including greater visibility of GPS satellites due to increased processing gain and greater accuracy in measurement of signal strength. The drawback of these longer samples is that they will produce very large volumes of data and introduce coherency problems over the sample length.

The relative pointing of the receive antenna will be varied depending on the altitude bin being sampled: Bin 0 (perigee) will require zenith pointing; Bin 1 (apogee) will use nadir (or Earth centred) pointing; Bins 2 and 3 will use cross track pointing, i.e. perpendicular to the velocity vector facing into the orbit plane: this will give Bitgrabber a view of the GPS satellites' side lobes.

4. STRV

The Space Technology Research Vehicles (STRVs) are designed, built and operated by the United Kingdom's Defence Evaluation and Research Agency (DERA). The objective of these missions is to provide an in flight test bed to evaluate and qualify new technologies for the space environment, applying the "Faster, Cheaper, Better" philosophy.

Two STRVs (1a and 1b) were launched into GTO by the Ariane 4 Auxiliary Structures and Payload (ASAP) ring in June of 1994. Each satellite weighs approximately 52 kg and took only 3 years from design to operations [4]. The mission supports a total of 14 experiments representing research from a wide range of national and international organisations including ESA.

Although the designed mission life of STRV 1a/b was only 12 months, over two and a half years on they are still operating, providing experimenters with high quality data. Furthermore, spacecraft operations has now been delegated to Colorado University as a training exercise prior to their Student Nitric Oxide Explorer (SNOE) mission. Whilst DERA maintains ownership and ultimate authority, it is believed this is one of the first times that daily operation of a spacecraft has been transferred between institutions, across international boundaries. The transfer was achieved in only 4 months and for a cost of less than US$ 200,000. This can be seen as a testimony for international standards since STRVs use the CCSDS compatible ESA Telemetry and Telecommand standards.

Two more STRV (1c and 1d) are in the design phase and due for launch in early 1999. These are slightly larger than the original craft, providing greater power and supporting more payloads. They will carry a total of 21 experiments, GAGE being one of these.

5. LINK BUDGETS

Prior to GPS satellite visibility simulation, link budgets were required for each of the three GPS signals under investigation (i.e. L1 C/A Code, L1 P(Y) Code and L2 P(Y) Code). In order to simplify the definition of the GPS transmit antenna within the simulation package being used, the antennae patterns were 'quantized' into four regions with broadly similar gain within each region; for the purposes of the link budget the minimum gain of each region was used [5]. The overall link budget can be described by Equation 1.

$$C/N_o = P_{Tx} + G_{Tx} - PL + G_{Rx} - FSL - L - T - K \text{ ....[1]}$$

P_{Tx} = Transmit Power
G_{Tx} = Max Gain of Transmit Antenna
PL = Pointing Loss
G_{Rx} = Gain of Receive Antenna
FSL = Free Space Loss
L = Implementation Losses
T = Noise Temperature
K = Boltzmann's Constant

The required Carrier to Noise power spectral density is given by Equation 2.

$$C/N_0 = SNR + 10 \log_{10}(1/T) \text{ ....[2]}$$

Where T = sample duration and SNR is that required by Bitgrabber for signal detection.

Table 1 describes the overall link budgets.

Description	Op.	L1 C/A	L1 P(Y)	L2 P(Y)	Units
Transmit Power	+	14.25	11.25	6.35	dBW
Gain of Tx Antenna	+	14.4	14.5	12.5	dBi
Gain of Rx Antenna	+	3	3	5	dBi
Implementation Losses	-	3	3	3	dB
Noise Temperature	-	22	22	22	dB-K
Boltzmann's Constant	-	-228.6	-228.6	-228.6	dBW/K-Hz
C/N_o + PL + FSL	=	**235.25**	**232.35**	**227.45**	**dB-Hz**

Table 1: Link Budget

With Table 1 complete, it was possible to construct a table of maximum effective ranges for every signal and all sample durations for each of the four regions. This enabled the antenna patterns to be specified for simulation purposes.

6. BLOCK IIA SATELLITE VISIBILITY STUDIES

In the past a number of studies have been conducted to establish the likely levels of GPS signal visibility achievable at GEO. Most recently an internal DERA study specific to GAGE and GTO was completed [5]. These simulations utilized the Aerospace Corporation's Satellite Orbit Analysis Program (SOAP). Best estimates of Bitgrabber performance and RF characteristics were combined with available data on GPS signal transmit powers and beam patterns to simulate a GPS constellation of 24 Block IIA satellites and an STRV hosting GAGE hardware.

Additional analysis software was developed to process the time logging files produced by SOAP such that visibility charts could be developed as shown in Figure 4.

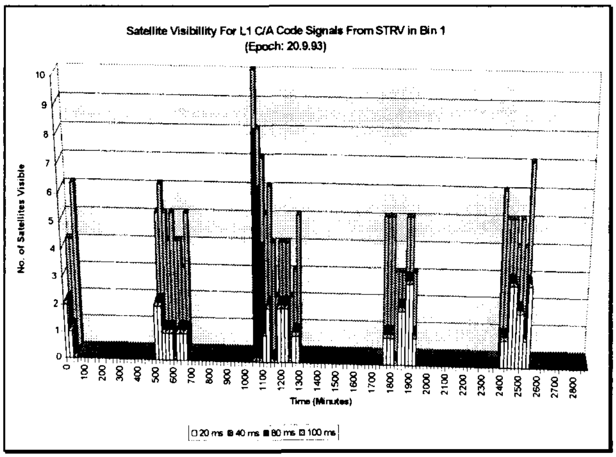

Figure 4: Visibility Chart 1

Figure 4 shows the Bin 1 passes in a 24 hour period. The GPS signal availability represents the visibility of the C/A Code signal. It is readily apparent that for the shorter sample durations (those at the front of the chart) visibility levels are low, with only one or two satellites available for the majority of the time. Extending the sample duration has little or no effect on visibility. However, when sampling for 100 ms the increased processing gain leads to much better visibility with at least four satellites available for the majority of the time. This apparent 'Threshold Effect' occurs at the point when GPS satellite sidelobes become visible due to the increase in processing gain. The point at which this occurs (100 ms in the above example) is dependent on the assumptions made in the link budget. GAGE will confirm the sample duration which can provide this highly desirable increase in visibility.

The L1 P(Y) Code signal is transmitted at half the power of the L1 C/A Code signal, hence visibility levels are reduced. Figure 5 shows this reduction in visibility, but the Threshold Effect is still apparent.

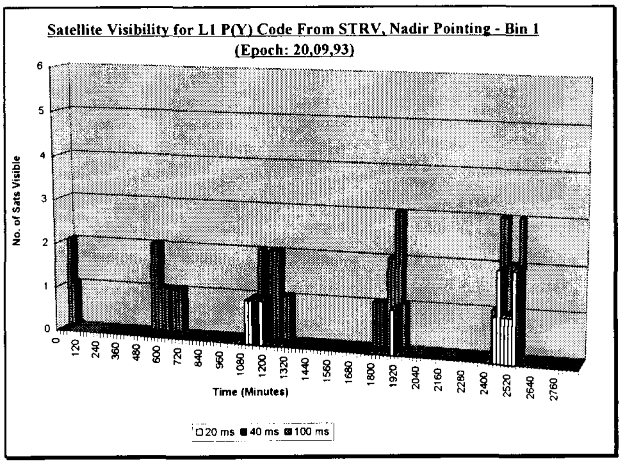

Figure 5: Visibility Chart 2

Figure 6 indicates the visibility levels for the L2 P(Y) Code signal at the same Epochs. Despite the L2 P(Y) Code signal being transmitted at an even lower power than the L1 P(Y) Code signal, the visibility levels are surprisingly good. This is due to the GPS antenna pattern for the L2 frequencies having significantly wider sidelobes compared to the L1 antenna patterns. This allows the sidelobes to be in the field of view of a geostationary receiver at a reduced range.

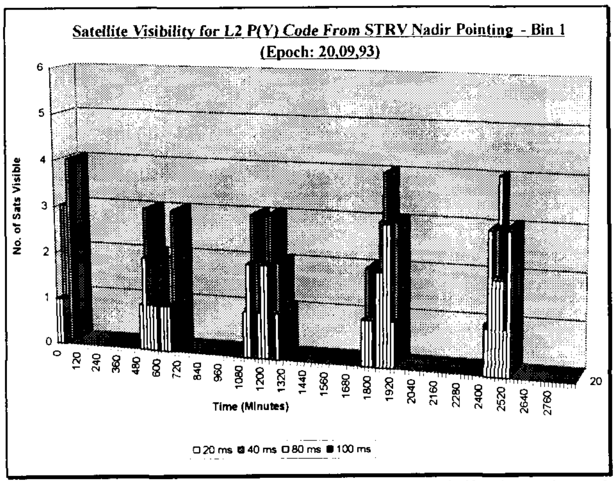

Figure 6: Visibility Chart 3

Simulations for Bins 2 and 3 revealed similar visibility levels to the Bin 1 case with an equivalent Threshold Effect; this time it occurred with 80 ms sample durations. It was also found that sample durations of 2 ms were adequate to give multiple satellite visibility in Bin 0. This confirms the findings of previous GPS receiver flights into LEO.

7. BLOCK IIR SATELLITE VISIBILITY STUDIES

The imminent introduction of the Block IIR satellites to the GPS constellation has the potential to effect the expected levels of visibility. Therefore, a further set of simulations assuming a constellation consisting entirely of Block IIR satellites was conducted, to establish if an adverse impact could be expected. Insufficient data regarding the L2 antenna patterns was available at the time of this work, however, L1 predictions could be made.

It was found that for the L1 C/A Code signal sampled over the shorter durations, and the L1 P(Y) Code signal generally, little or no impact on visibility was observed. This is because visibility in these cases depends largely on detection of the GPS signal through its mainlobe. There is significant margin in the link budget for mainlobe detection and so changes in the main lobe characteristics between Block IIA and IIR are likely to have negligible effect.

For the longer sample durations the visibility of the C/A code signal increases dramatically when assuming an all Block IIR constellation (Figure 7). This is because the visibility level is now dominated by detection through the GPS antenna side lobes. For the Block IIR satellites these sidelobes will apparently be significantly wider than those of the Block IIA satellites. This increase in sidelobe width allows a geostationary receiver to get closer to the GPS satellites before they drop out of the receiver's field of view.

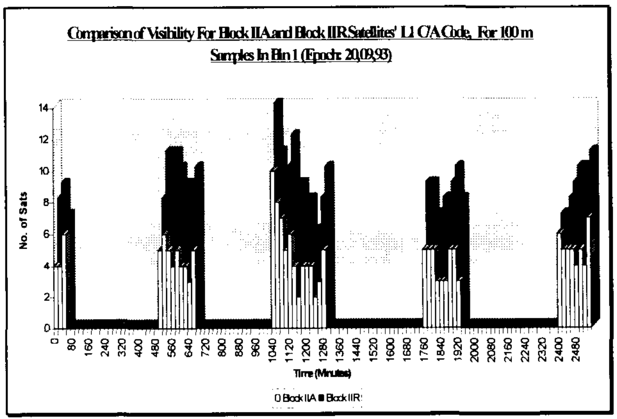

Figure 7: Visibility Chart 4

8. SAMPLING STRATEGY

An initial sampling strategy has been developed for the early stages of the mission. It begins with a period of sampling for 5 ms in Bin 0, for the purpose of calibrating GAGE hardware in orbit, and 100 ms samples in Bin 1. This is considered the maximum sample length which will sustain coherent integration given the stability of the clock within Bitgrabber. This will maximize the chance of GPS signal detection in the early stages of the mission enabling the primary objective to be achieved: measurement of GPS signal strengths at geostationary altitudes. Next will follow a series of samples using the full range of sample durations possible: this will validate the link budgets and simulation model whilst also indicating whether sample durations in excess of 100 ms offer any advantage (i.e. is loss of coherence outweighed by correlation gain ?).

Once the signal strengths at geostationary altitudes have been characterized to a satisfactory level, measurements at alternative altitudes will be made. Particular emphasis will be given to Bins 2 and 3 in an attempt to characterize the GPS transmit antennae sidelobes.

In addition to measuring the GPS signal strengths present around GTO, a variety of techniques will be used to define the orbit and provide GPS system time (not in real time). This will not only indicate the position and timing accuracies that could be achieved by a GPS receiver on an operational geostationary satellite, but will also benefit other STRV payloads.

It is envisaged that a number of samples can be taken around consecutive orbits providing a series of positional fixes. By taking alternate fixes, two orbits may be fitted giving an indication of accuracy and stability of orbit solution. Alternatively, by taking an orbit solution and dropping single fixes from the solution, examination of the residuals will indicate the accuracy of measurement at the altitude of the fix that has been dropped. External methods of verifying GAGE accuracy are under investigation.

Simulation has indicated that levels of visibility vary throughout the pass of an altitude Bin. Furthermore, work looking at the Positional Dilution of Precision (PDOP) has shown that this can vary dramatically from satisfactory levels to unacceptably high values [5]. The aim throughout the mission will be to sample at instants corresponding to high levels of visibility and low values of PDOP, thus maximizing the value of the data taken. This is highly desirable since the downlink from STRV will provide a data bottleneck, limiting the frequency of Bitgrabber operation. It is intended that continued simulation of GPS satellite and STRV orbits throughout the mission will indicate the optimum sample instants which will then be uplinked to Bitgrabber.

The experiment schedule and sampling strategy will be adaptive throughout the mission life. Command uplink sessions to Bitgrabber every three days will ensure the sampling strategy reflects the experience gained from previous data sets.

9. CONCLUSION

A number of feasibility studies have suggested that GPS receivers have potential for use on geostationary spacecraft with considerable benefit for the operator, payloads and the end user. The GPS at GTO experiment will investigate this potential.

GAGE is likely to be the first dual frequency P(Y) Code receiver to fly above the GPS constellation and as such will provide the GPS research community with valuable information regarding signal strengths and GPS satellite visibility at these altitudes. The findings from GAGE will confirm the feasibility (or otherwise) of using GPS as a means of orbit determination for geostationary spacecraft and potentially other missions which extend beyond the confines of the GPS constellation.

The mission will indicate the accuracy of position and timing that can be achieved in an operational navigation system at GEO. This will enable further investigation into applications of GPS beyond pure orbit determination. Of particular interest will be novel applications for the payloads and end user.

10. ACKNOWLEDGEMENTS

The advice and support of the JPL GPS team is gratefully acknowledged, especially Dr Larry Young and Jeff Srinivasan. The UK contribution to GAGE is funded by the Ministry of Defence.

11. REFERENCES

[1] "Experience with the use of GPS in a Low Earth Orbit" M. Unwin. UoSAT, CSER, University of Surrey. 1994

[2] "A Feasibility Analysis of Using GPS on Board a Geostationary Spacecraft" J. B. Magill DRA Contract Ref. RAE 1B/33. March 1992

[3] "Final Report, Tracking of Geostationary Satellites with GPS GPS-GEOTRACK" J..M^a .Legido. GMV, S.A GMVSA 2070/94, ESTEC contract no. 8609/89/NL/JG(SC). 6 July 1994

[4] "The Space Technology Research Vehicle: A Low Cost Mission to GTO" N.S. Wells N.P. Shave Space Department, DRA. 1995

[5] "A Study to Establish the 'GPS at GTO Experiment' Mission Strategy" P. Coulson August 1996

© British Crown Copyright 1996/DERA - Published with the permission of the Controller of Her Majesty's Stationery Office.